Electrochemical Reduction of Carbon Dioxide in Advanced Electrolyser Systems

Inaugural dissertation

of the Faculty of Science,

University of Bern

Presented by

Ivan Zelocualtecatl Montiel

From Mexico

Supervisor of the doctoral thesis:

Prof. Dr. Peter Broekmann

Department of Chemistry, Biochemistry and Pharmaceutical Sciences

Copyright Notice

This license does not apply for all Chapters, e.g., some Figures and Tables in Chapter 1; from Figure 1.6 to Figure 1.8, and Tables 1, 4 and 5. For Chapter 3, from Figure 3.1 to Figure 3.7 and from Figure 3.9 to Figure 3.13. And some Publications in chapter 7: Publications 7.1, 7.2, 7.3, 7.8, 7.10, 7.11, 7.12, 7.13. However, the corresponding copyrights to each Journal have been acquired.

Electrochemical Reduction of Carbon Dioxide in Advanced Electrolyser Systems

Inaugural dissertation

of the Faculty of Science,

University of Bern

Presented by

Ivan Zelocualtecatl Montiel

From Mexico

Supervisor of the doctoral thesis:

Prof. Dr. Peter Broekmann

Department of Chemistry, Biochemistry and Pharmaceutical Sciences

Accepted by the Faculty of Science

Bern, October 28th, 2022. **The Dean**

Prof. Dr. Marco Herwegh

Dedicated to my family,

for all the love they have always given me.

Where there is a tree to plant, plant it yourself.

Where there is an error to amend, amend it yourself.

Where there is an effort that everyone avoids, do it yourself.

Be the one to take the stone off the road.

Gabriela Mistral.

Abstract

The concentration of atmospheric CO_2 has increased alarmingly in the last few decades, triggering the search for new technologies that utilize CO_2 as a raw material. Electrochemical CO_2 reduction (ec-CO_2R) is one of the most promising approaches to mitigating the increase in atmospheric CO_2 levels. In this process, CO_2 is converted into valuable products such as carbon monoxide, methane, ethylene, methanol, ethanol, and formic acid by using renewable energy. Among these CO_2 electroreduction products, formate or formic acid is one of the most economically viable because it is an important chemical intermediate for many industrial processes and has promising applications in hydrogen storage.

Since the pioneering work of Hori et al., it is well known that various material catalysts such as Pd, Cd, In, Sn, and Pb have been studied for use in the production of formate via ec-CO_2R. However, these materials are too expensive and, in most cases, environmentally unfriendly. Recently, bismuth-based materials have received attention as catalysts for ec-CO_2R because of their low toxicity, low cost, excellent stability, and high selectivity for formate production from CO_2 in aqueous electrolytes.

In this work, I have focused on the synthesis of bismuth foam catalysts using the dynamic hydrogen bubble template (DHBT) electrodeposition approach, followed by thermal annealing in air at 300 °C for 12 h, which transforms the as-prepared metallic Bi foam into a completely oxidised Bi_2O_3 foam. The electrochemical performance of the Bi_2O_3 foam catalyst was carried out in a conventional H-type cell system and exhibited high faradaic efficiency ($FE_{formate}$ = ~100%) and high partial current density for formate ($PCD_{formate}$ = –84.1 mA cm^{-2}). The catalyst was also found to be highly stable after 100 h of continuous electrolysis.

The high $FE_{formate}$ and $PCD_{formate}$ achieved in these studies have been due to the presence of two reaction pathways, leading to high FE values across a broad potential window. The first reaction pathway involves the bismuth subcarbonate species at low cathodic potentials, while the second reaction pathway involves metallic bismuth species at high cathodic potentials. In this study, novel *operando* Raman spectroscopy was used for the first time to obtain information about the Bi_2O_3–Bi subcarbonate–Bi_{metal} transition as a function of the applied potential. In addition, the morphological changes of the catalyst before and after ec-CO_2R were monitored using identical location scanning electron microscopy (IL-SEM).

As high current densities on the order of –200 mA cm^{-2} cannot be achieved in H-type cell systems because of CO_2 mass transport limitations, the Bi_2O_3-GDE foam catalyst used in the

H-type cell was transferred to a flow cell (fluidic electrolyser). An excellent electrochemical performance was achieved in the flow cell electrolyser over a wide range of cathodic potentials, with high faradaic efficiencies and high partial current densities for formate production ($FE_{formate}$ = ~100% at –0.8 V *vs.* RHE and $PCD_{formate}$ = –414.7 mA cm^{-2} at –2.5 V *vs.* RHE in 1 M KOH). Importantly, an increase in the concentration of the electrolyte solution (5 M KOH) boosted the $PCD_{formate}$ values beyond –1 A cm^{-2}.

Ex situ XRD and Raman spectroscopy studies demonstrated that the subcarbonate reaction pathway for formate production was still active at high cathodic potentials (–1.5 V *vs.* RHE). This bismuth subcarbonate forms *in situ* and is highly stable due to the abundance of CO_2 under *operando* conditions in the gas-fed electrolyser. While, the metallic bismuth reaction pathway is also active at high cathodic potentials (up to –1.6 *vs.* RHE).

Finally, the use of advanced X-ray diffraction tomography (XRD-CT) revealed deeper insights into the spatial distribution of bismuth subcarbonate and metallic bismuth in the catalyst layer after ec-CO_2R.

Table of Content

List of Figures

List of Tables

List of Abbreviations

CCS	Carbon Capture and Storage	**MEA**	Membrane electrode assembly
ec-CO_2R	Electrochemical-CO_2 reduction	**GDE**	Gas diffusion electrode
FE	Faradaic efficiency	**GDL**	Gas diffusion layer
PCD	Partial current density	**CEM**	Cation exchange membrane
i	Current density	**AEM**	Anion exchange membrane
η	Overpotential	**BPM**	Bipolar membrane
EE	Energy efficiency	**HR-SEM**	High resolution scanning electron microscopy
OER	Oxygen evolution reaction	**ap-Bi/Bi_xO_y**	as prepared Bismuth/Bismuth oxide foam
HER	Hydrogen evolution reaction	**Bi_2O_3**	Bismuth oxide
OCP	Open circuit potential	**IL-SEM**	Identical location SEM
Rx	Resistance	**XRD**	X-ray diffraction
ΔG	Gibbs free energy	**DBHT**	Dynamic hydrogen bubble template
F	Faradaic constant	***oc-d***	Oxide derived
E	Potential (V)	**WLI**	White light interferometer
SHE	Standard hydrogen electrode	**XRD-CT**	X-ray Diffraction computed tomography
MOFs	Metal organic frameworks		
WE	Working electrode		
RE	Reference electrode		
CE	Counter electrode		
GC	Gas chromatography		
IC	Ion exchange chromatography		

1. INTRODUCTION

1.1. The Challenge: The Mitigation of Atmospheric CO_2 levels and Global Warming

Concerns about global warming, caused by the excess release of greenhouse gases into the Earth's atmosphere, have increased in recent years. A natural atmospheric phenomenon known as the greenhouse effect maintains the planet's temperature and consequently allows life on Earth to exist. When solar radiation reaches the Earth's atmosphere, some part of this radiation is reflected into outer space, while the rest is absorbed by the Earth's surface, warming it. However, the Earth also emits energy in the form of infrared radiation. Some of this radiation passes through the atmosphere, while the rest is absorbed and re-emitted towards the Earth's surface by greenhouse gases, such as methane (CH_4), nitrous oxide (N_2O), ozone (O_3), and, most notably, carbon dioxide (CO_2).[1-3] One of the greatest contributors to the anthropogenic greenhouse effect is the growing use of fossil fuels, which results in the emission of the aforementioned gases. The increasing concentration of greenhouse gases in the atmosphere strengthens the greenhouse effect, increasing global temperatures in a process known as global warming (Figure 1.1).[4]

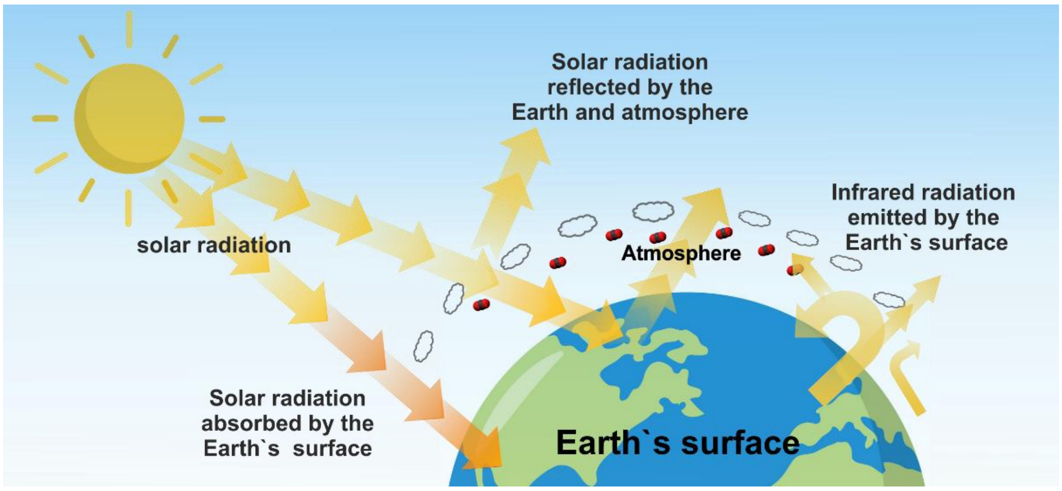

Figure 1.1. Schematic representation of the greenhouse effect.

Atmospheric CO_2 can be released naturally (e.g., by volcanic eruptions, forest fires, and biological respiration) or from anthropogenic sources (e.g., agricultural and industrial activities, the combustion of fossil fuels and solid waste, etc.). CO_2 contributes to the growth of plants and, consequently, the generation of oxygen in the process known as photosynthesis. However, the accumulation of CO_2 in the atmosphere leads to planetary warming, which has a wide range of adverse ecological, physical, and health impacts, including polar ice melting and consequent sea level increases, floods, droughts, storms, heatwaves, increased ocean acidity because of increased CO_2 intake, and the loss of crops due to water shortages. Thus, there is an urgent need for solutions that can help to decrease the atmospheric concentration of carbon dioxide.[5-7]

According to the Global Monitoring Laboratory in Hawaii, the concentration of atmospheric CO_2 is increasing at an alarming rate.[8-10] By the year 1958, CO_2 concentration was reported to be 315 ppm (parts per million). Since then, the Global Monitoring Laboratory has reported annual increases in CO_2 concentration at rates of approximately 1.6 ppm per year in the 1980s and 1.5 ppm per year in the 1990s. Furthermore, this rate has increased to 2.2 ppm per year in the last two decades. As a result, in April 2022, the total concentration was reported to be 420.23 ppm.[12] The Keeling curve represents the steady rise in the global atmospheric CO_2 concentration (in ppm) from 1958 to the present (Figure 1.2), and it represents the pioneering work of Charles Keeling (1928–2005), who developed precise analytical instruments and measurements protocols for the quantification of gaseous CO_2 in the atmosphere.[8, 11-12]

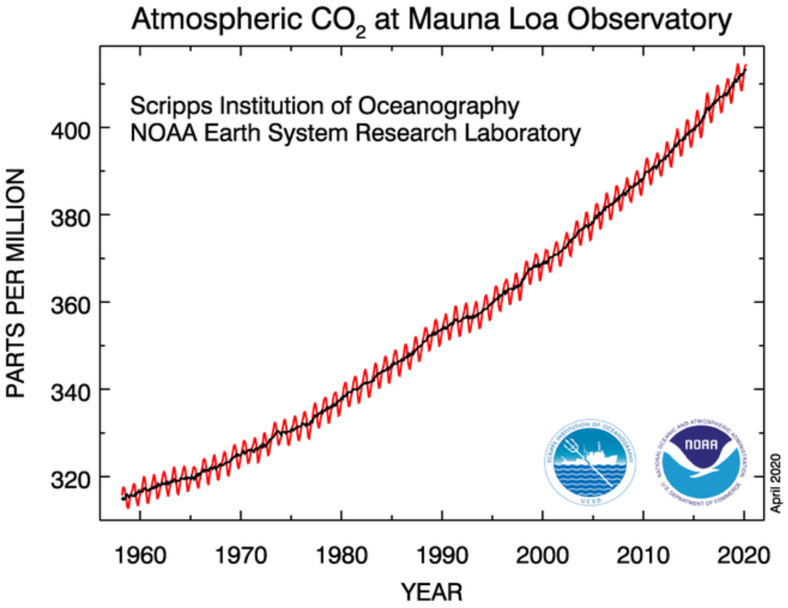

Figure 1.2. The Keeling curve describes the increase in atmospheric CO_2 concentration from 1958 to 2020. Reproduced from reference [12].

CO_2 is a linear molecule with a molecular weight of 44.0 g/mol, in which two oxygen (O) atoms are covalently bonded to a single carbon (C) atom. Each oxygen has two bonds with carbon, one of them σ and another one π, whose lengths are 116.3 pm. CO_2 is colourless, and at low concentrations, it is odourless; however, it has a sharp and acidic odour at high concentrations. Under standard conditions of temperature and pressure, it exists in a gaseous state and is stable unless chemically, electrocatalytically, or photocatalytically treated.[13]

Carbon dioxide molecule has four different modes of vibration: two stretching modes (symmetric and antisymmetric) and two flexing modes (Table 1). Symmetric stretching (1388 cm^{-1}) does not result in a change in the dipole moment; hence, this vibrational mode is inactive in the infrared spectrum. However, flexion stretching (667 cm^{-1}) and asymmetric stretching (2349 cm^{-1}) involve a change in the molecular dipole moment and are therefore active in the infrared spectrum. The infrared active vibrations of CO_2 are directly responsible for its ability to act as a greenhouse gas.[14]

Table 1. Vibrational modes of a CO_2 molecule[14]

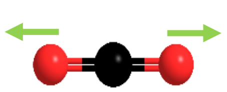	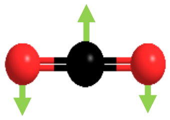	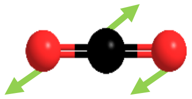	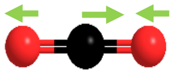
Stretching symmetric on the *z*-axis	Flexing Plane *xz*	Flexing Plane *yz*	Stretching antisymmetric
1388 cm^{-1} Inactive in the IR	667 cm^{-1} Active in the IR		2349 cm^{-1} Active in the IR

The main components of the Earth's atmosphere (oxygen and nitrogen) are transparent to infrared radiation. In contrast, CO_2 (and other atmospheric greenhouse gases) absorb some of this infrared radiation, trapping it within the Earth's atmosphere and resulting in global warming. CO_2 is by no means the most powerful greenhouse gas; however, it has a much higher atmospheric concentration than the other greenhouse gases and is thus responsible for approximately three-quarters of global warming.[1, 4]

1.2. Innovative Approaches towards CO_2 Capture and Valorization

Fossil fuel is a non-renewable energy source, and it is the principal driving force for the industrialization and economic growth of the world. Global fossil fuel consumption has increased rapidly since the Industrial Revolution, as shown in Figure 1.3. According to the Global Change Data Lab, it is estimated that only 60.7, 20.8, and 114 years of oil, natural gas, and coal remain, respectively.[15-16]

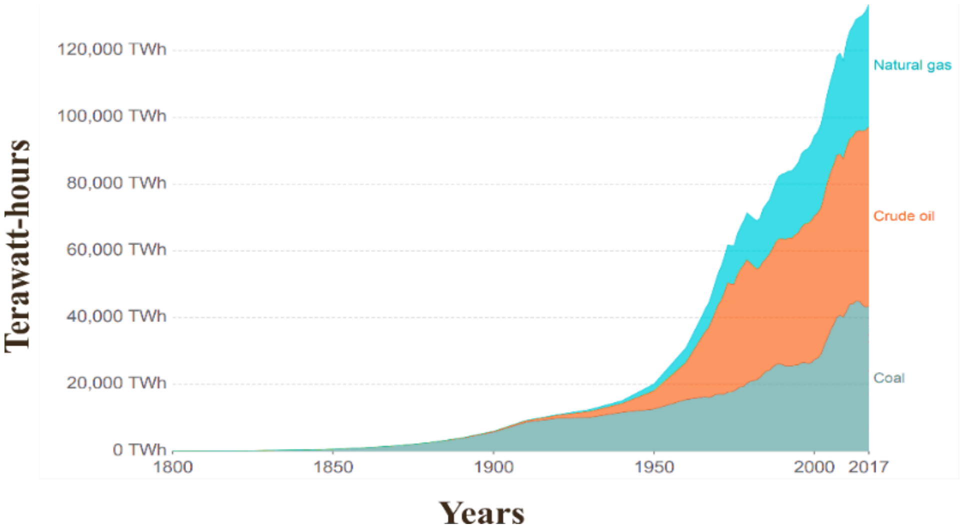

Figure 1.3. Global primary energy consumption by fossil fuel source, measured in terawatt-hours (TWh). Reproduced from reference [16].

From an environmental perspective, as well as considering the availability of these resources, the world must transition from a fossil fuel-denominated energy system to a low-carbon economy.[17] Consequently, the search for new alternative energies to those produced by fossil fuels are some of the proposals to contribute mitigating the increase of CO_2 concentration in the atmosphere.[15]

In this context, carbon capture and storage (CCS) has emerged as an attractive idea for reducing atmospheric CO_2 concentration caused principally by human activity.[18-20] However, since CCS involves the storage of CO_2 in the geological subsurface, CO_2 could still potentially leak back into the atmosphere, which is why the use of this method is a subject of discussion.[21-22]

An excellent example of CCS is the collaborative, pioneering work of Climeworks (Zürich, Switzerland) and Carbfix (Icelandic company). Climeworks developed an air-capture carbon dioxide machine in which CO_2 could either be recycled and used as a raw material or wholly removed from the air by storing it underground. As shown in Figure 1.4, the process starts with the capture of CO_2 (directly from the air) on a highly selective filter material located inside the collector. Once the filter is saturated with CO_2, the collector is closed and heated to 100 °C, releasing the CO_2; subsequently, the Carbfix method is used to mix the captured CO_2 with water and pump it deep underground, where it mineralizes and thus can be stored permanently.[23]

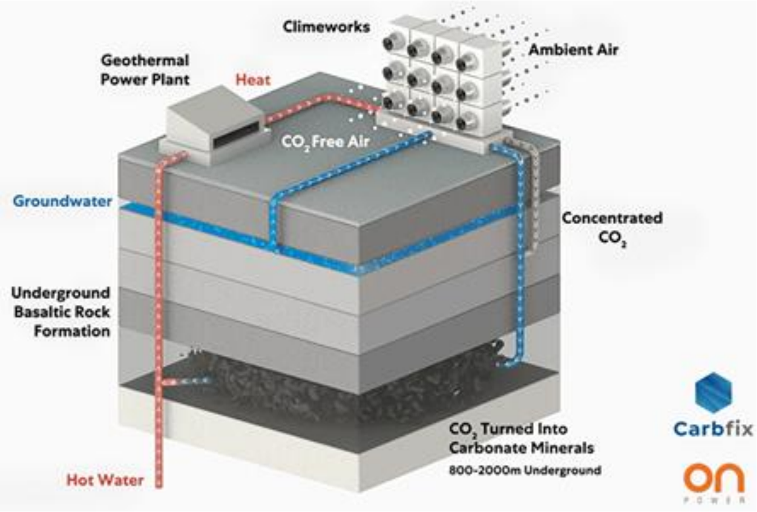

Figure 1.4. Schematic representation of the CO_2 capture technology combined with the storage process developed by Climeworks and Carbfix. Reproduced from reference [23].

The increased interest in finding new energy alternatives that can mitigate the rising levels of atmospheric CO_2 has also focused on CO_2 valorization using photochemical, biochemical, thermochemical, and electrochemical conversion routes. Photochemical CO_2 conversion involves reactions that occur on the surface of a semiconductor, that are induced by the absorption of photons; however, these are consumed as a reagent in the chemical reaction. Generally, a homogeneous photocatalytic CO_2 reduction requires a catalyst, an electron donor, and a light absorber.[24]

In biochemical CO_2 conversion, photosynthetic microorganisms (such as algae grown in non-oceanic environments) have the ability to capture sunlight and use it to store carbon in different ways, such that they can be used for the production of fuels, food additives and medicines. This photosynthetic process is very similar to that used by plants. That is, the energy from light is used to reduce CO_2 to another series of molecules that store energy. Some products obtained from this method include ethanol and hydrocarbons. However, the yields of products obtained through the biochemical conversion of CO_2 via algae fermentation processes are low, reducing their economic viability.[25-26]

Thermochemical conversion involves the use of high temperatures to convert CO_2 into useful products. One specific process is the reverse water-gas shift reaction (RWGS), which can be used to produce CO (main reactant in Fischer-Tropsch synthesis) and H_2O from CO_2 and H_2 at temperatures greater than 800 °C.[27-28, 132]

Electrochemical CO_2 reduction is the main topic of this work and will be discussed in more detail in the following section.

1.3. Electrochemical CO_2 Reduction

Electrochemical CO_2 reduction (denoted ec-CO_2R) is an innovative approach to mitigating the increase in atmospheric CO_2 levels. ec-CO_2R has attracted the attention of researchers because of its many advantages, such as the utilization of renewable electricity (e.g., wind, solar, geothermal, and hydroelectric energy) to convert CO_2 into high-value products and chemicals, allowing CO_2 to be recycled into compounds that can be utilised as energy sources. Figure 1.5 presents an overview of the electrochemical reduction of CO_2 to different high-value products and their respective applications.[29-30]

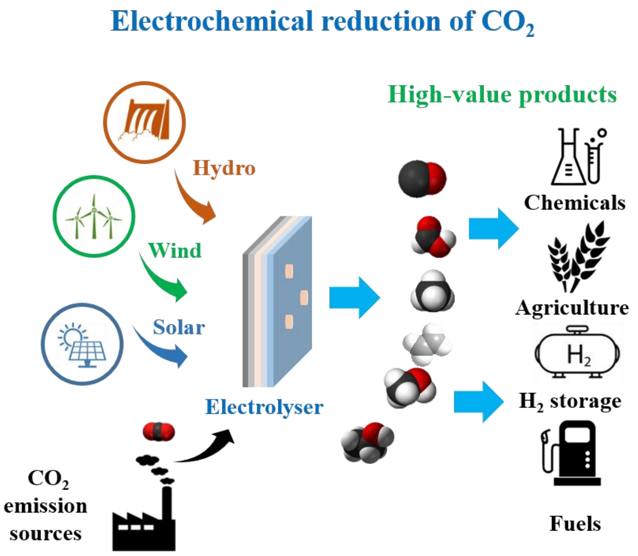

Figure 1.5. Schematic illustration of the electrochemical reduction of CO_2 powered by renewable energy sources such as solar, wind, and hydroelectric power. This process allows for the high concentration of CO_2 released by human activities to be recycled back and converted into value-added products.[29]

Despite the high chemical stability of CO_2, several researchers have demonstrated that CO_2 can be activated by an electrocatalytic processes. Specifically, the electrochemical reduction of CO_2 can proceed through two-, four-, six-, and eight- or even more electron-transfer reduction pathways, giving rise to a large spectrum of possible reduction products such as carbon monoxide (CO), methane (CH_4), ethylene (C_2H_4), methanol (CH_3OH), ethanol (C_2H_5OH), and formic acid (HCOOH).[29, 31-32] This process can take place in different phases such as gas or liquid, utilize aqueous and non-aqueous electrolytes at ambient pressure, and at high and low temperatures. Some advantages of utilizing the electrochemical reduction of CO_2 are:

- Electrode potentials and reaction temperatures control the reaction process.
- The supporting electrolyte can be recycled to minimize overall chemical waste.
- The energy used to drive the process can be obtained from renewable electricity.
- This system is compact and scalable to large-scale applications.

1.3.1. Figures of merit to describe ec-CO_2R

1. *Faradaic efficiency (FE)* is one of the most important parameters in the field of electrochemical CO_2 reduction, because it measures the product selectivity. FE is defined as the percentage of electrons consumed in the formation of a certain product. The FE can be calculated by dividing the amount of charge that was spent to obtain the product of interest by the total charge that passed through the electrochemical cell (Equation 1):[33-34]

$$FE_x = \frac{Q_x}{Q_{total}} = \frac{z_x\ n_x\ F}{Q_{total}} \qquad (1)$$

where:

- FE_x is the faradaic efficiency of component x.
- Q_x is the amount of charge consumed to produce the product of interest.
- Q_{total} is the total charge passed through the cell.
- z_x is the number of electrons transferred during the electrochemical reaction for the desired product.
- n_x is the number of moles of the desired product.
- F is the Faraday's constant (96485 C mol^{-1}).

It is important to mention that experimental results show that FE may be affected by the following:

- Catalysts themselves, e.g., the chemical composition.
- Morphology of the catalysts, such as its particle size and the thickness of the catalyst layer.
- Reaction conditions, e.g., temperature, the pH of the CO_2-saturated solution, reaction time, and the applied potential.

2. *Current density (i)* can be obtained by dividing the current by the surface area of the working electrode, which is a measure of the reaction rate. While the partial current density for a specific product n (i_n) is a direct measure of the rate at which a given product is generated, it can be calculated by multiplying the overall current density by the corresponding FE of the product (Equation 2).[33-34]

$$i_n = i * FE \qquad (2)$$

3. *Overpotential (η)* is the extra amount of voltage required to overcome the energy barrier which allows the reaction to occur. It is classified into two components: the result of activation polarization ($\eta_{activation}$) to overcome the activation energy barrier for reactions to occur on the catalytic electrode surface and the mass transfer limitation of dissolved CO_2 ($\eta_{diffusion}$).[30, 34]

4. *Energy efficiency (EE)* is defined as the ratio between the useful energy output (energy stored in the desired product) and total energy input, as shown in Equation 3, where E° is the standard potential and η is the overpotential.

$$EE = \frac{E^0}{E^0 + \eta} * FE \qquad (3)$$

This equation shows that *EE* is achieved through a combination of high selectivity (faradaic or current efficiency) and low overpotentials.[30, 34]

5. *Value of products*. A common question in ec-CO_2R research is which product is the best one to produce, and the answer depends on the product's intended application. Nevertheless, some products are likely to have a higher profit margin than others. Techno-economic analyses show that the two-electron products obtained from ec-CO_2R, such as formic acid and carbon monoxide, are the most economically viable options. In contrast, those C_2–C_4 products other than propanol are less profitable.[35-36] Table 2 shows the estimated production costs and the market prices for specific products obtained via ec-CO_2R compared to well-established chemical synthesis routes. Although, the global market for formic acid is smaller compared to carbon monoxide, there has recently been an increasing demand for this product because formic acid is an important chemical intermediate in many industrial processes and is widely used in leather, pesticide, medicine, and dyestuff. Most recently, it has attracted interest in the field of hydrogen storage.[29, 37-40]

Table 2. Current and estimated production costs for several ec-CO_2R products[41]

Product	Produced by	Current market price [$ kg^{-1}]	Current production volume [Mt y^{-1}]	Price of production via electrolysis [$ kg^{-1}]
H_2	Steam reforming, partial oxidation of methane or gasification of coal	2-4	65	4
CH_4	Methanogenesis or hydrogenation of CO_2	<0.08	2400	2-4
C_2H_4	Pyrolysis or vapourcracking	0.8 - 105	141	1.6-3.2
CO	Boudouard reaction	0.65	210000	0.27-0.54
$HCOO^-$ /HCOOH	Hydrolysis from methyl formate and formamide or by-product of acetic acid production	0.8-1.2	0.8	0.17-0.34
CH_3OH	From natural gas, coal biomass, waste	0.4-0.6	100	0.70-1.4

1.4. Thermodynamics and Kinetics of Electrochemical CO_2 Reduction

Electrochemistry refers to a branch of chemistry that studies the chemical reactions that occur at the interface of an electronic conductor (metal or semiconductor) and an ionic conductor, involving the transfer of the electrons between the electrode and the electrolyte or a species in solution.

Two types of electrolytic cells are studied in electrochemistry: galvanic and electrolytic. A galvanic cell is a device in which the reactions occur spontaneously at the electrodes when they are externally connected by a conductor. In contrast, an electrolytic cell is a device in which the reactions are triggered by the imposition of an external voltage greater than the open-circuit potential of the cell (OCP). Examples of this include the oxidation of methanol, the hydrogen and oxygen evolution reactions (denoted as HER and OER, respectively), nitrate reduction, and the electrochemical reduction of CO_2.[42-45] This thesis focuses on ec-CO_2R.

The ec-CO_2R involves an anode half-reaction for the oxidation of H_2O, and a cathode half-reaction for the reduction of CO_2, as described in Equation 4 and 5, respectively. Due to CO_2 electrolysis is usually performed in an aqueous environment, the hydrogen evolution reaction also takes place on the cathode (Equation 6), being a competing reaction to the ec-CO_2R:

$$\text{Anodic reaction: } 2H_2O \leftrightarrow O_2 + 4H^+ + 4e^- \tag{4}$$

$$\text{Cathodic reaction: } CO_2 + 2H^+ + 2e^- \leftrightarrow HCOOH \tag{5}$$

$$\text{HER: } 2H_2O + 2e^- \leftrightarrow H_2 + 2OH^- \tag{6}$$

The electrical potential supplied to the system results in the oxidation of water to molecular oxygen, hydrogen ions (H^+), and electrons (e^-) at the anode. Oxygen is released at the anode, while the electrons flow to the cathode, where they can combine with any of the H^+ ions that have travelled through the system membrane to form molecular hydrogen (H_2) or with CO_2 to form several reduced value-added products.

The product formed during ec-CO_2R is determined by the reaction conditions and the catalyst employed in the cathodic system. The CO_2 reduction reaction usually competes with the hydrogen evolution reaction, so if the reaction conditions and catalysts are not appropriate, the main reduced product would be hydrogen (H_2).

As mentioned previously, a driving force is required to convert a thermodynamically stable molecule, such as CO_2, into different products. For electrochemical processes, that driving force is the applied potential (ΔE^0_{cell}), defined as the equilibrium potential difference between the cathode and anode, which influences the reaction rate. The theoretical cell potential required to form a product via ec-CO_2R is described by Equation 7.[34, 46]

$$\Delta E^{o}_{cell} = E_{cathode} - E_{anode} \qquad (7)$$

The Gibbs free energy can be used to calculate the maximum amount of reversible work that a thermodynamic system can perform. When a system transforms reversibly from an initial state to a final state, the decrease in Gibbs free energy is equal to the work done by the system to its surroundings, minus the work of pressure forces. [46] Thus, the spontaneity of a given reaction can be measured by the change of Gibbs energy (ΔG°); specifically, a negative change in Gibbs energy indicates that the reaction is spontaneous. As the Gibbs energy is a complex function of temperature and pressure, it is normally difficult to precisely control the reaction spontaneity. However, in electrochemistry, ΔG° can be controlled by the applied potential as shown in Equation 8:

$$\Delta G° = -nFE° \qquad (8)$$

where *n* is the number of electrons involved in the reaction and *F* is the Faraday constant (96845 C/mol). In this way, electrochemistry allows for the direct control of a reaction's ΔG° and, consequently, its spontaneity. This equation describes the quantitative relationship between the chemical and the electrical energy in cell reactions; furthermore, other thermodynamic quantities can be derived from this equation. For example, the entropy change given by ΔG° can be derived as follows:

$$\Delta S° = -\left(\frac{\partial \Delta G}{\partial T}\right)_P \qquad (9)$$

$$\text{hence,} \qquad \Delta S° = nF\left(\frac{\partial E}{\partial T}\right)_P \qquad (10)$$

and

$$\Delta H° = \Delta G° + T\Delta S° = nF\left[T\left(\frac{\partial E}{\partial t}\right)_p - E\right] \qquad (11)$$

The equilibrium constant of the reaction can also be derived from Equation 12:

$$RT\ In\ K = -\Delta G° = nFE° \qquad (12)$$

This equation relates the electrochemical properties and thermodynamic properties of an electrochemical system. From thermodynamics is known that the Gibbs free energy is related to the concentration of the reactants and products (the reaction quotient, Q), which can be used to obtain the relationship between the electrode potential and the reaction quotient, known as the Nernst equation (Equation 13):

$$E = E° - \frac{RT}{nF}\, In\, \frac{C_r}{C_o} \qquad (13)$$

where C_r/C_o is the ratio of the bulk concentration of the reduced and oxidized species, $E°$ is the standard cell potential, R is the universal gas constant, and n is the number of electrons transferred. Table 3 shows the primary reactions that take place during the electrochemical reduction of CO_2, including the standard reduction potential (E°) versus standard hydrogen electrode (SHE) at 25 °C.[46]

Table 3. Selected Standard Potentials of CO_2 in Aqueous Solutions (V *vs.* SHE) at 1.0 atm and 25 °C According to the Standard Gibbs Energies of the Reactants in Reactions[47]

Cathodic half-cell reaction (reduction process)	Electrode potentials (V *vs.* SHE) at Standard Conditions	Product
$2H^+ + 2e^- \rightarrow H_2$	0.00	Hydrogen
$CO_2(g) + 2H^+ + 2e^- \rightarrow HCOOH(l)$	-0.250	Formic acid
$CO_2(g) + 2H_2O(l) + 2e^- \rightarrow HCOO^-(aq) + OH^-$	-1.078	Formate
$CO_2(g) + 2H^+ + 2e^- \rightarrow CO(g) + H_2O\ (l)$	-0.106	Carbon monoxide
$CO_2(g) + 2H_2O(l) + 2e^- \rightarrow CO(g) + 2OH^-$	-0.934	
$CO_2(g) + 4H^+ + 4e^- \rightarrow CH_2O(l) + H_2O\ (l)$	-0.070	Formaldehyde
$CO_2(g) + 3H_2O(l) + 4e^- \rightarrow CH_2O(l) + 4OH^-$	-0.898	
$CO_2(g) + 6H^+ + 6e^- \rightarrow CH_3OH(l) + H_2O\ (l)$	0.016	Methanol
$CO_2(g) + 5H_2O(l) + 6e^- \rightarrow CH_3OH(aq) + 6OH^-$	-0.812	
$CO_2(g) + 8H^+ + 8e^- \rightarrow CH_4(g) + 2H_2O\ (l)$	0.169	Methane
$CO_2(g) + 6H_2O(l) + 8e^- \rightarrow CH_4(g) + 8OH^-$	-0.659	
$2CO_2(g) + 12H^+ + 12e^- \rightarrow CH_2CH_2(g) + 4H_2O\ (l)$	0.064	Ethylene
$2CO_2(g) + 8H_2O(l) + 12e^- \rightarrow CH_2CH_2(g) + 12OH^-$	-0.764	
$2CO_2(g) + 12H^+ + 12e^- \rightarrow CH_3CH_2OH(l) + 3H_2O\ (l)$	0.084	Ethanol
$2CO_2(g) + 9H_2O(l) + 12e^- \rightarrow CH_3CH_2OH(l) + 12OH^-$	-0.744	
Anodic half-cell reaction $2H_2O(l) \rightarrow O_2 + 4H^+ + 4e^-$	1.23	OER

These interpretations are essential for the successful design of an electrochemical CO_2 reduction systems, as well as for estimating the energy required for the formation of specific products. In thermodynamics, the Gibbs free energy for CO_2 reduction is always positive; therefore, the theoretical potentials are negative.[41, 48-49]

1.4.1. Electrode Kinetics

An electrochemical reaction only proceeds once its activation barrier has been overcome; thus, such reactions require a sufficient electrical energy supply. Among these barriers, we found the electrical resistance of the circuit, activation energies of the electrochemical reactions occurring on the surface of the electrodes, availability of electrode surfaces coverage by gas bubbles formed, and the resistances to the ionic transfer within the electrolyte solution (Equation 14).

$$R_{total} = R_{cathode} + R_{bubble,H_2} + R_{membrane} + R_{anode} + R_{bubble,O_2} + R_{ions} + R_{circuit} \qquad (14)$$

Resistances in electrolysis systems are usually divided into three categories: electrical resistances ($R_{circuit}$), reaction resistances ($R_{bubble,H2}$, R_{ions}, $R_{membrane}$, and $R_{bubble,O2}$), and electrochemical reaction resistances ($R_{cathode}$ and R_{anode}).[33, 41, 46]

The electrochemical reaction occurs at the interface between the electrode and electrolyte solution and it can be described in three steps: 1) the transport of the reactant species from the bulk electrolyte to the electrode surface (first mass transfer process); 2) followed by the heterogeneous electron transfer across the interface, and 3) the transport of the products from the reaction area into the bulk solution (second mass transfer).[50-51] Some of these processes, such as electron transfer at the electrode surface, depend upon the electrode potential. Determination of a possible step order and the rate-determining step is crucial for the dynamic description of a specific electrode process.

For a given electrode reaction (Equation 15):

$$O + ne \underset{k_b}{\overset{k_f}{\leftrightarrow}} R \qquad (15)$$

where both the oxidized form (*O*) and the reduced form (*R*) of a redox couple are initially present in the bulk solution. The rate of the forward reduction process, v_f, is given for Equation 16:

$$v_f = k_f C_O(0,t) = \frac{i_c}{nFA} \qquad (16)$$

while the rate of the backward oxidation reaction, v_b, is given for equation 17:

$$v_b = k_b C_R(0,t) = \frac{i_a}{nFA} \qquad (17)$$

where k_f and k_b are the forward reduction and backward oxidation rate constants, respectively, C_O (0, t)/C_R (0, t) is the *O/R* surface concentration of the at time *t*, and i_c and i_a are the cathodic and anodic current, respectively. Both equations can be used to express the net rate of the reaction as follows (Equation 18):

$$v_{net} = v_f - v_b = k_f C_O(0,t) - k_b C_R(0,t) = \frac{i}{nFA} \qquad (18)$$

in which the overall current can be calculated by Equation 19:

$$i = i_c - i_a = nFA\left[k_f C_O\,(0,t) - k_b C_R\,(0,t)\right] \qquad (19)$$

An accurate kinetic expression of an electrode process can often be found by expressing current as a function of potential because there is a proportionality between the current and the net rate of an electrode reaction, and because the reaction rate is a strong function of the electrode potential. At equilibrium, the net current is zero, and the electrode potential is defined by the Nernst equation (Equation 13). Upon the passage of faradaic current, the electrode potential deviates from its equilibrium value in a process known as electrode polarization. The extent of polarization is determined by the overpotential, η (Equation 20):

$$\eta = E - E_{eq} \qquad (20)$$

Based on Butler–Volmer's model of electrode kinetics, the relationship between current density and overpotential can be represented by Equation 21:

$$i = i_0\left[\frac{C_O(0,t)}{C_O^*}\,e^{-\alpha f\eta} - \frac{C_R(0,t)}{C_R^*}\,e^{-(1-\alpha)f\eta}\right] \qquad (21)$$

where $f = F/RT$, α is the transfer coefficient, and i_0 is the exchange current, which represents the balanced Faradaic current at equilibrium and is equal to either component current, i_c or i_a, in magnitude. From equation 21, it can be concluded that the lower the exchange current, the higher the overpotential is required for a certain current to impede the kinetics of the reaction.[46, 52-53]

1.4.2. Role of the Catalysts in the Electrochemical CO_2 Reduction

The electrochemical CO_2 reduction is a complex multi-step reaction with multiple adsorbed intermediates, where a catalyst provides reactive sites that allow the reduction of CO_2 into different products. A catalyst accelerates a chemical reaction by decreasing the energy barrier without affecting the chemical equilibrium of the reaction by providing an alternative reaction pathway to the uncatalyzed reactions. Catalysts accomplish this by forming bonds with the reacting molecules and allowing these to react to a product, which detaches from the catalyst, and leaves it unaltered such that it is available for the subsequent reaction.[21] However, over time, catalysts experience a process known as ‘poisoning’ that makes them useless, especially working at high temperatures. Figure 1.6 shows the difference in the energy required to form a product in the presence and absence of a catalyst.

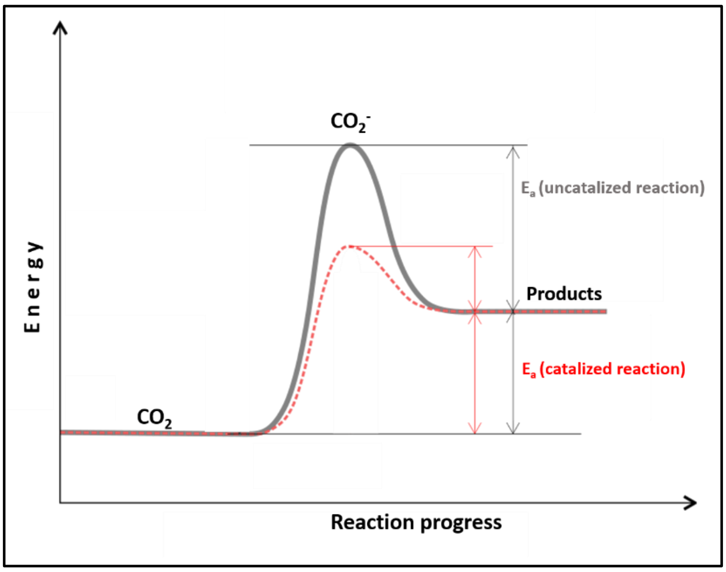

Figure 1.6. A schematic representation of the energy required for the electrochemical CO_2 reduction in the absence and presence of a catalyst. Readapted with permission from *J. Phys. Chem. Lett.* 2010, 1, 24, 3451–3458. Copyright 2010 American Chemical Society. [21]

Depending on the phase in which the catalyst is introduced, the catalytic processes can be classified as homogeneous and heterogeneous catalysis. Homogeneous catalysts are usually present as a species in solution (liquids or gases). In contrast, heterogeneous catalysts are generally solid, with chemical reactions between liquid or gaseous species occurring on the surface of the catalyst; the surface of the solid-liquid interface is of great importance in these processes.[54-57] In general, heterogeneous catalysts are preferred due to their stability, ease of separation, handling, and reusability. These advantages are manifested as lower costs in large-scale productions.

The first studies of the electrochemical CO_2 reduction were focused on using polycrystalline monometallic catalysts because they are structurally simple, easy to handle, and robust, making them attractive candidates for fundamental studies. According to Hori et al., monometallic catalysts can be divided into four groups, depending on the main CO_2 reduction product: 1) CO selective metals (e.g., Au, Ag, and Zn): 2) formate selective metals (e.g., Sn, In, and Pb); 3) hydrogen-selective metals (e.g., Fe, Ni, and Pt); and 4) Cu which has the unique catalytic ability to produce a wide range of CO_2 reduction products, including CO, formate, ethanol, and ethylene.[58-61] Table 4 shows the principal products obtained from ec-CO_2R in the presence of different metals at a current density of 5 mA cm^{-2}.

Table 4. Products generated from the electroreduction of CO_2 on different metals[58]

Electrode	Potential (V vs HNE)	Current density (mA cm^{-2})	Faradaic efficiency / %							
			CH_4	C_2H_4	EtOH	PrOH	CO	HCOOH	H_2	Total
Au	-1.14	5.0	0.0	0.0	0.0	0.0	87.1	0.7	10.2	98.0
Ag	-1.37	5.0	0.0	0.0	0.0	0.0	81.5	0.8	12.4	94.6
Zn	-1.54	5.0	0.0	0.0	0.0	0.0	79.4	6.1	9.9	95.4
Pd	-1.20	5.0	2.9	0.0	0.0	0.0	28.3	2.8	26.2	60.2
Ga	-1.24	5.0	0.0	0.0	0.0	0.0	23.2	0.0	79.0	102.0
Pb	-1.63	5.0	0.0	0.0	0.0	0.0	0.0	97.4	5.0	102.4
Hg	-1.51	0.5	0.0	0.0	0.0	0.0	0.0	99.5	0.0	99.5
In	-1.55	5.0	0.0	0.0	0.0	0.0	2.1	94.9	3.3	100.3
Sn	-1.48	5.0	0.0	0.0	0.0	0.0	7.1	88.4	4.6	100.1
Cd	-1.63	5.0	1.3	0.0	0.0	0.0	13.9	78.4	9.4	103.0
Tl	-1.60	5.0	0.0	0.0	0.0	0.0	0.0	95.1	6.2	101.3
Ni	-1.48	5.0	1.8	0.1	0.0	0.0	0.0	1.4	88.9	92.4[+]
Fe	-0.91	5.0	0.0	0.0	0.0	0.0	0.0	0.0	94.8	94.8
Pt	-1.07	5.0	0.0	0.0	0.0	0.0	0.0	0.1	95.7	95.8
Ti	-1.60	5.0	0.0	0.0	0.0	0.0	0.0	0.0	99.7	99.7
Cu	-1.44	5.0	33.3	25.5	5.7	3.0	1.3	9.4	20.5	103.5[*]

Electrolyte: 0.1 M $KHCO_3$; Temperature: 18.5 ± 0.5 °C. *The total value of the final product includes C_3H_5OH (1.4 %), CH_3CHO (1.1%) and C_2H_5CHO (2.3%) in addition to the tabulated substances. [+]The total value includes C_2H_6 (0.2%).

Catalysts are needed to bind and activate CO_2 to reduce the high overpotentials that are typical of these reactions. In addition, catalysts can drive the selective formation of desired products. For this reason, recent research on catalysts has mainly focused on different metal catalysts and the diverse products that can be formed. Researchers have also begun to study other materials, such as metal oxides, metal-organic frameworks (MOFs), and organometallic catalysts, for use in highly selective electrochemical CO_2 reduction processes.[25, 56]

1.4.3. Proposed Reaction Pathways for ec-CO_2R

Depending on the working electrode and the experimental conditions, ec-CO_2R can proceed through different reaction pathways that generate a different distribution of products. In general, the overall reaction involves three steps: 1) the chemical adsorption of the CO_2 on the surface of the catalyst, 2) the electron transfer and proton migration to break C=O bonds and form new C-O and C-H bonds, and 3) the desorption of the formed products from the catalyst surface and their diffusion into the electrolyte.[62] Reaction pathways have been studied both experimentally and theoretically over the last few decades.[63] These studies have shown that the rate determining step of ec-CO_2R is the first electron transfer to the surface-adsorbed $^*CO_2$ (where * denotes the adsorption site) to form $* CO_2^{\cdot -}$ intermediate, as shown in Figure 1.7.[64] The next step is determined by which atom binds to the electrode surface. If the oxygen atom of $* CO_2^{\cdot -}$ binds to the electrode surface, the carbon atom would be protonated to form *OCHO, which leads to the formation of formic acid or formate (Figure 1.7a). Conversely, if the carbon atom of $* CO_2^{\cdot -}$ binds to the electrode surface, the oxygen atom would be protonated to form *COOH, which leads to the formation *CO and eventually the release of CO from the surface of the catalyst (Figure 1.7b). In some catalytic materials such as Cu, the intermediate *CO can be reduced to form various hydrocarbons and alcohols.[29, 32]

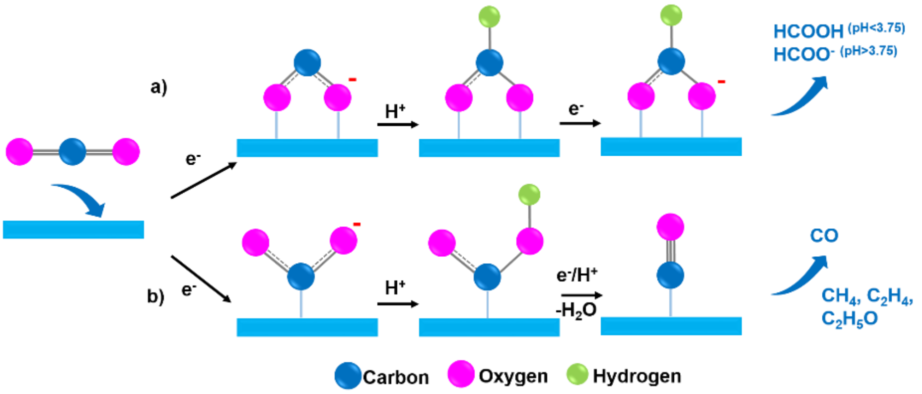

Figure 1.7. Possible reaction pathways for the electrochemical CO_2 reduction to formate, CO, and other products.[29]

In the work done in this thesis, the main product formed from ec-CO_2R was formate. According to the literature, the formation of formate involves an intermediate that binds to the electrode surface either through a single oxygen atom (monodentate) or two oxygen atoms (bidentate), as shown in Figure 1.8a. This intermediate can form by the reaction with *H via CO_2 insertion into the metal–hydrogen bond or by direct protonation with H^+ from the solution.[64] An alternative pathway proceeds via a $CO_2^{\cdot -}$ radical that reacts with a proton to generate $HCOO^-$ or HCOOH, as shown in Figure 1.8b (top).[65] And a third reaction pathway proposed consists of the presence of HCO_3 ions, which enhance $HCOO^-$ production, as shown Figure 1.8b (bottom).[65] Recently, Bocarsly et al. have proposed that forming a surface-bound tin carbonate is a key chemical step that is necessary for the reduction of CO_2 to $HCOO^-$ on tin electrodes, as shown in Figure 1.8c.[66] In light of this, our research group has proposed an alternative reaction pathway for Bi_2O_3 foam/film catalysts, which involves the formation of a so-called “bismuth subcarbonate” species that enhances formate formation. This reaction pathway will be discussed in the results and discussion section.[67]

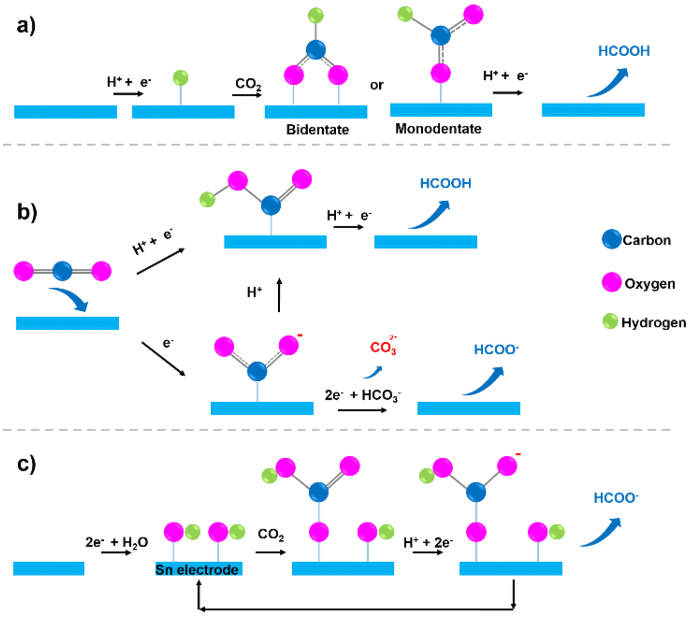

Figure 1.8. Possible reaction pathways for the electrochemical CO_2 reduction to formate or formic acid. a) The monodentate or bidentate intermediate route; b) the $CO_2^{\cdot-}$ radical intermediate route; and c) the surface-bound carbonate intermediate route (on Sn electrodes). Adapted from reference [62].

Recently, many research groups across the world have started to contribute more to the literature, creating a large catalogue of electrochemical conditions for the selectively reduction of CO_2 and the formation of products with high selectivity and high partial current densities, as well as the identification of catalysts that inhibit or suppress the HER. Figure 1.9 illustrates the increase in the number of publications related to electrochemical CO_2 reduction from the year 2000 to 2019.[68]

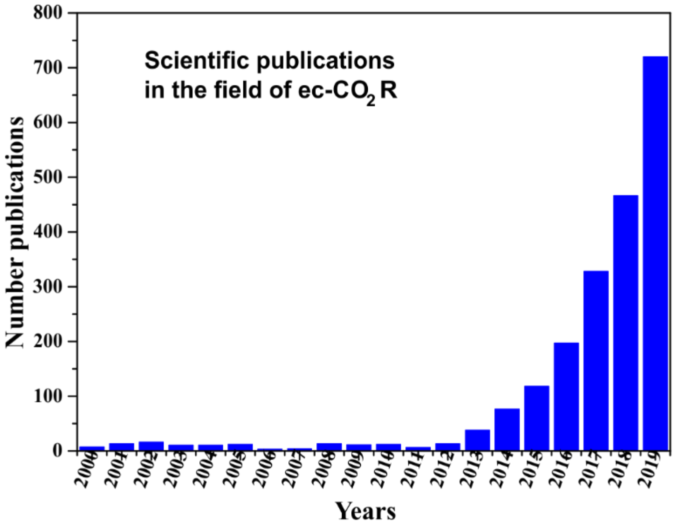

Figure 1.9. The number of scientific publications in the field of ec-CO_2R from the year 2000 to 2019. Adapted from reference [68].

1.5. The Electrochemical Cell and the Electrode Design for ec-CO_2R

Designing an appropriate electrochemical cell for ec-CO_2R is a crucial step that impacts the CO_2 reduction process as it determines the current density, faradaic efficiency, and stability of various catalytic materials. Over the years, different cell designs have been applied to ec-CO_2R. These systems can be mainly categorized into H-type and flow cell electrolysers (note that within the latter category, there is a further subcategorization).[63] The two systems for ec-CO_2R applied in this thesis are explained in detail below.

1.5.1. H-type cell system

The first studies in the field of ec-CO_2R were performed using H-type cells.[58] This type of cell is very commonly used as a lab-scale electrochemical reactor because of its ease of use for quick screening of catalysts.[29, 69-70]

An H-type cell is usually made of glass and consists of a cathode compartment, which contains the working electrode (WE) and the reference electrode (RE; Ag/AgCl); and an anode compartment, which contains the counter electrode (CE; Pt foil). These two compartments are usually connected through a salt bridge and separated by an ion-exchange membrane, which prevents the reduced products in the cathode compartment from being oxidized in the anode compartment, as shown in Figure 1.10.

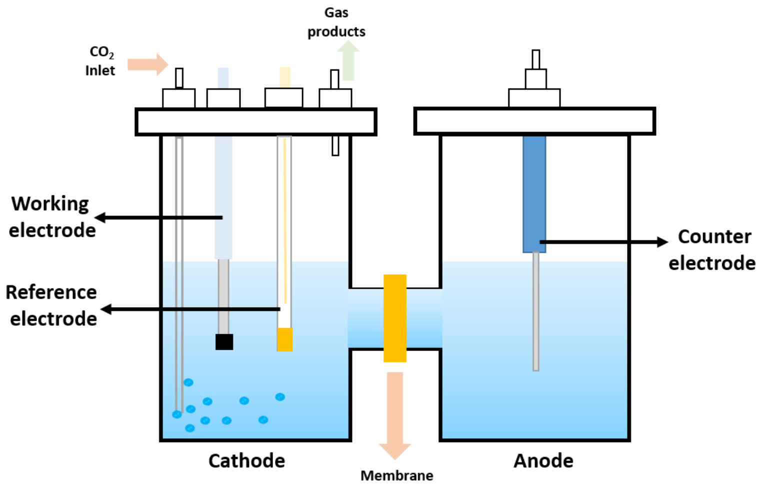

Figure 1.10. Schematic representation of a conventional H-type cell for ec-CO_2R.

In the cathode compartment, the reacting CO_2 is dissolved by bubbling in the liquid electrolyte during electrolysis. This system should be airtight for the products' faradaic efficiency (FE) to be calculated accurately. This is accomplished by collecting the gaseous products from the headspace and delivering them to a gas chromatograph (GC) for detection and quantification.

Conversely, the liquid products are collected from the electrolyte after the ec-CO_2R process and analysed by proton nuclear magnetic resonance (^{1}H-NMR), high-performance liquid chromatography (HPLC), or ion chromatography (IC).[71-75]

In an H-type cell, the current density for ec-CO_2R is restricted (<100 mA cm^{-2}) by the limited solubility (~0.03 mol kg^{-1} at ~300 K, 1 atm) and diffusion rate of CO_2 in aqueous electrolytes, especially under a large overpotentials where the reaction kinetics becomes relatively fast.[76] Therefore, the design a better system that enables higher current densities to be consider for industrial applications is required.

1.5.2. Flow Cell Electrolyser Systems

To overcome the mass transport issues presented in H-type cell systems, researchers have invested a significant amount of effort into the development of more efficient and economically viable ec-CO_2R systems.[77] This necessitates the transfer of studies carried out in H-type cell to flow cell systems. For example, in 2021, Tingting et al. reported an increase in the current density of formate production using $BiPO_4/Bi_2O_2CO_3$ catalysts from 28 mA cm^{-2} (H-type cell) to 930 mA cm^{-2} (flow cell).[78] Most recently, Wang et al. reported an increase in the partial current densities for formate from 61.7 mA cm^{-2} (H-type cell) to 590 mA cm^{-2} (flow cell) using bismuth nanosheets as a catalyst.[79]

Three electrochemical flow cell systems for ec-CO_2R have been studied: 1) the solid electrolyte electrolyser, 2) the membrane-electrode assembly electrolyser, and 3) the most widely used liquid-phase or fluidic electrolyser. The main flow cell studied in this thesis is the liquid-phase or fluidic electrolyser; however, all three systems are briefly described below.

1. *Solid electrolyte electrolyser*

The main feature of this electrolyser is that the electrolyte is solid, as shown in Figure 1.11. Some materials used as a solid electrolyte are zirconia and ceria-based oxides or lanthanum gallate-based oxides. The solid electrolyte can be either oxygen-ion conducting or proton-conducting. [80-81] In the oxygen-ion conducting electrolytes, H_2O molecules are reduced in the cathode, producing oxygen ions that pass through the solid electrolyte to the anode, where they are oxidised to molecular oxygen (O_2). Simultaneously, the adsorbed CO_2 is reduced by the activated hydrogen, as shown in Figure 1.11a. In proton-conducting electrolytes, water molecules are oxidised in the anode to produce molecular oxygen and protons. The protons produced in the anode pass through the solid electrolyte to the cathode, where they can react with the adsorbed CO_2 to produce high-value products, as shown in Figure 1.11b.

The main advantage of this electrolyser is the high current densities that can be achieved because of the enhanced kinetics at high temperatures (>600 °C), thus avoiding the mass transfer issues.[30, 63]

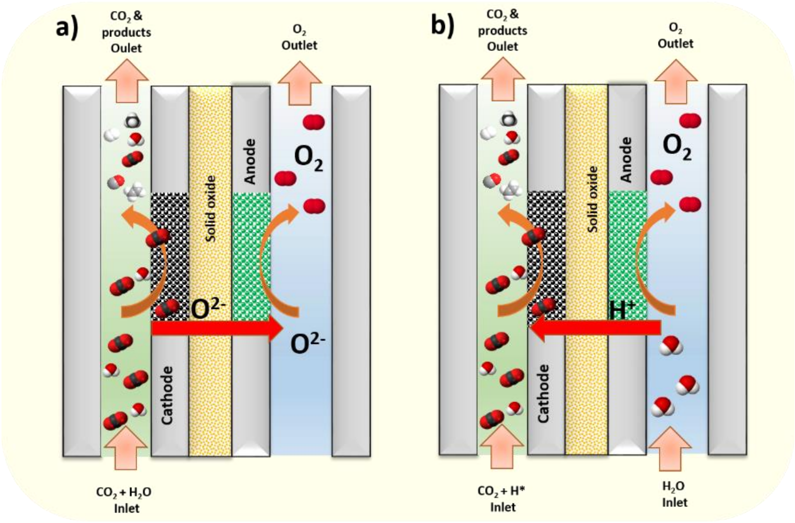

Figure 1.11. Solid electrolyte electrolysers. a) Oxygen-ion conducting and b) proton-conducting designs.

2. *Membrane-electrode assembly electrolyser*

In this type of electrolyser, the cathode and anode are separated by a polymer exchange membrane to avoid product crossover and re-oxidation. The electrodes and the membrane form a structure known as a membrane-electrode assembly (MEA), as shown in Figure 1.12. The membrane can transport ionic charges between the anode and cathode, enabling continuous and stable charge transfer.[82-83]

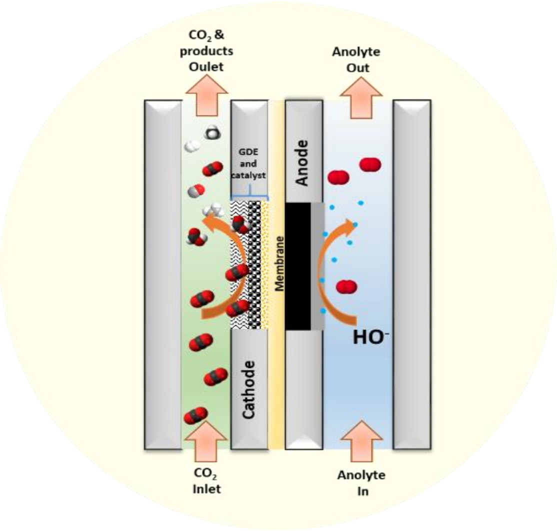

Figure 1.12. Membrane-electrode assembly electrolyser.

Humidified CO_2 is supplied to the cathode through a gas diffusion electrode (GDE; discussed in detail later in 1.5.3 section), allowing the gaseous products to leave the cell in the gas phase. Whereas, in the anode compartment, the primary reaction is the oxygen evolution reaction (OER), while the anolyte is recirculated by a peristaltic pump.

The membrane for this electrolyser could be a cation exchange membrane (CEM), an anion exchange membrane (AEM), or a bipolar membrane (BPM).[83-84] Some advantages of using this electrolyser are the improved partial current density and higher stability because of the elimination of the electrolyte in the cathode compartment and, consequently, avoiding any possibility of the electrolyte flooding into the GDE. The main disadvantage of these systems is their limited viability in the generation of liquid products, such as formate and alcohols, because these products can accumulate in the GDE and hamper gas diffusion.[29, 63]

3. *Liquid-phase or fluidic electrolyser*

The most common system for the electrochemical CO_2 reduction is the liquid-phase or fluidic electrolyser, shown in Figure 1.13. This type of electrolyser consists of an assembly gasket that are pressed together, forming three flow channels: one for the gas (CO_2), one for the catholyte, and one for the anolyte. An ion-exchange membrane separates the cathode and anode; like in the MEA electrolyser, the membrane serves to transport ionic charges between the electrodes. It also prevents ec-CO_2R products from crossing over to the anode.[30, 63, 71, 73-74]

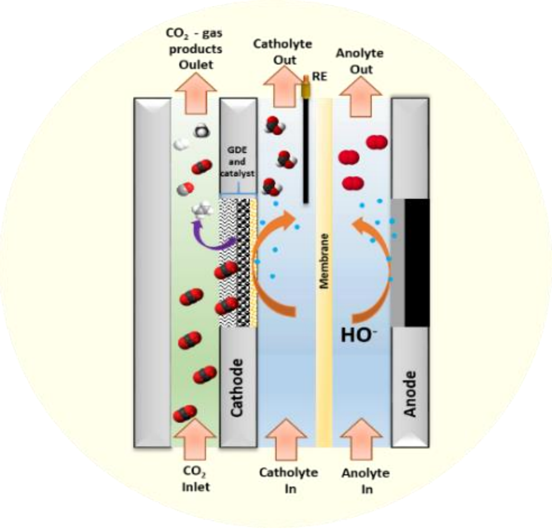

Figure 1.13. Liquid-phase or fluidic electrolyser.

A GDE separates the catholyte and gas channel. In this configuration, the catalyst layer is in direct contact with the flowing catholyte and, like in the MEA-electrolyser, the CO_2 is delivered to the catalyst through the back of the GDE. This makes CO_2 mass transfer to the catalyst more effective than with planar electrodes — which are commonly used in H-type cell — because the distance over which mass transfer through the electrolyte occurs is smaller. In addition, the liquid products are transported out of the reaction zone by circulating the catholyte with a peristaltic pump.[85]

One of the significant advantages of using this electrolyser is that the performance of the cathode and anode can be monitored using an external reference electrode. In addition, liquid-phase electrolysers can achieved high current densities (>1 A cm^{-2}) towards formate, CO and hydrocarbons.[78, 86-87] However, there are still some disadvantages in this design: for example, the presence of the liquid phase could be a source of instability in the system because of the deposition of impurities on the catalyst. It can also cause mechanical instability in the catalyst layer due to the continuous flow of electrolyte, as well as incur the risk of flooding the GDE, which is a common failure mode. In general, the operation of a flow cell demands a more complex periphery than an H-type cell. Table 5 shows a summary of the different advantages and disadvantages of each flow cell electrolyser system.

Table 5. Architectural comparison of different CO_2 electrolysers[30 63]

Electrolyser type	Electrolyte	Maximum current	Advantages	Disadvantages
H-type cell	Liquid electrolyte ($KHCO_3$ and ionic liquids)	<100 mA.cm^{-2}	▪ Easy to operate ▪ Used for quick screening of catalyst.	▪ Low solubility of CO_2 ▪ Low current density ▪ Cannot scale-up
Flow cell systems				
Solid electrolyte	Solid oxide	>1 A cm^{-2}	▪ High current density at high temperatures ▪ Avoiding mass transfer issue	▪ CO is the only product ▪ Carbon deposition ▪ Metal particles oxidation ▪ Cell degradation ▪ Energy-intensive at high temperatures, proper sealing is a challenge
Membrane-electrode assembly	Solid polymer (CEM, BPM, AEM)	>100 mA cm^{-2}	▪ High partial current densities. ▪ High stability. ▪ High stability to some products. ▪ Lower ohmic losses and less material cost due to the reduced flowing electrolyte.	▪ Need to humidified CO_2 or gas flow close to the aqueous anolyte. ▪ Unstable liquid outlet from the cathode. ▪ Liquid product crossover with MEA.
Liquid-phase/fluidic	Liquid electrolyte with various pH levels ($KHCO_3$, KOH, and ionic liquids).	>1 A cm^{-2}	▪ Possibility to engineer flowing electrolyte and pressurized setting ▪ Enhanced CO_2 diffusion with GDL, continuous liquid product sampling. ▪ Precise control of reaction environment. ▪ High current densities.	▪ GDL subject to potential crystallization of salts or flooding ▪ Ohmic losses

1.5.3. Gas Diffusion Electrodes

The electrode structure plays a crucial role in the reaction rate by supplying an adequate amount of gaseous reactants.[88] One way to overcome the mass transport limitations is by using a gas diffusion electrode (GDE). In general, a GDE consists of three different phases: 1) carbon nanofibers (macroporous substrate); 2) mesoporous carbon (microporous layer); and 3) the deposited catalyst layer that allows the formation of a three-phase boundary, where the catalyst, the electrolyte, and the gaseous reactant interact. Figure 1.14a describes the interactions that occur at the three-phase boundary during ec-CO_2R, while Figures 1.14b and 1.14c show the scanning electron microscopy (SEM) images of the GDE in the absence and presence of the catalyst layer, respectively.[89]

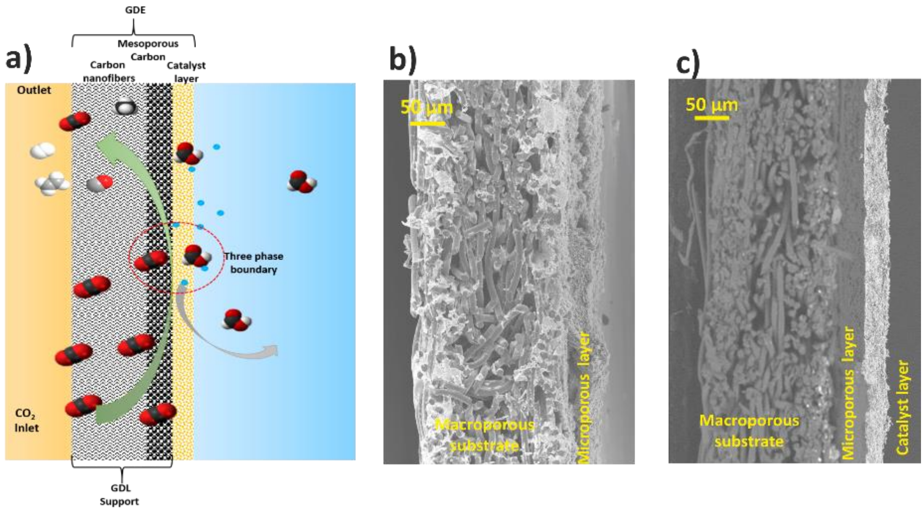

Figure 1.14. a) Three-phase boundary during ec-CO_2R. SEM images of the GDE in b) the absence and c) the presence of the catalyst layer.

In a GDE, the gas diffusion layer (GDL; carbon nanofibers and mesoporous carbon) is hydrophobic, porous, and conductive. The macroporous layer provides mechanical stability and electrical contact while distributing gas through its macroporous structure. Typical materials used for the construction of macroporous layer include carbon structures like carbon paper or carbon cloth.[90] The microporous layer is added to enhance the interfacial electrical connection and to prevent flooding. The microporous layer is composed of a mixture of carbon black nanoparticles and hydrophobic polymers (polytetrafluoroethylene; PTFE) and forms a layer with pores that are approximately 200 nm.[69, 90]

CO_2 reduction takes place on the catalyst layer in the GDE. In this work, the catalyst layer is composed of a bismuth nano-dendritic structure powder, mixed with a binder (such as Nafion) and deposited onto the microporous layer (Figure 1.14c). Different ionomers binders have been used to fixate the catalyst onto the surface, providing ionic conductivity within the catalyst layer.[91]

GDEs were first introduced and studied extensively in the context of fuel cells and water electrolysers.[92-93] In the case of fuel cells, the hydrophobic GDL played an important role in removing the excess of water. However, in GDEs applied to ec-CO_2R, the electrolyte must be kept in contact with the catalyst surface for sufficient time to allow the reaction to occur. While proper wetting is a prerequisite, too much hydrophilicity can lead to a flooding, which should also be avoided; otherwise, the HER would take place instead of ec-CO_2 reduction.[94-95] Recent studies have shown that for ec-CO_2R to be economically feasible, it is necessary to improve the current density (>200 mA cm^{-2}). Thus, the use of GDEs and flow cell systems are promising approaches to achieving this target.[96]

2. THESIS OUTLINE

Electrochemical CO_2 reduction is one of the most promising approaches to the mitigation of increased atmospheric CO_2 levels as it offers the potential to convert CO_2 into chemicals and fuels using different catalytic materials and renewable energy. In this context, metal foams have been studied as potentials catalysts for CO_2 reduction because they offer a large surface area that is not only accessible to reactants but also enables fast, multidimensional electron transport pathways.[97-100] Most importantly, is that metal foams can be directly used as cathodes for ec-CO_2R, without the need for additional mechanical support or binders, like Nafion, which are unnecessary in catalyst preparation.[99, 101]

In 2020, Dutta et al. reported that the activation of Cu foam by thermal annealing followed by the electroreduction of the oxidic precursors enhanced the reactivity and selectivity towards C2 and C3 products, such as ethylene, ethanol, and n-propanol, generated from the ec-CO_2R. Furthermore, the use of highly sensitive *operando* techniques such as X-ray absorption spectroscopy (XAS), X-ray diffraction (XRD), and Raman spectroscopy have demonstrated that, in the case of oxidized Cu foams, this catalyst pre-activation process is completed before to the formation of hydrocarbons and alcohols from CO_2.[102] This activation protocol has also been extended to bimetallic catalysts. Dutta et al. reported that the thermal activation of $Cu_{85}Ag_{15}$ catalysts enhanced the selectivity towards ethanol and n-propanol formation from CO_2 (total $FE_{alcohol}$= 40.6%). However, the use of *operando* XRD and Raman spectroscopy has demonstrated that the oxide reduction is completed before the electrochemical CO_2 reduction takes place.[103]

A variety of metal-based catalysts, such as Co_3O_4, SnO_2, ZnO, and In_2O_3, have been studied in the context of formate production in ec-CO_2R.[104-106] Among them, bismuth-based catalysts have attracted attention because of their large hydrogen evolution potential, low carbon monoxide (CO) adsorption energy, and their strong ability to stabilise CO_2^- intermediates.[107-109]

On this basis, I am going to focus on the synthesis of Bi_2O_3 foams for highly selective formate production from CO_2. Metallic Bi foams will be synthesized using the dynamic hydrogen bubble template (DHBT) electrodeposition approach, followed by thermal treatment in order to transform the “as-prepared Bi foam” (ap-Bi/Bi_xO_y) into a fully oxidised Bi_2O_3 foam.

The use of a conventional H-type cell configuration will provide information about the activity, selectivity, and stability of the Bi_2O_3 foam catalyst for ec-CO_2R over a wide potential window. The morphological changes that the catalyst undergoes during ec-CO_2R will be studied using identical location SEM. Furthermore, to study the role and stability of the oxidic species during ec-CO_2R, *operando* Raman spectroscopy will be used.

Once the appropriate conditions for synthesising Bi-foam based catalysts have been established, the next step is to transfer the knowledge acquired from the H-type cell experiments to more practical conditions using a flow cell electrolyser. To this end, a new catalyst preparation method will be developed, consisting of an airbrush coating of an ink on a GDL support followed by thermal treatment at 350 °C for 6 h in presence of air to form the Bi_2O_3. The electrochemical performance of the Bi_2O_3-GDE film will be carried out in a fluidic electrolyser (flow cell) in highly concentrated electrolyte solutions such as 1 M and 5 M KOH to reach the high current densities for the production of formate. The morphology of the catalyst will be analysed by SEM before and after thermal treatment, as well as post-ec-CO_2R. Finally, the use of complementary *ex situ* XRD, XRD-CT, and Raman spectroscopy will provide information about the composition of the catalyst at different stages of its preparation, providing clear evidence about the possible reaction pathways for formate production. Figure 2.1 represents the outline of this work.

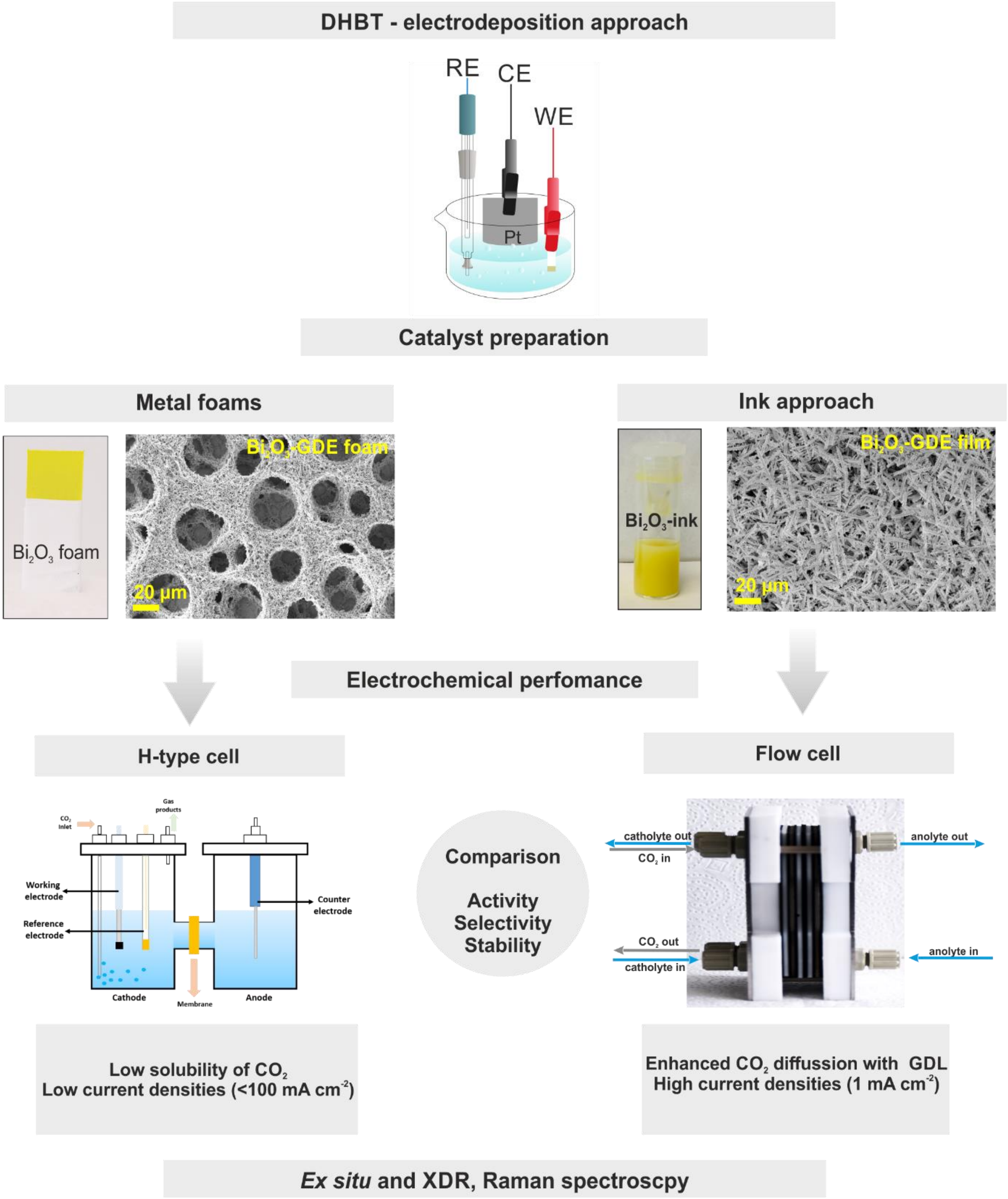

Figure 2.1. Thesis Outline.

3. RESULTS AND DISCUSSION

3.1. Electrochemical Performance of Bi_2O_3 Foam Catalyst in H-type Cell

The bismuth foam catalyst was electrodeposited on a gas a diffusion layer (GDL) support using the dynamic hydrogen bubble template (DHBT) electrodeposition approach with a plating bath containing 20 mM of ammonium bismuth citrate in 1.5 M H_2SO_4. The electrodeposition was carried out by applying high current densities of -3 A cm^{-2} for 20 s (exposed area 1 cm^2). Figure 3.1 illustrates the principle of metal deposition on a GDL.[67, 110-113]

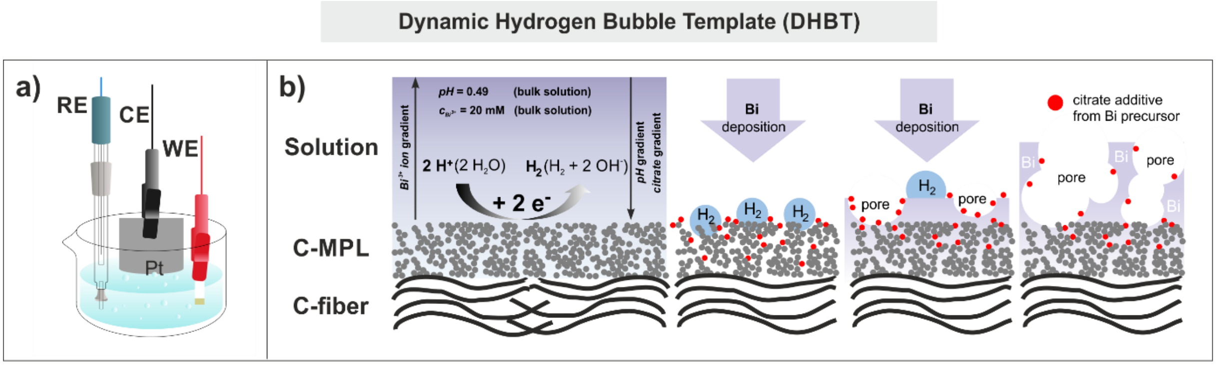

Figure 3.1. a) Schematic illustration of the set-up for the electrodeposition of Bi-foam catalyst. b) An illustration of the additive-assisted dynamic hydrogen bubble template (DHBT) electrodeposition carried out on the carbon fibre cloth support (gas diffusion layer, GDL). Readapted with permission from *ACS Catal.* 2021, 11, 9, 4988–5003. Copyright 2021 American Chemical Society. [67]

Note that due to the harsh experimental conditions, the metal deposition (primary process; Equation 22) is inevitably superimposed on the hydrogen evolution reaction (HER; secondary process). [67] The HER relies on the superposition of (i) proton reduction and (ii) water splitting (Equations 23 and 24, respectively) as follows:

Metal deposition: $$Bi^{3+} + 3e^- \rightarrow Bi^0 \qquad (22)$$

HER (proton reduction): $$2H^+ + 2e^- \rightarrow H_2 \qquad (23)$$

HER (water splitting): $$2H_2O + 2e^- \rightarrow H_2 + 2OH^- \qquad (24)$$

At these high current densities, proton reduction is mass transport-limited, which further activates the HER reaction pathway through water splitting.[114] Hydrogen gas bubbles, which temporarily form on the cathode, function as a transient geometric template for the actual metal foaming process.[101, 111] During the metal deposition, smaller H_2 bubbles tend to coalesce into larger bubbles, introducing dynamics to the metal deposition onto the template. It should be highlighted that the HER is a key factor in the formation of porous Bi/Bi_xO_y foams. For more details, please see **Publication 2**.[115]

Note that because of their oxophilicity and high surface area, metallic Bi foams readily undergo surface oxidation immediately after removal from the plating bath. Hence, they are denoted as 'ap-Bi/Bi_xO_y' foams to indicate that they are "as-prepared". The ap-Bi/Bi_xO_y foams were subjected to thermal annealing at 300 °C for 12 h in air to transform the catalytic material into a fully oxidised Bi_2O_3 foam (for details about the XRD and XPS characterisation of this material, please see **Publication 2**). Figure 3.2a–c shows the digital image and SEM images of the 'ap-Bi/Bi_xO_y' foam deposited on the GDL substrate. The Bi/Bi_xO_y foams obtained have a range of pore diameters from 15–25 µm, with small pores near the support electrode (GDL) and the largest pores at the outermost surface of the foam material (panel b). In contrast, the pore sidewalls consist of more loosely packed Bi dendrites (Figure 3.2c).

A digital image and SEM images (Figure 3.2 d–f) of the Bi_2O_3-GDE foam are also presented. It should be noted that the thermal treatment leads to a pronounced colour change, with the foam turning from black (ap-Bi/Bi_xO_y) to yellow (Bi_2O_3). Most importantly, the overall morphology of the foams remains preserved after thermal annealing, as evidenced by SEM inspection.

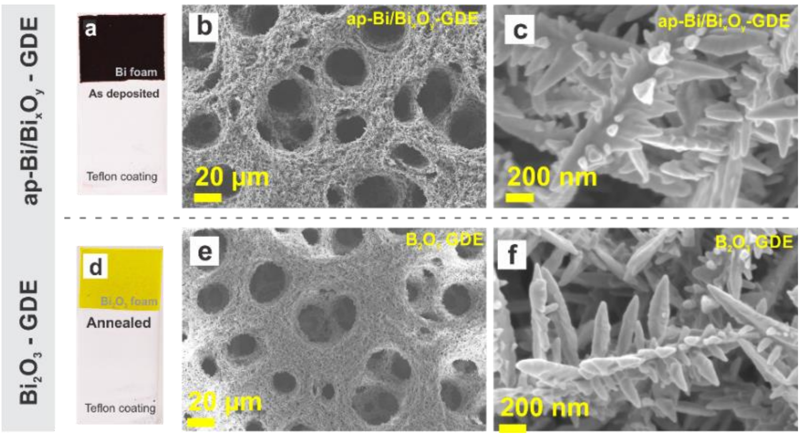

Figure 3.2. Morphology of the ap-Bi/Bi_xO_y and Bi_2O_3 foams deposited on GDL. a) Digital image of the ap-Bi/Bi_xO_y and its b-c) corresponding SEM images. d) Digital image of the Bi_2O_3-GDE foam and its e-f) corresponding SEM images. Readapted with permission from *ACS Catal.* 2021, 11, 9, 4988–5003. Copyright 2021 American Chemical Society. [67]

The Bi foams were electrodeposited on planar surfaces include copper and carbon foil as well as on highly porous surfaces, such as carbon cloth (GDL). It is important to mention that the dendritic nature of the pore sidewalls was not dependent on the chosen material. However, the pore size distribution did vary based on the supporting material: the pore size distribution of the

Bi foam was broader and less well defined on the GDL support material compared to the planar copper and carbon foil substrates. For more details, please see **Publication 2**.

The electrochemical catalyst testing was carried out for 1 h in a wide electrochemical potential window from –0.3 V to –2.0 V *vs.* RHE in a conventional H-type cell configuration using a CO_2-saturated solution of 0.5 M $KHCO_3$. The results for both catalysts, ap-Bi/Bi_xO_y and Bi_2O_3-GDE, are presented in Figure 3.3. The electrolysis results obtained for a planar Bi foil are also presented for comparison.

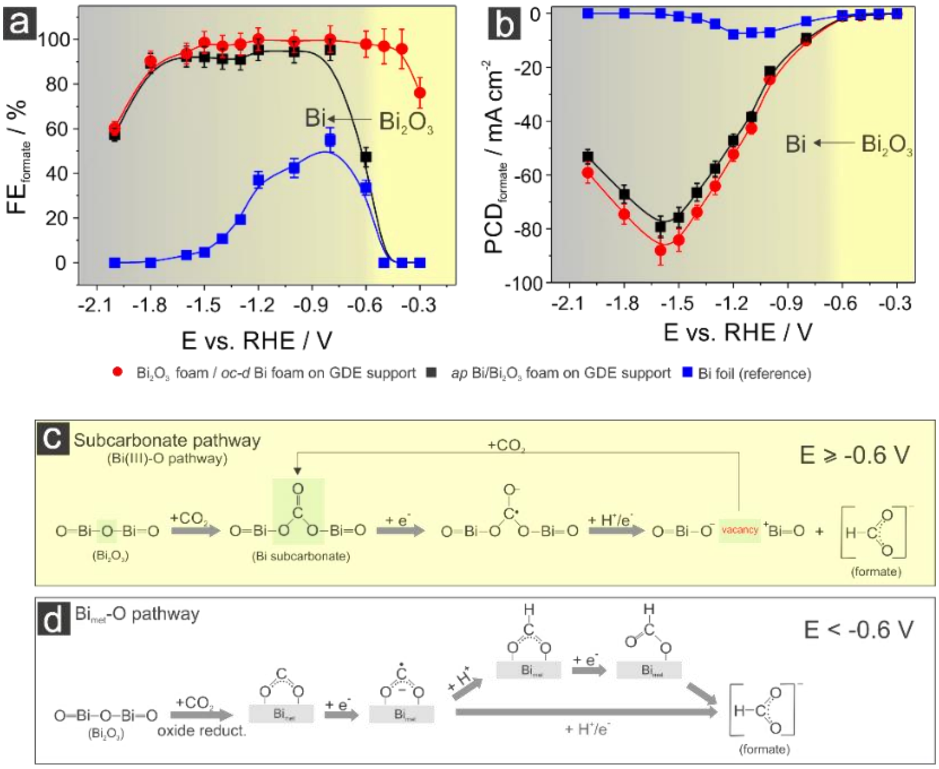

Figure 3.3. a) Product distribution of ec-CO_2R in terms of FE *vs.* E (V *vs.* RHE); results of the Bi_2O_3-GDE foam (red) are compared with the ap-Bi/Bi_xO_y foam (black) and a reference Bi foil catalyst (blue). b) Partial current densities for formate ($PCD_{formate}$) at different applied potentials. Note that all potentials are iR corrected. c) The subcarbonate reaction pathway for formate at low potentials. d) The Bi_{metal}–O reaction pathway at high potentials. Readapted with permission from *ACS Catal.* 2021, 11, 9, 4988–5003. Copyright 2021 American Chemical Society. [67]

Figures 3.3a and b illustrate the resulting ec-CO_2R product distribution in terms of the faradaic efficiency (FE; %) and the partial current densities (PCDs; mA cm^{-2}) versus the applied potential. The only electrolysis products are gaseous hydrogen (H_2) and non-volatile formate. For clarity, only the data for formate are presented.

From Figure 3.3a, it is clear that there are only small differences between ap-Bi/Bi_xO_y and Bi_2O_3-GDE catalysts at high overpotentials between –0.9 V to –2.0 V *vs.* RHE, where both catalysts exhibit $FE_{formate}$ that reaches ∼100%. However, substantial differences appear at low overpotentials; specially in the range of –0.3 V to –0.8 V *vs.* RHE. The most notable difference is the high formate efficiency for the thermally annealed sample (Bi_2O_3-GDE), reaching almost 100% in its low overpotential window (Figure 3.3a). This observation is indicative of a second reaction pathway for formate formation on the oxide-subcarbonate composite at these low overpotentials that is not active on the ap-Bi/Bi_xO_y catalyst. This statement was supported with the potential-dependent *operando* Raman spectroscopy, which it will be discussed in section 3.1.1. For more details, please see **Publication 2**.

Another important aspect is that the maximum PCDs for formate in the ap-Bi/Bi_xO_y and the oxide/carbonate-derived bismuth catalyst (*oc-d* Bi, a term referring to the Bi_2O_3-GDE catalyst after electrolysis) reached values of $PCD_{formate} = –75.8 \text{ mA cm}^{-2}$ and $PCD_{formate} = – 84.1 \text{ mA cm}^{- 2}$ at –1.5 V *vs.* RHE, respectively (Figure 3.3b). These values have not been reported in H-type cell systems.[67]

Figure 3.3c illustrates the proposed 'subcarbonate' reaction pathway for formate production on the composite material, assuming that the Bi oxide/carbonate species plays an active role in the CO_2 conversion at these low overpotentials. These subcarbonate species form in the CO_2–saturated bicarbonate solution through the partial surface exchange of oxidic Bi–O or Bi–OH species by Bi–CO_3–Bi ensembles according to Equation 25.[67]

$$Bi_2O_3 + CO_2 \rightarrow (BiO)_2CO_3 \qquad (25)$$

And Figure 3.3d shows the $Bi_{metallic}$–O reaction pathway for high overpotentials.[29] Note that, an alternative reaction pathway has also been proposed for the metallic Bi catalysts that involves Bi–C bond formation and the appearance of *COOH intermediates.[62, 116-118] For more details, please see **Publication 2**.

In addition to activity and selectivity, the durability of a catalyst plays an important role in its performance, specially over extended electrolysis time. To demonstrate the stability of the Bi_2O_3-GDE foam catalyst, two extended potentiostatic electrolysis experiments were carried out under experimental conditions where either the subcarbonate pathway or the $Bi_{metallic}$–O pathway were dominant at applied potentials of –0.6 V and –1.0 V *vs.* RHE for 100 h. These experiments showed that the catalyst studied in this work was highly stable under ec-CO_2R conditions.[67] Identical location SEM was used to study the changes in morphology of the catalyst before and after thermal treatment as well as after the electrolysis experiments. These studies show that on a µm-length scale, the "primary" macropore structure and the dendritic nature of the pore sidewalls were clearly preserved even after 45 min of electrolysis at –0.6 V *vs.* RHE. However, substantial changes occur on a nm-length scale because of the appearance of smaller nanoparticles (<10 nm) on the surface of the dendrite. For more details about the long-term experiment and IL-SEM, please see **Publication 2**.

3.1.1. Potential-dependent *operando* Raman Spectroscopy

Metal oxides have attracted considerable attention amongst researchers because they exhibit better activity than their metallic counterparts during ec-CO_2R.[119] For example, Su et al. reported that the synthetized Bi(III) nanosheets exhibited higher selectivity and partial current densities for formate compared to bulk Bi.[107] Similarly, Deng et al. reported that bismuth oxides exhibited improved selectivity and activity for CO_2 reduction to formate compared to metallic Bi spheres.[120] However, the role of the oxide in the process remains a subject of debate because the oxides can undergo structural and chemical changes during ec-CO_2R as reported by Dutta et al.[121] In the work done in this thesis, Raman spectroscopy was applied as a suitable technique to study the changes in the oxidation state of the Bi_2O_3 foam catalyst during the electrochemical CO_2 reduction.

Figure 3.4a compares the *ex situ* Raman spectra of the ap-Bi/Bi_xO_y and oxidized Bi_2O_3 foam catalysts as well as the commercial $Bi_2O_2CO_3$. In the ap-Bi/Bi_xO_y foam spectrum, only two bands at 119 cm^{-1} and 313 cm^{-1} were present with low intensities, corresponding to the vibrational modes of bismuth oxide; these formed because of surface oxidation as a consequence of exposure to air. In contrast, multiple Raman bands were observed in the Bi_2O_3 foam spectrum. These corresponded to the symmetric vibration mode of –Bi(III)– at 119 cm^{-1}, the vibrational modes of mononuclear –O– entities at 313 cm^{-1}, and the –Bi–O stretching mode at 475 cm^{-1}.[67, 122] Only one high-intensity band at 162 cm^{-1} was observed in the commercial $Bi_2O_2CO_3$, which corresponds to the subcarbonate fingerprint.[123]

The potential-dependent *operando* Raman experiments were performed to study the changes in the oxidation state of the Bi_2O_3 foam catalyst during ec-CO_2R (Figure 3.4b). The experiment was carried out in a Raman cell in a CO_2-saturated solution of 0.5 M $KHCO_3$ over a potential window between OCP and –1.0 V *vs.* RHE.[67, 121] It was found that all characteristic bands from the Bi_2O_3 foam (Figure 3.4a) were still preserved under these reaction conditions. However, a new band at 162 cm^{-1} (Figure 3.4b), corresponding to the bismuth subcarbonate, became the dominant band feature during the *operando* Raman experiments. This subcarbonate species can be regarded as the precursors of CO_2 electroreduction at low overpotentials (subcarbonate reaction pathway, please see Figure 3.3c).

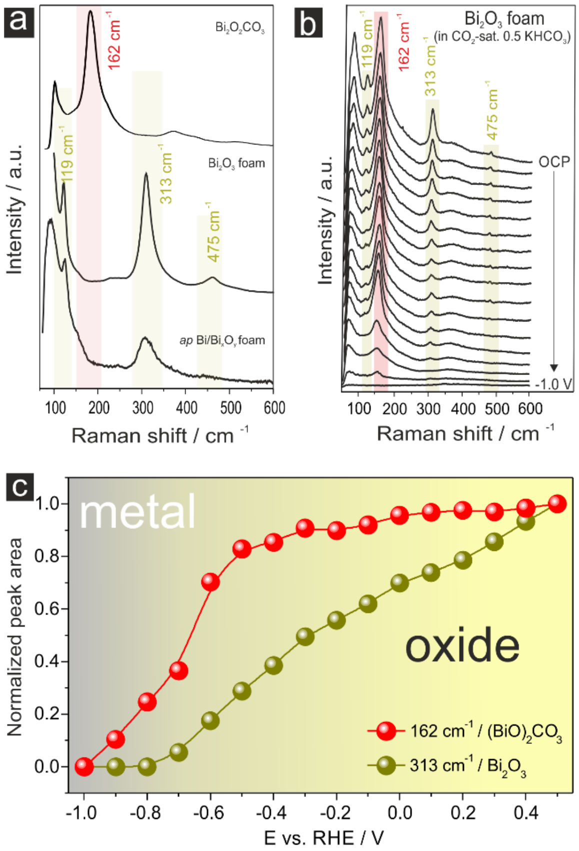

Figure 3.4. (a) *Ex situ* Raman spectrum of the ap-Bi/Bi$_x$O$_y$ and Bi$_2$O$_3$ foam catalysts and commercial Bi$_2$O$_2$CO$_3$ under dry conditions. b) A series of potential-dependent *operando* Raman spectra showing the oxide-subcarbonate-metal transition during ec-CO$_2$R, and c) Potential-dependent integrated intensities of the Raman bands at 162 cm^{-1} and 313 cm^{-1}, respectively. Readapted with permission from *ACS Catal.* 2021, 11, 9, 4988–5003. Copyright 2021 American Chemical Society. [67]

Both the oxide and subcarbonate species followed the same trend of decreasing intensities as the applied potentials increased. This suggests that the oxide-metal transition of the Bi_2O_3 foam is completed at approximately –0.8 V *vs.* RHE, while the subcarbonate band appeared to be even more stable than the corresponding oxides. To better illustrate the oxidation state changes of the Bi_2O_3 foam catalyst, Figure 3.4c shows the results of a quantitative analysis of the oxide-subcarbonate-metal (potential-dependent) transition based on the integrated intensities of the Raman features at 313 cm^{-1} (Bi_2O_3, fingerprint) and 162 cm^{-2} (subcarbonate, fingerprint).[67]

The oxide/subcarbonate-metal transition in the Bi_2O_3 foam catalyst during ec-CO_2R can also be monitored as a function of time and the applied potential by visual inspection at two different potentials. As expected, this compositional transition is faster at –0.6 V *vs.* RHE than at –0.3 V *vs.* RHE. For more details, please see **Publication 2**.

3.2. Electrochemical Performance of Bi_2O_3-GDE Catalyst in a Flow Cell Electrolyser

In this section, the Bi_2O_3-GDE foam catalyst studied in the H-type cell was transferred to a flow cell electrolyser to study the performance and stability of the Bi_2O_3/$Bi_2O_2CO_3$-GDE catalyst under ec- CO_2R conditions, as well as to increasing the current densities obtained in H-type cell studies.

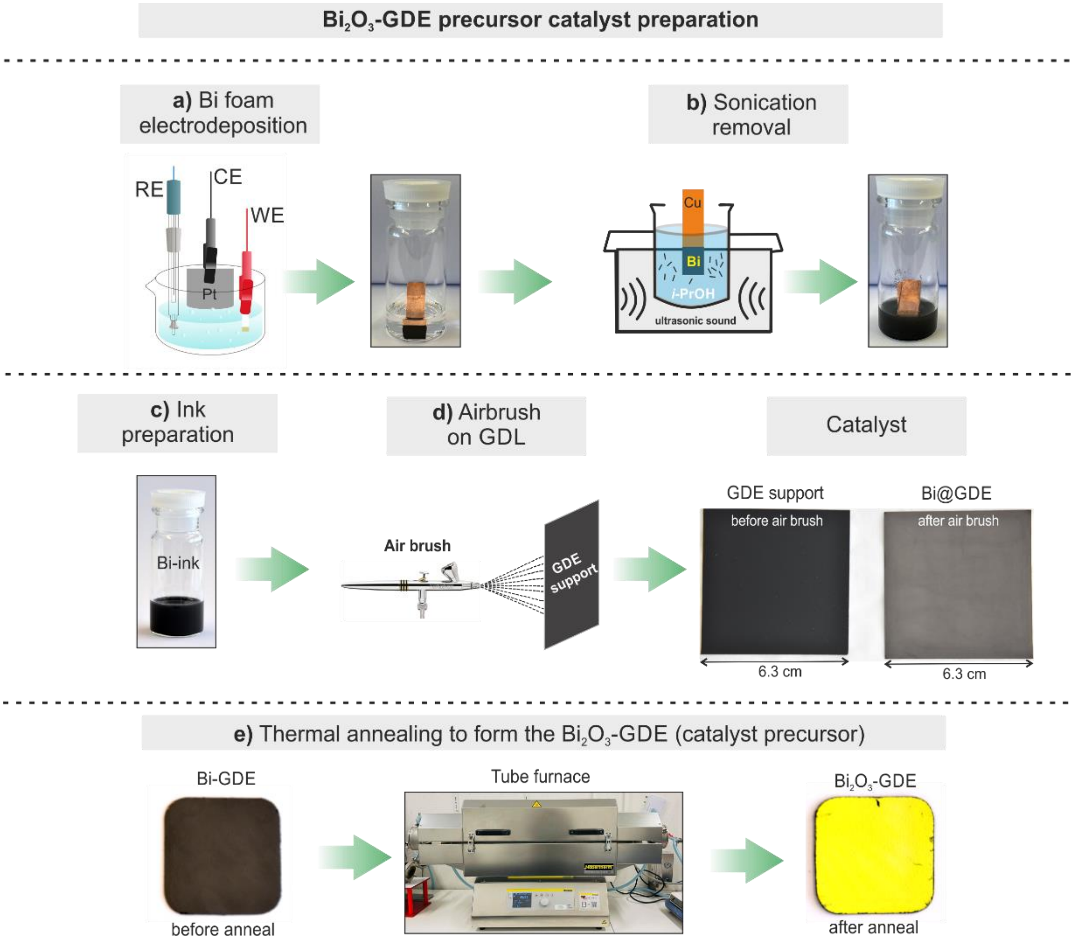

Figure 3.5. Schematic description of the step-by-step preparation of the Bi_2O_3-film on gas diffusion layer (GDL) support used in the fluidic electrolyser. Readapted with permission from *ACS Catal.* 2022, 12, 17, 10872-10886. Copyright 2022 American Chemical Society. [131]

Due to the scalability of flow cell systems, the methodology for Bi_2O_3-GDE catalyst preparation was adjusted. Figure 3.5 shows the new approach to preparing the ink-based catalyst:

a) Bismuth foam is electrodeposited on Cu foil support using the DHBT electrodeposition approach.
b) Mechanical removal after electrodeposition: the as-prepared Bi foam electrodes were transferred to a small vial and sonicated in the presence of isopropanol for 1 min to release all of the foam from the Cu foil support (24 electrodes of 1 cm^2 area were used to obtain approximately 90 mg of catalyst).

c) Ink preparation: the catalyst powder was sonicated for 30 min in 19.5 mL of isopropanol and 0.5 mL of Nafion.

d) A volume of 17 mL of the ink was spray-coated onto the GDL support. The loading of the catalyst was 1.06 mg/cm^{-2} as determined by inductively coupled plasma mass spectrometry (ICP-MS).

e) Thermal annealing at 350 °C for 6 h to form the Bi_2O_3-GDE (catalyst precursor).

The morphological structure of the ap-Bi/Bi_xO_y-film on GDE (ap-Bi-GDE) and the Bi_2O_3-film on GDE (Bi_2O_3-GDE) electrodes deposited by the airbrush was analysed by high-resolution scanning electron microscopy (HR-SEM). Figure 3.6 presents the SEM images for the ap-Bi-GDE and the Bi_2O_3-GDE. In contrast to the electrodeposited Bi foams, the catalyst no longer has a very well-distributed pore structure (Figure 3.6a and c). However, the dendritic nature of the Bi catalyst was preserved even after the catalyst had been subjected to 30 min of sonication. Most importantly, there were no morphological changes to the dendritic structure of the samples before and after thermal treatment (Figures 3.6b and d, respectively). Figure 3.6e shows a cross-sectional view of the Bi_2O_3-GDE catalyst, revealing that the thickness of the catalyst layer was approximately 28 μm. Figure 3.6f presents the EDX mapping of the bismuth oxide (yellow) on the GDL support material (red). [131] For more details, please see **Publication 1**.

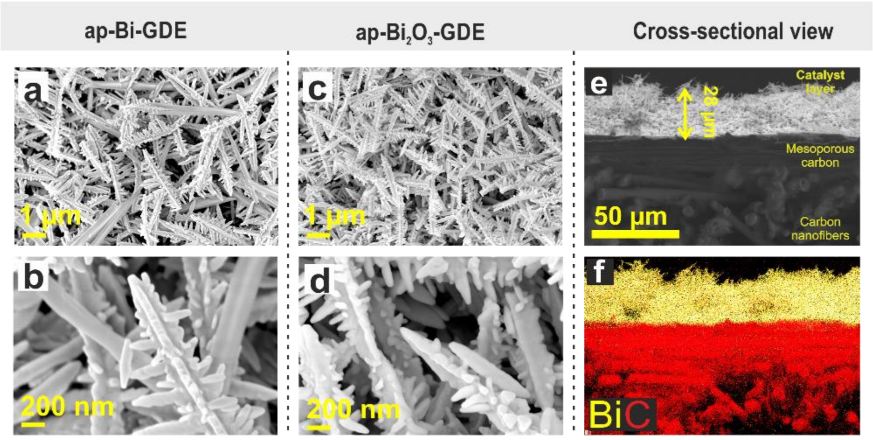

Figure 3.6. a-b) SEM images of the ap-Bi-GDE, c-d) SEM images of the Bi_2O_3-GDE (after thermal treatment) and the e-f) cross-sectional view and EDX mapping of the Bi_2O_3-GDE. Readapted with permission from *ACS Catal.* 2022, 12, 17, 10872-10886. Copyright 2022 American Chemical Society. [131]

The electrochemical performance of the new Bi_2O_3-GDE film catalyst for ec-CO_2R was studied in a fluidic electrolyser system. Figures 3.7a and b show an exploded view of the electrolyser as well as the assembled cell used in this work, respectively.

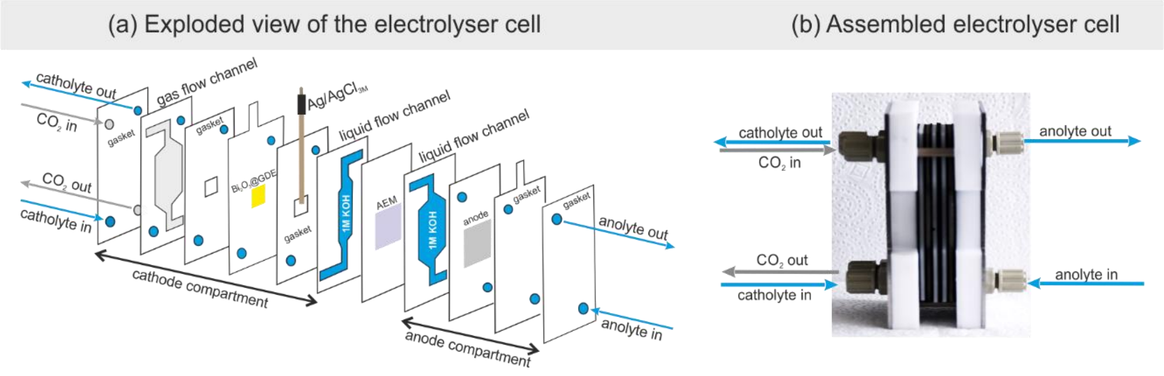
(a) Exploded view of the electrolyser cell

(b) Assembled electrolyser cell

Figure 3.7. a) Exploded view of the fluidic electrolyser cell used in this thesis. b) Assembled electrolyser cell. Readapted with permission from *ACS Catal.* 2022, 12, 17, 10872-10886. Copyright 2022. American Chemical Society.[131]

The electrolyte used in both compartments was passed through the electrolyte-flow channels to external containers using a peristaltic pump at a flow rate of 3.5 mL min^{-1}. Note that in this cell configuration, the anolyte was recirculated during the entire experiment, while the catholyte was not recirculated as it could promote formate crossover from the cathode to the anode compartment, where it can be re-oxidized.[124] The CO_2 gas flow was 25 mL min^{-1}, and it was controlled by a mass flowmeter. For more details about the experiments, please see **Publication 1**.[131]

The gaseous products were quantified during electrolysis by online gas chromatography (GC), while the liquid products were quantified after the electrolysis experiments by ion-exchange chromatography (IC). Over most of the potential window, the only detectable products of any significance were formate and H_2, with a very small amount of CO (~0.85%). Figure 3.8 shows a digital image of the installed fluidic electrolyser used in this work.

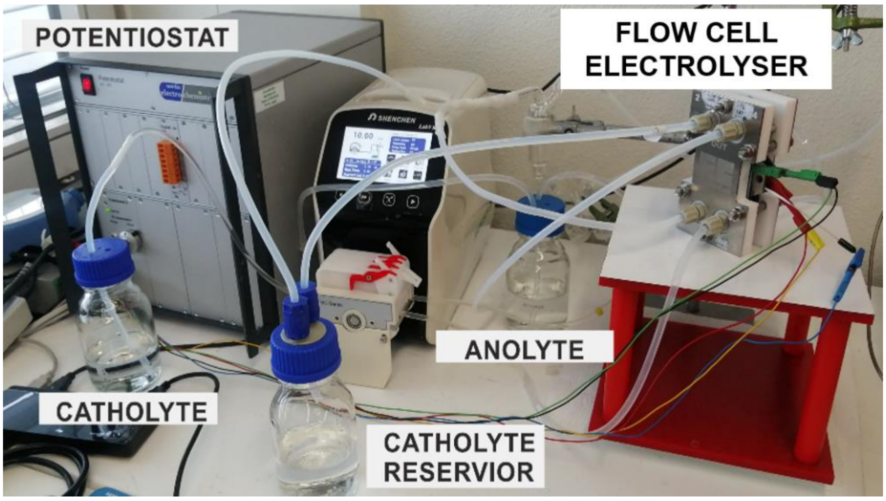

Figure 3.8. Digital image of the fluidic electrolyser system.

It is well known that in aqueous conditions, the ec-CO_2R is strongly influenced by the pH. Some studies have shown that the use of high-conductivity alkaline electrolytes, such as KOH, could suppress the HER and reduce ohmic losses.[71, 87] However, recent reports have demonstrated that the use of strongly acidic conditions (pH 1.0) with alkali cations can also suppressed HER during ec-CO_2R.[124-125]

In this work, the electrolyte used was either 1M KOH or 5 M KOH to evaluate the electrochemical performance of Bi_2O_3-GDE during ec-CO_2R. Figure 3.9 presents the product distribution of the Bi_2O_3-GDE in a flow cell electrolyser in terms of FE and PCD for both electrolyte concentrations.

Figure 3.9a shows an increase in $FE_{formate}$ when more negative potentials are applied, reaching a maximum $FE_{formate}$ = 97.35% at –0.8 V *vs.* RHE. These high FE values remain stable until – 1.4 V *vs.* RHE ($FE_{formate =}$ 84.5%). At more negative potentials, there is a decrease in FE, reaching $FE_{formate}$ = 62% at –2.5 V *vs.* RHE; this is accompanied by a complementary increase in H_2 production (FE_{H2} = 42%). Note that the partial flooding of the working electrode could be the main factor that promotes the HER. Similarly, Figure 3.9b shows that the PCDs follow the increasing trend at more cathodic potentials, with a maximum $PCD_{formate}$ = –441.23 mA cm^{-2} at –2.5 V *vs.* RHE (total current of –747.29 mA cm^{-2}). These current values are very promising for industrial applications. [131]

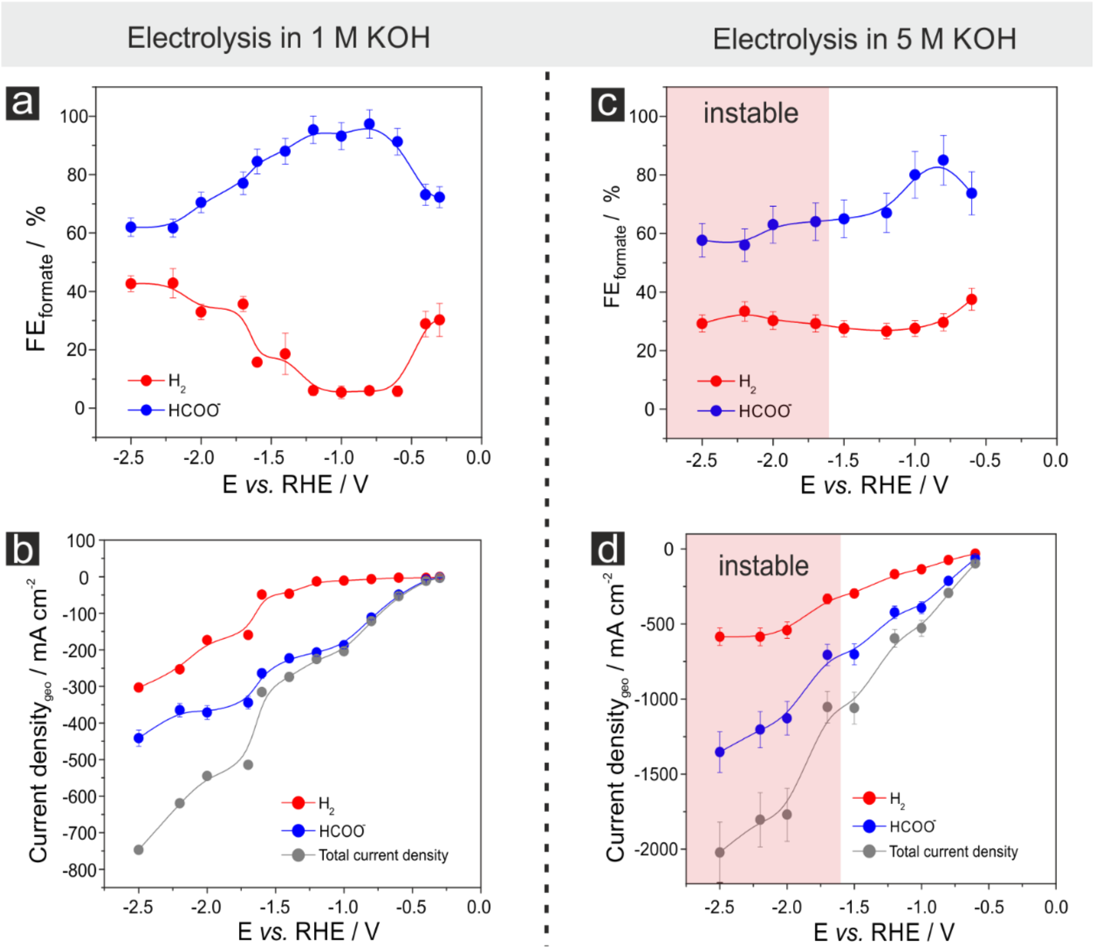

Figure 3.9. a and b) FE and PCD *vs.* RHE in 1 M KOH. And c and d) FE and PCD *vs.* RHE in 5 M KOH. The potentiostatic experiments were performed during 1 h of continuous electrolysis. A new Bi_2O_3-GDE electrode was used for each potential. For the sake of clarity, only the data for formate and H_2 are plotted. Readapted with permission from *ACS Catal.* 2022, 12, 17, 10872-10886. Copyright 2022 American Chemical Society. [131]

Highly concentrated KOH solutions have been reported to increase the electrolyte conductivity and reduce the activation energy barriers in ec-CO_2R.[126-127] Hence, to further improve the performance of ec-CO_2R in this work, a 5 M KOH electrolyte solution was also used. Figure 3.9c–d shows the electrochemical performance of the Bi_2O_3-GDE film catalyst in a 5 M KOH electrolyte solution. Both the FE and the PCDs (Figures 3.9c and d, respectively) for formate were different, with a significant decrease in FE compared to the experiments performed in 1 M KOH. However, the formate selectivity was maintained, with a maximum $FE_{formate}$ = 85% at – 0.8 V *vs.* RHE, as well as a gradual decrease in $FE_{formate}$ at more cathodic potentials ($FE_{formate}$ = 57.7% at –2.5 V *vs.* RHE). Interestingly, the total current density increased, with a maximum value of $PCD_{formate}$ = –1.35 A cm^{-2} at –2.5 V *vs.* RHE (total current density of –1938.3 A cm^{-2}).[131] For more details about these experiments, please see **Publication 1**.

As expected, it is possible to achieve high current densities while maintaining good formate selectivity when using extremely high concentrations of KOH. However, the HER increases drastically when high cathodic potentials are applied; as a result, the catalyst exhibits mechanical instability, which contributes to its detachment from the GDL support after 10 min of electrolysis. It should be noted that this mechanical instability is only present in the potential range between –1.6 V and –2.5 V *vs.* RHE. In contrast, the catalyst performs well under high alkaline conditions during 30 min of electrolysis in the potential range of –0.6 V to –1.5 V *vs.* RHE. In light of these findings, I will only focus on the data from the 1 M KOH electrolyte solution in the following discussions. [131]

3.2.1. *Ex situ* XRD and Raman Characterisation

Ex situ characterization techniques were used to better understand the high activity and selectivity of the Bi_2O_3-GDE towards formate production at high current densities. Figure 3.10 shows the results of potential-dependent *ex situ* XRD and Raman spectroscopy under CO_2 gas flow conditions, which demonstrated the predominant transformation of the oxidic Bi_2O_3 precursor catalyst into a bismuth subcarbonate phase (Equation 25). Note that the standard patterns for metallic Bi, Bi_2O_3, and $Bi_2O_2CO_3$ are also shown for comparison purposes. The *ex situ* XRD analysis revealed that in the potential range of –0.6 to –1.5 V *vs.* RHE, most of the diffractions peaks can be attributed to $Bi_2O_2CO_3$, with minor contributions from metallic Bi due to the applied cathodic potential. These results suggest that Bi_2O_3-GDE is not the actual catalyst during ec-CO_2R; instead, $Bi_2O_2CO_3$ is the primary catalyst involved in this reaction. The $Bi_2O_2CO_3$ is formed *in situ* when CO_2 gas, Bi_2O_3 (precursor catalyst), and the 1 M KOH electrolyte are in contact at the three-phase boundary within the flow cell electrolyser. However, when more cathodic potentials are applied from –1.6 V to –2.0 V *vs.* RHE, the features assigned to $Bi_2O_2CO_3$ disappear completely; instead, only features corresponding to metallic Bi are present (Figure 3.10a). [131] For more details, please see **Publication 1**.

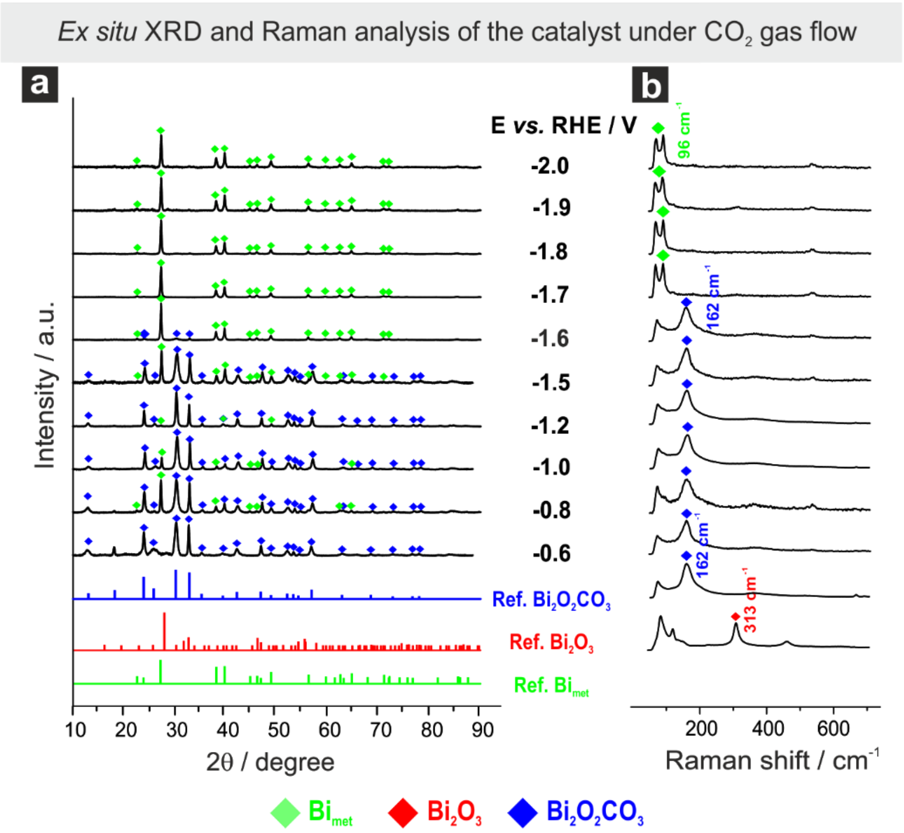

Figure 3.10. a) *Ex situ* XRD and b) *ex situ* Raman potential-dependent in the presence of CO_2 gas flow. The corresponding metallic Bi, Bi_2O_3, and $Bi_2O_2CO_3$ references for the XRD are shown (JPDS: 85-1331, 078-1793 and 41-1488, respectively), as well as the corresponding Raman references (purchased by Sigma Aldrich). Readapted with permission from *ACS Catal.* 2022, 12, 17, 10872-10886. Copyright 2022 American Chemical Society. [131]

Figure 3.10b shows the potential-dependent *ex situ* Raman spectra of the same samples as well as their corresponding references (Bi_2O_3 and $Bi_2O_2CO_3$). The peak observed at 162 cm^{-1} corresponds to the fingerprint of bismuth subcarbonate formed *in situ* during ec-CO_2R, which remains stable in the potential range between –0.6 V and –1.6 V *vs.* RHE. However, when more cathodic potentials are applied, the carbonate species is reduced, leaving only the peaks corresponding to metallic bismuth (64 and 96 cm^{-1}). Note that only $Bi_2O_2CO_3$ is detected in the potential range of –0.6 to –1.6 V *vs.* RHE, with no metallic bismuth present. As reported by Dutta et al. on the basis of oxidic Cu foams, [102] the (minor) deviations between XRD and Raman analyses likely originate from the different probing depths of these techniques. Raman spectroscopy is typically considered to be more surface-sensitive than XRD, which probes the entire three-dimensional "bulk" of the porous catalyst film. [102]

Both experiments demonstrate that the subcarbonate reaction pathway for formate formation (Figure 3.3c), which has already been described for H-type cells,[67] is also relevant for ec-CO_2R performed in a flow cell electrolyser. More importantly, these experiments show that the subcarbonate phase remains stable even at extremely cathodic potentials of –1.5 V *vs.* RHE. These results indicate that the CO_2 gas supply is the key factor for the stabilization of Bi(III) in the subcarbonate phase during ec-CO_2R. For more details, please see **Publication 1**. [131]

To confirm that the presence of CO_2 is essential for the formation of $Bi_2O_2CO_3$, potential-dependent *ex situ* XRD and Raman spectroscopy were performed in CO_2/Ar gas flow. For each potential, the first 30 min of electrolysis was performed in the presence of CO_2 and then changed to Ar for an additional 30 min (total electrolysis time 1 h). Figure 3.11 shows that only metallic Bi was present after electrolysis in both experiments, even at low potentials; this confirms that the formation of $Bi_2O_2CO_3$ (main catalyst) takes place only in the presence of CO_2.

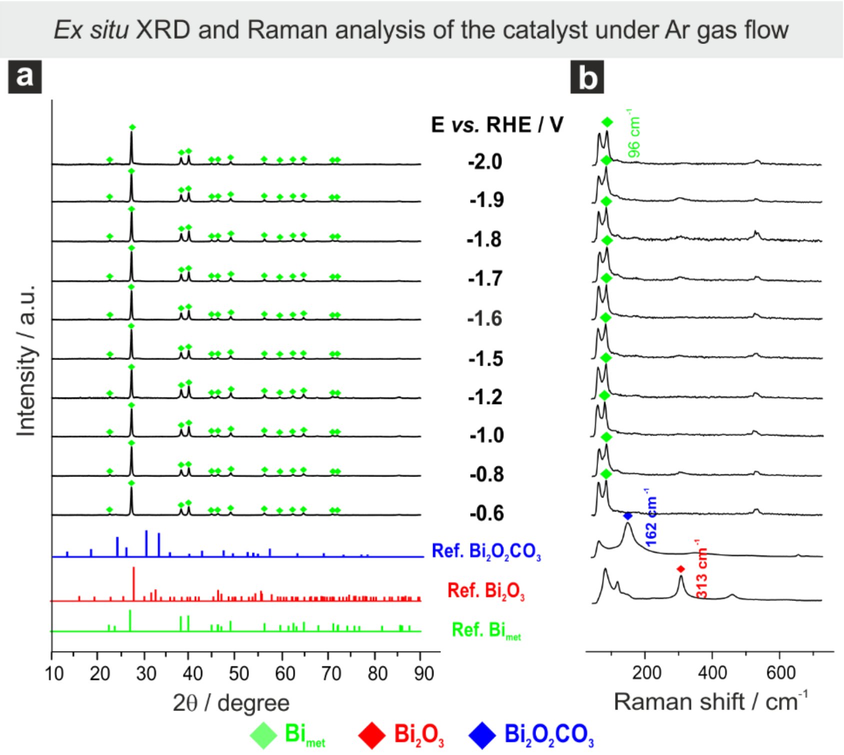

Figure 3.11. a) *Ex situ* XRD and b) *ex situ* Raman potential-dependent in presence of CO_2 (30 min) and Ar (30 min). The corresponding metallic Bi, Bi_2O_3, and $Bi_2O_2CO_3$ references for the XRD are shown (JPDS: 85-1331, 078-1793 and 41-1488, respectively), as well as the corresponding Raman references. Readapted with permission from *ACS Catal.* 2022, 12, 17, 10872-10886. Copyright 2022 American Chemical Society. [131]

To gain more insight into the kinetics of the $Bi_2O_2CO_3$ formation, selected potential-dependent *ex situ* XRD and Raman spectroscopy were performed at –1.0 V *vs.* RHE and at open circuit potential (OCP). The experiments at applied potential suggested a rapid transformation of the Bi_2O_3 into a $Bi_2O_2CO_3$ in the initial stage of CO_2 electrolysis (after 5 min). In addition, the experiments at OCP revealed that the exposure of the Bi_2O_3 precursor to CO_2 in the presence of 1 M KOH electrolyte solution was sufficient to initiate the subcarbonate formation. However, at OCP conditions the transformation of Bi_2O_3 to $Bi_2O_2CO_3$ is slower compared to applied potential. For more details about these experiments, please see **Publication 1**.

To support our hypothesis that $Bi_2O_2CO_3$ is stabilized by CO_2, potential-dependent *in situ* Raman spectroscopy was performed in the absence of CO_2 gas supply. Under such reaction conditions, the $Bi_2O_2CO_3$ demonstrated higher stability against electroreduction compared to the corresponding oxidic precursor. It is important to mention that the observed reduction potential of $Bi_2O_2CO_3$ and Bi_2O_3 was consistent with the Bi/water Pourbaix diagram. For more details, please see **Publication 1**.

3.2.2. Post-electrolysis SEM

The morphological changes involved in the transformation of Bi_2O_3-GDE (precursor catalyst) to $Bi_2O_2CO_3$-GDE (main catalyst) were studied before and after electrolysis at three different potentials. Figure 3.12 shows SEM images and contact angle measurements for the catalyst in their respective preparation stages. The SEM images for the ap-Bi-GDE and Bi_2O_3 show that there were no significant changes at the µm- and nm-scales (Figure 3.12a–e). The only remarkable difference between these two samples was the contact angle (Figure 3.12c and f), which was 157.7° for the ap-Bi-GDE and 28.2° for the fully oxidized Bi_2O_3-GDE. This was consistent with the fact that Bi_2O_3-GDE becomes more hydrophilic after thermal treatment.[128, 131] For more details, please see **Publication 1**.

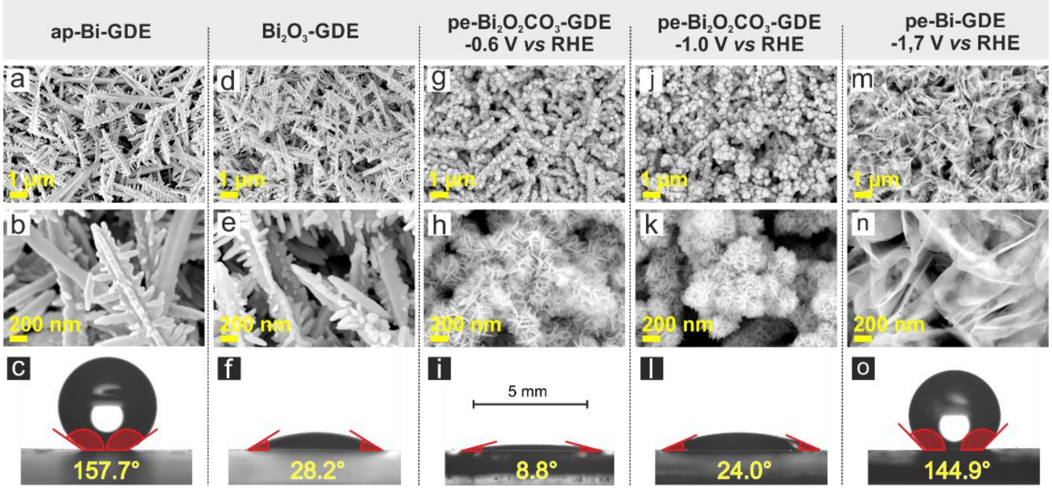

Figure 3.12. SEM and contact angle measurements images for the catalyst at specific preparation stages. a–c) ap-Bi-GDE, d–f) Bi_2O_3-GDE, g–i) $Bi_2O_2CO_3$-GDE after electrolysis at −0.6 V, j–l) $Bi_2O_2CO_3$-GDE after electrolysis at −1.0 V, and m–o) $Bi_2O_2CO_3$-GDE after electrolysis at −1.7 V *vs.* RHE, respectively. Reprinted with permission from *ACS Catal.* 2022, 12, 17, 10872-10886. Copyright 2022 American Chemical Society.[131]

There are significant morphological differences once cathodic potentials are applied (Figure 3.12g–n). Note that according to the *ex situ* XRD and Raman experiments at –0.6 V and –1.0 V *vs.* RHE, the main catalyst is the bismuth subcarbonate, while only metallic bismuth is present at –1.7 V *vs.* RHE. It is clear that the µm- and nm-scale morphology of the electrodes changed drastically for the three potentials chosen: the dendrite structure no longer exists; instead, a compact aggregate of subcarbonate nano-sheets is visible.

Another important difference is in the contact angle, which tends to increase gradually as the applied potential increases. The contact angle was found to be 8.8° at –0.6 V *vs.* RHE (Figure 3.12i) and 24.0° at –1.0 V *vs.* RHE (Figure 3.12l); this is due to the pronounced hydrophilic characteristics of bismuth subcarbonate.

The opposite was observed at –1.7 V *vs.* RHE, where only metallic Bi was present; the initial hydrophobic surface properties were recovered, with a contact angle of 144.9° (Figure 3.12o, 12.8° less than for the ap-Bi-GDE). The contact angle measurements suggest a facile electrolyte penetration on the catalyst layer when the Bi_2O_3 precursor was brought into contact with the aqueous electrolyte. [128, 131]

It should be noted that the high hydrophilicity of the catalyst could promote a degree of electrode flooding and lead to a reduction in the selectivity towards CO_2 products. During flooding, the pores in the GDL support become filled with the electrolyte, which not only blocks CO_2 from reaching the catalyst but also encourages salt precipitation, which further obstructs the pore walls of the GDE.[129] To monitor the electrolyte (KOH) penetration depth in the $Bi_2O_2CO_3$-GDE catalyst, EDX elemental analysis mapping was performed after the electrochemical experiments. The element mapping of the electrolyte's cation was performed by analysing the cross-sectional SEM of $Bi_2O_2CO_3$-GDE electrodes after electrolysis at potentials of –1.0 V and –1.7 V *vs.* RHE, as well as for Bi_2O_3-GDE.[95-96, 130] For more details about these experiments, please see **Publication 1**.

3.2.3. X-ray diffraction computed tomography (XRD-CT)

X-ray diffraction computed tomography (XRD-CT) was another technique employed in order to study the spacial depth distribution of the $Bi_2O_2CO_3$ and metallic Bi in the sample bulk. The maps in the Figure 3.13 illustrate the location of $Bi_2O_2CO_3$ (left column) and metallic Bi (right column) in the catalyst layer after 1 h of electrolysis at different applied potentials from –1.0 V to –1.8 V *vs.* RHE. To determine the concentration profile of $Bi_2O_2CO_3$ and metallic Bi as a function of depth, the intensities of the (1,0,3) and (0,1,3) peaks at $2\theta = 3.01°$ for $Bi_2O_2CO_3$, and the intensity of the (2,–1,0) peak at 2θ = 3.91° for metallic Bi were integrated in the XRD pattern corresponding to each voxel. From these experiments, it was clear that exist a homogeneous distribution of both phases as a function of the catalyst layer depth. Figure 3.13 also shows the coexistence of $Bi_2O_2CO_3$ and metallic Bi at the same positions in the GDE. Important to note that, a notable increase in the metallic Bi phase is observed at the expense of the carbonate phase at increasing the applied potentials. This experiment is consistent with the *ex situ* XRD and Raman spectroscopy, highlighting the preferential formation of the subcarbonate phase formation at low potentials as well as the continuous increase in the metallic phase at high potentials. [131] For more details, please see **Publication 1**.

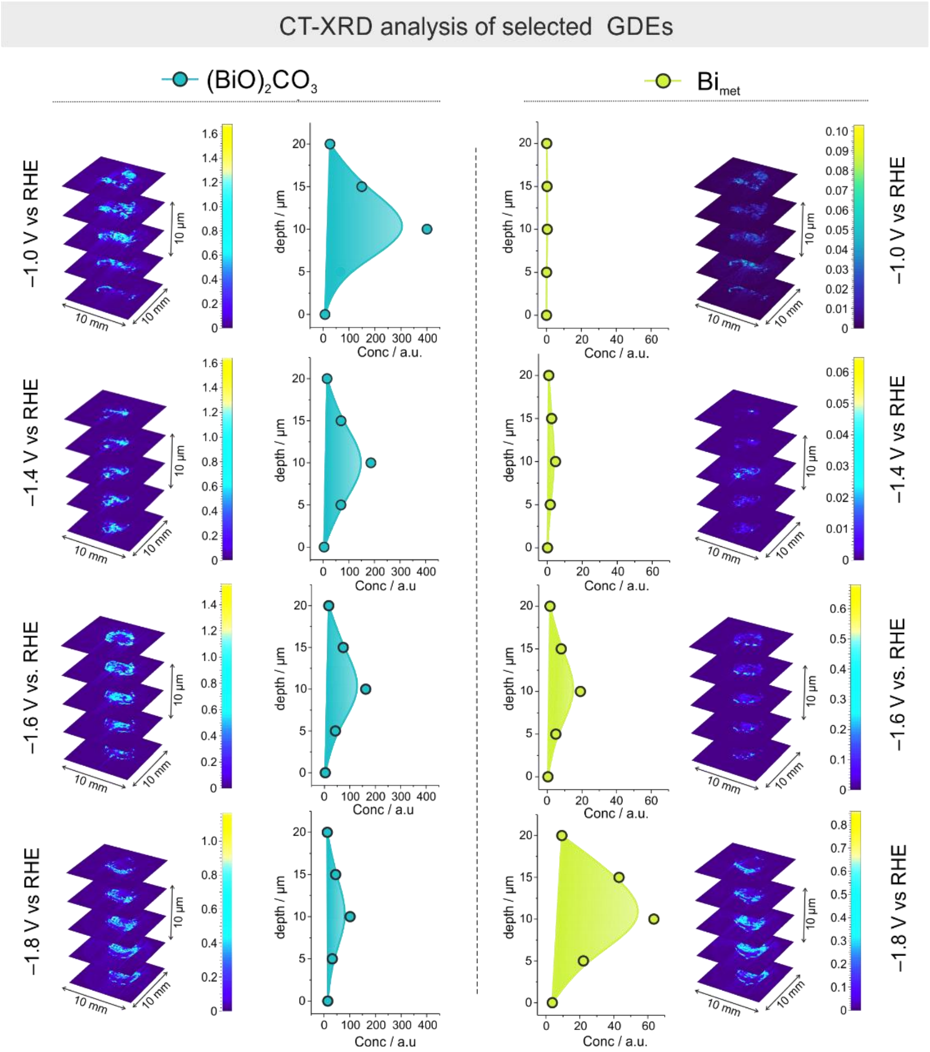

Figure 3.13. XRD-CT scans of the catalyst layer after ec-CO_2R at different applied potentials. The left column represents the spatial phase distribution of $Bi_2O_2CO_3$ at different depth profiles in selected areas of the sample, while, the right column represents the distribution of the metallic Bi phase. Reprinted with permission from *ACS Catal.* 2022, 12, 17, 10872-10886. Copyright 2022 American Chemical Society. [131]

4. CONCLUSION

The synthesis of bismuth foam catalysts was successfully performed on carbon cloth (GDL) using the dynamic hydrogen bubble template electrodeposition approach. After the metal deposition, the Bi foam was thermally treated at 300 °C for 12 h hours in the presence of air, which transformed the ap-Bi/Bi_xO_y foam catalyst into fully oxidised Bi_2O_3 foam. The initial electrochemical studies were performed in an H-type cell system, which revealed that the ap-Bi/Bi_xO_y and Bi_2O_3 foam catalysts exhibited high activity towards formate formation, reaching FEs close to 100% in the potential range of –0.7 V to –1.5 V *vs.* RHE. Notably, the Bi_2O_3 foam catalyst exhibited higher FEs at lower cathodic potentials compared to the ap-Bi/Bi_xO_y foam (from –0.3 V to –0.6 V *vs.* RHE). In addition, high partial current densities for formate (–84.1 mA cm^{-2}) were achieved in the H-type cells when using the Bi_2O_3 foam catalyst, which has not previously been reported. Complementary SEM analysis before and after electrolysis revealed a slight change in the nm-length scale of the catalyst structure, while no morphological alterations were observed at the µm-length scale.

For the first time, the oxidation state of the Bi_2O_3 foam catalyst during electrochemical CO_2 reduction was monitored by *operando* Raman spectroscopy. This study revealed that the high selectivity towards formate is directly related to the coupling of two reaction pathways: the subcarbonate reaction pathway at low cathodic potentials and the $Bi_{metallic}$-O pathway at high potentials.

The Bi_2O_3-GDE catalyst for ec-CO_2R was transferred to a flow cell electrolyser, which required the establishment of a new method of catalyst preparation: airbrush coating on a GDL support. The SEM analysis confirmed that the dendritic nature of the catalyst remained intact. However, the high porosity of the foams was completely lost.

The electrochemical performance of the Bi_2O_3-GDE film catalyst in the fluidic electrolyser revealed high selectivity towards formate production with FEs close to 100 % and 85% in 1 M and 5 M KOH electrolyte solution, respectively. In terms of PCDs, a maximum $PCD_{formate}$ = – 441.2 mA cm^{-2} was achieved in 1 M KOH, and $PCD_{formate}$ = –1353.4 mA cm^{-2} (–1938.3 A cm^{-2} total current density) was achieved in 5 M KOH at –2.5 V *vs.* RHE.

Complementary *ex situ* XRD and Raman spectroscopy revealed that the so-called subcarbonate reaction pathway for formate production was still active at high current densities in the fluidic electrolyser. It was also demonstrated that the abundance of CO_2 gas supply stabilized the bismuth subcarbonate catalyst, in which Bi is present in an oxidation state of +3. The bismuth subcarbonate forms *in situ,* during ec-CO_2R, from an oxidic CO_2-absorbing Bi_2O_3 precursor catalyst. Additionally, potential-dependent *ex situ* XRD and Raman experiments conducted using an Ar gas supply confirmed that the presence of CO_2 is the key factor in the stabilization of the $Bi_2O_2CO_3$ catalyst.

Post-electrolysis SEM analysis demonstrated that the morphology of the catalyst is affected as a consequence of the subcarbonate formation during ec-CO_2R, with more compact aggregates of subcarbonate appearing in the samples. Finally, the use of *ex situ* XRD-CT techniques revealed the homogeneous distribution of $Bi_2O_2CO_3$ and metallic Bi phases in the catalyst layer at different applied potentials.

5. OUTLOOK

The catalyst studied in this work demonstrated excellent activity and selectivity for formate production while also exhibiting extremely high current densities, making it unique and promising for applications across an extensive range of studies that can provide more information about its behaviour in ec-CO_2R. However, certain topics remain unexplored, and certain issues identified during this study must be addressed. Topics for future research include the following:

- Improving the mechanical stability of the catalyst for long-term experiments in 5 M KOH electrolyte solution using various binders or a mixture of them.
- Studying the transition of the catalyst from Bi_2O_3 to $Bi_2O_2CO_3$ using *operando* Raman and XRD experiments under flow conditions.
- Extending these studies to other metal oxides (e.g., InO_x, SnO_x, etc.) to know if it is possible to form carbonate species that would be active in ec-CO_2R.

6. REFERENCES

1. Miller, C. E.; Brown, L. R., Near infrared spectroscopy of carbon dioxide I. 16O12C16O line positions. *Journal of Molecular Spectroscopy* **2004,** *228* (2), 329-354.

2. Hallegatte, S.; Przyluski, V.; Vogt-Schilb, A., Building world narratives for climate change impact, adaptation and vulnerability analyses. *Nature Climate Change* **2011,** *1* (3), 151-155.

3. National Park Service, How Do Greenhouse Gasses Alter the Planet? **2021, October 8**.

4. Solomon, S.; Plattner, G.-K.; Knutti, R.; Friedlingstein, P., Irreversible climate change due to carbon dioxide emissions. *Proceedings of the National Academy of Sciences* **2009,** *106* (6), 1704-1709.

5. Yusuf, R. O.; Noor, Z. Z.; Abba, A. H.; Hassan, M. A. A.; Din, M. F. M., Methane emission by sectors: A comprehensive review of emission sources and mitigation methods. *Renewable and Sustainable Energy Reviews* **2012,** *16* (7), 5059-5070.

6. Shi, W.; Chen, Q.; Zhang, J.; Liu, D.; Yi, Q.; Chen, Y.; Ma, H.; Hu, L., Nitrous oxide emissions from cascade hydropower reservoirs in the upper Mekong River. *Water Research* **2020,** *173*, 115582.

7. Lindley, A. A.; McCulloch, A., Regulating to reduce emissions of fluorinated greenhouse gases. *Journal of Fluorine Chemistry* **2005,** *126* (11), 1457-1462.

8. Oreskes, N., The Scientific Consensus on Climate Change. *Science* **2004,** *306* (5702), 1686-1686.

9. Le Quéré, C.; Moriarty, R.; Andrew, R. M.; Canadell, J. G.; Sitch, S.; Korsbakken, J. I.; Friedlingstein, P.; Peters, G. P.; Andres, R. J.; Boden, T. A.; Houghton, R. A.; House, J. I.; Keeling, R. F.; Tans, P.; Arneth, A.; Bakker, D. C. E.; Barbero, L.; Bopp, L.; Chang, J.; Chevallier, F.; Chini, L. P.; Ciais, P.; Fader, M.; Feely, R. A.; Gkritzalis, T.; Harris, I.; Hauck, J.; Ilyina, T.; Jain, A. K.; Kato, E.; Kitidis, V.; Klein Goldewijk, K.; Koven, C.; Landschützer, P.; Lauvset, S. K.; Lefèvre, N.; Lenton, A.; Lima, I. D.; Metzl, N.; Millero, F.; Munro, D. R.; Murata, A.; Nabel, J. E. M. S.; Nakaoka, S.; Nojiri, Y.; O'Brien, K.; Olsen, A.; Ono, T.; Pérez, F. F.; Pfeil, B.; Pierrot, D.; Poulter, B.; Rehder, G.; Rödenbeck, C.; Saito, S.; Schuster, U.; Schwinger, J.; Séférian, R.; Steinhoff, T.; Stocker, B. D.; Sutton, A. J.; Takahashi, T.; Tilbrook, B.; van der Laan-Luijkx, I. T.; van der Werf, G. R.; van Heuven, S.; Vandemark, D.; Viovy, N.; Wiltshire, A.; Zaehle, S.; Zeng, N., Global Carbon Budget 2015. *Earth Syst. Sci. Data* **2015,** *7* (2), 349-396.

10. United States Environmental Protection Agency, Sources of Greenhouse Gas Emissions. **2020, April 11**.

11. National Oceanic & Atmospheric Administration, Trends in Atmospheric Carbon Dioxide. **2020, June 5**.

12. Global Monitoring Laboratory Earth System Research Laboratories Trends in Atmospheric Carbon Dioxide. https://gml.noaa.gov/ccgg/trends/mlo.html.

13. Liu, Y.; Qiao, J., Introduction to CO_2 Electroreduction. 2016; pp 1-46.

14. Zheng, Y.; Zhang, W.; Li, Y.; Chen, J.; Yu, B.; Wang, J.; Zhang, L.; Zhang, J., Energy related CO_2 conversion and utilization: Advanced materials/nanomaterials, reaction mechanisms and technologies. *Nano Energy* **2017,** *40*, 512-539.

15. Song, C., Global challenges and strategies for control, conversion and utilization of CO_2 for sustainable development involving energy, catalysis, adsorption and chemical processing. *Catalysis Today* **2006,** *115* (1), 2-32.

16. Our World in Data, Energy,. **2018, July 12**.

17. Sakimoto, K. K.; Kornienko, N.; Yang, P., Cyborgian Material Design for Solar Fuel Production: The Emerging Photosynthetic Biohybrid Systems. *Accounts of Chemical Research* **2017,** *50* (3), 476-481.

18. Baena-Moreno, F. M.; Rodríguez-Galán, M.; Vega, F.; Alonso-Fariñas, B.; Vilches Arenas, L. F.; Navarrete, B., Carbon capture and utilization technologies: a literature review and recent advances. *Energy Sources, Part A: Recovery, Utilization, and Environmental Effects* **2019,** *41* (12), 1403-1433.

19. Armstrong, K.; Styring, P., Assessing the Potential of Utilization and Storage Strategies for Post-Combustion CO_2 Emissions Reduction. *Frontiers in Energy Research* **2015,** *3* (8).

20. Takht Ravanchi, M.; Sahebdelfar, S., Carbon dioxide capture and utilization in petrochemical industry: potentials and challenges. *Applied Petrochemical Research* **2014,** *4* (1), 63-77.

21. Whipple, D. T.; Kenis, P. J. A., Prospects of CO_2 Utilization via Direct Heterogeneous Electrochemical Reduction. *The Journal of Physical Chemistry Letters* **2010,** *1* (24), 3451-3458.

22. Benson, S. M.; Surles, T., Carbon Dioxide Capture and Storage: An Overview With Emphasis on Capture and Storage in Deep Geological Formations. *Proceedings of the IEEE* **2006,** *94* (10), 1795-1805.

23. AG, C., Direct air capture: a technology to remove CO_2.

24. Scibioh, M. A.; Viswanathan, B., Chapter 8 - Photochemical Reduction of CO_2. In *Carbon Dioxide to Chemicals and Fuels*, Scibioh, M. A.; Viswanathan, B., Eds. Elsevier: 2018; pp 373-436.

25. Yaashikaa, P. R.; Senthil Kumar, P.; Varjani, S. J.; Saravanan, A., A review on photochemical, biochemical and electrochemical transformation of CO_2 into value-added products. *Journal of CO2 Utilization* **2019,** *33*, 131-147.

26. Reda, T.; Plugge, C. M.; Abram, N. J.; Hirst, J., Reversible interconversion of carbon dioxide and formate by an electroactive enzyme. *Proceedings of the National Academy of Sciences* **2008,** *105* (31), 10654-10658.

27. Rudnev, A. V.; Zhumaev, U. E.; Kuzume, A.; Vesztergom, S.; Furrer, J.; Broekmann, P.; Wandlowski, T., The promoting effect of water on the electroreduction of CO_2 in acetonitrile. *Electrochimica Acta* **2016,** *189*, 38-44.

28. Adamu, A.; Russo-Abegão, F.; Boodhoo, K., Process intensification technologies for CO_2 capture and conversion – a review. *BMC Chemical Engineering* **2020,** *2* (1), 2.

29. Han, N.; Ding, P.; He, L.; Li, Y.; Li, Y., Promises of Main Group Metal–Based Nanostructured Materials for Electrochemical CO_2 Reduction to Formate. *Advanced Energy Materials* **2020,** *10* (11), 1902338.

30. Lin, R.; Guo, J.; Li, X.; Patel, P.; Seifitokaldani, A., Electrochemical Reactors for CO_2 Conversion. *Catalysts* **2020,** *10* (5), 473.

31. Bushuyev, O. S.; De Luna, P.; Dinh, C. T.; Tao, L.; Saur, G.; van de Lagemaat, J.; Kelley, S. O.; Sargent, E. H., What Should We Make with CO_2 and How Can We Make It? *Joule* **2018,** *2* (5), 825-832.

32. Kuhl, K. P.; Cave, E. R.; Abram, D. N.; Jaramillo, T. F., New insights into the electrochemical reduction of carbon dioxide on metallic copper surfaces. *Energy & Environmental Science* **2012,** *5* (5), 7050-7059.

33. Garg, S.; Li, M.; Weber, A. Z.; Ge, L.; Li, L.; Rudolph, V.; Wang, G.; Rufford, T. E., Advances and challenges in electrochemical CO2 reduction processes: an engineering and design perspective looking beyond new catalyst materials. *Journal of Materials Chemistry A* **2020,** *8* (4), 1511-1544.

34. Küngas, R., Review—Electrochemical CO_2 Reduction for CO Production: Comparison of Low- and High-Temperature Electrolysis Technologies. *Journal of The Electrochemical Society* **2020,** *167* (4), 044508.

35. Spurgeon, J. M.; Kumar, B., A comparative technoeconomic analysis of pathways for commercial electrochemical CO_2 reduction to liquid products. *Energy & Environmental Science* **2018,** *11* (6), 1536-1551.

36. Verma, S.; Kim, B.; Jhong, H.-R. M.; Ma, S.; Kenis, P. J. A., A Gross-Margin Model for Defining Technoeconomic Benchmarks in the Electroreduction of CO2. *ChemSusChem* **2016,** *9* (15), 1972-1979.

37. Chen, C.; Khosrowabadi Kotyk, J. F.; Sheehan, S. W., Progress toward Commercial Application of Electrochemical Carbon Dioxide Reduction. *Chem* **2018,** *4* (11), 2571-2586.

38. Jouny, M.; Luc, W.; Jiao, F., General Techno-Economic Analysis of CO_2 Electrolysis Systems. *Industrial & Engineering Chemistry Research* **2018,** *57* (6), 2165-2177.

39. Nitopi, S.; Bertheussen, E.; Scott, S. B.; Liu, X.; Engstfeld, A. K.; Horch, S.; Seger, B.; Stephens, I. E. L.; Chan, K.; Hahn, C.; Nørskov, J. K.; Jaramillo, T. F.; Chorkendorff, I., Progress and Perspectives of Electrochemical CO_2 Reduction on Copper in Aqueous Electrolyte. *Chemical Reviews* **2019,** *119* (12), 7610-7672.

40. Joó, F., Breakthroughs in Hydrogen Storage—Formic Acid as a Sustainable Storage Material for Hydrogen. *ChemSusChem* **2008,** *1* (10), 805-808.

41. Durst, J.; Rudnev, A.; Dutta, A.; Fu, Y.; Herranz, J.; Kaliginedi, V.; Kuzume, A.; Permyakova, A. A.; Paratcha, Y.; Broekmann, P.; Schmidt, T. J., Electrochemical CO_2 Reduction - A Critical View on Fundamentals, Materials and Applications. *Chimia* **2015,** *69* (12), 769-776.

42. Araujo, R. B.; Martín-Yerga, D.; Santos, E. C. d.; Cornell, A.; Pettersson, L. G. M., Elucidating the role of Ni to enhance the methanol oxidation reaction on Pd electrocatalysts. *Electrochimica Acta* **2020,** *360*, 136954.

43. Zhu, J.; Hu, L.; Zhao, P.; Lee, L. Y. S.; Wong, K.-Y., Recent Advances in Electrocatalytic Hydrogen Evolution Using Nanoparticles. *Chemical Reviews* **2020,** *120* (2), 851-918.

44. Wang, Y.; Su, H.; He, Y.; Li, L.; Zhu, S.; Shen, H.; Xie, P.; Fu, X.; Zhou, G.; Feng, C.; Zhao, D.; Xiao, F.; Zhu, X.; Zeng, Y.; Shao, M.; Chen, S.; Wu, G.; Zeng, J.; Wang, C., Advanced Electrocatalysts with Single-Metal-Atom Active Sites. *Chemical Reviews* **2020,** *120* (21), 12217-12314.

45. Wu, Z.-Y.; Karamad, M.; Yong, X.; Huang, Q.; Cullen, D. A.; Zhu, P.; Xia, C.; Xiao, Q.; Shakouri, M.; Chen, F.-Y.; Kim, J. Y.; Xia, Y.; Heck, K.; Hu, Y.; Wong, M. S.; Li, Q.; Gates, I.; Siahrostami, S.; Wang, H., Electrochemical ammonia synthesis via nitrate reduction on Fe single atom catalyst. *Nature Communications* **2021,** *12* (1), 2870.

46. Lui, Y., Qiao, J., & Zhang, J,, Electrochemical Reduction of Carbon Dioxide: Fundamentals and Technologies (1 st ed.). CRC Press. **2016**.

47. Qiao, J.; Liu, Y.; Hong, F.; Zhang, J., A review of catalysts for the electroreduction of carbon dioxide to produce low-carbon fuels. *Chemical Society Reviews* **2014,** *43* (2), 631-675.

48. Ganesh, I., Electrochemical conversion of carbon dioxide into renewable fuel chemicals – The role of nanomaterials and the commercialization. *Renewable and Sustainable Energy Reviews* **2016,** *59*, 1269-1297.

49. Zeng, K.; Zhang, D., Recent progress in alkaline water electrolysis for hydrogen production and applications. *Progress in Energy and Combustion Science* **2010,** *36* (3), 307-326.

50. Bard, A. J. a. F., L. R., Electrochemical Methods: Fundamentals and Applications. *John Wiley & Sons, Inc., New York, NY.* **2001,** *2nd ed.*, 100.

51. Tao, G., Investigation of carbon dioxide electrolysis reaction kinetics in a solid oxide electrolyzer. **2003**.

52. Kas, R.; Yang, K.; Bohra, D.; Kortlever, R.; Burdyny, T.; Smith, W. A., Electrochemical CO_2 reduction on nanostructured metal electrodes: fact or defect? *Chemical Science* **2020,** *11* (7), 1738-1749.

53. Bohra, D.; Chaudhry, J. H.; Burdyny, T.; Pidko, E. A.; Smith, W. A., Modeling the electrical double layer to understand the reaction environment in a CO2 electrocatalytic system. *Energy & Environmental Science* **2019,** *12* (11), 3380-3389.

54. Lu, Q.; Jiao, F., Electrochemical CO_2 reduction: Electrocatalyst, reaction mechanism, and process engineering. *Nano Energy* **2016,** *29*, 439-456.

55. Ganesh, I., Conversion of carbon dioxide into methanol – a potential liquid fuel: Fundamental challenges and opportunities (a review). *Renewable and Sustainable Energy Reviews* **2014,** *31*, 221-257.

56. Jhong, H.-R. M.; Ma, S.; Kenis, P. J. A., Electrochemical conversion of CO_2 to useful chemicals: current status, remaining challenges, and future opportunities. *Current Opinion in Chemical Engineering* **2013,** *2* (2), 191-199.

57. Zhang, S.; Nguyen, L.; Liang, J.-X.; Shan, J.; Liu, J.; Frenkel, A. I.; Patlolla, A.; Huang, W.; Li, J.; Tao, F., Catalysis on singly dispersed bimetallic sites. *Nature Communications* **2015,** *6* (1), 7938.

58. Hori, Y.; Wakebe, H.; Tsukamoto, T.; Koga, O., Electrocatalytic process of CO selectivity in electrochemical reduction of CO_2 at metal electrodes in aqueous media. *Electrochimica Acta* **1994,** *39* (11), 1833-1839.

59. Cook, R. L., On the Electrochemical Reduction of Carbon Dioxide at In Situ Electrodeposited Copper. *Journal of The Electrochemical Society* **1988,** *135* (6), 1320.

60. Senocrate, A.; Battaglia, C., Electrochemical CO_2 reduction at room temperature: Status and perspectives. *Journal of Energy Storage* **2021,** *36*, 102373.

61. Whang, H. S.; Lim, J.; Choi, M. S.; Lee, J.; Lee, H., Heterogeneous catalysts for catalytic CO_2 conversion into value-added chemicals. *BMC Chemical Engineering* **2019,** *1* (1), 9.

62. Sun, Z.; Ma, T.; Tao, H.; Fan, Q.; Han, B., Fundamentals and Challenges of Electrochemical CO_2 Reduction Using Two-Dimensional Materials. *Chem* **2017,** *3* (4), 560-587.

63. Kibria, M. G.; Edwards, J. P.; Gabardo, C. M.; Dinh, C.-T.; Seifitokaldani, A.; Sinton, D.; Sargent, E. H., Electrochemical CO_2 Reduction into Chemical Feedstocks: From Mechanistic Electrocatalysis Models to System Design. *Advanced Materials* **2019,** *31* (31), 1807166.

64. Kortlever, R.; Shen, J.; Schouten, K. J. P.; Calle-Vallejo, F.; Koper, M. T. M., Catalysts and Reaction Pathways for the Electrochemical Reduction of Carbon Dioxide. *The Journal of Physical Chemistry Letters* **2015,** *6* (20), 4073-4082.

65. Zhang, S.; Kang, P.; Meyer, T. J., Nanostructured Tin Catalysts for Selective Electrochemical Reduction of Carbon Dioxide to Formate. *Journal of the American Chemical Society* **2014,** *136* (5), 1734-1737.

66. Baruch, M. F.; Pander, J. E.; White, J. L.; Bocarsly, A. B., Mechanistic Insights into the Reduction of CO_2 on Tin Electrodes using in Situ ATR-IR Spectroscopy. *ACS Catalysis* **2015,** *5* (5), 3148-3156.

67. Dutta, A.; Zelocualtecatl Montiel, I.; Kiran, K.; Rieder, A.; Grozovski, V.; Gut, L.; Broekmann, P., A Tandem (Bi_2O_3 → Bimet) Catalyst for Highly Efficient ec-CO_2 Conversion into Formate: Operando Raman Spectroscopic Evidence for a Reaction Pathway Change. *ACS Catalysis* **2021,** *11* (9), 4988-5003.

68. Perez, A. C.; Diaz-Perez, M. A.; Serrano-Ruiz, J. C., Electrochemical Reduction of CO_2: Overcoming Chemical Inertness at Ambient Conditions. *Electrochem* **2020,** *1* (1), 56-59.

69. Burdyny, T.; Smith, W. A., CO_2 reduction on gas-diffusion electrodes and why catalytic performance must be assessed at commercially-relevant conditions. *Energy & Environmental Science* **2019,** *12* (5), 1442-1453.

70. Yang, D.; Zhu, Q.; Chen, C.; Liu, H.; Liu, Z.; Zhao, Z.; Zhang, X.; Liu, S.; Han, B., Selective electroreduction of carbon dioxide to methanol on copper selenide nanocatalysts. *Nature Communications* **2019,** *10* (1), 677.

71. Bevilacqua, M.; Filippi, J.; Miller, H. A.; Vizza, F., Recent Technological Progress in CO_2 Electroreduction to Fuels and Energy Carriers in Aqueous Environments. *Energy Technology* **2015,** *3* (3), 197-210.

72. Yu, F.; Wei, P.; Yang, Y.; Chen, Y.; Guo, L.; Peng, Z., Material design at nano and atomic scale for electrocatalytic CO_2 reduction. *Nano Materials Science* **2019,** *1* (1), 60-69.

73. Ju, H.; Kaur, G.; Kulkarni, A. P.; Giddey, S., Challenges and trends in developing technology for electrochemically reducing CO_2 in solid polymer electrolyte membrane reactors. *Journal of CO2 Utilization* **2019,** *32*, 178-186.

74. Liang, S.; Altaf, N.; Huang, L.; Gao, Y.; Wang, Q., Electrolytic cell design for electrochemical CO_2 reduction. *Journal of CO2 Utilization* **2020,** *35*, 90-105.

75. Lee, J.; Tak, Y., Electrocatalytic activity of Cu electrode in electroreduction of CO_2. *Electrochimica Acta* **2001,** *46* (19), 3015-3022.

76. Duan, Z.; Sun, R., An improved model calculating CO_2 solubility in pure water and aqueous NaCl solutions from 273 to 533 K and from 0 to 2000 bar. *Chemical Geology* **2003,** *193* (3), 257-271.

77. Perry, S. C.; Leung, P.-k.; Wang, L.; Ponce de León, C., Developments on carbon dioxide reduction: Their promise, achievements, and challenges. *Current Opinion in Electrochemistry* **2020,** *20*, 88-98.

78. Fan, T.; Ma, W.; Xie, M.; Liu, H.; Zhang, J.; Yang, S.; Huang, P.; Dong, Y.; Chen, Z.; Yi, X., Achieving high current density for electrocatalytic reduction of CO2 to formate on bismuth-based catalysts. *Cell Reports Physical Science* **2021,** *2* (3), 100353.

79. Wang, D.; Liu, C.; Zhang, Y.; Wang, Y.; Wang, Z.; Ding, D.; Cui, Y.; Zhu, X.; Pan, C.; Lou, Y.; Li, F.; Zhu, Y.; Zhang, Y., CO_2 Electroreduction to Formate at a Partial Current Density up to 590 mA mg^{-1} via Micrometer-Scale Lateral Structuring of Bismuth Nanosheets. *Small* **2021,** *17* (29), 2100602.

80. Zhang, L.; Hu, S.; Zhu, X.; Yang, W., Electrochemical reduction of CO_2 in solid oxide electrolysis cells. *Journal of Energy Chemistry* **2017,** *26* (4), 593-601.

81. Zhang, X.; Song, Y.; Wang, G.; Bao, X., Co-electrolysis of CO_2 and H_2O in high-temperature solid oxide electrolysis cells: Recent advance in cathodes. *Journal of Energy Chemistry* **2017,** *26* (5), 839-853.

82. Weekes, D. M.; Salvatore, D. A.; Reyes, A.; Huang, A.; Berlinguette, C. P., Electrolytic CO_2 Reduction in a Flow Cell. *Accounts of Chemical Research* **2018,** *51* (4), 910-918.

83. Song, J. T.; Song, H.; Kim, B.; Oh, J., Towards Higher Rate Electrochemical CO_2 Conversion: From Liquid-Phase to Gas-Phase Systems. *Catalysts* **2019,** *9* (3), 224.

84. Kutz, R. B.; Chen, Q.; Yang, H.; Sajjad, S. D.; Liu, Z.; Masel, I. R., Sustainion Imidazolium-Functionalized Polymers for Carbon Dioxide Electrolysis. *Energy Technology* **2017,** *5* (6), 929-936.

85. Endrődi, B.; Bencsik, G.; Darvas, F.; Jones, R.; Rajeshwar, K.; Janáky, C., Continuous-flow electroreduction of carbon dioxide. *Progress in Energy and Combustion Science* **2017,** *62*, 133-154.

86. Grigioni, I.; Sagar, L. K.; Li, Y. C.; Lee, G.; Yan, Y.; Bertens, K.; Miao, R. K.; Wang, X.; Abed, J.; Won, D. H.; García de Arquer, F. P.; Ip, A. H.; Sinton, D.; Sargent, E. H., CO2 Electroreduction to Formate at a Partial Current Density of 930 mA cm–2 with InP Colloidal Quantum Dot Derived Catalysts. *ACS Energy Letters* **2021,** *6* (1), 79-84.

87. Löwe, A.; Schmidt, M.; Bienen, F.; Kopljar, D.; Wagner, N.; Klemm, E., Optimizing Reaction Conditions and Gas Diffusion Electrodes Applied in the CO_2 Reduction Reaction to Formate to Reach Current Densities up to 1.8 A cm^{-2}. *ACS Sustainable Chemistry & Engineering* **2021,** *9* (11), 4213-4223.

88. Rabiee, H.; Ge, L.; Zhang, X.; Hu, S.; Li, M.; Yuan, Z., Gas diffusion electrodes (GDEs) for electrochemical reduction of carbon dioxide, carbon monoxide, and dinitrogen to value-added products: a review. *Energy & Environmental Science* **2021,** *14* (4), 1959-2008.

89. Higgins, D.; Hahn, C.; Xiang, C.; Jaramillo, T. F.; Weber, A. Z., Gas-Diffusion Electrodes for Carbon Dioxide Reduction: A New Paradigm. *ACS Energy Letters* **2019,** *4* (1), 317-324.

90. Cindrella, L.; Kannan, A. M.; Lin, J. F.; Saminathan, K.; Ho, Y.; Lin, C. W.; Wertz, J., Gas diffusion layer for proton exchange membrane fuel cells—A review. *Journal of Power Sources* **2009,** *194* (1), 146-160.

91. Nwabara, U. O.; Hernandez, A. D.; Henckel, D. A.; Chen, X.; Cofell, E. R.; de-Heer, M. P.; Verma, S.; Gewirth, A. A.; Kenis, P. J. A., Binder-Focused Approaches to Improve the Stability of Cathodes for CO_2 Electroreduction. *ACS Applied Energy Materials* **2021,** *4* (5), 5175-5186.

92. Martín, A. J.; Larrazábal, G. O.; Pérez-Ramírez, J., Towards sustainable fuels and chemicals through the electrochemical reduction of CO_2: lessons from water electrolysis. *Green Chemistry* **2015,** *17* (12), 5114-5130.

93. Marini, S.; Salvi, P.; Nelli, P.; Pesenti, R.; Villa, M.; Berrettoni, M.; Zangari, G.; Kiros, Y., Advanced alkaline water electrolysis. *Electrochimica Acta* **2012,** *82*, 384-391.

94. Lundblad, A.; Björnbom, P., Wetting-in Studies on Alkaline-Fuel-Cell Cathodes Using a Potentiostatic-Galvanostatic Experimental Design. *Journal of The Electrochemical Society* **1994,** *141* (6), 1503-1508.

95. Shi, R.; Guo, J.; Zhang, X.; Waterhouse, G. I. N.; Han, Z.; Zhao, Y.; Shang, L.; Zhou, C.; Jiang, L.; Zhang, T., Efficient wettability-controlled electroreduction of CO_2 to CO at Au/C interfaces. *Nature Communications* **2020,** *11* (1), 3028.

96. Yang, K.; Kas, R.; Smith, W. A.; Burdyny, T., Role of the Carbon-Based Gas Diffusion Layer on Flooding in a Gas Diffusion Electrode Cell for Electrochemical CO_2 Reduction. *ACS Energy Letters* **2021,** *6* (1), 33-40.

97. Zhao, H.; Zhu, Y.-P.; Yuan, Z.-Y., Three-Dimensional Electrocatalysts for Sustainable Water Splitting Reactions. *European Journal of Inorganic Chemistry* **2016,** *2016* (13-14), 1916-1923.

98. Zhu, W.; Zhang, R.; Qu, F.; Asiri, A. M.; Sun, X., Design and Application of Foams for Electrocatalysis. *ChemCatChem* **2017,** *9* (10), 1721-1743.

99. Vesztergom, S.; Dutta, A.; Rahaman, M.; Kiran, K.; Zelocualtecatl Montiel, I.; Broekmann, P., Hydrogen Bubble Templated Metal Foams as Efficient Catalysts of CO_2 Electroreduction. *ChemCatChem* **2021,** *13* (4), 1039-1058.

100. Dutta, A.; Kiran, K.; Ramahan, M.; Zelocualtecatl Montiel, I.; Moreno-Garcia, P.; Vesztergom, S.; Drnec, J.; Oezaslan, M.; Broekmann, P., Insights from Operando and Identical Location (IL) Techniques on the Activation of Electrocatalysts for the Conversion of CO_2: A Mini-Review. *Chimia* **2021,** *75* (9), 733.

101. Dutta, A.; Morstein, C. E.; Rahaman, M.; Cedeño López, A.; Broekmann, P., Beyond Copper in CO_2 Electrolysis: Effective Hydrocarbon Production on Silver-Nanofoam Catalysts. *ACS Catalysis* **2018,** *8* (9), 8357-8368.

102. Dutta, A.; Rahaman, M.; Hecker, B.; Drnec, J.; Kiran, K.; Zelocualtecatl Montiel, I.; Jochen Weber, D.; Zanetti, A.; Cedeño López, A.; Martens, I.; Broekmann, P.; Oezaslan, M., CO_2 Electrolysis - Complementary operando XRD, XAS and Raman Spectroscopy Study on the Stability of CuxO Foam Catalysts. *Journal of Catalysis* **2020**.

103. Dutta, A.; Montiel, I. Z.; Erni, R.; Kiran, K.; Rahaman, M.; Drnec, J.; Broekmann, P., Activation of bimetallic AgCu foam electrocatalysts for ethanol formation from CO_2 by selective Cu oxidation/reduction. *Nano Energy* **2020,** *68*, 104331.

104. Gao, S.; Lin, Y.; Jiao, X.; Sun, Y.; Luo, Q.; Zhang, W.; Li, D.; Yang, J.; Xie, Y., Partially oxidized atomic cobalt layers for carbon dioxide electroreduction to liquid fuel. *Nature* **2016,** *529* (7584), 68-71.

105. Fu, Y.; Li, Y.; Zhang, X.; Liu, Y.; Qiao, J.; Zhang, J.; Wilkinson, D. P., Novel hierarchical SnO_2 microsphere catalyst coated on gas diffusion electrode for enhancing energy efficiency of CO_2 reduction to formate fuel. *Applied Energy* **2016,** *175*, 536-544.

106. Zha, B.; Li, C.; Li, J., Efficient electrochemical reduction of CO_2 into formate and acetate in polyoxometalate catholyte with indium catalyst. *Journal of Catalysis* **2020,** *382*, 69-76.

107. Su, P.; Xu, W.; Qiu, Y.; Zhang, T.; Li, X.; Zhang, H., Ultrathin Bismuth Nanosheets as a Highly Efficient CO_2 Reduction Electrocatalyst. *ChemSusChem* **2018,** *11* (5), 848-853.

108. Han, N.; Wang, Y.; Yang, H.; Deng, J.; Wu, J.; Li, Y.; Li, Y., Ultrathin bismuth nanosheets from in situ topotactic transformation for selective electrocatalytic CO_2 reduction to formate. *Nature Communications* **2018,** *9* (1), 1320.

109. Hori, Y., Electrochemical CO_2 Reduction on Metal Electrodes. In *Modern Aspects of Electrochemistry*, Vayenas, C. G.; White, R. E.; Gamboa-Aldeco, M. E., Eds. Springer New York: New York, NY, 2008; pp 89-189.

110. Kale, M. B.; Borse, R. A.; Gomaa Abdelkader Mohamed, A.; Wang, Y., Electrocatalysts by Electrodeposition: Recent Advances, Synthesis Methods, and Applications in Energy Conversion. *Advanced Functional Materials* **2021,** *31* (25), 2101313.

111. Abhijit Dutta, M. R., Carina Morstein, Nicolas Schlegel and Peter Broekmann, , Morphology Matters: Additive-Assisted Metal Foam Deposition for the Electrochemical CO_2 Conversion. *ECS Meeting Abstracts* **2018**.

112. Dutta, A.; Rahaman, M.; Kiran, K.; Zelocualtecatl Montiel, I.; Cedeño López, A.; Moreno-García, P.; Broekmann, P., (Invited) Power-to-Value: Metal Foam Catalysts for the Electrochemical Conversion of CO_2. *ECS Meeting Abstracts* **2020,** *MA2020-02* (15), 1409-1409.

113. Shin, H.-C.; Liu, M., Copper Foam Structures with Highly Porous Nanostructured Walls. *Chemistry of Materials* **2004,** *16* (25), 5460-5464.

114. de Jesus Gálvez-Vázquez, M.; Moreno-García, P.; Xu, H.; Hou, Y.; Hu, H.; Montiel, I. Z.; Rudnev, A. V.; Alinejad, S.; Grozovski, V.; Wiley, B. J.; Arenz, M.; Broekmann, P., Environment Matters: CO_2RR Electrocatalyst Performance Testing in a Gas-Fed Zero-Gap Electrolyzer. *ACS Catalysis* **2020,** *10* (21), 13096-13108.

115. Plowman, B. J.; Jones, L. A.; Bhargava, S. K., Building with bubbles: the formation of high surface area honeycomb-like films via hydrogen bubble templated electrodeposition. *Chemical Communications* **2015,** *51* (21), 4331-4346.

116. Koh, J. H.; Won, D. H.; Eom, T.; Kim, N.-K.; Jung, K. D.; Kim, H.; Hwang, Y. J.; Min, B. K., Facile CO_2 Electro-Reduction to Formate via Oxygen Bidentate Intermediate Stabilized by High-Index Planes of Bi Dendrite Catalyst. *ACS Catalysis* **2017,** *7* (8), 5071-5077.

117. Liu, M.; Pang, Y.; Zhang, B.; De Luna, P.; Voznyy, O.; Xu, J.; Zheng, X.; Dinh, C. T.; Fan, F.; Cao, C.; de Arquer, F. P. G.; Safaei, T. S.; Mepham, A.; Klinkova, A.; Kumacheva, E.; Filleter, T.; Sinton, D.; Kelley, S. O.; Sargent, E. H., Enhanced electrocatalytic CO_2 reduction via field-induced reagent concentration. *Nature* **2016,** *537* (7620), 382-386.

118. Yoo, J. S.; Christensen, R.; Vegge, T.; Nørskov, J. K.; Studt, F., Theoretical Insight into the Trends that Guide the Electrochemical Reduction of Carbon Dioxide to Formic Acid. *ChemSusChem* **2016,** *9* (4), 358-363.

119. Yan, S.; Abhilash, K. P.; Tang, L.; Yang, M.; Ma, Y.; Xia, Q.; Guo, Q.; Xia, H., Research Advances of Amorphous Metal Oxides in Electrochemical Energy Storage and Conversion. *Small* **2019,** *15* (4), 1804371.

120. Deng, P.; Wang, H.; Qi, R.; Zhu, J.; Chen, S.; Yang, F.; Zhou, L.; Qi, K.; Liu, H.; Xia, B. Y., Bismuth Oxides with Enhanced Bismuth–Oxygen Structure for Efficient Electrochemical Reduction of Carbon Dioxide to Formate. *ACS Catalysis* **2020,** *10* (1), 743-750.

121. Dutta, A.; Kuzume, A.; Kaliginedi, V.; Rahaman, M.; Sinev, I.; Ahmadi, M.; Roldán Cuenya, B.; Vesztergom, S.; Broekmann, P., Probing the chemical state of tin oxide NP catalysts during CO_2 electroreduction: A complementary operando approach. *Nano Energy* **2018,** *53*, 828-840.

122. Betsch, R. J.; White, W. B., Vibrational spectra of bismuth oxide and the sillenite-structure bismuth oxide derivatives. *Spectrochimica Acta Part A: Molecular Spectroscopy* **1978,** *34* (5), 505-514.

123. Taylor, P.; Sunder, S.; Lopata, V. J., Structure, spectra, and stability of solid bismuth carbonates. *Canadian Journal of Chemistry* **1984,** *62* (12), 2863-2873.

124. McCallum, C.; Gabardo, C. M.; O’Brien, C. P.; Edwards, J. P.; Wicks, J.; Xu, Y.; Sargent, E. H.; Sinton, D., Reducing the crossover of carbonate and liquid products during carbon dioxide electroreduction. *Cell Reports Physical Science* **2021,** *2* (8), 100522.

125. Huang, J. E.; Li, F.; Ozden, A.; Sedighian Rasouli, A.; García de Arquer, F. P.; Liu, S.; Zhang, S.; Luo, M.; Wang, X.; Lum, Y.; Xu, Y.; Bertens, K.; Miao, R. K.; Dinh, C. T.; Sinton, D.; Sargent, E. H., CO_2 electrolysis to multicarbon products in strong acid. *Science* **2021,** *372* (6546), 1074-1078.

126. Ma, M.; Clark, E. L.; Therkildsen, K. T.; Dalsgaard, S.; Chorkendorff, I.; Seger, B., Insights into the carbon balance for CO_2 electroreduction on Cu using gas diffusion electrode reactor designs. *Energy & Environmental Science* **2020,** *13* (3), 977-985.

127. Wei, X.; Zhang, W.; Liu, D.; Liu, D.; Yan, Y.; Zhang, J.; Yang, Y.; Yan, S.; Zou, Z., Bi particles with exposed (012) facet on 3D substrate as highly active and durable electrode for CO_2 reduction to formate. *Journal of CO2 Utilization* **2022,** *55*, 101797.

128. Cai, Z.; Zhang, Y.; Zhao, Y.; Wu, Y.; Xu, W.; Wen, X.; Zhong, Y.; Zhang, Y.; Liu, W.; Wang, H.; Kuang, Y.; Sun, X., Selectivity regulation of CO_2 electroreduction through contact interface engineering on superwetting Cu nanoarray electrodes. *Nano Research* **2019,** *12* (2), 345-349.

129. Kong, Y.; Hu, H.; Liu, M.; Hou, Y.; Kolivoška, V.; Vesztergom, S.; Broekmann, P., Visualisation and quantification of flooding phenomena in gas diffusion electrodes used for electrochemical CO_2 reduction: A combined EDX/ICP–MS approach. *Journal of Catalysis* **2022,** *408*, 1-8.

130. Bienen, F.; Löwe, A.; Hildebrand, J.; Hertle, S.; Schonvogel, D.; Kopljar, D.; Wagner, N.; Klemm, E.; Friedrich, K. A., Degradation study on tin- and bismuth-based gas-diffusion electrodes during electrochemical CO_2 reduction in highly alkaline media. *Journal of Energy Chemistry* **2021,** *62*, 367-376.

131. Zelocualtecatl Montiel, I.; Dutta, A.;Kiran, K.; Rieder, A.; Iarchuk, A.; Vesztergom, S.; Mirolo, M.; Martens, I; Drnec, J.; Broekmann, P., CO_2 Conversion at High Current Densities: Stabilization of Bi(III) Containing Electrocatalysts under CO_2 Gas Flow Conditions. *ACS Catalysis* **2022**, 10872-10886.

132. Inamuddin, A. M. A., Eric Lichtfouse, Conversion of Carbon Dioxide into Hydrocarbons Vol. 1 Catalysis. 1, 43-53.

7. PUBLICATIONS

This section highlights publications related to research in which I participated during my PhD studies. For each publication, I present a brief abstract and a statement of my contributions to the research effort.

7.1. CO_2 Conversion at High Current Densities: Stabilization of Bi(III) Containing Electrocatalysts under CO_2 Gas Flow Conditions

Reprinted with permission from ACS Catal. 2022, 12, 17, 10872-10886. Copyright 2022 American Chemical Society.

Authors: Iván Zelocualtecatl Montiel, Abhijit Dutta, Kiran Kiran, Alain Rieder, Anna Iarchuk, Soma Vesztergom, Marta Mirolo, Isaac Martens, Jakub Drnec, and Peter Broekmann

ACS Catal. ACS Catal. 2022, 12, 17, 10872-10886.

DOI: https://doi.org/10.1021/acscatal.2c02549

Highlights: This work reports the high performance of bismuth subcarbonate ($Bi_2O_2CO_3$) film catalysts for formate production using a flow cell system. The subcarbonate catalyst forms in situ from a CO_2-absorbing Bi_2O_3 precursor material during the electrochemical CO_2 reduction reaction. The electrochemical performance of this catalyst shows a maximum $FE_{formate}$ = 97.4% at -0.8 V *vs.* RHE ($PCD_{formate}$ = –111.6 mA cm^{-2} in 1 M KOH). Even higher values of $PCD_{formate}$ = –441.2 mA cm^{-2} ($FE_{formate}$ = 62%) were observed at more cathodic potential, –2.5 V *vs.* RHE. When the alkalinity of the electrolyte is increased (5 M KOH), the performance of formate production is boosted beyond $PCD_{formate}$ values of –1 A cm^{-2}. Complementary *ex situ* XRD and Raman spectroscopy investigations demonstrate high stability of Bi(III) in the subcarbonate catalyst phase at high cathodic potentials (–1.5 V vs. RHE). This stabilization effect can be attributed to the high abundance of gaseous CO_2 under the operating conditions of the gas-fed electrolyzer. Advanced X-ray diffraction computed tomography (XRD-CT) technique was applied to gain deeper insights into the spatial distribution of the metallic and carbonate phases comprising the active composite catalyst layer (CL) during the CO_2RR.

Contributions: In this project, I was one of the main persons responsible for the synthesis, characterization and electrochemical experiments. I contributed equally with Dr. Abhijit Dutta to the analysis and discussion of the data, and figure preparation of the paper.

ACS Catalysis

pubs.acs.org/acscatalysis

Research Article

CO_2 Conversion at High Current Densities: Stabilization of Bi(III)-Containing Electrocatalysts under CO_2 Gas Flow Conditions

Iván Zelocualtecatl Montiel,[⊥] Abhijit Dutta,[*,⊥] Kiran Kiran, Alain Rieder, Anna Iarchuk, Soma Vesztergom, Marta Mirolo, Isaac Martens, Jakub Drnec, and Peter Broekmann[*]

Cite This: *ACS Catal.* 2022, 12, 10872−10886

Read Online

ACCESS | Metrics & More | Article Recommendations | Supporting Information

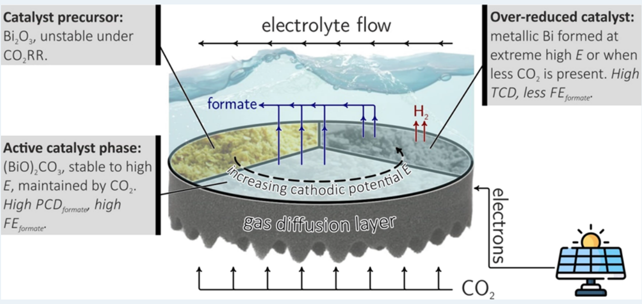

ABSTRACT: Herein, we demonstrate the superior performance of bismuth subcarbonate ($(BiO)_2CO_3$) layer catalysts for formate production using a fluidic CO_2-fed electrolyzer device. The subcarbonate catalyst readily forms in situ from a CO_2-absorbing Bi_2O_3 precursor material during the CO_2 reduction reaction (CO_2RR). In 1 mol dm^{-3} KOH electrolyte solution, a maximum Faradaic efficiency of $FE_{formate} = 97.4\%$ (corresponding partial current density of formate formation: $PCD_{formate} = -111.6$ mA cm^{-2}) was achieved at a comparably low applied electrolysis potential of −0.8 V vs the reversible hydrogen electrode (RHE). Even higher values of $PCD_{formate} = -441.2$ mA cm^{-2} ($FE_{formate}$ = 62%) were observed at a more cathodic potential, −2.5 V vs RHE. As the alkalinity of the liquid electrolyte is further increased (e.g., by using 5 mol dm^{-3} KOH solution), the performance of formate production is boosted beyond $PCD_{formate}$ values of −1 A cm^{-2}. Combined X-ray diffraction and Raman spectroscopic investigations demonstrate an extraordinarily high stability of Bi(III) cations in the catalytically active subcarbonate catalyst phase down to cathode potentials of −1.5 V vs RHE. This stabilization effect can clearly be attributed to the high abundance of gaseous CO_2 under the operating conditions of the gas-fed electrolyzer. In the absence of any CO_2 supply, the reductive Bi(III) → Bi(0) transition already occurs under much milder conditions of −0.3 V vs RHE, as evidenced by in situ Raman spectroscopy in CO_2-free 1 mol dm^{-3} KOH electrolyte solution. An advanced X-ray diffraction computed tomography technique was applied to gain deeper insights into the spatial distribution of the metallic and subcarbonate phases comprising the active composite catalyst layer during the CO_2RR.

KEYWORDS: *CO_2 electrolysis, formate production, gas-fed fluidic electrolyzer, subcarbonate pathway, Raman spectroscopy, X-ray diffraction computed tomography*

1. INTRODUCTION

In recent years, the electrochemical conversion of CO_2 into higher-value products has been introduced as a promising and technologically feasible approach for mitigating the negative climatic impact of the steadily increasing levels of atmospheric CO_2.[1−3] The CO_2 reduction reaction (CO_2RR) may become not only economically feasible but also truly sustainable if the surplus of renewable energy originating from solar radiation, wind power, and hydroelectric sources is used as energy input to drive the highly endergonic and kinetically hindered CO_2 conversion. The overall electrolysis reaction relies on an oxidative splitting of water (i.e., oxygen evolution reaction, OER) through

$$O_2 + 4e^- + 4H^+ \rightleftharpoons 2H_2O \text{ (acidic)} \tag{1}$$

or

$$O_2 + 2H_2O + 4e^- \rightleftharpoons 4OH^- \text{(alkaline)} \tag{2}$$

which is coupled to the reductive conversion of CO_2 (denoted hereafter as CO_2RR). In aqueous reaction environments, oxygen (O_2) is the only product that forms on the anode side regardless of the anode material used. However, a variety of CO_2RR products can be produced on the cathode, including but not limited to carbon monoxide (CO),[4−9] saturated[4,10−12] and nonsaturated hydrocarbons,[11,13−17] and alcohols with various chain lengths and energy densities (e.g., methanol,[12,18−20] ethanol,[16,21−23] and *n*-propanol[24]). Formate is another commodity chemical of high value that can be formed as a product of the CO_2RR.[25,26]

As recently noted by Chen et al.,[27] it is the liquid nature of the formate/formic acid product that enables the downstream product separation following primary electrolysis to be conducted with less effort, thus enhancing the profitability of

Received: May 25, 2022
Revised: August 6, 2022

https://doi.org/10.1021/acscatal.2c02549
ACS Catal. 2022, 12, 10872−10886

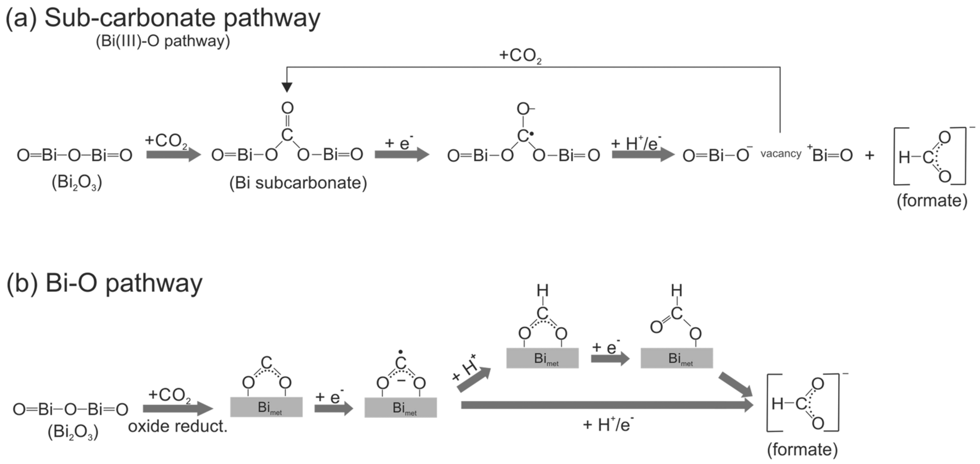

Figure 1. Reaction pathways of formate formation postulated for bismuth-type catalysts. (a) Subcarbonate pathway involving the in situ formation of $(BiO)_2CO_3$ from Bi_2O_3. (b) Bi–O pathway over metallic Bi catalysts.

the overall production process. Existing and potential future applications of formate/formic acid concern formic acid fuel cells,[28−30] related hydrogen storage technologies,[31] the chemical depolymerization of lignin (biomass valorization),[32] and its usage as a silage additive.[33] Particularly promising are recent developments aimed at coupling CO_2 electrolysis with approaches transforming formate into higher alcohols through biotechnological means, thus opening groundbreaking venues of future ($CO_2 \rightarrow$ formate) valorization.[34]

Not only are catalysts essential to accelerate the intrinsically slow CO_2RR, they are also required for a selective CO_2 transformation, directing the electrolysis toward the targeted product (e.g., formate) and minimizing the parasitic hydrogen evolution reaction (HER) that is typically superimposed on the CO_2RR in aqueous reaction environments. Depending on the solution pH, the HER can be fed either through reductive water splitting

$$2H_2O + 2e^- \rightleftharpoons H_2 + 2OH^- (\text{neutral/alkaline}) \quad (3)$$

or by the reduction of protons

$$2H^+ + 2e^- \rightleftharpoons H_2\ (\text{acidic}) \quad (4)$$

It has been shown that both the chemical nature of the catalyst material[35] and its morphology on various length scales[36,37] dictate the resulting CO_2RR product distribution. The catalyst porosity has been demonstrated to be particularly important for consecutive multiproton/multielectron reactions, e.g., the electrosynthesis of higher hydrocarbons and alcohols from CO_2, where the accumulation of key intermediates (e.g., CO) in confined reaction spaces of porous catalysts and related local pH effects determine the resulting CO_2RR product distribution.[10,38] However, a weaker impact of mesoscale porosity on the CO_2RR product distribution has been reported for coupled electron/proton transfer reactions of reduced complexity, e.g., the formation of formate/formic acid[39] from CO_2 according to

$$CO_2 + H_2O + 2e^- \rightleftharpoons HCOO^- + OH^- (\text{neutral/alkaline}) \quad (5)$$

Since the pioneering work by Hori et al.,[35] it has been known that particular oxophilic materials, e.g., Sn,[40−44] Pb,[45] Cd,[46] Tl, and In,[47] favor CO_2RR pathways toward formate production. However, debate continues regarding the mechanistic role of the respective metal oxides, which are either formed in situ during electrolysis or applied directly as the catalyst (precursor).[40−43] Advanced operando techniques, e.g., vibrational[40,48−50] and X-ray absorption spectroscopy,[49−51] have been successfully employed to gain deeper mechanistic insight into the electrolysis time, current density, and potential-dependent activation of CO_2RR catalysts under operating conditions.[40,52] A recent example is based on the use of oxidic bismuth electrocatalysts,[39,53,54] which had already demonstrated superior selectivities toward formate production in classical H-type cell testing environments, with Faradaic efficiencies (FEs) exceeding 95% within an extraordinarily (approximately 1.1 V)[39,55] wide potential window. For a CO_2-saturated 0.5 mol dm^{-3} $KHCO_3$ electrolyte solution, a combination of electrochemical analysis and operando Raman spectroscopy during CO_2RR revealed the coupling of two potential-dependent CO_2RR pathways as the origin of this superior catalytic performance.[39] At low applied overpotentials (−0.3 to −0.6 V vs the reversible hydrogen electrode (RHE)), the CO_2RR was shown to proceed predominantly via the so-called subcarbonate pathway (see Figure 1), where a pristine Bi_2O_3 precursor undergoes a rapid transformation into a bulk bismuth subcarbonate phase.[39,56−58] The term "bismuth subcarbonate" refers to a mixed oxide/carbonate compound in which bismuth has an oxidation state of +3. $(BiO)_2CO_3$ is formed (formally) through partial exchange of O^{2-} by CO_3^{2-} anions through the reaction of the oxidic precursor with gaseous or dissolved CO_2. With the aid of operando Raman spectroscopy, Dutta et al. could identify the $(BiO)_2CO_3$ subcarbonate phase as the active catalyst under these experimental conditions.[39] However, at electrolysis potentials more negative than −0.6 V vs RHE, the formed $(BiO)_2CO_3$ phase underwent a reductive transformation into metallic Bi, resulting in even higher partial current densities of formate formation (PCD_{formate}), i.e., reaching a remarkable value of −85 mA cm^{-2} at −1.6 V vs RHE.[39] In the presence of metallic Bi, the CO_2RR proceeds via the Bi–O pathway (Figure 1).[58] At first glance, these results seem to suggest that the so-called subcarbonate reaction pathway of formate formation remains limited to artificial experimental conditions, e.g., to those realized in H-type cell configurations. These conditions have only limited practical relevance for gas-fed electrolyzer systems. In gas-fed electrolyzers, the rate of CO_2RR is not limited by slow CO_2 mass transport, and as a consequence, much higher

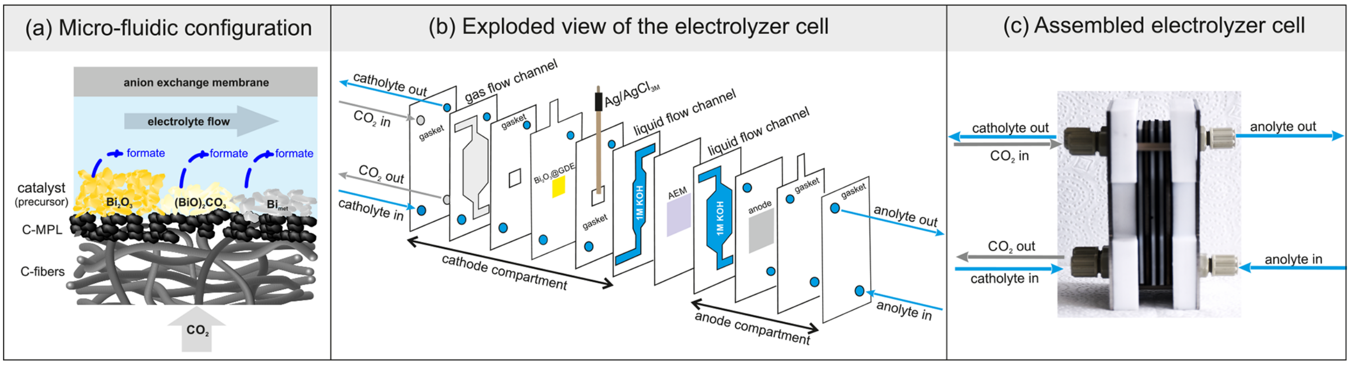

Figure 2. (a) Fluidic cathode configuration used in this study. (b) Exploded view of the flow cell electrolyzer. (c) Photograph of the assembled electrolyzer setup.

applied overpotentials (and current densities) can be achieved while still maintaining high formate selectivity.[55,56,59]

In the present study, we demonstrate that an accelerated mass transport of gaseous CO_2 not only boosts the formate production to values beyond $PCD_{formate} = -1$ A cm^{-2} but can also lead to a substantial stabilization of subcarbonate phases beyond the stability regime observed in classical CO_2RR test environments.[39] Our experimental results strongly suggest that observations previously made using H-type cell configurations cannot simply be transferred to experimental conditions realized in practical gas-fed electrolyzers. This conclusion is particularly relevant for the potential-dependent phase behavior of the used nonmetallic CO_2RR catalyst, which, as will be demonstrated hereinafter, depends not only on the applied electrode potential but also on the actual CO_2 gas supply.

2. EXPERIMENTAL SECTION

2.1. Fabrication of the Gas Diffusion Electrode (GDE). The initial catalyst preparation starts with repetitive Bi foam electrodeposition following established synthesis protocols based on the dynamic hydrogen bubble template (DHBT) metal deposition approach (see Figure S1).[39] For metal foaming, galvanostatic Bi deposition ($j_{geo} = -3.0$ A cm^{-2}) was performed in 100 cm^3 of 1.5 mol dm^{-3} H_2SO_4 (prepared from 96% H_2SO_4, ACS grade, Sigma-Aldrich) containing 20 mmol dm^{-3} ammonium bismuth citrate ($C_{12}H_{22}BiN_3O_{14}$, Sigma-Aldrich, purity ≥99.5%). Ammonium bismuth citrate was used as the Bi source as this precursor salt can be completely dissolved in sulfuric acid electrolyte solution. Other common bismuth precursors, by contrast, cannot be dissolved in sulfuric acid or tend to hydrolyze, leaving white precipitates in the plating bath behind (Figure S2).

The used three-electrode configuration consisted of a double junction Ag | AgCl | 3 mol dm^{-3} KCl reference electrode (Metrohm), a bright Pt anode (50 mm × 20 mm foil), and a Cu foil support (1 cm^2 geometric surface area) acting as the cathode. After completion of the metal foam deposition, the Bi-foam@Cu-foil samples were transferred to a vial containing 3 cm^3 of isopropanol (iPrOH, BASF SE, assay ≥99.0%) and then ultrasonicated until the porous foam material was completely removed from the Cu foil and dispersed in iPrOH. Metallic Bi powders were obtained through evaporation of the solvent at 50 °C for 12 h. To prepare the catalyst ink, 55 mg of the Bi powder was redispersed in a mixture of 19.5 cm^3 iPrOH and 0.5 cm^3 Nafion perfluorinated resin solution (~5 wt % Nafion in a mixture of lower aliphatic alcohols and 15−20 wt % water, purchased from Sigma-Aldrich), followed by 30 min of sonication at room temperature.

To fabricate the GDE, 17 cm^3 of the catalyst ink was spray-coated on the surface (6.3 cm × 6.3 cm) of a commercial gas diffusion layer (GDL, Freudenberg H23C8) via a hand-held airbrush pistole (Master Airbrush, G233) propelled with nitrogen gas (99.999%, Carbagas, Switzerland). The catalyst ink was dried with the assistance of vacuum applied to the backside of the GDL during the ink spray-coating process. The expected (nominal) Bi mass loading of $m_{Bi} = 1.17$ mg cm^{-2} agrees well with the experimental value obtained by inductively coupled plasma mass spectrometry (ICP-MS; $m_{Bi} = 1.06$ mg cm^{-2}).

The used H23C8-GDL reveals a characteristic bilayer structure composed of a supporting carbon fiber layer and a terminating microporous layer (MPL) on which the catalyst layer (CL) is deposited. MPLs are typically made hydrophobic by the manufacturer, e.g., via coating with polytetrafluoroethylene as a water-repelling agent, to minimize electrolyte flooding into deeper layers of the GDL, which may lead to an undesired blockage of CO_2 transport to the active catalyst sites during extended electrolyzer operation. The structural and physical characteristics of the H23C8-GDL are detailed in Figure S3. The most important feature of the used H23C8-GDL is the absence of cracks inside the MPL, which might facilitate massive permeation of liquid electrolyte into the GDL during the operation of the fluidic gas-fed electrolyzer.

For further use, pieces (6.3 cm × 6.3 cm) of these prepared GDEs (denoted as ap-Bi@GDEs) were cut into smaller segments (2 cm × 2 cm) with a punching blade. For further activation, the ap-Bi@GDEs were subjected to 6 h of in-air thermal annealing in a tube furnace (Nabertherm, Germany) at a temperature of 350 °C. The obtained oxidic layer is denoted as ap-Bi_2O_3@GDE and represents the starting point for all electrolyses discussed hereinafter. Of note, the transformation of metallic Bi into the corresponding Bi_2O_3 does not strongly affect the dendritic nature of the catalyst (precursor), as demonstrated in Figure S4. Similar observations were previously made for the thermal annealing of electrodeposited Cu foams.[10,37]

2.2. Electrolysis Experiments. All electrolysis experiments were performed in a potentiostatic operation mode utilizing a three-compartment flow cell electrolyzer (Electro-Cell, Denmark, see also Figure 2 and Figure S5). Cathode and anode compartments were separated from each other by an anion exchange membrane (Sustainion X37-50 Grade RT

Membrane). For the ap-Bi_2O_3@GDE, a geometric surface area of 1 cm^2 was exposed to the liquid electrolyte. A third compartment, required for the CO_2 gas supply, was assembled at the backside of the cathode.

With the aid of a peristaltic pump (LabV1, SHE-LabV1-MC4), the anolyte and catholyte were fed through the electrolyzer cell via two separated liquid flow channels at a flow rate of 3.3 cm^3 min^{-1}. Either 1 or 5 mol dm^{-3} KOH aqueous solution was used as the electrolyte. All solutions were produced using high-purity Milli-Q water (specific resistance of 18.2 MΩ cm, total organic carbon content below 5 ppb, Millipore).

For CO_2 electrolysis experiments, humidified CO_2 gas (Carbagas, 99.9999%) was fed at atmospheric pressure through the gas channels and the GDE. A gas flow rate of 30−35 cm^3 min^{-1} was applied and monitored with a mass flow controller unit (Vögtlin Instruments, GmbH, type GSC-A9SA-BB2). For selected reference experiments, the gas supply was switched during electrolysis from CO_2 to inert Ar gas (99.9999%, Carbagas, Switzerland).

All electrolysis experiments were conducted in a three-electrode configuration consisting of the ap-Bi_2O_3@GDE (working electrode, cathode), a Pt foil serving as the counter electrode (anode, geometric surface area of 1.5 cm^{-2}), and a leakless Ag | AgCl | 3 mol dm^{-3} KCl reference electrode (eDAQ). To ensure comparability, all potentials measured vs the named reference electrode were converted to the RHE scale according to

$$E_{\mathrm{RHE}} = E_{\mathrm{Ag\,|\,AgCl\,|\,3\,mol\,dm^{-3}\,KCl}} + 0.210\ \mathrm{V} + (0.0591\ \mathrm{V}\cdot\mathrm{pH}) \tag{6}$$

An ECi-200 potentiostat (Nordic Electrochemistry, Denmark) was used to establish potential control during electrolysis. For all measurements, *iR* compensation was applied.

During electrolysis, gaseous products (e.g., H_2 and CO) were detected and quantified in intervals of 20 min by means of online gas chromatography (GC). For this purpose, the gas flow outlet of the electrolyzer unit was connected to the sampling loop of a gas chromatograph (8610C, SRI Instruments). The GC instrument was equipped with both a packed Hayesep D column and a packed Molesieve 5A column. Argon (99.9999%, Carbagas) served as the carrier gas for GC analysis. To quantify gaseous CO and H_2 electrolysis products, a flame ionization detector coupled to a methanizer and a thermal conductivity detector were applied. Corresponding calibration measurements are provided in Figure S6.

The partial current for a given electrolysis product (I_i) can be determined from

$$I_i = \frac{x_i \cdot v \cdot F \cdot z}{V_{\mathrm{m}}} \tag{7}$$

where x_i refers to the mole fraction of the formed product in the out-flow gas, z represents the number of electrons transferred during the reaction, F = 96485.3 C mol^{-1} is the Faraday constant, v is the volumetric gas flow rate, and V_m represents the molar volume of the gas at 1 atm and room temperature.

The FE for a specific gaseous product was calculated by relating the partial current (I_i) to the corresponding total current (I_{total}) according to

$$\mathrm{FE} = \frac{I_i}{I_{\mathrm{total}}} \cdot 100\% \tag{8}$$

Nonvolatile electrolysis products (e.g., formate), accumulated in the catholyte, were quantified by ion exchange chromatography (IC) using a Metrohm 940 Professional IC Vario instrument equipped with a Metrosep A Supp 7 column and operated with MagicNet 3.1 software. For selected control experiments, the anolyte was also analyzed with the aim of monitoring possible formate crossover through the anion exchange membrane into the anolyte compartment during electrolysis. For IC analysis, aqueous solutions of 3 mmol dm^{-3} Na_2CO_3 and 0.1 mol dm^{-3} H_2SO_4 served as the eluent and the suppressor, respectively. The IC instrument was calibrated by injecting known standard formate concentrations in the range of 10−250 ppm prepared by dilution of a 1000 ppm IC standard solution (Sigma-Aldrich). Chromatograms, corresponding calibration plots, and further control measurements are presented in Figures S7 and S8. Sample aliquots were diluted (20- to 50-fold) with the eluent prior to IC analysis to inhibit matrix effects arising from the highly concentrated KOH working electrolyte.

FE values for nonvolatile products were derived from the integrated total charges (Q_{total}) of the electrolysis reaction and the partial charges (Q_i) corresponding to the formation of a specific product:

$$\mathrm{FE} = \frac{Q_i}{Q_{\mathrm{total}}} \cdot 100\% \tag{9}$$

The partial charge is calculated according to

$$Q_i = \frac{V_{\mathrm{cath}} \cdot F \cdot z}{M_i} \cdot c_i \tag{10}$$

V_{cath} is the total volume of the catholyte circulating in the electrolyzer, c_i denotes the mass concentration of the product i (usually expressed in mg dm^{-3} or "ppm"), and M_i is the molar mass of product i.

Electrolysis data presented hereinafter were acquired by averaging FE and PCD values obtained from three independent electrolysis experiments per applied electrolysis potential. Note that the FE vs E plots presented herein solely consider the formate accumulated in the catholyte. In most cases, the formate crossover through the membrane into the anolyte can be neglected (see the discussion below).

2.3. Structural and Compositional Characterization of the Catalyst.

X-ray diffraction (XRD) analyses were conducted using a STOE Stadi system equipped with a Cu K_α radiation source (λ = 0.1540 nm, 40 mA) and operated at 40 keV. X-ray diffractograms were recorded in reflection mode (Bragg−Brentano geometry) in steps of 1° min^{-1} with 2θ values ranging from 0° to 90°. Commercial β-Bi_2O_3 (Sigma Aldrich, purity ≥99.8%) and $(BiO)_2CO_3$ (Alfa Aesar, purity >98.5%) samples were used as internal references for the peak assignment. The obtained XRD patterns were further analyzed and compared with respective Joint Committee on Powder Diffraction Standards data for polycrystalline Bi, β-Bi_2O_3, and $(BiO)_2CO_3$ (file no. 85-1331, 78-1793, and 84-1752).

X-ray diffraction computed tomography (XRD-CT) experiments were performed at the high-energy beamline ID31 of the European Synchrotron Radiation Facility in Grenoble, France. The X-ray beam was monochromatized with a Laue monochromator to an energy of 80 keV and focused to a

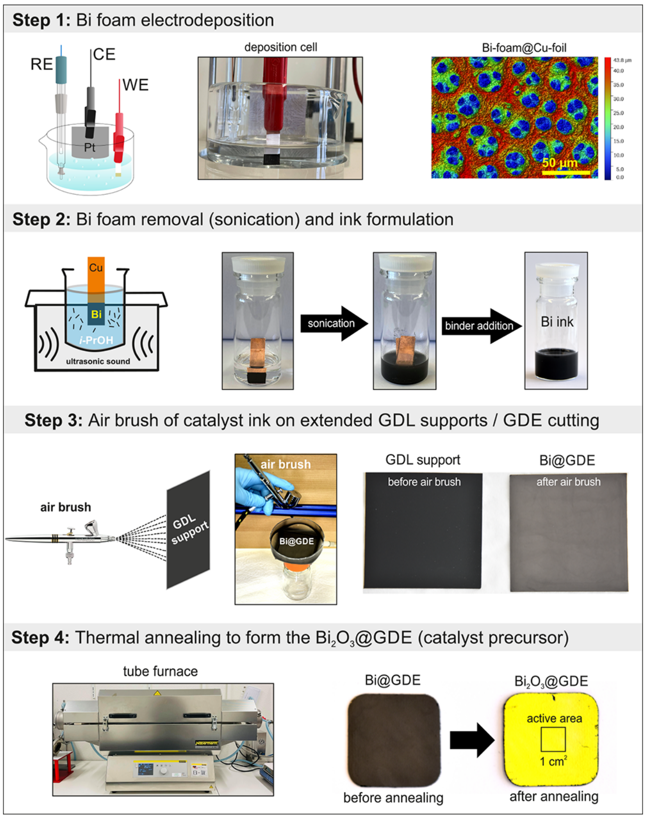

Figure 3. Individual preparation steps required for the fabrication of the GDE coated with the Bi_2O_3 film (denoted as ap-Bi_2O_3@GDE) serving as the catalyst precursor.

size of ~6 × 20 μm^2 (vertical × horizontal) at the sample position. Two-dimensional XRD patterns were collected with a Dectris Pilatus 2 M CdTe detector and radially integrated by pyFAI software.[60] Each slice is reconstructed from 62,500 diffraction patterns using a standard back-projection algorithm. Five slices for each sample are space by 5 μm to cover the whole volume of the CL.

Scanning electron microscopy (SEM)/energy-dispersive X-ray (EDX) analysis was performed with a Zeiss DSM 982 SEM equipped with a Noran SIX NSS200 EDX spectrometer.

The mesoscopic surface morphology of the foam was analyzed by means of white light interferometry (Contour GT, Bruker, see Figure 3). Vision64 software (Bruker) was used for operating the instrument and for data analysis.

Contact-angle measurements were conducted using a DSA25 Krüss Advance Drop Shape Analyzer (Krüss GmbH, Hamburg, Germany). Electrodes were mounted on a flat sample stage, and water drops (Milli-Q water, 1.4 μL) were deposited at room temperature.

Elemental analysis was performed by means of ICP-MS using a NExION 2000 ICP-MS instrument (Perkin Elmer). For the determination of the catalyst mass loading, GDE samples were dissolved in 3 cm^3 of conc. HNO_3 (69.3 wt %, BASF SE). For the analysis, aliquots of 5 mm^3 of this solution were dispersed in 10 cm^3 of 2 wt % HNO_3 solution (2000 times dilution). Sample solutions were measured 6 times each by ICP-MS.

For the postelectrolysis analysis of the electrolyte solution, aliquots of 20 mm^3 electrolyte were diluted in 10 cm^3 of 2 wt % HNO_3 solution (500 times dilution). Sample solutions were measured 4 times each by ICP-MS. Repetition measurements served as the basis for the determination of the relative standard deviation (RSD). ICP-MS-related RSD values are typically between 1 and 2%. An extra measuring error of ca. 1.5% needs to be taken into account and is due to the dilution treatment required for certain samples.

Raman spectroscopic analyses (ex situ) were conducted using a LabRAM HR800 confocal microscope (Horiba Jobin Yvon). Spectral data were collected with Lab Space 3.0 software via the Raman spectrometer coupled with a confocal microscope (Horiba Jobin Yvon). Calibration was carried out using a silicon wafer standard (520.6 cm^{-1}). A large-working-distance objective lens (50× magnification, 8-mm focal length) was applied with a numerical aperture of 0.1 in order to focus a diode-pumped solid-state laser beam (532 nm excitation wavelength, 3 mW power) on the sample and collect the incident and scattered laser light. The details of the in situ Raman spectroscopy experiments have been described previously.[39] An optical micrograph and a schematic of the in situ Raman cell are provided in Figure S9.

To identify the Bi_{metal}, Bi_2O_3, and $(BiO)_2CO_3$ phases, we used characteristic Raman features at 96 cm^{-1} (E_g mode of Bi_{metal}), 313 cm^{-1} (B_g mode ("Bi−O stretch") of Bi_2O_3), and 162 cm^{-1} (A_{1g} mode of the carbonate in $(BiO)_2CO_3$), respectively (Figure S10).[61,62] For comparison purposes, we added in addition a reference Raman spectrum of a commercial $Bi(OH)_3$ sample (CHEM-IMPEX INT'L INC).

3. RESULTS AND DISCUSSION

3.1. Characterization of the As-Prepared GDEs.

Several studies have already demonstrated superior CO_2RR performance of porous metal foam catalysts[36] electrodeposited with the aid of the DHBT method.[63−69] Herein, we have integrated the DHBT-assisted metal foam electrodeposition approach into a more general and versatile catalyst preparation scheme that is particularly suited for the fabrication of GDEs and that can be used in advanced electrolyzer setups. Owing to instrumental limitations, functionalizing more extended surface areas with the DHBT approach alone remains difficult, considering the required ultrahigh (geometric) current densities typically applied for such metal foam electrodeposition (e.g., −3 A cm^{-2}).[36,63,64] As detailed in Figure 3, the new GDE fabrication approach involves the repetitive deposition of metallic foams and their subsequent removal from the planar support electrode by ultrasonication.

Of note, this foam removal method destroys the initially formed primary macroporosity of the metal foam without affecting the dendritic nature of the electrodeposited material. In particular, for CO_2RR processes in which the primary macroporosity of the foam is less important, e.g., in the case of formate production, the excellent catalytic performance and selectivity of the electrodeposited material are preserved, as it was recently shown by Dutta et al.[39] This dendritic catalyst material is used for the formulation of catalyst (precursor) inks, which are subsequently spray-coated onto extended gas diffusion layer supports, thereby yielding homogeneous CLs. Further catalyst activation can often be achieved through thermal annealing, e.g., yielding a Bi_2O_3 film with a characteristic yellow appearance in the present case (Figure 3).[39]

Bi_2O_3 crystallizes in various polymorphic forms, denoted as α-Bi_2O_3 (monoclinic), β-Bi_2O_3 (tetragonal), γ-Bi_2O_3 (bcc), δ-Bi_2O_3 (cubic), ε-Bi_2O_3 (triclinic), and ω-Bi_2O_3 (triclinic).[70−73] Amorphous Bi_2O_3 has also been reported in the literature.[74]

https://doi.org/10.1021/acscatal.2c02549

These studies emphasize the necessity of combining XRD analyses with complementary techniques, e.g., Raman spectroscopy/microscopy, that are sensitive to phases lacking any long-range transitional order. Interestingly, the combination of DHBT-assisted bismuth electrodeposition and thermal annealing (e.g., at 350 °C in air) exclusively yields the β-Bi_2O_3 phase, which has been described in the literature as the most valuable phase among the known modifications (e.g., for photocatalytic applications) because it shows the smallest band gap (~2.58 eV).[70,74] The synthesis of this phase in a pure form, for instance through wet chemistry (precipitation routes), is often considered difficult in the literature.[70]

Figure 4 depicts top−down SEM and cross-sectional SEM/EDX micrographs as well as representative X-ray diffractograms and Raman data of the as-prepared bismuth oxide film on the GDE (denoted as ap-Bi_2O_3@GDE). This ap-Bi_2O_3@GDE was the starting point for all electrolysis experiments discussed hereinafter. On a macroscopic length scale, the SEM data reveal a homogeneous catalyst precursor film (panel a), whereas dendritic features govern the catalyst morphology on a submicrometer length scale (panel b). The catalyst (precursor) layer must be porous and permeable for both gases and liquids to enable (i) rapid CO_2 transport through the GDL toward the active catalyst sites and (ii) (partial) permeation of the catalyst material by the liquid electrolyte. The inward transport of CO_2 and liquid electrolyte into such a three-dimensional CL is considered vital for establishing triple-phase boundaries in the CL, thereby facilitating CO_2RR.[75,76] As shown by panels c and d of Figure 4, the ap-Bi_2O_3 CL has an average thickness of about 28 μm, with the bismuth oxide not penetrating the carbon MPL. The X-ray diffractogram (panel e) and the Raman spectrum (panel f) of the ap-Bi_2O_3 CL closely resemble the reference diffractogram and spectrum of β-Bi_2O_3.

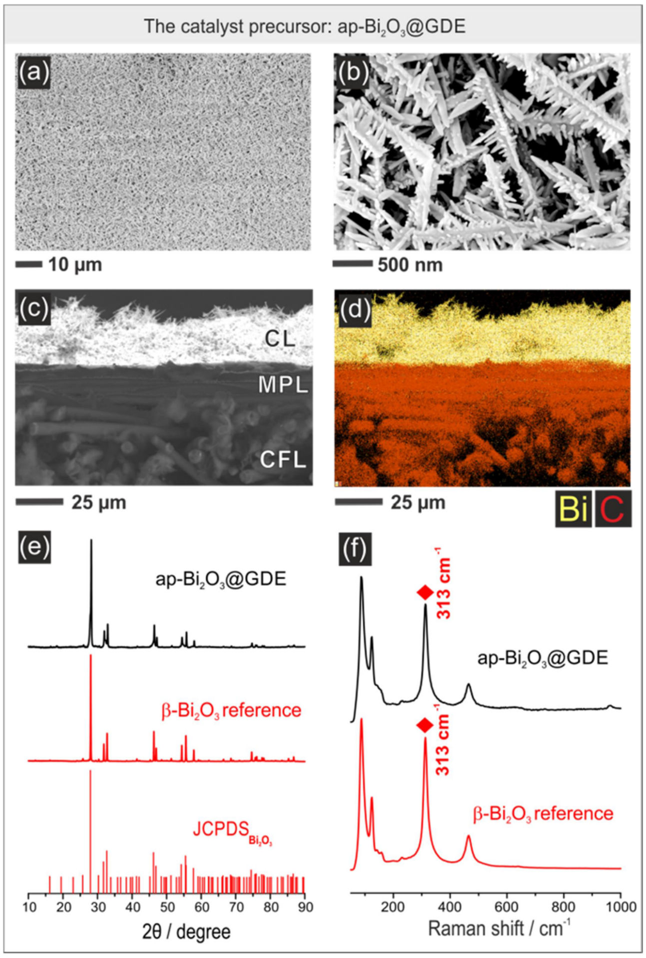

Figure 4. (a,b) Top−down SEM micrographs of ap-Bi_2O_3@GDE. (c,d) Cross-sectional SEM and EDX mapping of ap-Bi_2O_3@GDE. (e) X-ray diffractogram of ap-Bi_2O_3@GDE including references for β-Bi_2O_3. (f) Representative Raman spectrum of the ap-Bi_2O_3@GDE.

3.2. Electrochemical Performance Testing.

Catalyst performance testing was conducted in 1 and 5 mol dm^{-3} KOH electrolyte solutions using the fluidic electrolyzer system depicted in Figure 2. Unless otherwise stated, electrolysis was carried out for a duration of 1 h with the application of a freshly prepared ap-Bi_2O_3@GDE in each case. The catalyst testing results are presented in Figure 5 and confirm the superior selectivity of the dendritic Bi_2O_3 catalyst (precursor) toward formate production that has already been reported for H-type cell experiments.[39,57] Representative current (density) versus time traces are provided in Figure S11. In 1 mol dm^{-3} KOH solution, the formate efficiency ($FE_{formate}$) increases from an initial value of 72.2% to a maximum of 97.4% as the applied potential was changed from −0.3 to −0.8 V vs RHE. It is important to note that within a rather broad potential window that spans from −0.6 to −1.2 V vs RHE, the formate efficiency does not fall below 90%. The main (parasitic) byproduct of this electrolysis reaction is hydrogen. CO was also detected as a CO_2RR byproduct but only in trace amounts, never exceeding a Faradaic yield of 2.7% (Table S1). At more negative potentials, the formate efficiency decreases to 62% at −2.5 V vs RHE. Note that the FEs sum up to ca. 100% (Table S1), indicating that formate crossover through the membrane into the anolyte can safely be neglected for these electrolyses (see also discussion below).

The beneficial effect of using gas-fed electrolyzer systems becomes more obvious when we consider the corresponding PCDs (Figure 5a and Table S2), which greatly exceed those obtained in the H-type cell configuration. In H-type cells, such high CO_2RR rates cannot be achieved due to reactant mass transport limitations in the CO_2-saturated aqueous bicarbonate solution.[39] The $PCD_{formate}$ values steadily increase with the applied potential and reach in the 1 mol dm^{-3} KOH electrolyte solution a value of $PCD_{formate} = -441.2$ mA cm^{-2} at the most negative applied potential of −2.5 V vs RHE (Table S2). Throughout the entire potential range studied herein, the FEs of formate production and the corresponding PCD values remain above those of the parasitic HER.

Further improvement of the $PCD_{formate}$ values can be achieved using a 5 mol dm^{-3} KOH aqueous solution as the electrolyte (Figure 5b, Tables S3 and S4). In the present case, a superior formate current density of $PCD_{formate} = -1353.4$ mA cm^{-2} was found for an applied electrolysis potential of −2.5 V vs RHE. Compared to the results for 1 mol dm^{-3} KOH, the corresponding FEs are slightly lower in the 5 mol dm^{-3} KOH solution, reaching a maximum of 85% also at −0.8 V vs RHE. Note that the actual $PCD_{formate}$ and $FE_{formate}$ values might be even higher than those reported in Figure 5b. In particular, at high current densities, formate crossover through the membrane into the anolyte cannot be neglected anymore.[77] This is why the total Faradaic efficiency (FE_{tot}), determined from the IC analysis of the catholyte and online GC, remains clearly below 100%, e.g., $FE_{tot} = 87.0\%$ at −2.5 V vs RHE (Table S3). Figure S12 demonstrates the detection of formate

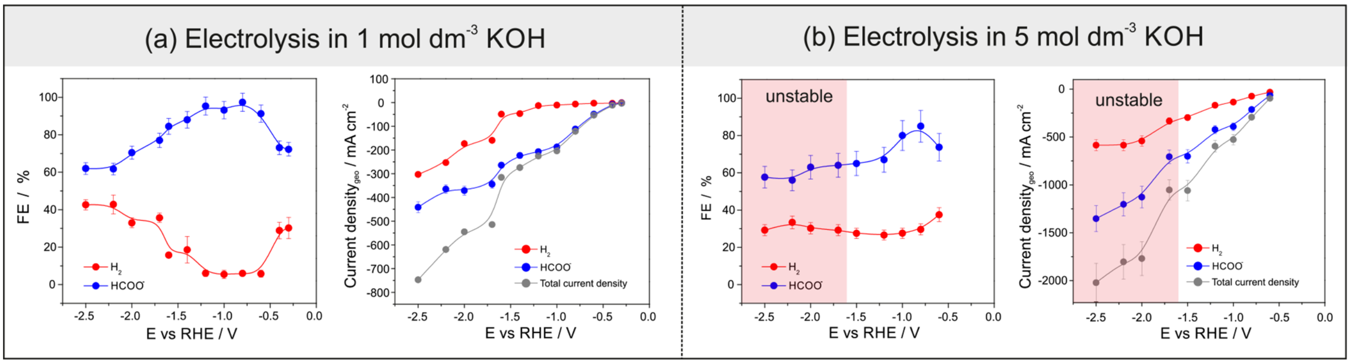

Figure 5. (a) Potential-dependent product distribution of potentiostatic CO_2 electrolysis experiments performed in 1 mol dm^{-3} KOH aqueous electrolyte. The data are represented as plots of FE values or corresponding (partial) current densities vs the applied electrolysis potential (*E* vs RHE). Of note, the applied potentials are *iR*-compensated. (b) Data set obtained for electrolysis conducted in 5 mol dm^{-3} KOH aqueous electrolyte. Electrolysis results for which the catalyst undergoes structural degradation (mechanical instability under massive hydrogen evolution) are highlighted in red. Numerical data for this figure are presented in Tables S1−S4.

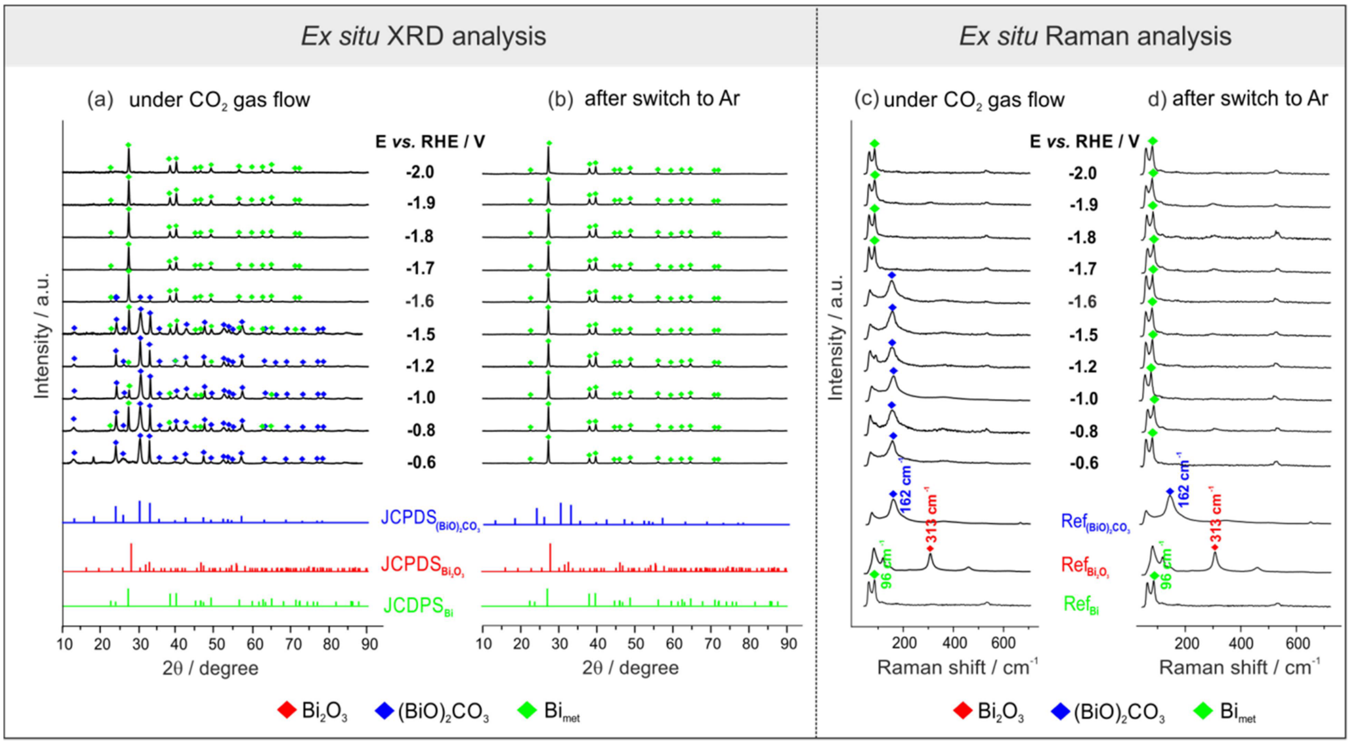

Figure 6. (a) Ex situ X-ray diffractograms recorded after 60 min of potentiostatic electrolysis in 1 mol dm^{-3} KOH solution under a continuous CO_2 gas flow; the *iR*-compensated electrolysis potentials are indicated next to the diffractograms. (b) Corresponding X-ray diffractograms of catalyst films subjected to 30 min of electrolysis under a CO_2 flow followed by an additional 30 min of electrolysis under an inert Ar gas flow. (c) Ex situ Raman spectra recorded after 60 min of potentiostatic electrolysis in 1 mol dm^{-3} KOH solution under a continuous CO_2 gas flow (corresponding to panel a). (d) Raman spectra of catalyst films subjected to 30 min of electrolysis under a CO_2 flow followed by an additional 30 min of electrolysis under an inert Ar gas flow (corresponding to panel b). Diffractogram and Raman spectroscopy features corresponding to Bi_2O_3, $(BiO)_2CO_3$, and metallic Bi are highlighted in red, blue, and green, respectively.

in the anolyte. The precise quantification of formate in the anolyte stemming from the crossover process is, however, hindered due to possible formate oxidation on the anode.

Figure S13 compares the excellent performance of the ap-Bi_2O_3@GDE catalyst precursor presented herein with data published in the literature with an emphasis on gas-fed electrolyzer studies (see also Table S5).

It is important to note that under the harsh experimental conditions applied here, the CLs become structurally unstable (highlighted in red in Figure 5b). This particular form of catalyst degradation is due to the parasitic HER (e.g., PCD_{H2} = −584.9 mA cm^{-2} at −2.5 V vs RHE), which involves massive gas evolution and H_2 bubble formation on and inside the porous CL, leading to structural disintegration of the catalyst film. For this reason, all mechanistic studies discussed hereinafter were performed in the 1 mol dm^{-3} KOH electrolyte, in which CLs remain structurally intact.

3.3. Structural Alterations within the CL. To gain insight into the structural and compositional changes occurring to the ap-Bi_2O_3@GDE precursor during the CO_2RR, processed GDEs were subjected to rigorous ex situ XRD and Raman spectroscopic analysis after electrolysis. To demonstrate the influence of CO_2 exposure on the compositional and structural alterations of the catalyst, 1 h electrolyses were performed in two different ways: (i) under a continuous flow of CO_2 for the whole duration of the experiment and (ii) under an initial CO_2 flow (30 min) followed by an additional 30 min of electrolysis in a stream of inert Ar gas (see Figure 6). Note that after switching from CO_2 to the Ar gas supply, the resulting electrolysis currents stem solely from the HER. For electrolyses that were fully performed under CO_2 flow (panels a and c in Figure 6), both XRD and Raman data point to a predominant transformation of the oxidic Bi_2O_3 precursor into a bismuth subcarbonate phase according to

$$Bi_2O_3 + CO_2 \rightleftharpoons (BiO)_2CO_3 \tag{11}$$

No characteristic features of the original Bi_2O_3 phase remained visible in the respective X-ray diffractograms or Raman spectra when the electrolyses were performed in the potential range of −0.6 to −1.5 V vs RHE (panels a and c). To gain more insight into the kinetics of $(BiO)_2CO_3$ formation, selected Raman/XRD analyses were carried out for a series of time-dependent electrolyses performed at −1.0 V vs RHE (Figure S14), which suggested a rapid Bi_2O_3 transformation into subcarbonate in the initial stage of CO_2 electrolysis. Additional control experiments performed under CO_2 gas flow at the open circuit potential (OCP) further revealed that exposure of the Bi_2O_3 precursor to gaseous CO_2 in the presence of 1 mol dm^{-3} KOH electrolyte solution is already sufficient to initiate subcarbonate formation (Figure S15). Exposure of Bi_2O_3 to the humidified CO_2 gas stream is, however, not sufficient to initiate subcarbonate formation that further emphasizes the important role of the liquid electrolyte for this phase transition (Figure S16). Although neither potential control nor an ongoing CO_2RR seems to be a prerequisite for the observed $(BiO)_2CO_3$ formation in the alkaline electrolyte solution under CO_2 gas flow, CO_2RR clearly accelerates this in situ transformation. A noteworthy difference between the phase transitions occurring under potential control and at OCP is observed in the appearance of metallic Bi, which forms only under reductive conditions (e.g., at −1.0 V vs RHE) but not at OCP (Figure S15). In agreement with this reasoning, metallic Bi is also found as a second (minor) component of the CL in addition to $(BiO)_2CO_3$ in all diffractograms recorded after 1 h of electrolysis in the potential range of −0.6 to −1.5 V vs RHE (panel a and panel c of Figure 6). This experimental observation points to a (formal) (oxo-anion → carbonate-anion) exchange process during the CO_2RR, which is superimposed by a (competing) reductive transformation of Bi(III) to Bi(0) according to

$$Bi_2O_3 + 6e^- + 3H_2O \rightleftharpoons 2Bi + 6OH^- \tag{12}$$

At lower applied overpotentials (−0.6 to −1.5 V vs RHE), the anion exchange under a continuous CO_2 flow is obviously the faster process, whereas the Bi(III) electroreduction to metallic Bi determines the final chemical composition of the CL at higher applied overpotentials. Notably, only $(BiO)_2CO_3$ is detected in the Raman spectroscopy experiments for samples processed at lower applied overpotentials (Figure 6c), with no metallic bismuth present. As recently discussed by Dutta et al. on the basis of oxidic Cu foams,[49] the (minor) deviations between XRD and Raman analyses likely originate from the different probing depths of these techniques. Raman spectroscopy is typically considered to be more surface-sensitive than XRD, which probes the entire three-dimensional "bulk" of the porous catalyst film.[49] This would suggest that the surface regions in contact with the aqueous electrolyte are mainly in the subcarbonate form, while the more buried "bulk" regions can be both metallic and $(BiO)_2CO_3$. Also, in-plane chemical inhomogeneities in the CL (discussed in detail below) can be partially responsible for observed differences (Figure 6) given the different volume probing depths by different techniques.

$(BiO)_2CO_3$-related features disappear completely from the diffractograms and Raman spectra of GDEs subjected to electrolysis potentials below −1.5 V vs RHE (panels a and c of Figure 6). Our results demonstrate that the subcarbonate reaction pathway of formate formation (Figure 1), already described for liquid-flow and H-type cell test beds,[39,55,78] is also relevant for the CO_2RR performed in gas-fed electrolyzer devices. Intriguingly, in the present case, the subcarbonate phase remains stable even at an extremely cathodic potential of −1.5 V vs RHE (Figure 6a,c). This behavior hints to a further stabilization of the $(BiO)_2CO_3$ catalyst in the CO_2 gas-fed electrolyzer. Our results indicate that the CO_2 abundance may be the key factor for the stabilization of Bi(III) in the subcarbonate phase during the CO_2RR. $(BiO)_2CO_3$ electroreduction involves the (formal) release of CO_2 according to

$$(BiO)_2CO_3 + 6e^- + 3H_2O \rightleftharpoons 2Bi + 6OH^- + CO_2 \tag{13}$$

which actually rationalizes the observed cathodic shift of the reduction potential in the presence of gaseous CO_2 for the gas-fed electrolyzer. Of note, the bismuth subcarbonate electroreduction can also be formulated by assuming a carbonate anion release according to

$$(BiO)_2CO_3 + 6e^- + 2H_2O \rightleftharpoons 2Bi + 4OH^- + CO_3^{2-} \tag{14}$$

The assumed CO_2-mediated stabilization of the subcarbonate occurs in the latter case through the carbonic acid/bicarbonate/carbonate/CO_2 equilibria in the alkaline electrolyte solution.

To experimentally prove our working hypothesis of a CO_2-mediated stabilization of the subcarbonate phase, we performed dedicated control experiments in which 30 min CO_2 electrolyses were followed by additional 30 min electrolyses under an Ar gas flow. Under these "inert" conditions, electrolysis continues exclusively through the HER. Panels b and d in Figure 6 depict the corresponding ex situ XRD and Raman data of these processed GDEs. The results indeed confirm the complete reductive transformation of $(BiO)_2CO_3$, formed in the initial phase of electrolysis under CO_2 supply, into metallic Bi at all applied potentials after the switch from CO_2 to an inert Ar gas supply (Figure 6b,d). Corresponding time-dependent experiments (Figure S17) indicate a reduction process that occurs rapidly on the outermost catalyst surface being in contact with aqueous electrolyte (preferentially probed by Raman spectroscopy) with, however, a certain time delay in the three-dimensional bulk of the catalyst material (probed by XRD).

To further support our working hypothesis of a stabilizing effect of CO_2, we conducted additional potential-dependent in situ Raman spectroscopy experiments in the absence of any CO_2 gas supply. Under these conditions, $(BiO)_2CO_3$ reduction already occurs in the CO_2-free 1 mol dm^{-3} KOH electrolyte solution under relatively mild cathodic conditions, at an applied potential of approximately −0.3 V vs RHE (Figure S18). Of note, corresponding stability Raman experiments

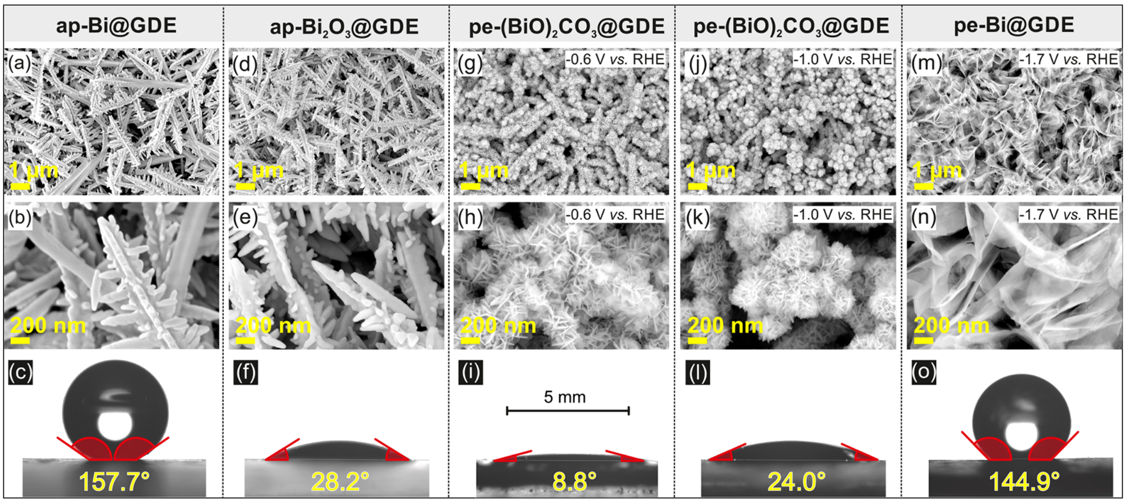

Figure 7. Top−down SEM inspection and corresponding contact-angle measurements of the catalyst (precursor) layers. (a−c) As-prepared porous metallic Bi film (denoted as ap-Bi@GDE). (d−f) As-prepared Bi_2O_3 film on the GDL after thermal annealing (denoted as ap-Bi_2O_3@GDE). (g−i) Postelectrolysis (pe) inspection of the CL after 60 min of electrolysis at −0.6 V vs RHE (denoted as pe-$(BiO)_2CO_3$@GDE). (j−l) Results obtained after 60 min of electrolysis at −1.0 V vs RHE. (m−o) Results obtained after 60 min of electrolysis at −1.7 V vs RHE (denoted as pe-Bi@GDE).

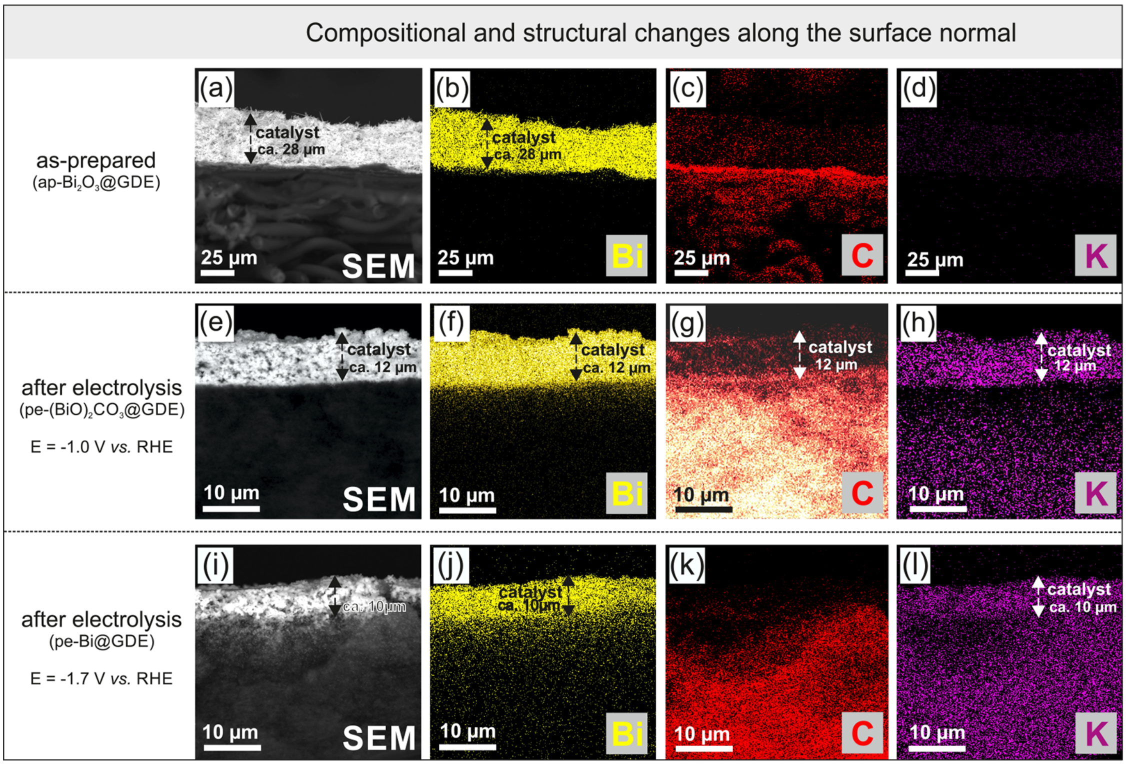

Figure 8. Representative cross-sectional SEM and EDX analyses of the GDEs. (a−d) Data for the ap-Bi_2O_3@GDE sample (after thermal annealing of the metallic Bi sample). (e−h) Postelectrolysis data for a sample subjected to 60 min of electrolysis in 1 mol dm^{-3} KOH electrolyte at −1.0 V vs RHE; this sample is representative of a predominant presence of the subcarbonate phase. (i−l) Postelectrolysis data for a sample subjected to 60 min of electrolysis in 1 mol dm^{-3} KOH at −1.7 V vs RHE; this sample is representative of a predominant presence of the metallic Bi phase.

using the Bi_2O_3 film demonstrate a higher stability of $(BiO)_2CO_3$ against electroreduction compared to the corresponding oxidic precursor (Figure S18), even in the absence of any stabilizing CO_2 gas dissolved in the electrolyte or in direct contact with the subcarbonate phase. The observed reduction potential of Bi_2O_3 agrees fairly well with the Bi/water Pourbaix diagram depicted in Figure S19.

Our ex situ XRD analysis clearly indicates that the subcarbonate formation affects the entire three-dimensional bulk of the Bi_2O_3 precursor material. Complementary top−down SEM analysis reveals that both the CO_2-mediated transformation of Bi_2O_3 and the potential-induced electroreduction of the subcarbonate phase into metallic Bi lead to substantial alterations in film morphology across various length scales (Figure 7). The dendritic appearance, which is characteristic for films of the as-prepared metallic Bi (panels a and b) and annealed Bi_2O_3 (panels d and e), disappears in the course of $(BiO)_2CO_3$ formation and is replaced by more

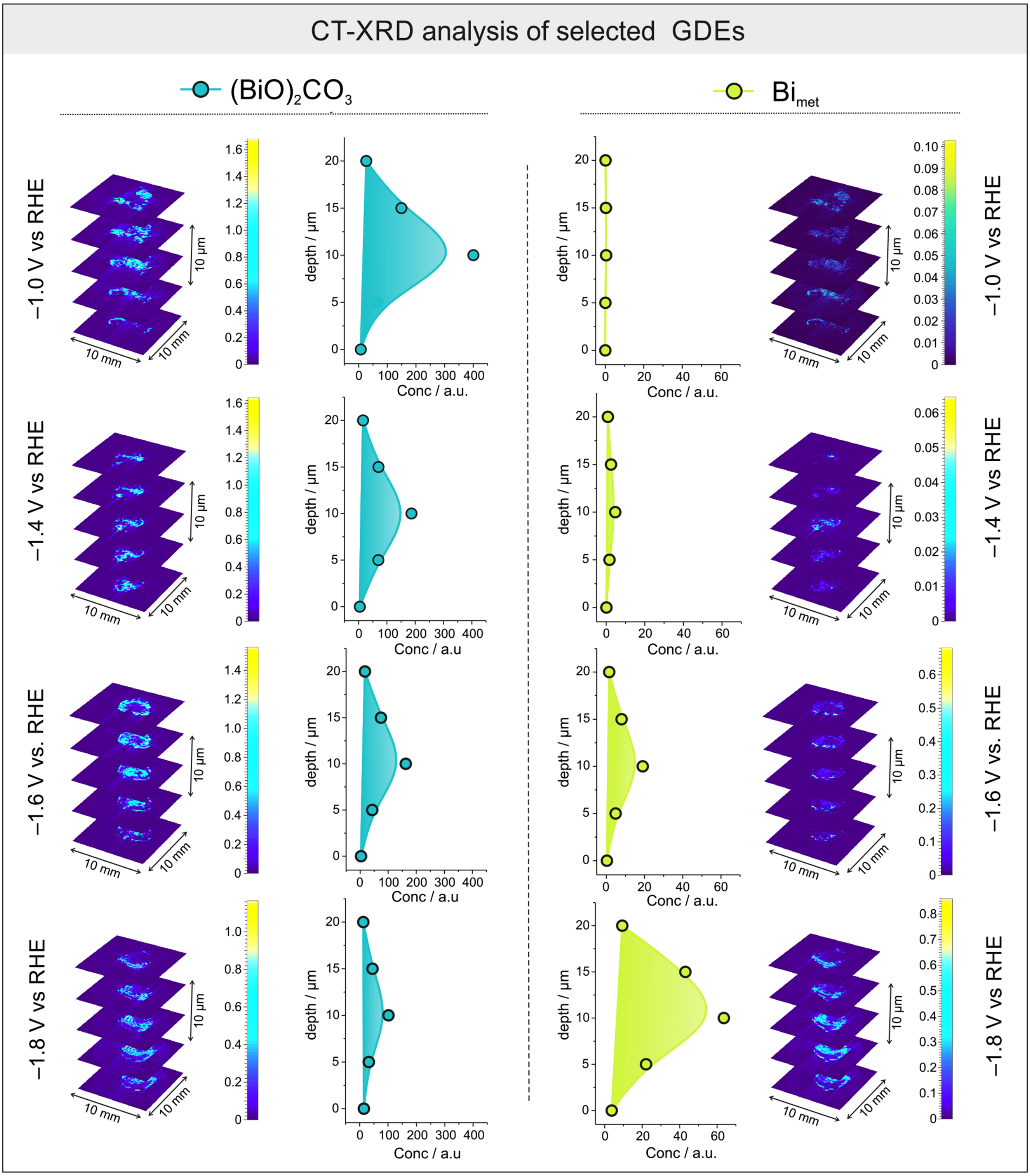

Figure 9. XRD-CT scans of the CL after CO$_2$RR (1 h) at various potentials. A series of plane scans (in the *xy*-plane) have been performed at different sample heights (vertical positions). The left column shows the distribution of (BiO)$_2$CO$_3$ in different depths and corresponding depth profiles determined at the selected areas of the sample. The right column shows the same for the Bi metal phase.

compact aggregates of subcarbonate nanosheets (panels g and k). Further electroreduction of the in situ formed (BiO)$_2$CO$_3$ at −1.7 V vs RHE leaves more extended micron-sized sheets of metallic Bi behind (panels m and n). Complementary contact-angle measurements (panels c and f) hint at a transition from initially hydrophobic to pronounced hydrophilic surface characteristics as a consequence of thermal annealing of the as-prepared metallic Bi (ap-Bi@GDE: Θ = 157.7°). The contact angle of this ap-Bi$_2$O$_3$@GDE decreased to Θ = 28.2°. Moreover, also the formed bismuth subcarbonate shows pronounced hydrophilic characteristics (pe-Bi$_2$O$_3$@GDE: Θ = 8.8°/−0.6 V vs RHE, Θ = 24.0°/−1.0 V vs RHE, panel i and panel l, respectively). Interestingly, the initial hydrophobic surface properties of the as-prepared Bi were largely recovered after subcarbonate electroreduction back into metallic Bi (denoted as pe-Bi@GDE: Θ = 144.9°, after electrolysis at −1.7 V vs RHE, panel o), although the film morphology showed substantial changes, e.g., compared to the as-prepared dendritic Bi. These contact angle analyses suggest a facile electrolyte permeation of the three-dimensional structure of the CL when the oxidic Bi_2O_3 precursor is brought into contact with the aqueous electrolyte. This statement is confirmed by a further control experiment provided in Figure S20. It can be further assumed that such catalyst wetting is sustained even if the oxidic catalyst precursor is transformed into the hydrophilic subcarbonate phase during the CO_2RR. To probe the extent to which the interior of the micrometer-thick CL is wetted by the alkaline electrolyte, we applied cross-sectional SEM/EDX analysis, with a focus on potassium concentration profiles along the surface normal (Figure 8). The exclusive source of potassium cations is the KOH electrolyte solution; therefore, the presence of potassium cations in the GDE serves as a "chemical fingerprint" for the permeation of the CL with electrolyte and further points to an (undesired) electrolyte flooding into deeper layers of the GDE. This approach represents an extension of the recently developed analysis technique applied for postelectrolysis visualization of potassium carbonate precipitates in the GDE interior.[79] Indeed, the K-EDX mapping suggests complete wetting of the Bi_2O_3 precursor layer, the formed subcarbonate, and the metallic bismuth layer down to the MPL (see Figure 8h and l). Of note, our above considerations of the wetting characteristics are based solely on (postelectrolysis) ex situ contact-angle measurements and neglect additional electrocapillary effects under potential control, which might transform an intrinsically hydrophobic material (e.g., metallic Bi film) into a more hydrophilic one. The extent to which the electrolyte is expelled from the CL after the Bi(III) reduction into Bi metal takes place cannot be ultimately determined by the ex situ measurements presented herein.

Interestingly, after electrolyses, potassium is also detected inside the MPL of the GDE (Figure 8h and l). This observation indicates a partial electrolyte permeation into the MPL during the CO_2RR. However, considering the observed high PCDs and FEs of formate production at these applied electrolysis potentials (see also Figure 5a), it appears unlikely that the micropores of the MPL (Figure S3) would become completely blocked by the electrolyte. The CO_2 gas supply through the micropores of the GDL toward the CL is still apparently sufficient, and it is likely that the electrolyte entering the MPL and the fibrous layer during electrolyzer operation perspirates out of the electrolyzer with the outward CO_2 gas stream. Such electrolyte perspiration typically prevents massive electrolyte flooding and complete blockage of the micropores, which would result in substantial CO_2RR performance losses.

As a consequence of the described phase transitions, the CL also experiences a further structural alteration in film thickness. Cross-sectional SEM analysis reveals a substantial decrease in CL thickness occurring with subcarbonate formation at −1.0 V vs RHE and Bi_2O_3 reduction to metallic Bi at −1.7 V vs RHE (Figure 8a,e,i). The film thickness decreases from an initial value of ~28 μm (ap-Bi_2O_3@GDE) to ~12 μm (pe-$(BiO_2)CO_3$@GDE) and ~10 μm (pe-Bi@GDE). However, complementary ICP-MS analyses of the electrolyte to which the CL was exposed during electrolysis reveal only a minor loss (<3%) of catalyst material in the liquid electrolyte (Figure S21), which cannot account for the thickness changes observed in the cross-sectional SEM analysis (Figure 8a,e,i). From this comparison, it can safely be concluded that the density of the CL increases during the transformation of Bi_2O_3 into either $(BiO)_2CO_3$ or metallic Bi. This substantial structural alteration obviously does not compromise the facile transport of CO_2 through the GDL into the CL (see Figure 5a).

To better understand the differences observed between XRD and Raman spectroscopy (Figure 6) and to gain information on the heterogeneous distribution of $(BiO)_2CO_3$ and metallic Bi in the CL, a series of XRD-CT scans have been collected for samples that were made subject to electrolysis at different potentials. By using this technique,[80,81] we can image the chemical composition with a relatively high spatial resolution (40 μm) in the whole bulk of the sample. The maps in Figure 9 represent the location of the $(BiO)_2CO_3$ (left column) and metallic Bi (right column) in the CL after 1 h of CO_2RR at increasing cathodic potentials, from −1.0 to −1.8 V vs RHE for each sample.

To derive the concentration profile of $(BiO)_2CO_3$ and metallic Bi as a function of depth, the intensities of the (1,0,3) and (0,1,3) peaks at $2\theta = 3.01°$ for $(BiO)_2CO_3$ and that of the (2,−1,1) peak at $2\theta = 3.91°$ for Bi were integrated in the XRD pattern corresponding to each voxel (X-ray probe energy of 80 keV). The result confirms that the distribution of the phases is rather homogeneous as a function of the CL depth. The coexistence of $(BiO)_2CO_3$ and metallic Bi in the same positions in the GDE is highlighted in Figure 9, with a general increase in the metallic phase at the expense of the carbonate phase for CO_2RR at lower potentials. A relatively higher concentration of metallic Bi on the CL surface (in contact with the electrolyte) is observed at an extremely negative potential (−1.8 V vs RHE). This is in agreement with the Raman and ex situ XRD measurements showing the preferential subcarbonate phase formation on the same CL-electrolyte interface at lower CO_2RR potentials, even though both phases are present in the bulk. The interesting observation that the phases in the bulk are mixed and, therefore, not in thermodynamic equilibrium can likely be explained by diffusion effects occurring in the CL that lead to uneven potential distribution and a strong in-plane phase inhomogeneity. The potential distribution on the surface of the CL, in contact with the electrolyte solution, is relatively homogeneous, allowing subsequent phase transformations toward the thermodynamic equilibrium. However, the bulk of the CL can be subjected to much larger concentration and potential differences that can lead to the mixing of crystalline phases.

Hints to phase mixing in particular at "intermediate potentials" can clearly be seen in Figure 10, showing (in panels a and b) the phase distribution of $(BiO)_2CO_3$ and Bi, respectively, in a CL sample following 1 h electrolysis at −1.6 V vs RHE. These maps reveal locations where either one of the phases is completely missing, marked by white ovals, which can only be explained by assuming that these areas were subject to different CO_2 concentrations and/or potentials. Apart from these areas, the sample contains both phases, mixed with uneven distribution (panel c). In certain regions, the phase transformation proceeded from the surface in contact with the electrolyte to the bulk. This is demonstrated by the line profiles in panel (d), where we plotted the phase distribution and the relative difference along the gray line shown in panel (c). In

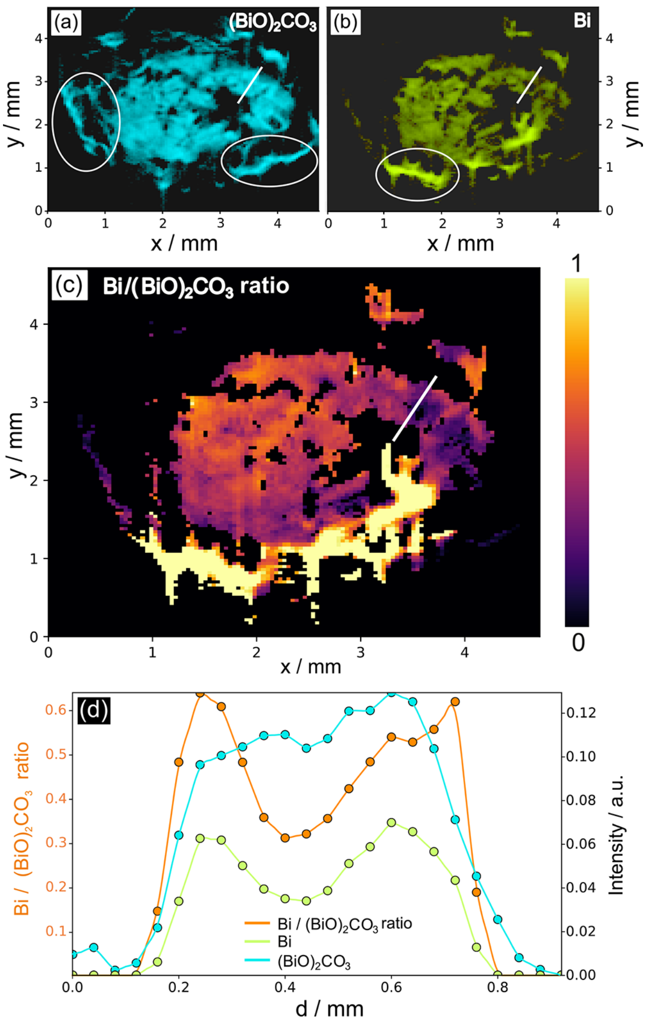

Figure 10. In-plane distribution of (a) $(BiO)_2CO_3$ and (b) Bi of the CL after CO_2RR (1 h) at −1.6 V vs RHE. The inhomogeneous nature of the phase distribution is highlighted in (c) by showing the Bi/$(BiO)_2CO_3$ ratio. Plot (d) presents line profiles along the white line in (a−c).

this area, the Bi phase is much more abundant close to the electrolyte than in the center of the region. As we observe these effects only at larger scales of several hundred microns, areas of smaller scales are likely homogeneous, as supported by SEM measurements, and this explains the relative homogeneity of phases in the out-of-plane direction. These considerations are important in the CL design, as the slow phase mixing can lead to the degradation of catalyst selectivity and may play a role in long-time catalyst deactivation.

4. CONCLUSIONS AND OUTLOOK

In this work, we have integrated for the first time the DHBT-assisted metal foam deposition of CO_2RR catalyst materials into a more general preparation scheme for the preparation of GDEs that can be used in gas-fed electrolyzer setups. The so-called subcarbonate reaction pathway of CO_2-to-formate electroreduction is shown to be prevalent also at high current densities (e.g., $PCD_{formate}$ = −207.1 mA cm^{-2} and $FE_{formate}$ = 95.3% at −1.2 V vs RHE) in these gas-fed electrolyzer systems. We have demonstrated that the local abundance of gaseous CO_2 during operation of a gas-fed electrolyzer leads to substantial stabilization of the bismuth subcarbonate catalyst in which Bi is present in an oxidation state of +3. The active subcarbonate phase ($(BiO)_2CO_3$) readily forms in situ, during CO_2RR, from an oxidic CO_2-absorbing Bi_2O_3 precursor material. Under a continuous CO_2 gas flow in the electrolyzer, the $(BiO)_2CO_3$ phase transforms into metallic Bi only under harsh reductive conditions at applied electrolysis potentials more negative than −1.5 V vs RHE, whereas this cathodic transformation occurs in the absence of CO_2 under much milder conditions, at −0.3 V vs RHE, as evidenced by in situ Raman spectroscopy. After electroreduction of the $(BiO)_2CO_3$ phase into metallic Bi, even higher partial current densities were observed, e.g., a value of $PCD_{formate}$ = −441.2 mA cm^{-2} at −2.5 V vs RHE. Increasing the alkalinity of the liquid electrolyte further (e.g., by using 5 mol dm^{-3} KOH solution) boosts the $PCD_{formate}$ values beyond −1 A cm^{-2}. Although the transformation of the subcarbonate phase to metallic Bi does increase the PCD of formate production, the metallic Bi catalyst has a substantially lower FE as it also facilitates hydrogen evolution. It is a novel result of this study that a constant, high-rate CO_2 feed has to be maintained in order to uphold the stability of the highly selective subcarbonate phase at stringent cathodic potentials.

Postelectrolysis K-EDX mapping of cross-sectioned GDEs demonstrated complete permeation of the CL with 1 mol dm^{-3} KOH electrolyte solution as a prerequisite for the formation of triple-phase boundaries facilitating CO_2RR.

Ex situ CT-XRD techniques were applied to GDEs following electrolysis and confirmed the appearance of heterogeneous composite catalyst films consisting of metallic Bi and $(BiO)_2CO_3$. Relative phase abundances are not only potential-dependent but also show great variance across the sample, which can compromise the long-term stability of the catalyst.

This present study lays the foundation for future work, which will apply advanced operando XRD-CT techniques addressing highly important in-plane and out-of-plane inhomogeneity effects, which appear in particular in the intermediate potential regimes where phase transitions in the catalyst film take place. Also, the important issue of the electrolyte transport into and through the catalyst film (e.g., into the carbon support) will be addressed by operando XRD-CT, introducing a high spatial resolution under reactive conditions into the diffraction experiment.

■ ASSOCIATED CONTENT

SI Supporting Information

The Supporting Information is available free of charge at https://pubs.acs.org/doi/10.1021/acscatal.2c02549.

Experimental procedures, extra control and reference experiments, and supporting data extracted from the literature (PDF)

■ AUTHOR INFORMATION

Corresponding Authors

Abhijit Dutta − *Department of Chemistry, Biochemistry and Pharmaceutical Science, University of Bern, 3012 Bern, Switzerland*; orcid.org/0000-0002-3054-0492;
Email: abhijit.dutta@unibe.ch
Peter Broekmann − *Department of Chemistry, Biochemistry and Pharmaceutical Science and National Centre of Competence in Research (NCCR) Catalysis, University of*

Bern, 3012 Bern, Switzerland; orcid.org/0000-0002-6287-1042; Email: peter.broekmann@unibe.ch

Authors

Iván Zelocualtecatl Montiel − *Department of Chemistry, Biochemistry and Pharmaceutical Science and National Centre of Competence in Research (NCCR) Catalysis, University of Bern, 3012 Bern, Switzerland*

Kiran Kiran − *Department of Chemistry, Biochemistry and Pharmaceutical Science, University of Bern, 3012 Bern, Switzerland*

Alain Rieder − *Department of Chemistry, Biochemistry and Pharmaceutical Science and National Centre of Competence in Research (NCCR) Catalysis, University of Bern, 3012 Bern, Switzerland*

Anna Iarchuk − *Department of Chemistry, Biochemistry and Pharmaceutical Science and National Centre of Competence in Research (NCCR) Catalysis, University of Bern, 3012 Bern, Switzerland*

Soma Vesztergom − *Department of Chemistry, Biochemistry and Pharmaceutical Science, University of Bern, 3012 Bern, Switzerland; Department of Physical Chemistry, Eötvös Loránd University, 1117 Budapest, Hungary*

Marta Mirolo − *European Synchrotron Radiation Facility (ESRF), 38000 Grenoble, France*

Isaac Martens − *European Synchrotron Radiation Facility (ESRF), 38000 Grenoble, France*

Jakub Drnec − *European Synchrotron Radiation Facility (ESRF), 38000 Grenoble, France*

Complete contact information is available at:
https://pubs.acs.org/10.1021/acscatal.2c02549

Author Contributions

$^{\perp}$I.Z.M. and A.D. contributed equally.

Notes

The authors declare no competing financial interest.

The raw data to this paper are made fully accessible to the public via Zenodo at doi 10.5281/zenodo.6908494 along with the publication of this manuscript.

■ ACKNOWLEDGMENTS

This publication was created as part of NCCR Catalysis (grant number 180544), a National Centre of Competence in Research funded by the Swiss National Science Foundation. A.I. acknowledges financial support from the State Secretariat for Education, Research, and Innovation through a Swiss Government Excellence Scholarship for Foreign Scholars. S.V. acknowledges financial support from the National Research, Development and Innovation Office of Hungary under the grant FK135375.

■ REFERENCES

(1) Appel, A. M.; Bercaw, J. E.; Bocarsly, A. B.; Dobbek, H.; DuBois, D. L.; Dupuis, M.; Ferry, J. G.; Fujita, E.; Hille, R.; Kenis, P. J. A.; Kerfeld, C. A.; Morris, R. H.; Peden, C. H. F.; Portis, A. R.; Ragsdale, S. W.; Rauchfuss, T. B.; Reek, J. N. H.; Seefeldt, L. C.; Thauer, R. K.; Waldrop, G. L. Frontiers, Opportunities, and Challenges in Biochemical and Chemical Catalysis of CO_2 Fixation. *Chem. Rev.* **2013**, *113*, 6621−6658.

(2) Whipple, D. T.; Kenis, P. J. A. Prospects of CO_2 Utilization via Direct Heterogeneous Electrochemical Reduction. *J. Phys. Chem. Lett.* **2010**, *1*, 3451−3458.

(3) Karl, T. R.; Trenberth, K. E. Modern Global Climate Change. *Science* **2003**, *302*, 1719−1723.

(4) Hori, Y.; Kikuchi, K.; Suzuki, S. Production of CO and CH_4 in Electrochemical Reduction of CO_2 at Metal-Electrodes in Aqueous Hydrogencarbonate Solution. *Chem. Lett.* **1985**, *11*, 1695−1698.

(5) Dutta, A.; Morstein, C. E.; Rahaman, M.; Cedeño López, A.; Broekmann, P. Beyond Copper in CO_2 Electrolysis: Effective Hydrocarbon Production on Silver-Nanofoam Catalysts. *ACS Catal.* **2018**, 8357−8368.

(6) Mistry, H.; Choi, Y. W.; Bagger, A.; Scholten, F.; Bonifacio, C. S.; Sinev, I.; Divins, N. J.; Zegkinoglou, I.; Jeon, H. S.; Kisslinger, K.; Stach, E. A.; Yang, J. C.; Rossmeisl, J.; Cuenya, B. R. Enhanced Carbon Dioxide Electroreduction to Carbon Monoxide over Defect-Rich Plasma-Activated Silver Catalysts. *Angew. Chem., Int. Ed.* **2017**, *56*, 11394−11398.

(7) Hoshi, N.; Kato, M.; Hori, Y. Electrochemical reduction of CO_2 on single crystal electrodes of silver Ag(111), Ag(100) and Ag(110). *J. Electroanal. Chem.* **1997**, *440*, 283−286.

(8) Ma, M.; Djanashvili, K.; Smith, W. A. Selective electrochemical reduction of CO_2 to CO on CuO-derived Cu nanowires. *Phys. Chem. Chem. Phys.* **2015**, *17*, 20861−20867.

(9) Ma, M.; Trześniewski, B. J.; Xie, J.; Smith, W. A. Selective and Efficient Reduction of Carbon Dioxide to Carbon Monoxide on Oxide-Derived Nanostructured Silver Electrocatalysts. *Angew. Chem., Int. Ed.* **2016**, *55*, 9748−9752.

(10) Dutta, A.; Rahaman, M.; Luedi, N. C.; Mohos, M.; Broekmann, P. Morphology Matters: Tuning the Product Distribution of CO_2 Electroreduction on Oxide-Derived Cu Foam Catalysts. *ACS Catal.* **2016**, *6*, 3804−3814.

(11) Dewulf, D. W.; Jin, T.; Bard, A. J. Electrochemical and Surface Studies of Carbon-Dioxide Reduction to Methane and Ethylene at Copper Electrodes in Aqueous-Solutions. *J. Electrochem. Soc.* **1989**, *136*, 1686−1691.

(12) Hirunsit, P.; Soodsawang, W.; Limtrakul, J. CO_2 Electrochemical Reduction to Methane and Methanol on Copper-Based Alloys: Theoretical Insight. *J. Phys. Chem. C* **2015**, *119*, 8238−8249.

(13) Dinh, C.-T.; Burdyny, T.; Kibria, M. G.; Seifitokaldani, A.; Gabardo, C. M.; García de Arquer, F. P.; Kiani, A.; Edwards, J. P.; De Luna, P.; Bushuyev, O. S.; Zou, C.; Quintero-Bermudez, R.; Pang, Y.; Sinton, D.; Sargent, E. H. CO_2 electroreduction to ethylene via hydroxide-mediated copper catalysis at an abrupt interface. *Science* **2018**, *360*, 783−787.

(14) Mistry, H.; Varela, A. S.; Bonifacio, C. S.; Zegkinoglou, I.; Sinev, I.; Choi, Y. W.; Kisslinger, K.; Stach, E. A.; Yang, J. C.; Strasser, P.; Cuenya, B. R. Highly Selective Plasma-Activated Copper Catalysts for Carbon Dioxide Reduction to Ethylene. *Nat. Commun.* **2016**, *7*, 12123.

(15) Hori, Y.; Takahashi, I.; Koga, O.; Hoshi, N. Selective Formation of C2 Compounds from Electrochemical Reduction of CO_2 at a Series of Copper Single Crystal Electrodes. *J. Phys. Chem. B* **2002**, *106*, 15−17.

(16) Hori, Y.; Murata, A.; Takahashi, R.; Suzuki, S. Enhanced Formation of Ethylene and Alcohols at Ambient Temperature and Pressure in Electrochemcial Reduction of Carbondioxide at a Copper Electrode. *J. Chem. Soc., Chem. Commun.* **1988**, 17−19.

(17) Yano, H.; Shirai, F.; Nakayama, M.; Ogura, K. Efficient electrochemical conversion of CO_2 to CO, C_2H_4 and CH_4 at a three-phase interface on a Cu net electrode in acidic solution. *J. Electroanal. Chem.* **2002**, *519*, 93−100.

(18) Frese, K. W.; Leach, S. Electrochemical Reduction of Carbondioxide to Methane, Methanol, and CO on Ru Electrodes. *J. Electrochem. Soc.* **1985**, *132*, 259−260.

(19) Ohta, K.; Kawamoto, M.; Mizuno, T.; Lowy, D. A. Electrochemical reduction of carbon dioxide in methanol at ambient temperature and pressure. *J. Appl. Electrochem.* **1998**, *28*, 717−724.

(20) Albo, J.; Irabien, A. Cu_2O-loaded gas diffusion electrodes for the continuous electrochemical reduction of CO_2 to methanol. *J. Catal.* **2016**, *343*, 232−239.

(21) Hoang, T. T. H.; Verma, S.; Ma, S.; Fister, T. T.; Timoshenko, J.; Frenkel, A. I.; Kenis, P. J. A.; Gewirth, A. A. Nanoporous Copper−Silver Alloys by Additive-Controlled Electrodeposition for the Selective Electroreduction of CO_2 to Ethylene and Ethanol. *J. Am. Chem. Soc.* **2018**, *140*, 5791−5797.

(22) Ren, D.; Ang, B. S.-H.; Yeo, B. S. Tuning the Selectivity of Carbon Dioxide Electroreduction toward Ethanol on Oxide-Derived Cu_xZn Catalysts. *ACS Catal.* **2016**, *6*, 8239−8247.

(23) Ma, S.; Sadakiyo, M.; Luo, R.; Heima, M.; Yamauchi, M.; Kenis, P. J. A. One-Step Electrosynthesis of Ethylene and Ethanol from CO_2 in an Alkaline Electrolyzer. *J. Power Sources* **2016**, *301*, 219−228.

(24) Rahaman, M.; Kiran, K.; Montiel, I. Z.; Grozovski, V.; Dutta, A.; Broekmann, P. Selective n-propanol formation from CO_2 over degradation-resistant activated PdCu alloy foam electrocatalysts. *Green Chem.* **2020**, *22*, 6497−6509.

(25) Chi, L.-P.; Niu, Z.-Z.; Zhang, X.-L.; Yang, P.-P.; Liao, J.; Gao, F.-Y.; Wu, Z.-Z.; Tang, K.-B.; Gao, M.-R. Stabilizing indium sulfide for CO_2 electroreduction to formate at high rate by zinc incorporation. *Nat. Commun.* **2021**, *12*, 5835.

(26) Yan, S.; Peng, C.; Yang, C.; Chen, Y.; Zhang, J.; Guan, A.; Lv, X.; Wang, H.; Wang, Z.; Sham, T.-K.; Han, Q.; Zheng, G. Electron Localization and Lattice Strain Induced by Surface Lithium Doping Enable Ampere-Level Electrosynthesis of Formate from CO_2. *Angew. Chem., Int. Ed.* **2021**, *60*, 25741−25745.

(27) Chen, Y.; Vise, A.; Klein, W. E.; Cetinbas, F. C.; Myers, D. J.; Smith, W. A.; Deutsch, T. G.; Neyerlin, K. C. A Robust, Scalable Platform for the Electrochemical Conversion of CO_2 to Formate: Identifying Pathways to Higher Energy Efficiencies. *ACS Energy Lett.* **2020**, *5*, 1825−1833.

(28) Rice, C.; Ha, S.; Masel, R. I.; Waszczuk, P.; Wieckowski, A.; Barnard, T. Direct formic acid fuel cells. *J. Power Sources* **2002**, *111*, 83−89.

(29) Rice, C.; Ha, S.; Masel, R. I.; Wieckowski, A. Catalysts for direct formic acid fuel cells. *J. Power Sources* **2003**, *115*, 229−235.

(30) Zhu, Y.; Ha, S. Y.; Masel, R. I. High power density direct formic acid fuel cells. *J. Power Sources* **2004**, *130*, 8−14.

(31) Fellay, C.; Dyson, P. J.; Laurenczy, G. A Viable Hydrogen-Storage System Based On Selective Formic Acid Decomposition with a Ruthenium Catalyst. *Angew. Chem., Int. Ed.* **2008**, *47*, 3966−3968.

(32) Rahimi, A.; Ulbrich, A.; Coon, J. J.; Stahl, S. S. Formic-acid-induced depolymerization of oxidized lignin to aromatics. *Nature* **2014**, *515*, 249−252.

(33) Muck, R. E.; Nadeau, E. M. G.; McAllister, T. A.; Contreras-Govea, F. E.; Santos, M. C.; Kung, L. Silage review: Recent advances and future uses of silage additives. *J. Dairy Sci.* **2018**, *101*, 3980−4000.

(34) Li, H.; Opgenorth Paul, H.; Wernick David, G.; Rogers, S.; Wu, T.-Y.; Higashide, W.; Malati, P.; Huo, Y.-X.; Cho Kwang, M.; Liao James, C. Integrated Electromicrobial Conversion of CO_2 to Higher Alcohols. *Science* **2012**, *335*, 1596−1596.

(35) Hori, Y. Electrochemical CO_2 Reduction on Metal Electrodes. In *Modern Aspects of Electrochemistry*; Springer: New York, 2008; pp 89−189.

(36) Vesztergom, S.; Dutta, A.; Rahaman, M.; Kiran, K.; Zelocualtecatl Montiel, I.; Broekmann, P. Hydrogen Bubble Templated Metal Foams as Efficient Catalysts of CO_2 Electroreduction. *ChemCatChem* **2021**, *13*, 1039−1058.

(37) Dutta, A.; Rahaman, M.; Mohos, M.; Zanetti, A.; Broekmann, P. Electrochemical CO_2 Conversion Using Skeleton (Sponge) Type of Cu Catalysts. *ACS Catal.* **2017**, *7*, 5431−5437.

(38) Liu, X.; Schlexer, P.; Xiao, J.; Ji, Y.; Wang, L.; Sandberg, R. B.; Tang, M.; Brown, K. S.; Peng, H.; Ringe, S.; Hahn, C.; Jaramillo, T. F.; Nørskov, J. K.; Chan, K. pH effects on the electrochemical reduction of CO_2 towards C2 products on stepped copper. *Nat. Commun.* **2019**, *10*, 32.

(39) Dutta, A.; Zelocualtecatl Montiel, I.; Kiran, K.; Rieder, A.; Grozovski, V.; Gut, L.; Broekmann, P. A Tandem ($Bi_2O_3 \rightarrow Bi_{met}$) Catalyst for Highly Efficient ec-CO_2 Conversion into Formate: Operando Raman Spectroscopic Evidence for a Reaction Pathway Change. *ACS Catal.* **2021**, *11*, 4988−5003.

(40) Dutta, A.; Kuzume, A.; Kaliginedi, V.; Rahaman, M.; Sinev, I.; Ahmadi, M.; Cuenya, B. R.; Vesztergom, S.; Broekmann, P. Probing the chemical state of tin oxide NP catalysts during CO_2 electroreduction: A complementary operando approach. *Nano Energy* **2018**, *53*, 828−840.

(41) Dutta, A.; Kuzume, A.; Rahaman, M.; Vesztergom, S.; Broekmann, P. Monitoring the Chemical State of Catalysts for CO_2 Electroreduction: An In Operando Study. *ACS Catal.* **2015**, *5*, 7498−7502.

(42) Sen, S.; Brown, S. M.; Leonard, M.; Brushett, F. R. Electroreduction of carbon dioxide to formate at high current densities using tin and tin oxide gas diffusion electrodes. *J. Appl. Electrochem.* **2019**, *49*, 917−928.

(43) Lee, S.; Ocon, J. D. Alkaline CO_2 Electrolysis toward Selective and Continuous $HCOO^-$ Production over SnO_2 Nanocatalysts. *J. Phys. Chem. C* **2015**, *119*, 4884−4890.

(44) Zhao, S.; Li, S.; Guo, T.; Zhang, S.; Wang, J.; Wu, Y.; Chen, Y. Advances in Sn-Based Catalysts for Electrochemical CO_2 Reduction. *Nano-Micro Lett.* **2019**, *11*, 62.

(45) García, J.; Jiménez, C.; Martínez, F.; Camarillo, R.; Rincón, J. Electrochemical reduction of CO_2 using Pb catalysts synthesized in supercritical medium. *J. Catal.* **2018**, *367*, 72−80.

(46) Chen, Z.; Wang, N.; Yao, S.; Liu, L. The flaky Cd film on Cu plate substrate: An active and efficient electrode for electrochemical reduction of CO_2 to formate. *J. CO2 Util.* **2017**, *22*, 191−196.

(47) Li, J.; Zhu, M.; Han, Y.-F. Recent Advances in Electrochemical CO_2 Reduction on Indium-Based Catalysts. *ChemCatChem* **2021**, *13*, 514−531.

(48) Kuzume, A.; Dutta, A.; Vesztergom, S.; Broekmann, P. *Operando Raman spectroscopy: studies on the reactivity and stability of SnO_2 nanoparticles during electrochemical CO_2 reduction reaction*; Elsevier, 2018; pp 217−226.

(49) Dutta, A.; Rahaman, M.; Hecker, B.; Drnec, J.; Kiran, K.; Zelocualtecatl Montiel, I.; Jochen Weber, D.; Zanetti, A.; Cedeño López, A.; Martens, I.; Broekmann, P.; Oezaslan, M. CO_2 electrolysis − Complementary operando XRD, XAS and Raman spectroscopy study on the stability of Cu_xO foam catalysts. *J. Catal.* **2020**, *389*, 592−603.

(50) Zou, Y.; Wang, S. An Investigation of Active Sites for electrochemical CO_2 Reduction Reactions: From In Situ Characterization to Rational Design. *Adv. Sci.* **2021**, *8*, No. 2003579.

(51) Timoshenko, J.; Roldan Cuenya, B. In Situ/Operando Electrocatalyst Characterization by X-ray Absorption Spectroscopy. *Chem. Rev.* **2021**, *121*, 882−961.

(52) Dutta, A.; Kiran, K.; Rahaman, M.; Montiel, I. Z.; Moreno-Garcí, P.; Vesztergom, S.; Drnec, J.; Oezaslan, M.; Broekmann, P. Insights from Operando and Identical Location (IL) Techniques on the Activation of Electrocatalysts for the Conversion of CO_2: A Mini-Review. *Chimia* **2021**, *75*, 733−743.

(53) Feng, X.; Zou, H.; Zheng, R.; Wei, W.; Wang, R.; Zou, W.; Lim, G.; Hong, J.; Duan, L.; Chen, H. Bi_2O_3/BiO_2 Nanoheterojunction for Highly Efficient Electrocatalytic CO_2 Reduction to Formate. *Nano Lett.* **2022**, *22*, 1656−1664.

(54) Deng, P.; Wang, H.; Qi, R.; Zhu, J.; Chen, S.; Yang, F.; Zhou, L.; Qi, K.; Liu, H.; Xia, B. Y. Bismuth Oxides with Enhanced Bismuth−Oxygen Structure for Efficient Electrochemical Reduction of Carbon Dioxide to Formate. *ACS Catal.* **2020**, *10*, 743−750.

(55) Zhang, Y.; Zhang, X.; Ling, Y.; Li, F.; Bond, A. M.; Zhang, J. Controllable Synthesis of Few-Layer Bismuth Subcarbonate by Electrochemical Exfoliation for Enhanced CO_2 Reduction Performance. *Angew. Chem., Int. Ed.* **2018**, *57*, 13283−13287.

(56) Fan, T.; Ma, W.; Xie, M.; Liu, H.; Zhang, J.; Yang, S.; Huang, P.; Dong, Y.; Chen, Z.; Yi, X. Achieving high current density for electrocatalytic reduction of CO_2 to formate on bismuth-based catalysts. *Cell Rep. Phys. Sci.* **2021**, *2*, No. 100353.

(57) Shi, Y.; Wen, C. F.; Wu, X.; Zhao, J. Y.; Mao, F.; Liu, P. F.; Yang, H. G. In situ reconstruction of vegetable sponge-like Bi_2O_3 for

efficient CO_2 electroreduction to formate. *Mater. Chem. Front.* **2022**, *6*, 1091−1097.

(58) Lv, W.; Bei, J.; Zhang, R.; Wang, W.; Kong, F.; Wang, L.; Wang, W. $Bi_2O_2CO_3$ Nanosheets as Electrocatalysts for Selective Reduction of CO_2 to Formate at Low Overpotential. *ACS Omega* **2017**, *2*, 2561−2567.

(59) Lin, J.; Yan, S.; Zhang, C.; Hu, Q.; Cheng, Z. Electroreduction of CO_2 toward High Current Density. *Processes* **2022**, *10*, 826.

(60) Ashiotis, G.; Deschildre, A.; Nawaz, Z.; Wright, J. P.; Karkoulis, D.; Picca, F. E.; Kieffer, J. The fast azimuthal integration Python library: pyFAI. *J. Appl. Crystallogr.* **2015**, *48*, 510−519.

(61) Reyes-Contreras, A.; Camacho-López, M.; Camacho-López, S.; Olea-Mejía, O.; Esparza-García, A.; Bañuelos-Muñetón, J. G.; Camacho-López, M. A. Laser-induced periodic surface structures on bismuth thin films with ns laser pulses below ablation threshold. *Opt. Mater. Express* **2017**, *7*, 1777−1786.

(62) Taylor, P.; Sunder, S.; Lopata, V. J. Structure, spectra, and stability of solid bismuth carbonates. *Can. J. Chem.* **1984**, *62*, 2863−2873.

(63) Shin, H. C.; Dong, J.; Liu, M. Porous Tin Oxides Prepared Using an Anodic Oxidation Process. *Adv. Mater.* **2004**, *16*, 237−240.

(64) Shin, H. C.; Liu, M. Copper foam structures with highly porous nanostructured walls. *Chem. Mater.* **2004**, *16*, 5460−5464.

(65) Dutta, A.; Montiel, I. Z.; Erni, R.; Kiran, K.; Rahaman, M.; Drnec, J.; Broekmann, P. Activation of bimetallic AgCu foam electrocatalysts for ethanol formation from CO_2 by selective Cu oxidation/reduction. *Nano Energy* **2020**, *68*, No. 104331.

(66) Rudnev, A. V.; Kiran, K.; Cedeño López, A.; Dutta, A.; Gjuroski, I.; Furrer, J.; Broekmann, P. Enhanced electrocatalytic CO formation from CO_2 on nanostructured silver foam electrodes in ionic liquid/water mixtures. *Electrochim. Acta* **2019**, *306*, 245−253.

(67) Luo, W.; Xie, W.; Mutschler, R.; Oveisi, E.; De Gregorio, G. L.; Buonsanti, R.; Züttel, A. Selective and Stable Electroreduction of CO_2 to CO at the Copper/Indium Interface. *ACS Catal.* **2018**, *8*, 6571−6581.

(68) Luo, W.; Zhang, J.; Li, M.; Züttel, A. Boosting CO Production in Electrocatalytic CO_2 Reduction on Highly Porous Zn Catalysts. *ACS Catal.* **2019**, *9*, 3783−3791.

(69) Kottakkat, T.; Klingan, K.; Jiang, S.; Jovanov, Z. P.; Davies, V. H.; El-Nagar, G. A. M.; Dau, H.; Roth, C. Electrodeposited AgCu Foam Catalysts for Enhanced Reduction of CO_2 to CO. *ACS Appl. Mater. Interfaces* **2019**, *11*, 14734−14744.

(70) Barrera-Mota, K.; Bizarro, M.; Castellino, M.; Tagliaferro, A.; Hernández, A.; Rodil, S. E. Spray deposited β-Bi_2O_3 nanostructured films with visible photocatalytic activity for solar water treatment. *Photochem. Photobiol. Sci.* **2015**, *14*, 1110−1119.

(71) Vila, M.; Díaz-Guerra, C.; Piqueras, J. α-Bi_2O_3 microcrystals and microrods: Thermal synthesis, structural and luminescence properties. *J. Alloys Compd.* **2013**, *548*, 188−193.

(72) Divya, J.; Shivaramu, N. J.; Purcell, W.; Roos, W. D.; Swart, H. C. Effects of annealing temperature on the crystal structure, optical and photocatalytic properties of Bi_2O_3 needles. *Appl. Surf. Sci.* **2020**, *520*, No. 146294.

(73) Liu, G.; Li, S.; Lu, Y.; Zhang, J.; Feng, Z.; Li, C. Controllable synthesis of α-Bi_2O_3 and γ-Bi_2O_3 with high photocatalytic activity by α-Bi_2O_3→γ-Bi_2O_3→α-Bi_2O_3 transformation in a facile precipitation method. *J. Alloys Compd.* **2016**, *689*, 787−799.

(74) Leontie, L.; Caraman, M.; Delibaş, M.; Rusu, G. I. Optical properties of bismuth trioxide thin films. *Mater. Res. Bull.* **2001**, *36*, 1629−1637.

(75) Lu, Q.; Jiao, F. Electrochemical CO_2 reduction: Electrocatalyst, reaction mechanism, and process engineering. *Nano Energy* **2016**, *29*, 439−456.

(76) Nesbitt, N. T.; Burdyny, T.; Simonson, H.; Salvatore, D.; Bohra, D.; Kas, R.; Smith, W. A. Liquid−Solid Boundaries Dominate Activity of CO_2 Reduction on Gas-Diffusion Electrodes. *ACS Catal.* **2020**, *10*, 14093−14106.

(77) McCallum, C.; Gabardo, C. M.; O'Brien, C. P.; Edwards, J. P.; Wicks, J.; Xu, Y.; Sargent, E. H.; Sinton, D. Reducing the crossover of carbonate and liquid products during carbon dioxide electroreduction. *Cell Rep. Phys. Sci.* **2021**, *2*, No. 100522.

(78) Zhang, M.; Wei, W.; Zhou, S.; Ma, D.-D.; Cao, A.; Wu, X.-T.; Zhu, Q.-L. Engineering a conductive network of atomically thin bismuthene with rich defects enables CO_2 reduction to formate with industry-compatible current densities and stability. *Energy Environ. Sci.* **2021**, *14*, 4998−5008.

(79) Kong, Y.; Hu, H.; Liu, M.; Hou, Y.; Kolivoška, V.; Vesztergom, S.; Broekmann, P. Visualisation and quantification of flooding phenomena in gas diffusion electrodes used for electrochemical CO_2 reduction: A combined EDX/ICP−MS approach. *J. Catal.* **2022**, *408*, 1−8.

(80) Martens, I.; Vamvakeros, A.; Martinez, N.; Chattot, R.; Pusa, J.; Blanco, M. V.; Fisher, E. A.; Asset, T.; Escribano, S.; Micoud, F.; Starr, T.; Coelho, A.; Honkimäki, V.; Bizzotto, D.; Wilkinson, D. P.; Jacques, S. D. M.; Maillard, F.; Dubau, L.; Lyonnard, S.; Morin, A.; Drnec, J. Imaging Heterogeneous Electrocatalyst Stability and Decoupling Degradation Mechanisms in Operating Hydrogen Fuel Cells. *ACS Energy Lett.* **2021**, *6*, 2742−2749.

(81) Vamvakeros, A.; Jacques, S. D. M.; Di Michiel, M.; Matras, D.; Middelkoop, V.; Ismagilov, I. Z.; Matus, E. V.; Kuznetsov, V. V.; Drnec, J.; Senecal, P.; Beale, A. M. 5D operando tomographic diffraction imaging of a catalyst bed. *Nat. Commun.* **2018**, *9*, 4751.

Supporting Information

CO_2 Conversion at High Current Densities: Stabilization of Bi(III) Containing Electrocatalysts under CO_2 Gas Flow Conditions

Iván Zelocualtecatl Montiel[1,2#], Abhijit Dutta[1#]*, Kiran Kiran[1], Alain Rieder[1,2], Anna Iarchuk[1,2], Soma Vesztergom[1,3], Marta Mirolo[4], Isaac Martens[4], Jakub Drnec[4], and Peter Broekmann[1,2]*

[1]*Department of Chemistry, Biochemistry and Pharmaceutical Science, University of Bern, Freiestrasse 3, 3012 Bern, Switzerland*

[2]*National Centre of Competence in Research (NCCR) Catalysis, University of Bern, Freiestrasse 3, 3012 Bern, Switzerland*

[3]*Department of Physical Chemistry, Eötvös Loránd University, Pázmány Péter sétány 1/A, 1117 Budapest, Hungary*

[4]*European Synchrotron Radiation Facility (ESRF), 71 Avenue des Martyrs, 38000, Grenoble, France*

[#]*Contributed equally*

[*]*Corresponding authors: abhijit.dutta@unibe.ch (A. Dutta) and*

peter.broekmann@unibe.ch (P. Broekmann)

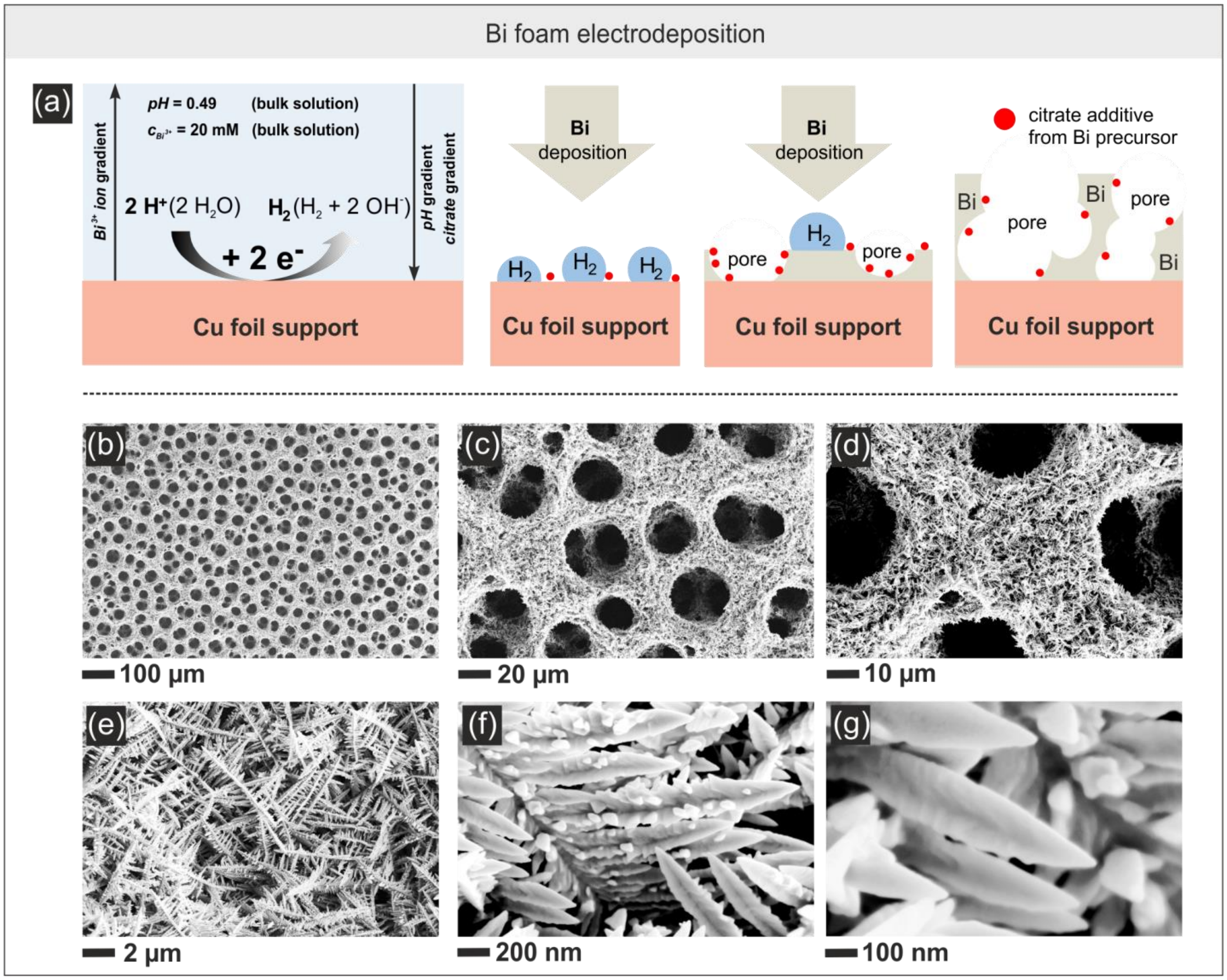

Figure S1. a) Schematic demonstrating the concept of the Dynamic Hydrogen Bubble Template (DHBT) assisted Bi foam electrodeposition process.[1] b) – g) Top-down SEM inspection of the Bi foam obtained after 20 s of Bi deposition at –3 A cm^{-2}. For this experiment a Cu foil served as the support electrode (see also Figure 3).

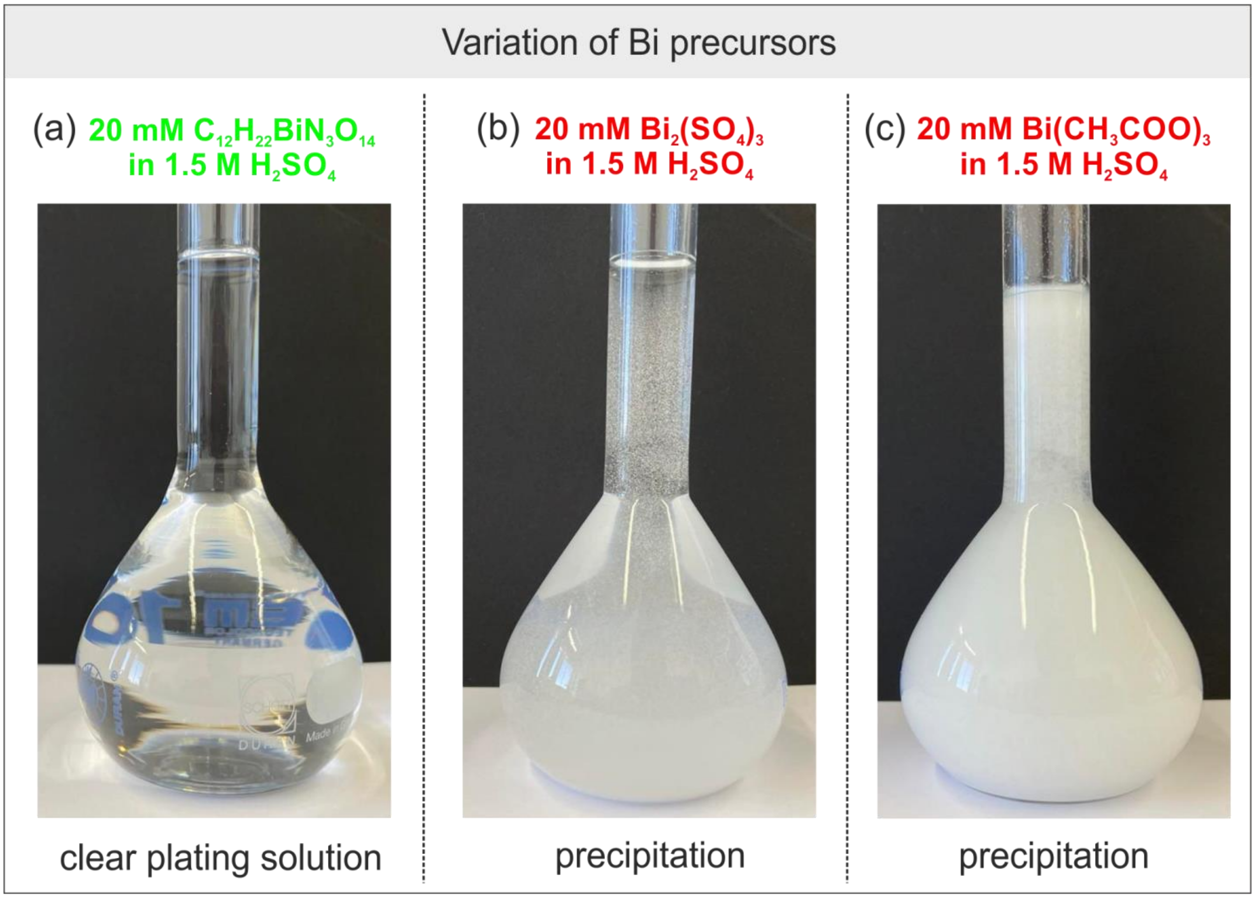

Figure S2. Optical micrographs demonstrating the excellent solubility of ammonium bismuth citrate (panel a) whereas corresponding sulfate and acetate precursors either tend to hydrolyze or are not soluble at all (panel b and c).

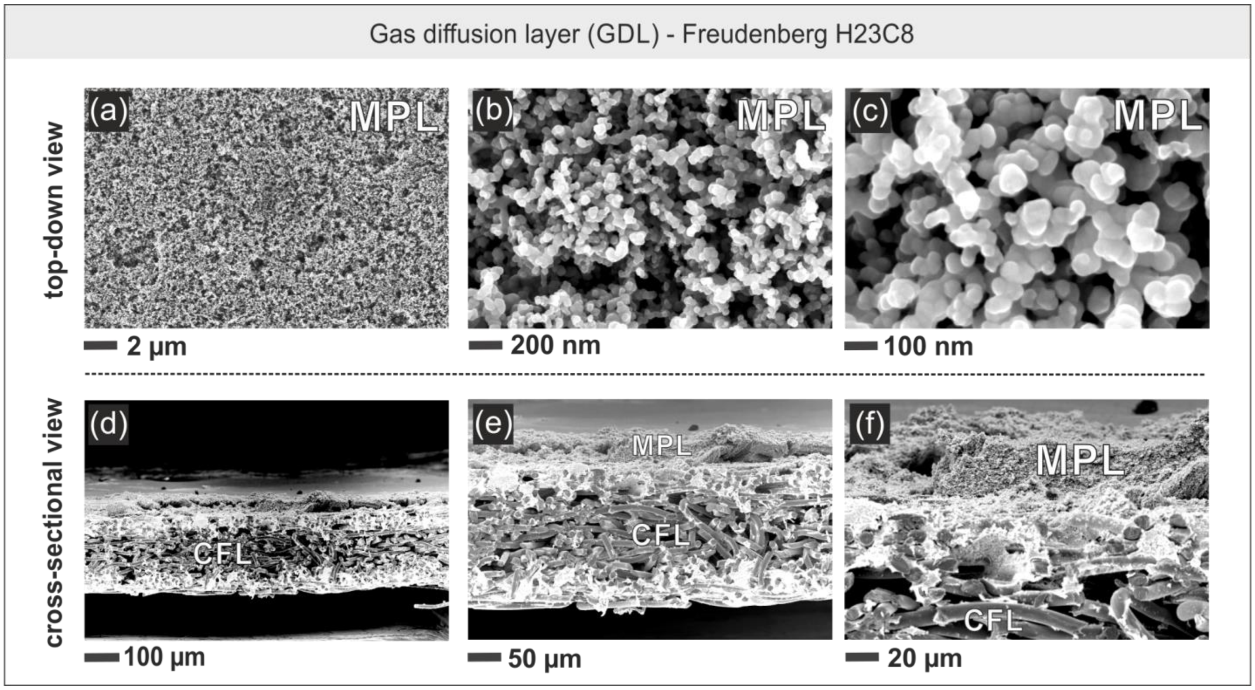

Figure S3. SEM inspection of the gas diffusion layer (GDL, Freudenberg H23C8) used in this study as the support electrode. a) – c) Top-down inspection showing the microporous layer (MPL) of the GDL. d) – f) Cross-sectional view showing both the carbon fibrous layer (CFL) and the MPL.

Physical characteristics (according to the manufacturer): entire thickness: (235 ± 3) µm; entire void ratio: (60 ± 4)%; MPL thickness: (41 ± 2) µm; MPL void ratio: (30 ± 8)%; MPL crack ratio: 0.0%; CFL thickness: (194 ± 5) µm; CFL void ratio: (67 ± 4)%; CFL crack ratio: 0.0%.

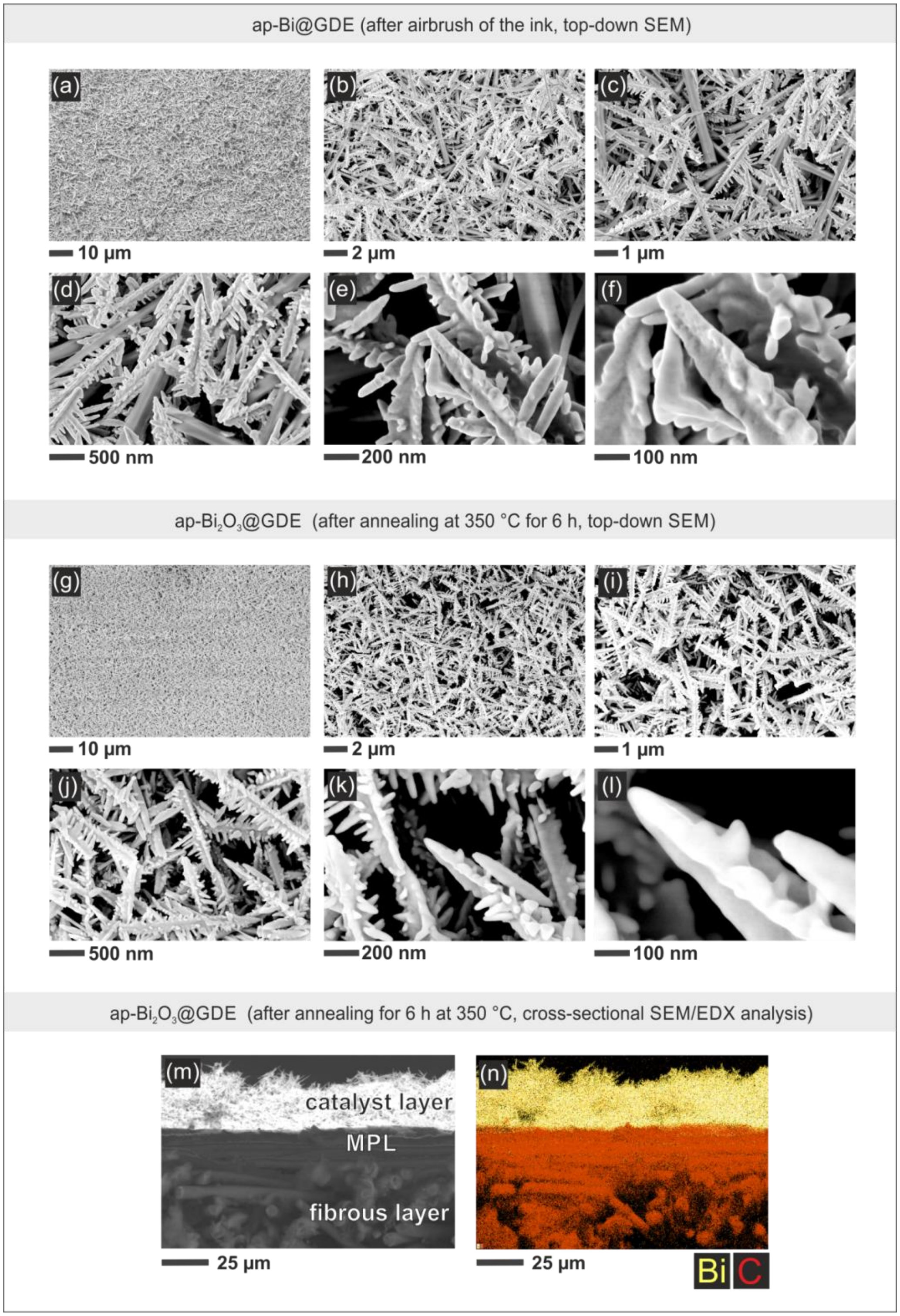

Figure S4. a) – f) Top-down SEM inspection of as-prepared dendritic catalyst (precursor) material deposited on the MPL (denoted ap-Bi@GDE). g) – l) Top-down SEM inspection of dendritic Bi_2O_3 layer after the thermal annealing. m) – n) Cross-sectional SEM/EDX inspection of the ap-Bi_2O_3@GDE after thermal annealing.

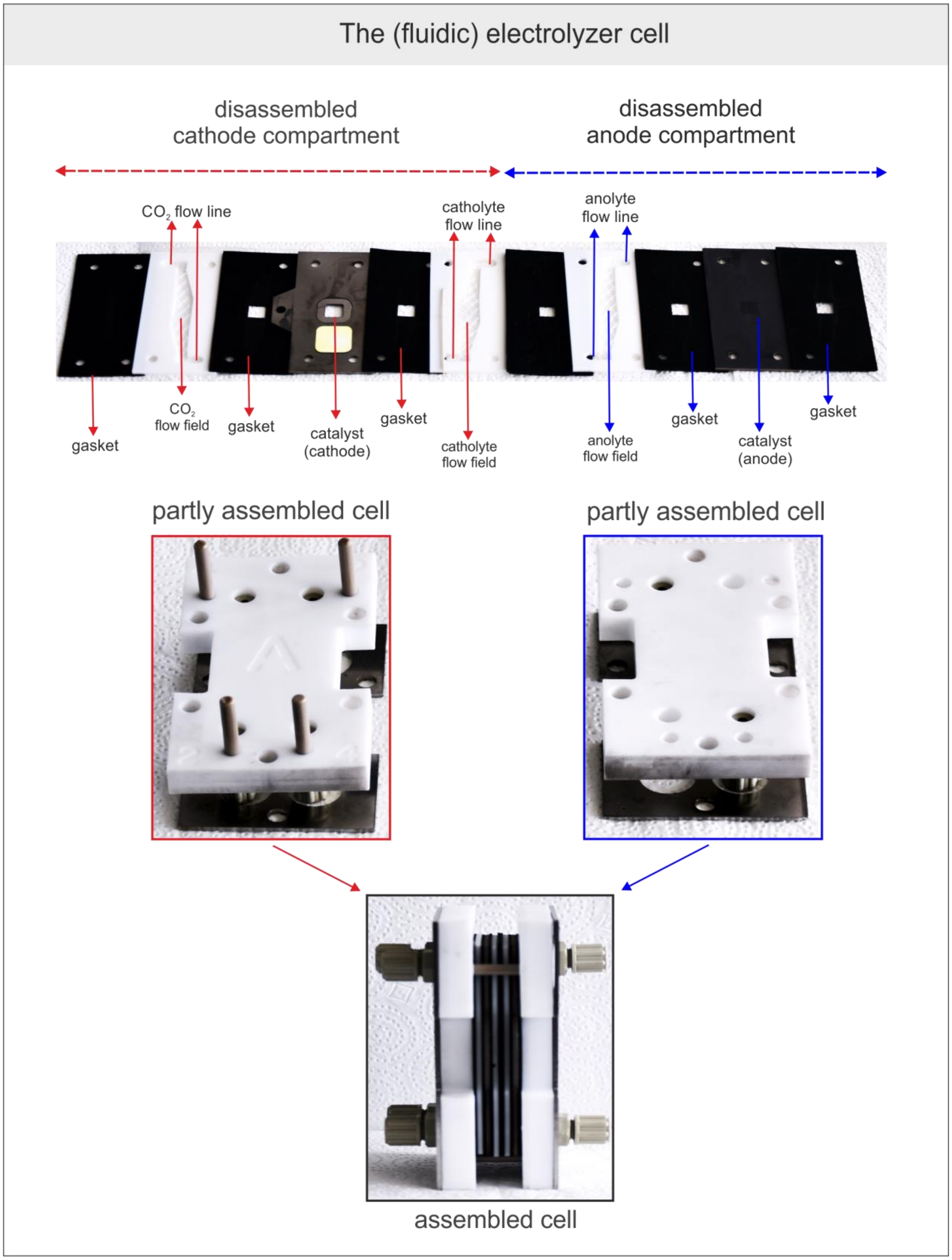

Figure S5. Disassembled, partly assembled, and completely assembled electrolyzer cell used in this study. Of note, the anion exchange membrane is not shown here.

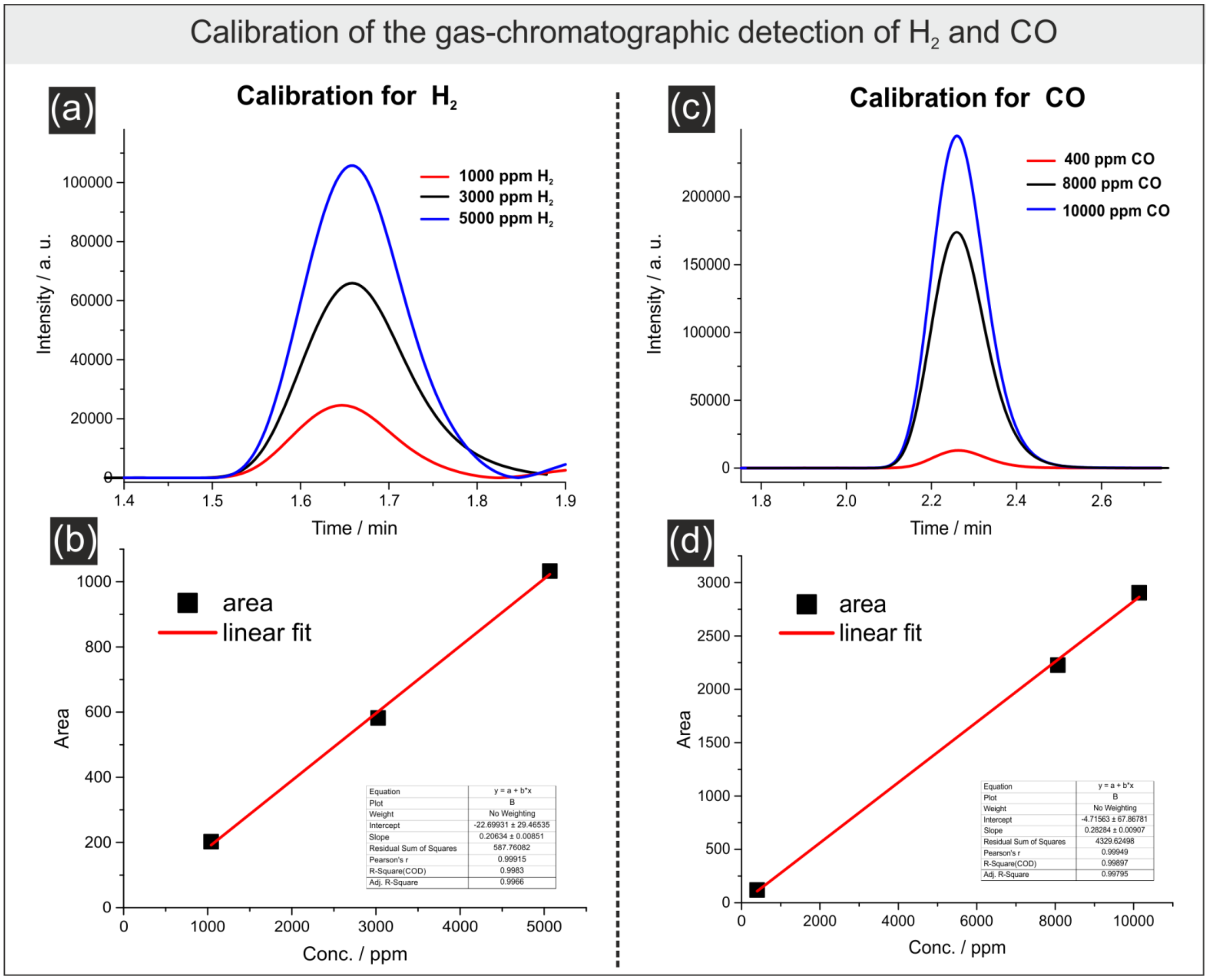

Equation	y = a + b*x
Plot	B
Weight	No Weighting
Intercept	-22.69931 ± 29.46535
Slope	0.20634 ± 0.00851
Residual Sum of Squares	587.76082
Pearson's r	0.99915
R-Square(COD)	0.9983
Adj. R-Square	0.9966

Equation	y = a + b*x
Plot	B
Weight	No Weighting
Intercept	-4.71563 ± 67.86781
Slope	0.28284 ± 0.00907
Residual Sum of Squares	4329.62498
Pearson's r	0.99949
R-Square(COD)	0.99897
Adj. R-Square	0.99795

Figure S6. (a) Gas-chromatograms of standard hydrogen reference samples used for calibration purposes. (b) Corresponding plot of the integrated surface area versus the nominal concentration of the standard solutions. (c) Gas-chromatograms of standard CO reference samples used for calibration purposes. (d) Corresponding plot of the integrated surface area versus the nominal concentration of the standard solutions.

Calibration of the ionchromatographic detection of formate

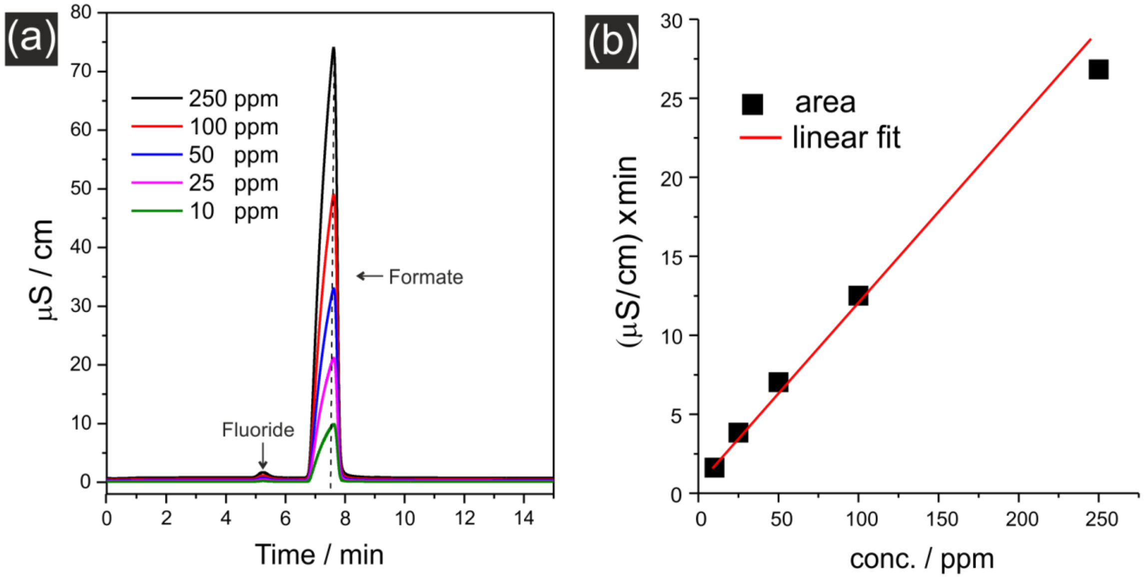

(c)

Formate Conc (ppm)	Retention time (minute)	Height (µS/cm)	Area (µS/cm) x min
10	7.57	9.241	1.624
25	7.56	20.052	3.845
50	7.57	32.240	7.029
100	7.58	47.757	12.513
250	7.58	73.138	26.833

Figure S7. (a) Chromatograms of standard formate reference samples used for calibration purposes. Chromatograms were measured for aqueous solutions containing 10, 25, 50, 100, and 250 ppm formate. These solutions were prepared from 1000 ppm IC standard solution purchased from Sigma Aldrich. (b) Calibration curve derived from the measurements shown in panel a; (c) Table showing the results of the calibration measurements in terms of formate retention times, peak heights, and peak areas.

Note that traces of fluoride are also detected (highlighted as satellite peaks in panel a). These fluoride traces in the sub-ppm range originate from the Milli-Q water itself and from the KOH source (see Figure S8 and S12).

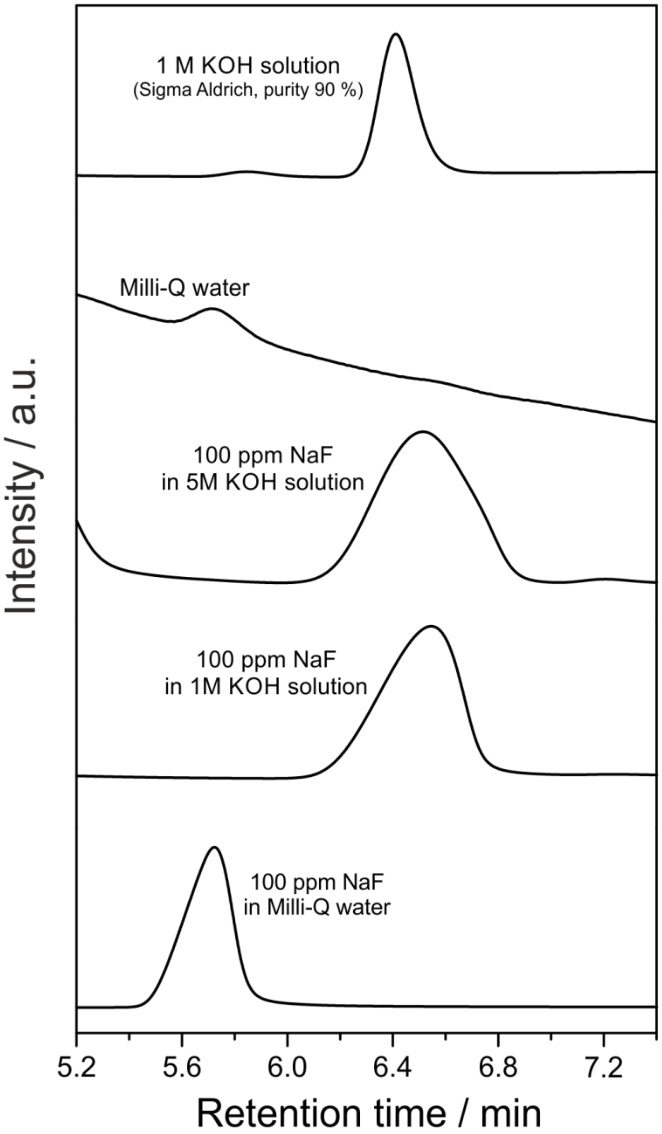

Figure S8. Reference measurements based on ion exchange chromatography used for the identification of the satellite peak observed on the chromatograms for the formate detection. The satellite peak stems from traces of fluoride (sub-ppb range) being present in the Milli-Q water and the KOH source. Note that the retention time of the fluoride changes slightly with the pH (see also Figure S7 and S12).

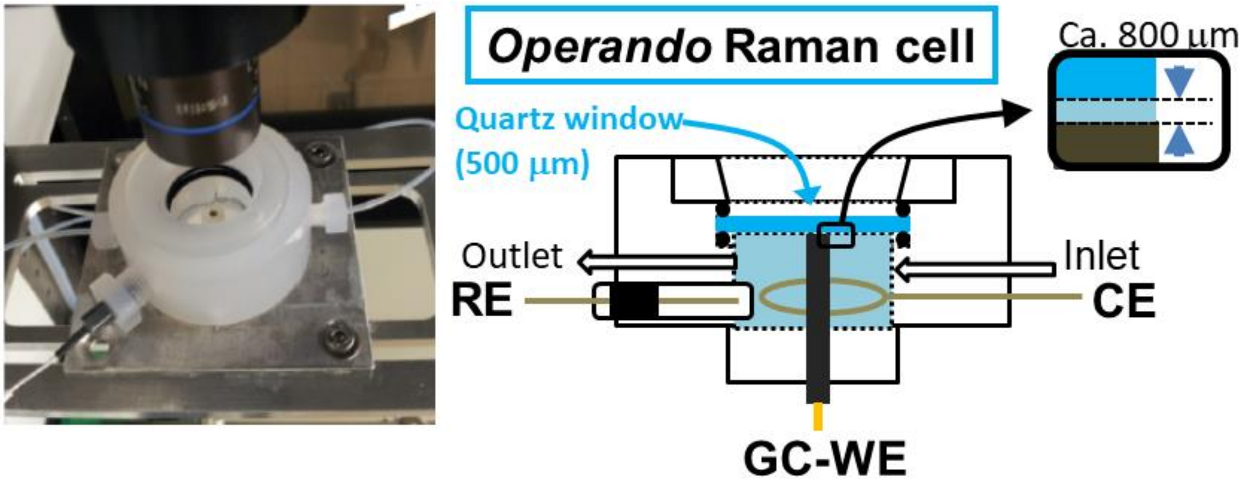

Figure S9. Optical micrograph and schematics of the *operando* Raman cell used in this study. RE: reference electrode; CE: counter electrode; GC-WE: glassy carbon working electrode

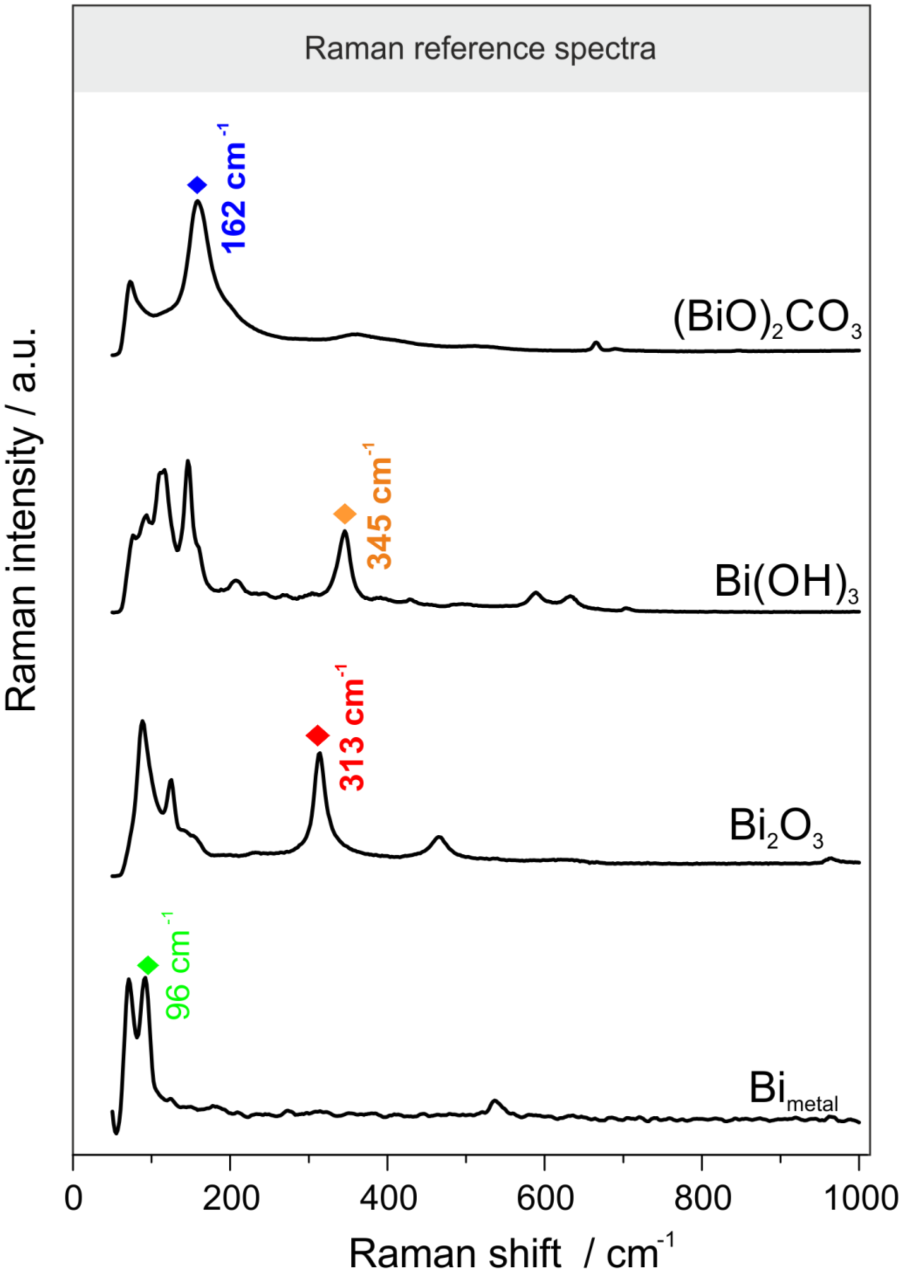

Figure S10. Raman reference spectra for (i) metallic Bi, (ii) for β-Bi_2O_3, (iii) for $Bi(OH)_3$, and (iv) for a $(BiO)_2CO_3$ (subcarbonate) sample. The characteristic Raman features at 96 cm^{-1}, 313 cm^{-1}, 345 cm^{-1} and 162 cm^{-1} served as spectroscopic fingerprints for the presence of metallic Bi, the corresponding bismuth oxide, the bismuth hydroxide, and the subcarbonate phase, respectively. These spectra are consistent with published Raman data in the literature.[2-5]

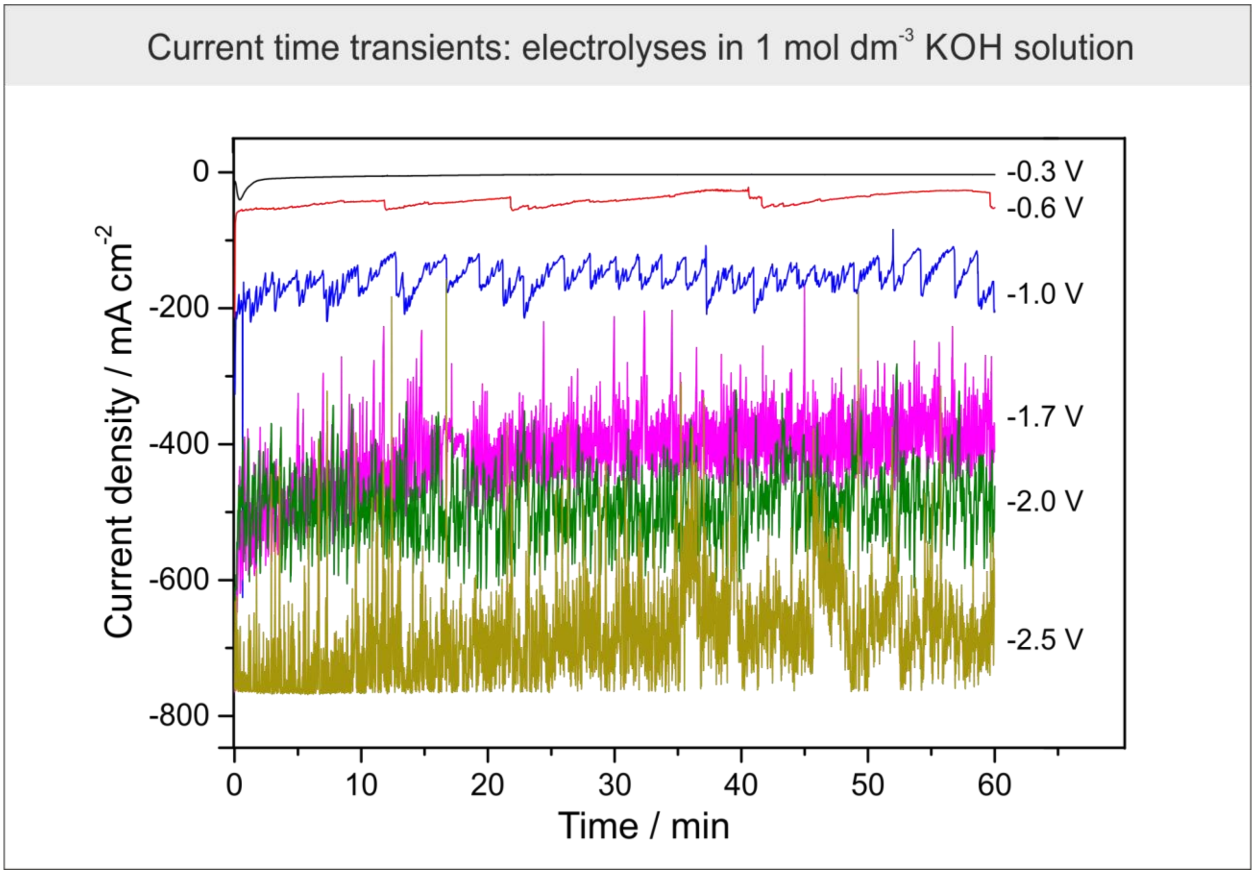

Figure S11. Representative current density time traces measured for potentiostatic electrolyses in 1 mol dm^{-3} KOH solution. Note that the fluctuation of the current density scales with the applied electrolysis potential. The origin of these fluctuations is the HER which becomes more pronounced at higher overpotentials. Hydrogen gas bubble formation on and inside the catalyst film leads to temporal changes of the active surface area (formation and release of gas bubbles).

Formate detection in the anolyte (formate crossover)

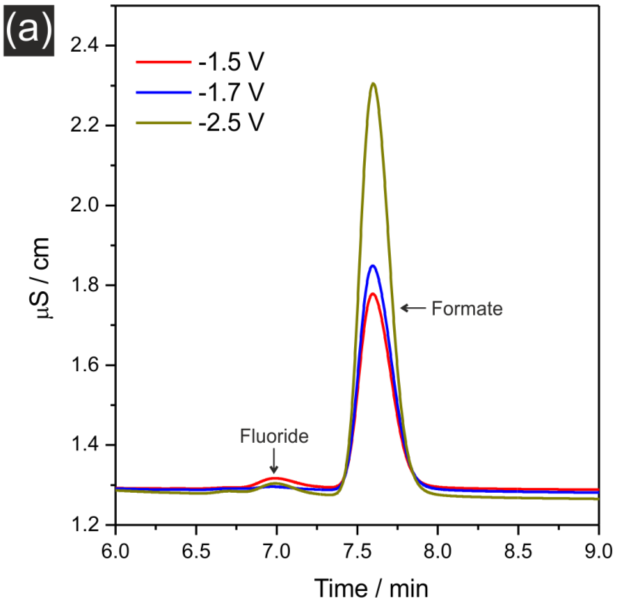

(b)

Potential *vs.* RHE	Retention time (minute)	Height (µS/cm)	Area (µS/cm) x min	Formate Conc (ppm)
-1.5	7.58	0.485	0.114	14.90
-1.7	7.56	0.562	0.134	17.52
-2.5	7.58	1.031	0.228	21.83

Figure S12. Experimental evidence for possible formate crossover through the anion exchange membrane into the anolyte during CO_2RR. CO_2RR was carried out in 5 mol dm^{-3} KOH solution at three different applied potentials. (a) Measured ion chromatograms of the anolyte. (b) Table showing the formate retention time, the peak height, the peak area, and the resulting formate concentration in ppm.

Note that the precise formate quantification in the anolyte is hindered by the possible formate oxidation on the anode.

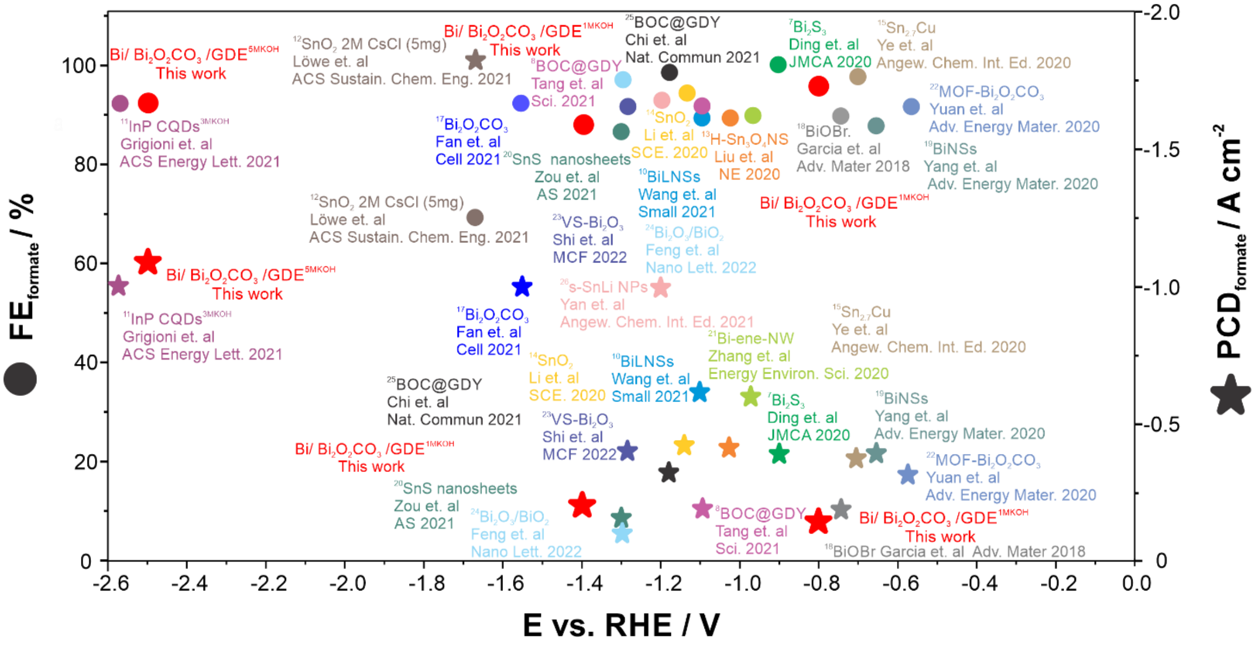

Figure S13. Comparison of electrocatalytic performance of the Bi/(BiO)$_2$CO$_3$@GDE used in this study (highlighted in red) with literature data. See also Table S5.

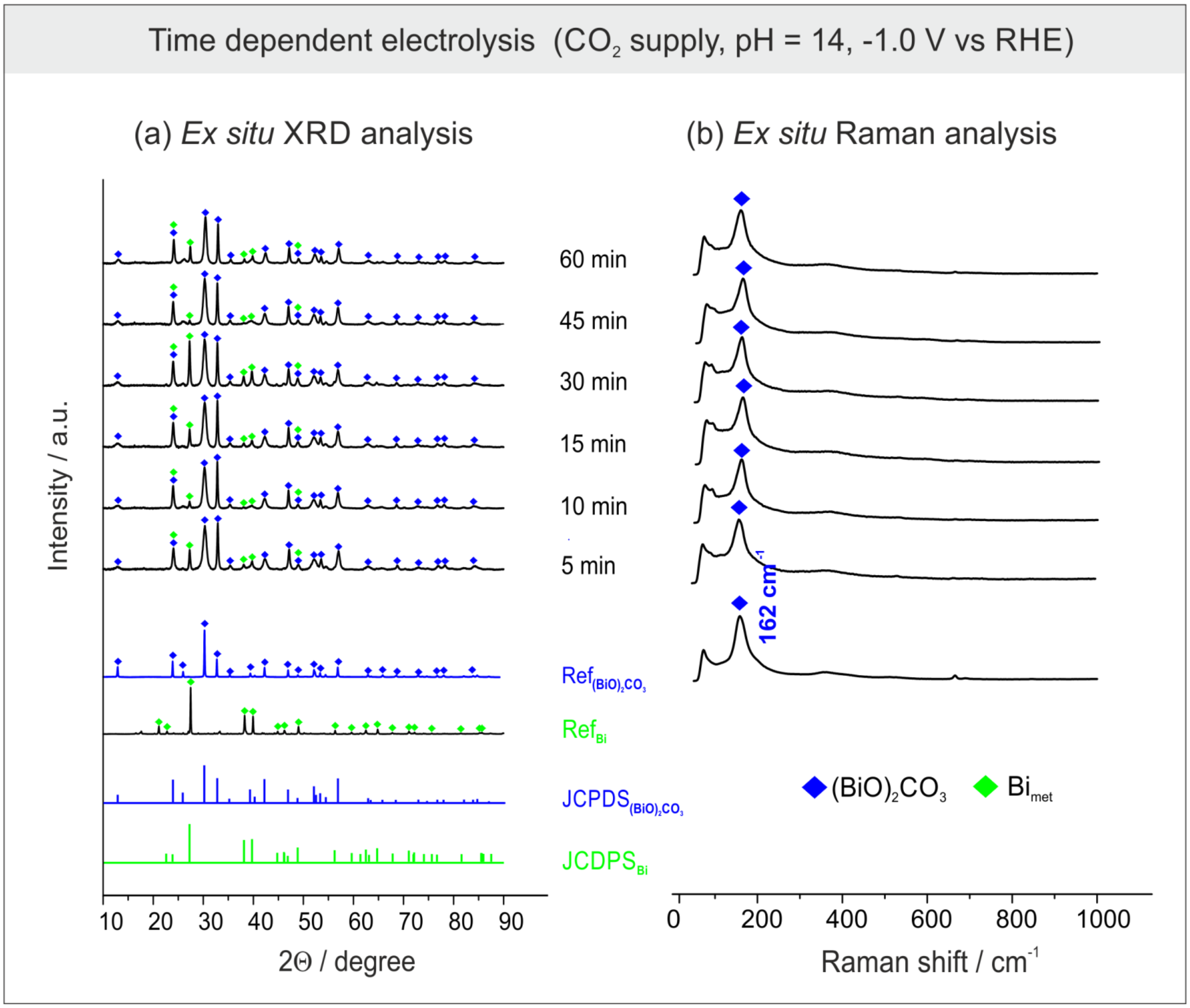

Figure S14. Time-dependent electrolyses carried out in 1 mol dm^{-3} KOH electrolyte at –1.0 V vs RHE under continuous CO_2 flow conditions. Of note, a fresh ap-Bi_2O_3@GDE sample was used in each electrolysis experiment. Experiments were stopped after different electrolysis times indicated next to the diffractograms/spectra. After electrolysis, the processed GDEs were subjected to *ex situ* XRD (panel a) and Raman spectroscopy (panel b) analysis. These results suggest a rapid $(BiO)_2CO_3$ phase formation taking place within a couple of minutes after initiating the electrolysis under potential control and continuous CO_2 gas flow. Of note, no XRD features of the pristine Bi_2O_3 precursor were visible any more after 5 min of electrolysis. By contrast to that, contributions of metallic Bi appeared in all XRD patterns suggesting that the $(BiO)_2CO_3$ phase formation at –1.0 V vs RHE is accompanied by a reductive transformation of the Bi(III) to Bi(0) as a competing process to the (oxo-anion→carbonate anion) exchange. The presence of metallic Bi is not visible in the corresponding Raman data (panel b); this can be rationalized by differences in the specific probing depths of both analysis techniques. Raman spectroscopy is considered more surface sensitive than XRD analysis which probes the entire bulk of the catalyst film.

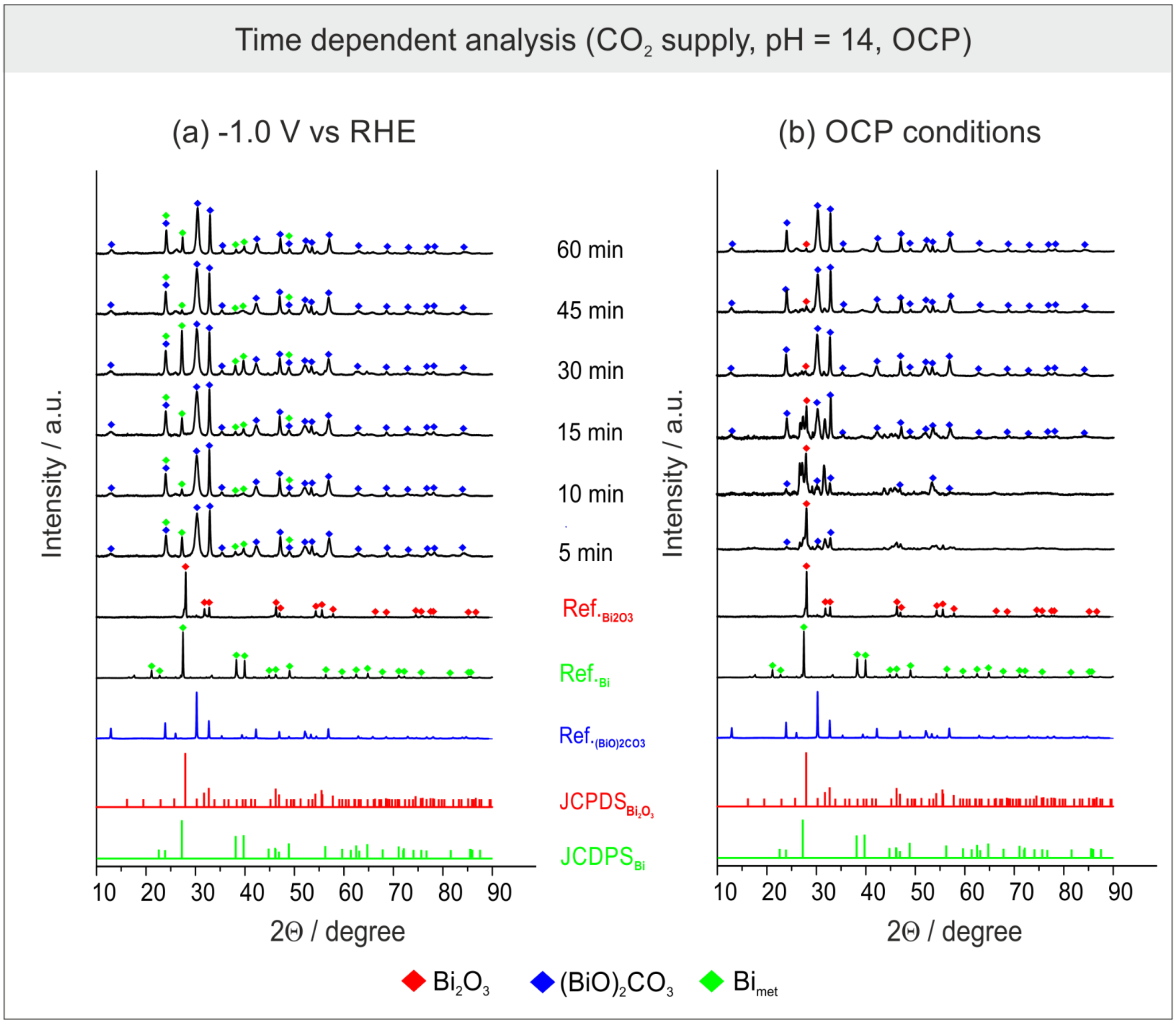

Figure S15. Time-dependent alterations of ap-Bi_2O_3@GDEs due to CO_2 exposure at –1.0 V vs RHE (panel a) and under open circuit (OCP) conditions (panel b). 1 mol dm^{-3} KOH aqueous solution was used as the electrolyte. Of note, a freshly prepared Bi_2O_3@GDE sample was applied in each experiment. The comparison of XRD data suggests a faster subcarbonate formation under CO_2RR conditions at –1.0 V vs RHE than at OCP (*e.g.*, see data after 5 min of electrolysis). In addition, metallic Bi forms under reductive conditions at –1.0 V vs RHE, pointing to that the competing processes of subcarbonate formation (anion exchange) and Bi(III) reduction take place in parallel. The active catalyst at –1.0 V vs RHE is a composite film of metallic Bi (minor phase) and $(BiO)_2CO_3$ (major phase). In contrast to the experiments carried out under potential control (panel a) trace amounts of Bi_2O_3 remain visible in the diffractograms even after extended CO_2 exposure times (panel b).

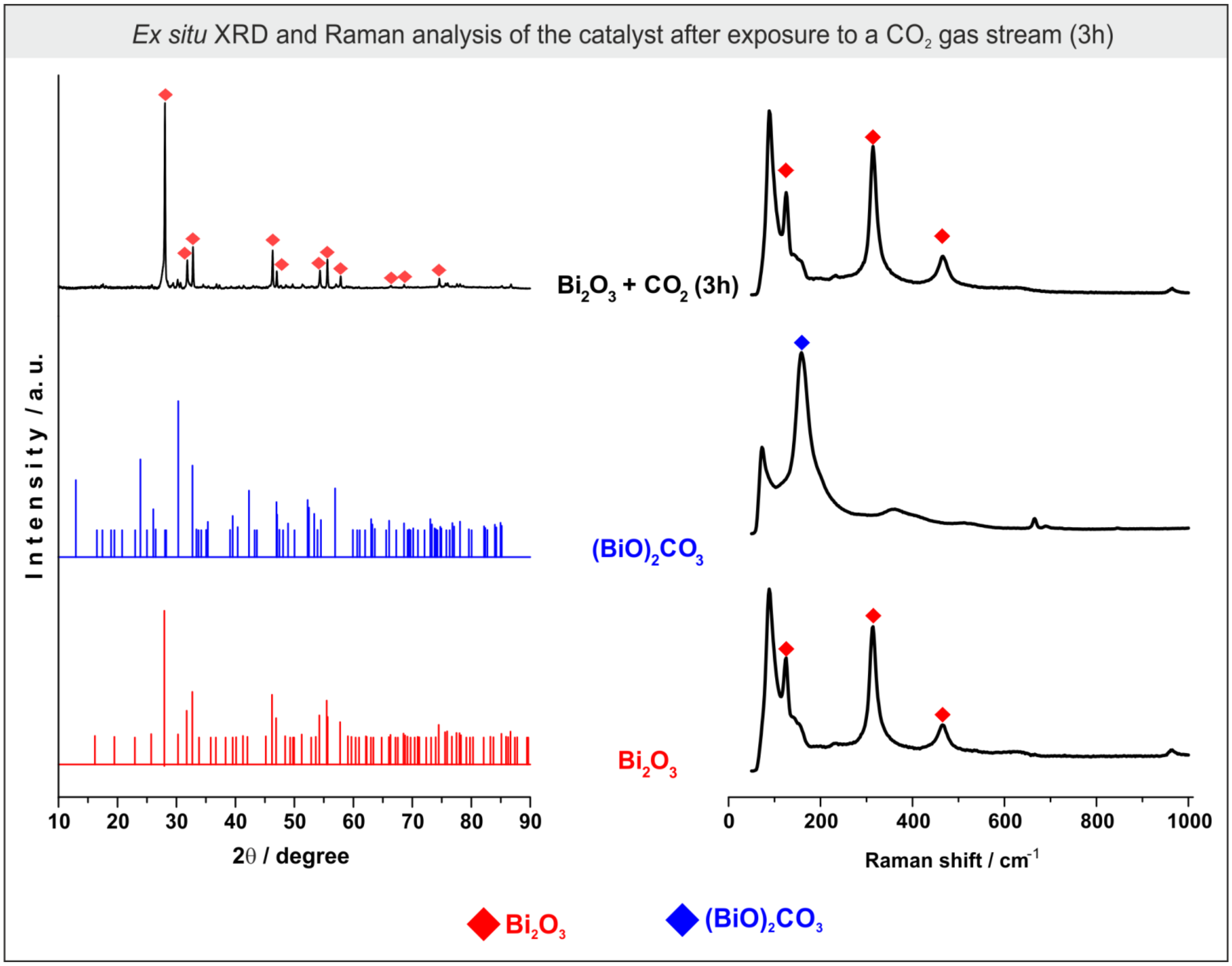

Figure S16. Control experiment where the as prepared Bi_2O_3 sample was exposed for 3h at RT to a stream of humidified CO_2 in the absence of liquid electrolyte. Under these conditions no bismuth subcarbonate formation takes place indicating that the presence of the alkaline liquid electrolyte is mandatory for the subcarbonate formation (at least at RT).

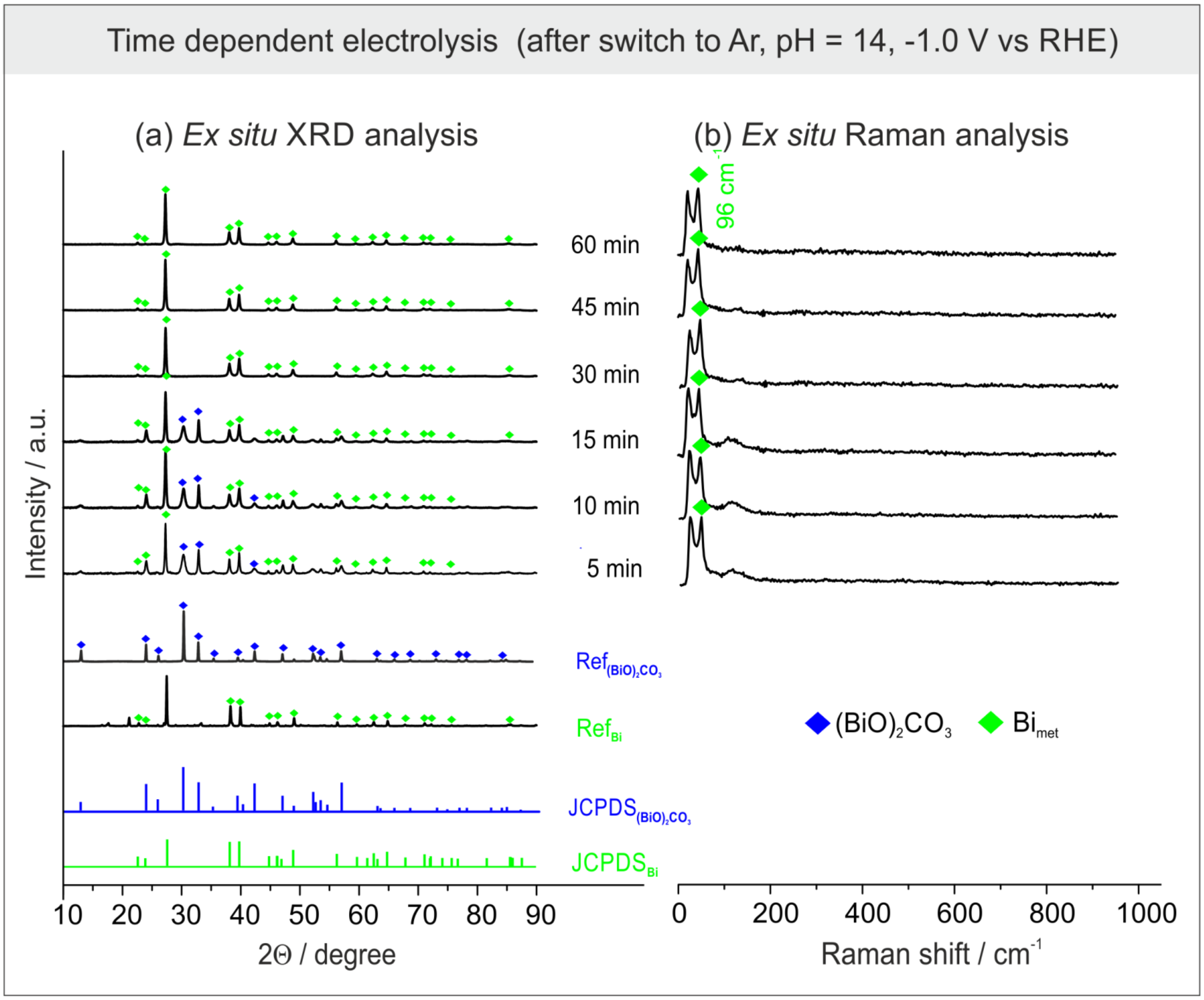

Figure S17. *Ex situ* XRD (panel a) and Raman spectroscopic analysis (panel b) of GDEs subjected to 30 min electrolysis under CO_2 gas flow conditions followed by a further electrolysis under Ar gas flow of variable duration. The switch from CO_2 to Ar gas supply was carried out under electrolysis conditions at –1.0 V vs RHE. The extra time spent for the electrolysis under Ar gas flow is indicated next to the diffractograms/Raman spectra. The Raman data indicate a rapid transition into the metallic Bi (panel b) whereas as the Bi(III) reduction is completed in the "bulk" of the CL only after 30 min of electrolysis under Ar gas flow. Differences in the time dependent changes of the CL are rationalized by different probing depths of the XRD and Raman spectroscopic techniques.

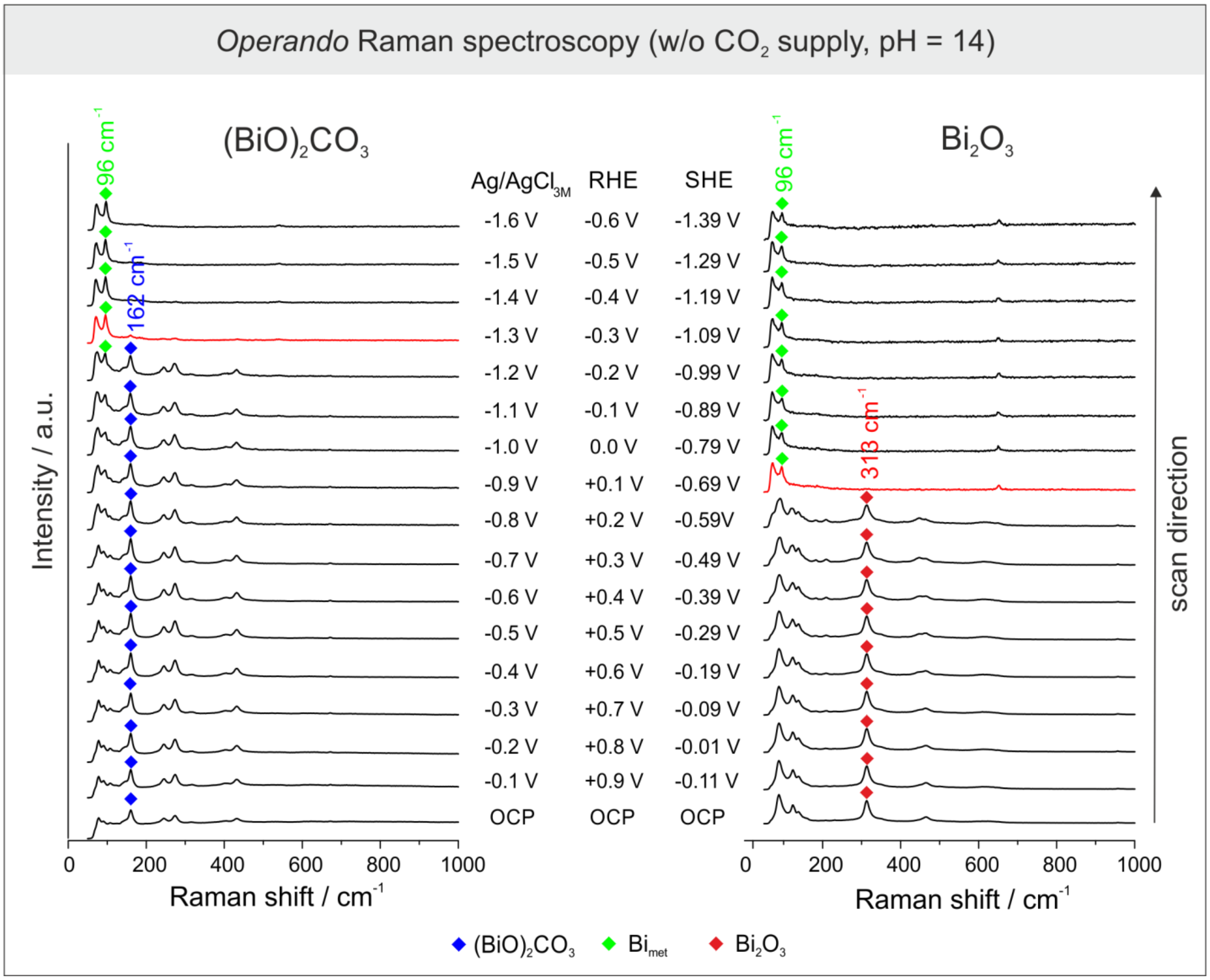

Figure S18. Potential-dependent stability of $(BiO)_2CO_3$ and Bi_2O_3 films exposed to a 1 mol dm^{-3} KOH electrolyte (pH = 14) in the absence of a CO_2 gas supply probed by *in situ* Raman spectroscopy in a liquid flow Raman cell. The experimental Raman set-up has been detailed elsewhere.[1] The $(BiO)_2CO_3$ film has been prepared in the gas-fed electrolyzer cell prior to the Raman spectroscopic measurements by exposing the ap-Bi_2O_3@GDE to 1 mol dm^{-3} KOH electrolyte solution at the OCP for 1 h under continuous CO_2 supply. After the subcarbonate formation in the electrolyzer cell the $(BiO)_2CO_3$@GDE was transferred to the liquid flow cell for the *in situ* Raman investigation under potential control. Highlighted in red are those Raman spectra indicating the respective transformation of the subcarbonate/oxide into the metallic bismuth.

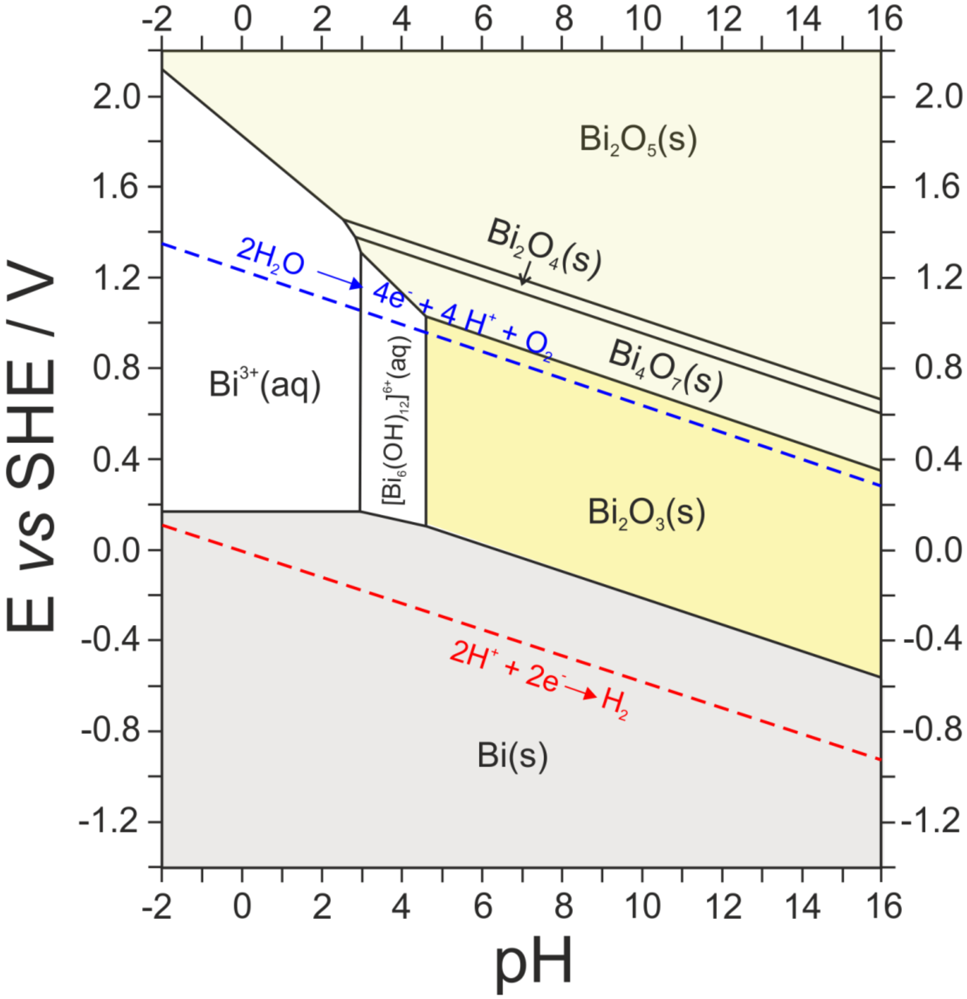

Figure S19. Pourbaix diagram of the bismuth/water system according to Nam et al.[6]

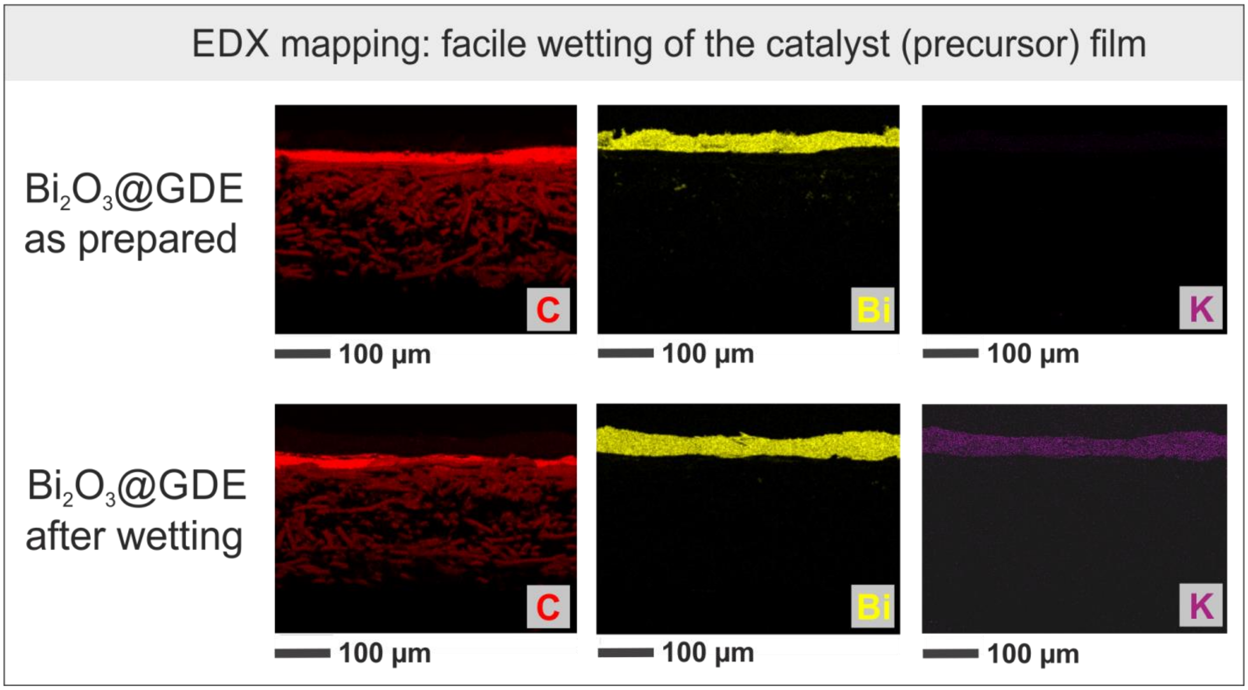

Figure S20. Control experiment demonstrating the facile and complete wetting of the Bi_2O_3 precursor film on the GDE after exposure to an electrolyte droplet (1 M KOH solution). The K-mapping indicates penetration of the electrolyte down to the GDL carbon support. The K elemental maps were re-normalized location-wise, using the maximum pixel intensity detected in the map recorded after dropping as a normalization factor.

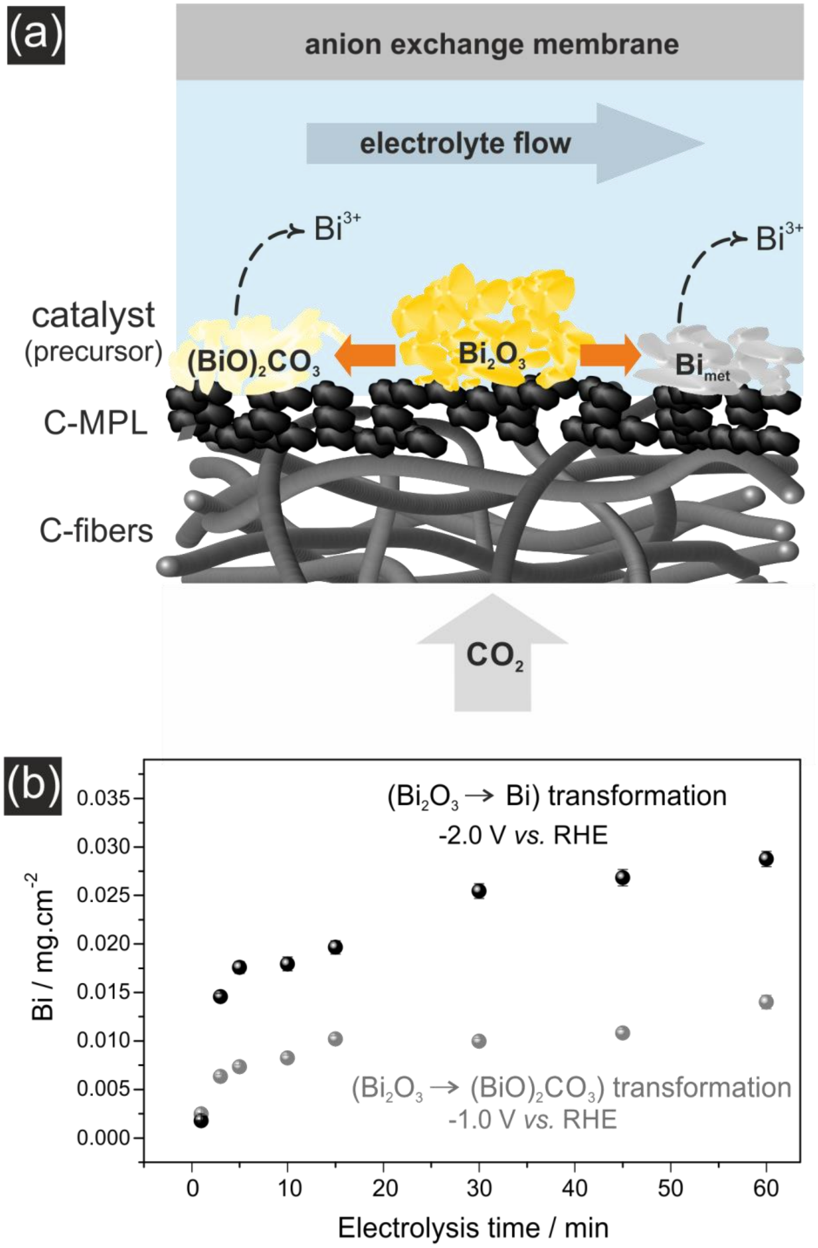

Figure S21. a) Graphical representation of the fluidic cathode configuration demonstrating the release of Bi^{3+} ions into the electrolyte as consequence of the subcarbonate formation (–1.0 vs RHE) and metallic Bi from the Bi_2O_3 precursor. b) Bi content in the electrolyte determined by means of ICP-MS. The Bi content increases within the first couple of minutes of the electrolysis and reaches then saturation. The saturation concentrations remain on a low level. The concentrations are normalized to the geometric surface area of 1 cm^2 exposed to the 1 mol dm^{-3} KOH electrolyte solution. For comparison note that the experimentally determined Bi mass loading was $m_{\mathrm{Bi}} = 1.06\ \mathrm{mg\ cm^{-2}}$.

Table S1. Potential-dependent product distribution represented as Faradaic efficiencies (*FE*s) after potentiostatic CO_2RR in 1 mol dm^{-3} KOH over the ap-Bi_2O_3@GDE.

(*E* vs RHE) / V	**FE_{H_2} / %**	**FE_{CO} / %**	**$FE_{formate}$ %**	**FE_{tot} / %**
–0.3	30.2 ± 7	—	72.2 ± 4	102.2 ± 6
–0.4	28.8 ± 4	2.0 ± 0.3	73.1 ± 3	101.3 ± 5
–0.6	5.8 ± 2	2.6 ± 0.5	91.3 ± 4	99.7 ± 1
–0.8	5.9 ± 1	2.7 ± 0.1	97.4 ± 5	106.0 ± 1
–1.0	5.4 ± 2	2.7 ± 0.2	93.2 ± 5	101.3 ± 2
–1.2	6.0 ± 2	2.4 ± 0.1	95.3 ± 5	103.8 ± 1
–1.4	18.6 ± 7	1.5 ± 0.1	88.0 ± 4	108.0 ± 7
–1.6	15.8 ± 1	0.6 ± 0.7	84.5 ± 4	100.9 ± 2
–1.7	35.7 ± 2	2.3 ± 0.8	77.0 ± 4	115.0 ± 3
–2.0	32.9 ± 3	—	70.5 ± 4	103.4 ± 2
–2.2	42.8 ± 5	0.3 ± 0.2	61.7 ± 3	104.8 ± 5
–2.5	42.6 ± 3	0.4 ± 0.3	62.0 ± 3	105.0 ± 2

Table S2. Total (TCD) and partial (PCD) current densities corresponding to Table S1.

(*E* vs RHE) / V	**PCD_{H_2} / (mA cm^{-2})**	**PCD_{CO} / (mA cm^{-2})**	**$PCD_{formate}$ / (mA cm^{-2})**	***TCD* / (mA cm^{-2})**
–0.3	–1.0 ± 6	—	–2.4 ± 0.1	–3.5 ±6
–0.4	–3.2 ± 4	–0.2 ± 0.2	–7.9 ± 0.3	–11.4 ± 5
–0.6	–3.1 ± 2	–1.4 ± 0.4	–48.9 ± 2	–53.5 ± 1
–0.8	–6.8 ± 1	–3.1 ± 0.5	–111.6 ± 5	–121.6 ± 1
–1.0	–10.9 ± 2	–5.3 ± 0.2	–187.5 ± 9	–203.9 ± 2
–1.2	–13.1 ± 2	–5.1 ± 0.1	–207.1 ± 10	–225.4 ± 1
–1.4	–47.1 ± 7	–3.8 ± 0.1	–223.2 ± 11	–274.2 ± 7
–1.6	–49.2 ± 1	–2.0 ± 0.7	–264.2 ± 13	–315.4 ± 2
–1.7	–159.5 ± 3	–10.1 ± 0.6	–344.4 ± 17	–514.4 ± 3
–2.0	–173.5 ± 3	—	–371.1 ± 18	–545.1 ± 2
–2.2	–253.0 ± 5	–1.7 ± 0.2	–364.9 ± 18	–619.7 ± 4
–2.5	–303.4 ± 3	–2.6 ± 0.3	–441.2 ± 22	–747.2 ± 2

Table S3. Potential-dependent product distribution represented as Faradaic efficiencies (FEs) after potentiostatic CO_2RR in 5 mol dm^{-3} KOH over the ap-Bi_2O_3@GDE.

(*E* vs RHE) / V	**FE_{H_2} / %**	**FE_{CO} / %**	**$FE_{formate}$ %**	**FE_{tot} / %**
–0.6	37.5 ± 4	1.4 ± 0.1	73.7 ± 7	112.7 ± 11
–0.8	29.6 ± 3	2.3 ± 0.2	85.0 ± 8	117.0 ± 11
–1.0	27.5 ± 3	—	80.0 ± 8	107.5 ± 10
–1.2	26.6 ± 2	3.4 ± 0.3	67.0 ± 6	97.0 ± 9
–1.5	27.4 ± 3	—	65.0 ± 6	92.4 ± 9
–1.7	29.2 ± 3	2.1 ± 0.2	64.0 ± 6	95.4 ± 9
–2.0	30.2 ± 3	—	63.0 ± 6	93.2 ± 9
–2.2	33.3 ± 3	1.19 ± 0.1	56.0 ± 5	90.5 ± 9
–2.5	29.2 ± 2	—	57.6 ± 5	86.9 ± 8

Table S4. Total (TCD) and partial (PCD) current densities corresponding to Table S3.

(*E* vs RHE) / V	**PCD_{H2} / (mA cm^{-2})**	**PCD_{CO} / (mA cm^{-2})**	**$PCD_{formate}$ / (mA cm^{-2})**	***TCD* / (mA cm^{-2})**
–0.6	–31.8 ± 3	–1.20 ± 0.1	–62.5 ± 6	–95.5 ± 9
–0.8	–74.2 ± 7	–5.96 ± 0.5	–212.7 ± 21	–292.9 ± 29
–1.0	–135.1 ± 13	—	–392.0 ± 39	–527.0 ± 52
–1.2	–167.6 ± 16	–21.46 ± 2	–422.1 ± 42	–594.9 ± 59
–1.5	–296.9 ± 29	—	–702.0 ± 70	–998.9 ± 106
–1.7	–332.6 ± 33	–23.95 ± 2	–706.1 ± 70	–1052.7 ± 105
–2.0	–541.1 ± 54	—	–1127.7 ± 112	–1668.8 ± 177
–2.2	–585.2 ± 58	–17.36 ± 1	–1203.1 ± 120	–1803.5 ± 180
–2.5	–584.9 ± 58	—	–1353.4 ± 135	–1938.3 ± 202

Table S5. Literature survey: formate production utilizing gas-fed electrolyzer systems (corresponding to Figure S8).

Catalyst	**Electrolyte**	**FE$_{formate}$ / %**	**E / V**	**PCD$_{formate}$ / mA·cm^{2}**	**Ref.**
Bi_2S_3 nanostructures	1 M, KOH	~100	–0.9 V vs RHE	~–400	7
BOC@GDY	1 M KOH	93.5	–1.1 V vs RHE	–200	8
C-supported SnO_2	0.25 M K_2SO_4	< 90	E_{cell} 5.9 V	–500	9
Bi LNSs	1 M KOH	92.2	–1.1 V vs RHE	–590	10
InP CQDs	3M KOH	93.1	–2.6 V vs RHE	–1000	11
SnO_2 NPs	2 M CsCl (pH10)	70	–1.6 V vs SHE	–1800	12
H-Sn_3O_4 NS	1 M KOH	91.1	–1.02 V vs RHE	–465	13
SnO_2 nanosheets	1 M KOH	94.2	–1.13 V vs RHE	–471	14
SnO_x shell / $Sn_{2.7}Cu$	1 M KOH	98	–0.70 V vs RHE	–406.7	15
Bi_2O_3 NP/Bi-$Bi_2O_2CO_3$	DI water	75.9	3.52 V	–200	16
$BiPO_4$ to $Bi_2O_2CO_3$	1 M KOH	93	–1.55 V vs RHE	–1000	17
BiOBr-templated	2 M $KHCO_3$	90	–	–200	18
Bi NSs	1 M KOH	89	–0.67 V vs RHE	–405	19
SnS nanosheets	1 M KOH	88	–1.3 V vs RHE	–120	20
Bi-ene-NW	1 M KOH	91	–0.97 V vs RHE	–570	21
MOF-derived $Bi_2O_2CO_3$	1 M KOH	93	–0.59 V vs RHE	–280	22
VS-Bi_2O_3	1 M KOH	93.7	–1.29 vs RHE	–400	23
Bi_2O_3/BiO_2	0.5 M HCO_3	98.1	–1.3 V vs RHE	–111.3	24
$ZnIn_2S_4$	1 M $KHCO_3$	99.3	-1.18 V vs RHE	-298	25
s-SnLi NPs	1 M KOH	92 %	-1.2 V vs RHE	-1000	26

References

1. Dutta, A.; Zelocualtecatl Montiel, I.; Kiran, K.; Rieder, A.; Grozovski, V.; Gut, L.; Broekmann, P., A Tandem (Bi_2O_3 → Bi_{met}) Catalyst for Highly Efficient ec-CO_2 Conversion into Formate: *Operando* Raman Spectroscopic Evidence for a Reaction Pathway Change. *ACS Catal.* **2021,** *11* (9), 4988-5003.

2. Rodríguez-Fernández, C.; Akius, K.; Morais de Lima, M.; Cantarero, A.; van Ruitenbeek, J. M.; Sabater, C., Raman signal reveals the rhombohedral crystallographic structure in ultra-thin layers of bismuth thermally evaporated on amorphous substrate. *Mater. Sci. Eng., B* **2021,** *270*, 115240.

3. Madhusudan, P.; Yu, J.; Wang, W.; Cheng, B.; Liu, G., Facile synthesis of novel hierarchical graphene–$Bi_2O_2CO_3$ composites with enhanced photocatalytic performance under visible light. *Dalton Trans.* **2012,** *41* (47), 14345-14353.

4. Harwig, H. A., On the Structure of Bismuthsesquioxide: The α, β, γ, and δ-phase. *Z. Anorg. Allg. Chem.* **1978,** *444* (1), 151-166.

5. Reyes-Contreras, A.; Camacho-López, M.; Camacho-López, S.; Olea-Mejía, O.; Esparza-García, A.; Bañuelos-Muñetón, J. G.; Camacho-López, M. A., Laser-induced periodic surface structures on bismuth thin films with ns laser pulses below ablation threshold. *Opt. Mater. Express* **2017,** *7* (6), 1777-1786.

6. Nam, D.-H.; Choi, K.-S., Bismuth as a New Chloride-Storage Electrode Enabling the Construction of a Practical High Capacity Desalination Battery. *J. Am. Chem. Soc.* **2017,** *139* (32), 11055-11063.

7. Ding, P.; Zhang, J.; Han, N.; Zhou, Y.; Jia, L.; Li, Y., Simultaneous power generation and CO_2 valorization by aqueous Al–CO_2 batteries using nanostructured Bi_2S_3 as the cathode electrocatalyst. *J. Mater. Chem. A* **2020,** *8* (25), 12385-12390.

8. Tang, S.-F.; Lu, X.-L.; Zhang, C.; Wei, Z.-W.; Si, R.; Lu, T.-B., Decorating graphdiyne on ultrathin bismuth subcarbonate nanosheets to promote CO_2 electroreduction to formate. *Sci. Bull.* **2021**.

9. Chen, Y.; Vise, A.; Klein, W. E.; Cetinbas, F. C.; Myers, D. J.; Smith, W. A.; Deutsch, T. G.; Neyerlin, K. C., A Robust, Scalable Platform for the Electrochemical Conversion of CO_2 to Formate: Identifying Pathways to Higher Energy Efficiencies. *ACS Energy Lett.* **2020,** *5* (6), 1825-1833.

10. Wang, D.; Liu, C.; Zhang, Y.; Wang, Y.; Wang, Z.; Ding, D.; Cui, Y.; Zhu, X.; Pan, C.; Lou, Y.; Li, F.; Zhu, Y.; Zhang, Y., CO_2 Electroreduction to Formate at a Partial Current Density up to 590 mA mg^{-1} via Micrometer-Scale Lateral Structuring of Bismuth Nanosheets. *Small* **2021,** *17* (29), 2100602.

11. Grigioni, I.; Sagar, L. K.; Li, Y. C.; Lee, G.; Yan, Y.; Bertens, K.; Miao, R. K.; Wang, X.; Abed, J.; Won, D. H.; García de Arquer, F. P.; Ip, A. H.; Sinton, D.; Sargent, E. H., CO_2 Electroreduction to Formate at a Partial Current Density of 930 mA cm^{-2} with InP Colloidal Quantum Dot Derived Catalysts. *ACS Energy Lett.* **2021,** *6* (1), 79-84.

12. Löwe, A.; Schmidt, M.; Bienen, F.; Kopljar, D.; Wagner, N.; Klemm, E., Optimizing Reaction Conditions and Gas Diffusion Electrodes Applied in the CO_2 Reduction Reaction to Formate to Reach Current Densities up to 1.8 A cm^{-2}. *ACS Sustainable Chem. Eng.* **2021,** *9* (11), 4213-4223.

13. Liu, L.-X.; Zhou, Y.; Chang, Y.-C.; Zhang, J.-R.; Jiang, L.-P.; Zhu, W.; Lin, Y., Tuning Sn_3O_4 for CO_2 reduction to formate with ultra-high current density. *Nano Energy* **2020,** *77*, 105296.

14. Li, J.; Jiao, J.; Zhang, H.; Zhu, P.; Ma, H.; Chen, C.; Xiao, H.; Lu, Q., Two-Dimensional SnO_2 Nanosheets for Efficient Carbon Dioxide Electroreduction to Formate. *ACS Sustainable Chem. Eng.* **2020,** *8* (12), 4975-4982.

15. Ye, K.; Zhou, Z.; Shao, J.; Lin, L.; Gao, D.; Ta, N.; Si, R.; Wang, G.; Bao, X., In Situ Reconstruction of a Hierarchical Sn-Cu/SnO_x Core/Shell Catalyst for High-Performance CO_2 Electroreduction. *Angew. Chem. Int. Ed.* **2020,** *59* (12), 4814-4821.

16. Yang, H.; Kaczur, J. J.; Sajjad, S. D.; Masel, R. I., Performance and long-term stability of CO_2 conversion to formic acid using a three-compartment electrolyzer design. *J. CO2 Util.* **2020,** *42*, 101349.

17. Fan, T.; Ma, W.; Xie, M.; Liu, H.; Zhang, J.; Yang, S.; Huang, P.; Dong, Y.; Chen, Z.; Yi, X., Achieving high current density for electrocatalytic reduction of CO_2 to formate on bismuth-based catalysts. *Cell Rep. Phys. Sci.* **2021,** *2* (3), 100353.

18. García de Arquer, F. P.; Bushuyev, O. S.; De Luna, P.; Dinh, C.-T.; Seifitokaldani, A.; Saidaminov, M. I.; Tan, C.-S.; Quan, L. N.; Proppe, A.; Kibria, M. G.; Kelley, S. O.; Sinton, D.; Sargent, E. H., 2D Metal Oxyhalide-Derived Catalysts for Efficient CO_2 Electroreduction. *Adv. Mater.* **2018,** *30* (38), 1802858.

19. Yang, J.; Wang, X.; Qu, Y.; Wang, X.; Huo, H.; Fan, Q.; Wang, J.; Yang, L.-M.; Wu, Y., Bi-Based Metal-Organic Framework Derived Leafy Bismuth Nanosheets for Carbon Dioxide Electroreduction. *Adv. Energy Mater.* **2020,** *10* (36), 2001709.

20. Zou, J.; Lee, C.-Y.; Wallace, G. G., Boosting Formate Production from CO_2 at High Current Densities Over a Wide Electrochemical Potential Window on a SnS Catalyst. *Adv. Sci.* **2021,** *8* (15), 2004521.

21. Zhang, M.; Wei, W.; Zhou, S.; Ma, D.-D.; Cao, A.; Wu, X.; Zhu, Q.-L., Engineering conductive network of atomically thin bismuthene with rich defects enables CO_2 reduction to formate with industry-compatible current densities and stability. *Energy Environ. Sci.* **2021,** *14* (9), 4998-5008.

22. Yuan, W.-W.; Wu, J.-X.; Zhang, X.-D.; Hou, S.-Z.; Xu, M.; Gu, Z.-Y., In situ transformation of bismuth metal–organic frameworks for efficient selective electroreduction of CO_2 to formate. *J. Mater. Chem. A* **2020,** *8* (46), 24486-24492.

23. Shi, Y.; Wen, C. F.; Wu, X.; Zhao, J. Y.; Mao, F.; Liu, P. F.; Yang, H. G., In situ reconstruction of vegetable sponge-like Bi_2O_3 for efficient CO_2 electroreduction to formate. *Mater. Chem. Front.* **2022,** *6* (8), 1091-1097.

24. Feng, X.; Zou, H.; Zheng, R.; Wei, W.; Wang, R.; Zou, W.; Lim, G.; Hong, J.; Duan, L.; Chen, H., Bi_2O_3/BiO_2 Nanoheterojunction for Highly Efficient Electrocatalytic CO_2 Reduction to Formate. *Nano Lett.* **2022,** *22* (4), 1656-1664.

25. Chi, L.-P.; Niu, Z.-Z.; Zhang, X.-L.; Yang, P.-P.; Liao, J.; Gao, F.-Y.; Wu, Z.-Z.; Tang, K.-B.; Gao, M.-R., Stabilizing indium sulfide for CO_2 electroreduction to formate at high rate by zinc incorporation. *Nat. Comm.* **2021,** *12* (1), 5835.

26. Yan, S.; Peng, C.; Yang, C.; Chen, Y.; Zhang, J.; Guan, A.; Lv, X.; Wang, H.; Wang, Z.; Sham, T.-K.; Han, Q.; Zheng, G., Electron Localization and Lattice Strain Induced by Surface Lithium Doping Enable Ampere-Level Electrosynthesis of Formate from CO_2. *Angew. Chem. Int. Ed.* **2021,** *60* (49), 25741-25745.

7.2. A Tandem ($Bi_2O_3 \rightarrow Bi_{met}$) Catalyst for Highly Efficient ec-CO_2 Conversion into Formate: Operando Raman Spectroscopic Evidence for a Reaction Pathway Change

Reprinted with permission from ACS Catal. 2021, 11, 9, 4988–5003. Copyright 2021 American Chemical Society.

Authors: Abhijit Dutta, **Iván Zelocualtecatl Montiel,** Kiran Kiran, Alain Rieder, Vitali Grozovski, Lukas Gut, and Peter Broekmann

ACS Catal. 2021, **11**, 9, 4988–5003. DOI: https://doi.org/10.1021/acscatal.0c05317

Highlights: A novel bismuth oxide foam on GDL support was synthesized through the dynamic hydrogen bubble template (DHBT) electrodeposition approach followed by thermal annealing at 300˚C for 12h. The oxidic Bi_2O_3 foam and the reduced metallic Bi_{met} foam revels high selectivity towards formate with values that never fall below 90% with an extended potential window of ~1100 mV (maximum $FE_{formate}$ = 100% at –0.6 V *vs.* RHE). The highly porous nature of the Bi_2O_3 foam combined with GDL support leads to a high electrochemically active surface area. As a result, excellent partial current densities were achieved (~90 mA cm^{-2}). These promising electrocatalytic characteristics result from coupling two distinct reaction pathways of formate formation in the aqueous CO_2-saturated 0.5 M $KHCO_3$ electrolyte, which is active on (i) the partly reduced Bi_2O_3 foam at low overpotentials (the subcarbonate pathway) and (ii) on the corresponding metallic $Bi_{metallic}$ foam catalyst at medium and high overpotentials (the Bi-O pathway). For the first time, *operando* Raman spectroscopy provides experimental evidence for the embedment of CO_2 into the oxidic Bi_2O_3 matrix (subcarbonate formation) at low overpotentials prior to and during the CO_2RR. The gradual transition of the formed carbonate/oxide composite catalyst into its fully metallic state was monitored by *operando* Raman spectroscopy as a function of electrolysis time and applied potential. IL-SEM was used to monitor morphological changes at the nm-length scale upon subcarbonate formation and partial electroreduction of the oxidic precursor during the CO_2RR. However, the macroporous structure of the foam catalyst remains unaffected by the (oxide/carbonate→metal) transition and the catalytic CO_2RR.

Contributions: In this project, I was one of the main persons responsible for the synthesis, characterization and electrochemical experiments. I contributed equally with Dr. Abhijit Dutta to the analysis and discussion of the data, and figure preparation of the paper.

ACS Catalysis

pubs.acs.org/acscatalysis Research Article

A Tandem (Bi_2O_3 → Bi_{met}) Catalyst for Highly Efficient *ec*-CO_2 Conversion into Formate: *Operando* Raman Spectroscopic Evidence for a Reaction Pathway Change

Abhijit Dutta,* Iván Zelocualtecatl Montiel, Kiran Kiran, Alain Rieder, Vitali Grozovski, Lukas Gut, and Peter Broekmann*

Cite This: *ACS Catal.* 2021, 11, 4988−5003 **Read Online**

ACCESS | Metrics & More | Article Recommendations | Supporting Information

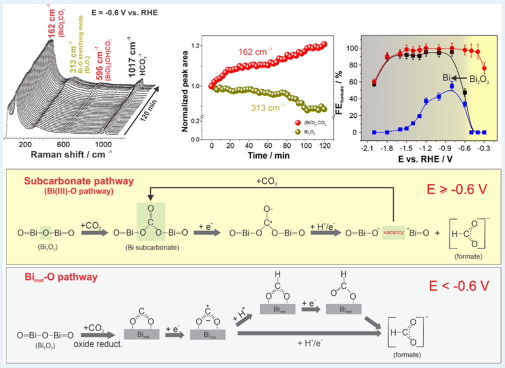

ABSTRACT: A novel bismuth oxide nanofoam, produced by means of the dynamic hydrogen bubble template (DHBT) electrodeposition approach followed by thermal annealing at 300 °C for 12 h, demonstrates excellent electrocatalytic selectivity toward formate production with faradaic efficiencies (FEs) never falling below 90% within an extended potential window of ∼1100 mV (max. $FE_{formate}$ = 100% at −0.6 V vs RHE). These promising electrocatalytic characteristics result from the coupling of two distinct reaction pathways of formate formation in the aqueous CO_2-sat. 0.5 M $KHCO_3$ electrolyte, which are active on (i) the partly reduced Bi_2O_3 foam at low overpotentials (sub-carbonate pathway) and (ii) on the corresponding metallic Bi_{met} foam catalyst at medium and high overpotentials (Bi−O pathway). For the first time, *operando* Raman spectroscopy provides experimental evidence for the embedment of CO_2 into the oxidic Bi_2O_3 matrix (sub-carbonate formation) at low overpotentials prior to and during the CO_2 reduction reaction (CO_2RR). The gradual transition of the formed carbonate/oxide composite catalyst into its fully metallic state is monitored by *operando* Raman spectroscopy as a function of electrolysis time and applied potential. The observed structural and compositional alterations correlate with changes in the faradaic efficiency and partial current density of formate production ($PCD_{formate}$), which reaches a maximum value of $PCD_{formate}$ = −84.1 mA cm^{-2} at −1.5 V vs RHE. The so-called identical location scanning electron microscopy technique was applied to monitor morphological changes that take place on the nanometer length scale upon sub-carbonate formation and partial electro-reduction of the oxidic precursor during the CO_2RR. However, the macroporous structure of the foam catalyst remains unaffected by the (oxide/carbonate → metal) transition and the catalytic CO_2RR.

KEYWORDS: *ec-CO_2 reduction, operando Raman spectroscopy, identical location (IL) SEM, formate production, carbon fiber cloth, $(BiO)_2CO_3$, Bi_2O_3 nanofoam*

INTRODUCTION

Societal, economic, and technological advancements over the last several decades have led to the extensive use of fossil fuels and, consequently, to substantially enhanced emissions of the greenhouse gas carbon dioxide (CO_2), which is the primary origin of global climate change.[1,2] Furthermore, alternative energy sources need to be explored due to the limited supply of fossil fuels. In principle, synthetic fuels (e.g., oxygenates[3] and hydrocarbons[3,4]) and other valuable platform chemicals (e.g., formate[5]) can be produced by means of the electrochemical reduction of CO_2 (denoted hereinafter CO_2RR), a process that has significant potential to contribute in the future to the necessary closing of the anthropogenic CO_2 cycle.[6] It is the use of renewable energy sources as the input for the highly endergonic CO_2RR that will render the overall CO_2 conversion process truly sustainable.[7−10]

Formate, one of the targeted liquid CO_2RR products, is currently synthesized in the industry on a large scale from CO.[11] The "green" electrochemical approach of formate production via the CO_2RR (electrochemical synthesis route) can be considered a promising alternative to the mature but environmentally unfriendly process of formate production (CO synthesis route).

It is known that electrocatalysts are essential not only to accelerate the inherently slow CO_2RR process but also to direct the reaction selectivity toward the targeted product.

Received: December 4, 2020
Revised: March 17, 2021
Published: April 8, 2021

https://doi.org/10.1021/acscatal.0c05317
ACS Catal. 2021, 11, 4988−5003

Early studies by Azuma et al.[12] and Hori et al.[13] focused primarily on the CO_2RR in an aqueous reaction environment and mono-metallic "bulk" materials as the catalysts. Based on their pioneering work, CO_2RR catalysts were classified into three major groups depending on the resulting product distribution: (i) carbon monoxide (CO) forming catalysts (e.g., Ag, Au, and Zn), (ii) hydrocarbon and oxygenate producing catalysts (Cu), and (iii) formate producing metals (e.g., Pb, Sn, Tl, Hg, and In).[12,14]

Recently, several more complex CO_2RR catalysts for formate production have been developed, such as nitrogen- and sulfur-doped reduced graphene oxide,[15] molecular catalysts,[16] nanocomposite materials,[17] and Pd-based composites.[5] Intriguingly, transition metal oxides, such as Co_3O_4,[18,19] SnO_2,[20] ZnO,[21] and In_2O_3,[22] have also been identified as promising candidates for the electrosynthesis of formate from CO_2.

Among the formate-producing catalysts studied thus far, Bi and Bi-based materials stand out, in particular because of their ability to stabilize the adsorbed $CO_2^{\cdot -}$ radical anion, which is considered to be a key intermediate in the reaction pathway of formate production.[23−25]

Previous studies have focused on two-dimensional (2D) Bi materials, e.g., foils,[26] nanosheets,[23,24,27] thin layers of Bi,[28] and dendritic Bi catalysts.[29] However, in most of these cases, an excellent formate efficiency was achieved only within a rather narrow potential window (e.g., a faradaic efficiency of ~86% and $PCD_{formate}$ of approximately −13.33 mA cm^{-2} at −1.1 V vs RHE)[27] and on a comparably short electrolysis time scale of a few hours.[24,27,30−32] The latter suggests substantial catalyst degradation over more extended electrolysis times.[23,24,27,31,33]

In the present work, we apply the additive-assisted dynamic hydrogen bubble template (denoted hereinafter DHBT)[34,35] approach for the electrosynthesis of three-dimensional (3D) dendritic Bi foams. As substrates of choice, we chose carbon fiber cloths, which often find use as gas diffusion electrodes (GDEs, see Figure S1) in electrolyzer systems. The results obtained on the GDE are further compared to Bi foams deposited on ideal planar support electrodes (e.g., Cu and C foils). Herein, we demonstrate that the combination of a GDE support material with the DHBT approach for catalyst preparation results in electrodes of particularly high electrochemically active surface area (ECSA), thus leading to excellent partial current densities of formate production ($PCD_{formate}$) that reach values of ~−84.1 mA cm^{-2} (normalized to the geometric surface area of the support material).

From previous electrochemical and *operando* spectroscopic studies, e.g., on SnO_2-based precursor materials, it is known that (transient) intermediate oxide species can play a crucial role in the catalytic mechanism of formate formation.[36,37] Similar to Sn, Bi and Bi-based materials are also highly oxophilic and therefore prone to rapid surface oxidation after their (electro) synthesis. The specific role of oxygen and oxidic species in the CO_2RR mechanism on Bi-based electrocatalysts has, however, not yet been addressed. For this purpose, we compare the as-prepared Bi foams with foams that were treated by a further thermal annealing step at 300 °C, thus transforming the pristine and largely metallic Bi foams into well-defined Bi_2O_3 oxide foams.

By analyzing the CO_2RR product distribution in combination with *operando* Raman spectroscopy, we demonstrate that both the oxidic Bi_2O_3 and the metallic Bi are highly selective catalyst materials toward formate production. However, the underlying CO_2RR mechanisms on the Bi_2O_3 and Bi catalyst are found to be substantially different. Herein, we present for the first time *operando* spectroscopic evidence for the so-called bismuth sub-carbonate[30] reaction pathway of formate production involving the absorptive embedment of CO_2 into the oxide matrix prior to its electro-conversion into formate.

RESULT AND DISCUSSION

Synthesis and *Ex Situ* Structural Characterization of Bi/Bi_xO_y and Bi_2O_3 Foams. Using the dynamic hydrogen bubble template (DHBT) electrodeposition approach, Bi foams were first deposited on planar copper (Cu) and carbon (C) foil supports. This process was subsequently transferred to a porous carbon fiber cloth that often finds use as a gas diffusion electrode (GDE) in electrolyzer systems.

When applying high current densities of j = −3 A cm^{-2} in a highly acidic environment (1.5 M H_2SO_4), the actual metal deposition is inevitably superimposed on the hydrogen evolution reaction (HER). Under the applied harsh experimental conditions, the HER relies on the superposition of (i) proton reduction and (ii) water splitting according to

$$\text{HER(proton reduction)}:\ 2H^+ + 2e^- \rightarrow H_2 \quad (1)$$

$$\text{HER(water splitting)}:\ 2H_2O + 2e^- \rightarrow H_2 + 2OH^- \quad (2)$$

$$\text{metal deposition}:\ Bi^{3+} + 3e^- \rightarrow Bi_{met} \quad (3)$$

At these high current densities, proton reduction is mass transport-limited, thus further activating the HER reaction pathway through water splitting.[38,39] Hydrogen gas bubbles, which temporarily form on the cathode, function as a transient geometric template for the actual metal foaming process.[34,35,40−42] In the course of the metal deposition process, smaller H_2 bubbles tend to coalesce into larger bubbles, thus introducing dynamics into the templated metal deposition process.[38,43] Importantly, the local pH close to the electrode surface significantly changes as a consequence of the massive H^+ consumption (eq 1) and OH^- formation (eq 2). The basic principle of the additive and DHBT-assisted metal foaming process is illustrated in Figure 1 for a carbon fiber cloth (gas diffusion electrode, GDE, see also Figure S1) serving as the support electrode. In this work, a citrate-based salt (ammonium bismuth citrate) was used as the Bi precursor to avoid undesirable hydrolysis processes, which are typical of most inorganic Bi salts (e.g., $Bi_2(SO_4)_3$ and $Bi(NO_3)_3$) during solution preparation in aqueous media. Although citrate anions transform almost completely into citric acid in the highly acidic environment of the bulk electrolyte solution, nonetheless anionic citrate forms in the interfacial boundary layer under vigorous HER conditions due to local pH changes (Figure 1).[34] Therefore, it can be assumed that the actual metal foaming process occurs from a complexed bismuth solution because citrate readily forms chelating complexes with Bi^{3+} ions.[40] These complexing ligands are released from the reduced Bi and remain temporarily chemisorbed on the metallic surface during metal electrodeposition, which might further alter the nucleation and growth characteristics of the Bi.[34] Note that, due to their oxophilicity and high surface area, metallic Bi foams readily undergo surface oxidation immediately after their emersion from the plating bath (see discussion

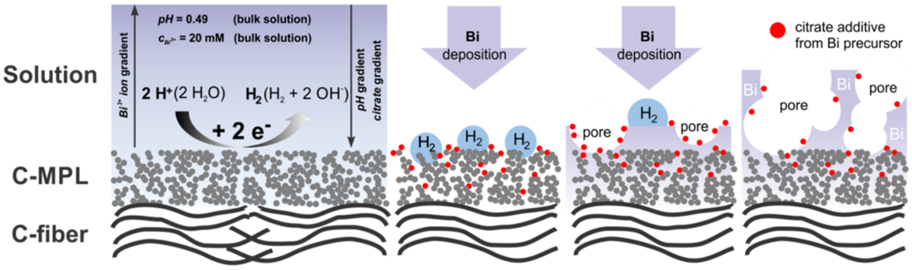

Figure 1. Scheme illustrating the additive-assisted dynamic hydrogen bubble template (DHBT) electrodeposition approach carried out on the carbon fiber cloth support (gas diffusion electrode, GDE).

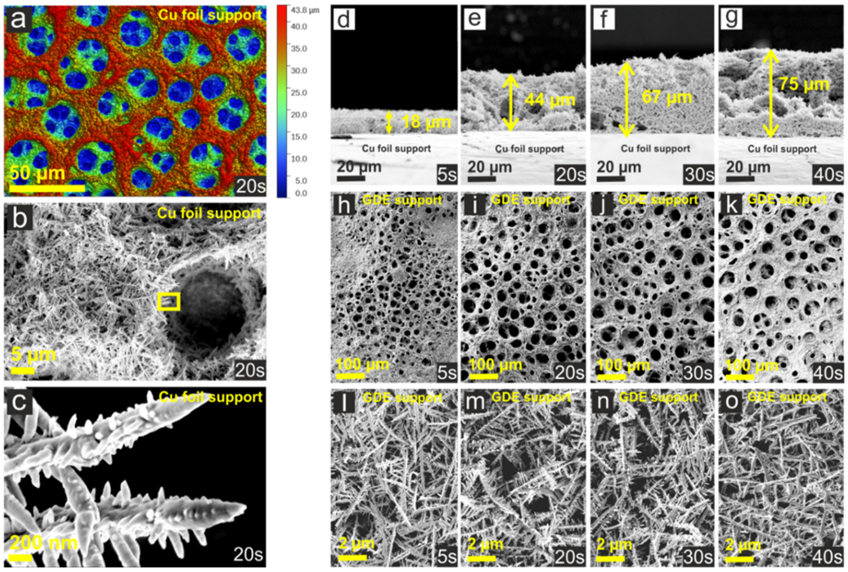

Figure 2. Morphology of the as-prepared (*ap*) Bi/Bi$_x$O$_y$ foam. (a) White light interferometry image of the *ap* Bi/Bi$_x$O$_y$ foam deposited on a Cu foil support (denoted *ap* Bi/Bi$_x$O$_y$@Cu). (b, c) Corresponding SEM images. (d−g) Side view of the *ap* Bi/Bi$_x$O$_y$@Cu foams, foam thickness as a function of the deposition time. (h−o) *ap* Bi/Bi$_x$O$_y$ foam deposited on a carbon fiber cloth support (denoted Bi/Bi$_x$O$_y$@GDE).

of the XPS results below). For this reason, we denote them in the following "as-prepared" (*ap*) "Bi/Bi$_x$O$_y$" foams.

Figure 2 depicts white light interferometry (WLI) (panel a) and SEM images (panels b and c) of the *ap* Bi/Bi$_x$O$_y$ foam deposited on the planar Cu foil substrate. Similar to the morphologies of the related Cu, Ag, Sn, and Zn systems,[34,35,42,44,45] the obtained Bi/Bi$_x$O$_y$ foams also show a distinct gradient in the pore diameters along the surface normal, with the smallest pores near the support electrode (Cu foil) and the largest pores at the outermost surface of the foam material. Two distinct levels of interconnected open-cell pores are visible with surface pore diameters ranging from 15 to 25 μm, thus representing the "primary" macroscale porosity of the formed *ap* Bi/Bi$_x$O$_y$ foam (Figure 2a). The pore side-walls consist of more loosely packed Bi dendrites, thus introducing a "secondary" nanoscale porosity to the *ap* Bi/Bi$_x$O$_y$ foam (Figure 2b,c). Dendritic metal growth results from the applied harsh experimental conditions ($j = -3$ A cm^{-2}), in which the rate of metal deposition is limited by mass transport of Bi^{3+} ions along with the decreased mobility of the formed adatoms on the emerging electrode surface. Both the thickness of the *ap* foams and the respective size distribution of the surface pores increase with elapsed deposition time, at least in the initial time period of metal foaming (Figure 2d−g, Figures S2 and S3). Figure 2h−o depicts top-down SEM images of four selected *ap* Bi/Bi$_x$O$_y$@GDE samples differing in the thickness of the covering Bi foams. Obviously, the dendritic nature of the pore side-walls does not depend on the chosen support material. However, the primary macroporosity (e.g., pore size distribution) experiences certain alterations when changing the support material. This can in principle be due to the ratio of faradaic efficiencies (FE_{H2}/FE_{Bi}) and the so-called "bubble break-off diameter", both of which depend on the chemical nature and the surface morphology of the support material.[34,35,38,44−46] In general, the pore size distribution of the Bi foams is broader and less well defined on the porous GDE support compared to the planar Cu and C foil substrates (see Figure S5). However, the gravimetric analysis of the deposits suggests that the amount of Bi material is similar for all three support materials used (Figure S6).

Obviously, the formed hydrogen bubbles are more stable on the rough GDE support and tend further to coalesce during the concerted metal deposition/HER processes, thus explaining the bigger surface pores in case of the GDE support compared to the Cu and C foils substrates (Figure S5).

Note that both sides of the carbon fiber cloths used in this work were coated with a microporous carbon layer (denoted C-MPL, Figure S1). Due to the porous nature of this support material, it can be assumed that Bi is also deposited to some extent inside the outermost C-MPL (Figure 1). For the electrochemical catalyst performance testing, discussed below, we restrict our study to foams obtained by 20 s of deposition

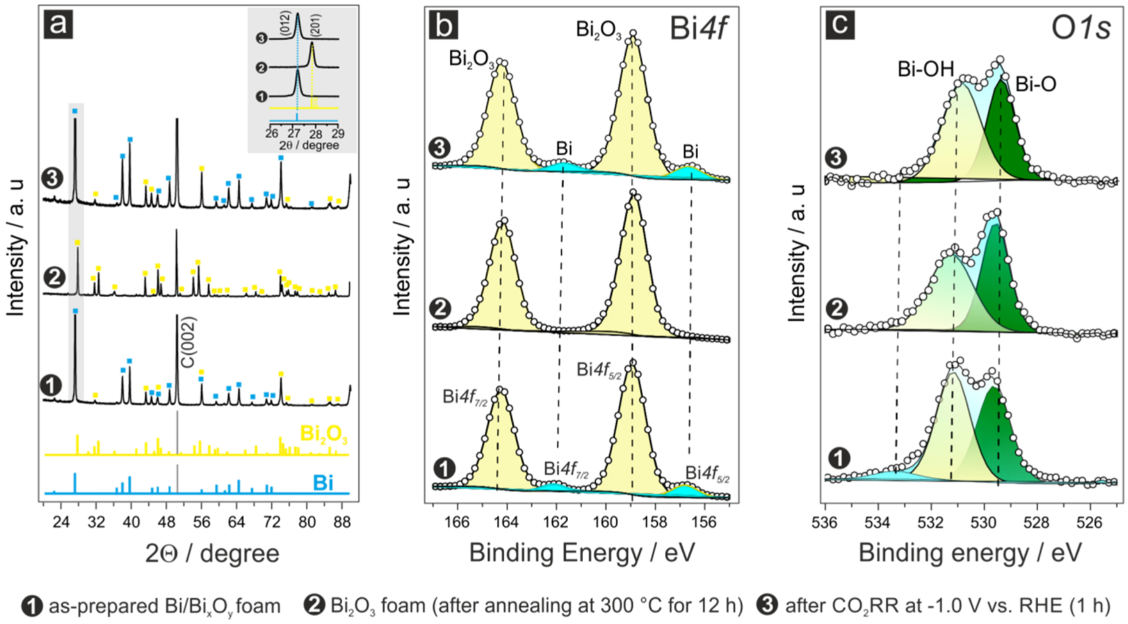

Figure 3. (a) X-ray diffraction (XRD) inspection of the Bi foams depending on their stage of preparation, as indicated by the numbers. The foams were deposited on a carbon foil support; for comparison purposes, the references for metallic Bi (blue) and Bi_2O_3 (yellow) are also provided. (b) Corresponding Bi4f X-ray photo-emission spectra. (c) Corresponding O1s X-ray photo-emission spectra. Note that for the 1 h CO_2RR, the Bi_2O_3 foam was used as the catalyst.

time, yielding on the Cu foil support a thickness of the active catalyst materials of ~44 μm (Figure 2e and Figure S4). Thicker catalyst films often become mechanically instable under harsh CO_2RR conditions in particular when gases evolve as reaction products (e.g., hydrogen gas bubbles at higher overpotentials).

The *ap* Bi/Bi_xO_y foams were further subjected to thermal annealing at 300 °C for 12 h in air, thus transforming the catalyst material into a fully oxidized Bi_2O_3 foam. This assumption is confirmed by TEM analyses of the *ap* Bi/Bi_xO_y and the Bi_2O_3 foams (see Figure S7). The overall morphology of the foams remains preserved upon thermal annealing, as evidenced by SEM inspection (Figure S8). It should be noted that the thermal treatment leads to a pronounced color change of the foam from black (*ap* Bi/Bi_xO_y) to yellowish (Bi_2O_3, Figure S9).

In the corresponding X-ray diffraction (XRD) analysis (Figure 3a, Table S1) the diffraction patterns of three Bi foams in distinct preparation stages are compared. The *ap* sample yields a diffraction pattern that is dominated by features of polycrystalline Bi (rhombohedral crystal structure, space group *P*21/c).[47−49] These are superimposed by minor contributions from α-Bi_2O_3 that likely forms on the surface of the foam following its immersion in the plating bath and exposure to air. The diffractogram of the thermally annealed sample, by contrast, exclusively shows contributions from the monoclinic α-Bi_2O_3 phase. Post-electrolysis XRD inspection (after 1 h at −1.0 V vs RHE in CO_2-sat. 0.5 M $KHCO_3$) suggests an electro-reduction of the α-Bi_2O_3 bulk phase back into metallic Bi. Again, the minor contributions of α-Bi_2O_3 to the XRD patterns most likely result from post-electrolysis surface oxidation of the oxophilic Bi under ambient conditions. Also, trace residuals of the formed Bi_2O_3, which were not in proper contact to the support during electrolysis, might add to the observed minor oxide features visible in the XRD patterns after the electrolysis (Figure 3a). Similar effects have recently been discussed for SnO_2-based CO_2RR catalysts.[36]

Whereas XRD is sensitive only to the "bulk" of the catalyst material exhibiting long-range transitional order, XPS selectively probes the chemical composition of the catalyst surface, which does not necessarily exhibit a lateral order. Panels b and c in Figure 3 show the spin-orbit split (5.3 eV) Bi4f and the O1s photoemissions of the Bi foams depending on their preparation state (see also Figures S10 and S11). It is noteworthy that, even for the as-prepared sample, Bi(III) species (BE ($Bi4f_{5/2}$) = 162.1 eV) govern the Bi4f emission (Figure 3b-1) superimposed by minor contributions from metallic Bi(0), which appear as a satellite peak at BE ($Bi4f_{5/2}$) = 156.8 eV. This particular feature can be assigned to photoemissions from the near-surface "bulk" of the metallic Bi foam. The ratio of integrated intensities ($I_{Bi(III)}/I_{Bi(o)}$ = 6.92), derived from the quantitative analysis of the $Bi4f_{5/2}$ emissions, confirms a largely oxidized Bi foam surface. The corresponding O1s spectrum, shown in panel c, indicates the presence of two different oxygen components, which are attributed to Bi−OH (BE (O1s) = 530.7 eV) and oxidic Bi−O species (BE (O1s) = 529.5 eV); the latter can be assigned to the surface-confined α-Bi_2O_3 phase, which has already been observed in the respective XRD analysis of the as-prepared foam sample (panel a-1). Bi−OH species most likely originate from the partial hydrolysis of the oxide on the outermost surface of the foam when exposed, even for a short time, to (humid) air prior to the XPS inspection.

Annealing the foam sample for 12 h at 300 °C transforms the mixed Bi/Bi_xO_y foam into its fully oxidized α-Bi_2O_3 state (panel a-2) and lets the Bi(0) contribution completely disappear from the respective Bi4f photoemission spectrum (panel b-2). However, the corresponding O1s emission is only marginally affected by the thermal treatment (panel c-2). The presence of hydroxy species on the surface of the foam even after the annealing treatment is again supportive of a mixed

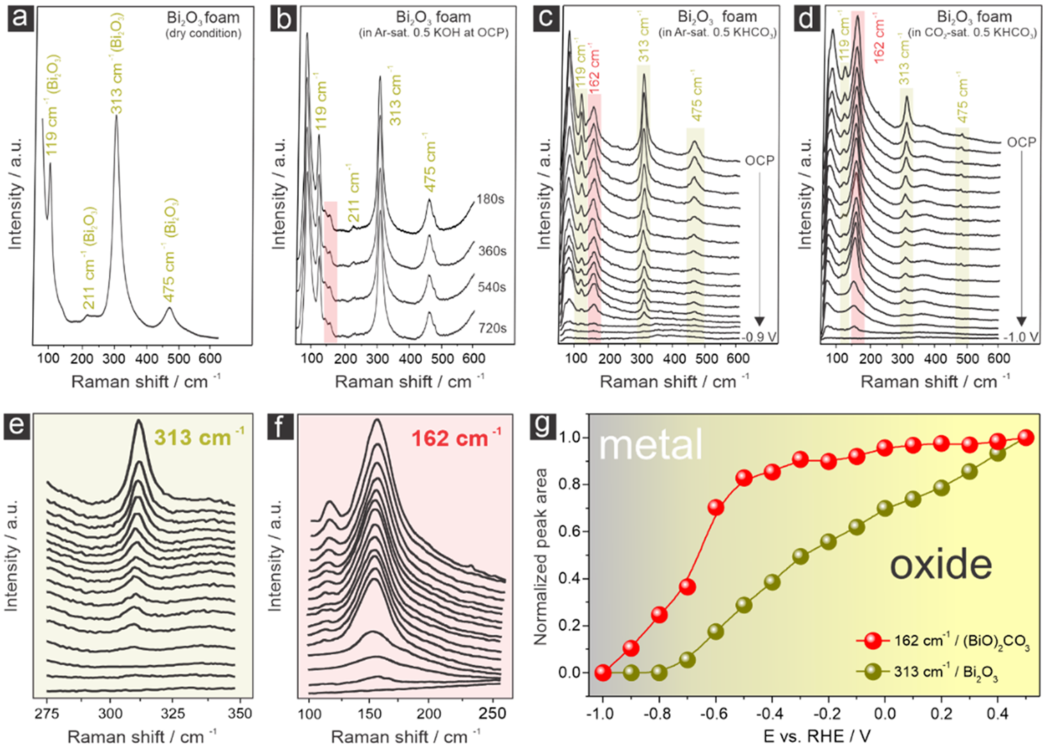

Figure 4. (a) *Ex situ* Raman spectrum of the Bi_2O_3 foam under dry conditions after annealing the *ap* Bi/Bi_2O_3 foam at 300 °C for 12 h. (b) Time-resolved Raman spectra of the Bi_2O_3 foam at the open-circuit potential (OCP) in the Ar-sat. 0.5 M KOH solution. (c) Series of potential-dependent Raman spectra showing the (oxide → metal) transition of the Bi_2O_3 foam in the Ar-sat. 0.5 M $KHCO_3$ solution; the holding time at each potential was 3 min. (d) Series of potential-dependent Raman spectra showing the respective (oxide/carbonate → metal) transition in the CO_2-sat. 0.5 M $KHCO_3$ solution; the holding time at each potential was 3 min. (e) Potential-dependent changes of the Raman peak at 313 cm^{-1} used as the fingerprint for the presence of Bi_2O_3 (enlarged section of spectra shown in panel (d)). (f) Potential-dependent changes of the Raman peak at 162 cm^{-1} used as the fingerprint for the presence of the sub-carbonate species on the catalyst (enlarged section of spectra shown in panel (d)). (g) Potential-dependent integrated intensities of the Raman peaks shown in panels (e) and (f).

hydroxy/oxide surface layer that instantaneously forms on the foam surface when exposed to air. Obviously, the presence of hydroxy species on the foam surface does not require any exposure to an aqueous electrolyte prior to XPS analysis.

Post-electrolysis XPS inspection of the foam sample shows the re-appearance of satellite peaks in the Bi4$f_{5/2}$ emissions assigned to the metallic Bi(0) (panel b-3), thus resembling the photoemission characteristics of the as-prepared sample, in full accordance with the XRD analysis. As expected, the corresponding O1s spectrum again shows the presence of both hydroxy and oxidic species on the foam surface (panel c-3), supporting our assumption of a surface chemical composition of the Bi foam, which is governed more by exposure to environmental air prior to XPS inspection than by the particular experimental history of the sample (e.g., thermal annealing or electrolysis).

These findings call for more advanced *in situ* (*operando*) investigations of the Bi foams to probe the chemical state of the catalyst under potential control prior to and during the CO_2RR.

Potential- and Time-Dependent *Operando* Raman Spectroscopy. The porous nature of the metallic or oxidic Bi foams facilitates the method of Raman spectroscopy.[50,51] Note that, due to the finite penetration depth of the laser light, Raman spectroscopy probes both the surface and to some extent also the bulk properties of the catalyst sample.[36,37] The Supporting Information contains several reference measurements on the optimization of the Raman experiment in terms of laser light source and laser power (see Figures S12 and S13).

Figure 4a depicts a representative *ex situ* Raman spectrum of the dry Bi_2O_3 foam sample after 12 h of annealing at 300 °C in air (internal reference). Several prominent peaks are visible in the range between 100 and 700 cm^{-1}, which can be attributed to the vibrational modes of the α-Bi_2O_3 phase and its double refraction biaxial crystal structure, revealing a low symmetry of monoclinic geometry.[52−54] According to the literature,[46,47,55,56] the observed Raman bands can be grouped into three types of features: (i) strong Raman bands appearing at wavenumbers <120 cm^{-1}, which are typically assigned to displacements of cationic −Bi(III)− entities with regard to the surrounding oxide matrix (e.g., at 119 cm^{-1});[53] (ii) weaker bands appearing between 120 and 155 cm^{-1} that are due to the concerted vibrational motions of binuclear Bi−O entities;[47,55] and (iii) vibrational modes of mononuclear −O− entities that are typically found at wavenumbers >155 cm^{-1} (e.g., the Bi−O stretching mode at 313 cm^{-1}).[46,53,56] As expected from the *ex situ* XRD and XPS analysis (Figure 3), the Raman spectrum of the corresponding dry *ap* Bi/Bi_xO_y foam (*ex situ* characterization) shows qualitatively the same Raman features as the thermally annealed foam (see Figure S14). However, the oxide-related Raman features are broader, less well defined, and weaker in intensity in the case of the surface oxides on the *ap* sample.

Figure 4b displays a time-dependent series of Raman spectra of the Bi_2O_3 foam exposed to an Ar-saturated 0.5 M KOH solution at the open-circuit potential (pH = 13.5, OCP ≈ +0.79 V vs RHE, Figure S15a). A CO_2/bicarbonate-free potassium hydroxide electrolyte was chosen for this measurement to selectively study the effect of the exposure of the foam to an alkaline electrolyte on its surface composition, independent of the additional alteration resulting from CO_2/bicarbonate adsorption phenomena (see discussion below). The Raman characteristics of the dry Bi_2O_3 foam sample (panel a) are, in principle, preserved in the alkaline aqueous electrolyte of pH = 13.5. Very minor alterations appear at the OCP in the range from 120 to 170 cm^{-1} and are due to a more extended surface hydrolysis in the aqueous electrolyte involving the exchange of Bi−O by Bi−OH species. Further alterations concern the less intense Raman band at 475 cm^{-1}, which shows a small satellite feature in the alkaline electrolyte environment. These minor changes in the Raman characteristics that are visible in the first spectrum of the time-resolved series are already completed after 180 s of exposure. There are no further alterations observed in the subsequently recorded spectra at exposure times >180 s, thus proving the stability of the Bi_2O_3 foam at OCP and pH of 13.5 in full accordance with the thermodynamic predictions represented in the respective Pourbaix diagram.[57] This observation is full in agreement with the corresponding OCP measurement which reaches a plateau value at exposure times >200 s (Figure S15a). The Raman spectra acquired in the CO_2 and bicarbonate-free 0.5 M KOH electrolyte serve as further reference for the potential-dependent Raman experiments of the Bi_2O_3 foam carried out in an Ar-saturated aqueous 0.5 M $KHCO_3$ electrolyte (Figure 4c). Again, all main Raman features at 119, 313, and 475 cm^{-1} attributed the Bi_2O_3 phase are preserved in the Ar-saturated bicarbonate solution even at the OCP of ca. +0.60 V vs RHE (see Figures S15b and S16a). However, a new strong Raman feature appears at 162 cm^{-1} (highlighted red in panel c), which can be assigned to the so-called sub-carbonate species[58] that forms in the Ar-sat. bicarbonate solution even at the OCP through the partial surface exchange of oxidic Bi−O or Bi−OH species by $Bi-CO_3-Bi$ ensembles according to

$$Bi_2O_3 + CO_2 \rightarrow (BiO)_2CO_3 \qquad (4)$$

This assignment could be further corroborated by *ex situ* Raman measurements using a commercial $(BiO)_2CO_2$ powder sample as the reference material. Clearly visible in Figure S17 is the strong Raman feature at 162 cm^{-1}. Less intense vibrational modes at 366 and 574 cm^{-1}, visible in the reference spectra (Figure S17), are typically not detected in the *in situ* (e.g., at OCP) and *operando* Raman experiments under CO_2RR conditions. These observations (Figure 4c) imply a direct adsorptive interaction of either dissolved CO_2 or the bicarbonate anion with the Bi_2O_3 foam even in the Ar-saturated 0.5 M $KHCO_3$ electrolyte under non-reactive conditions at the OCP (Figure S16a). Note that traces of gaseous CO_2 are present even in the Ar-saturated bicarbonate solution. Both the oxide-related Raman features at 119, 313, and 475 cm^{-1}, and the new sub-carbonate vibrational mode at 162 cm^{-1} gradually disappear when changing the potential from the OCP to −0.9 V vs RHE (Figure 4c). A quantitative analysis of this (oxide/sub-carbonate → metal) transition is provided in the Supporting Information (see Figures S18 and S19). Note that the derived integrated intensities do not exactly correlate with the abundance of a certain Raman active species on the electrode. Integrated intensities also depend on other factors, e.g., the surface roughness or changes thereof (e.g., during the oxide → metal transition). Plots of the integrated Raman intensity versus the applied electrode potential (e.g., Figure S18) provide, however, valuable qualitative trends in the stability of the oxidic and carbonate phases present on the electrode.

Hereinafter, we restrict the discussion to analogue Raman experiments carried out in the CO_2-saturated 0.5 $KHCO_3$ electrolyte solution (Figure 4d and Figure S15c), which served as the working electrolyte for mechanistic studies and the actual catalyst performance testing (discussed below). The main difference to the Raman spectra acquired in the Ar-saturated bicarbonate solution (panel c) is the intensity of the sub-carbonate Raman band at 162 cm^{-1}, which becomes the dominant Raman feature in the CO_2−sat. (~35 mM)[59] electrolyte. Our *operando* spectroscopic results strongly suggest substantial "non-reactive" CO_2 adsorption on the Bi_2O_3 prior to the actual CO_2RR onset (see also Figure S16b). These results also imply a (partial) displacement of the oxide and surface hydroxide features by the sub-carbonate at the OCP, which is not restricted to the outermost catalyst surface but extends further into deeper layers and the near-surface bulk of the Bi_2O_3 foam catalyst. This hypothesis is further supported by Figure S20, comparing the integrated intensities of the Raman spectra acquired from the *ap* Bi/Bi_xO_y foam and the corresponding thermally annealed Bi_2O_3 foam at the OCP. Interesting to note is that, in the case of the largely metallic *ap* Bi/Bi_xO_y foam, which is covered only by a thin oxidic skin, the oxide-related Raman features instantaneously disappear when brought into contact with the CO_2-sat 0.5 M $KHCO_3$ electrolyte (Figure S21). As a result, a thin bismuth sub-carbonate skin is formed on the otherwise *ap* metallic Bi foam. Note that, for the sub-carbonate formation under non-reactive conditions (at OCP), also the electrolyte pH is of importance (see discussion of Figure S22).

Formed sub-carbonate species can be regarded as precursors of CO_2 electroreduction at low overpotentials in the initial stage of the CO_2RR. A quantitative analysis of the potential-dependent (oxide/sub-carbonate → metal) transition is based on the integrated intensities of the Raman features at 313 cm^{-1} (Bi_2O_3 fingerprint, Figure 4e) and 162 cm^{-1} (sub-carbonate fingerprint; Figure 4f). The results of this analysis are presented in Figure 4g. Both the oxide and the sub-carbonate features follow the same qualitative trend of decreasing intensities with increasing CO_2RR overpotentials (decreasing applied potentials). The potential-dependent Raman data suggest that the (oxide → metal) transition of the Bi_2O_3 foam is completed at approximately −0.8 V vs RHE. By using Bi_2O_3 microsphere particles as the CO_2RR catalyst, Deng et al. have recently demonstrated that the Bi−O Raman mode at 313 cm^{-1} can persist, at least to an extent, even to applied potentials beyond −0.9 V vs RHE.[60] Sub-carbonate-related Raman features were, however, not discussed in that study. On the Bi_2O_3 foam, these sub-carbonate species appear to be even more stable than the corresponding oxides. This can be concluded from the quasi-plateau behavior of the 162 cm^{-1} features in the intensity vs potential plot at potentials ranging from the OCP to −0.6 V vs RHE (Figure 4g). The significant decrease in intensity at potentials less than −0.6 V vs RHE spectra is completed only at −1.0 V vs RHE. We do consider the formed metallic Bi foam catalyst present at potentials less than −1.0 V vs RHE as oxide/sub-carbonate derived (denoted hereinafter as *oc-d*).

Note that the data shown in Figure 4d−g do not necessarily present steady-state conditions; the holding time at each applied potential was 3 min (see the Experimental Section). The exchange of the oxide (surface hydroxide) species by the sub-carbonate might therefore further proceed even during an ongoing CO_2RR in the low overpotential regime. This is demonstrated by the series of time-dependent Raman spectra in Figure 5, which further support our working hypothesis that the oxide/sub-carbonate exchange is not restricted to the outermost surface but proceeds deeper into the bulk of the foam catalyst with time. Note that the observed Raman feature at 1017 cm^{-1} is due to bicarbonate in the solution phase, as evidenced by the additional control experiments depicted in Figure S23.

The transition from the oxidic Bi_2O_3 foam to the oxide/sub-carbonate/Bi_{met} composite at low applied overpotentials can be monitored as a function of time and applied potential by using visual inspection. Figure 6 depicts representative optical photographs of the oxidic Bi_2O_3 foam exposed to the CO_2-sat. 0.5 M $KHCO_3$ electrolyte. The yellowish color gradually disappears with time and turns into black, which is characteristic not only of the *ap* Bi/Bi_xO_y foam (see Figure S9 and the corresponding multimedia file) but also for the corresponding oxide/sub-carbonate/Bi_{met} composite formed in this potential regime (see Figure 4g). As expected, this compositional transition is faster at −0.6 V vs RHE than at −0.3 vs RHE.

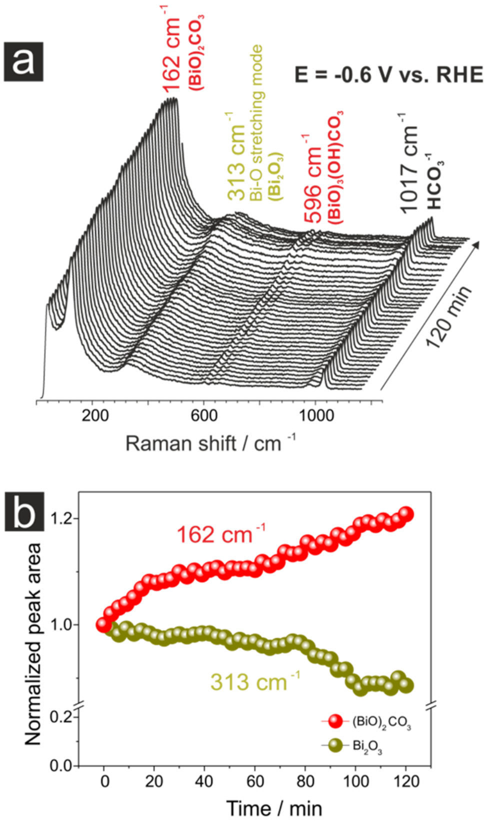

Figure 5. (a) Series of time-resolved Raman spectra acquired over 120 min at E = −0.6 V vs RHE. (b) Integrated intensities of the Raman peaks at 162 cm^{-1} (sub-carbonate) and 313 cm^{-1} (Bi_2O_3) as functions of time. This experiment confirms the non-steady-state characteristics of the Raman measurements shown in Figure 4.

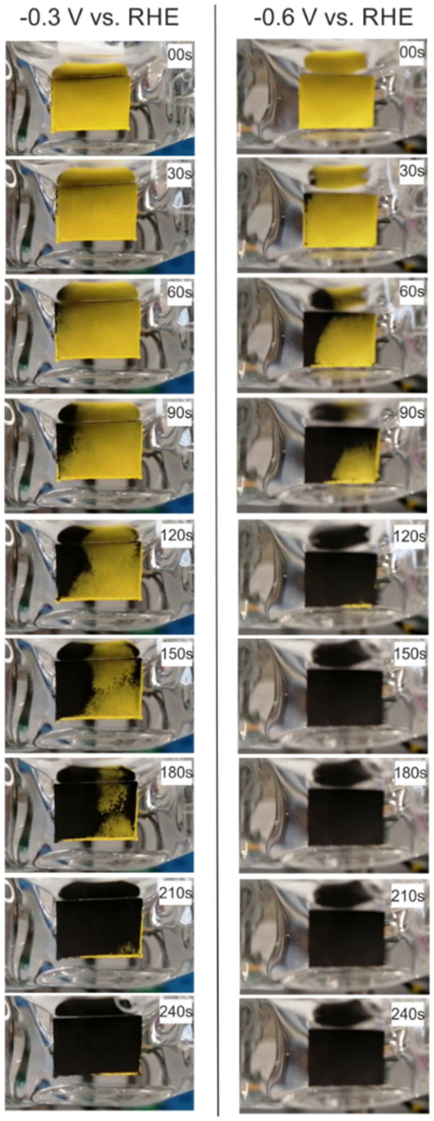

Figure 6. *Operando* optical inspection of the time-dependent (oxide → sub-carbonate/metal) transition in the CO_2-sat. 0.5 M $KHCO_3$ solution at low overpotentials.

ICP-MS Analysis of the Electrolyte during the CO_2RR. *Operando* Raman spectroscopy is sensitive to the compositional and structural alterations that the oxidic catalyst undergoes upon sub-carbonate formation and potential-induced oxide/sub-carbonate reduction. As known from the work by Mayrhofer et al.,[61−63] the electroreduction of oxidic species can lead to the release of metal ions into the electrolyte. Under the harsh cathodic conditions typically applied for the CO_2RR, these metal ions might be re-deposited on the catalyst surface during the ongoing CO_2 electrolysis reaction. To probe these effects, a series of potentiostatic electrolysis reactions was carried out in CO_2-saturated 0.5 M $KHCO_3$ solution using freshly prepared Bi_2O_3 foams as the catalysts. Aliquots of the bicarbonate electrolyte were analyzed by means of ICP-MS as a function of electrolysis time in the range of applied potentials between −0.3 and −1.8 V vs RHE. The results of this analysis are presented in Figure 7 and Table S2.

Clearly, the amount of Bi ions released into the electrolyte upon oxide reduction strongly depends on the applied electrolysis potential. Interestingly, we find the highest amount of Bi ions in the electrolyte at the lowest applied electrolysis potentials (−0.3 V vs RHE), reaching a maximum Bi content

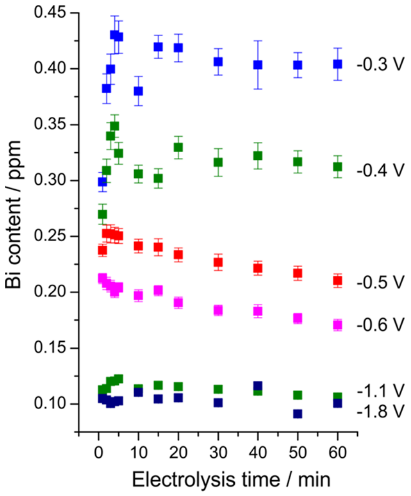

Figure 7. Time evolution of the Bi content in the CO_2-sat. 0.5 M $KHCO_3$ electrolyte solution under potentiostatic conditions determined by ICP-MS. The potentials applied during potentiostatic electrolysis are indicated in the graph. Freshly prepared Bi_2O_3 foams (20 s deposition time, annealing at 300 °C for 12 h in air) were used as the catalyst (single catalyst approach).

of 0.430 ppm after 4 min followed by a slow drop-down in concentration. In this potential regime, we observed the (partial) displacement of the oxidic bismuth species by the respective sub-carbonate (see Figures 4 and 5). Apparently, it is this oxide/sub-carbonate displacement at low overpotentials that provokes the massive release of Bi ions into the electrolyte, as observed by ICP-MS.

Note that, due to the CO_2 purging of the electrolyte during electrolysis, the released metal ions are homogeneously distributed in the electrolyte solution after their release from the electrode surface. A similar peak-like behavior in the Bi content evolution can be observed for the electrolyses at −0.4 and −0.5 V vs RHE, respectively. The maximum detected Bi content decreases to 0.100 ppm at −1.8 V vs RHE, suggesting that rapid oxide reduction and rapid metal ion deposition at the lowest potentials applied effectively prevented the massive release of Bi into the solution.

CO_2 Electrolysis. The results of the electrochemical catalyst performance testing, carried out in a broad potential range from −0.3 V down to −2.0 vs RHE, are presented in Figure 8a,b for the *ap* Bi/Bi_xO_y foam and the thermally annealed foam. In both cases, carbon cloths (GDE, Figure S1) served as the support material for the initial catalyst preparation. For comparison purposes, also the electrolysis results obtained for a planar Bi foil are presented (reference). Panel a in Figure 8 depicts the resulting CO_2RR product distribution in the form of a FE vs *E* plot (faradaic efficiency versus applied electrolysis potential), whereas in panel b, the corresponding partial current densities (PCDs) are considered. The only electrolysis products are gaseous hydrogen (H_2) and non-volatile formate. Within the entire potential range studied in this work, the faradaic efficiencies of formate and H_2 production sum up to ~100% (see Table S3). For the sake of clarity, in Figure 8, we present only the respective formate data.

In the FE vs *E* plot (panel a), the Bi foil shows a characteristic peak-like behavior in the product distribution with a maximum formate efficiency of $FE_{formate}$ = 55.0% ($PCD_{formate}$ = −2.92 mA cm^{-2}) at −0.8 V vs RHE. This is in agreement with the results recently reported by Zhang et al., using a sulfide-derived Bi catalyst.[64]

A significant improvement in the formate efficiency is achieved when using the foam-type Bi catalyst. Both *ap* Bi/Bi_xO_y and Bi_2O_3/*oc-d* Bi exhibit faradaic efficiencies of formate production that reach ~100% (Table S3). Quite intriguingly, this excellent product selectivity is observed not only within a narrow potential regime, as typical, e.g., for 2D systems like Bi foil, but within a rather broad range of applied electrolysis potentials ("plateau" regime), that is substantially broader in the case of the Bi_2O_3/*oc-d* Bi foam (~1100 mV) compared to the *ap* Bi/Bi_xO_y catalyst (~800 mV). Only marginal differences between both foam catalysts are noted for electrolysis potentials less than −0.9 V, whereas substantial differences in their product distributions appear at low overpotentials in the range from −0.3 to −0.7 V vs RHE. Under these electrolysis conditions, the product distribution of the *ap* Bi/Bi_xO_y foam better resembles the Bi foil with negligible formate production. It can safely be assumed that the metallic Bi foil is partly oxidized on its surface prior to the CO_2RR, thus rationalizing the qualitative similarity to the *ap* Bi/Bi_xO_y foam. However, a high level of formate efficiency is observed for the fully oxidized Bi_2O_3 foam catalyst, which also reaches almost 100% in this low-overpotential regime (Figure 8a and Table S3). This observation is indicative of the opening of a second reaction pathway of formate formation on the oxide/sub-carbonate/Bi_{met} composite at these low overpotentials that is not active on the *ap* Bi/Bi_xO_y catalyst. The thin surface oxide layer of the latter catalyst is obviously not sufficient to mimic the catalytic properties of the fully oxidized Bi foam in the electrochemical screening experiment at low overpotentials. The most prominent difference between the *ap* Bi/Bi_xO_y and the fully oxidized Bi_2O_3 foam concerns the capability of the Bi_2O_3 to adsorb/absorb dissolved CO_2 from the electrolyte phase,[65] giving rise to the appearance of prominent features in the Raman spectra assigned to sub-carbonate species (Figure 4d and Figure S20).

Based on the presented Raman data, it can be concluded that the near-surface oxide phase is partially converted into a mixed oxide/carbonate phase, even under non-reactive conditions, prior to the actual CO_2RR onset (Figure 4d). The Raman data further suggest a partial reduction of the mixed $(BiO)_2CO_3$-Bi_2O_3 at the CO_2RR onset (−0.4 V to −0.8 V vs RHE; Figure 4g) to metallic Bi, thus leading to a complex oxide/sub-carbonate/Bi_{met} composite on which the CO_2RR takes place in the low-overpotential regime. Figure 8d depicts the proposed "sub-carbonate" reaction pathway of formate production on the composite material assuming that the Bi oxide/carbonate species play an active role in the CO_2 conversion at these low overpotentials.[30] The overall reaction rates and the $PCD_{formate}$ remain at low levels within this low overpotential regime (Figure 8b and Table S4), also likely due to the limited conductivity of the oxide/sub-carbonate/Bi_{met} composite. Local pH changes at the catalyst/electrolyte interface as the driving force for the observed sub-carbonate formation at low overpotentials (Figures 4d−g and 5) can therefore be excluded due to the low overall reaction rates (Table S3) and in particular due to negligible faradaic efficiencies for hydrogen production at low overpotentials (Table S3).

It is the compositional transformation from the mixed oxide/carbonate composite to a fully metallic Bi state, evidenced by the *operando* Raman data (Figure 4), that allows

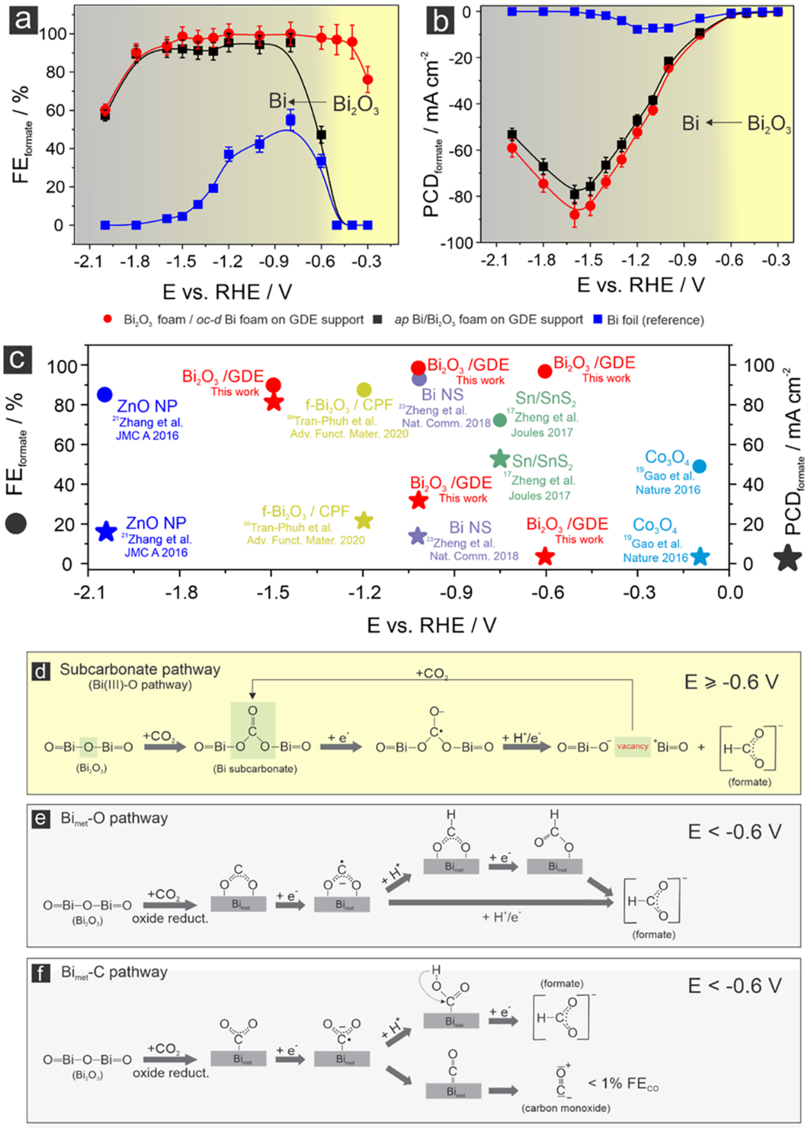

Figure 8. (a) CO_2RR product distribution represented as FE vs E plot (single catalyst approach); results of the Bi_2O_3/oc-d Bi foam are compared with the *ap* Bi/Bi_xO_y foam and a Bi foil catalyst (reference). (b) CO_2RR product distribution represented as $PCD_{formate}$ vs E plot; note that the potential-dependent product distributions shown in panels (a) and (b) are averaged over three individual electrolysis experiments per potential applied. (c) Performance overview for formate-producing CO_2RR catalysts (for detailed discussion in terms of long-term electrolysis, see text and Table 1). (d) Proposed CO_2RR mechanism at low overpotentials, $E \geq -0.6$ V vs RHE (Bi_2O_3 catalyst). (e) Dominant CO_2RR mechanism at high overpotentials, $E < -0.6$ V vs RHE (Bi_{met} catalyst; Bi_{met}−O pathway). (f) Alternative CO_2RR mechanism at high overpotentials (Bi_{met} catalyst; Bi_{met}−C pathway).

the partial current densities of formate production to substantially increase (Figure 8b). In the following, we denote the activated metallic Bi catalyst as “oxide/carbonate-derived” (*oc-d*). Note that the observed PCDs are systematically higher for the *oc-d* Bi foam compared to the *ap* Bi/Bi_xO_y (Figure 8b). This trend is due to the increased electrochemically active surface area (ECSA) after the reduction of the “bulk” oxide phases (see also Figure S24). Similar trends of increasing ECSA were reported for other oxide-derived CO_2RR catalysts, e.g., Cu-based materials.[35,44] Particularly noteworthy are the maximum PCDs of formate production for the *ap* Bi/Bi_xO_y and the *oc-d* Bi, reaching values of $PCD_{formate} = -75.8$ mA cm^{-2} and $PCD_{formate} = -84.1$ mA cm^{-2} at -1.5 V vs RHE, respectively. At potentials less than -1.5 V vs RHE, both the $FE_{formate}$ and $PCD_{formate}$ values decrease, and the HER becomes the dominant electrolysis process (see Table S4). This peak-like behavior in the CO_2RR efficiency plot is typically rationalized by the onset of CO_2 mass transport limitations appearing at elevated total reaction rates and high overpotentials as the CO_2 concentration is limited to only ∼35 mM in the aqueous electrolyte.[59] In contrast, the competing water splitting reaction (HER) does not become diffusion-limited.

It should be emphasized that both foam catalysts outperform other Bi-based electrocatalysts in terms of faradaic efficiency and with regard to the maximum partial current densities ($PCD_{formate}$) when considering classical half-cell measurements. Figures of merit for the Bi_2O_3 foam catalyst are presented in Figure 8c along with the performance data of recently reported benchmark catalysts for formate formation in the half-cell configuration, e.g., partially oxidized/ultrathin Co_3O_4,[18,19] Sn/SnS_2,[17] fractal-Bi_2O_3,[66] Au−Bi_2O_3[67] and ultrathin Bi-NS,[23] and ZnO.[21] Partial current densities of formate formation, higher than those reported herein, were only achieved when using gas/liquid flow electrolyzer systems.[68] In this context, Gong et al. have recently reported a $PCD_{formate}$ of −288 mA cm^{-2} using a high concentration of KOH in combination with an oxidic Bi double-wall nanotube catalyst.[69]

The most striking characteristic of the Bi_2O_3 foam catalyst, reported herein, is clearly the extraordinarily broad potential window of ∼1100 mV in which the faradaic efficiency of formate formation never falls below 90%. This unique feature is the direct result of the coupling of the two formate reaction pathways operative either on the oxidic catalyst ("sub-carbonate" pathway, low overpotentials, Figure 8d) or on its metallic form (Bi_{met}−O pathway; high overpotentials, Figure 8e). Note that, for the metallic Bi catalyst, also an alternative reaction pathway has also been proposed that involves Bi−C bond formation and the appearance of *COOH intermediates (Figure 8f).[29,70,71] However, in light of the high oxophilicity of Bi and the presented Raman data, proving Bi−O bond formation, we consider the Bi−O reaction pathway (Figure 8e) to be the dominant one at high overpotentials where the oxide/carbonates are fully reduced. This conclusion becomes further supported by the absence of significant amounts of CO as a CO_2RR byproduct (< 1%) that enables formate production through the Bi_{met}−O pathway.[29,70,71]

It should be noted that the choice of the support material (e.g., Cu foil or carbon fiber cloth) and related to the fact that differences in the macroporosity have only a marginal impact on the resulting product distribution (ratio of FE_{HE} and $FE_{formate}$, see Figure S5, Figure S25, Figure S26, Table S5, and Table S6). This is a major difference to other foam-type catalysts, e.g., copper-based systems, in which changes of the macroporosity lead to severe alterations in the respective CO_2RR product distribution. The latter effect was rationalized by Dutta et al.[35] by particular "trapping" phenomena of CO_2RR intermediates (e.g., CO or C_2H_4) inside the porous foam catalyst, thus facilitating the re-adsorption and further coupling and hydrogenation of trapped intermediates.[35] In the present case, there are no significant amount of electrolysis products observed other than formate and hydrogen. Morphology-induced "trapping" effects are therefore not relevant for the catalysts and reaction pathways discussed herein. The beneficial role of the porous foam structure remains restricted in the present case to the increase of the electrochemically active surface area (ECSA) and the resulting increased partial current densities whereas the reaction pathways remain unaltered.

Electrochemical Durability and Morphological (In)-Stability of the Bi_2O_3 Foam Catalyst. Not only are the resulting product distribution and the observed activity/product selectivity of importance for the overall catalyst performance evaluation but also the catalyst durability over more extended electrolysis times than typically applied in the standard catalyst screening approach (Figure 8). To demonstrate the excellent stability of the Bi_2O_3 foam catalyst, two extended potentiostatic electrolysis experiments were carried out under experimental conditions where either the "sub-carbonate" pathway (Figure 8d) or the Bi_{met}−O pathway (Figure 8e) was dominant at applied potentials of −0.6 V vs RHE and −1.0 V vs RHE, respectively.

The corresponding current vs time traces (Figure 9a) suggest quasi-steady-state conditions after passing an initial cathodic event indicating the partial or even complete reduction of the oxidic precursor. Due to the varying applied electrolysis potentials, also the resulting quasi-steady-state current densities are different and reach values of j_{mean} = −0.88 ± 0.2 mA cm^{-2} (−0.6 V vs RHE) and j_{mean} = −26.2 ± 2.1 mA cm^{-2} (−1.0 V vs RHE). However, a slight trend toward higher total current densities over time can be noted for both cases (see also discussion of the IL inspection below).

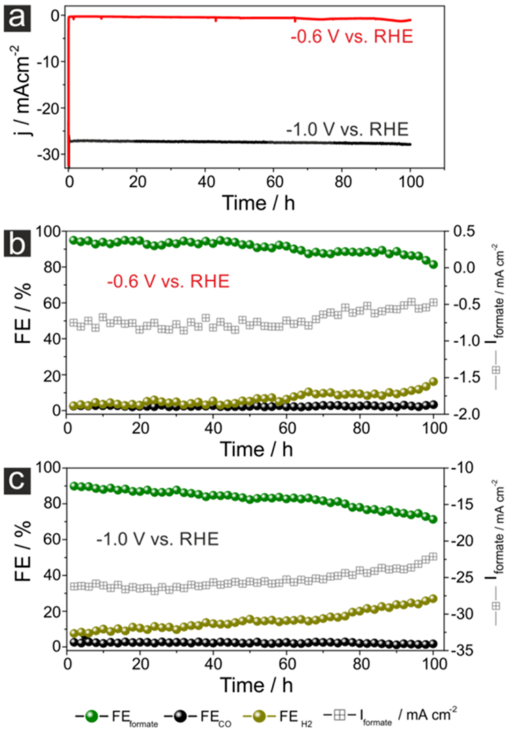

Figure 9. (a) Current transient curves representing the potentiostatic CO_2RR at −0.6 V and −1.0 V vs RHE, respectively. (b) FE/PCD vs *t* plot of the CO_2RR at −0.6 V vs RHE. (c) FE/PCD vs *t* plot of the CO_2RR at −1.0 V vs RHE. Bi_2O_3 foams (20 s deposition time, annealing at 300 °C for 12 h in air) were used as catalysts for the extended electrolysis experiments.

In particular, for the electrolysis at −0.6 V vs RHE (Figure 9b), the $FE_{formate}$ values decrease by only <10% within 100 h of electrolysis time (from an initial 97.3% to a final 89.1%), thus indicating the excellent stability of the mixed oxide/sub-carbonate/Bi_{met} composite catalyst (sub-carbonate pathway). Note that trends in the time-dependent FE_{H2} and $FE_{formate}$ changes are anti-correlated to each other.

More substantial is the catalyst degradation, however, when the electrolysis is carried out at −1.0 V vs RHE (Figure 9c). In this case, we observe a decrease from the initial $FE_{formate}$ = 91.7% to final $FE_{formate}$ = 79.1% after 100 h of electrolysis. Accordingly, the corresponding partial current density decreases from $j_{formate}$ = −28.67 mA cm^{-2} to a final $j_{formate}$ = −21.06 mA cm^{-2}. Table 1 summarizes the stability characteristics of various Bi catalysts. It demonstrates that the foams, presented in this work, reveal an excellent stability in the electrochemical electrolysis experiment over other Bi-based electrocatalysts.

Although the extended electrolysis experiments (Figure 9b) suggest reaching stable quasi-steady-state conditions, at least on the scale of a few hours, the Raman data have already indicated substantial compositional changes of the foam catalyst in particular in the initial phase of the CO_2RR. Under these conditions, the CO_2RR is obviously superimposed by a continued exchange of oxide by the carbonate (Figure 5).

Table 1. Comparison of Some Representative Studies Conducted in Recent Years for the Electrochemical Reduction of CO_2 to Formate or Formic Acid

catalysts	Pot. vs RHE (V)	partial current density$_{formate}$ (mA cm^{-2})	FEs of formate (%)	FEs (over extended electrolysis period of time in hour)	references
Bi_2O_3 NF @GDE	−0.60	−00.88	97.3	100 h (dropped to 91% after 80 h)	this work
Bi_2O_3 NF @GDE	−1.00	−26.11	91.7	100 h (dropped to 80% after 80 h)	this work
f-Bi_2O_3 @ CFP	−1.20	−24.0	87.0	16 h	Tran-Phu et al.[66]
Bi_2O_3NSs@ MCCM	−0.96	−05.58	77.3	12 h	Liu et al.[31]
ultra-thin Bi NS	−1.74	−24.00	89.8	10 h	Han et al.[23]
ultra-thin Bi NS	−1.10	−16.5	95.5	10 h	Zhang et al.[27]
ultra-thin Bi_2O_3 NS	−1.00	−12.3	95.1	05 h	Su et al.[24]
Bi nanostructure	−0.90	−13.33	92.3	30 h	Lu et al.[32]

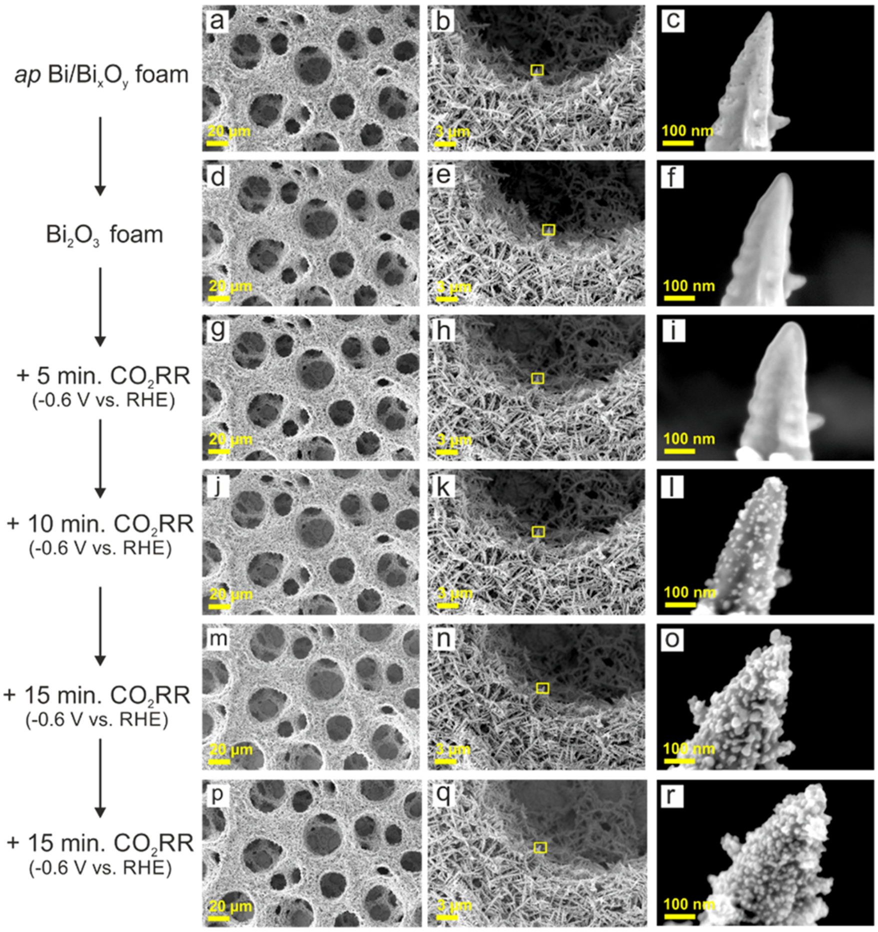

Figure 10. (a−r) Identical location (IL) SEM inspection of morphological changes associated to the thermal annealing of the *ap* Bi/Bi_xO_y foam and subsequent potentiostatic CO_2 electrolysis in the CO_2-sat. 0.5 M $KHCO_3$ solution at −0.6 V vs RHE.

These results prove that stable current vs time and the corresponding FE vs time traces (Figure 9) alone are not conclusive for monitoring the actual catalyst stability.

The *operando* Raman results are therefore further complemented by so-called identical location (IL) SEM investigations. Figure 10 displays the changes in the catalyst morphology due to the thermal annealing of the *ap* Bi/Bi_xO_y foam and, within the first 45 min of electrolysis, a time scale that is comparable to the Raman experiment shown in Figure 5. For this purpose, the CO_2RR was interrupted at defined electrolysis times (after 15, 30, and 45 min total electrolysis time) and then subjected to *ex situ* SEM inspection, focusing on the same spot on the catalyst surface.

On a larger µm length scale (panel a, d, g, j, m, and p), severe morphological alterations are neither observed for the thermal annealing nor for the electrolysis itself. Both the "primary" macropore structure and the dendritic nature of the pore sidewalls are clearly preserved even after 45 min of electrolysis at −0.6 V vs RHE.

Substantial changes occur, however, on the nanometer length scale, as evidenced by the SEM images shown in panels c, f, i, l, o, and r. One characteristic feature of these morphological changes under CO_2RR conditions is the appearance of smaller nanoparticles (<10 nm) on the surface of the dendrite. In addition, it seems that the apparent volume of the dendrite increases, which is indicative of increased porosity. Note that the ECSA is further increased upon oxide reduction. Nanoparticle growth and surface roughening effects are reported for the activation for foam-type and dendritic Cu catalysts by Cu_xO precursor reduction.[35,44] In the present case, a further process needs to be considered, which might also contribute to the nanoscale changes in the catalyst morphology. The *operando* Raman shows the continued embedment of CO_2 into the oxidic Bi_2O_3 precursor material (Figure 5), forming sub-carbonate species at the expense of oxidic Bi−O. Note that this process also involves an inward (CO_2) and outward (e.g., oxygen species) mass transport, which might further roughen the catalyst. These microscopic data support our working hypothesis that the observed sub-carbonate formation (Figure 5) is not restricted to the outermost surface of the oxidic precursor but also affects the near-surface bulk of the catalyst material.

The SEM image in Figure 10r represents the oxide/sub-carbonate/Bi_{met} composite (see also Figure 4g), which is considered the active catalyst in the low overpotential regime.

A similar IL-SEM analysis but comparing the initial oxidic catalyst morphology and the one after 100 h of electrolysis (Figure S27) confirm the morphological changes already observed on a shorter time scale, suggesting that the most severe changes occur in the initial stage of the CO_2RR (approximately the first hour).

CONCLUSIONS

By means of *operando* Raman spectroscopy combined with electrochemical performance testing, we have demonstrated that three-dimensional Bi_2O_3 foams, produced by an additive-assisted dynamic hydrogen bubble template approach and thermal annealing (12 h at 300 °C), show a "tandem" electrocatalytic activity toward formate formation. The (partly) oxidic Bi_2O_3 foam and the reduced metallic Bi_{met} foam reveal both a high selectivity toward formate, reaching faradaic efficiencies close of 100%. It is the porous nature of the foam catalyst in combination with the use of a carbon fiber cloth (GDE) as the support material that leads to a particularly high electrochemically active surface area and, accordingly, to excellent partial current densities $PCD_{formate}$ of approximately -90 mA cm^{-2} (normalized to the geometric surface area) in the CO_2 electrolysis. However, what makes this catalyst unique is the extraordinarily broad potential window of astonishing ~1100 mV in which the $FE_{formate}$ values do not fall below 90%. This was proven herein to be directly related to the coupling of two different formate reaction pathways, being operative either at low overpotentials (sub-carbonate pathway) and medium/high overpotentials (Bi_{met}−O pathway). For the first time, experimental evidence was provided to demonstrate the displacement of oxidic species by carbonate species, which is not only restricted to the outermost surface but further extends into the near surface bulk of the foam material. The formed sub-carbonate serves as the reactant in the course of the CO_2RR, at least at low overpotentials. The so-called identical location (IL) SEM inspection proves severe morphological alterations upon sub-carbonate formation and partial oxide-reduction during an ongoing CO_2RR at low overpotentials.

In our future studies, we will apply synchrotron-based *operando* X-ray absorption and X-ray diffraction techniques in combination with Raman spectroscopy to reveal in more detail the mechanism of sub-carbonate formation during the CO_2RR.

EXPERIMENTAL SECTION

Chemicals and Materials. For metal foaming the following support materials have been used: (i) a 20 cm × 20 cm carbon fiber cloth (gas diffusion electrode, GDE) was purchased from Fuel Cell (USA). This carbon fiber cloth is covered on both sides with an extra mesoporous carbon layer (C-MPL, see Figure S1) facilitating the adhesion of the electrodeposited metallic foam to the support. The total thickness of the carbon cloth is ~385 μm. The carbon fiber cloths were used as received. (ii) Cu foils were purchased from Alfa Aesar (thickness 0.25 mm, 200 × 200 mm, purity ≥99.95%) and subjected to an electropolishing treatment in ortho-phosphoric acid (50 w%, ACS grade, Sigma Aldrich) to remove the native oxide layer prior their use. A graphite foil thereby served as the counter (cathode) electrode and the Cu foil as the working electrode (anode). A constant potential difference of 2.0 V was applied between both electrodes for the duration of 2 min. (iii) Graphitic carbon foils were purchased from Alfa Aesar (0.25 mm thickness) and activated by annealing in air at 550 °C for 12 h in a tube furnace prior to the Bi electrodeposition.

Electrolyte Solutions. The standard plating bath for the Bi foam deposition was composed of 1.5 M H_2SO_4 (prepared from 96% H_2SO_4, ACS grade, Sigma-Aldrich) serving as the supporting electrolyte and 20 mM bismuth ammonium citrate ($C_{12}H_{22}BiN_3O_{14}$, Sigma Aldrich, purity ≥99.5%). The CO_2RR experiments were carried out in 0.5 M $KHCO_3$ (ACS grade, Sigma-Aldrich) electrolyte solutions saturated with CO_2 gas (99.999%, Carbagas, Switzerland). For blank experiments, the same electrolyte was saturated with inert Ar gas (99.999%, Carbagas, Switzerland). Ar saturated potassium hydroxide (KOH, ACS grade, Sigma Aldrich) is also used for performing blank experiments.

Electrochemical Experiments. The galvanostatic Bi foam deposition was carried out in a 100 mL glass beaker by applying a current density of $j = -3.0$ A cm^{-2} (referred to the geometric surface area of the support electrode). The three-electrode arrangement consisted of a leakless $Ag/AgCl_{3M}$ reference electrode (EDAQ), a bright Pt foil (15 mm × 5 mm) serving as the anode, and the support electrode (GDE, Cu foil, and C foil) as the cathode. The electrodeposition was performed in a face-to-face configuration (distance between the anode and cathode: 3.5 mm) similar to the Ag foam electrodeposition process described elsewhere.[34] Important to note is that the deposited Bi foam is thick enough to avoid any undesired contribution from the support material (carbon and copper) to the resulting CO_2RR product distribution (see discussion of Figure S26). All voltammetric and CO_2RR electrolysis experiments were carried out in a custom-built, air-tight glass-cell (H-type) described elsewhere.[35] Possible chloride ion cross-contaminations in the working electrolytes originating from the $Ag/AgCl_{3M}$ reference electrode were monitored and excluded by ion exchange (IC) chromatography (Metrohm). All potentials given herein are *iR*-corrected (~85% of the cell resistance). The cell resistance was determined by means of the current interrupt method (Autolab NOVA 2.1 software).

For comparison purposes, all potentials measured versus the $Ag/AgCl_{3M}$ reference are referenced to the reversible hydrogen electrode (RHE) and calculated according to

$$E_{\mathrm{RHE}}(\mathrm{V}) = E_{\mathrm{Ag/AgCl(3M)}}(\mathrm{V}) + 0.210\ \mathrm{V} + (0.059\ \mathrm{V} \times \mathrm{pH}) \quad (5)$$

A reversible redox probe (dimethyl viologen (DMV^{2+})) was used for the determination of the electrochemically active surface area (ECSA) by means of cyclic voltammetric (CV) measurements (Figure S24). Scan-rate dependent CVs were measured in an H-type glass cell containing aqueous 1 M Na_2SO_4 (ACS grade, Sigma-Aldrich) solution and 10 mM $DMVCl_2$ (Sigma-Aldrich). The ECSA was determined on the basis of the Randles− Ševčik equation according to

$$i_{\mathrm{p}} = 2.69 \times 10^5 n^{3/2} A c D^{1/2} \nu^{1/2} \quad (6)$$

with i_p representing the peak current, n is the number of transferred electrons (n = 1), c is the concentration of the redox-active DMV^{2+} species, D is the DMV^{2+} diffusion coefficient, and ν is the potential sweep rate. ^{1}H DOSY NMR measurements were carried to estimate the diffusion coefficient of dimethyl viologen ($D = 5.5 \times 10^{-10}\ \mathrm{m^2\ s^{-1}}$). We note that the Randles−Ševčik equation was originally derived for planar macroelectrodes (e.g., discs) and not for highly porous electrode materials. The ECSA was derived from the linear regression of the respective i_p vs $\nu^{1/2}$ plots with A (ECSA) serving as a free fit parameter (see discussion of Figure S24 in the Supporting Information).

Annealing Treatment. Electrodeposited Bi metal foams were further activated by thermal annealing in air at 300 °C for 12 h using a tube furnace (GERO Hochtemperaturofen GmbH, Germany).

Structural and Compositional Characterization. *X-ray Diffraction (XRD) Analysis.* STOE Stadi system with a Cu Kα radiation source (λ = 0.1540 nm, 40 mA) operated at 40 keV was used for XRD analysis. Diffractograms were recorded in reflection mode (Bragg−Brentano geometry) in steps of 1° $\mathrm{min^{-1}}$ with 2θ values ranging from 0 to 90°. For the XRD analysis of the Bi foams, a carbon foil substrate was used. The obtained XRD patterns were analyzed and compared to JCPDS (Joint Committee on Powder Diffraction standards) data of polycrystalline Bi and Bi_2O_3 (file nos. 44-1246 and 41-1449).

Elemental Analysis. Elemental analysis of the electrolytes after the electrolysis was carried out by means of inductively coupled plasma mass spectrometry (ICP-MS, Perkin Elmer NexION 2000 instrument). For the ICP-MS analysis, aliquots of 20 μL of electrolyte (CO_2-sat. 0.5 M $KHCO_3$ solution) were diluted in 3% nitric acid solutions (501 times dilution). Each ICP-measurement was repeated four times by default; these repetitive measurements served as the basis for the determination of the sample-specific values of the relative standard deviation (RSD). ICP-MS-related RSD values are typically between 1 and 2%. An extra measuring error of ca. 1.5% needs to be taken into account and is due to the dilution treatment required for certain samples. Error bars in Figure 7 include both the instrumental error (ICP-MS) and the additional error resulting from the dilution procedure.

X-ray Photoelectron Spectroscopy (XPS). XPS measurements were carried out using a PHI VersaProbeII scanning XPS micro-probe (Physical Instruments AG, Germany) equipped with a monochromatic Al Kα X-ray source operated at 24.8 W with a spot size of 100 μm. The spherical capacitor analyzer was set at 45° take-off angle with respect to the sample surface. The pass energy was 46.95 eV. Peak positions were referenced to the carbon C1s peak at 285.5 eV. The curve fitting was performed using the Casa-XPS software.

SEM, EDX, and TEM. The morphology of the alloy foams was characterized by means of scanning electron microscopy (SEM) and energy-dispersive X-ray spectroscopy (EDX) using a Hitachi S-3000 N scanning electron microscope and a Noran SIX NSS200 energy-dispersive X-ray spectrometer. For the high-resolution (HR) identical location (IL) SEM imaging, a Zeiss DSM 982 instrument was used. For HR-TEM imaging, a FEI Tecnai G^2 F20 instrument equipped with a thermal (Schottky) field-emission source was used and operated at a 200 kV accelerating voltage. The microscope objective lens was a FEI Tecnai "Twin" lens type. A spherical aberration coefficient of Cs = 2.2 mm permitted a point resolution of 2.7 Å and a line resolution of 1.44 Å. The images were taken on a CETA CCD camera.

White Light Interferometry Analysis. The mesoscopic surface morphology of the foam electrodes was analyzed by means of white light interferometry (Contour GT, Bruker). Vision64 software (Bruker) was used for operating the instrument and the data analysis.

Quantification of Gaseous Electrolysis Products. During electrolysis, CO_2 was continuously purged through the catholyte at a flow rate of 13 mL $\mathrm{min^{-1}}$. The headspace of the electrolysis cell was directly connected to the gas sampling loop of the gas chromatograph (GC 8610C, SRI Instruments). GC measurements were conducted in intervals of 20 min. The GC was equipped with both (i) a packed Hayesep D column and (ii) a packed Molesieve 5A column. Argon (99.9999%, Carba Gas) was used as the carrier gas. A thermal conductivity detector (TCD) was applied for the quantification of the formed H_2. Partial current (I_i) of each gaseous product, formed during the electrochemical CO_2 reduction, was determined according to

$$I_i = \frac{c_i \cdot \nu \cdot F \cdot z}{10^6 \cdot V_{\mathrm{m}}} \quad (7)$$

where I_i is the partial current for a given product i, c_i refers to the amount of product in ppm, z represents the number of electrons transferred during the electron transfer reaction, F is the Faraday constant in C $\mathrm{mol^{-1}}$, ν is the flow rate in L $\mathrm{s^{-1}}$, and V_m represents the molar volume of gas at 1 atm and room temperature in L $\mathrm{mol^{-1}}$.

The faradaic efficiency (FE) for a given gaseous product was calculated by dividing its partial current density by the total current density (I_{total}), derived from the respective current vs time traces.

$$\mathrm{FE} = \frac{I_i}{I_{\mathrm{total}}} \cdot 100\% \quad (8)$$

Quantification of Liquid Products. In order to determine the yield of the non-volatile products (formate), aliquots were taken from the known volume of the catholyte after (see, e.g., Figures 8a and 8b) or during the electrolysis (see, e.g., Figure 9). The concentration of the liquid product was determined by an ion exchange chromatograph (Metrohm 940 Professional IC Vario) equipped with a Metrosep A Supp 7 column and controlled by the MagicNet 3.1 software. A 3 mM Na_2CO_3/0.1 M H_2SO_4 solution served as the eluent and suppressor, respectively. The instrument was calibrated by injecting known std. concentrations in the range from 2 to 10 ppm formate solution (see Figure S28). The standard solution was prepared by dilution of 1000 ppm ICstd. solution (Sigma Aldrich). The electrolysis samples were diluted 20 times by the eluent prior to the analysis in order to reduce solvent effects by the bicarbonate solution.

The faradaic efficiency for the non-volatile products was derived on the basis of the integrated partial (Q_i) and total charges (Q_{total}) of the electrolysis reaction according to

$$Q_i = \frac{V_{\text{cath}} \cdot F \cdot z}{10^3 \cdot M} \cdot c_i \tag{9}$$

$$\text{FE} = \frac{Q_i}{Q_{\text{total}}} \cdot 100\% \tag{10}$$

where Q_i is the partial charge involved for the formation of a certain product i, V_{cath} is the total volume of the catholyte in L, c_i is the amount of the product i in ppm, M refers to the molar mass of the product, F is the Faraday constant, and z is the number of electron transferred to form the product. Q_{total} is the total charge transferred during the electrolysis experiment (see Figure S29).

Note that, for all potential-dependent CO_2RR experiments, a single catalyst approach was used (e.g., Figures 7, 8a, and 8b). A freshly prepared catalyst was used for each electrolysis experiment.

***Operando* Raman Spectroscopy.** Raman spectroscopic analyses were conducted using a LabRAM HR800 confocal microscope (Horiba Jobin Yvon). Spectral data were collected with the Raman spectrometer coupled to a confocal microscope (Horiba Jobin Yvon) and operated by the Lab Space 3.0 software. The calibration was carried out using a silicon wafer standard (520.6 cm^{-1}). A large working distance objective lens (50 × magnification, 8 mm focal length) has been applied with a numerical aperture of 0.1 in order to focus a diode-pumped solid-state (DPSS) laser beam (excitation wavelength of 532 nm; laser power of 3 mW for standard Raman measurements) on the sample and to collect both the incident and scattered laser light. For comparison purposes, also a He-Ne laser (excitation wave length of 633 nm) was used (see Figure S13).

A home-made spectro-electrochemical cell made of Kel-F was used for spectroscopic analysis.[46] The spectro-electrochemical cell consisted of a Ag/AgCl reference (EDAQ) electrode and an Au wire and the Bi foam (*ap* Bi/Bi_xO_y or Bi_2O_3) as the counter and working electrode, respectively.

A μ-Autolab III (EcoChemie) potentiostat was used for the electrochemical Raman measurements. The ohmic resistances of about 17 Ω were determined by the current interrupt method and compensated (~85%) during the measurement via GPES 4.0 software. Unless otherwise stated, Raman spectra were collected in the spectral range from 100 to 1200 cm^{-1} at a 3 mW laser power and an excitation wavelength of 532 nm (DPSS laser). For the data acquisition in the potentiostatic experiments (Figure 4c–g), the holding time was 180 s at each applied electrolysis potential. The actual Raman spectroscopic measurements were started only after 2 min holding the potential in order to reach (quasi) steady-state conditions after the potential step (see also discussion of Figure 5). To improve the signal-to-noise ratio, 10 individual spectra (10 s recording time each) were recorded at a given potential, averaged, and displayed (e.g., in Figures 4c and 4d). Time-resolved Raman spectroscopy experiments under OCP conditions were performed with an interval time of ca. 90 s (e.g., in Figure 4b and Figure S16). For the data acquisition, 10 spectra were recorded (10 s recording time each), averaged, and displayed (e.g. in Figure 4b).

All Raman spectra were baseline corrected in the Lab Space 3.0 software using a polynomial fit function. The normalization of the integrated peak intensities (Figure 4g and Figure S18) was carried out using the integrated intensity data at the OCP as the reference point.

■ ASSOCIATED CONTENT

Supporting Information

The Supporting Information is available free of charge at https://pubs.acs.org/doi/10.1021/acscatal.0c05317.

SEM images, reference measurements on the optimization of the Raman experiment in terms of laser light source and laser power, quantitative analysis of this (oxide/sub-carbonate → metal) transition, and additional supporting results and discussion (PDF)

Corresponding media file of Figure S9 (MP4)

■ AUTHOR INFORMATION

Corresponding Authors

Abhijit Dutta – *Department of Chemistry and Biochemistry, University of Bern, Bern 3012, Switzerland;* orcid.org/0000-0002-3054-0492; Email: abhijit.dutta@dcb.unibe.ch

Peter Broekmann – *Department of Chemistry and Biochemistry, University of Bern, Bern 3012, Switzerland;* orcid.org/0000-0002-6287-1042; Email: peter.broekmann@dcb.unibe.ch

Authors

Iván Zelocualtecatl Montiel – *Department of Chemistry and Biochemistry, University of Bern, Bern 3012, Switzerland*

Kiran Kiran – *Department of Chemistry and Biochemistry, University of Bern, Bern 3012, Switzerland*

Alain Rieder – *Department of Chemistry and Biochemistry, University of Bern, Bern 3012, Switzerland*

Vitali Grozovski – *Department of Chemistry and Biochemistry, University of Bern, Bern 3012, Switzerland*

Lukas Gut – *Department of Chemistry and Biochemistry, University of Bern, Bern 3012, Switzerland*

Complete contact information is available at: https://pubs.acs.org/10.1021/acscatal.0c05317

Notes

The authors declare no competing financial interest.

■ ACKNOWLEDGMENTS

The financial support by the CTI Swiss Competence Centre for Energy Research (SCCER Heat and Electricity Storage) is gratefully acknowledged. P.B. acknowledges the financial support by the Swiss National Science Foundation (SNSF) via the project no. 200020_172507.

■ REFERENCES

(1) Wang, W.-H.; Himeda, Y.; Muckerman, J. T.; Manbeck, G. F.; Fujita, E. CO_2 Hydrogenation to Formate and Methanol as an Alternative to Photo- and Electrochemical CO_2 Reduction. *Chem. Rev.* **2015**, *115*, 12936–12973.

(2) Karl, T. R.; Trenberth, K. E. Modern Global Climate Change. *Science* **2003**, *302*, 1719.

(3) Gurudayal; Bullock, J.; Srankó, D. F.; Towle, C. M.; Lum, Y.; Hettick, M.; Scott, M. C.; Javey, A.; Ager, J. Efficient solar-driven electrochemical CO_2 reduction to hydrocarbons and oxygenates. *Energy Environ. Sci.* **2017**, *10*, 2222–2230.

(4) Peterson, A. A.; Abild-Pedersen, F.; Studt, F.; Rossmeisl, J.; Nørskov, J. K. How copper catalyzes the electroreduction of carbon dioxide into hydrocarbon fuels. *Energy Environ. Sci.* **2010**, *3*, 1311−1315.

(5) Rahaman, M.; Dutta, A.; Broekmann, P. Size-Dependent Activity of Palladium Nanoparticles: Efficient Conversion of CO_2 into Formate at Low Overpotentials. *ChemSusChem* **2017**, *10*, 1733−1741.

(6) Daggash, H. A.; Patzschke, C. F.; Heuberger, C. F.; Zhu, L.; Hellgardt, K.; Fennell, P. S.; Bhave, A. N.; Bardow, A.; Mac Dowell, N. Closing the carbon cycle to maximise climate change mitigation: power-to-methanol vs. power-to-direct air capture. *Sustain. Energy Fuels* **2018**, *2*, 1153−1169.

(7) Seh, Z. W.; Kibsgaard, J.; Dickens, C. F.; Chorkendorff, I.; Nørskov, J. K.; Jaramillo, T. F. Combining theory and experiment in electrocatalysis: Insights into materials design. *Science* **2017**, *355*, No. eaad4998.

(8) García de Arquer, F. P.; Dinh, C.-T.; Ozden, A.; Wicks, J.; McCallum, C.; Kirmani, A. R.; Nam, D.-H.; Gabardo, C.; Seifitokaldani, A.; Wang, X.; Li, Y. C.; Li, F.; Edwards, J.; Richter, L. J.; Thorpe, S. J.; Sinton, D.; Sargent, E. H. CO_2 electrolysis to multicarbon products at activities greater than 1 A cm^{-2}. *Science* **2020**, *367*, 661.

(9) Liu, C.; Colón, B. C.; Ziesack, M.; Silver, P. A.; Nocera, D. G. Water splitting−biosynthetic system with CO_2 reduction efficiencies exceeding photosynthesis. *Science* **2016**, *352*, 1210.

(10) Pan, F.; Yang, Y. Designing CO_2 reduction electrode materials by morphology and interface engineering. *Energy Environ. Sci.* **2020**, 2275.

(11) Qiao, J.; Liu, Y.; Hong, F.; Zhang, J. A review of catalysts for the electroreduction of carbon dioxide to produce low-carbon fuels. *Chem. Soc. Rev.* **2014**, *43*, 631−675.

(12) Azuma, M.; Hashimoto, K.; Hiramoto, M.; Watanabe, M.; Sakata, T. Electrochemical Reduction of Carbon Dioxide on Various Metal Electrodes in Low-Temperature Aqueous $KHCO_3$ Media. *J. Electrochem. Soc.* **1990**, *137*, 1772−1778.

(13) Hori, Y.; Kikuchi, K.; Suzuki, S. Production of CO and CH_4 in electrochemical reduction of CO_2 at metal electrodes in aqueous hydrogencarbonate solution. *Chem. Lett.* **1985**, *14*, 1695−1698.

(14) Hori, Y.; Wakebe, H.; Tsukamoto, T.; Koga, O. Electrocatalytic process of CO selectivity in electrochemical reduction of CO_2 at metal electrodes in aqueous media. *Electrochim. Acta* **1994**, *39*, 1833−1839.

(15) Chai, G.-L.; Guo, Z.-X. Highly effective sites and selectivity of nitrogen-doped graphene/CNT catalysts for CO_2 electrochemical reduction. *Chem. Sci.* **2016**, *7*, 1268−1275.

(16) Sun, Z.; Ma, T.; Tao, H.; Fan, Q.; Han, B. Fundamentals and Challenges of Electrochemical CO_2 Reduction Using Two-Dimensional Materials. *Chem* **2017**, *3*, 560−587.

(17) Zheng, X.; De Luna, P.; García de Arquer, F. P.; Zhang, B.; Becknell, N.; Ross, M. B.; Li, Y.; Banis, M. N.; Li, Y.; Liu, M.; Voznyy, O.; Dinh, C. T.; Zhuang, T.; Stadler, P.; Cui, Y.; Du, X.; Yang, P.; Sargent, E. H. Sulfur-Modulated Tin Sites Enable Highly Selective Electrochemical Reduction of CO_2 to Formate. *Joule* **2017**, *1*, 794−805.

(18) Gao, S.; Jiao, X.; Sun, Z.; Zhang, W.; Sun, Y.; Wang, C.; Hu, Q.; Zu, X.; Yang, F.; Yang, S.; Liang, L.; Wu, J.; Xie, Y. Ultrathin Co_3O_4 Layers Realizing Optimized CO_2 Electroreduction to Formate. *Angew. Chem., Int. Ed.* **2015**, *128*, 708−712.

(19) Gao, S.; Lin, Y.; Jiao, X.; Sun, Y.; Luo, Q.; Zhang, W.; Li, D.; Yang, J.; Xie, Y. Partially oxidized atomic cobalt layers for carbon dioxide electroreduction to liquid fuel. *Nature* **2016**, *529*, 68.

(20) Fu, Y.; Li, Y.; Zhang, X.; Liu, Y.; Qiao, J.; Zhang, J.; Wilkinson, D. P. Novel hierarchical SnO_2 microsphere catalyst coated on gas diffusion electrode for enhancing energy efficiency of CO_2 reduction to formate fuel. *Appl. Energy* **2016**, *175*, 536−544.

(21) Zhang, T.; Zhong, H.; Qiu, Y.; Li, X.; Zhang, H. Zn electrode with a layer of nanoparticles for selective electroreduction of CO_2 to formate in aqueous solutions. *J. Mater. Chem. A* **2016**, *4*, 16670−16676.

(22) Zha, B.; Li, C.; Li, J. Efficient electrochemical reduction of CO_2 into formate and acetate in polyoxometalate catholyte with indium catalyst. *J. Catal.* **2020**, *382*, 69−76.

(23) Han, N.; Wang, Y.; Yang, H.; Deng, J.; Wu, J.; Li, Y.; Li, Y. Ultrathin bismuth nanosheets from in situ topotactic transformation for selective electrocatalytic CO_2 reduction to formate. *Nat. Commun.* **2018**, *9*, 1320.

(24) Su, P.; Xu, W.; Qiu, Y.; Zhang, T.; Li, X.; Zhang, H. Ultrathin Bismuth Nanosheets as a Highly Efficient CO_2 Reduction Electrocatalyst. *ChemSusChem* **2018**, *11*, 848−853.

(25) Zhang, H.; Ma, Y.; Quan, F.; Huang, J.; Jia, F.; Zhang, L. Selective electro-reduction of CO_2 to formate on nanostructured Bi from reduction of BiOCl nanosheets. *Electrochem. Commun.* **2014**, *46*, 63−66.

(26) Rudnev, A. V.; Kiran, K.; Broekmann, P. Specific Cation Adsorption: Exploring Synergistic Effects on CO_2 Electroreduction in Ionic Liquids. *ChemElectroChem* **2020**, *7*, 1897−1903.

(27) Zhang, W.; Hu, Y.; Ma, L.; Zhu, G.; Zhao, P.; Xue, X.; Chen, R.; Yang, S.; Ma, J.; Liu, J.; Jin, Z. Liquid-phase exfoliated ultrathin Bi nanosheets: Uncovering the origins of enhanced electrocatalytic CO_2 reduction on two-dimensional metal nanostructure. *Nano Energy* **2018**, *53*, 808−816.

(28) Yang, F.; Elnabawy, A. O.; Schimmenti, R.; Song, P.; Wang, J.; Peng, Z.; Yao, S.; Deng, R.; Song, S.; Lin, Y.; Mavrikakis, M.; Xu, W. Bismuthene for highly efficient carbon dioxide electroreduction reaction. *Nat. Commun.* **2020**, *11*, 1088.

(29) Koh, J. H.; Won, D. H.; Eom, T.; Kim, N.-K.; Jung, K. D.; Kim, H.; Hwang, Y. J.; Min, B. K. Facile CO_2 Electro-Reduction to Formate via Oxygen Bidentate Intermediate Stabilized by High-Index Planes of Bi Dendrite Catalyst. *ACS Catal.* **2017**, *7*, 5071−5077.

(30) Zhang, Y.; Zhang, X.; Ling, Y.; Li, F.; Bond, A. M.; Zhang, J. Controllable Synthesis of Few-Layer Bismuth Subcarbonate by Electrochemical Exfoliation for Enhanced CO_2 Reduction Performance. *Angew. Chem., Int. Ed.* **2018**, *57*, 13283−13287.

(31) Liu, S.; Lu, X. F.; Xiao, J.; Wang, X.; Lou, X. W. Bi_2O_3 Nanosheets Grown on Multi-Channel Carbon Matrix to Catalyze Efficient CO_2 Electroreduction to HCOOH. *Angew. Chem., Int. Ed.* **2019**, *58*, 13828−13833.

(32) Lu, P.; Gao, D.; He, H.; Wang, Q.; Liu, Z.; Dipazir, S.; Yuan, M.; Zu, W.; Zhang, G. Facile synthesis of a bismuth nanostructure with enhanced selectivity for electrochemical conversion of CO_2 to formate. *Nanoscale* **2019**, *11*, 7805−7812.

(33) Li, L.; Ma, D.-K.; Qi, F.; Chen, W.; Huang, S. Bi nanoparticles/Bi_2O_3 nanosheets with abundant grain boundaries for efficient electrocatalytic CO_2 reduction. *Electrochim. Acta* **2019**, *298*, 580−586.

(34) Dutta, A.; Morstein, C. E.; Rahaman, M.; Cedeño López, A.; Broekmann, P. Beyond Copper in CO_2 Electrolysis: Effective Hydrocarbon Production on Silver-Nanofoam Catalysts. *ACS Catal.* **2018**, *8*, 8357−8368.

(35) Dutta, A.; Rahaman, M.; Luedi, N. C.; Mohos, M.; Broekmann, P. Morphology Matters: Tuning the Product Distribution of CO_2 Electroreduction on Oxide-Derived Cu Foam Catalysts. *ACS Catal.* **2016**, *6*, 3804−3814.

(36) Dutta, A.; Kuzume, A.; Kaliginedi, V.; Rahaman, M.; Sinev, I.; Ahmadi, M.; Roldán Cuenya, B.; Vesztergom, S.; Broekmann, P. Probing the chemical state of tin oxide NP catalysts during CO_2 electroreduction: A complementary operando approach. *Nano Energy* **2018**, *53*, 828−840.

(37) Dutta, A.; Kuzume, A.; Rahaman, M.; Vesztergom, S.; Broekmann, P. Monitoring the Chemical State of Catalysts for CO_2 Electroreduction: An In Operando Study. *ACS Catal.* **2015**, *5*, 7498−7502.

(38) Plowman, B. J.; Jones, L. A.; Bhargava, S. K. Building with bubbles: the formation of high surface area honeycomb-like films via hydrogen bubble templated electrodeposition. *Chem. Commun.* **2015**, *51*, 4331−4346.

(39) Gálvez-Vázquez, M. D. J.; Grozovski, V.; Kovács, N.; Broekmann, P.; Vesztergom, S. Full Model for the Two-Step

Polarization Curves of Hydrogen Evolution, Measured on RDEs in Dilute Acid Solutions. *J. Phys. Chem. C* **2020**, *124*, 3988−4000.

(40) Asato, E.; Katsura, K.; Mikuriya, M.; Turpeinen, U.; Mutikainen, I.; Reedijk, J. Synthesis, Structure, and Spectroscopic Properties of Bismuth Citrate Compounds and the Bismuth-Containing Ulcer-Healing Agent Colloidal Bismuth Subcitrate (CBS). 4. Crystal Structure and Solution Behavior of a Unique Dodecanuclear Cluster $(NH_4)_{12}[Bi_{12}O_8(cit)_8](H_2O)_{10}$. *Inorg. Chem.* **1995**, *34*, 2447−2454.

(41) Vesztergom, S.; Dutta, A.; Rahaman, M.; Kiran, K.; Zelocualtecatl Montiel, I.; Broekmann, P. Hydrogen Bubble Templated Metal Foams as Efficient Catalysts of CO_2 Electroreduction. *ChemCatChem* **2021**, *13*, 1039−1058.

(42) Dutta, A.; Rahaman, M.; Mohos, M.; Zanetti, A.; Broekmann, P. Electrochemical CO_2 Conversion Using Skeleton (Sponge) Type of Cu Catalysts. *ACS Catal.* **2017**, *7*, 5431−5437.

(43) Zhang, H.; Ye, Y.; Shen, R.; Ru, C.; Hu, Y. Effect of Bubble Behavior on the Morphology of Foamed Porous Copper Prepared via Electrodeposition. *J. Electrochem. Soc.* **2013**, *160*, D441−D445.

(44) Sen, S.; Liu, D.; Palmore, G. T. R. Electrochemical Reduction of CO_2 at Copper Nanofoams. *ACS Catal.* **2014**, *4*, 3091−3095.

(45) Shin, H.-C.; Liu, M. Copper Foam Structures with Highly Porous Nanostructured Walls. *Chem. Mater.* **2004**, *16*, 5460−5464.

(46) Dutta, A.; Montiel, I. Z.; Erni, R.; Kiran, K.; Rahaman, M.; Drnec, J.; Broekmann, P. Activation of bimetallic AgCu foam electrocatalysts for ethanol formation from CO_2 by selective Cu oxidation/reduction. *Nano Energy* **2020**, *68*, 104331.

(47) Harwig, H. A. On the Structure of Bismuthsesquioxide: The α, β, γ, and δ-phase. *Z. Anorg. Allg. Chem.* **1978**, *444*, 151−166.

(48) Kumar, P.; Singh, J.; Pandey, A. C. Rational low temperature synthesis and structural investigations of ultrathin bismuth nanosheets. *RSC Adv.* **2013**, *3*, 2313−2317.

(49) Pereira, A. L. J.; Errandonea, D.; Beltrán, A.; Gracia, L.; Gomis, O.; Sans, J. A.; García-Domene, B.; Miquel-Veyrat, A.; Manjón, F. J.; Muñoz, A.; Popescu, C. Structural study of α-Bi_2O_3 under pressure. *J. Phys.: Condens. Matter* **2013**, *25*, 475402.

(50) Jiang, S.; Klingan, K.; Pasquini, C.; Dau, H. New aspects of operando Raman spectroscopy applied to electrochemical CO_2 reduction on Cu foams. *J. Chem. Phys.* **2018**, *150*, No. 041718.

(51) Dutta, A.; Rahaman, M.; Hecker, B.; Drnec, J.; Kiran, K.; Zelocualtecatl Montiel, I.; Jochen Weber, D.; Zanetti, A.; Cedeño López, A.; Martens, I.; Broekmann, P.; Oezaslan, M. CO_2 electrolysis – Complementary operando XRD, XAS and Raman spectroscopy study on the stability of Cu_xO foam catalysts. *J. Catal.* **2020**, *389*, 592−603.

(52) Denisov, V. N.; Ivlev, A. N.; Lipin, A. S.; Mavrin, B. N.; Orlov, V. G. Raman spectra and lattice dynamics of single-crystal. *J. Phys.: Condens. Matter* **1997**, *9*, 4967−4978.

(53) Betsch, R. J.; White, W. B. Vibrational spectra of bismuth oxide and the sillenite-structure bismuth oxide derivatives. *Spectrochim. Acta, Part A* **1978**, *34*, 505−514.

(54) Schröder, F.; Bagdassarov, N.; Ritter, F.; Bayarjargal, L. Temperature dependence of Bi_2O_3 structural parameters close to the α−δ phase transition. *Phase Transitions* **2010**, *83*, 311−325.

(55) Ho, C.-H.; Chan, C.-H.; Huang, Y.-S.; Tien, L.-C.; Chao, L.-C. The study of optical band edge property of bismuth oxide nanowires α-Bi_2O_3. *Opt. Express* **2013**, *21*, 11965−11972.

(56) Steele, J. A.; Lewis, R. A. In situ micro-Raman studies of laser-induced bismuth oxidation reveals metastability of β-Bi_2O_3 microislands. *Opt. Mater. Express* **2014**, *4*, 2133−2142.

(57) Ibl, N. Atlas d'équilibres électrochimiques à 25 °C. Von M. Pourbaix, unter Mitwirkung zahlreicher Fachgelehrter. Verlag: Gauthier-Villars & Cie., Paris 1963. 1. Aufl., 644 S., zahlr. Abb., geb. NF 140.—. *Angew. Chem., Int. Ed.* **1964**, *76*, 444−444.

(58) Taylor, P.; Sunder, S.; Lopata, V. J. Structure, spectra, and stability of solid bismuth carbonates. *Can. J. Chem.* **1984**, *62*, 2863−2873.

(59) Wiebe, R.; Gaddy, V. L. The Solubility of Carbon Dioxide in Water at Various Temperatures from 12 to 40° and at Pressures to 500 Atmospheres. Critical Phenomena*. *J. Am. Chem. Soc.* **1940**, *62*, 815−817.

(60) Deng, P.; Wang, H.; Qi, R.; Zhu, J.; Chen, S.; Yang, F.; Zhou, L.; Qi, K.; Liu, H.; Xia, B. Y. Bismuth Oxides with Enhanced Bismuth−Oxygen Structure for Efficient Electrochemical Reduction of Carbon Dioxide to Formate. *ACS Catal.* **2020**, *10*, 743−750.

(61) Cherevko, S.; Reier, T.; Zeradjanin, A. R.; Pawolek, Z.; Strasser, P.; Mayrhofer, K. J. J. Stability of nanostructured iridium oxide electrocatalysts during oxygen evolution reaction in acidic environment. *Electrochem. Commun.* **2014**, *48*, 81−85.

(62) Cherevko, S.; Mayrhofer, K. J. J., On-Line Inductively Coupled Plasma Spectrometry in Electrochemistry: Basic Principles and Applications. In *Encyclopedia of Interfacial Chemistry*; Wandelt, K., Ed. Elsevier: Oxford, 2018; pp. 326−335, DOI: 10.1016/B978-0-12-409547-2.13292-5.

(63) Löffler, M.; Khanipour, P.; Kulyk, N.; Mayrhofer, K. J. J.; Katsounaros, I. Insights into Liquid Product Formation during Carbon Dioxide Reduction on Copper and Oxide-Derived Copper from Quantitative Real-Time Measurements. *ACS Catal.* **2020**, *10*, 6735−6740.

(64) Zhang, Y.; Li, F.; Zhang, X.; Williams, T.; Easton, C. D.; Bond, A. M.; Zhang, J. Electrochemical reduction of CO_2 on defect-rich Bi derived from Bi_2S_3 with enhanced formate selectivity. *J. Mater. Chem. A* **2018**, *6*, 4714−4720.

(65) Ortiz-Quiñonez, J. L.; Vega-Verduga, C.; Díaz, D.; Zumeta-Dubé, I. Transformation of Bismuth and β-Bi_2O_3 Nanoparticles into $(BiO)_2CO_3$ and $(BiO)_4(OH)_2CO_3$ by Capturing CO_2: The Role of Halloysite Nanotubes and "Sunlight" on the Crystal Shape and Size. *Cryst. Growth Des.* **2018**, *18*, 4334−4346.

(66) Tran-Phu, T.; Daiyan, R.; Fusco, Z.; Ma, Z.; Amal, R.; Tricoli, A. Nanostructured β-Bi2O3 Fractals on Carbon Fibers for Highly Selective CO_2 Electroreduction to Formate. *Adv. Funct. Mater.* **2020**, *30*, 1906478.

(67) Tran-Phu, T.; Daiyan, R.; Fusco, Z.; Ma, Z.; Rahim, L. R. A.; Kiy, A.; Kluth, P.; Guo, X.; Zhu, Y.; Chen, H.; Amal, R.; Tricoli, A. Multifunctional nanostructures of Au−Bi_2O_3 fractals for CO_2 reduction and optical sensing. *J. Mater. Chem. A* **2020**, *8*, 11233−11245.

(68) Del Castillo, A.; Alvarez-Guerra, M.; Solla-Gullón, J.; Sáez, A.; Montiel, V.; Irabien, A. Sn nanoparticles on gas diffusion electrodes: Synthesis, characterization and use for continuous CO_2 electroreduction to formate. *J. CO2 Util.* **2017**, *18*, 222−228.

(69) Gong, Q.; Ding, P.; Xu, M.; Zhu, X.; Wang, M.; Deng, J.; Ma, Q.; Han, N.; Zhu, Y.; Lu, J.; Feng, Z.; Li, Y.; Zhou, W.; Li, Y. Structural defects on converted bismuth oxide nanotubes enable highly active electrocatalysis of carbon dioxide reduction. *Nat. Commun.* **2019**, *10*, 2807.

(70) Liu, M.; Pang, Y.; Zhang, B.; De Luna, P.; Voznyy, O.; Xu, J.; Zheng, X.; Dinh, C. T.; Fan, F.; Cao, C.; de Arquer, F. P. G.; Safaei, T. S.; Mepham, A.; Klinkova, A.; Kumacheva, E.; Filleter, T.; Sinton, D.; Kelley, S. O.; Sargent, E. H. Enhanced electrocatalytic CO_2 reduction via field-induced reagent concentration. *Nature* **2016**, *537*, 382−386.

(71) Yoo, J. S.; Christensen, R.; Vegge, T.; Nørskov, J. K.; Studt, F. Theoretical Insight into the Trends that Guide the Electrochemical Reduction of Carbon Dioxide to Formic Acid. *ChemSusChem* **2016**, *9*, 358−363.

Supporting Information

to the paper entitled

A tandem ($Bi_2O_3 \rightarrow Bi_{met}$) catalyst for highly efficient *ec*-CO_2 conversion into formate: *Operando* Raman spectroscopic evidence for a reaction pathway change

Abhijit Dutta[a]*, Iván Zelocualtecatl Montiel[a], Kiran Kiran[a], Alain Rieder[a], Vitali Grozovski[a], Lukas Gut[a], and Peter Broekmann[a]*

[a]Department of Chemistry and Biochemistry, University of Bern, Freiestrasse 3, Bern 3012 Switzerland

*Corresponding authors: abhjit.dutta@dcb.unibe.ch (Dr. Abhijit Dutta)

peter.broekmann@dcb.unibe.ch (Prof. Dr. Peter Broekmann)

Keywords: ec-CO_2 reduction, *operando* Raman spectroscopy, *Identical location* (IL) SEM, formate production, Carbon fiber cloth, $(BiO)_2CO_3$, Bi_2O_3 nano foam

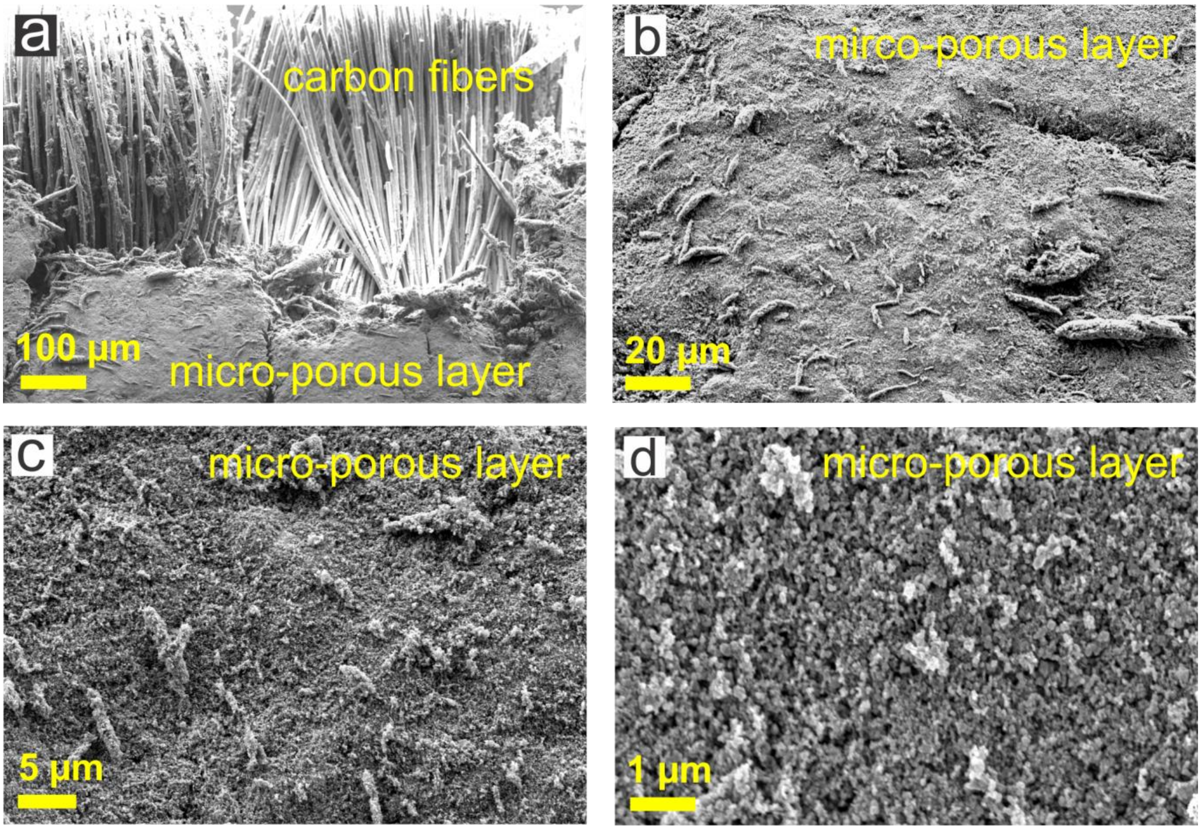

Figure S1. (a) Top-down SEM image of the carbon fiber cloth covered by a micro-porous carbon layer (C-MPL); note that carbon fibers are visible due to a local removal of the C-MPL; (b) – (d) Top-down SEM inspection of the structurally intact C-MPL. Note that in the manuscript this support material is referred to as GDE (gas diffusion electrode).

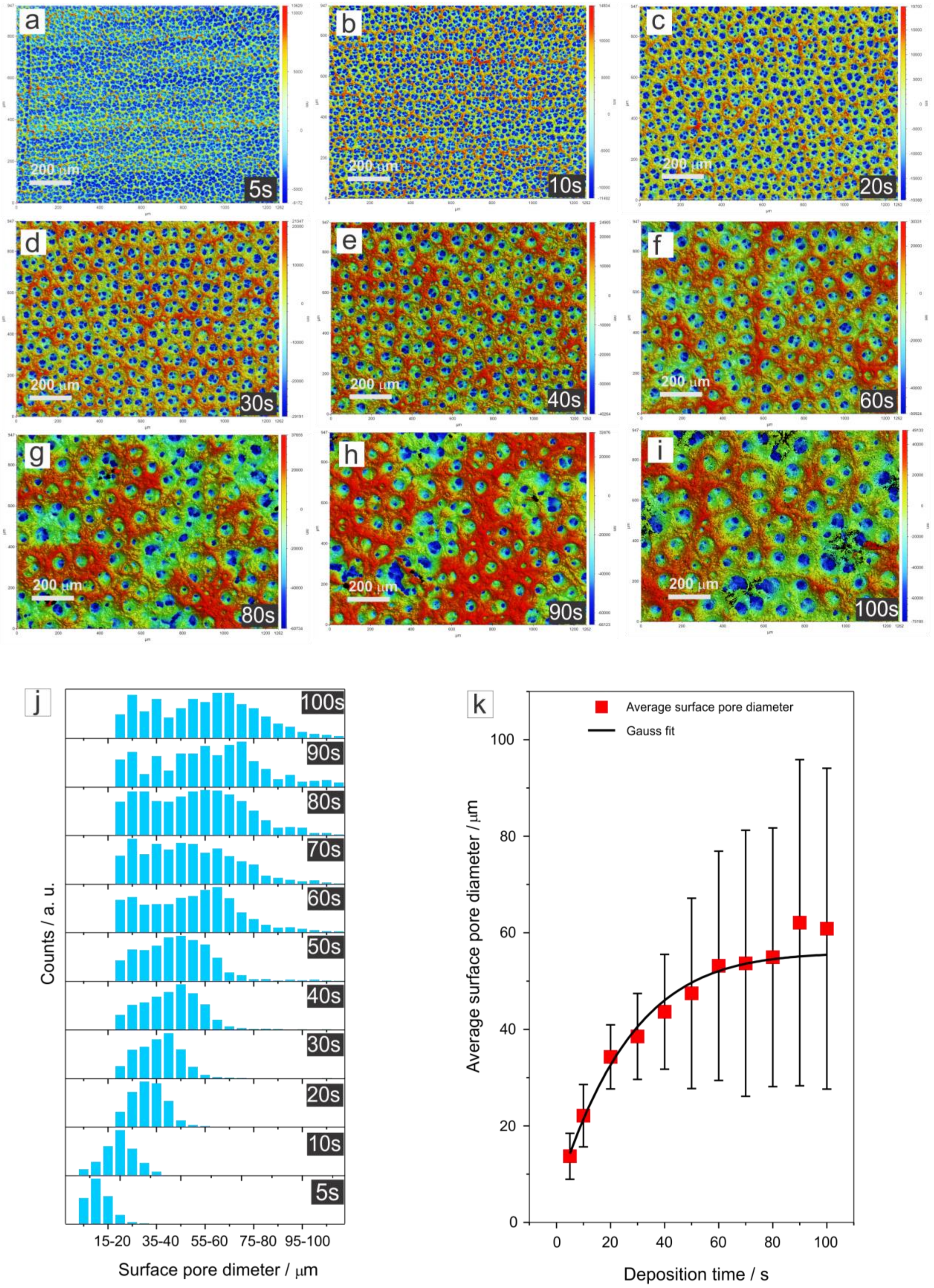

Figure S2. (a) - (i) White light interferometry inspection of the *ap* Bi/Bi$_x$O$_y$ foams deposited on the Cu foil support (the respective deposition times are indicated in the images); note that the pore size distributions are well-defined up to a deposition time of ~ 40s; above that value the surface becomes increasingly inhomogeneous; (j) Pore size distributions derived from the WLI images; (k) Mean pore sizes as function of the deposition time. The increasing error bars are indicative for the increasing inhomogeneity of the foams at higher deposition times.

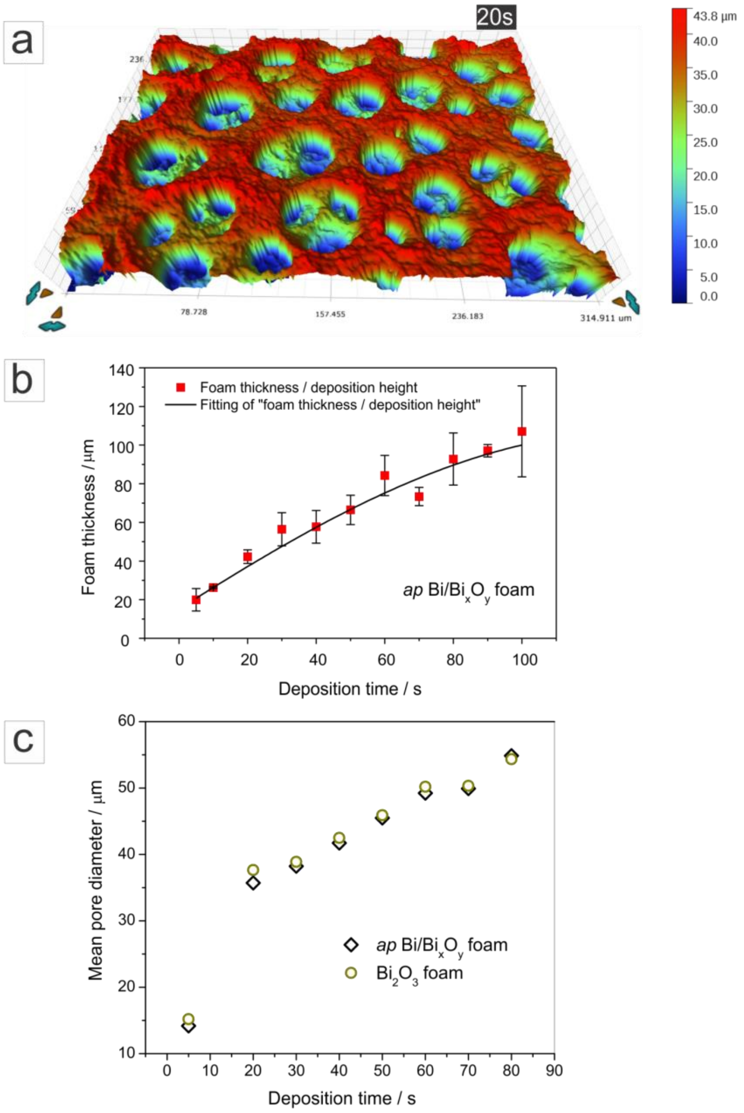

Figure S3. (a) Three-dimensional representation of the WLI image shown in Figure S2c; (b) Evolution of the foam thickness as function of the deposition time (Cu foil support); (c) Comparison of the mean surface pore diameters as function of the deposition time determined for the *ap* Bi/Bi$_x$O$_y$ foam and the thermally annealed (12 h at 300 °C in air) Bi$_2$O$_3$ foam. This comparison confirms that the thermal treatment does not affect the macro-porosity of the Bi foam.

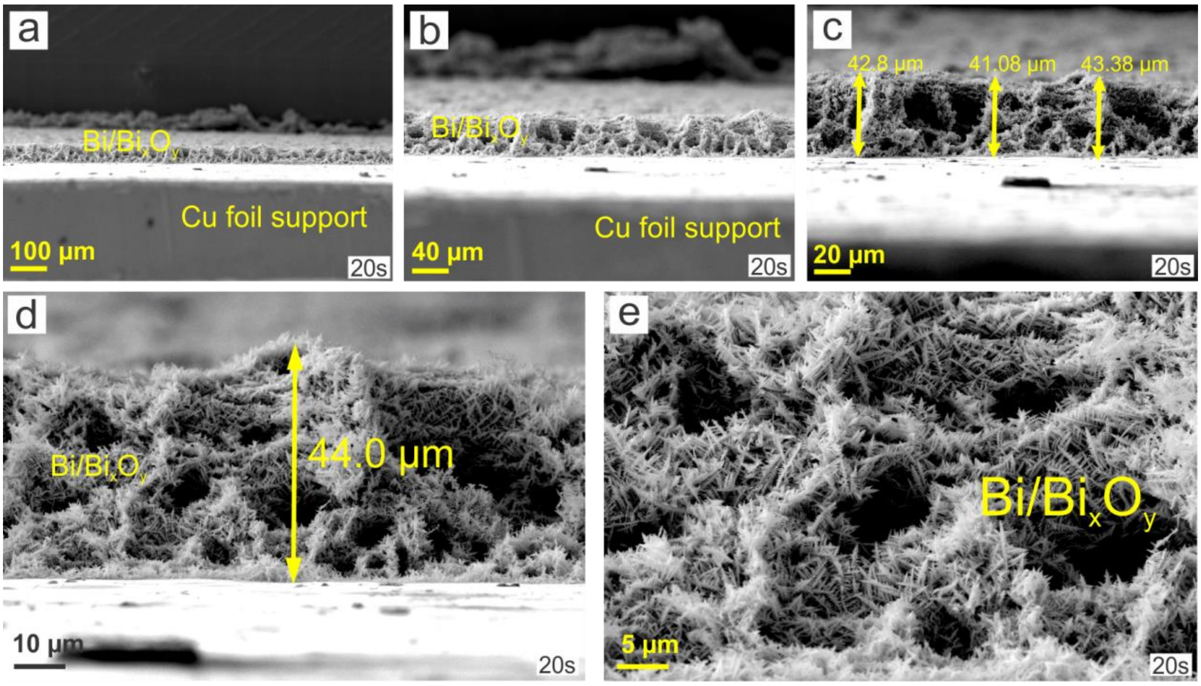

Figure S4. (a) - (e) Side-view SEM inspection of the *ap* Bi/Bi$_x$O$_y$ foam (20s deposition time). The observed thickness agrees well with the results of the white-light interferometry.

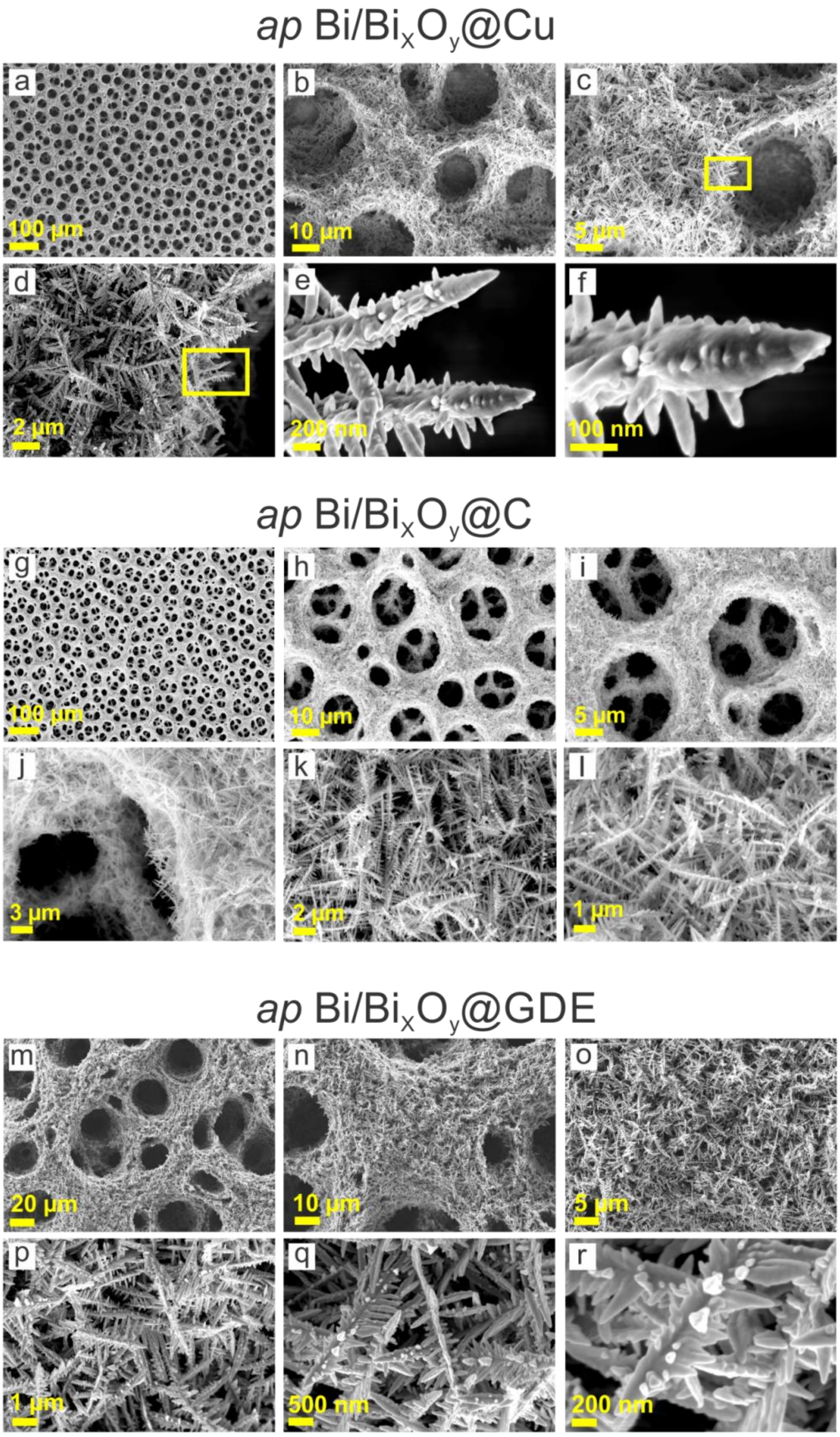

Figure S5. (a) - (f) SEM inspection of the *ap* Bi/Bi_xO_y foam deposited on the Cu foil support (20 s deposition time); (g) - (l) SEM inspection of the *ap* Bi/Bi_xO_y foam deposited on the C foil support (20 s deposition time); (m) - (r) SEM inspection of the *ap* Bi/Bi_xO_y foam deposited on the carbon fiber cloth (GDE, 20 s deposition time).

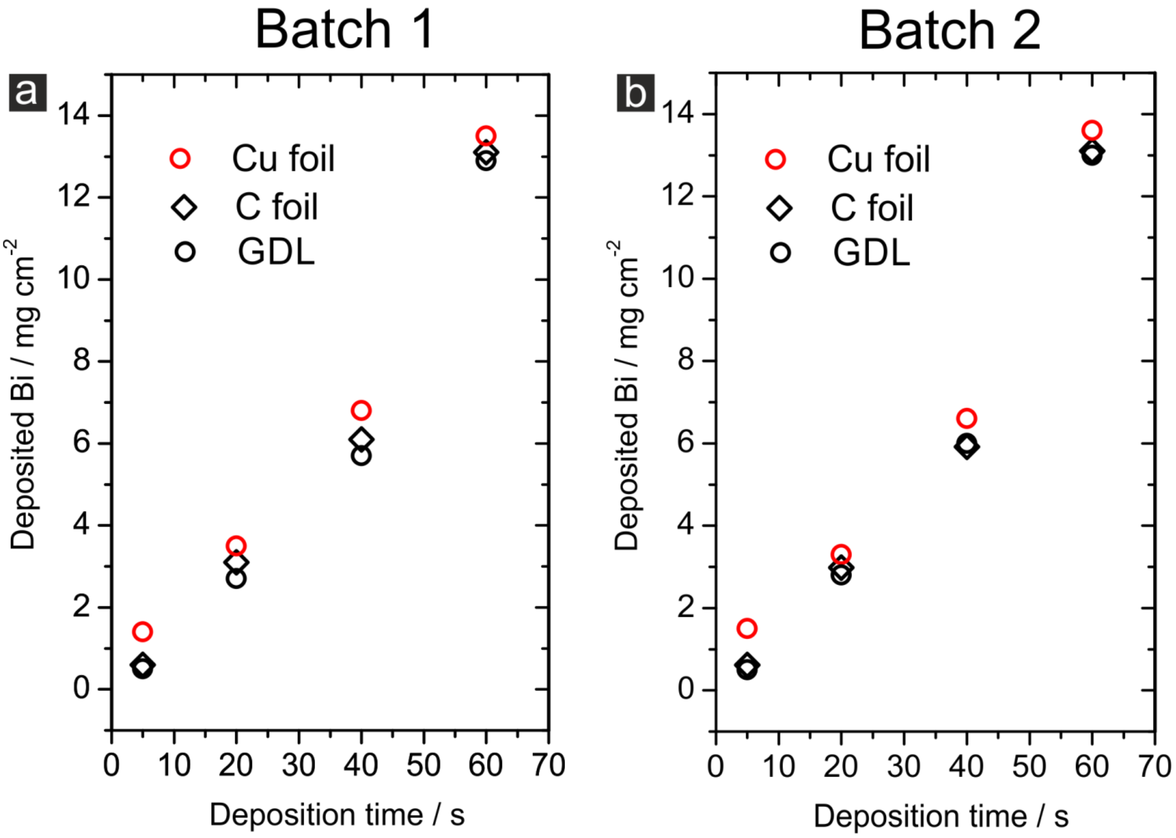

Figure S6. Gravimetrically determined masses of electrodeposited Bi as function of the deposition time and the chemical nature of the support material (see also Table S5). Panel (a) and (b) show two different batches of Bi foam samples. A comparison of batch 1 and 2 reveals that the reproducibility of the Bi deposition by means of the additive-assisted DHBT approach is excellent. The amounts of deposited Bi are in principle comparable for the Cu foil, C foil and GDE supports. The faradaic efficiency towards metal deposition seems to be slightly higher for the Cu support compared to both carbon supports.

Comparing these results with the SEM analysis in Figure S5 reveals that the observed differences in the foam morphology are mainly due to differences in the so-called bubble break-off diameter which seems to be higher on the rougher surface of the GDE support than on the planar Cu and C foil substrates. Minor differences in the total amount of Bi deposited on the support materials alone cannot explain the huge differences in the foam morphology observed in the top-down SEM inspection (Figure S5).

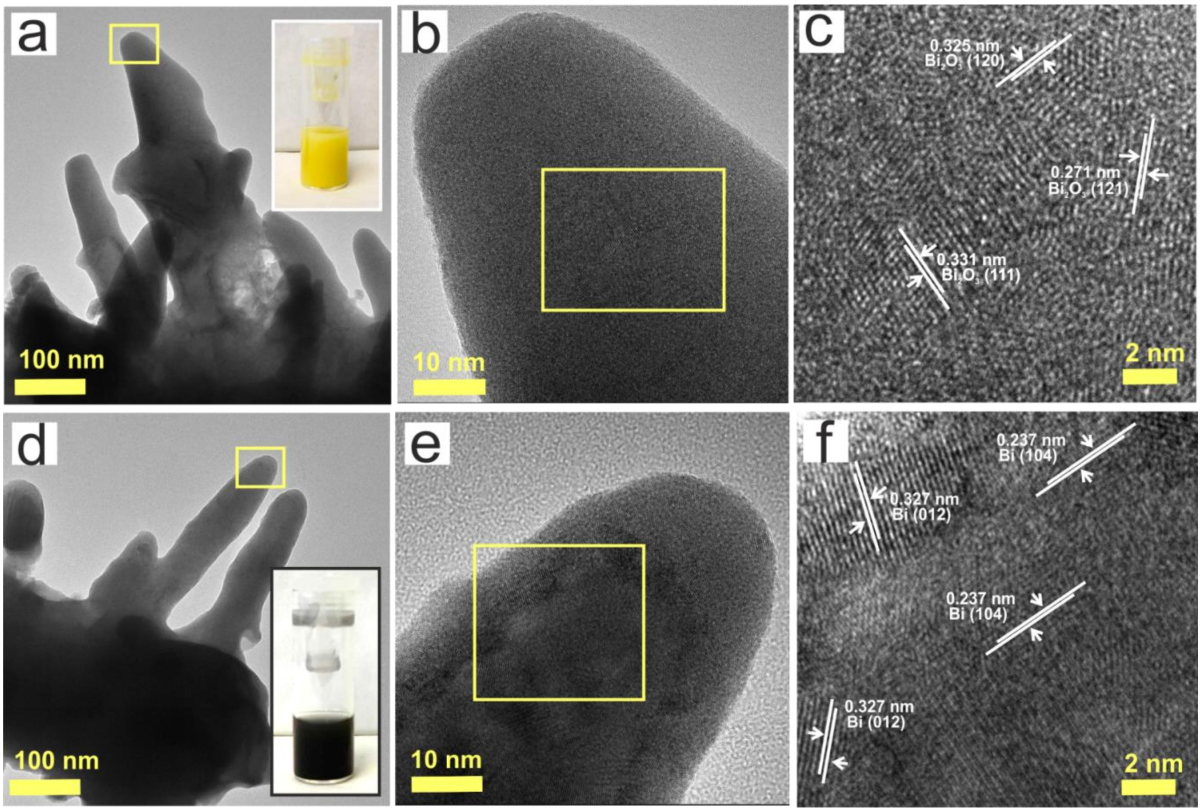

Figure S7. (a) - (c) TEM inspection of the Bi_2O_3 foam. For this purpose the metallic Bi foam catalyst was electrodeposited (20 s deposition time) on a Cu foil support, thermally annealed (12 h at 300 °C in air), mechanically removed from the support and subsequently dispersed in ethanol. The obtained yellow ink (see inset in panel a) was then drop-cast on a carbon-coated Cu-grid (300 mesh) for further microscopic inspection; (d) – (f) Corresponding TEM inspection of the *ap* Bi/Bi_xO_y sample. The inset in panel d shows the black ethanol ink of the dispersed *ap* Bi/Bi_xO_y sample.

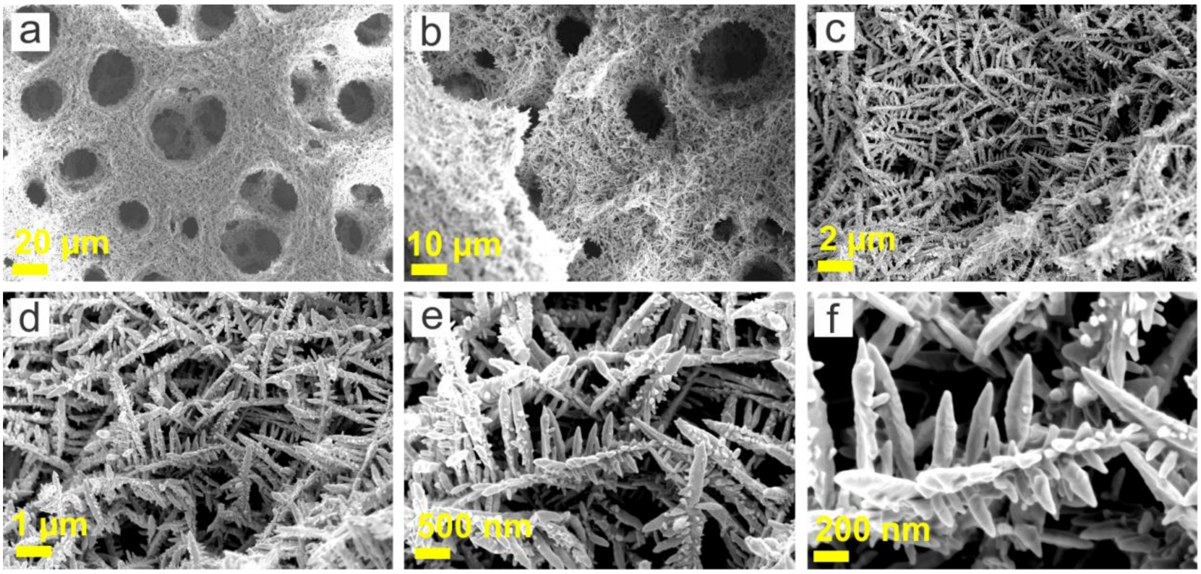

Figure S8. (a) - (f) SEM inspection of the Bi_2O_3@GDE foam after annealing of the pristine *ap* Bi/Bi_xO_y sample (20 s deposition time) for 12 h at 300 °C in air.

Figure S9. (a) Black appearance of the *ap* Bi/Bi$_x$O$_y$ foam; (b) Yellow appearance of the Bi$_2$O$_3$ foam after annealing the Bi/Bi$_x$O$_y$@GDE at 300 °C in air (12 h). Note that a geometric area of ~1 cm^2 was exposed to the electrolyte.

.

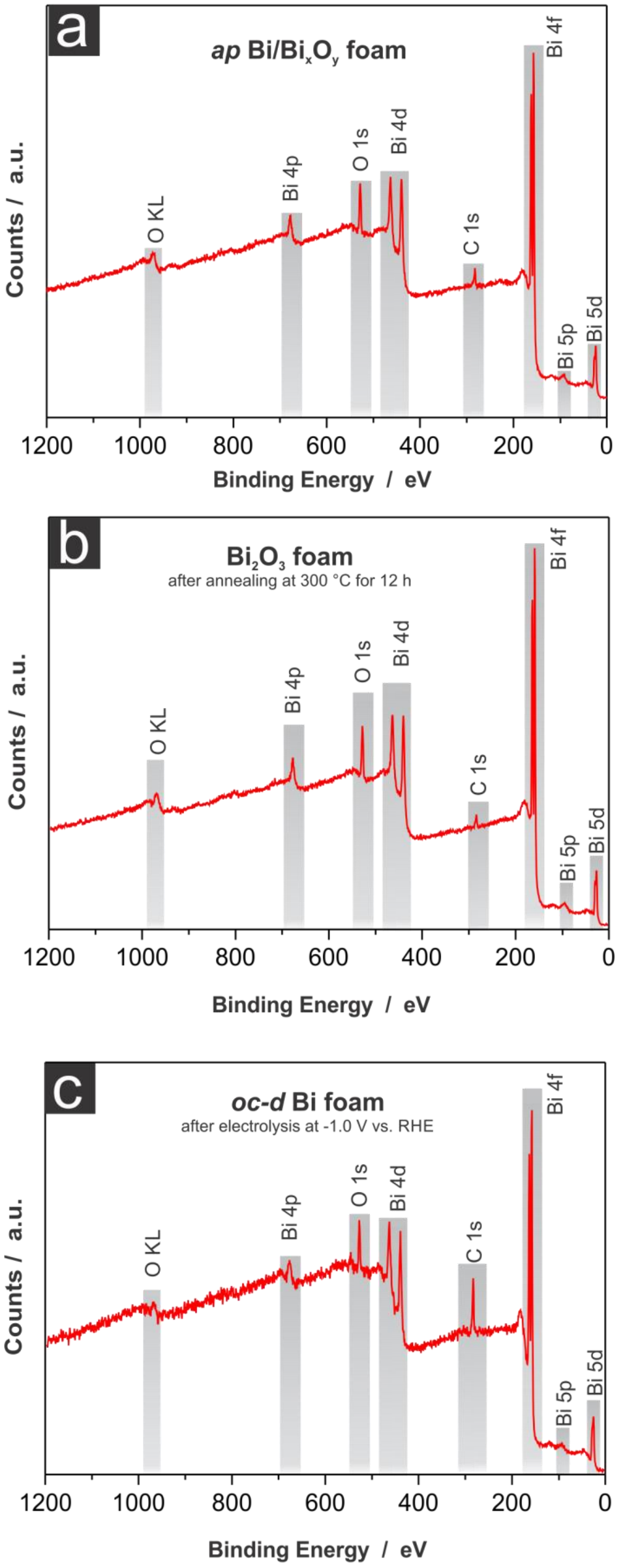

Figure S10 Survey XPS spectra of (a) the *ap* Bi/Bi$_x$O$_y$ foam (20 s deposition time), (b) the thermally annealed foam (Bi$_2$O$_3$), and (c) the oxide-carbonate derived (*oc-d*) foam after 1h electrolysis in CO$_2$-sat. 0.5 KHCO$_3$ at -1.0 V vs. RHE using the Bi$_2$O$_3$ foam as the catalyst. Note that both the *ap* Bi/Bi$_x$O$_y$ foam and the *oc-d* foam undergo rapid surface (re-)oxidation after emersion from the electrolyte bath.

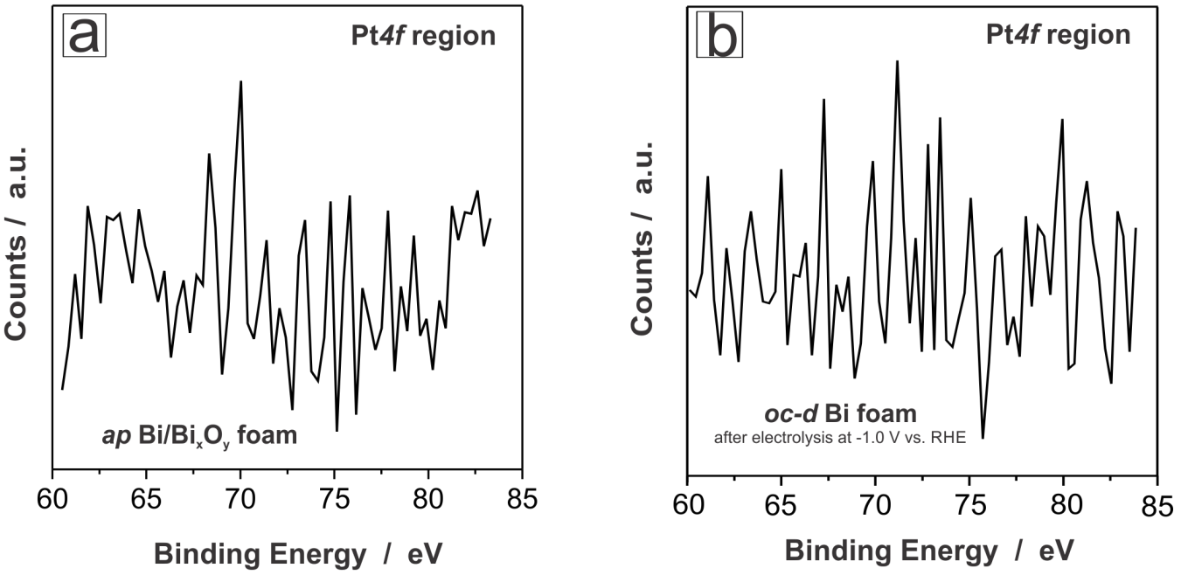

Figure S11. XPS spectra of the *ap* Bi/Bi$_x$O$_y$ foam (a) and the oxide-carbonate derived (*oc-d*) foam sample after electrolysis at -1.0 V vs. RHE in CO_2-sat. 0.5 $KHCO_3$ focussing on the Pt*4f* region.

These spectra demonstrate that Pt is dissolved from the anode and re-deposited on the cathode/catalyst surface neither during the initial foam electrodeposition nor during the CO_2RR.

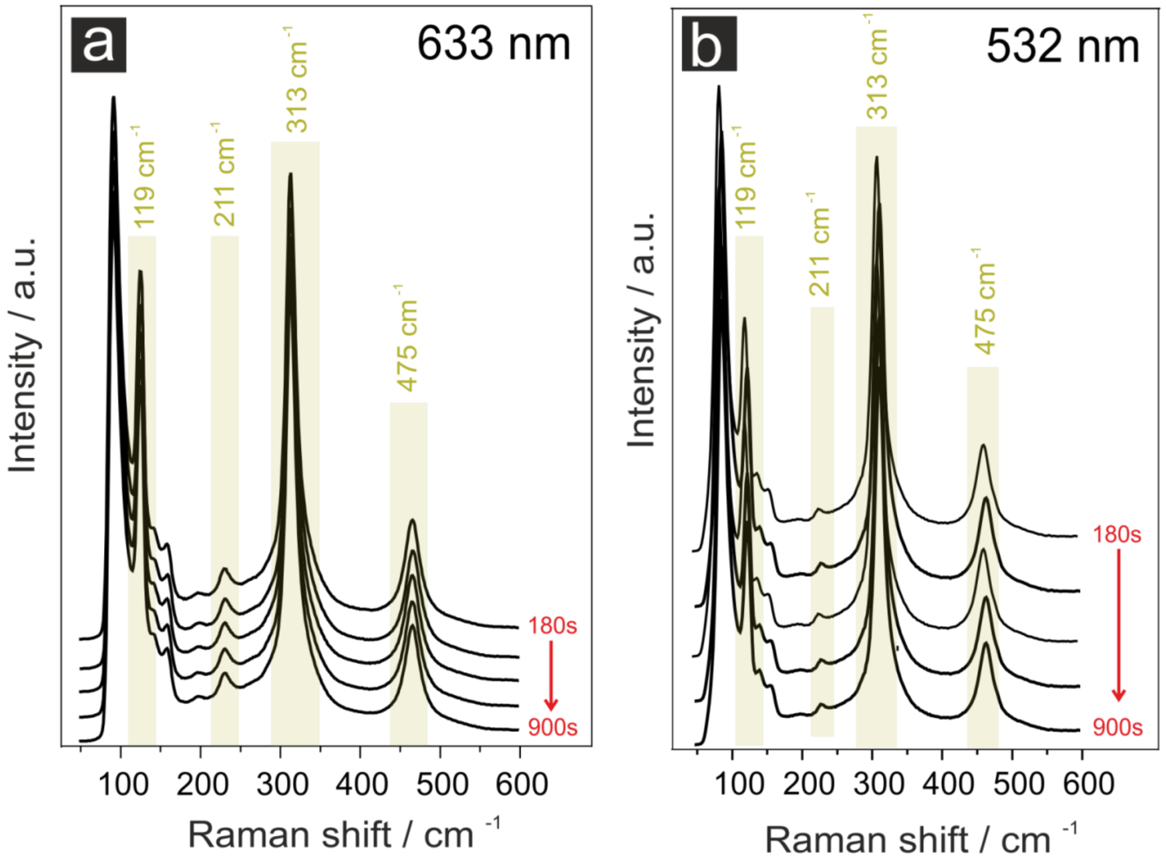

Figure S12. Comparison of *ex situ* Raman spectra (dry conditions) acquired from the dry Bi_2O_3 foam sample (20 s deposition time; after annealing at 300 °C in air for 12 h) using two different laser light excitations; a) red laser (633 nm); b) green laser (532 nm). The oxide-related Raman features are well resolved in both cases indicating that both laser sources are in principle suited for the Raman investigation of this Bi-based foam material. Note that the Raman features do not change upon repeated acquisition of the Raman spectra. A laser power of 3 mW does not lead to a beam induced degradation of the Bi foam material.

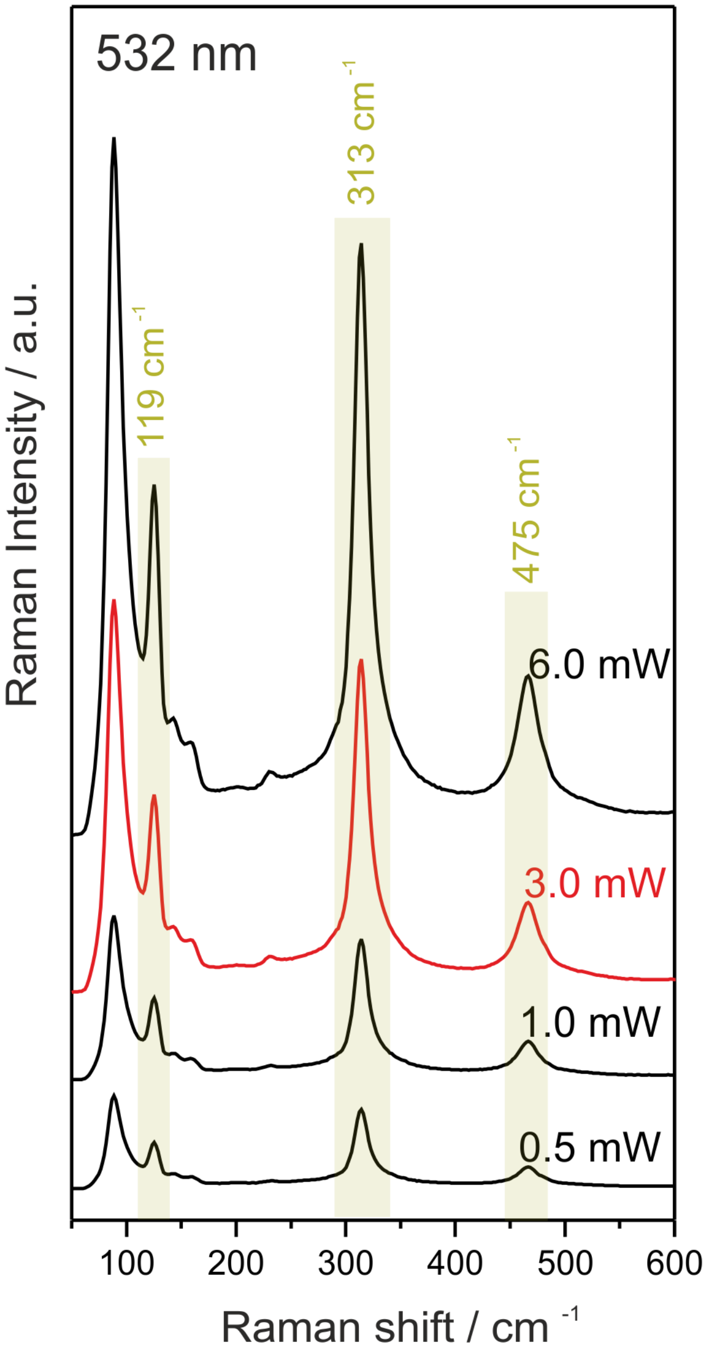

Figure S13. Comparison of the Raman spectra acquired under dry conditions (*ex situ*) from the *ap* Bi/Bi$_x$O$_y$ foam (20 s deposition time) using the ‘green’ laser (532 nm excitation wave length) at different laser powers ranging from 0.5 mW to 6.0 mW.

As standard setting for the *ex situ*, *in situ* (at OCP) and *operando* (under CO$_2$RR conditions) Raman experiments a laser power of 3 mW was chosen (highlighted red) providing reasonable Raman signal intensities while avoiding undesired local heating and laser induced degradation of the catalyst sample. A laser power of 6 mW might already lead to an undesired ‘burning’ (structural and compositional degradation) of the Bi foams.

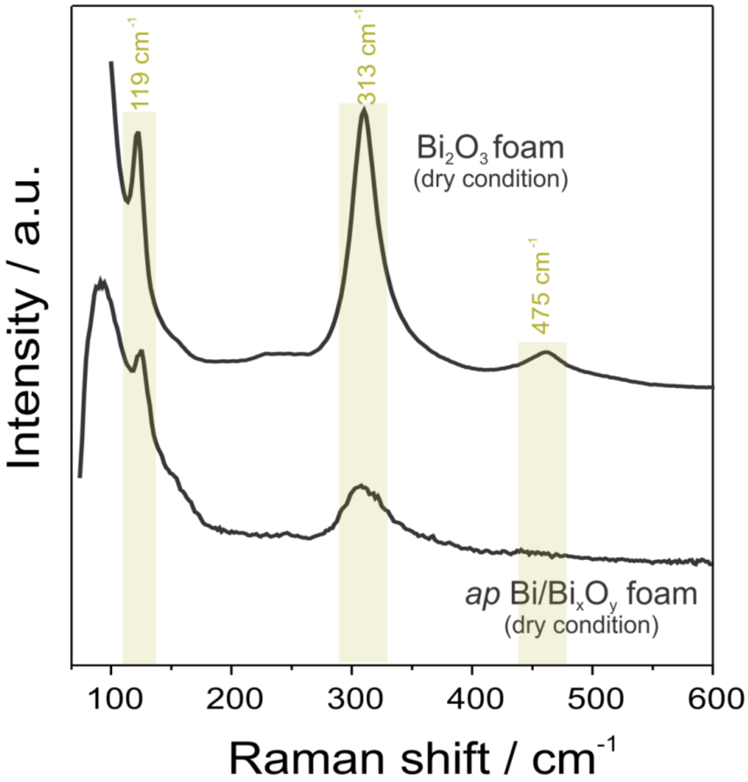

Figure S14. Comparison of the Raman spectra (laser wave length: 532 nm; laser power: 3 mW) acquired under dry conditions (*ex situ*) from the *ap* Bi/Bi_xO_y foam (20 s deposition time) and from the Bi_2O_3 foam after the annealing at 300 °C in air (12 h). Characteristic Raman features corresponding to the bismuth oxide are highlighted green. Clearly the oxide-related Raman features are more intense in case of the annealed sample thus pointing to a fully oxidised sample after the thermal annealing in accordance to the XRD analysis (see Figure 3a).

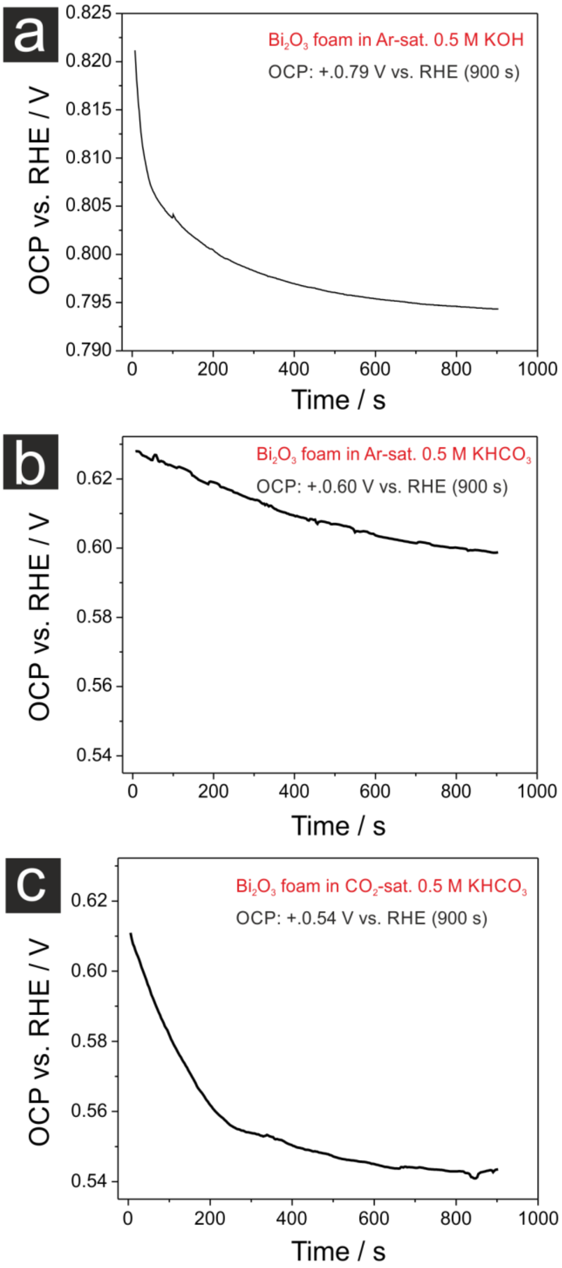

Figure S15. Time-dependent OCP measurements of the Bi_2O_3 foam (20 s deposition time; after annealing at 300 °C in air for 12 h) in the Ar-sat. 0.5 M KOH (panel a), the Ar-sat. 0.5 M $KHCO_3$ (panel b), and the CO_2-saturated 0.5 M $KHCO_3$ solution (panel c). The time-dependent changes of the OCP are most pronounced in case of the Ar-sat. 0.5 M KOH (panel a) due to surface hydrolysis (exchange of oxide by hydroxides) at pH = 13.5 and in the CO_2-sat. 0.5 M $KHCO_3$ solution. The latter effect is attributed to the rapid exchange of oxidic species by sub-carbonate species which does not remain restricted to the outermost surface of the foam material but affects also deeper layers of the 'bulk' of the foam material. Note that the pH values are slightly different both electrolytes: pH(Ar-saturated 0.5 M $KHCO_3$) =8.3; pH(CO_2-saturated 0.5 M $KHCO_3$) = 7.8.

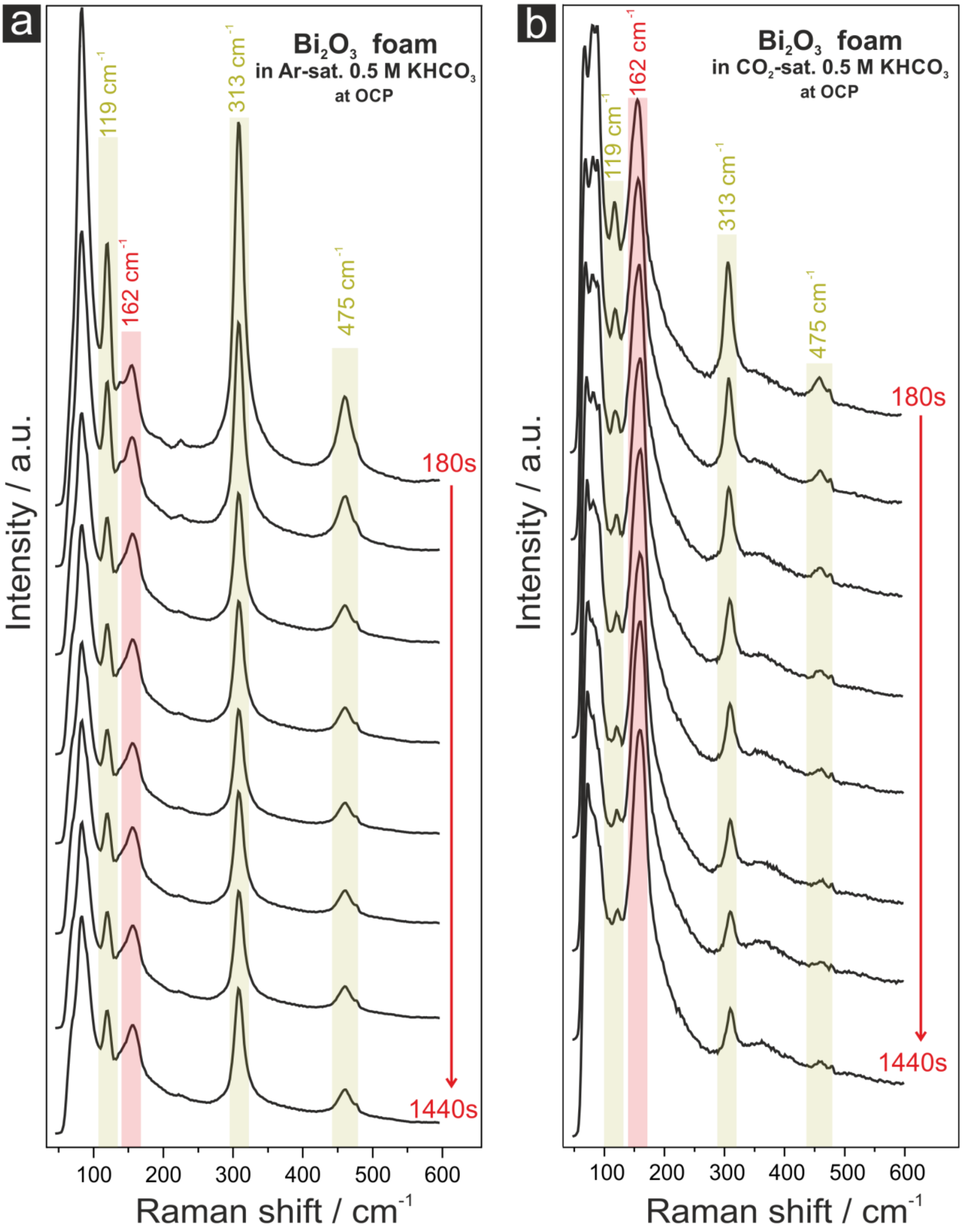

Figure S16. Comparison of the Raman spectra (laser wave length: 532 nm; laser power: 3 mW) of the Bi_2O_3 foam (20s deposition time; after annealing at 300 °C in air for 12 h) at OCP in Ar-saturated (panel a) and CO_2-sat. 0.5 M $KHCO_3$ (panel b). Note that the pH values are slightly different in both electrolytes: pH (Ar-saturated 0.5 M $KHCO_3$) = 8.3; pH (CO_2-saturated 0.5 M $KHCO_3$) = 7.8. Note that a weak sub-carbonate Raman feature at 162 cm^{-1} is also visible in the Ar-saturated electrolyte (a). Trace amounts of dissolved CO_2 are also present in the Ar-saturated solution; the bicarbonate indirectly serves as the CO_2 source. The drop down of the oxide-related Raman features with elapsed time in panel a is likely due the partial hydrolysis of the surface oxides (exchange of oxide by hydroxide species).

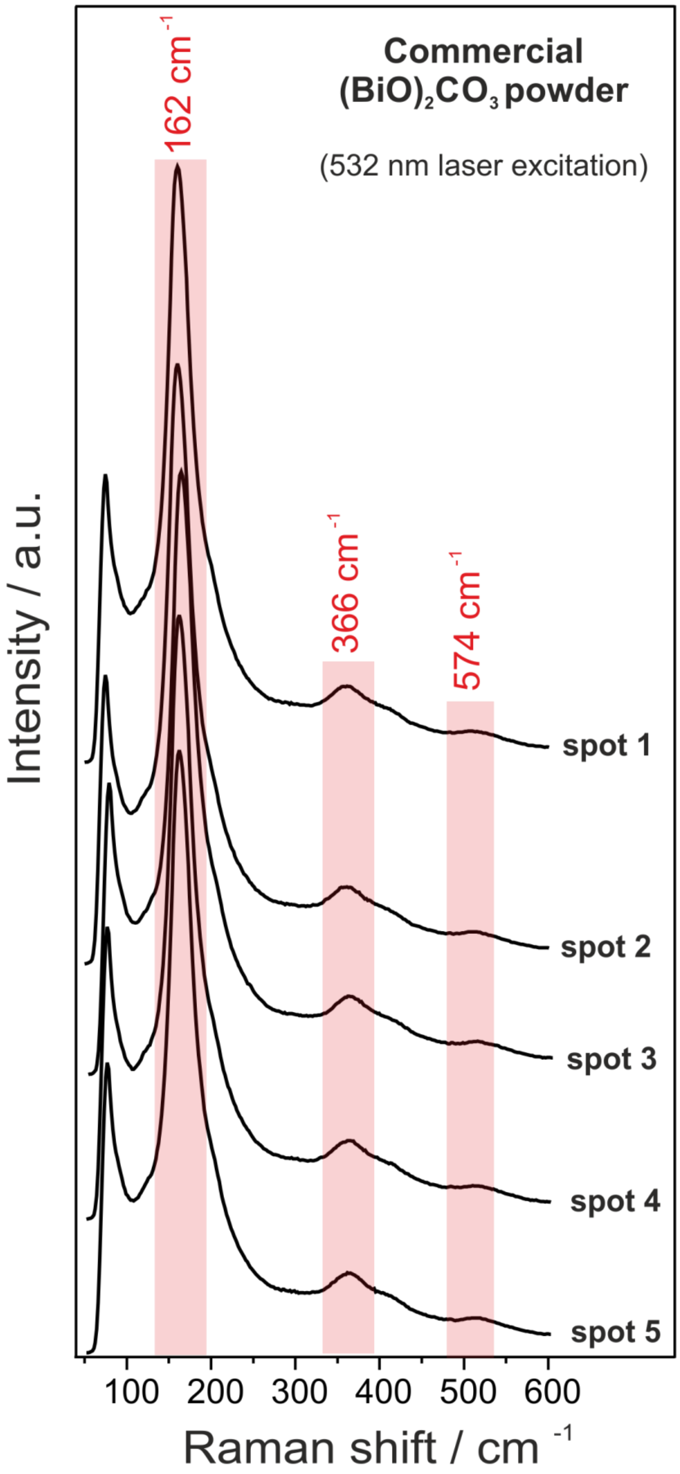

Figure S17. *Ex situ* Raman spectra (laser wave length: 532 nm; laser power: 3 mW) of a dry $(BiO)_2CO_3$ reference powder sample (Sigma Aldrich) recorded at different spots on the sample. Clearly visible are a strong Raman feature at 162 cm^{-1} (used as fingerprint for the presence of sub-carbonate in this study) and two weaker features at 366 cm^{-1} and 574 cm^{-1}. The latter two (less intense) Raman features are usually not observed in the *operando* Raman spectra (see e.g. Figure 4d).

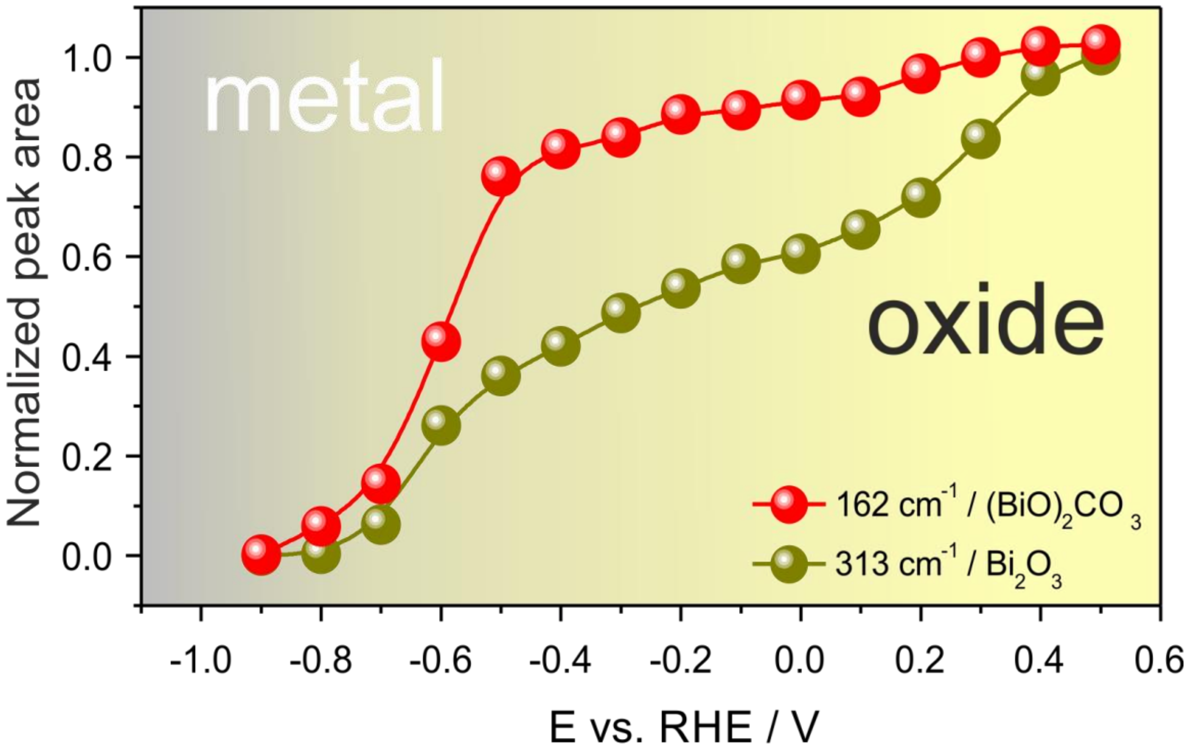

Figure S18. Quantitative analysis of the Raman spectra presented in Fig. 4c and S19a (analogue to the analysis presented in Fig. 4g). The graph shows changes of the potential-dependent Raman intensities for the Bi_2O_3 foam catalyst (20 s deposition time; after annealing at 300 °C in air for 12 h) in the Ar-sat. 0.5 M $KHCO_3$ electrolyte.

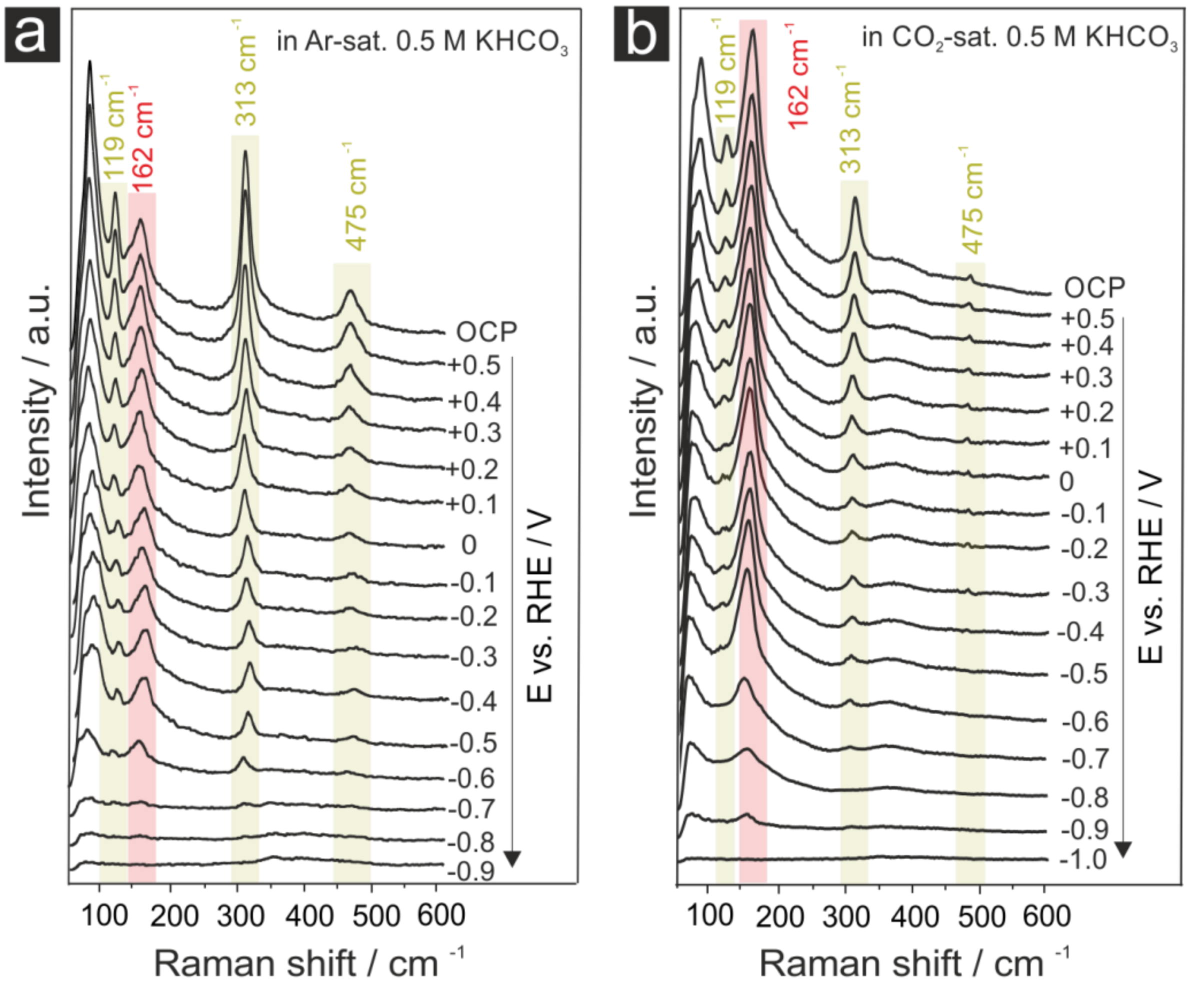

Figure S19. Potential dependent Raman spectra acquired in the Ar- (panel a) and CO$_2$-saturated (panel b) 0.5 M KHCO$_3$ electrolyte. The applied electrolysis potential versus RHE is indicated at the respective spectrum. These Raman plots correspond to Figure 4c and 4d in the main manuscript.

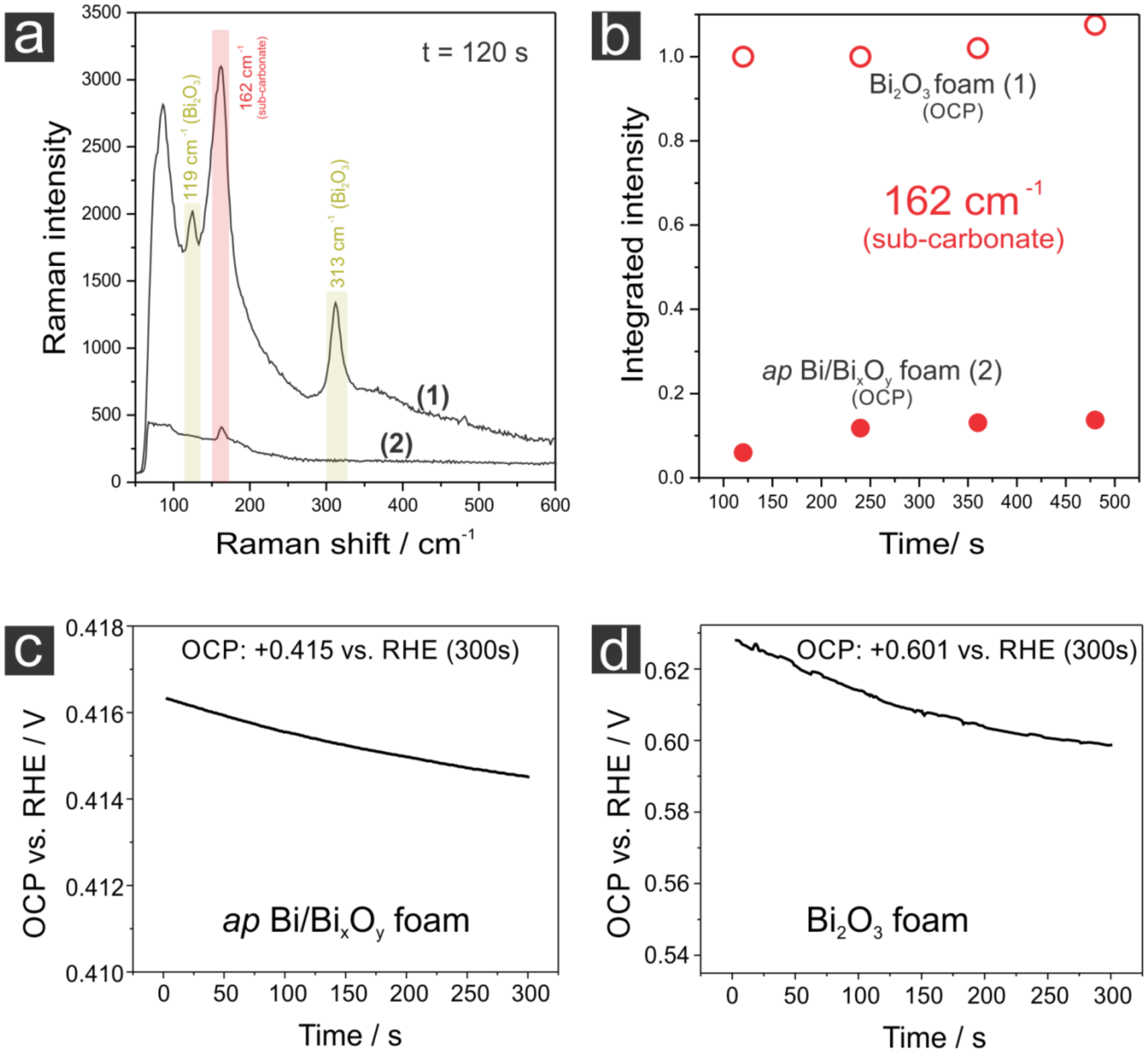

Figure S20. (a) Comparison of the Raman spectra of the Bi_2O_3 foam (spectrum 1) and the *ap* Bi/Bi_xO_y foam (spectrum 2) after their exposure to the CO_2-saturated 0.5 M $KHCO_3$ solution at OCP. Note that the oxide-related peaks have completely disappeared in case of the *ap* Bi/Bi_xO_y foam after exposure to the electrolyte (see Figure S14). The substantially higher intensity of the oxide-related Raman features in the spectrum of the Bi_2O_3 sample (spectrum 1) compared to the *ap* Bi/Bi_xO_y foam (spectrum 2) suggests that the sub-carbonate formation does not remain restricted to the outermost surface of the catalyst material but further extends into the 'bulk' of the Bi_2O_3 matrix. (b) Time dependent evolution of the integrated intensities of the Raman band at 162 cm^{-1} (Raman 'fingerprint' for the presence of sub-carbonate species) indicating a slight increase in intensity in both cases as function of time; (c) Time-dependent OCP-measurement for the *ap* Bi/Bi_xO_y foam exposed to the CO_2-saturated 0.5 M $KHCO_3$ solution; (d) Time-dependent OCP-measurement for the Bi_2O_3 foam exposed to the CO_2-saturated 0.5 M $KHCO_3$ solution.

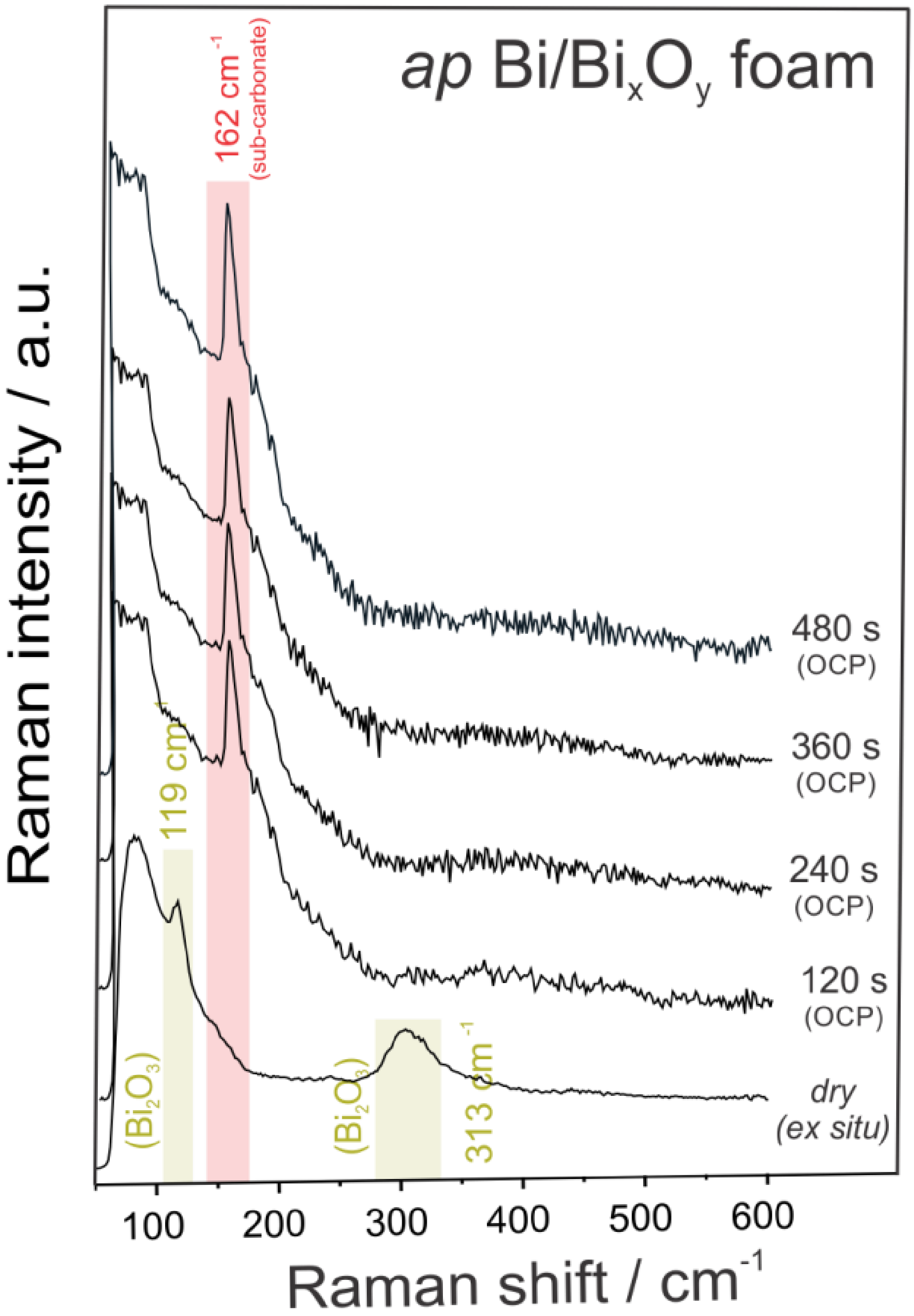

Figure S21. Changes of the Raman spectrum of the *ap* Bi/Bi$_x$O$_y$ sample after exposure to the CO_2-sat. 0.5 M $KHCO_3$ electrolyte at OCP (~ +0.415 vs. RHE, see Fig. S20c).

Note that the surface oxide related features completely disappear after the exposure to the electrolyte at the OCP. Only subcarbonate features are visible when exposed to the electrolyte environment. This is indicative for a complete exchange of the surface oxide/hydroxide by sub-carbonate species in case of the *ap* Bi/Bi$_x$O$_y$ sample. The surface exchange process seems to be fast as there is not oxide-related feature visible already in the first Raman spectrum at 120 s.

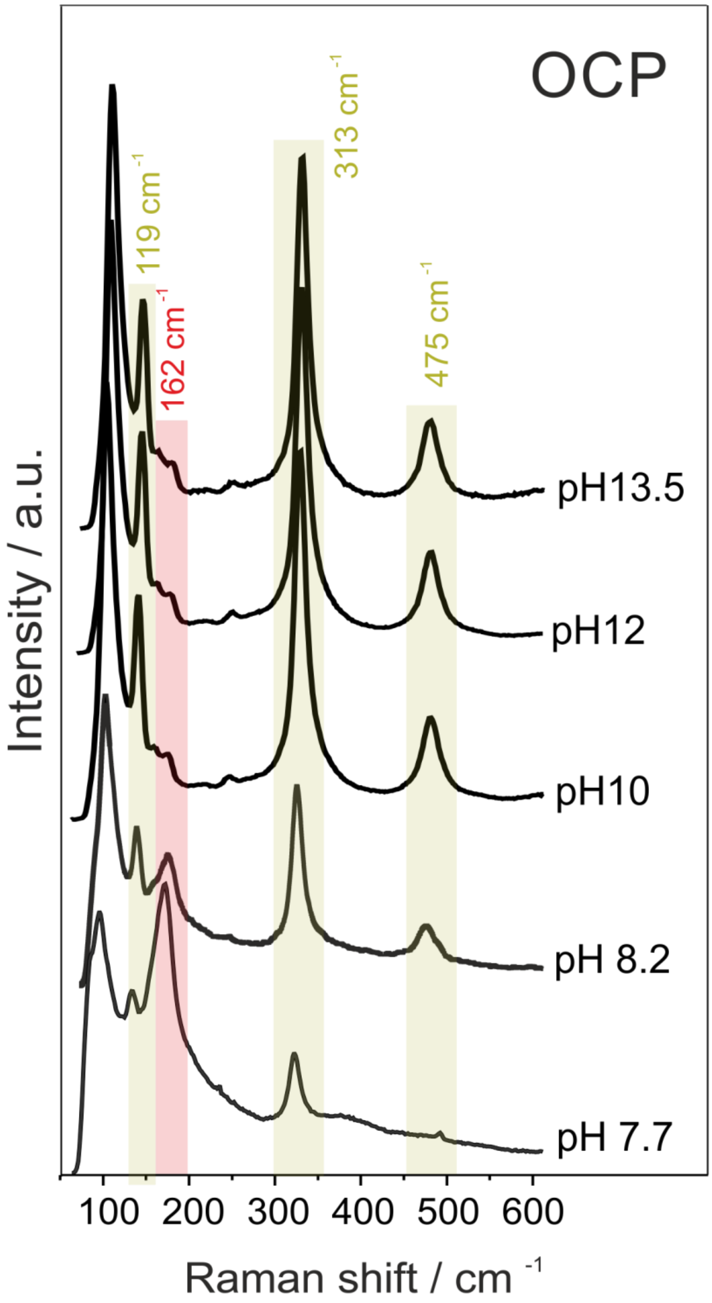

Figure S22. Series of *in situ* Raman spectra of the Bi_2O_3 foams (20 s deposition time; after annealing at 300 °C in air for 12 h) at OCP in 0.5 KOH solution. The spectrum at pH 13.5 serves as a reference in the CO_2-/carbonate-free alkaline electrolyte. The lower pH values were adjusted by bubbling gaseous CO_2 through the 0.5 KOH solution. Depending on the bubbling time different pHs and CO_2/bicarbonate/carbonate/hydroxide concentrations are adjusted due to the shift in the CO_2/bicarbonate/carbonate equilibrium. Sub-carbonate formation is observed solely at moderately alkaline pH values (8.2 and 7.7). This suggests that dissolved CO_2 is mandatory for the exchange of the oxide by the sub-carbonate on the Bi_2O_3 foam surface. Obviously no direct exchange of oxidic/hydroxy species by carbonate anions takes place at higher pH values (> 8.2).

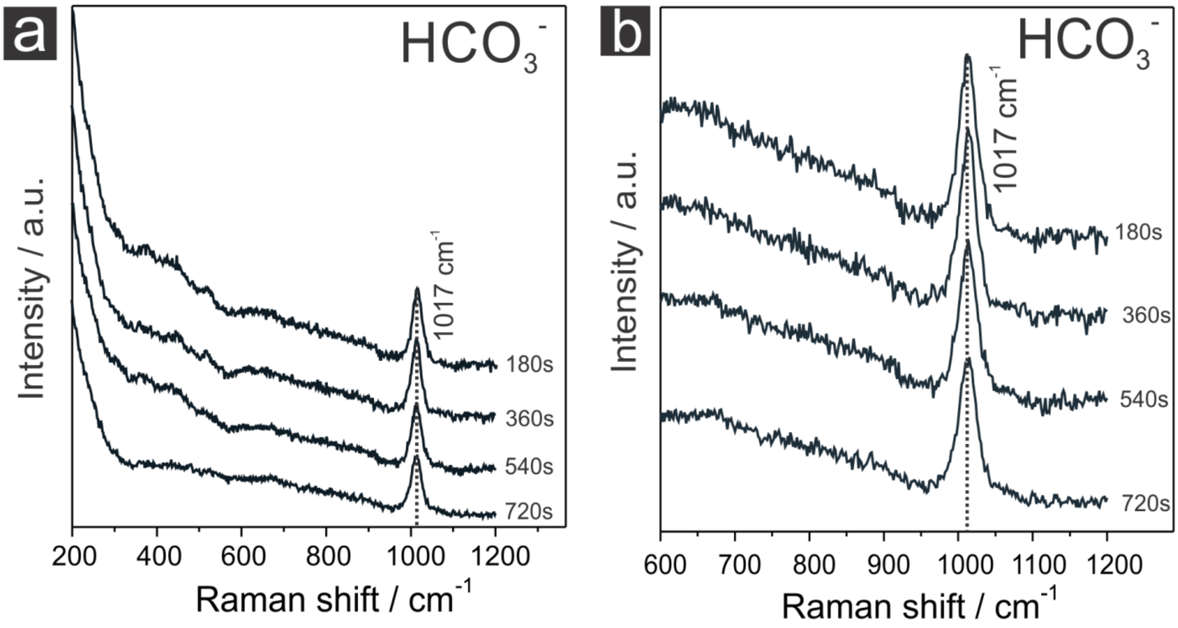

Figure S23. (a) – (b) Control Raman experiment in CO$_2$-sat. 0.5 M KHCO$_3$ solution at OCP using an Al foil as the substrate. This experiment demonstrates that the presence of the bicarbonate Raman feature at 1017 cm^{-1} is independent of the chosen electrode material (Al foil, Bi$_2$O$_3$ foam, etc.). It is therefore likely that the Raman band at 1017 cm^{-1} is a 'solution' feature and not due a chemisorbed species. In the latter case one would expect changes in the Raman shift and intensity depending on the chemical nature and structure of the electrode/substrate surface used.

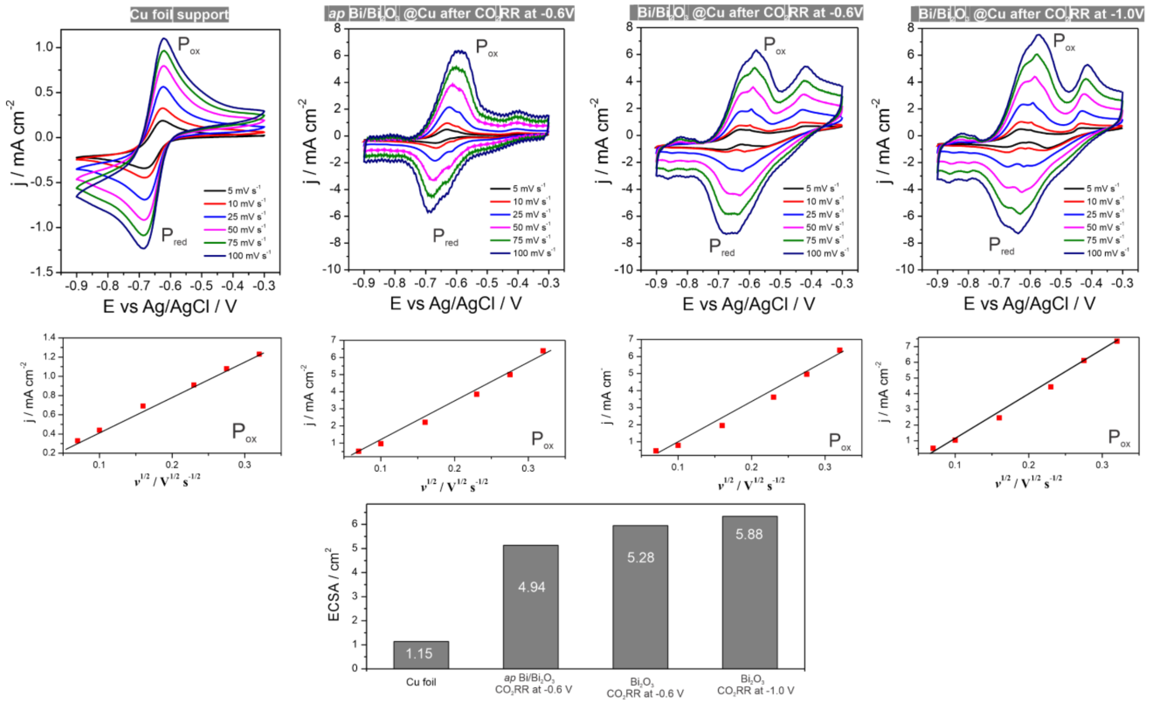

Figure S24. Representative determination of the electrochemically active surface area (ECSA) for the *ap* Bi/Bi_xO_y@Cu and the Bi_2O_3@Cu catalysts using the so-called viologen method (for details see Experimental section). The ECSA was determined after CO_2RR (1 h electrolysis) as indicated in the graphs.

These results strongly suggest that the resulting ECSA of the Bi_2O_3 foams also depends on the actual electrolysis potential/condition.

This is actually the reason why we do not normalize the electrolysis data (e.g. in Figure 8a and 8ab) to the respective ESCA.

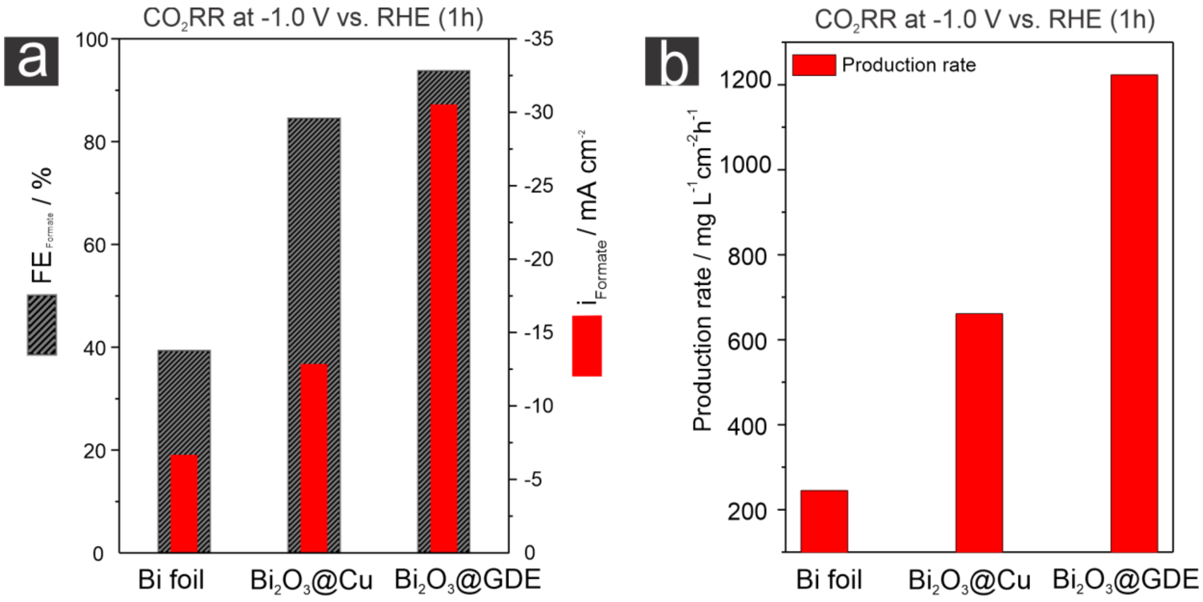

Figure S25. (a) Comparison of the FE$_{formate}$ and PCD$_{formate}$ values for the Bi foil (reference), the Bi_2O_3@Cu, and the Bi_2O_3@GDE catalysts (20s deposition time; after annealing at 300 °C in air for 12 h). These results demonstrate that the product selectivity is only marginally affected by changes of the support material (Cu foil versus GDE); the resulting PCDs are, however, depending on the support material as the ECSA is also altered; (b) Corresponding formate production rates.

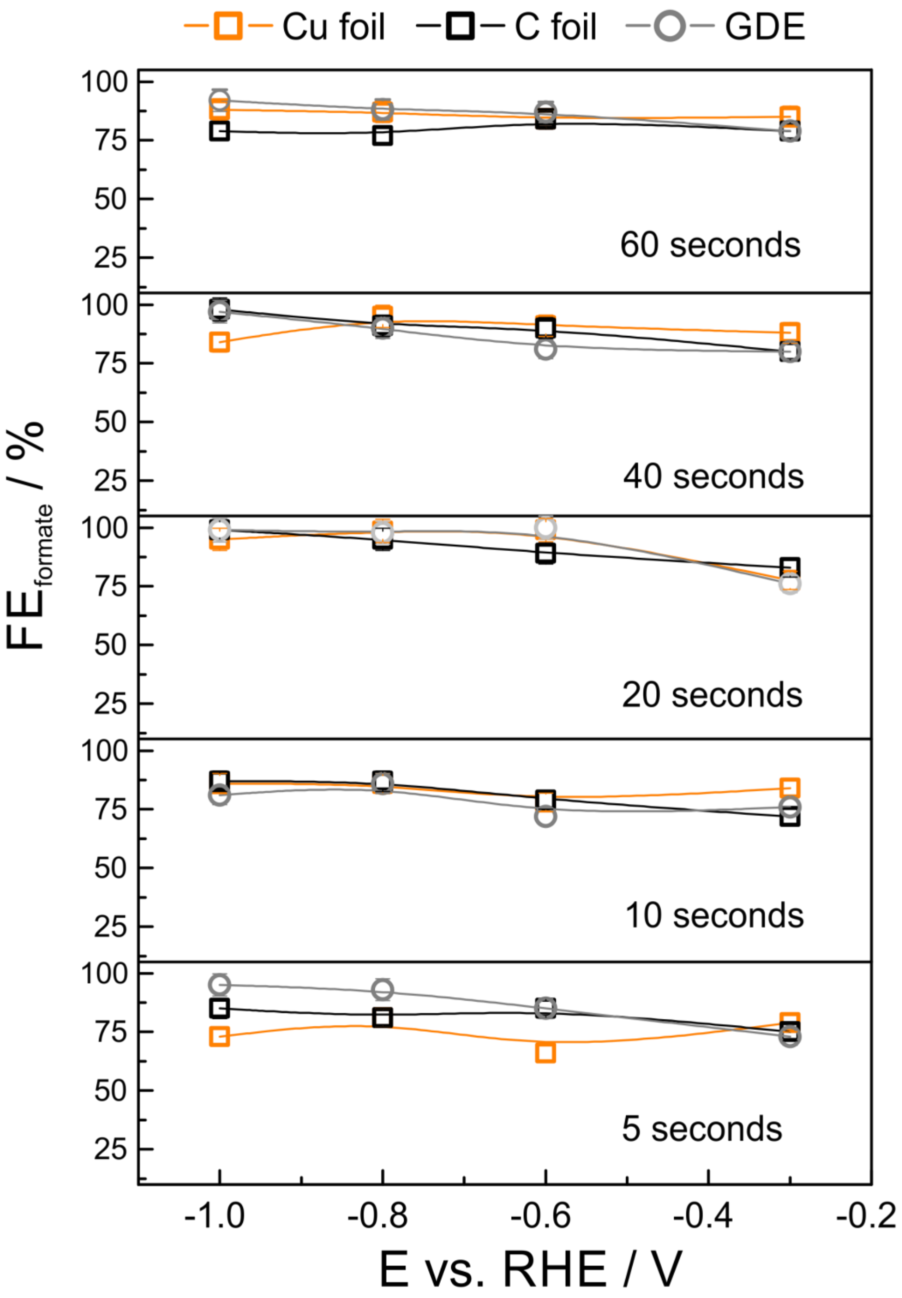

Figure S26. Comparison of the FE$_{formate}$ values for the Bi_2O_3 catalysts (after annealing at 300 °C in air for 12 h) after 1 h electrolysis in CO_2-sat. 0.5 M $KHCO_3$ electrolyte (single catalyst approach). In this measurement campaign we varied the support material and deposition time (indicated in the respective graph, see also Table S6). The results shown in the graphs represent single-electrolysis experiments (no repetitions).

The optimum performance is achieved for a deposition time of 20 s. Note that thicker foams (deposition > 20 s) often suffer from mechanical instability under harsh CO_2RR conditions. At low deposition times (e.g. 5 s) the support material starts to contribute to the CO_2RR in the form of an increased faradaic efficiency towards hydrogen (e.g. Cu at 5 s deposition time).

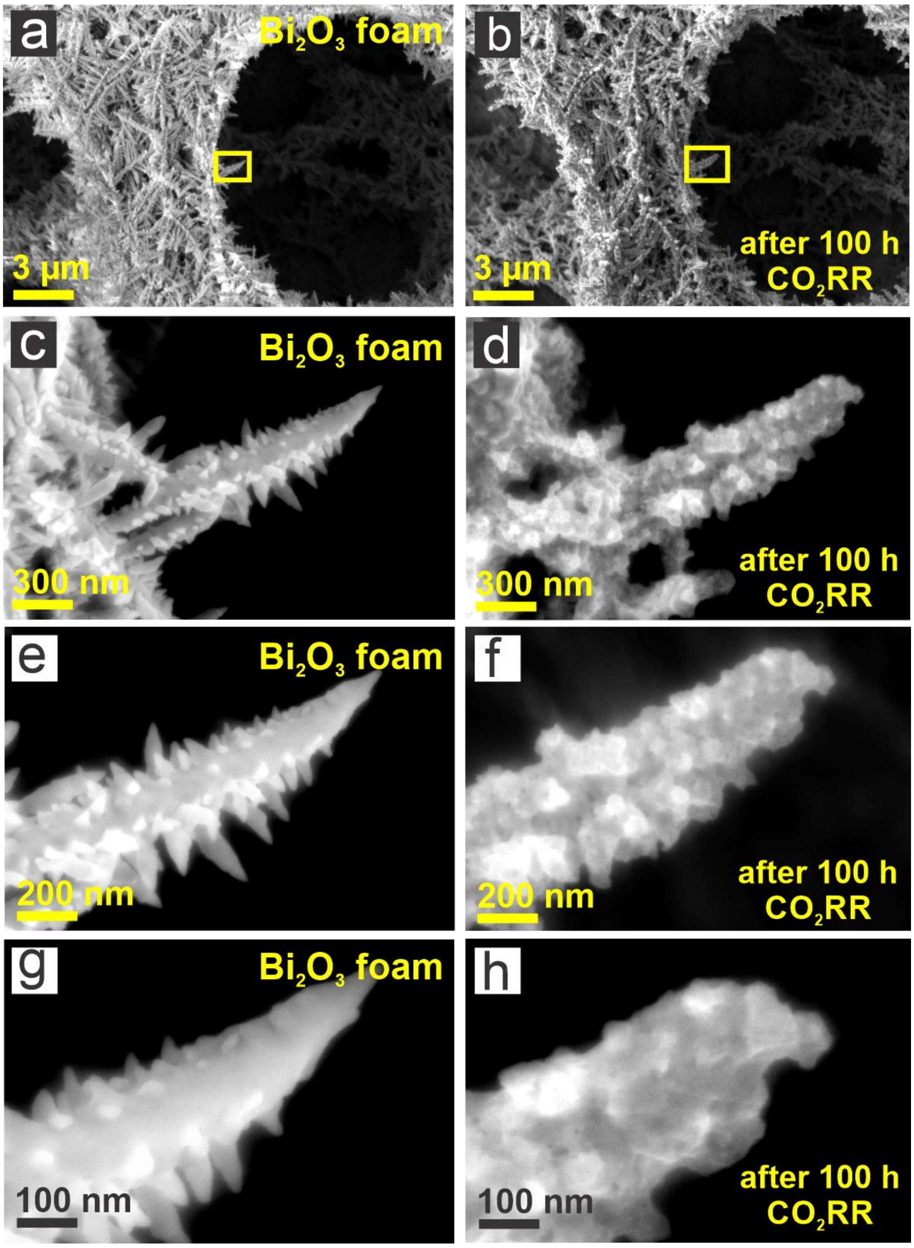

Figure S27. Identical location (IL) SEM inspection of the Bi_2O_3 foam catalyst on GDE (20 s deposition time; after annealing at 300 °C in air for 12 h) before and after 100 h of electrolysis at –0.6 V vs. RHE in the CO_2-sat. 0.5 M $KHCO_3$ electrolyte. The morphology of the catalyst after 100 h of electrolysis is representative for the oxide/sub-carbonate/Bi_{met} composite.

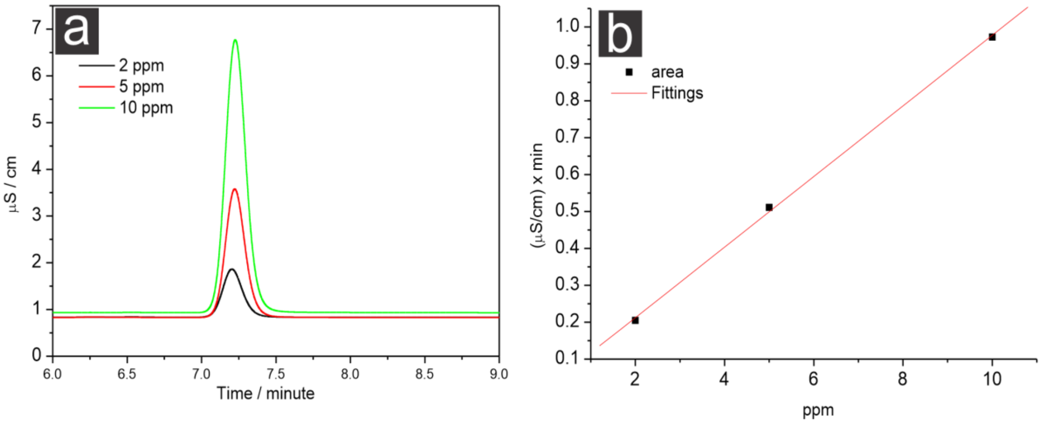

c

Formate conc (ppm)	Retention time (minute)	Height (µS/cm)	Area, (µS/cm)x min
2	7.31	1.257	0.205
5	7.32	3.140	0.511
10	7.32	5.911	0.973

Figure S28. (a) Chromatograms of standard formate reference samples used for calibration purposes. Chromatograms were measured for calibration solution containing 2, 5, and 10 ppm formate, respectively. These solutions were prepared from 1000 ppm IC standard solution purchased from Sigma Aldrich. (b) The calibration curve was obtained from the measurement of the standard samples; (c) Table showing the results of the calibration measurements in terms of formate retention times, peak heights and peak areas.

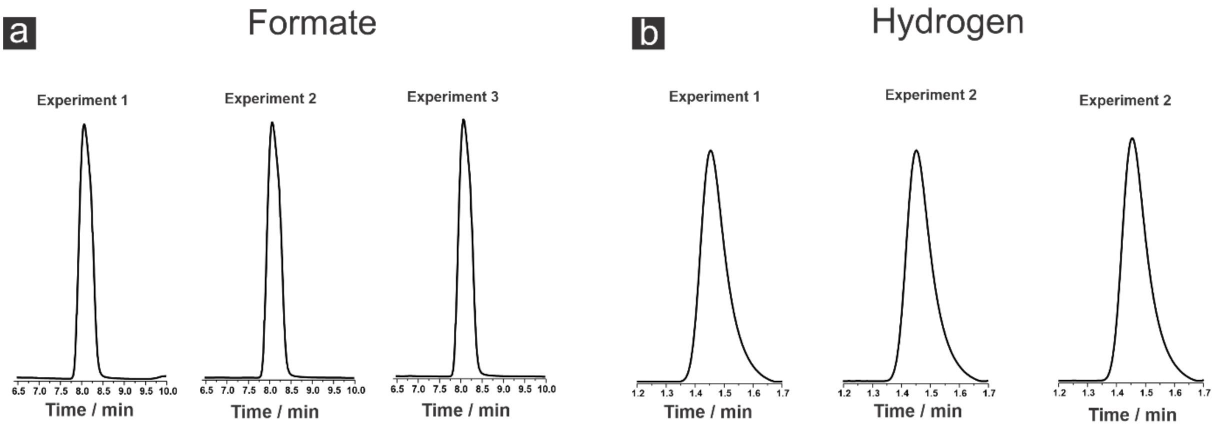

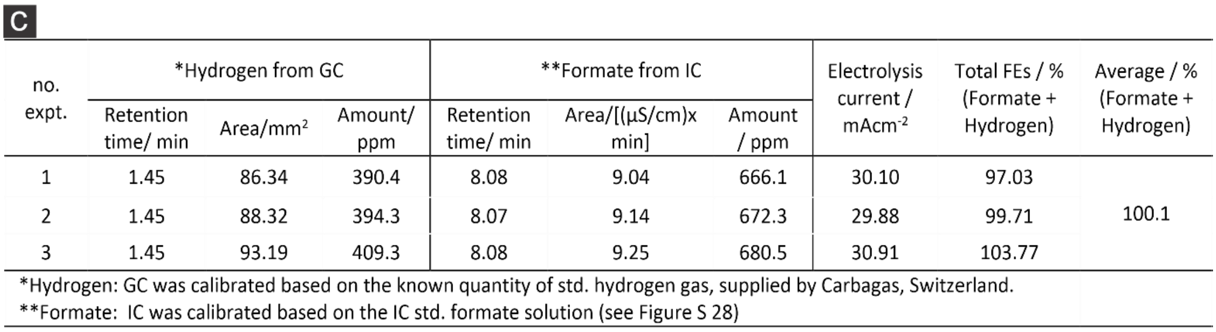

no. expt.	*Hydrogen from GC			**Formate from IC			Electrolysis current / mAcm^{-2}	Total FEs / % (Formate + Hydrogen)	Average / % (Formate + Hydrogen)
	Retention time/ min	Area/mm^2	Amount/ ppm	Retention time/ min	Area/[(µS/cm)x min]	Amount / ppm			
1	1.45	86.34	390.4	8.08	9.04	666.1	30.10	97.03	100.1
2	1.45	88.32	394.3	8.07	9.14	672.3	29.88	99.71	
3	1.45	93.19	409.3	8.08	9.25	680.5	30.91	103.77	

*Hydrogen: GC was calibrated based on the known quantity of std. hydrogen gas, supplied by Carbagas, Switzerland.
**Formate: IC was calibrated based on the IC std. formate solution (see Figure S 28)

Figure S29. Chromatograms of electrolysis experiments on Bi_2O_3 foam at -1.0 V vs RHE (a) formate (b) hydrogen, obtained from ion-exchange (IC) and gas chromatograph, respectively (c) Table, showing the results of the quantification of hydrogen and formate in terms of retention times, peak areas, and total amount of products in three consecutive repetition of experiments (Electrolysis at -1.0 V, 1 h) for obtaining the average FEs values within the error margin.

Table S1. XRD inspection of 'as prepared' Bi foams and 'Bi_2O_3 foam (after annealing). The 2ϴ values corresponding to the phases of Bi and Bi_2O_3. The presented data correspond to Fig. 3a.

'as prepared' Bi foams		Bi_2O_3 foam (after annealing)	
2ϴ	**h k l**	**2ϴ**	**h k l**
22.46	(003)	27.92	(201)
27.29	(012)	31.65	(220)
38.05	(104)	32.56	(211)
39.61	(110)	38.29	(301)
44.57	(015)	41.08	(212)
45.99	(006)	41.85	(320)
48.68	(202)	44.91	(321)
56.03	(024)	46.15	(222)
59.24	(107)	46.67	(400)
61.09	(205)	48.21	(410)
62.12	(116)	51.01	(411)
64.66	(122)	54.05	(203)
67.50	(018)	55.36	(431)
70.70	(214)	57.61	(421)
71.85	(300)	58.88	(412)
74.14	(027)	59.51	(431)
75.41	(303)	61.80	(430)
85.31	(220)	66.15	(004)
86.97	(217)	68.32	(440)
89.98	(131)	69.05	(432)
91.54	(312)	74.01	(610)
-	-	75.39	(601)
-	-	75.81	(224)
-	-	77.28	(442)
-	-	77.82	(620)
-	-	85.75	(631)
-	-	86.55	(622)

Table S2. Time evolution of the Bi content in the CO_2-sat. 0.5 M $KHCO_3$ electrolyte solution determined by ICP-MS under potentiostatic conditions. Freshly-prepared Bi_2O_3 foams (after annealing at 300 °C for 12 h in air) were used as the catalyst. The presented data correspond to Fig. 7.

	Bi content in ppm at different electrolysis time during ec-CO_2RR at different applied potentials (V vs. RHE)					
Electrolysis time / min	**-0.3 V**	**-0.4 V**	**-0.5 V**	**-0.6 V**	**-1.1 V**	**-1.8 V**
1	0.298±0.008	0.269±0.009	0.237±0.005	0.212±0.004	0.112±0.003	0.104±0.002
2	0.382±0.013	0.308±0.010	0.252±0.007	0.207±0.005	0.113±0.003	0.103±0.002
3	0.399±0.013	0.339±0.012	0.252±0.008	0.205±0.005	0.120±0.003	0.100±0.003
4	0.430±0.016	0.348±0.010	0.251±0.006	0.200±0.004	0.120±0.003	0.102±0.002
5	0.428±0.014	0.324±0.009	0.250±0.006	0.204±0.004	0.122±0.003	0.102±0.003
10	0.380±0.013	0.305±0.007	0.241±0.006	0.196±0.005	0.113±0.002	0.110±0.002
15	0.419±0.010	0.301±0.008	0.240±0.007	0.201±0.004	0.116±0.003	0.104±0.003
20	0.418±0.012	0.329±0.010	0.233±0.006	0.190±0.005	0.115±0.003	0.105±0.003
30	0.406±0.011	0.316±0.012	0.226±0.007	0.183±0.004	0.113±0.003	0.100±0.002
40	0.403±0.021	0.322±0.011	0.221±0.006	0.183±0.005	0.111±0.003	0.116±0.003
50	0.403±0.011	0.316±0.009	0.216±0.006	0.176±0.004	0.107±0.002	0.091±0.002
60	0.404±0.014	0.312±0.009	0.210±0.006	0.170±0.005	0.106±0.002	0.100±0.003

Table S3. Faradaic efficiency (FE) values at different applied electrolysis potential of 1 h potentiostatic *ec*-CO_2RR over the *ap* Bi/Bi_2O_3 foam, Bi_2O_3 /*oc-d* Bi foam on GDE support (300 °C, 12 h, in air) and Bi foil (reference). The presented data correspond to Fig. 8a.

	Faradaic efficiency (FE) %					
Potential (vs. RHE)	*ap* Bi/Bi_2O_3 foam on GDE support		Bi_2O_3 foam /*oc-d* Bi foam on GDE support		Bi foil (reference)	
	H_2	Formate	H_2	Formate	H_2	Formate
-0.3	-	-	23.93±1.33	76.07±3.33	-	-
-0.4	-	-	04.25±0.23	95.75±5.14	-	-
-0.5	-	-	03.09±0.16	96.91±5.24	-	-
-0.6	53.00±2.10	47.30±2.23	0.9±0.051	100.09±05.0	66.40±6.64	33.60±3.36
-0.8	05.00±0.50	95.33±5.13	02.14±0.11	97.86±4.38	45.00±4.50	55.00±5.50
-1.0	05.70±0.57	94.30±4.43	01.00±0.1	99.01±4.45	57.60±2.76	42.40±4.24
-1.2	04.66±0.46	95.34±4.13	1.0±0.05	100.10±5.0	62.88±3.14	37.12±3.71
-1.3	09.16±0.61	90.84±3.28	02.15±0.12	97.85±4.38	80.68±4.03	19.32±1.93
-1.4	08.78±0.77	91.22±3.31	03.08±0.30	96.92±4.37	89.16±4.51	10.84±1.08
-1.5	07.88±0.58	92.12±3.11	01.37±0.09	98.63±4.33	95.35±4.73	04.65±0.46
-1.6	07.71±0.57	92.30±2.63	06.33±0.33	93.67±4.18	96.55±5.75	0
-1.8	10.50±0.55	89.30±4.13	09.67±0.26	90.33±4.01	100±5.0	0
-2.0	42.67±2.16	57.33±4.21	39.81±1.28	60.19±3.01	100±5.0	0

Table S4. Partial current density values at different applied electrolysis potential of 1 h potentiostatic *ec*-CO_2RR over the *ap* Bi/Bi_2O_3 foam, Bi_2O_3 /*oc-d* Bi foam on GDE support (300 °C, 12 h, in air) and Bi foil (reference). The presented data correspond to Fig. 8b.

	Partial Current Density (mA cm^{-2})		
Potential (vs. RHE)	*ap* Bi/Bi_2O_3 foam on GDE support	Bi_2O_3 foam /*oc-d* Bi foam on GDE support	Bi foil (reference)
-0.3	-	-0.17±0.01	-
-0.4	-	-0.49±0.04	-
-0.5	-	-0.85±0.08	-
-0.6	-0.95±0.09	-1.06±0.10	-0.667±0.066
-0.8	-9.12±0.91	-10.13±0.61	-2.924±0.292
-1.0	-27.49±2.74	-30.53±3.16	-7.144±0.714
-1.2	-47.10±3.11	-52.31±5.23	-7.741±0.774
-1.3	-57.72±4.17	-64.11±6.41	-3.927±0.392
-1.4	-66.47±5.64	-73.82±5.23	-1.794±0.179
-1.5	-75.80±4.58	-84.18±5.11	-1.139±0.113
-1.6	-79.27±6.92	-88.04±6.31	0.000
-1.8	-67.15±5.71	-74.57±5.15	0.000
-2.0	-53.22±4.25	-59.11±4.31	0.000

Table S5 Gravimetrically determined masses (mg/cm^{-2}) of electrodeposited Bi as a function of deposition time

Batch 1			
Dep. Time (s)	**C foil (mg/cm^{-2})**	**Cu foil (mg/cm^{-2})**	**GDE (mg/cm^{-2})**
5	0.6±0.01	1.4±0.05	0.5±0.001
20	3.1±0.06	3.5±0.1	2.7±0.05
40	6.1±0.09	6.8±0.1	5.7±0.15
60	13.1±0.05	13.5±0.05	12.9±0.05

Batch 2			
Dep. time (s)	**C foil (mg/cm^{-2})**	**Cu foil (mg/cm^{-2})**	**GDE (mg/cm^{-2})**
5	0.62±0.01	1.5±0.01	0.5±0.01
20	2.98±0.06	3.3±0.06	2.8±0.06
40	5.92±0.09	6.6±0.1	6.0±0.09
60	13.1±0.05	13.6±0.05	13±0.05

Table S6 Comparison of the $FE_{formate}$ values for the Bi_2O_3 catalysts (after annealing at 300 °C in air for 12 h) on three different substrates at different deposition times.

E *vs* RHE	**5 s**	**10 s**	**20 s**	**40 s**	**60 s**
			Cu foil		
-0.3 V	79±3.95	84±4.20	77.5±3.87	88±4.40	85±4.25
-0.6 V	66±3.30	78±3.90	99±4.95	91±4.55	84±4.20
-0.8 V	81±4.05	86±4.30	98.6±4.93	95±4.75	87±4.35
-1.0 V	73±3.65	86±4.30	95±4.75	84±4.20	88±4.40
			Carbon foil		
-0.3 V	75±3.75	72±3.60	83±4.15	80±4.01	79±3.95
-0.6 V	85±4.25	79±3.95	89±4.45	90±4.50	84±4.20
-0.8 V	81±4.05	87±4.35	95±4.75	91±4.55	77±3.85
-1.0 V	85±4.25	87±4.35	99±4.95	98±4.90	79±3.95
			GDE		
-0.3 V	73±3.65	76±3.80	76.07±3.80	80±4.00	79±3.95
-0.6 V	85±4.25	72±3.60	100.0±5.00	81±4.05	87±4.35
-0.8 V	93±4.65	86±4.30	97.86±4.89	90±4.50	88±4.40
-1.0 V	95±4.75	81±4.05	99.01±4.95	97±4.85	92±4.60

7.3. Activation of bimetallic AgCu foam electrocatalysts for ethanol formation from CO_2 by selective Cu oxidation/reduction

Authors: Abhijit Dutta, **Iván Zelocualtecatl Montiel**, Rolf Erni, Kiran Kiran, Motiar Rahaman, Jakub Drnec, Peter Broekmann

Nano Energy **68** (2020) 104331. DOI: https://doi.org/10.1016/j.nanoen.2019.104331

Highlights: This paper reports the synthesis, characterization, and electrochemical performance of a bimetallic $Ag_{15}Cu_{85}$ foam catalyst produced using the dynamic hydrogen bubble template electrodeposition approach. The as-deposited catalyst is selective for CO at low overpotentials ($FE_{CO} = 81.45\%$, $PCD_{CO} = –0.24$ mA cm^{-2} at –0.3 V *vs.* RHE) and for C_2H_4 at higher overpotentials ($FE_{C2H4} = 36.56\%$, $PCD_{C2H4} = –11.32$ mA cm^{-2} at –1.1 V *vs.* RHE). The $Ag_{15}Cu_{85}$ foam thermally activated at 200˚C for 12 h presents high selectivity for alcohol formation ($FE_{EtOH} = 33.7\%$, $PCD_{EtOH} = –8.67$ mA cm^{-2} and $FE_{PrOH} = 6.9\%$ and $PCD_{PrOH} = –0.3$ mA cm^{-2} at –1.0 V and –0.9 V *vs.* RHE, respectively). The corresponding thermal activation transforms the Cu in the bimetallic system into a mixture of crystalline Cu_2O and amorphous CuO. In contrast, Ag remains in its metallic state because of the thermal instability of Ag_2O. This thermal activation provides high stability and selectivity of the $Ag_{15}Cu_{85}$ catalyst towards ethanol formation for 100 h of continuous electrolysis. Scanning electron microscopy images before and after electrolysis experiments show structural and composition changes. The catalyst morphology seems to be unaffected at the µm-length scale; however, minor morphological changes are visible at the nm-length scale (small particles appearing) after extended electrolysis times. Both *operando* X-ray diffraction and *operando* Raman spectroscopy demonstrate that the oxide reduction is completed before the electrochemical CO_2 reduction sets in.

Contributions: In this project, I was one of the main persons responsible for the synthesis, characterization, and electrochemical experiments. I contributed equally with Dr. Abhijit Dutta to the analysis and discussion of the data, figure preparation, and redaction of the paper.

Nano Energy 68 (2020) 104331

Contents lists available at ScienceDirect

Nano Energy

journal homepage: http://www.elsevier.com/locate/nanoen

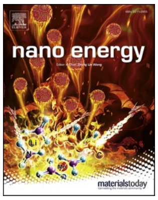

Full paper

Activation of bimetallic AgCu foam electrocatalysts for ethanol formation from CO_2 by selective Cu oxidation/reduction

Abhijit Dutta[a,*,1], Iván Zelocualtecatl Montiel[a,1], Rolf Erni[b], Kiran Kiran[a], Motiar Rahaman[a], Jakub Drnec[c], Peter Broekmann[a,**]

[a] Department of Chemistry and Biochemistry, University of Bern, Freiestrasse 3, Bern, 3012, Switzerland
[b] Electron Microscopy Center, Swiss Federal Laboratories for Materials Science and Technology (EMPA), Überlandstrasse 129, 8600, Dübendorf, Switzerland
[c] European Synchrotron Radiation Facility (ESRF), 71 Avenue des Martyrs, 38000, Grenoble, France

ARTICLE INFO

Keywords:
CO_2 electro-reduction
AgCu catalyst
Ethanol
Operando X-ray diffraction
Operando Raman spectroscopy

ABSTRACT

Bimetallic AgCu metal foams (15 at% Ag, 85 at% Cu) have been synthesized by means of an additive-assisted electrodeposition process using the dynamic hydrogen bubble template approach. Ag and Cu remain fully phase-segregated in the as deposited bimetallic foam exhibiting a high degree of dispersion of pure nm-sized Ag domains embedded in the Cu matrix. An activation of this bimetallic material towards ethanol formation is achieved by thermal annealing of the as deposited foam under mild conditions (200 °C for 12 h). Such annealing quantitatively transforms the Cu in the bimetallic system into a mixture of crystalline Cu_2O and amorphous CuO whereas the Ag remains in its metallic state due to the thermal instability of Ag_2O above temperatures of 180 °C. The selective oxidation of Cu in the bimetallic $Ag_{15}Cu_{85}$ catalyst goes along with an enrichment of Cu oxides on the surface of the formed mixed $AgCu_xO$ foam.

Both *operando* X-ray diffraction and *operando* Raman spectroscopy demonstrate, however, that the oxide reduction is completed before the electrochemical CO_2 reduction sets in. The thus formed oxide-derived (OD) bimetallic $Ag_{15}Cu_{85}$ foam catalyst shows high selectivity towards alcohol formation with Faradaic efficiencies of $FE_{EtOH} = 33.7\%$ and $FE_{n\text{-}PrOH} = 6.9\%$ at −1.0 V and −0.9 V vs RHE, respectively. Extended electrolysis experiments (100 h) indicate a superior degradation resistance of the oxide-derived bimetallic catalyst which is ascribed to the effective suppression of the C1 hydrocarbon reaction pathway thus avoiding irreversible carbon contaminations appearing in particular during methane production.

1. Introduction

In recent years, the electrochemical conversion of environmentally harmful CO_2 into products of higher value is considered a promising and technologically feasible approach to mitigate the increase of atmospheric CO_2 [1–3] which reaches already levels above 410 ppm [4]. Because of this global threat, a paradigm shift currently drives both the energy and mobility sectors away from fossil-based (coal, oil, and natural gas) towards renewables (hydro, wind, and solar) energy sources. The chemistry sector follows this trend which will surely affect entire production chains of most commodity and fine chemicals. This so-called ‘energy transition’ can therefore be considered as a truly intersectorial challenge which calls for new transsectorial strategies. Several technologies including capture [5] and sequestration [6] have already been devised in order to reduce levels of CO_2 in the atmosphere. Amongst these, CO_2 reduction by electrochemical means [7] deserves particular attention as it can transform CO_2 directly back into synthetic fuels (so-called e-fuels) or other platform chemicals of high value [1,2]. In particular the electrochemical co-electrolysis of water and CO_2 has a great potential to directly interlink the energy sector to the chemistry sector (see ‘Rheticus’ process as a prime example thereof) [8]. The CO_2 reduction reaction might become not only economically feasible in the future but also truly sustainable, in particular when the surplus of renewables originating from solar radiation, wind power, and hydro sources is used as energy input to drive this electrochemical CO_2 conversion. This so-called ‘power to value’ concept might, in future, become

---

* Corresponding author.
** Corresponding author.
E-mail addresses: abhijit.dutta@dcb.unibe.ch (A. Dutta), peter.broekmann@dcb.unibe.ch (P. Broekmann).
[1] Authors contributed equally to this work.

https://doi.org/10.1016/j.nanoen.2019.104331
Received 23 August 2019; Received in revised form 23 October 2019; Accepted 25 November 2019

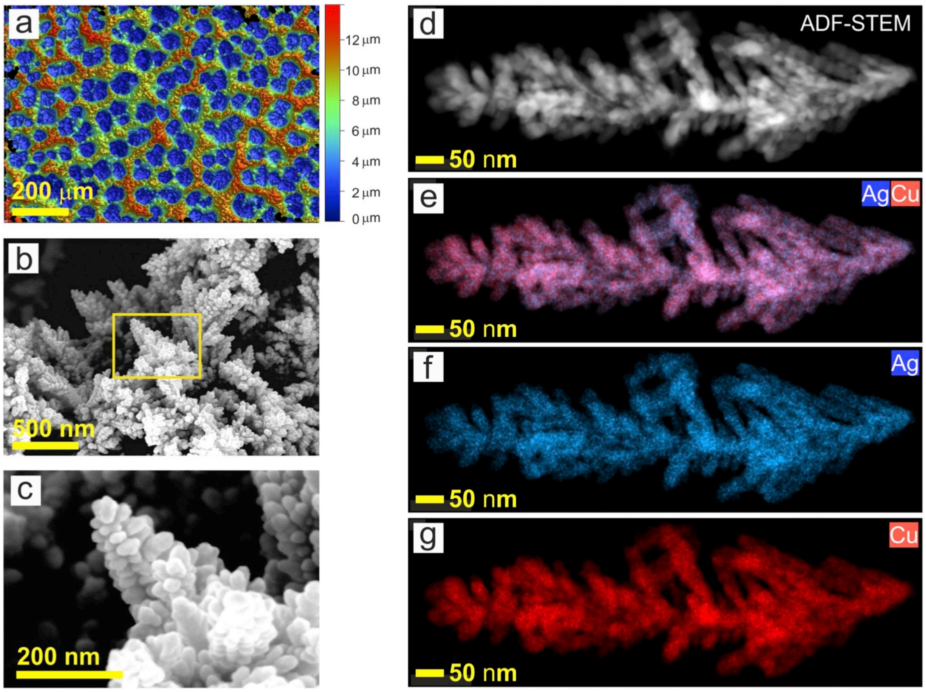

Fig. 1. Morphological and compositional analysis of the as deposited $Ag_{15}Cu_{85}$ foam deposited on a Cu foil substrate. a) White-light interferometric image of the bimetallic foam; b) and c) SEM analysis; d) ADF-STEM analysis of an individual dendrite; e) EDX mapping of the dendrite (Ag, Cu); f) spatial distribution of the Ag component; g) spatial distribution of the Cu component.

one important element among others contributing to the closing of the anthropogenic carbon cycle [3,9,10].

This electrocatalytic process typically relies on the oxidative splitting of water (OER: Oxygen Evolution Reaction) and the reductive conversion of CO_2 (CO_2RR: CO_2 Reduction Reaction). Oxygen (O_2) is the only product that can form on the anode side when using aqueous environments, irrespective of which anode material is used (e.g., RuO_2, IrO_2, or FeNi based systems) [11,12]. However, a variety of different CO_2RR products are typically produced on the cathode side [7], ranging from formate [13–15], carbon monoxide (CO) [16–27], saturated and non-saturated hydrocarbons (e.g. methane [16,20,28], ethylene [29–32]) to oxygenates of various chain length and energy density (e.g., methanol [20,28,33], ethanol [29,34,35], and n-propanol [34,36]). The specific CO_2RR product distribution is mainly governed by chemical nature [7], the structure, and the morphology [30] of the electrocatalyst. Cu stands out in the group of monometallic CO_2RR catalysts [7] as it is capable to produce hydrocarbons [7,16,37–41] and oxygenates [32–35] of variable C–C chain length.

In particular, the multi-hydrocarbon and oxygenate formation from CO_2 typically requires the balanced interaction between catalyst active sites and chemisorbed *CO (Sabatier principle), the latter being considered as the key intermediate in the CO_2RR. Such balance guarantees a sufficiently high abundance and residence time of the *CO at the reactive sites as mechanistic pre-requisites to undergo further C–C coupling and reductive hydrogenation reactions [42]. For several CO_2RR catalysts, Kuhl et al. [28] derived a Volcano like interrelation between the *CO binding strength and experimentally determined CO_2RR current densities at -0.8 V vs RHE. Au and Ag were found on the low binding energy side of the volcano curve, rationalizing the facile release of the formed CO as main product when the CO_2RR is carried out over Ag and Au. Cu was found on the high binding energy side next to the volcano maximum with the right balance of the *CO binding strength to prevent irreversible poisoning of the catalyst (e.g., as in case of Pd [13,15]) but allowing for C–C coupling reactions.

One major drawback of the Cu catalysts is, however, their poor product selectivity [7]. One recently discussed experimental concept towards improved selectivity of C–C coupled hydrocarbons (e.g., ethylene) is based on the use of bimetallic materials consisting of a CO producer (e.g., Ag, Au, or Zn) and the C–C coupler (Cu) [29,43–46]. A high abundance of CO is achieved, e.g. through selective CO_2RR on the Ag component in the bimetallic system. CO is subsequently transported to Cu sites in close proximity that are active for the C–C coupling. Short diffusion paths from Ag to Cu on the catalyst surface are essential for this 'CO spillover' concept. Further, CO_2RR efficiencies are per se improved when using AgCu bimetallics as the Ag reveals an intrinsically higher overpotential for the parasitic hydrogen evolution reaction (HER). It is the high surface concentration of chemisorbed *CO which leads to a further suppression of the HER by blocking surface sites, at least within a certain range of potentials applied [44].

In this present study, we further develop this approach by selectively activating the Cu component in the bimetallic AgCu system for alcohol formation. This can be achieved by thermal annealing, which leads to the selective formation of Cu oxides, whereas the Ag remains in its metallic state. Electroreduction of the formed oxidic Cu precursor under CO_2RR conditions transforms the bimetallic AgCu system into a C–C coupling and alcohol forming catalyst. The latter is denoted in the following as oxide-derived (OD) $Ag_{15}Cu_{85}$.

A combination of *operando* Raman spectroscopy and X-ray diffraction is used, along with TEM, STEM and so-called identical location (*IL*)-SEM imaging, to probe compositional and structural changes of the catalyst which go along with its activation for alcohol production.

For the preparation of model catalysts we apply the so-called dynamic hydrogen bubble template approach, originally developed for the electrodeposition of monometallic metal foams [47,48], to the bimetallic AgCu system [27]. Also we will show that the use of complexing plating additives (e.g., citrate) plays a vital role for the required dispersion of the Ag in the Cu matrix.

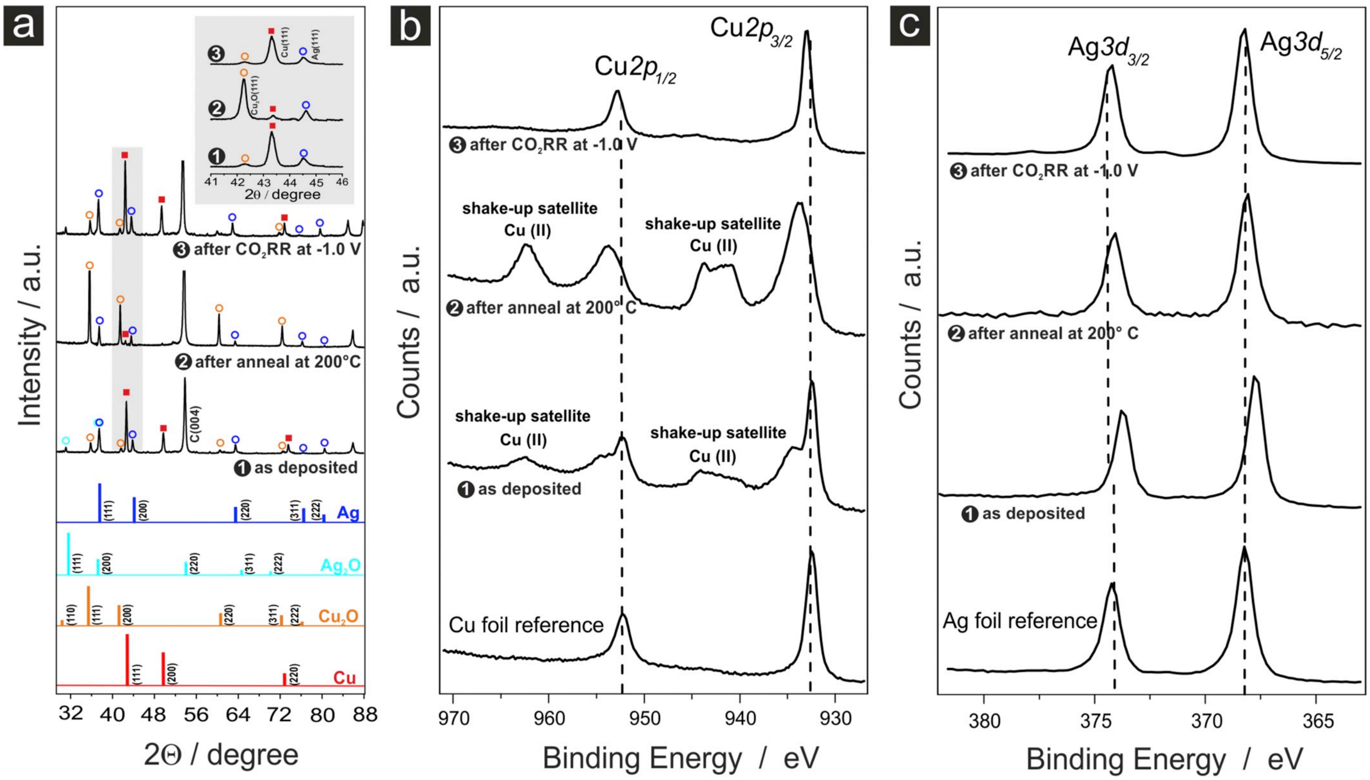

Fig. 2. a) *Ex situ* XRD analysis of the as deposited $Ag_{15}Cu_{85}$ foam, the annealed foam (12 h at 200 °C), and the OD-$Ag_{15}Cu_{85}$ (after 1 h CO_2RR at −1.0 V vs RHE); b) and c) Corresponding XPS analysis of the bimetallic foam.

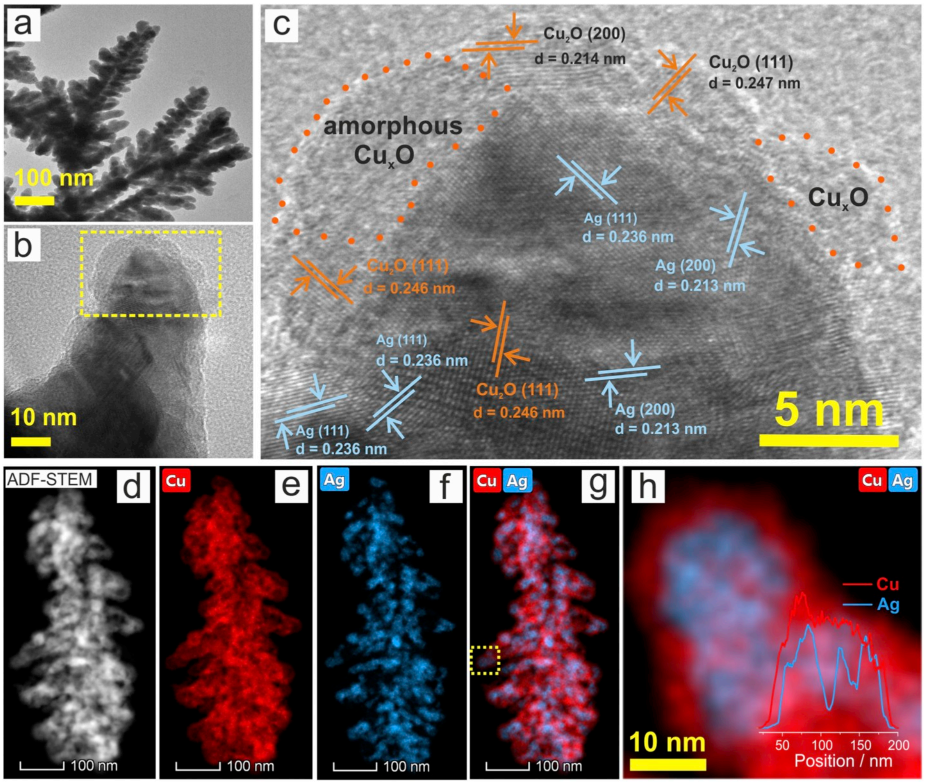

Fig. 3. Structural and compositional analysis of the thermally annealed $Ag_{15}Cu_{85}$ (12 h at 200 °C) foam; a) - c) HR-TEM micrographs of the thermally annealed $Ag_{15}Cu_{85}$ foam; d) ADF-STEM micrograph of the annealed $Ag_{15}Cu_{85}$ foam; e) – h) EDX mapping of an isolated dendrite of the annealed $Ag_{15}Cu_{85}$ foam. The yellow square in panel g highlights the section shown in panel h. The inset in panel h depicts one-dimensional line-scans over the feature (exhibited from panel g).

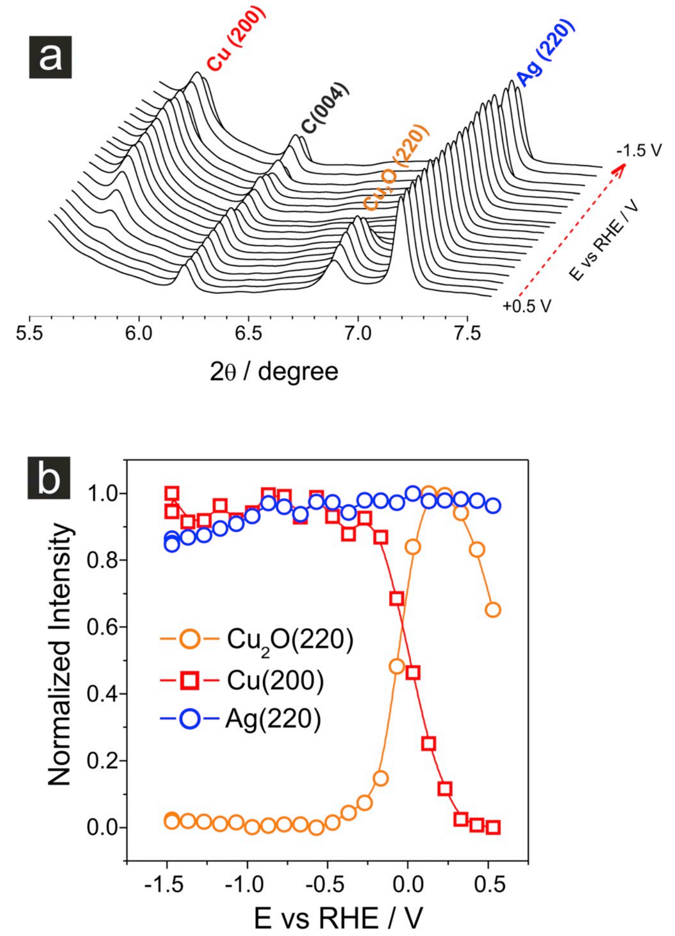

Fig. 4. *Operando* XRD experiment demonstrating the electro-reduction of Cu_2O in the annealed $Ag_{15}Cu_{85}$ foam as function of the applied electrode potential; a) Potential dependent XRD spectra; b) Integrated and normalized intensities derived from spectra shown in panel a (orange: integrated intensity of the Cu_2O (220) peak; red: integrated intensity of the Cu (200) peak; blue: integrated intensity of the Ag (220) peak).

2. Results and discussion

2.1. Synthesis and activation of the $Ag_{15}Cu_{85}$ foam catalyst

The as deposited $Ag_{15}Cu_{85}$ foam - The bimetallic $Ag_{15}Cu_{85}$ foam catalyst (this notation refers to the bulk composition derived from the ICP-OES analysis, see Table S1) has been electrodeposited on a Cu foil substrate at $j = -3$ A cm^{-2} (20 s) using a plating bath containing 1.5 M H_2SO_4, 20 mM $CuSO_4$, 2 mM Ag_2SO_4, and 0.1 M $Na_3C_6H_5O_7$. Key to this process is the hydrogen evolution reaction (HER, secondary process) that is superimposed on the metal deposition (primary process) when such high cathodic current densities are applied [30,47,48]. Hydrogen bubbles, which appear on the cathode during the massive HER, thereby serve as transient geometric template for the metal foaming process [30,47,48]. Proton consumption and water splitting (OH^- formation) lead to the appearance of pronounced *pH* gradients at the interface thus resulting into the deprotonation of the citric acid (10^{-1} M tri-sodium citrate di-hydrate) in the reaction boundary layer [18]. The formed citrate tends to chemisorb on the cathode thus altering the nucleation and growth characteristics of the emerging foam deposit [18]. In addition, citrate anions undergo fast chelating reactions with the Ag^+ and Cu^{2+} cations in the near electrode surface reaction boundary layer [18]. It can therefore be assumed that the actual deposition process occurs from a complexed metal ion solution produced *in situ* in the near surface electrolyte (see schematic in Fig. S1) [18]. In this present study, we restrict ourselves to the discussion of one particular composition of the bimetallic AgCu foam catalyst containing 15 at% Ag and 85 at% Cu. Detailed compositional studies of this kind of catalysts are hampered by the fact that any changes of the bath composition (e.g., the Ag^+: Cu^{2+} ion ratio or the citrate additive concentration) will inevitably affect the Faradaic efficiencies of hydrogen production and metal deposition [27]. As a consequence of that not only the chemical composition of the deposit is altered but also its morphology on various length scales [27]. Compositional and morphological effects (e.g., pore size distribution, morphology of the pore side-walls) can therefore not be studied independently from each other when applying the dynamic hydrogen bubble approach [48] to these bimetallic systems.

Fig. 1 shows representative white-light interferometry (panel a) and SEM micrographs (panels b and c) of the as deposited $Ag_{15}Cu_{85}$ foam which resembles in appearance to the pure Cu foams with their multilevel 3D architecture of interconnected pores [30,48,49]. A cross-sectional SEM inspection reveals a thickness of ~18 μm (see Fig. S2) of the as deposited $Ag_{15}Cu_{85}$ foam. A similar bimetallic AgCu foam has recently been reported by Kottakat et al. [27] which has, however, been deposited from an additive-free plating bath and showed therefore different structural and morphological characteristics compared to the one discussed herein. The mean outermost surface pore diameter of the $Ag_{15}Cu_{85}$ foam discussed herein amounts to ~25 μm. Note that these metal foams typically reveal a gradient in pore size along the surface normal due to the coalescence of hydrogen bubbles in the course of the metal deposition [30,48]. Similar to the pure Cu metal foams deposited from an additive-free Cu plating bath [30,48,49], also the sidewalls of the bimetallic $Ag_{15}Cu_{85}$ foam reveal a dendritic nature with individual dendrites composed of AgCu particles having dimensions of <50 nm (panel c). Note that individual dendrites in the pure Cu foams deposited from additive-free plating baths are composed of shaped Cu crystallites showing preferential (111) and (100) facets on their surface [49]. No such texturing is, however, visible on the bimetallic $Ag_{15}Cu_{85}$ foam. Also note that pure Cu catalysts deposited under identical plating conditions (current density and plating time) in the presence of the citrate additive do not show a well-developed foam morphology at all (Fig. S3) thus demonstrating that the presence of the citrate not only impacts the nucleation and growth of the metal deposition process but also the formation and release of the hydrogen bubbles from the electrode.

The correlation between the catalyst morphology and its composition has been achieved by means of ADF-STEM imaging (Fig. 1d) combined with EDX mapping, the latter providing information on the spatial distribution of Cu and Ag, respectively (Fig. 1e–g). The EDX analysis confirms that the electrodeposition approach yields bimetallic foams with a high degree of dispersion of Ag in the Cu matrix, which is considered as a crucial prerequisite for the intended CO 'spillover' concept [50]. The presence of the citric acid additive in the plating bath is found to be essential to yield a bimetallic catalyst material where the nm-sized Ag and Cu domains form a maximum of phase boundaries. By contrast, the respective metal foam deposited in the absence of citric acid resembles more a physical mixture of loosely packed Ag and Cu particles (see Fig. S4).

Activation of the $Ag_{15}Cu_{85}$ foam: ex situ XRD and XPS analysis - An activation of the as deposited $Ag_{15}Cu_{85}$ foam for the selective formation of ethanol from CO_2 requires a further treatment which is typically based on an oxidation of the catalyst material. Both thermal annealing [34,49,51–55] and the exposure of Cu-based catalysts to oxygen plasma [40,56,57] have already been demonstrated to be beneficial for the formation of oxidic catalyst precursors which, under CO_2RR conditions, reductively transform into their metallic form thereby creating those reactive sites which are actually active towards C–C coupling and the formation of alcohols [34]. In addition, the C1 hydrocarbon (methane) reaction pathway gets effectively suppressed by this oxidation/reduction cycle [34]. This side effect of the thermal treatment has been found to be particularly beneficial for the degradation stability of the

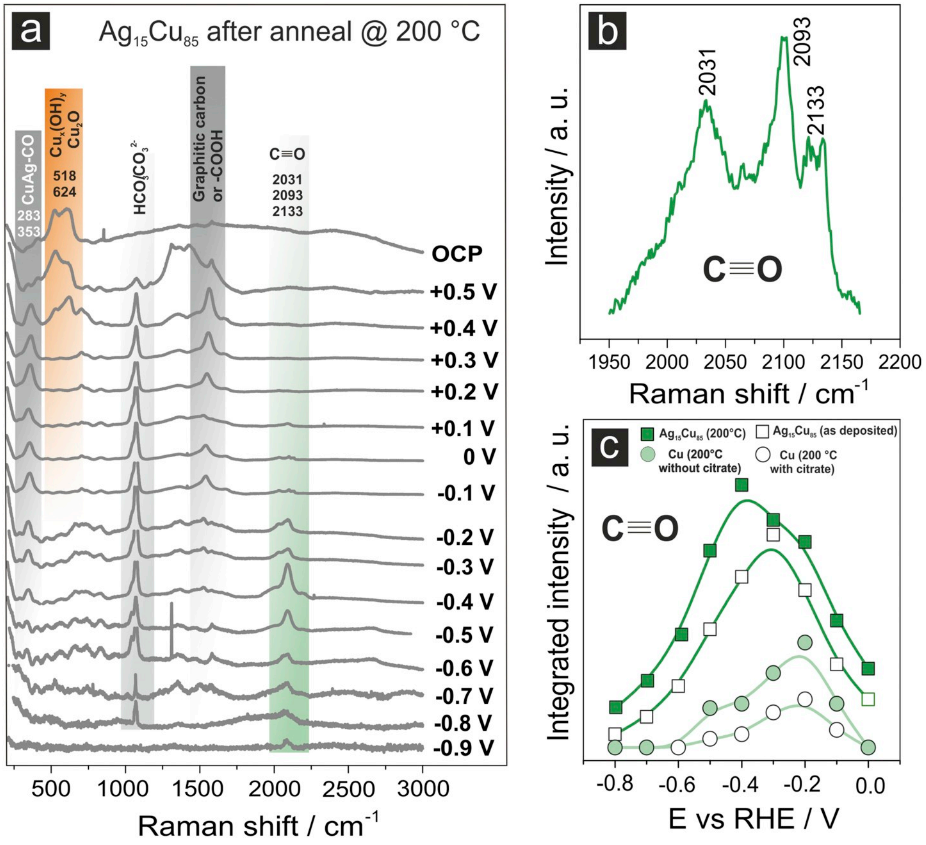

Fig. 5. a) Representative *Operando* Raman spectra of the thermally annealed $Ag_{15}Cu_{85}$ foam (12 h at 200 °C) as function of the applied electrode potential; b) Enlarged section of the operando Raman spectrum of the thermally annealed sample at −0.2 V vs RHE focusing on the intramolecular stretching mode of chemisorbed CO demonstrating three different adsorption sites; c) Integrated intensities of Raman peaks assigned to the intramolecular CO stretching modes. For comparison purposes also the results for the as deposited $Ag_{15}Cu_{85}$ foam and for the pure Cu catalysts (deposited in the presence and absence of citrate and thermally annealed at 200 °C for 12 h) are presented.

CO_2RR catalysts [34]. The formation of methane via the coupled C1/C2 reaction pathway [34,58] typically involves an undesired and irreversible carbonization of the catalyst surface [59–61].

A mild thermal annealing treatment in air at 200 °C was applied for 12 h to the as deposited $Ag_{15}Cu_{85}$ foam. Fig. 2a depicts representative diffraction patterns of the as deposited $Ag_{15}Cu_{85}$ foam, the thermally annealed one, and the catalyst after 1 h of CO_2RR at −1.0 V vs RHE (OD-$Ag_{15}Cu_{85}$ foam). For the sake of interpretability also the respective JCPDS reference data for *fcc* Cu, fcc Ag, Cu_2O and Ag_2O are presented (see also Table S1). From the XRD analysis, it can be concluded that the as deposited $Ag_{15}Cu_{85}$ foam is composed of pure Cu and Ag phases with minor contributions originating from Cu_2O and Ag_2O. Qualitatively similar diffraction patterns of bimetallic CuAg thin films were recently reported by Clark et al. also showing peaks coinciding with those of pure *fcc* Ag and Cu [44]. In the latter case, a small contribution from an AgCu surface alloying was observed. In the present case there are, however, no experimental hints in the XRD analysis for any alloying (see Table S1) in agreement with recent results by Kottakat et al. [27]. These different experimental observations can be rationalized by the particular preparation route of AgCu film formation used by Clark et al. which actually facilitates AgCu surface alloy formation [44]. The phase-segregation of Cu and Ag is indeed expected as the respective binary phase diagram indicates an immiscibility of Ag and Cu for a wide range of temperatures and compositions relevant to this study [50]. Minor oxidic components visible in the diffractogram of the as deposited sample might originate in particular at the surface of the deposit after its emersion from the metal ion containing plating bath and the subsequent drying procedure in air [30,49].

Thermal annealing in air at 200 °C partly transforms the Cu into crystalline Cu_2O whereas the diffraction pattern of metallic Cu almost disappears. Diffraction patterns of crystalline Ag_2O are not detected due to thermal instability of the Ag_2O which decomposes at temperatures above 180 °C [62]. From the XRD analysis it can be concluded that the thermally annealed $Ag_{15}Cu_{85}$ is a mixed metal/oxide ($AgCu_xO$) composite material.

As expected, the post-electrolysis XRD analysis reveals again major contributions from metallic Cu and Ag whereas the oxidic components have almost been disappeared (see also the inset in Fig. 2a). Only trace amounts of crystalline Cu_2O can be detected which have likely been formed on the catalyst surface after the CO_2 electrolysis during exposure of the catalyst to air.

As the XRD experiment is only sensitive to bulk phases revealing long-range translational order, complementary XPS analysis has been applied being more sensitive to the chemical state of the catalyst surface. Panels b and c of Fig. 2 depict Cu*2p* and Ag*3d* core level emissions of the bimetallic catalyst material representing different stages of its preparation and use. As reference, also XPS spectra of pure Ag and Cu foil samples are provided. Obviously, Cu(II) species are already present on the as deposited foam.

This can be deduced from the satellite features on the high binding energy side of the Cu(0)/Cu(I) related Cu*2p* emission. In addition, characteristic shake-up features are visible in the XPS spectrum of the as deposited sample, thus further confirming the presence of Cu(II). Cu(II) related XPS features might originate from residuals of the complexed Cu (II) precursors which were trapped inside the metal foam after its emersion from the plating bath. Note that Cu foams deposited from a non-complexed (citric acid free) solution do not show these characteristic Cu(II) features in the XPS (Fig. S5) [49]. Further, the annealed $Ag_{15}Cu_{85}$ foam sample contains Cu(I) and Cu(II) species which, in this case, can be assigned to oxidic Cu as product of the thermal treatment [49]. The annealing temperature of 200 °C is, however, not high enough to induce sufficient translational order in the formed CuO phase to be detected in the XRD (Fig. 2a) in full agreement with the literature [49]. After the electrolysis, the sample contains metallic Cu as well as minor amounts of cuprous and cupric oxides. The latter can be attributed to the post-electrolysis re-oxidation of the sample when exposed to air in

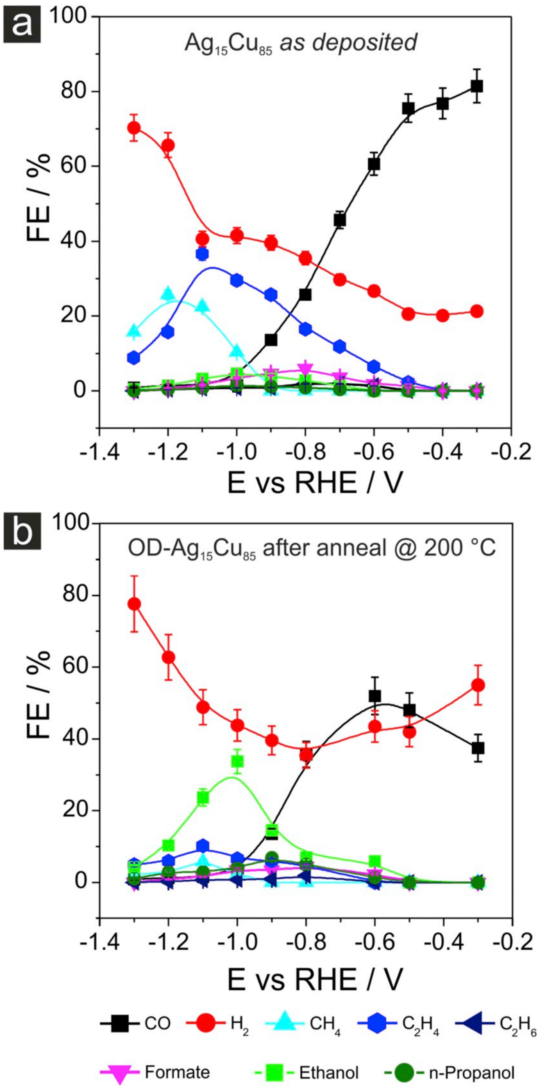

Fig. 6. Potential dependent CO_2RR product distribution for (a) the as deposited $Ag_{15}Cu_{85}$ foam and (b) the (oxide-derived) OD-$Ag_{15}Cu_{85}$ foam catalyst after the annealing at 200 °C.

agreement with the XRD analysis.

Also the Ag*3d* core level emissions of the $Ag_{15}Cu_{85}$ foam (panel c) confirm our *ex situ* XRD analysis. After electrodeposition of the $Ag_{15}Cu_{85}$ foam both Ag(0) and Ag(I) species are observed in the XPS. For instance, the $Ag3d_{5/2}$ peak at BE = 367.9 eV is downward-shifted by ΔBE ≈0.3 eV with respect to the Ag reference (BE($Ag3d_{5/2}$) = 368.2 eV thus indicating the presence of Ag(I) species. One possible origin of the Ag(I) might be residual Ag(I) complexes trapped inside the metal foam after the deposition. Note that similar Ag(I) features appear in the photoemission spectra of pure Ag metal foams deposited from a citrate containing plating bath [18]. In accordance with the XRD analysis, the Ag*3d* core level emission of the annealed $Ag_{15}Cu_{85}$ foam does not show any contribution of Ag(I). This once more confirms the thermal instability of the Ag_2O phase and the $AgCu_xO$ composite nature after its annealing at 200 °C. For the discussion of the CO_2RR product distribution (see below) it is important to note that the relative abundance of Cu and Ag on the catalyst surface differs from the respective bulk composition determined by ICP-OES and further changes in the course of the thermal oxidation/*ec* reduction treatment as evidenced by the quantitative analysis of the Cu*2p* and the Ag*3d* core level emissions. Their integrated intensities (I_{Cu2p}:I_{Ag3d}) change from 62:38 (as deposited) to 91:9 (annealed at 200 °C) and 77:23 (after 1 h CO_2RR at −1.0 V vs RHE). In particular the surface of the annealed foam sample seems to be substantially enriched by (oxidic) Cu. Basis for this quantification was the XPS data set presented in Fig. S6.

This scenario becomes further supported by a combined HR-TEM and ADF-STEM inspection of the annealed $Ag_{15}Cu_{85}$ foam sample (Fig. 3) providing information of the spatial distribution of the metallic Ag and oxidic Cu_xO domains in the bimetallic foam. From the HR-TEM image in Fig. 3c it can be seen that the surface of the dendrite is composed of amorphous Cu_xO and crystalline Cu_2O whereas metallic Ag is found predominantly in the interior of the dendrite (see also the EDX analysis in Fig. 3h). Diameters of the Cu_xO and the metallic Ag domains in the composite are in the range of 4–8 nm. Spatially resolved EDX analysis combined with ADF-STEM imaging (Fig. 3) confirms a uniform dispersion of nm-sized Ag and Cu_xO domains in the bulk of the dendrite as already concluded from the EDX analysis of the as deposited sample (Fig. 1).

Activation of the $Ag_{15}Cu_{85}$ foam: operando XRD and Raman spectroscopic analysis - Applying cathodic electrode potentials relevant for the CO_2RR leads to further structural and compositional changes in the mixed metal-oxide foam involving in particular the electro-reduction of the cupric and cuprous oxides. These compositional changes can be probed under reactive conditions by means of the *operando* XRD technique using characteristic diffraction features of the crystalline Cu_2O as fingerprint for the presence of oxidic copper (Fig. 4a). Fig. 4b depicts the normalized intensities of the (220) diffraction peak of Cu_2O as well as intensities of the Ag and Cu related to (220) and (200) reflections, respectively, as a function of the applied electrode potential. Again, crystalline CuO was not detectable in the XRD due to its amorphous state (see also Fig. 3c). The intensity of Cu_2O related diffraction peaks first increase when going from +0.5 V to +0.25 V vs RHE before dropping down to zero at potentials < −0.5 V vs RHE. Such initial rise in the normalized intensity of the Cu_2O related diffraction peaks can be attributed to the reduction of amorphous CuO to metallic Cu which proceeds via crystalline Cu_2O as an intermediate. In general, the decrease of the Cu_2O related diffraction intensity at potentials < +0.25 V vs RHE is anti-correlated to the raise in the integrated peak intensity of the metallic Cu. Fig. 4 suggests that the reduction of the oxidic Cu 'precursor' is already completed before the CO_2RR sets in (≈-0.3 V vs RHE). The normalized intensity of the Ag related (220) peak remains constant, at least in the potential range relevant for the Cu oxide-metal transition (+0.5 V vs RHE to −0.5 V vs RHE). A certain decrease in the integrated intensity is, however, observed at potentials < −1.0 V vs RHE. One possible explanation might be a preferential leaching of the Ag component under CO_2RR/HER conditions.

Operando Raman spectroscopy further supports the conclusion on the metal-oxide transition occurring at potentials more anodic than the CO_2RR onset. Not only is this technique more sensitive to the chemical state of the catalyst surface than the XRD, it is in addition suitable to probe chemisorbed intermediates of the CO_2RR [27]. Fig. 5a shows a series of potential dependent steady-state Raman spectra covering a potential window from the open circuit potential (OCP) down to −0.9 V vs RHE. According to the literature, the vibrational modes observed at 518 and 624 cm^{-1} originate from $Cu_x(OH)_y$ and Cu_2O species at the catalyst surface [63]. Their peak intensities drop down to zero already at potentials < +0.2 V vs RHE (Fig. 5a). This value is even more positive than the oxide-metal transition probed by the *operando* XRD (Fig. 4). Differences in the observed oxide-metal transition potential might be related to technique specific. Also note that neither the *operando* XRD nor the *operando* Raman spectroscopy can exclude the presence of traces of so-called sub-surface oxygen after completion of the potential-induced oxide-metal transition [64].

CO stretching modes of chemisorbed carbon monoxide appear in the *operando* Raman spectra at applied potentials < +0.1 V vs RHE. The discernable Raman peaks at 2031 cm^{-2}, 2093 cm^{-2}, and 2133 cm^{-2} (Fig. 5b) are due to different adsorption sites of CO chemisorbed either on metallic Cu or on Ag of the $Ag_{15}Cu_{85}$ foam [65,66]. A clear

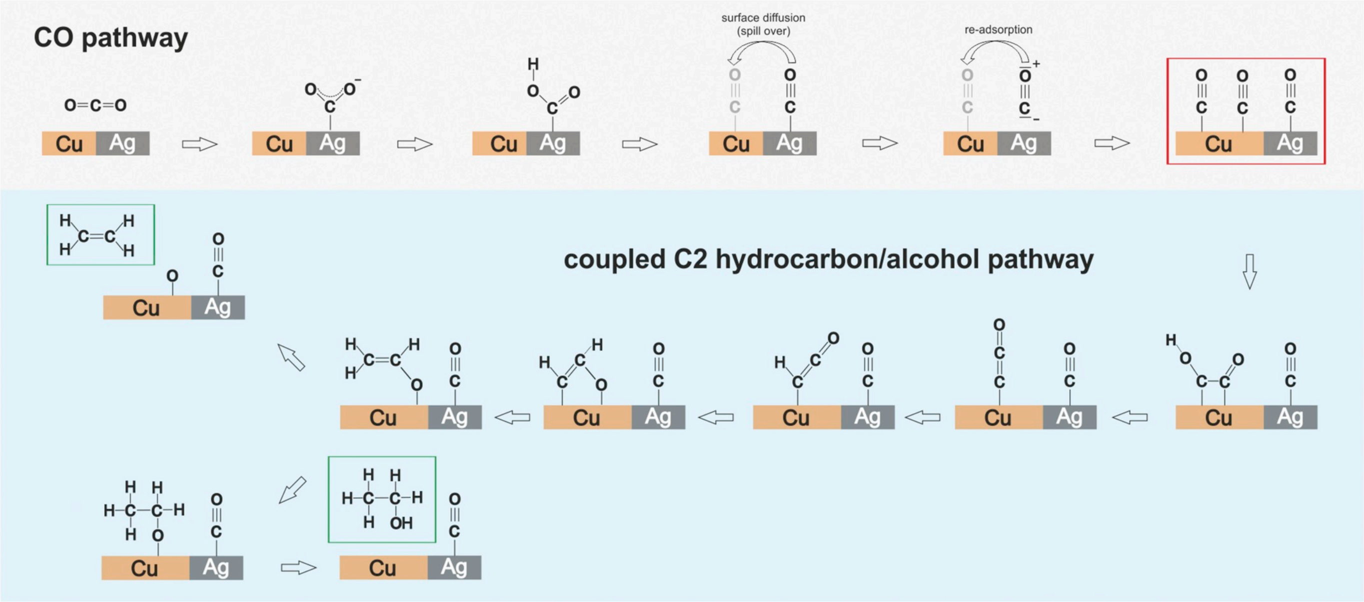

Fig. 7. Proposed reaction scheme illustrating the coupling of the CO pathway and the C2 hydrocarbon/alcohol reaction pathways.

improvement of the bimetallic $Ag_{15}Cu_{85}$ foam with regard to pure Cu catalysts is a higher abundance of chemisorbed CO at more cathodic potentials (Fig. 5c, Fig. S7). Note that the peak maximum of the integrated peak intensity of the CO stretching mode is shifted by ~200 mV towards more cathodic potentials in case of the thermally annealed $Ag_{15}Cu_{85}$ foam. A similar increased abundance of chemisorbed CO is observed for the as deposited $Ag_{15}Cu_{85}$ foam (Fig. 5c). This characteristic feature of the bimetallic $Ag_{15}Cu_{85}$ foams can be regarded as beneficial for the ethylene and the alcohol formation which require both a high abundance of chemisorbed CO on the catalyst surface [67]. The stabilization of chemisorbed CO on the catalyst surface under CO_2RR conditions can be regarded as crucial mechanistic prerequisite for any further improvement of the ethanol efficiency.

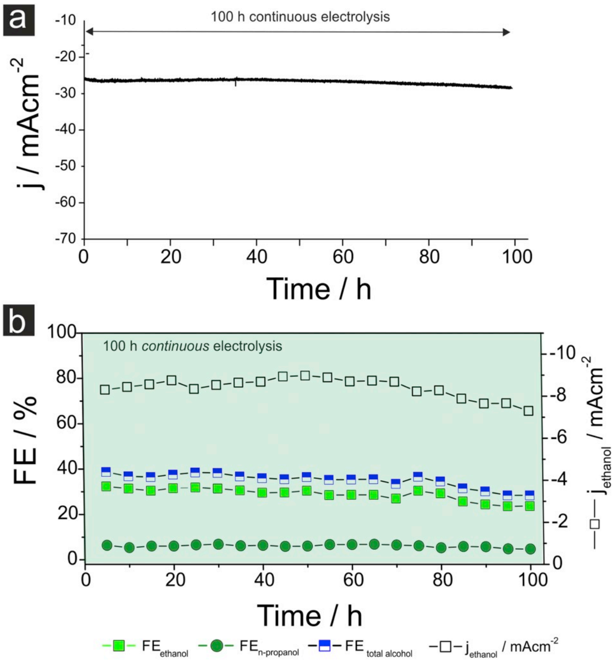

Fig. 8. a) Current density/time transient curve of the 100 h lasting catalyst stressing experiment at −1.0 V vs RHE (note the electrolysis current is normalized to the geometric surface area); b) Corresponding CO_2RR product distribution focusing on the alcohols (ethanol and n-propanol).

2.2. *Electrochemical performance of the $Ag_{15}Cu_{85}$ foam catalysts*

The electrocatalytic performance of the $Ag_{15}Cu_{85}$ foam has been evaluated by means of potential dependent electrolysis experiments (1 h duration) from CO_2-saturated 0.5 M $KHCO_3$ electrolytes (pH = 7.2). Results of these electrolysis experiments are shown in Fig. 6a for as deposited $Ag_{15}Cu_{85}$ foam. In principle, the potential dependent product distribution can be subdivided into three distinct potential regimes. In the range from −0.3 to −0.7 V vs RHE CO is the predominant CO_2RR product reaching a maximum Faradaic efficiency of $FE_{CO} = 81.45\%$ (Table S2) at −0.3 V, which corresponds to a partial CO current density of $j_{CO} = -\ 0.24$ mA cm^{-2} (Table S3). It can be assumed that it is the Ag component in the as deposited $Ag_{15}Cu_{85}$ foam catalyst on which the CO_2RR preferentially takes place at these low overpotentials. This bimetallic catalyst outperforms pure Cu catalysts in terms of CO production at low overpotentials. One reason might be related to the almost quantitative suppression of the formate production (Fig. 6a, Table S2) which is typically produced over pure Cu electrocatalysts at these conditions (e.g. $FE_{formate} = 49.2\%$ at −0.7 V vs RHE [34]). Comparably high efficiencies of formate formation are also observed for pure Cu catalysts deposited in the presence of citrate additives (see Fig. S3 and Fig. S8 in supplementary information).

A similar effect of suppressed formate production has recently been discussed by Kottakat et al. for electrodeposited bimetallic AgCu foams [27]. In this latter case a maximum CO efficiency of $\sim FE_{CO} = 58.4\%$ at −0.6 V vs RHE was reported [27]. Highest CO efficiencies at particularly low overpotentials similar to those reported herein were so far reported only for pure Au [68] or Ag [69] electrocatalysts. An example related to this present work is the pure Ag foam electrocatalyst also deposited from a citrate-containing plaiting bath [18]. In this latter case the FE_{CO} values did not fall below 90% within a 800 mV broad potential window ranging from −0.3 to −1.2 V vs RHE [18]. It should be emphasized, however, that the bimetallic AgCu foams are superior over the pure Ag catalyst in terms of Ag mass activity [27].

In the present case the FE_{CO} values start to drop down at potentials $<$ −0.5 V vs RHE not only because of the HER which becomes more favored with increasing cathodic potentials, but also because of the C1 (methane) and C2 (ethylene, ethane) hydrocarbon pathways which are opened at potentials < -0.4 V and < -0.9 V vs RHE, respectively. The

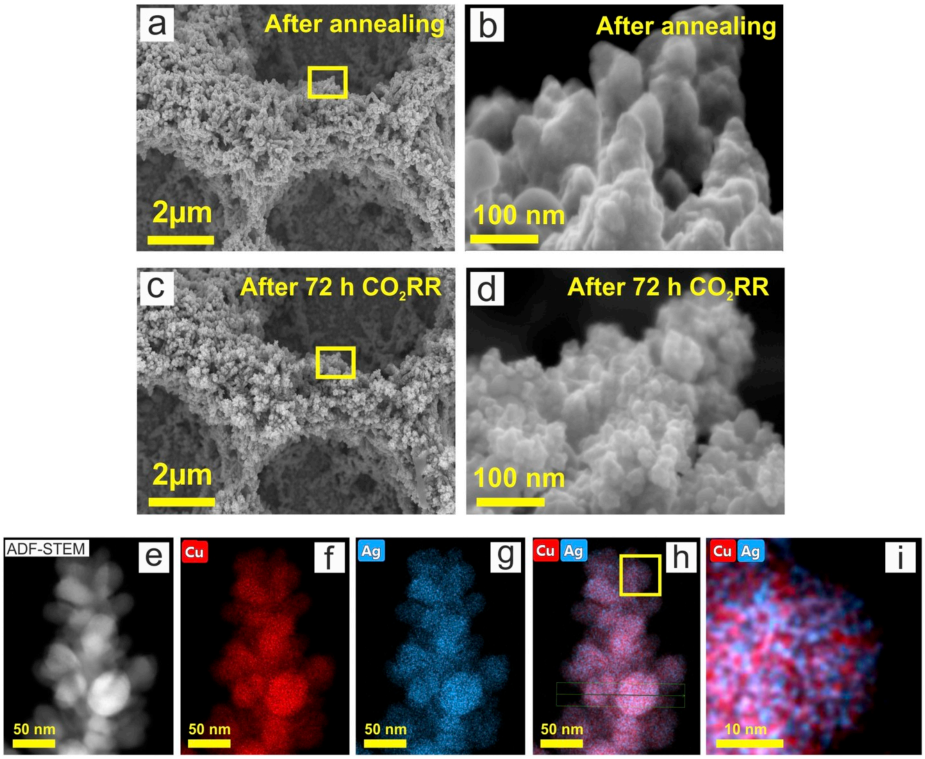

Fig. 9. a) – d) Identical location (IL) SEM analysis of the catalyst before (panel a and b) and after (panel c and d) 72 h CO_2RR at −1.0 V vs RHE; e) – i) ADF-STEM micrograph and EDX mapping of a single dendrite after CO_2RR at −1.0 V vs. RHE. The yellow square in panel h highlights the section shown in panel i.

ethylene efficiency reaches its maximum of $FE_{C2H4} = 36.56\%$ ($j_{C2H4} = -11.32$ mA cm^{-2}) at −1.1 V vs RHE. These efficiencies are comparable to those reported for Cu nano-foams [70] or Cu nano-cubes with (100) surface orientation [71,72]. Table S4 provides an overview on the best performing Cu-based catalysts for ethylene production. Interesting to note is that, in contrast to pure Cu foams [30], the C_2H_6 formation remains on a low level on the bimetallic catalyst within the entire potential range studied herein never exceeding 1% (Table S2).

As known from polycrystalline Cu electrocatalysts [73], methane production sets in at slightly higher overpotentials as compared to ethylene reaching on as deposited $Ag_{15}Cu_{85}$ a maximum of $FE_{CH4} = 25.6\%$ at −1.2 V vs RHE (Fig. 6a). C2 and C3 alcohol formation is negligible on the as deposited $Ag_{15}Cu_{85}$ foam. The n-propanol efficiencies never exceed 1% whereas a maximum ethanol efficiency of $FE_{EtOH} = 4.6\%$ ($j_{EtOH} = -1.11$ mA cm^{-2}) is obtained at −1.0 V vs RHE. The second characteristic potential regime in the product CO_2RR distribution (<-0.7 V vs RHE) is obviously dominated by the Cu component in the as deposited $Ag_{15}Cu_{85}$ foam with its capability of enabling C–C coupling reactions. It can be assumed that the C–C coupling reaction benefits from the high abundance of CO inside the porous catalyst. Due to the small domain sizes of the metallic components of the as deposited $Ag_{15}Cu_{85}$ foam (Fig. 1, see also below discussion on Fig. 9i) the CO intermediate is rapidly transported from the Ag (CO producer) to the Cu domains (C–C coupler) either by surface diffusion ('spillover') or by diffusion through the liquid electrolyte phase inside the pores of the bimetallic foam (re-adsorption of trapped CO).

In principle, this basic concept holds true also for the thermally annealed (oxide-derived) $Ag_{15}Cu_{85}$ foam (Fig. 6b). The C1 and C2 hydrocarbon pathways are, however, substantially suppressed on the OD-$Ag_{15}Cu_{85}$ foam (Table S5). A maximum value of only $FE_{C_2H_4} = 10.2\%$ ($j_{C2H4} = -3.1$ mA cm^{-2}) is observed at −1.1 V vs RHE. Instead, ethanol is the predominant CO_2RR product at electrolysis potentials < −0.8 V vs RHE reaching a maximum value of $FE_{EtOH} = 33.7\%$ ($j_{EtOH} = -8.67$ mA cm^{-2}) at −1.0 V vs RHE. Important to note is that the efficiency for n–propanol formation remains on a low level (e.g., $FE_{n\text{-}PrOH} = 6.9\%$, $j_{n\text{-}PrOH} = -1.8$ mA cm^{-2} at −0.9 V vs RHE) thus pointing to a catalyst which is selective towards C2 alcohol formation (Table S5 and Table S6). Rahaman et al. recently reported a high alcohol efficiency for thermally annealed dendritic Cu of $FE_{alcohol} = 24.8\%$ ($j_{alcohol} = -7.73$ mA cm^{-2}) at −1.0 V vs RHE [34]. The alcohol selectivity itself was, however, poor with almost equivalent efficiencies for ethanol and n-propanol [34].

The OD-$Ag_{15}Cu_{85}$ is currently among the best performing catalysts for the production of higher alcohols (an overview is provided in Table S7 and Table S8).

A certain drawback of the thermal annealing of the $Ag_{15}Cu_{85}$ foam is the decrease of the Ag (CO producer) content at the catalyst surface in the course of the thermal oxidation/ec reduction treatment (see discussion of the XPS data). This structural and compositional alteration of the catalyst surface becomes apparent also from the CO_2RR product distribution, in particular in the low overpotential regime ranging from −0.3 V to −0.8 V vs RHE (Fig. 6b). In comparison to the as deposited sample (Fig. 6a) the Faradaic yield of CO production is substantially lower for the oxide-derived catalyst at lowest overpotentials, e.g. at −0.3 V vs RHE ($FE_{CO} = 37.4\%$ instead of $FE_{CO} = 81.45\%$ (as deposited)) and slightly lower at medium overpotentials, e.g. at −0.6 V vs RHE ($FE_{CO} = 52.0\%$ instead of $FE_{CO} = 60.7\%$ (as deposited)). However, the Ag content on the catalyst surface after the reduction of the oxides seems to be sufficient to substantially improve the total alcohol efficiency $FE_{alcohol}$ compared to pure Cu foams (see also discussion of Fig. 9).

Fig. 7 summarizes the suggested mechanism of alcohol formation on the bimetallic AgCu catalyst surface which is consistent with published models on alcohol formation on Cu [34]. CO forms selectively on the Ag domains and is subsequently transported to the Cu via surface diffusion ('spillover') or alternatively via CO transport through the solution phase (desorption/re-adsorption). Besides the increased abundance of CO intermediates it is the stabilization of the chemisorbed *CO on the catalyst surface which further directs the CO_2RR towards C–C coupling and alcohol formation. This stabilization is deduced from the potential dependent integrated intensity of the CO stretching mode (Fig. 5c). Its maximum is downward-shifted on the potential scale in case of the

$Ag_{15}Cu_{85}$ foam compared to the pure Cu foam (Fig. 5c). Note that the Raman experiment does not allow for a direct comparison of the CO surface concentration on the pure Cu and the $Ag_{15}Cu_{85}$ foam due to differences in the surface morphology (e.g. roughness) and chemical composition of both catalyst materials.

2.3. *Stability of the annealed $Ag_{15}Cu_{85}$ foam catalyst*

Besides the CO_2RR product selectivity and activity, it is the long term stability of the catalyst which defines its overall performance. Therefore, long term CO_2 electrolysis experiments were performed at −1.0 V vs RHE corresponding to the maximum ethanol efficiency in the potential dependent screening experiment (Fig. 6b). Fig. 8 depicts the current/time transient curve (panel a) and the corresponding *FE/PCD vs t* plot (panel b) of a 100 h continuous electrolysis experiment. The partial current density (PCD) for ethanol formation drops down slightly from -8.4 mA/cm^2 to -7.3 mA/cm^2 thus pointing to an excellent degradation stability of the bimetallic catalyst. Note that, when the electrolysis is carried out in a discontinuous fashion, the degradation process proceeds faster (see discussion on Fig. S9 in the supplementary information).

Structural and compositional changes upon catalyst activation via the precursor reduction and the CO_2 electrolysis itself become apparent from identical location IL-SEM analyses of the $Ag_{15}Cu_{85}$ foam in Fig. 9 after anneal at 200 °C (panel a–b) and after 72 h of continuous CO_2 electrolysis (panel c–d). The electroreduction of the precursor and the CO_2 electrolysis at −1.0 V vs RHE leaves the mesoscopic pore structure on the μm scale fully unaffected (panel a and c) similar to what is known from Cu and Ag foams [18,30]. Distinct structural changes are, however, visible on the nm length scale (panel b and d). After the 72 h of electrolysis (panel d) smaller particles have been evolved, most likely in the initial stage of the electrolysis where the CO_2RR is superimposed on the Cu oxide reduction (see e.g. Fig. 4). Similar morphological changes become apparent from an extended IL-analysis of the catalyst carried out at discontinuous operation mode (Fig. S10 in the supplementary information).

Combined ADF-STEM imaging and EDX mapping (Fig. 9) clearly indicate a high degree of dispersion of Ag and Cu domains. The preferential segregation of Cu in the form of cuprous and cupric oxides has disappeared under CO_2RR conditions in full agreement also with the XPS analysis.

3. Conclusions

Bimetallic $Ag_{15}Cu_{85}$ foam catalysts have been produced by means of an additive (citrate) assisted electrodeposition approach utilizing the dynamic hydrogen bubble template approach. Whereas the as deposited catalyst is selective towards CO at particularly low overpotentials ($FE_{CO} = 81.45\%$, $j_{CO} = -0.24$ mA cm^{-2} at −0.3 V vs RHE) and towards C_2H_4 at higher overpotentials ($FE_{C2H4} = 36.56\%$, j_{C2H4} = - 11.32 mA cm^{-2} at −1.1 V vs RHE) an activation of the catalyst for selective alcohol formation is achieved by thermal annealing of the $Ag_{15}Cu_{85}$ at 200 °C for 12 h. This treatment leads to a metal/oxide composite material consisting of metallic Ag and oxidized Cu (denoted as $AgCu_xO$ foam), the latter being accumulated at the surface of the foam. Electroreduction of the oxidic components in the $AgCu_xO$ precursor leads to an oxide-derived (OD) bimetallic AgCu catalyst which outperforms in terms of ethanol selectivity ($FE_{EtOH} = 33.7\%$, $j_{EtOH} = -8.67$ mA cm^{-2} at −1.0 V vs RHE) and durability (100 h).

A key feature of the OD-$Ag_{15}Cu_{85}$ foam catalyst is the high dispersion of nm-sized domains of metallic Ag (CO producer) and Cu (C–C coupler, alcohol former) in the bimetallic catalyst thus allowing for a facile transport of the CO intermediate to those Cu surface sites that are particularly active for C–C coupling and ethanol formation (CO spillover concept). The excellent performance of the OD-$Ag_{15}Cu_{85}$ foam catalyst is due to the synergistic effects of an increased CO abundance at higher overpotentials and the selective activation of the Cu component by the oxide formation and its electroreduction under CO_2RR conditions.

Operando Raman spectroscopy and X-ray diffraction both clearly demonstrate that the activation (electro-reduction) of the annealed $Ag_{15}Cu_{85}$ foam is completed before the CO_2RR sets in.

4. Experimental section

4.1. *Chemical and materials*

Cu foils were purchased from Alfa Aesar (thickness 0.25 mm, purity ≥ 99.95%) and cut into pieces having dimensions of ~8 mm × 22 mm. Prior to the electrodeposition of the CuAg foam, Cu foils were subjected to an electropolishing treatment in ortho-phosphoric acid (50w%, ACS grade, SigmaAldrich) using a two-electrode arrangement. A graphite foil thereby served as counter (cathode) and the Cu foil as working electrodes (anode), respectively. A constant potential difference of 2.0 V was applied between both electrodes for the duration of 2 min. During the electropolishing treatment, the Cu foil was gently moved in the phosphoric acid solution to remove oxygen bubbles formed upon electrode polarization on the Cu. The resulting surface morphology was characterized by means of atomic force microscopy (AFM, NanoSurf, see Fig. S11 in the supplementary information).

4.2. *Electrolyte solutions*

The standard plating bath for the bimetallic AgCu foam deposition was composed of 1.5 M H_2SO_4 (prepared from 96% H_2SO_4, ACS grade, Sigma-Aldrich) serving as supporting electrolyte, 20 mM $CuSO_4$ (Fluka), 2 mM Ag_2SO_4 (Sigma Aldrich, purity ≥ 99.5%), and 0.1 M $Na_3C_6H_5O_7 \cdot 2H_2O$ (tri-sodium citrate di-hydrate, >99.7%, Merck). For comparison purposes AgCu electroplating experiments were performed also in the additive-free bath. Furthermore also pure Cu catalysts were deposited from a plating bath in the absence of Ag containing 1.5 M H_2SO_4 (ACS grade, Sigma-Aldrich) and 20 mM $CuSO_4$ (Fluka). This deposition was carried out in the presence and the absence of 0.1 M $Na_3C_6H_5O_7 \cdot 2H_2O$ (tri-sodium citrate di-hydrate, >99.7%, Merck). See the *operando* Raman results in Fig. 5c and SEM images in Fig. S3 in the supplementary information.

The electrochemically active surface area (denoted hereinafter as ECSA) was estimated by means of cyclic voltammetry (CV) using dimethyl viologen dichloride ($DMVCl_2$) as reversible redox-probe following a protocol described previously [30]. Scan-rate dependent CVs were measured in aqueous 1 M Na_2SO_4 (ACS grade, Sigma-Aldrich) solution containing 10 mM $DMVCl_2$ (Sigma-Aldrich). The estimated ECSA of the bimetallic AgCu foams (as deposited) used herein amounts to 2.66 cm^{-2} (referring to 1 cm^{-2} geometric surface area). Note that the ECSA further increases to 4.45 cm^{-2} after the thermal annealing. For details of the ECSA determination see Fig. S12 in the supplementary information.

All CO_2RR experiments were carried out in 0.5 M $KHCO_3$ (ACS grade, Sigma-Aldrich) electrolyte solutions saturated with CO_2 gas (99.999%, Carbagas, Switzerland). For blank experiments the same electrolyte was saturated with inert Ar gas.

4.3. *Electrochemical experiments*

The AgCu foam deposition was carried out in a glass-beaker containing 100 mL of the plating solution. For the galvanostatic deposition process, a nominal current density of $j = -3.0$ A cm^{-2} (referred to the geometric surface area of the Cu foil support electrode) was applied for 20 s. The three-electrode arrangement consisted of a leakless $Ag/AgCl_{3M}$ reference electrode (RE, EDAQ), a bright Pt-foil (15 mm × 5 mm) serving as counter electrode (CE), and the Cu foil (substrate of the bimetallic AgCu foam) catalysts serving as working electrode (WE). The electrodeposition was performed in a face-to-face configuration (WE-CE) as indicated in Fig. S13 in the supplementary information. Note that the deposited bimetallic foam is sufficiently thick (>15 μm) so that any contribution from the substrate to the resulting CO_2RR product distribution is excluded.

Electrodeposited bimetallic AgCu and the pure Cu foams were further activated by thermal annealing in air at 200 °C for 12 h using a tube furnace (GERO Hochtemperaturofen GmbH, Germany).

All voltammetric and CO_2RR electrolysis experiments were carried out in a custom-built, air-tight glass-cell (H-type) described elsewhere [30].

Possible chloride ion cross-contaminations in the working electrolytes originating from the $Ag/AgCl_{3M}$ reference electrode were monitored and excluded by ion exchange (IC) chromatography (Metrohm). Technical details of the CO_2RR product analysis based on online gas-chromatography and ion exchange (IC) chromatography were described elsewhere [30].

All potentials given herein are iR-corrected and referenced to the reversible hydrogen electrode (RHE) by using the following equation:

$$E_{RHE}\ (V) = E_{Ag/AgCl(3M)}\ (V) + 0.210\ V + (0.059\ V \times pH)$$

4.4. Structural and compositional characterization

For the XRD analysis an STOE Stadi P system with a Cu Kα radiation source (λ = 0.1540 nm, 40 mA) operated at 40 keV was used. XRD spectra were recorded in reflection mode (Bragg-Brentano geometry) in steps of 1° min^{-1} with 2θ values ranging from 0 to 90°. To exclude Cu diffraction peaks originating from the Cu foil support, the bimetallic foam was deposited onto a graphite substrate (99.8%, Alfa Aesar, 0.13 mm thickness). The obtained XRD patterns were analyzed and compared to JCPDS (Joint Committee on Powder Diffraction standards) data of polycrystalline Ag, Ag_2O, AgO, Cu, Cu_2O, and CuO (File No. 04–0783, 43–0997, 43–1038, 04–0836, 05–0667, 41–0254).

Elemental analysis of the bimetallic foams was carried out by means of inductively coupled plasma optical emission spectrometry (Agilent 5110 inductively coupled plasma optical emission spectrometry (ICP-OES)).

X-ray photoelectron spectroscopy (XPS) studies were carried out using a PHI VersaProbeII scanning XPS micro-probe (Physical Instruments AG, Germany) equipped with a monochromatic Al Kα X-ray source operated at 24.8 W with a spot size of 100 μm. Peak positions were referenced to the carbon C1s peak at 285.5 eV and curve fitting was performed using the Casa-XPS software.

The morphology of the bimetallic foams was characterized by means of Scanning Electron Microscopy (SEM) and Energy-Dispersive X-ray spectroscopy (EDX) using a Hitachi S-3000 N Scanning Electron Microscope and a Noran SIX NSS200 energy-dispersive X-ray spectrometer. For the high-resolution identical location IL-SEM imaging a Zeiss DSM 982 instrument was used. In addition the mesoscopic surface morphology of the bimetallic AgCu foam was analyzed by means of a white light interferometry (Contour GT, Bruker).

For the transmission electron microscopy (TEM), the $Ag_{15}Cu_{85}$ catalyst was dispersed on a carbon coated TEM Au grid (200 mesh) after initial electrodeposition on a Cu foil substrate, followed by dispersion in absolute ethanol. For the HR-TEM imaging an FEI Tecnai F2 instrument was used with an accelerating voltage of 200 kV. Annular dark-field scanning transmission electron microscopy (ADF-STEM) in combination with EDX measurements were carried out using a FEI Titan Themis operated at 300 kV equipped with a SuperEDX detector.

4.5. Operando Raman spectroscopy

Raman spectroscopic measurements were performed using a LabRAM HR800 confocal microscope (Horiba Jobin Yvon). A large working distance objective lens (50 times magnification, 8 mm focal length) has been applied with a numerical aperture of 0.1 in order to focus a diode-pumped solid-state laser beam (excitation wavelength 632 nm, power 3 mW) on the sample. The Raman signal was collected in backscattering geometry using a home-made spectro-electrochemical cell (see Fig. S14 in the supplementary information) [74,75].

4.6. Operando X-ray diffraction (XRD)

Operando XRD experiments (see Fig. S15 in the supplementary information) were performed at the European Synchrotron Radiation Facility ID31 high energy beamline. The 69 keV monochromatic X-ray beam was focused to the size of 5 × 20 $μm^2$ (vertical x horizontal) at the sample position. The 2D XRD patterns were collected with a Dectris Pilatus 2 M CdTe detector. A custom made PEEK electrochemical cell consists of a Pt counter electrode, an Ag/AgCl (3 M KCl) reference electrode (EDAQ) and the sample working electrode supported on carbon paper electrically connected with an Au wire. The measurements were performed in CO_2-saturated 0.5 M $KHCO_3$ electrolyte and in grazing incidence geometry. The sample was first measured at OCP after the electrolyte was introduced to the cell and then at subsequently decreasing potentials in steps of 0.1 V. The resting time at each potential before the measurement was 2 min. The raw 2D diffraction patterns were radially integrated to the final 1D patterns using the pyFAI package [76]. The 1D patterns were further analyzed by integrating the characteristic peak intensities and fitting the Gaussian function to determine the FWHM.

Declaration of competing interest

No conflict of interest exists.

Acknowledgements

The financial support by the CTI Swiss Competence Center for Energy Research (SCCER Heat and Electricity Storage) is gratefully acknowledged. PB acknowledges the financial support by the Swiss National Science Foundation (SNSF) via the project No. 200020_172507. This study was performed with the support of the interfaculty Microscopy Imaging Centre (MIC) of the University of Bern.

Appendix A. Supplementary data

Supplementary data to this article can be found online at https://doi.org/10.1016/j.nanoen.2019.104331.

References

[1] D.T. Whipple, P.J.A. Kenis, Prospects of CO_2 utilization via direct heterogeneous electrochemical reduction, J. Phys. Chem. Lett. 1 (2010) 3451–3458.
[2] A.M. Appel, J.E. Bercaw, A.B. Bocarsly, H. Dobbek, D.L. DuBois, M. Dupuis, J. G. Ferry, E. Fujita, R. Hille, P.J.A. Kenis, C.A. Kerfeld, R.H. Morris, C.H.F. Peden, A. R. Portis, S.W. Ragsdale, T.B. Rauchfuss, J.N.H. Reek, L.C. Seefeldt, R.K. Thauer, G. L. Waldrop, Frontiers, opportunities, and challenges in biochemical and chemical catalysis of CO_2 fixation, Chem. Rev. 113 (2013) 6621–6658.
[3] H.-R.M. Jhong, S. Ma, P.J.A. Kenis, Electrochemical conversion of CO_2 to useful chemicals: current status, remaining challenges, and future opportunities, Curr. Opin. Chem. Eng. 2 (2013) 191–199.
[4] National oceanic and atmospheric administration. https://www.noaa.gov/.
[5] H. Yang, Z. Xu, M. Fan, R. Gupta, R.B. Slimane, A.E. Bland, I. Wright, Progress in carbon dioxide separation and capture: a review, J. Environ. Sci. 20 (2008) 14–27.
[6] M. Mikkelsen, M. Jørgensen, F.C. Krebs, The teraton challenge. A review of fixation and transformation of carbon dioxide, Energy Environ. Sci. 3 (2010) 43–81.
[7] Y. Hori, in: R.E.W.C.G. Vayenas, M.E. Gamboa-Aldeco (Eds.), Modern Aspects of Electrochemistry, Springer, New York, 2008, pp. 89–189.
[8] T. Haas, R. Krause, R. Weber, M. Demler, G. Schmid, Technical photosynthesis involving CO_2 electrolysis and fermentation, Nat. Catal. 1 (2018) 32–39.
[9] J.-P. Jones, G.K.S. Prakash, G.A. Olah, Electrochemical CO_2 reduction: recent advances and current trends, Isr. J. Chem. 54 (2014) 1451–1466.
[10] G. Centi, S. Perathoner, Opportunities and prospects in the chemical recycling of carbon dioxide to fuels, Catal. Today 148 (2009) 191–205.
[11] S. Cherevko, S. Geiger, O. Kasian, N. Kulyk, J.-P. Grote, A. Savan, B.R. Shrestha, S. Merzlikin, B. Breitbach, A. Ludwig, K.J.J. Mayrhofer, Oxygen and hydrogen

evolution reactions on Ru, RuO_2, Ir, and IrO_2 thin film electrodes in acidic and alkaline electrolytes: a comparative study on activity and stability, Catal. Today 262 (2016) 170–180.

[12] M. Görlin, M. Gliech, J.F. de Araújo, S. Dresp, A. Bergmann, P. Strasser, Dynamical changes of a Ni-Fe oxide water splitting catalyst investigated at different pH, Catal. Today 262 (2016) 65–73.

[13] M. Rahaman, A. Dutta, P. Broekmann, Size-dependent activity of palladium nanoparticles: efficient conversion of CO_2 into formate at low overpotentials, ChemSusChem 10 (2017) 1733–1741.

[14] A. Dutta, A. Kuzume, M. Rahaman, S. Vesztergom, P. Broekmann, Monitoring the chemical state of catalysts for CO_2 electroreduction: an in operando study, ACS Catal. 5 (2015) 7498–7502.

[15] X.Q. Min, M.W. Kanan, Pd-catalyzed electrohydrogenation of carbon dioxide to formate: high mass activity at low overpotential and identification of the deactivation pathway, J. Am. Chem. Soc. 137 (2015) 4701–4708.

[16] Y. Hori, K. Kikuchi, S. Suzuki, Production of CO and CH_4 in electrochemical reduction of CO_2 at metal-electrodes in aqueous hydrogencarbonate solution, Chem. Lett. (1985) 1695–1698.

[17] S. Ma, Y. Lan, G.M.J. Perez, S. Moniri, P.J.A. Kenis Silver, Supported on titania as an active catalyst for electrochemical carbon dioxide reduction, ChemSusChem 7 (2014) 866–874.

[18] A. Dutta, C.E. Morstein, M. Rahaman, A. Cedeño López, P. Broekmann, Beyond copper in CO_2 electrolysis: effective hydrocarbon production on silver-nanofoam catalysts, ACS Catal. (2018) 8357–8368.

[19] S. Liu, H. Tao, L. Zeng, Q. Liu, Z. Xu, Q. Liu, J.-L. Luo, Shape-dependent electrocatalytic reduction of CO_2 to CO on triangular silver nanoplates, J. Am. Chem. Soc. 139 (2017) 2160–2163.

[20] K.W. Frese, S. Leach, Electrochemical reduction of carbon dioxide to methane, methanol, and CO on Ru electrodes, J. Electrochem. Soc. 132 (1985) 259–260.

[21] T. Hatsukade, K.P. Kuhl, E.R. Cave, D.N. Abram, T.F. Jaramillo, Insights into the electrocatalytic reduction of CO_2 on metallic silver surfaces, Phys. Chem. Chem. Phys. 16 (2014) 13814–13819.

[22] N. Hoshi, M. Kato, Y. Hori, Electrochemical reduction of CO_2 on single crystal electrodes of silver Ag(111), Ag(100) and Ag(110), J. Electroanal. Chem. 440 (1997) 283–286.

[23] H. Mistry, Y.W. Choi, A. Bagger, F. Scholten, C.S. Bonifacio, I. Sinev, N.J. Divins, I. Zegkinoglou, H.S. Jeon, K. Kisslinger, E.A. Stach, J.C. Yang, J. Rossmeisl, B. R. Cuenya, Enhanced carbon dioxide electroreduction to carbon monoxide over defect-rich plasma-activated silver catalysts, Angew. Chem. Int. Ed. 56 (2017) 11394–11398.

[24] Y. Hori, H. Wakebe, T. Tsukamoto, O. Koga, Electrocatalytic process of CO selectivity in electrochemical reduction of CO_2 at metal electrodes in aqueous media, Electrochim. Acta 39 (1994) 1833–1839.

[25] M. Li, J.J. Wang, P. Li, K. Chang, C.L. Li, T. Wang, B. Jiang, H.B. Zhang, H.M. Liu, Y. Yamauchi, N. Umezawa, J.H. Ye, Mesoporous palladium-copper bimetallic electrodes for selective electrocatalytic reduction of aqueous CO_2 to CO, J. Mater. Chem. 4 (2016) 4776–4782.

[26] S. Verma, X. Lu, S. Ma, R.I. Masel, P.J.A. Kenis, The effect of electrolyte composition on the electroreduction of CO_2 to CO on Ag based gas diffusion electrodes, Phys. Chem. Chem. Phys. 18 (2016) 7075–7084.

[27] T. Kottakkat, K. Klingan, S. Jiang, Z.P. Jovanov, V.H. Davies, G.A.M. El-Nagar, H. Dau, C. Roth, Electrodeposited AgCu foam catalysts for enhanced reduction of CO_2 to CO, ACS Appl. Mater. Interfaces 11 (2019) 14734–14744.

[28] K.P. Kuhl, T. Hatsukade, E.R. Cave, D.N. Abram, J. Kibsgaard, T.F. Jaramillo, Electrocatalytic conversion of carbon dioxide to methane and methanol on transition metal surfaces, J. Am. Chem. Soc. 136 (2014) 14107–14113.

[29] T.T.H. Hoang, S. Verma, S. Ma, T.T. Fister, J. Timoshenko, A.I. Frenkel, P.J. A. Kenis, A.A. Gewirth, Nanoporous copper–silver alloys by additive-controlled electrodeposition for the selective electroreduction of CO_2 to ethylene and ethanol, J. Am. Chem. Soc. 140 (2018) 5791–5797.

[30] A. Dutta, M. Rahaman, N.C. Luedi, M. Mohos, P. Broekmann, Morphology matters: tuning the product distribution of CO_2 electroreduction on oxide-derived Cu foam catalysts, ACS Catal. 6 (2016) 3804–3814.

[31] Y. Hori, A. Murata, R. Takahashi, S. Suzuki, Enhanced formation of ethylene and alcohols at ambient temperature and pressure in electrochemcial reduction of carbon dioxide at a copper electrode, J. Chem. Soc., Chem. Commun. (1988) 17–19.

[32] D. Ren, Y. Deng, A.D. Handoko, C.S. Chen, S. Malkhandi, B.S. Yeo, Selective electrochemical reduction of carbon dioxide to ethylene and ethanol on copper(I) oxide catalysts, ACS Catal. 5 (2015) 2814–2821.

[33] J. Albo, A. Irabien, Cu_2O-loaded gas diffusion electrodes for the continuous electrochemical reduction of CO_2 to methanol, J. Catal. 343 (2016) 232–239.

[34] M. Rahaman, A. Dutta, A. Zanetti, P. Broekmann, Electrochemical reduction of CO_2 into multicarbon alcohols on activated Cu mesh catalysts: an identical location (IL) study, ACS Catal. 7 (2017) 7946–7956.

[35] S. Ma, M. Sadakiyo, R. Luo, M. Heima, M. Yamauchi, P.J.A. Kenis, One-step electrosynthesis of ethylene and ethanol from CO_2 in an alkaline electrolyzer, J. Power Sources 301 (2016) 219–228.

[36] D. Ren, N.T. Wong, A.D. Handoko, Y. Huang, B.S. Yeo, Mechanistic insights into the enhanced activity and stability of agglomerated Cu nanocrystals for the electrochemical reduction of carbon dioxide to n-propanol, J. Phys. Chem. Lett. 7 (2016) 20–24.

[37] Y. Hori, I. Takahashi, O. Koga, N. Hoshi, selective formation of C2 compounds from electrochemical reduction of CO_2 at a series of copper single crystal electrodes, J. Phys. Chem. B 106 (2002) 15–17.

[38] Y. Hori, I. Takahashi, O. Koga, N. Hoshi, Electrochemical reduction of carbon dioxide at various series of copper single crystal electrodes, J. Mol. Catal. A Chem. 199 (2003) 39–47.

[39] Y. Hori, R. Takahashi, Y. Yoshinami, A. Murata, Electrochemical reduction of CO at a copper electrode, J. Phys. Chem. B 101 (1997) 7075–7081.

[40] H. Mistry, A.S. Varela, C.S. Bonifacio, I. Zegkinoglou, I. Sinev, Y.W. Choi, K. Kisslinger, E.A. Stach, J.C. Yang, P. Strasser, B.R. Cuenya, Highly selective plasma-activated copper catalysts for carbon dioxide reduction to ethylene, Nat. Commun. 7 (2016).

[41] R. Reske, H. Mistry, F. Behafarid, B. Roldan Cuenya, P. Strasser, Particle size effects in the catalytic electroreduction of CO_2 on Cu nanoparticles, J. Am. Chem. Soc. 136 (2014) 6978–6986.

[42] A.A. Peterson, F. Abild-Pedersen, F. Studt, J. Rossmeisl, J.K. Norskov, How copper catalyzes the electroreduction of carbon dioxide into hydrocarbon fuels, Energy Environ. Sci. 3 (2010) 1311–1315.

[43] Z.-Y. Chang, S.-J. Huo, J.-M. He, J.-H. Fang, Facile synthesis of Cu–Ag bimetallic electrocatalyst with prior C2 products at lower overpotential for CO_2 electrochemical reduction, Surf. Interfaces 6 (2017) 116–121.

[44] E.L. Clark, C. Hahn, T.F. Jaramillo, A.T. Bell, Electrochemical CO_2 reduction over compressively strained CuAg surface alloys with enhanced multi-carbon oxygenate selectivity, J. Am. Chem. Soc. 139 (2017) 15848–15857.

[45] J. Huang, M. Mensi, E. Oveisi, V. Mantella, R. Buonsanti, Structural sensitivities in bimetallic catalysts for electrochemical CO_2 reduction revealed by Ag–Cu nanodimers, J. Am. Chem. Soc. 141 (2019) 2490–2499.

[46] D. Ren, B.S.-H. Ang, B.S. Yeo, Tuning the selectivity of carbon dioxide electroreduction toward ethanol on oxide-derived CuxZn catalysts, ACS Catal. 6 (2016) 8239–8247.

[47] H.C. Shin, J. Dong, M. Liu, Porous tin oxides prepared using an anodic oxidation process, Adv. Mater. 16 (2004) 237–240.

[48] H.C. Shin, M. Liu, Copper foam structures with highly porous nanostructured walls, Chem. Mater. 16 (2004) 5460–5464.

[49] A. Dutta, M. Rahaman, M. Mohos, A. Zanetti, P. Broekmann, Electrochemical CO_2 conversion using skeleton (sponge) type of Cu catalysts, ACS Catal. 7 (2017) 5431–5437.

[50] E.L. Clark, A.T. Bell, Electrochemical reduction of CO_2 over phase segregated cuag bimetallic electrodes with enhanced oxygenate selectivity by CO spillover, Meet. Abstr. (2016). MA2016-02 3339-3339.

[51] K.W. Frese, Electrochemical reduction of CO_2 at intentionally oxidized copper electrodes, J. Electrochem. Soc. 138 (1991) 3338–3344.

[52] A. Verdaguer-Casadevall, C.W. Li, T.P. Johansson, S.B. Scott, J.T. McKeown, M. Kumar, I.E.L. Stephens, M.W. Kanan, I. Chorkendorff, Probing the active surface sites for CO reduction on oxide-derived copper electrocatalysts, J. Am. Chem. Soc. 137 (2015) 9808–9811.

[53] C.W. Li, J. Ciston, M.W. Kanan, Electroreduction of carbon monoxide to liquid fuel on oxide-derived nanocrystalline copper, Nature 508 (2014) 504–507.

[54] C.W. Li, M.W. Kanan, CO_2 reduction at low overpotential on Cu electrodes resulting from the reduction of thick Cu_2O films, J. Am. Chem. Soc. 134 (2012) 7231–7234.

[55] R. Kas, R. Kortlever, A. Milbrat, M.T.M. Koper, G. Mul, J. Baltrusaitis, Electrochemical CO_2 reduction on Cu_2O-derived copper nanoparticles: controlling the catalytic selectivity of hydrocarbons, Phys. Chem. Chem. Phys. 16 (2014) 12194–12201.

[56] D. Gao, F. Scholten, B. Roldan Cuenya, Improved CO_2 electroreduction performance on plasma-activated Cu catalysts via electrolyte design: halide effect, ACS Catal. 7 (2017) 5112–5120.

[57] D. Gao, I. Zegkinoglou, N.J. Divins, F. Scholten, I. Sinev, P. Grosse, B. Roldan Cuenya, Plasma-activated copper nanocube catalysts for efficient carbon dioxide electroreduction to hydrocarbons and alcohols, ACS Nano 11 (2017) 4825–4831.

[58] R. Kortlever, J. Shen, K.J.P. Schouten, F. Calle-Vallejo, M.T.M. Koper, Catalysts and reaction pathways for the electrochemical reduction of carbon dioxide, J. Phys. Chem. Lett. 6 (2015) 4073–4082.

[59] Y. Hori, A. Murata, R. Takahashi, formation of hydrocarbons in the electrochemical reduction of carbon dioxide at a copper electrode in aqueous solution, J. Chem. Soc., Faraday Trans. 1 85 (1989) 2309–2326.

[60] S.A. Akhade, W. Luo, X. Nie, N.J. Bernstein, A. Asthagiri, M.J. Janik, Poisoning effect of adsorbed CO during CO_2 electroreduction on late transition metals, Phys. Chem. Chem. Phys. 16 (2014) 20429–20435.

[61] D.W. Dewulf, T. Jin, A.J. Bard, Electrochemical and surface studies of carbon-dioxide reduction to methane and ethylene at copper electrodes in aqueous-solutions, J. Electrochem. Soc. 136 (1989) 1686–1691.

[62] J.F. Weaver, G.B. Hoflund, Surface characterization study of the thermal decomposition of Ag_2O, Chem. Mater. 6 (1994) 1693–1699.

[63] S. Jiang, K. Klingan, C. Pasquini, H. Dau, New aspects of operando Raman spectroscopy applied to electrochemical CO_2 reduction on Cu foams, J. Chem. Phys. 150 (2018), 041718.

[64] A. Eilert, F. Cavalca, F.S. Roberts, J. Osterwalder, C. Liu, M. Favaro, E.J. Crumlin, H. Ogasawara, D. Friebel, L.G.M. Pettersson, A. Nilsson, Subsurface oxygen in oxide-derived copper electrocatalysts for carbon dioxide reduction, J. Phys. Chem. Lett. 8 (2017) 285–290.

[65] Y. Ichinohe, T. Wadayama, A. Hatta, Electrochemical reduction of CO_2 on silver as probed by surface-enhanced Raman scattering, J. Raman Spectrosc. 26 (1995) 335–340.

[66] K.G. Schmitt, A.A. Gewirth, In situ surface-enhanced Raman spectroscopy of the electrochemical reduction of carbon dioxide on silver with 3,5-diamino-1,2,4-triazole, J. Phys. Chem. C 118 (2014) 17567–17576.

[67] X. Nie, M.R. Esopi, M.J. Janik, A. Asthagiri, Selectivity of CO_2 reduction on copper electrodes: the role of the kinetics of elementary steps, Angew. Chem. Int. Ed. 52 (2013) 2459–2462.
[68] S. Verma, Y. Hamasaki, C. Kim, W. Huang, S. Lu, H.-R.M. Jhong, A.A. Gewirth, T. Fujigaya, N. Nakashima, P.J.A. Kenis, Insights into the low overpotential electroreduction of CO_2 to CO on a supported gold catalyst in an alkaline flow electrolyzer, ACS Energy Lett. 3 (2018) 193–198.
[69] Q. Lu, J. Rosen, Y. Zhou, G.S. Hutchings, Y.C. Kimmel, J.G. Chen, F. Jiao, A selective and efficient electrocatalyst for carbon dioxide reduction, Nat. Commun. 5 (2014) 3242.
[70] S. Sen, D. Liu, G.T.R. Palmore, Electrochemical reduction of CO_2 at copper nanofoams, ACS Catal. 4 (2014) 3091–3095.
[71] J. Huang, N. Hörmann, E. Oveisi, A. Loiudice, G.L. De Gregorio, O. Andreussi, N. Marzari, R. Buonsanti, Potential-induced nanoclustering of metallic catalysts during electrochemical CO_2 reduction, Nat. Commun. 9 (2018) 3117.
[72] A. Loiudice, P. Lobaccaro, E.A. Kamali, T. Thao, B.H. Huang, J.W. Ager, R. Buonsanti, Tailoring copper nanocrystals towards C2 products in electrochemical CO_2 reduction, Angew. Chem. Int. Ed. 55 (2016) 5789–5792.
[73] K.P. Kuhl, E.R. Cave, D.N. Abram, T.F. Jaramillo, New insights into the electrochemical reduction of carbon dioxide on metallic copper surfaces, Energy Environ. Sci. 5 (2012) 7050–7059.
[74] A. Kuzume, A. Dutta, S. Vesztergom, P. Broekmann, Operando Raman spectroscopy: studies on the reactivity and stability of SnO_2 nanoparticles during electrochemical CO_2 reduction reaction, in: K. Wandelt (Ed.), Encyclopedia of Interfacial Chemistry,Surface Science and Electrochemistry, Elsevier, Amsterdam, 2018, pp. 217–226.
[75] A. Dutta, A. Kuzume, V. Kaliginedi, M. Rahaman, I. Sinev, M. Ahmadi, B.R. Cuenya, S. Vesztergom, P. Broekmann, Probing the chemical state of tin oxide NP catalysts during CO_2 electroreduction: a complementary operando approach, Nano Energy 53 (2018) 828–840.
[76] G. Ashiotis, A. Deschildre, Z. Nawaz, J.P. Wright, D. Karkoulis, F.E. Picca, J. Kieffer, The fast azimuthal integration Python library: pyFAI, J. Appl. Crystallogr. 48 (2015) 510–519.

Dr. Abhijit Dutta obtained his PhD degree in chemistry from the Indian Institute of Engineering Science and Technology, Kolkata. During his PhD study, his research mainly focused on the development of Pt and Pd based nanostructured for the application to Fuel cell such as alcohol electro oxidation, hydrogen oxidation and oxygen reduction reaction. He worked as a post-doctoral fellow at the National University of Singapore, Singapore. In 2015 he joined the interfacial electrochemistry group of Prof. Peter Broekmann at University of Bern, Switzerland, where he focuses on the development of various operando spectroscopies (Raman, XAS, and XRD) to characterize novel electrocatalysts for the selective conversion of CO_2 to value-added products.

Iván Zelocualtecatl Montiel received his B.S and M.Sc. in Chemistry from Meritorious Autonomus University of Puebla (BUAP) in 2013 and 2016, respectively. He is currently a Ph.D. candidate in the Department of Chemistry and Biochemistry at University of Bern under the supervision of Prof. Dr. Peter Broekmann. His research interest is focused on the development of novel catalyst for the CO_2 electroreduction.

Dr. Rolf Erni received his doctoral degree from the Swiss Federal Institute of Technology Zurich (ETH Zurich) in the Institute of Applied Physics. He carried out postdoctoral studies at the University of California, Davisand at the National Center for Electron Microscopy (NCEM), Lawrence Berkeley National Laboratory. He then joined FEI Company as an application specialist and senior system engineer. Before returning to NCEM as a staff scientist, he spent a period of time as a faculty member at the EMAT Institute of the University of Antwerp. Rolf Erni is now head of the Electron Microscopy Center at Empa. His research interests cover various topics in electron microscopy, such as diffraction physics, ultra-high resolution and low-voltage (scanning) transmission electron microscopy as well as valence electron energy-loss spectroscopy (VEELS).

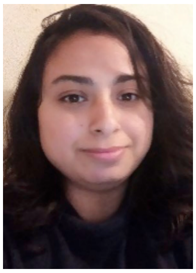

Kiran Kiran received her M.Sc in Physics from Maharshi Dayanand University (M.D.U) India in 2015. She is currently pursuing her Ph.D. at the Department of Chemistry and Biochemistry at University of Bern under the supervision of Prof. Peter Broekmann. Her research interests is focused on the synthesis of novel electrocatalyst for CO_2RR.

Dr. Motiar Rahaman received his M.Sc. in chemistry (2013) from the Indian Institute of Technology Madras, India. He obtained his PhD (2018) on the electrochemical conversion of CO_2 into value-added products from the University of Bern (group of Peter Broekmann). Currently he works as a post-doctoral fellow at the University of Cambridge (UK).

Dr. Jakub Drnec obtained his PhD degree at University of Victoria, Canada, in the field of surface electrochemistry. He is a beamline scientist at European Synchrotron (ESRF) in Grenoble (France), developing new high energy X-rays experimental techniques to study materials for energy conversion and storage. His main goal is to probe materials in their working environment in order to better understand their functioning. His current projects involve operando investigations of fuel cells and batteries, fundamental studies of electrocatalyst's degradation and structure-activity relationships, and development of operando electrochemical cells and data analysis routines.

Prof. Dr. Peter Broekmann obtained his M.Sc. in chemistry (1998) and a PhD (2000) from the University of Bonn. After a post-doctoral stay at the University of Twente (The Netherlands) in 2001, he became project leader at the Institute of Physical Chemistry in Bonn. Since 2008 he holds a lecturer position for electrochemistry at the University of Bern (Switzerland). His research is focused on metal deposition processes for semiconductor and electrocatalysis applications.

Appendix A. Supplementary material

to the paper entitled

Activation of Bimetallic AgCu Foam Electrocatalysts for Ethanol Formation from CO_2 by Selective Cu Oxidation/Reduction

Abhijit Dutta[a]*[±], Iván Zelocualtecatl Montiel[a ±], Rolf Erni[b], Kiran Kiran[a], Motiar Rahaman[a], Jakub Drnec[c], and Peter Broekmann[a]*

[a]Department of Chemistry and Biochemistry, University of Bern, Freiestrasse 3, Bern 3012 Switzerland

[b]Electron Microscopy Center, Swiss Federal Laboratories for Materials Science and Technology (EMPA), Überlandstrasse 129, 8600 Dübendorf, Switzerland

[c]European Synchrotron Radiation Facility (ESRF), 71 Avenue des Martyrs, 38000 Grenoble, France

[±]Authors contributed equally to this work

*Corresponding authors: abhijit.dutta@dcb.unibe.ch (A.Dutta)

peter.broekmann@dcb.unibe.ch (P. Broekmann)

Keywords

CO_2 electro-reduction, AgCu catalyst, ethanol, operando X-ray diffraction, operando Raman spectroscopy

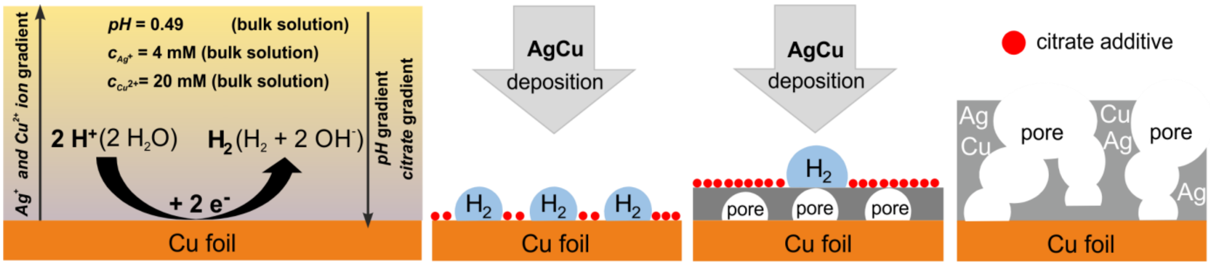

Fig. S1 Schematic showing the working principle of the additive-assisted metal foam deposition.

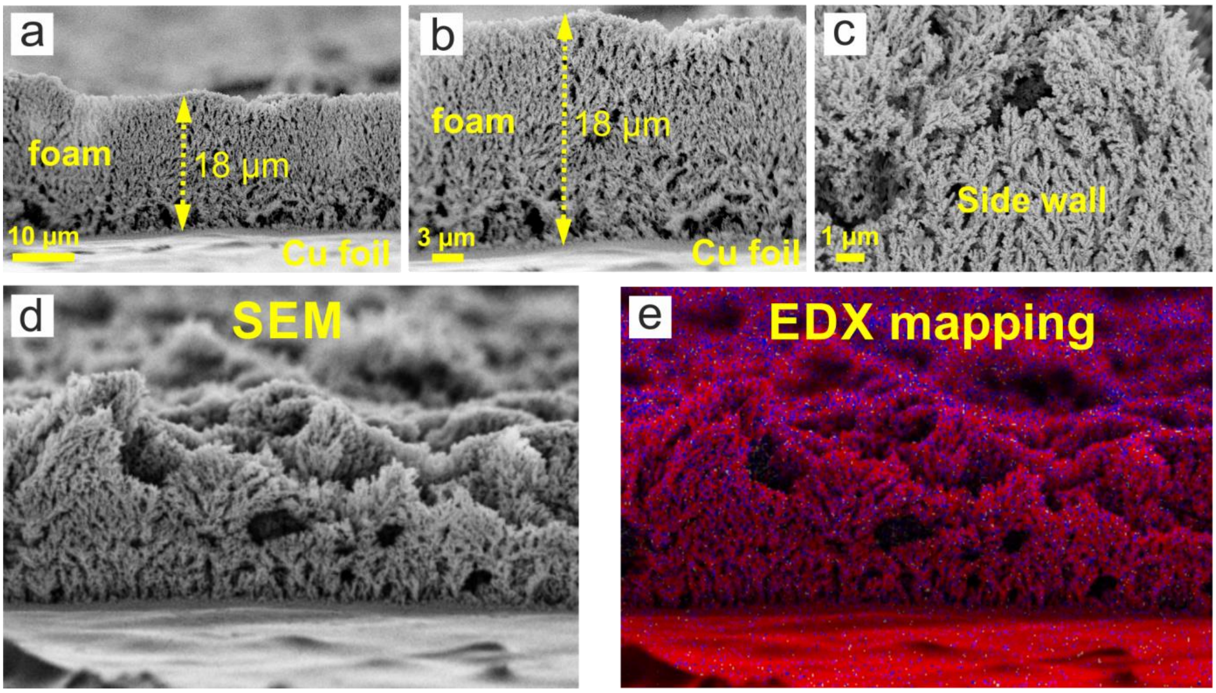

Fig. S2 (a-d) Cross-sectional SEM and (e) EDX analysis of the as deposited $Ag_{15}Cu_{85}$ foam. This catalyst has been electrodeposited on a Cu foil substrate at $j = -3$ A cm^{-2} (20 sec.) using a plating bath containing 1.5 M H_2SO_4, 20 mM $CuSO_4$, 2 mM Ag_2SO_4, and 0.1 M $Na_3C_6H_5O_7$.

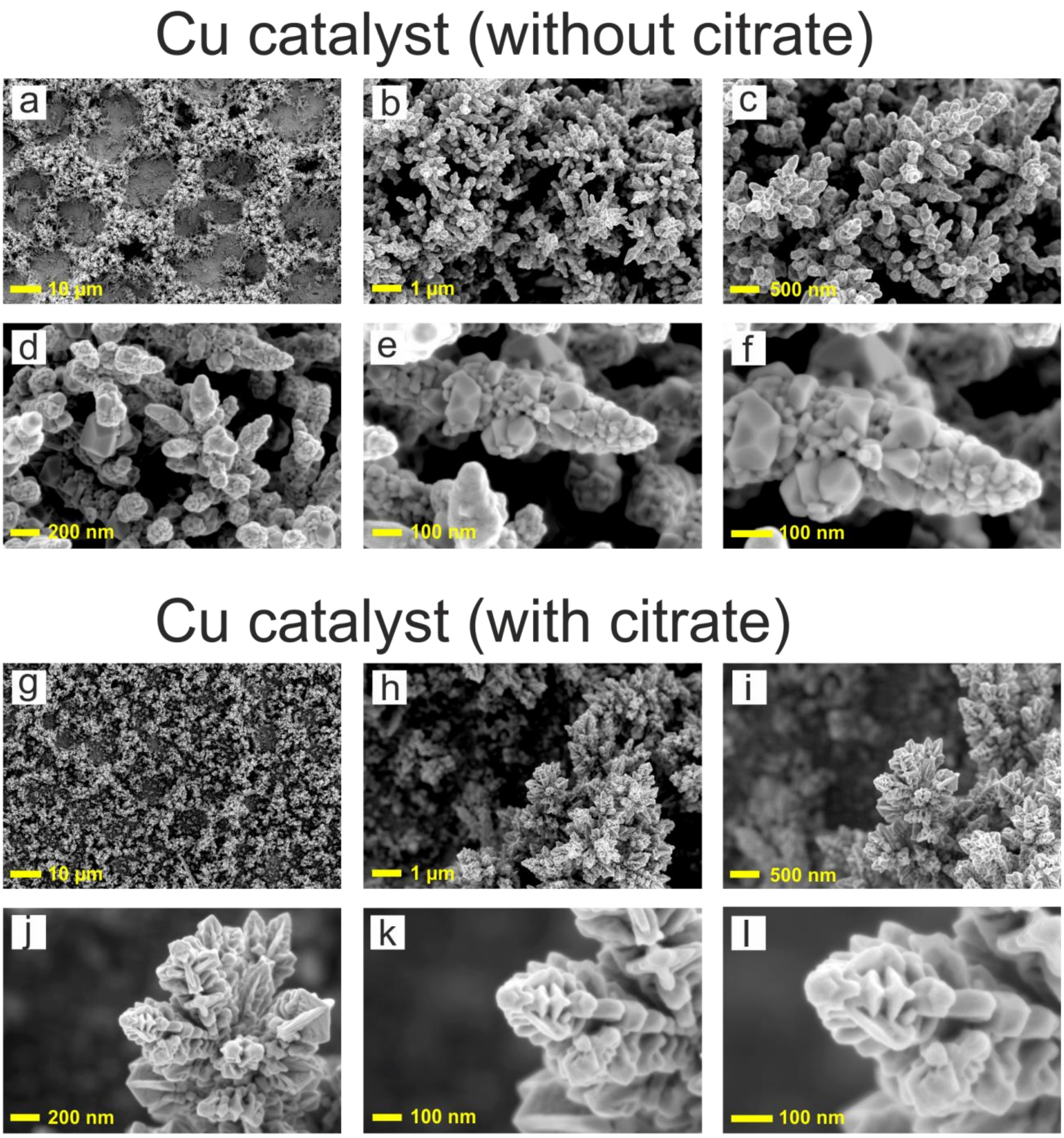

Fig. S3: a) – f) Series of top-down SEM micrographs showing the meso-porosity and micro-porosity of the respective pure Cu catalyst deposited in the *absence* of the citrate additive (Cu foil substrate, j = – 3 A cm-^{2}, 20 sec. deposition time) using a plating bath containing 1.5 M H_2SO_4 and 20 mM $CuSO_4$

g) – h) Series of top-down SEM micrographs showing the meso-porosity and micro-porosity of the respective pure Cu catalyst deposited in the *presence* of the citrate additive (Cu foil substrate, j = – 3 A cm-^{2}, 20 sec. deposition time) using a plating bath containing 1.5 M H_2SO_4, 20 mM $CuSO_4$ and 0.1 M $Na_3C_6H_5O_7 \cdot 2\ H_2O$). Note that no well-developed pores were formed under the given experimental conditions demonstrating that the citrate additive has a substantial influence on the HER and the metal deposition. Not only is the morphology of the Cu deposit affected by the citrate but also the hydrogen bubble formation.

These catalysts were further activated by thermal annealing at 200° C in air and served as reference samples for the Raman study presented in Fig. 5c.

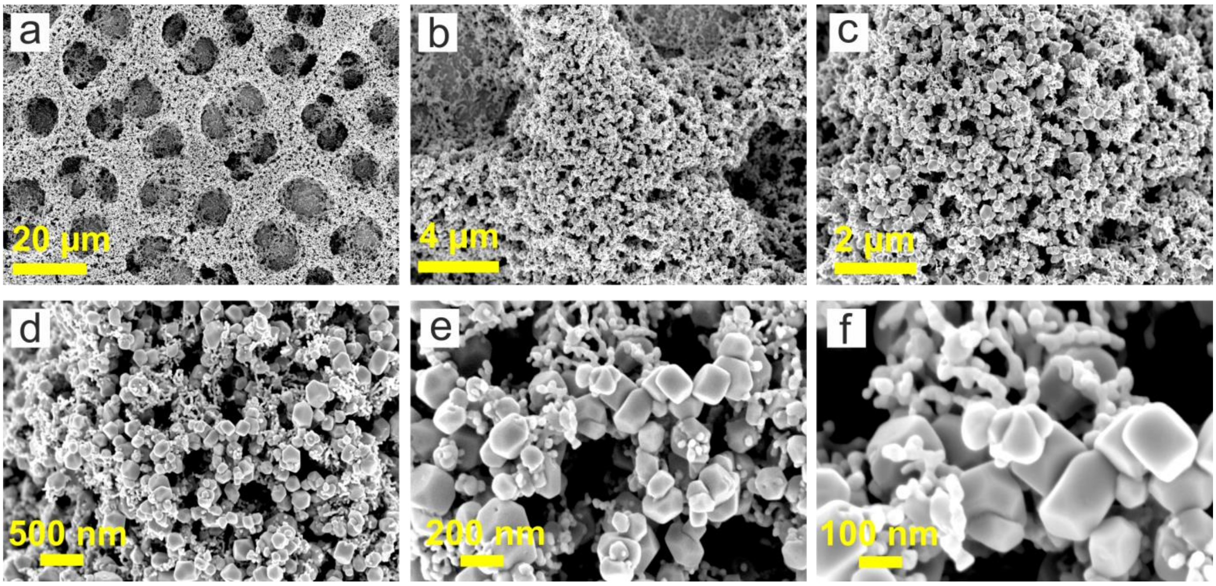

Fig. S4: Series of top-down SEM micrographs showing the meso-porosity and micro-porosity of the respective bimetallic AgCu foam deposited in the absence of the citrate additive (Cu foil substrate, j = – 3 A cm^{-2}, 20 sec. deposition time) using a plating bath containing 1.5 M H_2SO_4, 20 mM $CuSO_4$, 2 mM Ag_2SO_4,). Note that both the pore size distribution and the pore side-wall morphology are altered compared to the electro deposited from the additive-containing bath (see Fig. 1).

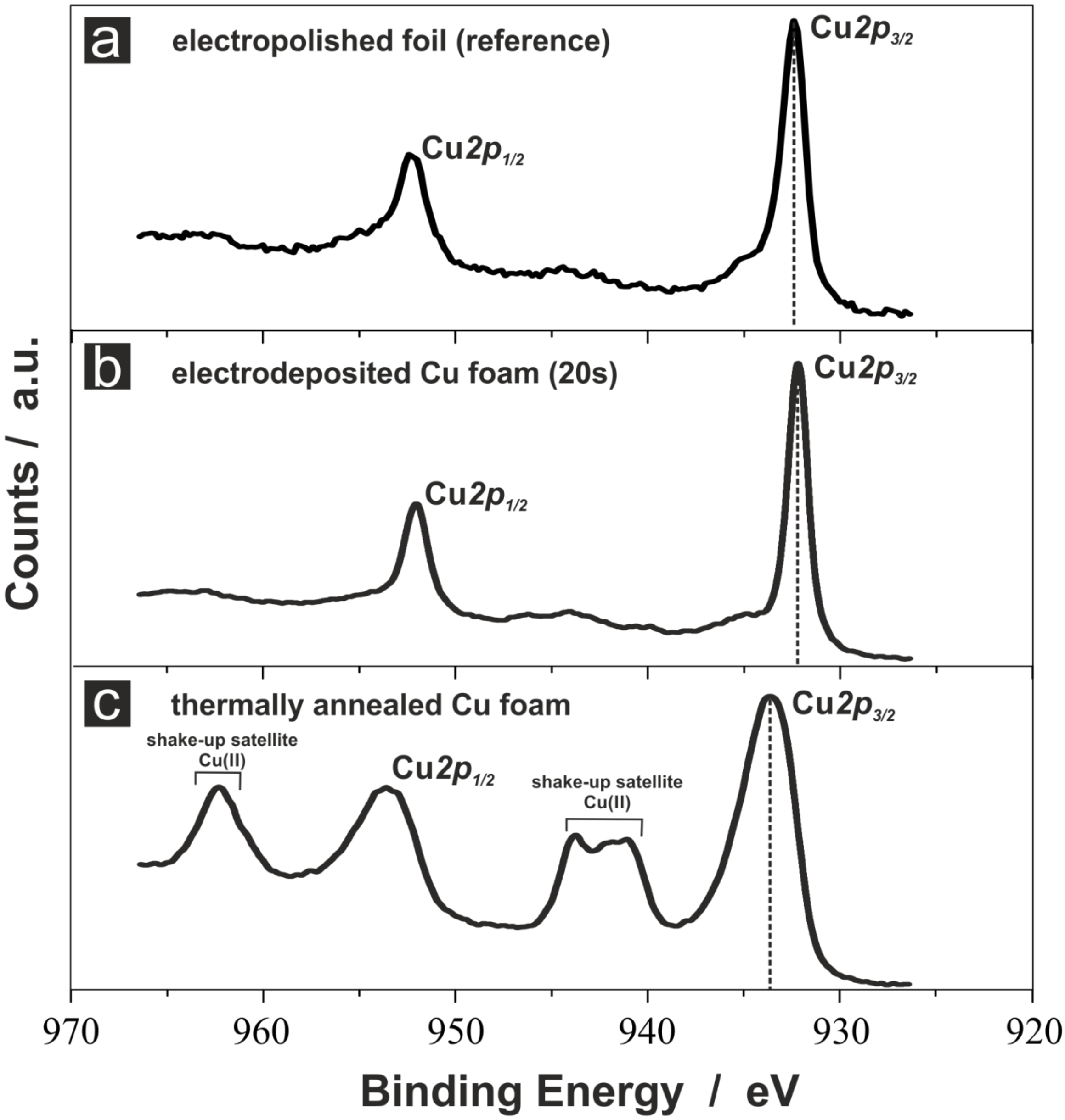

Fig. S5: Representative ex situ XPS analysis of a pure as deposited Cu catalyst and an annealed Cu catalyst deposited at -3 A cm^{-2} (20 s) in the absence of citrate. The upper panel displays the XPS spectrum of an electro-polished Cu foil.

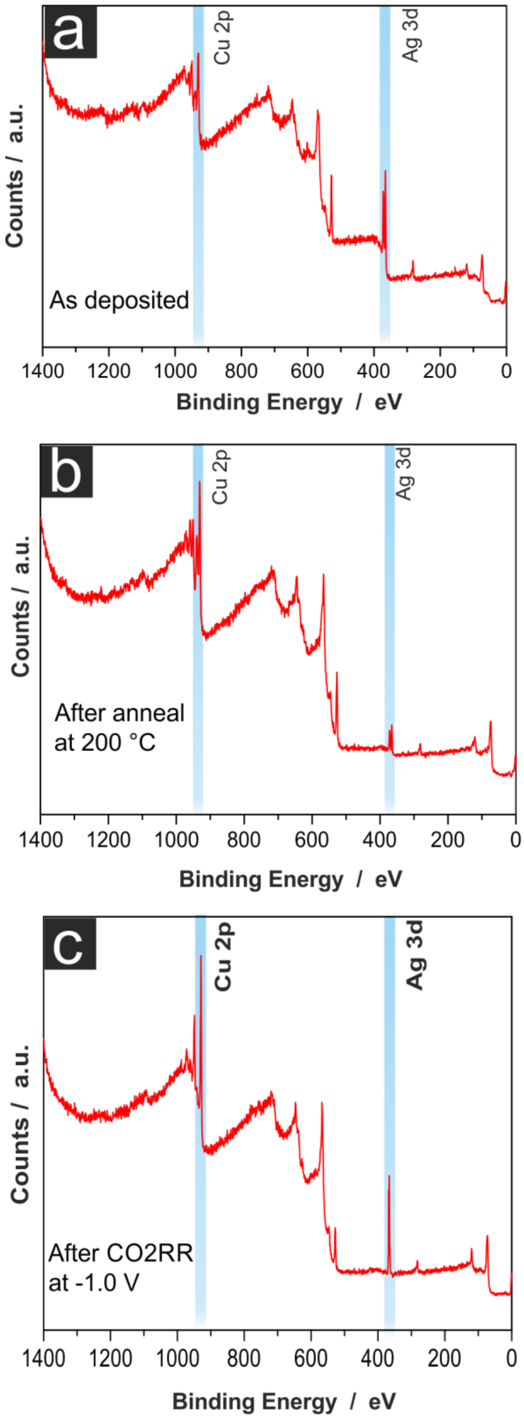

Fig. S6: Survey XPS spectra of the $Ag_{15}Cu_{85}$ foam on which the determination of the I_{Cu2p}:I_{Ag3d} ratio was based on (panel a: as deposited; panel b: after anneal at 200 °C; panel c: after 1 h CO_2RR at -1.0 V vs RHE).

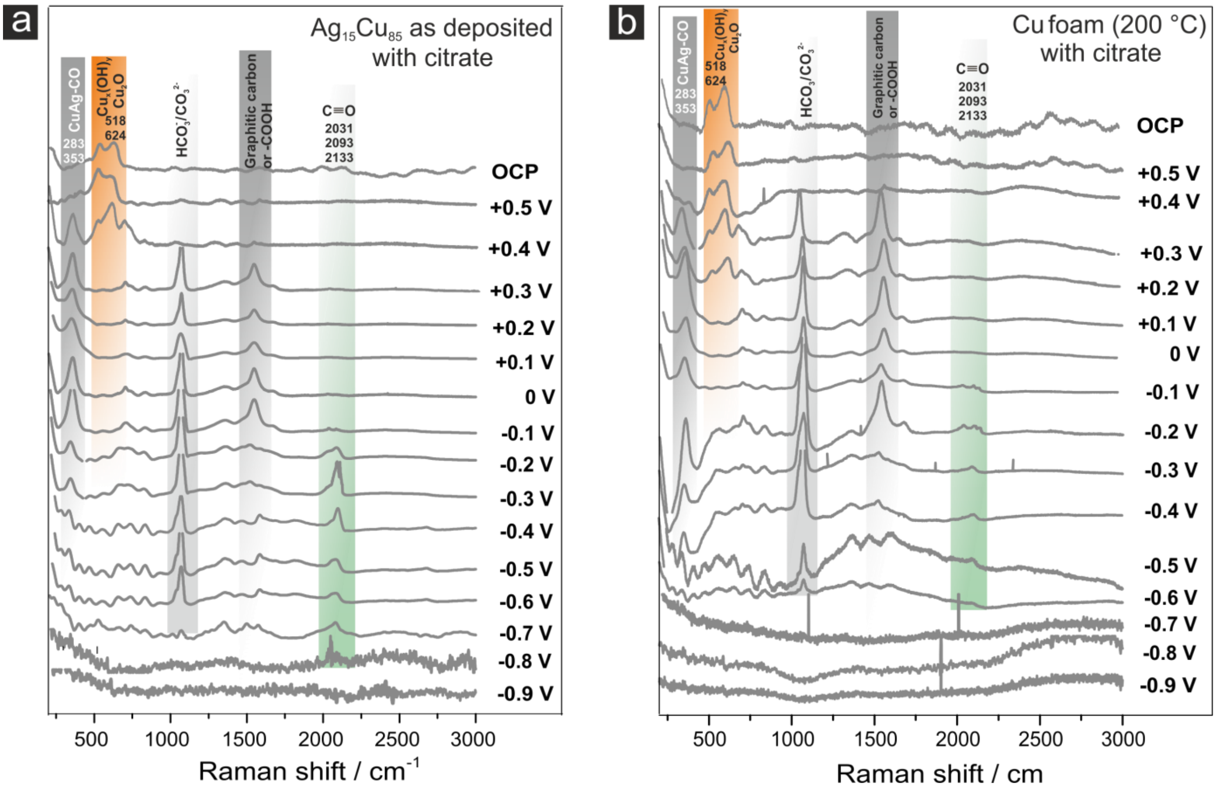

Fig. S7 Representative operando Raman spectra of (a) as deposited $Ag_{15}Cu_{85}$ foam and (b) Cu foam (12 h at 200 °C) as function of the applied electrode potentials. Citrate additive is used during deposition of Cu and bimetallic AgCu foam.

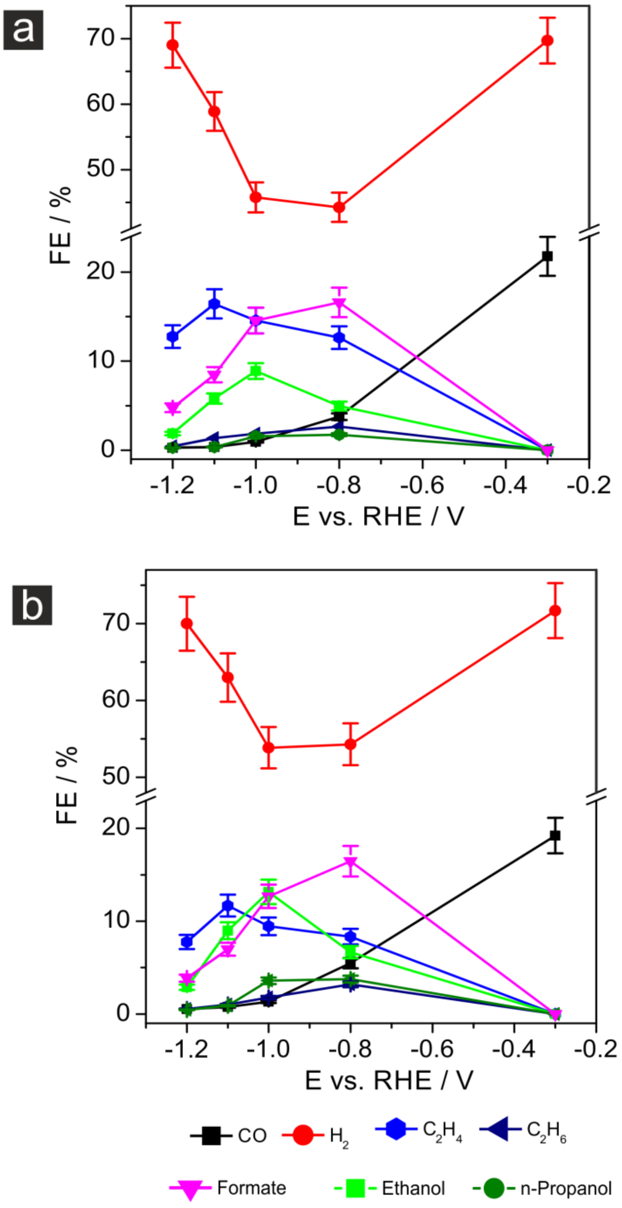

Fig. S8: a) Product distribution of the CO_2RR carried out over the Cu catalyst deposited in the presence of the citrate additive (see Fig. S3); b) Product distribution of the CO_2RR carried out over the thermally annealed (oxide-derived) Cu catalyst. The annealing temperature was 200 °C (12 h).

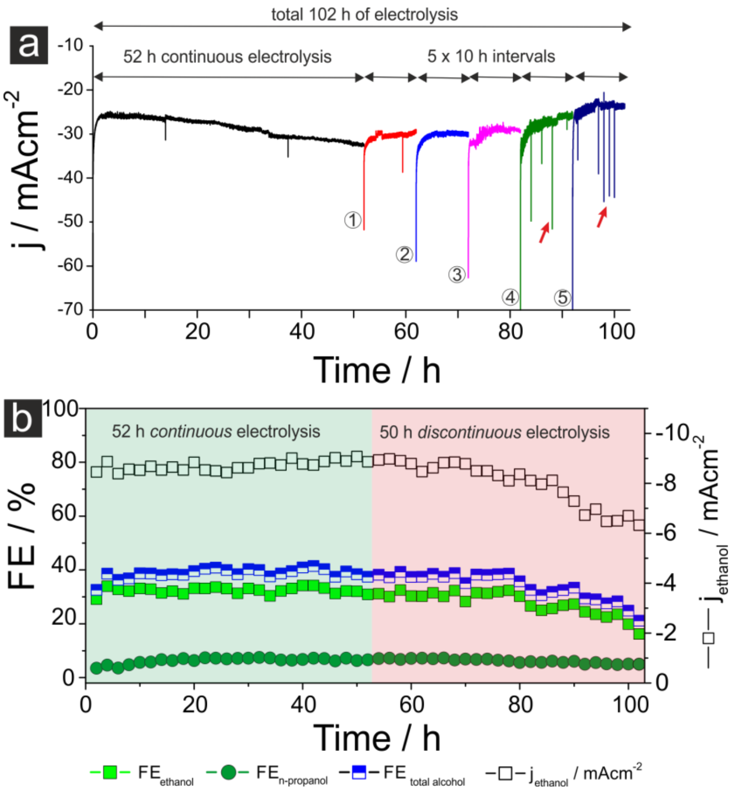

Fig. S9: a) Current density/time transient curve of the 102 h lasting catalyst stressing experiment at -1.0 V vs RHE (note that the electrolysis current is normalized to the geometric surface area); b) Corresponding CO_2RR product distribution focusing on the alcohol production and hydrogen formation.

The catalyst stressing experiment consists of two major parts. The first one represents a continuous electrolysis over 52 h followed by an extra sequence of 5 discontinuous electrolysis intervals of 10 h duration each. In between the electrolysis was interrupted for 6-8 h and the catalyst was kept in Milli-Q water at the OCP. Larger cathodic current spikes (labeled 1-5 in panel a) correspond to the reduction of oxides formed during the electrolysis off-time and the exposure of the catalyst to Milli-Q water at the OCP. During the second half of the stressing experiment the catalyst undergoes several surface oxidation/reduction cycles. Extra cathodic events in current/time transient (highlighted by red arrows in panel a) are due to short unintentional losses of the potential control, likely caused by gas bubbles formed upon electrolysis.

The product distribution during the first 52 h of continuous electrolysis remains largely constant with FE_{EtOH} values of 33 ± 3% (main alcohol component) and efficiencies for n-propanol (minor alcohol component) formation of $FE_{n\text{-}PrOH} = 5 \pm 2\%$. Catalyst degradation starts to occur when the electrolysis was carried out in the discontinuous mode. Obviously, it is not the CO2RR and the alcohol production which induce the observed drop-down of the FE_{acohol} values but the repeated oxidation/reduction cycles in the discontinuous electrolysis experiment. Our quantitative XPS analysis on the catalyst activation already demonstrated that the oxidation/reduction of the bimetallic catalyst goes along with severe morphological and compositional changes which might also involve the partial loss of Ag on the catalyst surface (Fig. 2 and Fig. S7). It can be assumed that similar compositional changes on the catalyst surface are the origin of the observed degradation at extended electrolysis times of > 70 h (panel b).

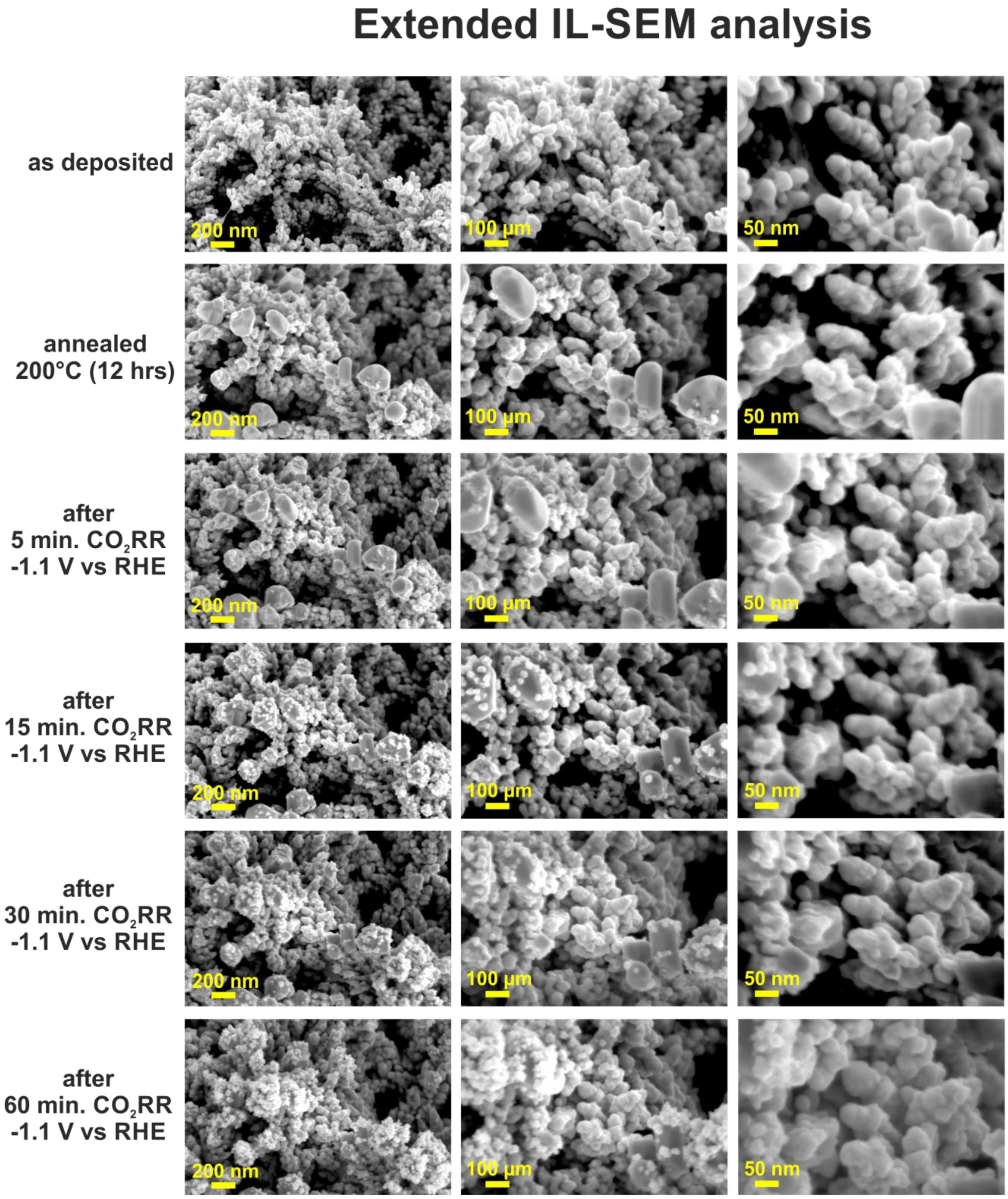

Fig. S10: Series of top-down SEM images showing the morphological changes as consequence of a discontinuous electrolysis experiment.

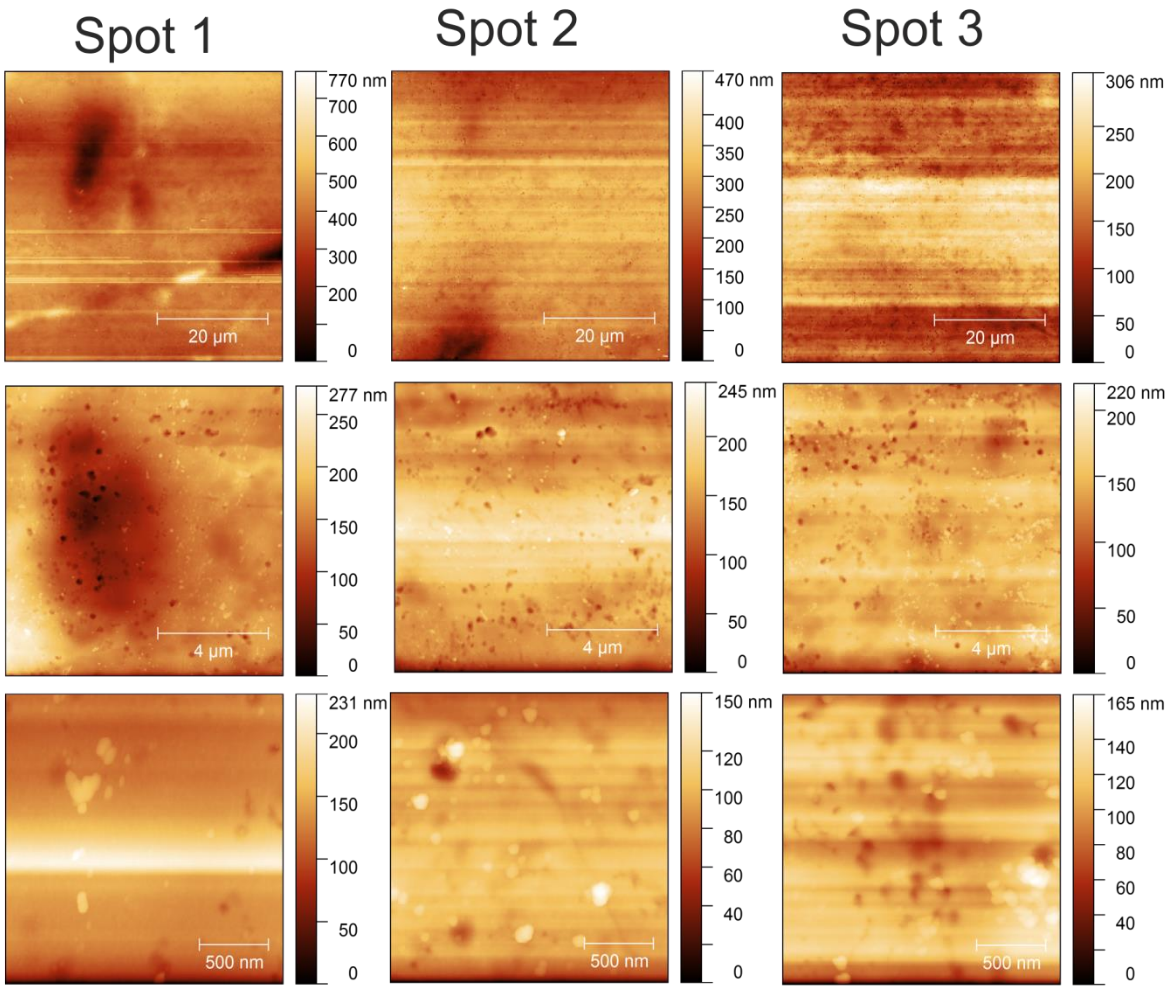

Fig. S11: Representative AFM images showing the surface morphology of the electropolished Cu foil which serves as substrate for the AgCu foam electrodeposition.

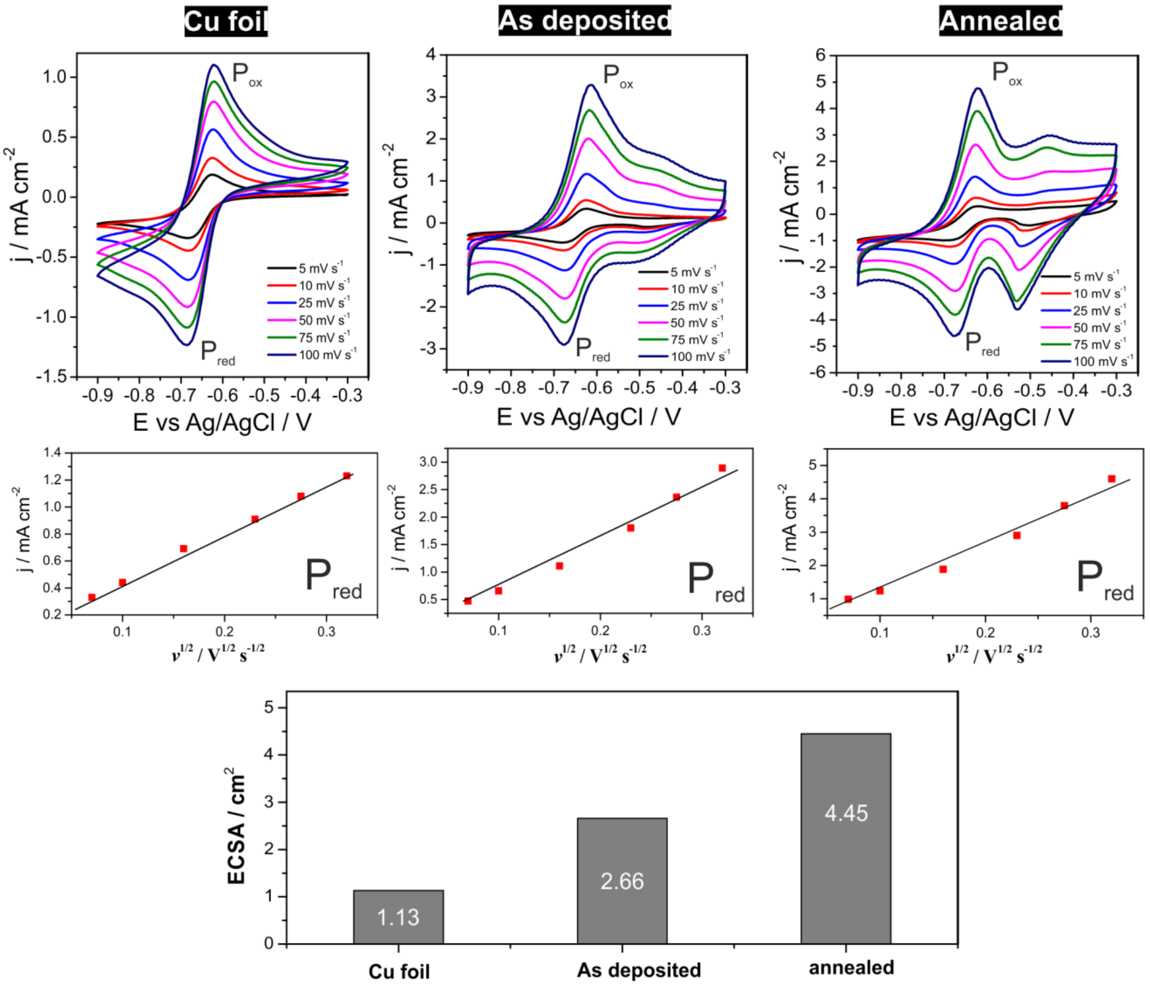

Fig. S12: Scan-rate dependent cyclic voltammograms (CVs) of the Cu foil substrate, the as deposited $Ag_{15}Cu_{85}$ foam and the respective annealed bimetallic foam in aqueous 1 M Na_2SO_4 (ACS grade, Sigma-Aldrich) solution containing 10 mM $DMVCl_2$. The electrochemically active surface area was estimated on the basis of the Randles–Sevcik equation relating the peak current density (referred to the geometric surface area) of the voltammogram to the square root of the applied potential sweep rate. We are aware the Randles–Sevcik equation was originally derived for ideally planar electrode surfaces and not for roughened metal foams. However, this approach might be yet applicable as there is a clear linear relation between the peak current density and the square root of the potential sweep rate.

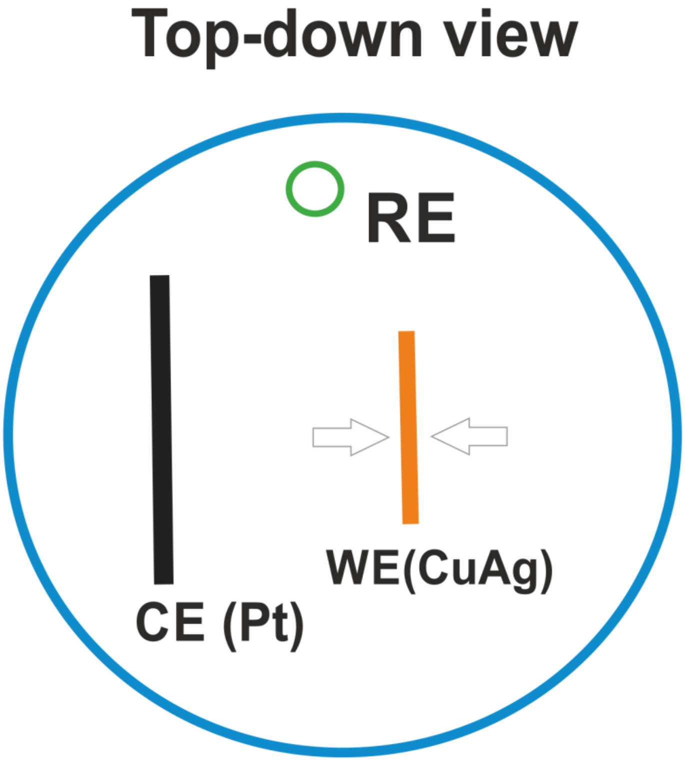

Fig. S13: Schematics showing the face-to-face arrangement of WE, RE, and CE in the glass beaker used for the metal foam electrodeposition. The distance between CE and WE electrode was 3.5 cm.

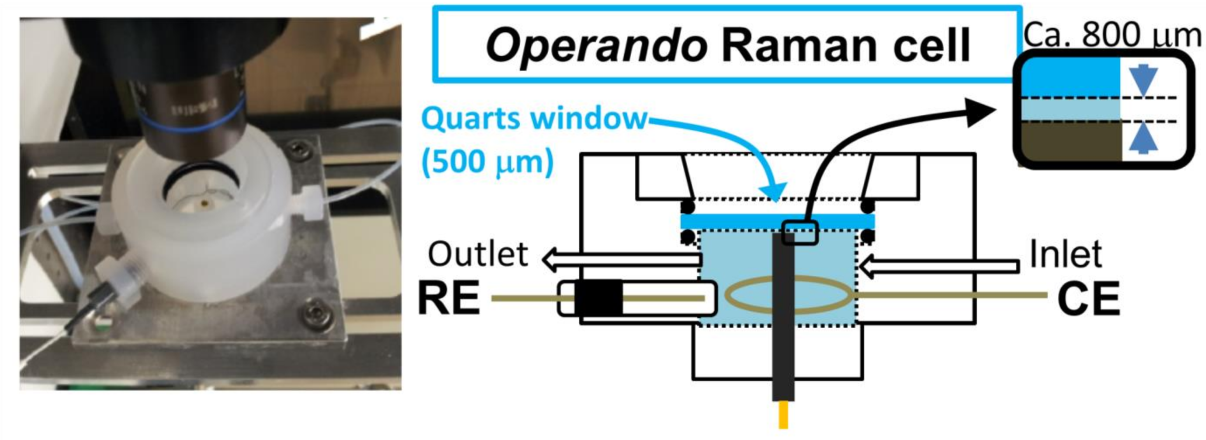

Fig. S14: Optical micrograph and schematics of the *operando* Raman cell used in this study.

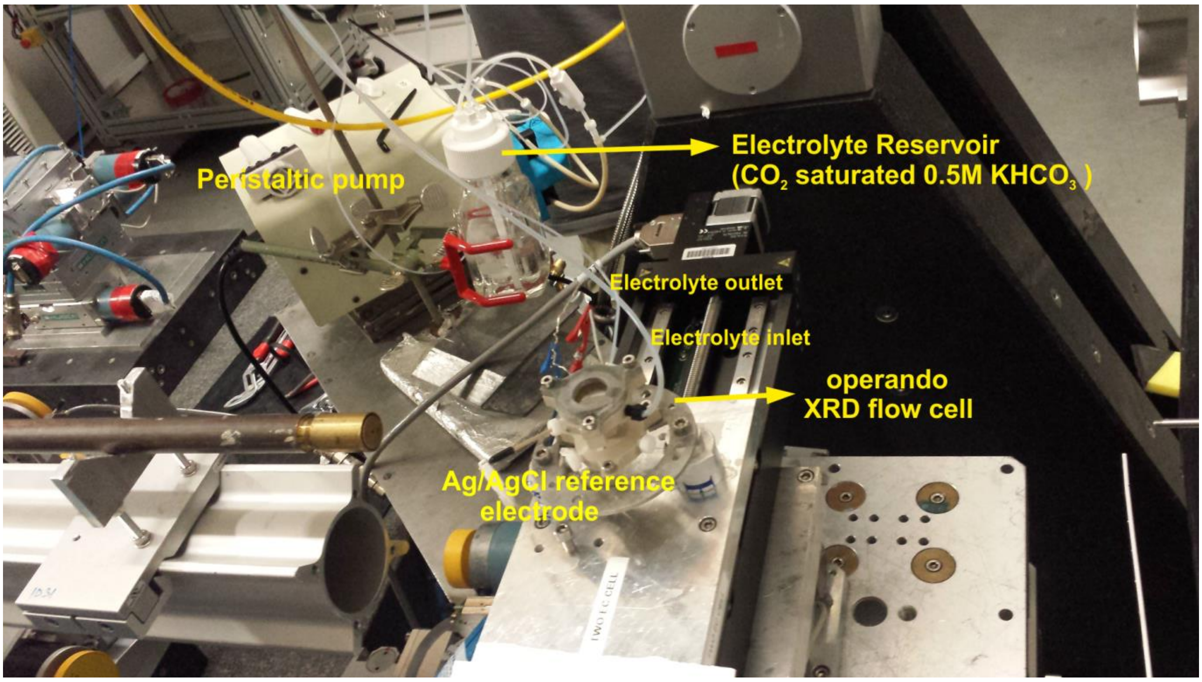

Fig. S15: Optical micrograph showing the *operando* XRD experimental set-up at the ESRF (ID31) used in this study.

Table S1: Structural characteristics of catalysts obtained from EDX, ICP-OES, and ex-situ XRD

Catalysts	Metal composition CuAg (at%)		2θ / degree ; (hkl) CuKα radiation (λ = 0.1540 nm)					
	From EDX	From ICP-OES	(110)	(111)	(200)	(220)	(311)	(222)
^{i}Ag	-	-	-	38.11	44.27	64.42	77.47	81.57
^{ii}Cu	-	-	-	43.29	50.43	74.12	89.92	95.13
^{iii}Ag_2O	-	-	26.60	32.79	38.04	54.90	65.44	68.74
^{iv}Cu_2O	-	-	29.56	36.41	42.29	61.34	73.52	77.32
CuAg (as deposited)	89/11	85/15	-	38.08/43.25/36.39	50.41/44.3	74.10/64.44	-	-
CuAg (annealed)	87/13	84/16	-	36.43/38.08/43.22	42.31/44.29	61.36/64.45	-	-
CuAg (after electrolysis)	88/12	83/17	-	38.13/43.33/36.37	44.29/50.40/42.33	74.15/64.39	-	-

^{i}JCPDS Ag : 040-783 ; ^{ii}JCPDS Cu: 040-836; ^{iii}JCPDS $_{Ag_2O}$: 430-997; ^{iv}JCPDS $_{Cu_2O}$: 05-0667

Table S2: Faradaic efficiency (FE) values at different applied electrolysis potential of the *ec*-CO_2RR on '*as deposited $Ag_{15}Cu_{85}$ foam*' (1h potentiostatic *ec*-CO_2RR)

$Ag_{15}Cu_{85}$ (as deposited)								
Potentials (vs. RHE)	Faradaic Efficiency (FE) %							
	CO	H_2	Formate	C_2H_4	C_2H_6	CH_4	Ethanol	1-Propanol
-0.3	81.45	21.3	0	0	0	0	0	0
-0.4	76.8	20.1	0	0	0	0	0	0
-0.5	75.56	20.56	1.36	2.2	0	0	0	0
-0.6	60.67	26.67	1.87	6.45	1.34	0	0	0
-0.7	45.657	29.76	3.66	11.786	1.85	0	1.33	0.43
-0.8	25.67	35.45	5.98	16.45	1.89	0	2.77	0.89
-0.9	13.56	39.56	4.66	25.67	0.874	0	3.89	1.1
-1	3.45	41.5	3.45	29.56	0.78	10.33	4.67	1.5
-1.1	1.56	40.6	1.563	36.56	0.67	22.45	3.22	0.78
-1.2	1.44	65.67	0.564	15.67	0.34	25.67	1.35	0.35
-1.3	0.89	70.33	0	8.895	0	15.67	0.52	0

Table S3. Partial current density values at different applied electrolysis potential of the *ec*-CO_2RR on '*as deposited $Ag_{15}Cu_{85}$ foam*' (1h potentiostatic *ec*-CO_2RR)

$Ag_{15}Cu_{85}$ (As deposited)								
Potentials (vs. RHE)	**Partial current density ($mAcm^{-2}$)**							
	CO	H_2	Formate	C_2H_4	C_2H_6	CH_4	Ethanol	1-Propanol
-0.3	-0.24	-0.16	0	0	0	0	0	0
-0.4	-0.46	-0.24	0	0	0	0	0	0
-0.5	-1.28	-0.31	-0.0023	-0.0037	0	0	0	0
-0.6	-2.79	-1.23	-0.0087	-0.290	-0.06	0	0	0
-0.7	-2.78	-1.83	-0.223	-0.71	-0.11	0	-0.08	-0.026
-0.8	-2.13	-3.12	-0.49	-1.37	-0.15	0	-0.23	-0.07
-0.9	-1.97	-6.04	-0.70	-3.81	-0.13	0	-0.58	-0.166
-1	-0.73	-8.85	-0.73	-6.33	-0.16	-2.20	-1.11	-0.14
-1.1	-0.42	-11.1	-0.42	-11.32	-0.18	-6.12	-0.87	-0.21
-1.2	-0.53	-24.42	-0.20	-6.80	-0.12	-9.77	-0.50	-0.12
-1.3	-0.43	-31.24	0	-3.87	0	-7.04	-0.22	0

Table S4: Overview of the performances of Cu-based catalysts for ethylene production for *ec*-CO_2RR

Catalysts	**FE_{C2H4}**	**E (V vs. RHE)**	**Partial current ($mAcm^{-2}$)**	**Ref.**
O_2 plasma treated Cu foil	~61 %	-0.92 V	~ -7.2	[1]
40 wt % Cu NP/vulcan C	~47 %	-1.77 V	-18.9	[2]
Cu dendrite	~35 %	-1.1 V	-10.8	[3]
Oxide derived Cu	~30 %	-1.0 V	-7.98	[4]
Cu Single Crystal (Orientation 711)	~59 %	-1.0 V	-	[5]
Redeposited Cu from $Cu_2(OH)_3Cl$ sol−gel	~39 %	-1.2 V	-29.6	[6]
Cu nanocube (44 nm)	~42 %	-1.1 V	-	[7]
C supported Cu nanoparticle	57 %	-1.1 V	~ -12.1	[8]

Table S5: Faradaic efficiency (FE) values at different applied electrolysis potential of the *ec*-CO_2RR on '*annealed $Ag_{15}Cu_{85}$ foam (200 °C, 12 h)'* (1h potentiostatic *ec*-CO_2RR)

$Ag_{15}Cu_{85}$ (annealed)								
Potentials (vs. RHE)	**Faradaic Efficiency (FE) %**							
	CO	H_2	Formate	C_2H_4	C_2H_6	CH_4	Ethanol	1-Propanol
-0.3	37.44	55.00	0	0	0	0	0	0
-0.5	48	42.00	0	0	0	0	0	0
-0.6	52	43.45	2.33	0	0	0	5.87	1.33
-0.8	35.67	35.45	4.45	4.78	1.89	0	6.98	5.01
-0.9	13.56	39.56	3.34	5.89	0.874	0	14.56	6.9
-1	3.45	43.8	3.45	6.60	0.78	2.33	33.71	3.98
-1.1	1.56	48.86	1.563	10.20	0.67	2.11	23.65	2.9
-1.2	1.21	62.76	0.88	5.88	0.23	2.98	10.33	2.876
-1.3	0.89	77.65	0	4.895	0	2.12	4.22	1.056

Table S6: Partial current density values at different applied electrolysis potential of the *ec*-CO_2RR on '*annealed $Ag_{15}Cu_{85}$ foam (200° C, 12 h)'* (1h potentiostatic *ec*-CO_2RR)

$Ag_{15}Cu_{85}$ (annealed)								
Potentials (vs. RHE)	**Partial current density ($mAcm^{-2}$)**							
	CO	H_2	Formate	C_2H_4	C_2H_6	CH_4	Ethanol	1-Propanol
-0.3	-0.18	-0.27	0	0	0	0	0	0
-0.5	-0.90	-0.84	0	0	0	0	0	0
-0.6	-2.87	-2.40	-0.128	0	0	0	-0.324	-0.07
-0.8	-4.75	-4.72	-0.59	-0.63	-0.25	0	-0.93	-0.67
-0.9	-2.65	-7.74	-0.65	-1.15	-0.17	0	-3.85	-1.79
-1	-0.910	-11.55	-0.91	-2.40	-0.20	-0.61	-8.67	-1.01
-1.1	-0.50	-15.96	-0.50	-3.11	-0.21	-0.68	-7.70	-0.94
-1.2	-0.46	-26.27	-0.36	-2.45	-0.09	-1.28	-4.30	-1.19
-1.3	-0.41	77.65	-36.0	4.895	0	-0.98	-1.96	-0.49

Table S7: Overview of the performances of Cu-based catalysts for the electroreduction of CO_2 to ethanol and propanol

Catalysts	**Pot. (vs. RHE)**	**FE$_{\mathbf{EtOH}}$ / %**	**FE$_{\mathbf{Propanol}}$ / %**	**Ref.**
Cu_2O/rGO NC	-0.1 V	9.93	-	[9]
Cu_2O-ZnO	-0.8 V	10.1	2.12	[10]
3.6 µm Cu_2O	-1.0 V	16.37	-	[11]
Cu_4Zn	-1.0 V	29.1	-	[12]
CuAg porous	-0.7 V	25 (in electrolyzer flow cell)	-	[13]
Cu Nanocrystals	-0.95 V	7.7	8.8 to 10.1	[14]
Cu dendrite	-1.0 V	13%	11.3	[3]
PYD]@Cu–Pt	-0.65 V	25 %	4	[15]
Cu NPs	-81.0 V	15.5	6.1	[16]

Table S8: Overview of the performances of different CuAg catalysts for the electroreduction of CO_2.

Catalysts	**FE$_{\mathbf{CO}}$**	**FE$_{\mathbf{C2H4}}$ at E (RHE)**	**FE$_{\mathbf{EtOH}}$**	**FE$_{\mathbf{Propanol}}$**	**Ref.**
CuAg dendrite	18 % at -0.75 V	14 % at -0.75 V	-	-	[17]
Nano porous CuAg alloy	27 % at -0.3 V (in electrolyzer flow cell)	60 % at -0.7 V (in electrolyzer flow cell)	25 % at -0.7 V (in electrolyzer flow cell)	-	[13]
Ag–Cu dendrite	43 % at -0.9 V	-	-	-	[18]
Cu-Ag Foam	63 % at -0.6 V	-	-	-	[19]
Cu-Ag Foam	17.8% at -0.6 V	-	-	-	[20]
Cu_{80}-Ag_{20} Film	14 % at -1.05 V	22 % at -1.05 V	18 % at -1.05 V	3 % at -1.05 V	[21]

References:

[1] H. Mistry, A.S. Varela, C.S. Bonifacio, I. Zegkinoglou, I. Sinev, Y.-W. Choi, K. Kisslinger, E.A. Stach, J.C. Yang, P. Strasser, B.R. Cuenya, Nature Communications 7 (2016) 12123.

[2] O.A. Baturina, Q. Lu, M.A. Padilla, L. Xin, W. Li, A. Serov, K. Artyushkova, P. Atanassov, F. Xu, A. Epshteyn, T. Brintlinger, M. Schuette, G.E. Collins, ACS Catalysis 4 (2014) 3682-3695.

[3] M. Rahaman, A. Dutta, A. Zanetti, P. Broekmann, ACS Catalysis 7 (2017) 7946-7956.

[4] A.D. Handoko, C.W. Ong, Y. Huang, Z.G. Lee, L. Lin, G.B. Panetti, B.S. Yeo, The Journal of Physical Chemistry C 120 (2016) 20058-20067.

[5] Y. Hori, I. Takahashi, O. Koga, N. Hoshi, The Journal of Physical Chemistry B 106 (2002) 15-17.

[6] P. De Luna, R. Quintero-Bermudez, C.-T. Dinh, M.B. Ross, O.S. Bushuyev, P. Todorović, T. Regier, S.O. Kelley, P. Yang, E.H. Sargent, Nature Catalysis 1 (2018) 103-110.

[7] A. Loiudice, P. Lobaccaro, E.A. Kamali, T. Thao, B.H. Huang, J.W. Ager, R. Buonsanti, Angew. Chem. Int. Ed. 55 (2016) 5789-5792.

[8] H. Jung, S.Y. Lee, C.W. Lee, M.K. Cho, D.H. Won, C. Kim, H.-S. Oh, B.K. Min, Y.J. Hwang, J. Am. Chem. Soc. 141 (2019) 4624-4633.

[9] R.A. Geioushy, M.M. Khaled, A.S. Hakeem, K. Alhooshani, C. Basheer, J. Electroanal. Chem. 785 (2017) 138-143.

[10] J. Albo, A. Irabien, J. Catal. 343 (2016) 232-239.

[11] D. Ren, Y. Deng, A.D. Handoko, C.S. Chen, S. Malkhandi, B.S. Yeo, ACS Catalysis 5 (2015) 2814-2821.

[12] D. Ren, B.S.-H. Ang, B.S. Yeo, ACS Catalysis 6 (2016) 8239-8247.

[13] T.T.H. Hoang, S. Verma, S. Ma, T.T. Fister, J. Timoshenko, A.I. Frenkel, P.J.A. Kenis, A.A. Gewirth, J. Am. Chem. Soc. 140 (2018) 5791-5797.

[14] D. Ren, N.T. Wong, A.D. Handoko, Y. Huang, B.S. Yeo, The Journal of Physical Chemistry Letters 7 (2016) 20-24.

[15] H.-P. Yang, Y.-N. Yue, S. Qin, H. Wang, J.-X. Lu, Green Chemistry 18 (2016) 3216-3220.

[16] D. Kim, C.S. Kley, Y. Li, P. Yang, Proceedings of the National Academy of Sciences 114 (2017) 10560.

[17] Z.-Y. Chang, S.-J. Huo, J.-M. He, J.-H. Fang, Surfaces and Interfaces 6 (2017) 116-121.

[18] J. Choi, M.J. Kim, S.H. Ahn, I. Choi, J.H. Jang, Y.S. Ham, J.J. Kim, S.-K. Kim, Chem. Eng. J. 299 (2016) 37-44.

[19] T. Kottakkat, K. Klingan, S. Jiang, Z.P. Jovanov, V.H. Davies, G.A.M. El-Nagar, H. Dau, C. Roth, ACS Applied Materials & Interfaces 11 (2019) 14734-14744.

[20] H. Lee, S.H. Ahn, Bull. Korean Chem. Soc. 38 (2017) 1085-1090.

[21] E.L. Clark, C. Hahn, T.F. Jaramillo, A.T. Bell, J. Am. Chem. Soc. 139 (2017) 15848-15857.

7.4. Size-dependent Structural Alterations in Ag Nanoparticles During CO_2 Electrolysis in a Gas-fed Zero-gap Electrolyzer

Authors: Huifang Hu, Menglong Liu, Ying Kong, **Iván Zelocualtecatl Montiel**, Yuhui Hou, Alexander V. Rudnev, Peter Broekmann

Highlights: This work reports the role of the catalyst degradation for Ag-NPs with different particle sizes during CO_2RR in a zero-gap electrolyzer. For this purpose, galvanostatic electrolyzes of the PVP-capped Ag-NPs were performed using three different particle sizes of 10, 40 and 100 nm. The combination of SEM and size distribution analyses of the Ag-NP_S@GFE electrodes before and after electrolysis showed that the NPs with a particle size of 10 nm underwent agglomeration during electrolyzes, giving place to the formation of larges agglomerates of 200 nm of distance. For the 40 nm NPs, fragmentation was more noticed with the formation of smaller clusters. While, for the 100 nm NPs, two pathways were observed; 1) agglomeration of two or three initial particles giving place to particles sizes of 170-200 nm, and 2) fragmentation of the initial NPs giving place to smaller NPs of 11-13 nm size. The fragmentation could be associated with cathodic corrosion of Ag-NPs at negative potentials under CO_2RR and HER conditions. The use of ICP-MS demonstrated that the Ag-NPs loading of the electrodes did not show considerable change before and after electrolyzes experiments, which does not affect the CO_2RR.

Contributions: In this project, I was involved in conducting ICP-MS. In addition, I participated in the manuscript revision process.

ChemElectroChem

Chemistry Europe
European Chemical Societies Publishing

Accepted Article

Title: Size-dependent Structural Alterations in Ag Nanoparticles During CO2 Electrolysis in a Gas-fed Zero-gap Electrolyzer

Authors: Huifang Hu, Menglong Liu, Ying Kong, Iván Zelocualtecatl Montiel, Yuhui Hou, Alexander V. Rudnev, and Peter Broekmann

To be cited as: *ChemElectroChem* **2022**, e202200615

Link to VoR: https://doi.org/10.1002/celc.202200615

WILEY-VCH

ChemElectroChem 10.1002/celc.202200615

Size-Dependent Structural Alterations in Ag Nanoparticles During CO_2 Electrolysis in a Gas-Fed Zero-Gap Electrolyzer

Huifang Hu,[a] Menglong Liu,[a,b] Ying Kong,[a,b] Iván Zelocualtecatl Montiel,[a,b] Yuhui Hou,[a] Alexander V. Rudnev,*[a,c] Peter Broekmann*[a,b]

[a] H. Hu, M. Liu, Y. Kong, I. Zelocualtecatl Montiel, Dr. Y. Hou, Dr. A.V. Rudnev, Prof. P. Broekmann
Department of Chemistry, Biochemistry and Pharmaceutical Sciences
University of Bern
Freiestrasse 3, 3012 Bern, Switzerland
E-mail: peter.broekmann@unibe.ch, alexander.rudnev@unibe.ch
[b] M. Liu, Y. Kong, I. Zelocualtecatl Montiel, Prof. P. Broekmann
National Centre of Competence in Research (NCCR) Catalysis
University of Bern
Freiestrasse 3, 3012 Bern, Switzerland
[c] Dr. A.V. Rudnev
A.N. Frumkin Institute of Physical Chemistry and Electrochemistry
Russian Academy of Sciences
Leninskii pr. 31 bld. 4, 119071 Moscow, Russia

Supporting information for this article is given via a link at the end of the document.

Abstract: Ag nanoparticles (NPs) are efficient electrocatalysts for electrochemical CO_2-to-CO conversion. However, NPs are thermodynamically unstable and can undergo structural alterations under electrolysis operating conditions. These structural changes may play a crucial role in the deterioration of CO_2 reduction reaction (CO_2RR) performance on the long-term electrolysis time scale. Here, we studied the effect of NP size on NP degradation during CO_2RR. Polyvinylpyrrolidone-capped 10-, 40, and 100-nm Ag NPs deposited on a gas diffusion electrode were used as testbed catalysts in a gas-fed zero-gap electrolyzer. Inductively coupled plasma mass spectrometry indicated insignificant catalyst-material detachment after galvanostatic CO_2 electrolysis. Scanning electron microscopy analysis showed that smaller NPs tended to agglomerate during CO_2 electrolysis. 100-nm NPs formed agglomerates consisting of only two-three NPs and underwent pronounced fragmentation with the formation of particles several nanometers in size. The fragmentation was associated with cathodic corrosion of Ag NPs under conditions of intensive CO_2RR and hydrogen evolution.

Introduction

Electrochemical CO_2 conversion is a promising approach for the storage of renewable electricity in a sustainable manner and the production of synthetically or industrially valuable platform chemicals.[1] Currently, research on the electrochemical approach is driven primarily by the technological demand for catalyst and electrolyzer configurations that provide selective and stable progress of CO_2 reduction reaction (CO_2RR).

CO_2RR in H-type electrochemical cells (two-compartment cells with a membrane separating the cathode and anode compartments) suffers from mass transport limitations, owing to the low concentration of CO_2 in electrolyte solutions. The use of a zero-gap gas-flow electrolyzer unit with a gas diffusion electrode (GDE) overcomes these limitations, thus resulting in current densities of CO_2RR above 300 mA cm^{-2}.[2-5] Modern commercial GDEs consist of a carbon fiber support (CFS) and a microporous layer (MPL) with the catalyst layer deposited on the MPL.[6] In the zero-gap configuration, a humidified CO_2 gas diffuses through a porous gas diffusion layer (CFS and MPL) of the GDE to the active sites of the catalyst.

Metallic nanoparticles (NPs) deposited on a GDE can be used as efficient electrocatalysts for CO_2 reduction. High selectivity for CO_2-to-CO conversion has been achieved, for example with nanoparticulate or nanostructured Ag catalysts.[7-11] Relatively low loading of nanoparticulate catalyst material can be used to achieve a CO_2RR current density at an industrially relevant level. However, owing to their small size, NPs can be thermodynamically unstable and undergo structural alterations under electrolysis operating conditions. Degradation mechanisms for fragmentation, reshaping, poisoning, agglomeration, dissolution (redeposition), detachment, and Oswald ripening have been reported for NPs under CO_2RR at negative potentials [12, 13]. NP fragmentation can be considered as a phenomenon of cathodic corrosion.[14]

Although NP-catalyst degradation behavior during CO_2RR has been intensively studied in H-type and one-compartment cells (e.g., see refs.[12, 15-20]), the conclusions obtained in these studies might not be directly applicable to the zero-gap electrolyzer configuration.[2] In the latter case, the investigation of catalyst degradation has been hindered by the precipitation of (bi)carbonate salt at a three-phase GDE interface within several or few tens of minutes, thus severely suppressing CO_2RR.[2, 3, 21-23] Nevertheless, the study of NP-catalyst structural changes during CO_2RR in a zero-gap electrolyzer under harsh conditions (high current densities) is extremely important, because NP degradation is crucial for CO_2RR performance on the long-term electrolysis time scale.

Multiple factors affect NP degradation behavior. In our previous work, we have studied the effect of a capping agent on structural alterations of spherical Ag NPs after CO_2RR in a zero-gap electrolyzer.[3] Ag NPs 40 nm in size were stabilized by four capping agents: branched polyethylenimine (PEI), polyvinylpyrrolidone (PVP), polyethylene glycol (PEG), and citrate. Although the NPs displayed identical size distributions, they differed in their activity toward CO_2RR in terms of faradaic efficiency for CO formation, FE_{CO}, and current densities in the course of potentiostatic electrolysis. Thus, the structural changes in NPs occurring during electrolysis were also affected by the chemical nature of the capping agent. Here, continuing our investigation of the degradation behavior of Ag NP catalysts, we focused on the effect of NP size on structural changes during CO_2RR in a zero-gap electrolyzer (the corresponding configuration has been described in detail in refs.[3, 23], Figure S1). Catalyst inks were prepared from commercially available PVP-capped 10-, 40-, and 100-nm Ag NPs. Through a set of post-electrolysis analyses of the NP-catalyst, we show that degradation pathways substantially depend on the initial NP size. Smaller NPs tend to agglomerate during CO_2 electrolysis; in particular, 10-nm NPs form agglomerates up to 200 nm in the longest dimension. In addition, 100-nm NPs form agglomerates consisting of only two or three NPs, and undergo pronounced fragmentation, thus forming large amounts of particles several nanometers in size, which are redeposited on the MPL. The fragmentation appears to be associated with cathodic corrosion of Ag NPs at negative potentials under conditions of intensive CO_2RR and hydrogen evolution reaction (HER).

Results and Discussion

Characterization of the as-prepared Ag NP catalysts deposited on the GDE

The as-prepared Ag NP catalyst deposited on the GDE (Figure S2) was analyzed with scanning electron microscopy (SEM) (Figure 1a,e,i). The respective size distributions are shown in Figure 2. SEM images before electrolysis indicated that the Ag NPs were fairly uniformly distributed over the MPL surface. Size analysis demonstrated a normal distribution of NP sizes on the GDE surface before electrolysis. The estimated mode values were close to the values indicated by the manufacturer (the values are given in the graphs, Figure 2). Inductively coupled plasma mass spectrometry (ICP-MS) data demonstrated that the actual mass loading for NPs of different sizes was nearly identical (Table 1). However, according to SEM data the number of NPs on the GDE surface (in terms of volume or mass) appeared dissimilar. The amount (volume and mass) of 10-nm NPs on the GDE surface seemed to be significantly less than those of 40- and 100-nm NPs. This finding is explained by the greater penetration of smaller NPs inside the GDE layers during drop-cast deposition. The cross-sectional SEM images in Figure 3 distinguished the boundary between MPL and CFS. The EDX mapping of Ag demonstrated the presence of Ag NPs inside both MPL and CFS (Figure 3). Moreover, 10-nm NPs were distributed fairly uniformly in the microporous layer, with greater density around cracks and at the boundaries between microporous and microfiber layers. The amount of 10-nm NPs on the surface of the GDE was similar to that inside the microporous layer. This finding was supported by individual EDX spectra (cf. spectrum 1 with spectra 2 and 6 in Figure 3b). Spectrum 3 recorded at the area close to the microporous/microfiber layer boundary showed an enhanced Ag signal. The EDX mapping and spectra 4 and 5 unambiguously indicated that 10-nm NPs penetrated into the CFS.

A slightly less uniform distribution of 40-nm NPs was observed inside MPL (Figure 3c) with increased density on the top surface of MPL, at cracks, and around the MPL/CFS boundary. A smaller amount of Ag NPs was observed in CFS. This observation was supported by individual EDX spectra (Figure 3d). Spectra 1 to 3 showed Ag signals of slightly higher intensity than those in the spectra recorded at areas 4 and 5. A large fraction of 100-nm NPs after deposition were located on top of the MPL (Figure 3e). High density of NPs was also observed at cracks and at the MPL/CFS boundary, whereas NPs were scarcely detected inside MPL and CFS far from large cracks. This result was confirmed by EDX spectra (Figure 3f): spectra recorded at areas inside the layers (2 and 7 in MPL and 5 and 6 in CFS) showing weak or absent Ag signal, whereas the signal was stronger on the top of MPL (spectrum 1) or around the MPL/CFS boundary (spectra 3 and 4). These findings indicated that larger particles (such as 100 nm) scarcely penetrated through/into micropores of MPL, but a portion of these NPs passed through the MPL via cracks and accumulated at the MPL/CFS boundary.

Note that we used the same Ag mass loading for all NP-catalysts. Thus, the surface area of NP-catalysts would certainly depend on their initial size. In addition, the data in Figure 3 clearly show that a large fraction of particles penetrates the GDE and might not participate in the electrolysis reaction. Moreover, the amount of Ag NPs penetrated in CFS layer strongly depends on initial NP size. Estimation of the electroactive area of Ag NPs and the appropriate comparison of surface areas are hardly possible when solely based on the mass loading and size distribution data.

Table 1. Loading of Ag in NP-catalyst as calculated from the drop-cast amount and as estimated by ICP-MS.

Ag NP-catalyst	Calculated loading / µg cm^{-2}	Loading by ICP-MS / µg cm^{-2}		
		as-prepared	after electrolysis[a]	after recovery experiments[b]
10 nm	300	290.52±11.8	267.80±20.7	266.65±9.4
40 nm	300	297.31±16.6	289.43±17.0	277.04±18.0
100 nm	300	303.02±4.8	287.78±18.2	270.68±13.8

[a] After electrolysis at -283 mA cm^{-2} for 60 min. [b] After 2nd electrolysis at -283 mA cm^{-2} for 60 min.

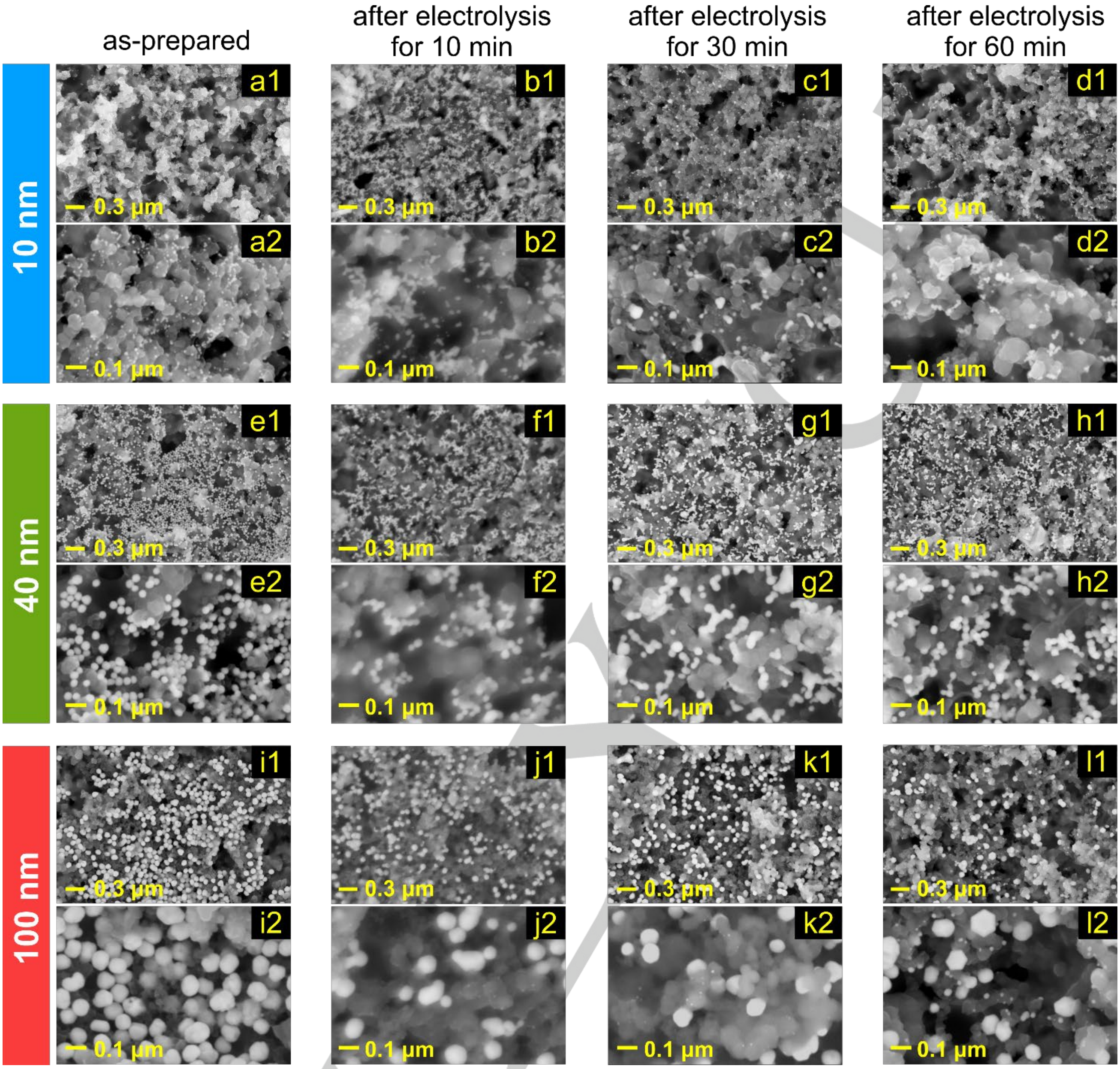

Figure 1. Representative SEM images of Ag NP-catalyst on GDEs. The size of NPs: (a-d) 10 nm, (e-h) 40 nm, (i-l) 100 nm. The SEM images were recorded (a,e,i) before ("as-prepared") and (b-d, f-h, j-l) after galvanostatic CO_2 electrolyses (j = -283 mA cm^{-2}) for different time (different passed charge): (b,f,j) 10 min (169.7 C cm^{-2}), (c,g,k) 30 min (509.2 C cm^{-2}), (d,h,l) 60 min (1018.4 C cm^{-2}). Two images of different magnification are shown for each sample.

CO_2 electrolysis: loss of CO_2RR performance

Figure 4 shows the *FE*s of three detected products (CO, H_2, and $HCOO^-$) forming during CO_2 galvanostatic electrolysis at j = -283 mA cm^{-2} for 60 min (passed charge q = 1018.4 C cm^{-2}). The initial FE_{CO} was ~90–93% and was nearly identical for NPs of different sizes (Figure 4), in agreement with findings form studies on the size effect on CO_2RR. Au NPs and Cu NPs ~5 nm or larger have been reported to show similar CO_2RR performance in terms of faradaic efficiency.[24, 25] Only smaller NPs showed a significant change in the product distribution. Typically, the use of Cu and Au NPs with sizes below 5 nm markedly increased faradaic efficiency of hydrogen formation, FE_{H2}, and decreased CO_2RR efficiency.[24, 25]

However, over time or with a passed charge, the FE_{CO} drastically decreased, whereas the FE_{H2} correspondingly increased. No clear correlation was observed between the NP size and the CO_2RR performance deterioration. The fastest deterioration occurred for 40-nm NPs, whereas the slowest deterioration was observed for 100-nm NPs. The rate of FE_{CO} decrease over time was moderate for 10-nm NPs. Formate was also produced in a detectable amount in our experiments. Typically, FE_{HCOO-} increased over time, reaching ~11% after 60 min of CO_2 electrolysis (1018.4 C cm^{-2}).

The rapid loss in CO_2RR performance has been found to be associated primarily with potassium (bi)carbonate precipitation on the GDE.[2, 3, 21-23] The (bi)carbonate precipitation is caused by increased local alkalinity leading to an undesirable reaction of CO_2 with hydroxide ions. Several processes induce an increase in local pH. (i) CO_2RR and HER consume protons from water molecules, thus forming hydroxide ions. (ii) Driven by both chemical and electric potential gradients, K^+ ions penetrate even the anion exchange membrane.[26] (iii) Finally, the percolation of anolyte (KOH) from the anode compartment via membrane defects leads to flooding of the GDE. The electrolyte solution

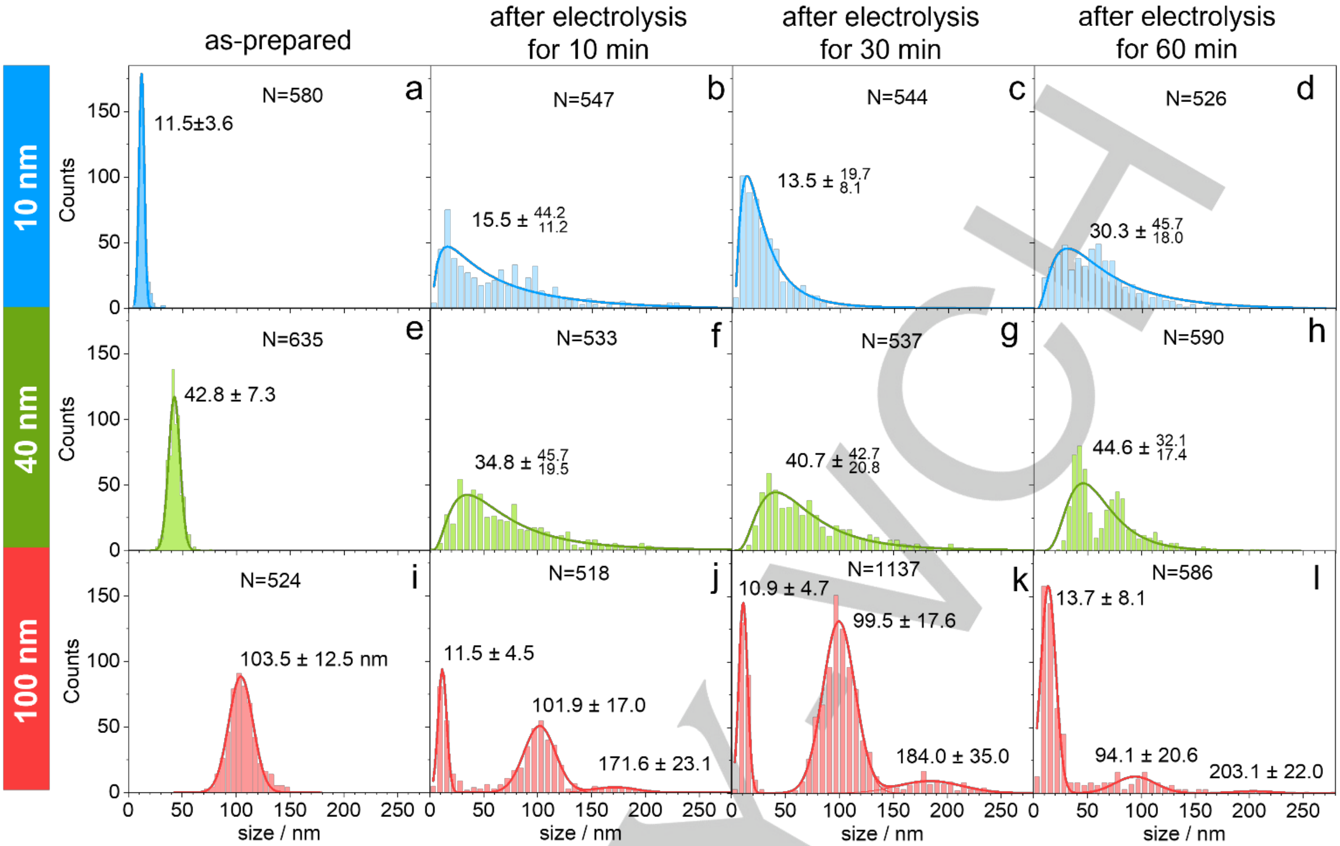

Figure 2. Histograms showing the particle size distribution of Ag NPs of different size: (a-d) 10 nm, (e-h) 40 nm, (i-l) 100 nm. The data were obtained for NP-catalysts (a,e,i) before and (b-d, f-h, j-l) after CO_2 electrolysis at *j* = -283 mA cm^{-2} for a certain time: (different passed charge): (b,f,j) 10 min (169.7 C cm^{-2}), (c,g,k) 30 min (509.2 C cm^{-2}), (d,h,l) 60 min (1018.4 C cm^{-2}). Expectation ranges of the particle size are shown for the fitted peak(s). Number of particles analyzed (N) is given in the graphs.

penetrating into GDE substantially slow down CO_2 diffusion to the active catalytic sites in MPL, thus, hindering CO_2RR consequently promoting HER.[23] On the other hand, the flooding of GDE induces the formation of (bi)carbonate at the three-boundary GDE interface. Because of the limited solubility of potassium (bi)carbonate (lower than the solubility of KOH), the salt precipitates and also leads to blocking of CO_2RR active sites.[21] The precipitation also results in a decreasing electrode potential during the galvanostatic CO_2 electrolysis (Figure S3). The potential at the beginning of the electrolysis at *j* = -283 mA cm^{-2} is around -1.7 V irrespective of the NP size and decreases with time, as the precipitate forms.

We also note that the precipitation issue may be affected by the amount of PVP-capping agent in the catalyst ink. Previously, we reported that PVP is present in ink not only as a capping agent adsorbed on Ag NPs but also in a dissolved/dispersed form (excess PVP).[3] The adsorption of PVP from ink on the GDE after catalyst drop-casting may change the interfacial properties of the electrode and influence the precipitation behavior. Alinejad et al. have recently demonstrated that a PVP-capped Au NP-catalyst displays worse CO_2RR performance (in terms of FE_{CO} and current density) than a PVP-free Au NP-catalyst in both an H-cell and a zero-gap electrolyzer.[27] Herein, we estimated the PVP content in supernatant solutions (Table 2). To quantify PVP surfactant, we determined the total nitrogen content in the supernatant solution (TN_{sup}), i.e. excess PVP, and in the solution of NPs redispersed in water after removal of excess PVP (TN_{NP}). We assumed that TN_{NP} corresponded to PVP directly attached to NPs. The data indicated that TN_{sup} (excess PVP) was approximately an order of magnitude higher than TN_{NP} (PVP on NPs) (Table 2). The results also indicated that the excess PVP decreased with NP size. That is, the concentration calculated for a PVP monomer, $c_{VP,sup}$, in the case of 100-nm NPs was half that for 10-nm NPs (135 vs 250 ppm). Thus, the relatively slow deterioration of CO_2RR performance in the case of 100-nm NPs (Figure 4c) might also have been due to the smaller amount of PVP in the catalyst ink. The effect of PVP on the precipitation issue during CO_2 electrolysis in a zero-gap electrolyzer will be the focus of our follow-up work.

Table 2. TN values for supernatant (TN_{sup}) and redispersed NPs (TN_{NP}) solutions after the removal of excess PVP and calculated respective concentrations of PVP monomers (vinylpyrrolidone, $c_{VP,sup}$ and $c_{VP,NP}$) assuming one nitrogen atom per monomer. The Ag content in the samples was 0.5 mg mL^{-1}.

Samples	TN_{sup} / ppm	$c_{VP,sup}$ / ppm	TN_{NP} / ppm	$c_{VP,NP}$ / ppm
10 nm	31.5	250	2.8	22
40 nm	21.7	172	2.3	18
100 nm	17.0	135	1.3	10

Despite the deterioration in CO_2RR performance associated with (bi)carbonate precipitation at the GDE, clear alterations in the NP-catalyst structure occurred after CO_2 electrolysis. These

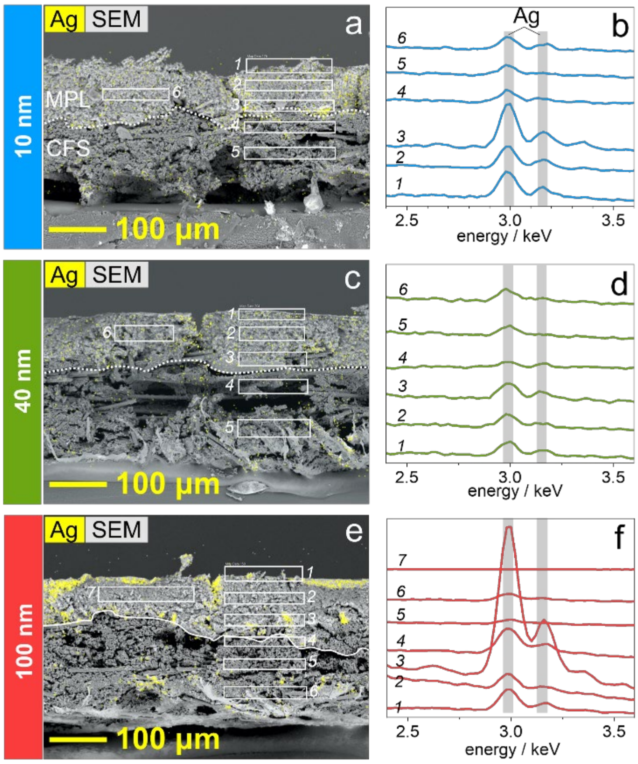

Figure 3. (a, c, e) Representative cross-sectional side-view SEM images and overlapped EDX Ag mapping of the microporous and microfiber GDE layers with deposited Ag NPs of different sizes: (a) 10 nm, (c) 40 nm, (e) 100 nm. Dotted lines indicate boundaries between MPL and CFS. (b,d,f) EDX spectra recorded for respective areas of GDE cross-sections (see numbering).

structural changes might lead to CO_2RR performance losses, which occur less rapidly than losses due to salt precipitation but can become considerable during long-term CO_2 electrolysis. Of particular concern, NPs with certain preferential orientations (e.g., cubic NPs) display higher activity (lower overpotential) toward CO_2RR.

The structural disordering of such shaped NPs leads to catalyst deactivation.[20] In contrast, the degradation of even spherical NPs with no preferential surface orientation can lead to performance losses. For example, NP agglomeration decreases the electrochemically active surface area, whereas corrosion may promote the detachment of NPs, i.e. the loss of the contact between the catalyst and the support.

To confirm the fact that the large decrease in FE_{CO} within 60 min of CO_2 electrolysis (as shown in Figure 4) was associated primarily with (bi)carbonate precipitation, we performed so-called "recovery" experiment (Figures S4-S6). In this experiment, the GDE after the 1st electrolysis was washed accurately in water to remove the salt precipitate and used again in the 2nd electrolysis (details in Experimental section). Of note, the washing procedure did not lead to any loss in Ag NP catalysts. ICP-MS data demonstrated nearly identical mass loading of Ag after the 1st and 2nd electrolyses (Table 1). Simultaneously, the washing allowed for removal of nearly all (bi)carbonate precipitate (as previously demonstrated by EDX analysis in ref.[3]). Figure S4 shows the comparison of *FE*s for CO and H_2 production in the 1st and 2nd galvanostatic electrolyses at j = -283 mA cm^{-2}. The CO_2RR performance almost completely recovered for the washed GDE: the initial FE_{CO} in the 2nd electrolysis was equal to or slightly less than that in the 1st electrolysis. The FE_{CO} decrease and the FE_{H2} increase over time (passed charge) were slightly faster in the case of the washed GDE in the 2nd electrolysis. However, beyond structural changes in NP catalysts, these effects may be associated with many other factors such as (partial) removal of the capping agent, PVP, slight changes in hydrophilicity of GDE, and/or remaining residual salt precipitate after the washing procedure.

CO_2 electrolysis was also performed at two other current densities in addition to j = -283 mA cm^{-2}: -141 and -566 mA cm^{-2} (Figures S7-S12). In all cases, the charge passed during electrolysis was 509.2 C cm^{-2}, and therefore the electrolysis duration differed: 60 min at -141 mA cm^{-2}, 30 min at -283 mA cm^{-2}, and 15 min at -566 mA cm^{-2}. When the FE_{CO} and FE_{H2} were plotted vs electrolysis time (Figure S8), the deterioration rate of CO_2RR performance was higher at higher applied current density. However, when we compared data for the same charge passed, the decrease in FE_{CO} was highest for the lowest current density used (Figure S7). Overall, we concluded that the size of NPs had no considerable effect on CO_2RR performance deterioration, regardless of electrolysis duration or current density. This finding is in agreement with the conclusion that performance losses were due mainly to salt precipitation. We also observed that increasing the current density of CO_2 electrolysis increased in FE_{HCOO-} up to 17–19% (Figure S9). However, this change in the product distribution did not appear to depend on NP size: FE_{HCOO-} increased with

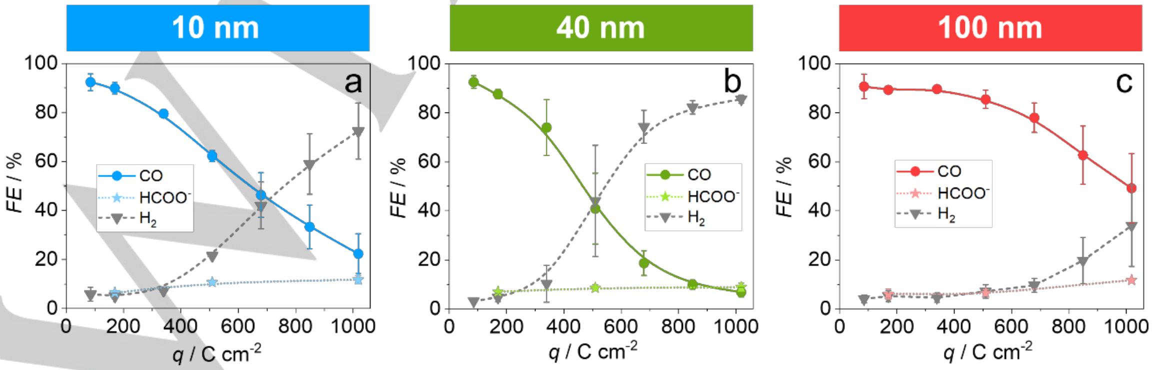

Figure 4. FEs of CO, $HCOO^-$, and H_2 versus charge passed during galvanostatic CO_2 electrolyses (at j = -283 mA cm^{-2}) employing Ag NP-catalysts. The size of NPs: (a) 10 nm, (b) 40 nm, (c) 100 nm. The total electrolysis time is 60 min.

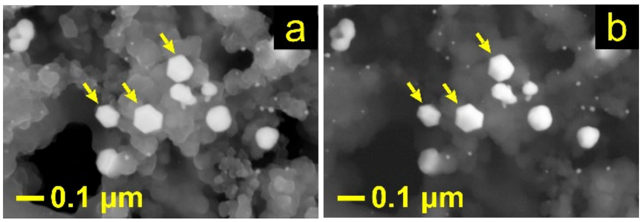

Figure 5. Representative SEM images of 100-nm Ag NP-catalysts on GDE after passing 1018.4 C cm^{-2} during CO_2 electrolysis (60 min) at *j* = -283 mA cm^{-2}. NPs indicated by arrows display clear faceting. Images were acquired using (a) InLens SE and (b) BSD detectors.

current density similarly for 10-, 40-, and 100-nm NPs. The dependencies of the electrode potential on the passed charge or time are also rather similar for NPs of different sizes (Figure S10). In general, the potential decreases during the galvanostatic electrolysis reaction. This decrease scales with the cathodic current applied.

Structural changes in Ag NPs after CO_2 electrolysis

The structural changes in NP catalysts were analyzed by SEM after CO_2 electrolyses. Because of massive salt precipitation, the GDE underwent the water washing procedure, as in the "recovery" experiments. A comparison of Ag mass loading estimated by ICP-MS before and after electrolysis indicated only a minor decrease (Table 1).

Representative SEM images of the Ag NP-catalyst layer after CO_2 electrolysis at j = -283 mA cm^{-2} are shown in Figure 1 for the three studied sizes of NPs. The size distributions of NPs are presented in Figure 2. Expected particle size ranges (mode ± deviation) were determined from the histograms shown in Figure 2, fitted by either symmetric Gaussians or asymmetric (skewed) log-normal functions.

The SEM images demonstrated that Ag NPs underwent agglomeration after CO_2 electrolysis even within 10 min (Figure 1). The agglomeration was characteristic for all three sizes of NPs under study. Furthermore, we observed the appearance of smaller particles after electrolysis with 100-nm NP catalyst (Figure 1j-l). From the fitting of NP size distribution, we made the following observations. In the case of 10-nm NPs, the size distribution was fitted by a log-normal function. The mode value increased with increasing electrolysis time (charge passed) from 11.5 up to 30.3 nm (Figure 2b-d), with some particles/agglomerates reaching 100 nm or greater (the longest dimension). Such agglomerated NPs were not observed before electrolysis, and as-prepared NPs had a fairly narrow expected range. In the case of 40-nm NPs (Figure 2f-h), the size distribution was also log-normal. Nevertheless, the mode value did not substantially shift after electrolysis; thus, a large fraction of NPs retained their initial size. Simultaneously, the expected range became broader, and skewness appeared with a larger contribution from agglomerated particles (as in the case of 10-nm NPs). The number of NPs smaller than 40 nm also increased after CO_2 electrolysis, thus indicating a degradation mechanism associated with partial NP fragmentation. The degradation behavior of 100-nm NPs was different. Three populations of NPs were distinguished and fitted with Gaussians (Figure 2j-l). The size distribution in the population with the mode value close to

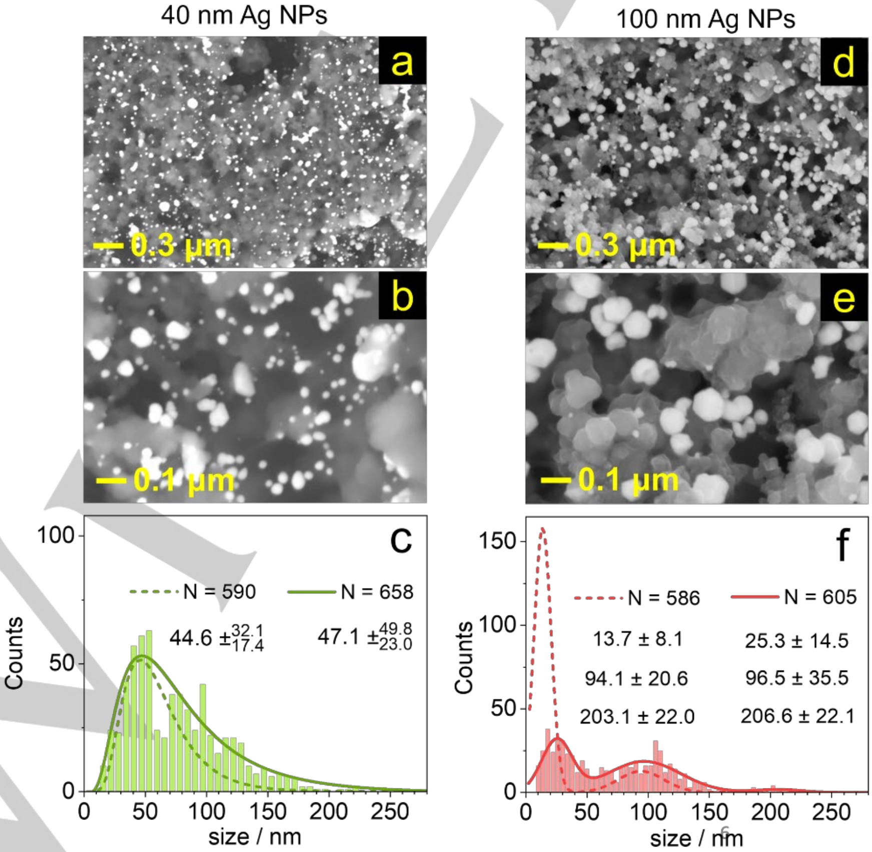

Figure 6. (a,b, d,e) SEM images and (c,f) size histograms and fitting (solid line) of (a-c) 40-nm and (d-f) 100-nm NP-catalysts after "recovery" experiment, i.e. 2nd electrolysis at j = -283 mA cm^{-2}. The fitting curves of size distribution for NP-catalysts after the 1st electrolysis are also shown by dashed lines. Number of particles analyzed (N), mode values, and deviations are given in the graphs.

the initial value (100 nm) became broader after electrolysis: the deviation increased from 12.5 nm for the as-prepared catalyst up to 20.6 nm for the catalyst after 60-min electrolysis. Simultaneously, the mode value of this population slightly decreased from 103.5 to 94.1 nm after electrolysis, thus, suggesting fragmentation of the NPs. A new population with a mode value of approximately 11–13 nm appeared after 10 min of CO_2 electrolysis. The number of these small NPs and the expected range of the population appeared to increase with electrolysis time (charge passed). SEM images in Figure 1j-l clearly displayed an increased number of small NPs. The formation of the small NPs was consistent with the decrease in the mode value of the initial NP distribution. Additionally, we resolved the third population with the mode value, which changed from 171.6 nm to 203.1 nm with increasing electrolysis time (Figure 2j-l). This population typically consisted of two or three agglomerated NPs. The agglomeration of 10-nm NPs was much more severe during CO_2 electrolysis: a large fraction of agglomerates exceeded the initial NP size by factors of 10 to 20 (Figure 2b-d). Thus, the agglomeration of 100-nm particles was a slower process than that for 10-nm NPs. On the basis of our results, we concluded that 100-nm NPs are more likely to undergo fragmentation than agglomeration.

Interestingly, we also observed the faceting of individual 100-nm NPs after electrolysis. For the as-prepared samples, virtually all NPs were spherical without any distinguishable facets. SEM images in Figure 5 (more images in Figure S13) showed that NPs underwent extensive restructuring and, after 60 min of electrolysis, acquired clear facets. Facet formation was characteristic of the cathodic corrosion process [28, 29]. Although the mechanism of cathodic corrosion is not yet fully understood, it has been observed for many metals including Ag.[30] Elnagar et al. have demonstrated the formation of a (111) facet on a polycrystalline Au wire after cathodic polarization in concentrated KOH solution (5–20 M).[31] Au faceting was observed at -1.5 V vs RHE and became more pronounced at more negative potentials. After polarization at -3.5 V vs RHE for just 60 s, the voltammetric response of Au wire was nearly identical to that for an Au(111) single crystal electrode. The authors in ref.[31] have concluded that HER and high near-surface concentration of K^+ ions are essential for the cathodic corrosion process and faceting. Such conditions can be fulfilled during CO_2 electrolysis in a gas-fed electrolyzer. Typically, the GDE cathode potential during galvanostatic polarization at j = -283 mA cm^{-2} is between -1.75 and -1.95 V, whereas high alkalinity and K^+ concentration are achieved because of HER and CO_2RR, K^+ ion penetration and KOH solution flooding via the membrane. In the case of 40-nm NPs the faceting was observed but in much less extent than for 100-nm NPs. Figure S14 demonstrates a few faceted NPs for a sample after the “recovery” experiment, i.e. two electrolyses at j = -283 mA cm^{-2} for 60 min each. For small NPs (10 nm), we did not observe pronounced faceting after CO_2 electrolysis, possibly because of insufficient SEM resolution as well as the tendency of the smaller particles to agglomerate.

The faceting of spherical NPs in this study (Figure 5) was opposite from the degradation behavior of cubic Ag NPs with the initial facet orientation of (100) [2]. During electrolysis, the Ag nanocubes underwent fragmentation and changed their cubic shape, becoming more spherical during CO_2 electrolysis. Similarly, the fragmentation and destruction of (100) facets were found for cubic Cu NPs [20].

In addition, we performed a reference experiment employing the 100-nm NP-catalyst, where we fed the GDE with Ar+H_2O (no CO_2). Under these conditions only HER takes place at the cathode. Note, no precipitate was observed at the cathode after 60 min of electrolysis at j = -283 mA cm^{-2}. This might be the reason why the electrode potential was much more stable during the water electrolysis than that in the course of CO_2 electrolysis (Figure S15a). Nevertheless, the MPL layer of the GDE was wet after the water electrolysis probably likely due to the KOH flooding. The SEM analysis after the electrolysis in the absence of CO_2 demonstrates much less pronounced formation of small clusters as compared to the samples after the CO_2 electrolysis at the same current density (Figure S15). This finding suggests that the fragmentation of 100-nm Ag NPs is more pronounced during CO_2RR (on CO_2-fed GDE). One possible explanation of this observation is that the (bi)carbonate precipitation on the CO_2-fed GDE blocks diffusion pathways for CO_2, H_2O, K^+, and OH^- ions and, thus, may lead to a greater local increase in alkalinity as compared to the situation where only Ar and H_2O are fed through the GDE.

Recently, we have reported that excess PVP influences the degradation behavior of 40-nm Ag NPs: the removal of excess PVP leads to more pronounced agglomeration of NPs after CO_2 electrolysis [3]. We assumed that excess PVP adsorbed on the carbon support rendered NPs immobile and thus hindered their agglomeration. The estimation of TN in NP-catalyst samples demonstrated a smaller amount of excess PVP in the case of larger NPs (*cf.* TN_{sup} values in Table 2). Thus, a greater tendency for agglomeration might be expected for NP catalysts containing smaller amounts of excess PVP. However, we observed an opposite trend: although the 100-nm NP-catalyst contained a smaller amount of excess PVP, the agglomeration was more characteristic for 10- and 40-nm NP catalysts (Figures 1 and 2). This result indicated that NP size plays a more decisive role in degradation behavior than excess PVP content observed in our experiments.

The SEM analysis of Ag NP catalysts after CO_2 electrolysis at different current densities (but with the same passed charge equal to 509.2 C cm^{-2}) is shown in Figures S11 and S12. For the 10-nm NPs, the increase in current density (-141, -283, and -566 mA cm^{-2}) had a minor effect on the degradation behavior: the NPs tended to agglomerate at any current density (Figures S11a-d, S12a-d). The agglomeration of 40-nm NPs appeared to be more severe with increasing current density of electrolysis (Figures S11e-f, S12e-f). At j = -566 mA cm^{-2}, the NP size could scarcely be estimated because of massive agglomeration, whereas at j = -141 mA cm^{-2}, many agglomerates consisted of two NPs, thus resulting in an additional peak in the size distribution histogram at 79.7 nm (Figure S12f). For 100-nm NPs, the agglomeration was insignificant at low current density j = -141 mA cm^{-2} (Figure S12j). At higher current densities (-283 and -566 mA cm^{-2}), the difference in degradation behavior was minor (Figure S12k,l). At all current densities, the 100-nm NPs tended toward fragmentation with the formation of small particles with a mode size of 11–18 nm (Figure S12j-l).

We also performed SEM analysis of 40-nm catalyst after the “recovery” experiment, i.e., after the 2nd electrolysis at j = -283 mA cm^{-2} (product distribution data are shown in Figures S4, S5). The comparison of the morphology and size distribution of the

NP catalysts after the 1st and 2nd electrolyses (Figure 6a-c) demonstrated further agglomeration and fragmentation of NPs in the 2nd electrolysis: the expected range became broader, and the deviations increased for both directions (toward smaller and larger sizes; Figure 6c). Thus, the continuation of CO_2 electrolysis after reactivation of GDE by removal of (bi)carbonate precipitate led to further degradation (agglomeration and fragmentation) of Ag NPs. SEM analysis of the 100-nm catalyst after the “recovery” experiment demonstrates even more pronounced changes in size distribution as compared to that after the 1st electrolysis (Figure 6d-f). The mode value of the population of small particles formed in the 1st electrolysis increased from 13.7 to 25.3 nm accompanied by a broadening of the expectation range. This finding suggests that at least part of small clusters agglomerated (in parallel to the formation of new small clusters due to fragmentation) in the course of the 2nd electrolysis. Moreover, some 100-nm NPs display signs of severe degradation of after the 2nd electrolysis as indicated in Figure S6.

Raw data and unprocessed measurement files serving as a basis of this article can be found elsewhere.[32]

Conclusion

Herein, we studied the effect of NP size on NP degradation behavior during CO_2 electrolysis in a gas-fed zero-gap electrolyzer. For this purpose, we performed galvanostatic electrolyses with PVP-capped spherical Ag NPs of different initial sizes (10, 40, and 100 nm). Post-electrolysis SEM and size-distribution analyses were used to explore structural changes. ICP-MS analysis of Ag loading before and after electrolysis showed no considerable detachment of the NP-catalyst, regardless of the NP size. However, SEM data demonstrated clear structural changes in NPs on the surface of GDE after electrolysis. The smallest 10-nm NPs underwent mainly agglomeration during galvanostatic CO_2 electrolysis, thus leading to the formation of larger agglomerates with the longest distance up to 200 nm. For 40-nm NPs, agglomeration was also prevalent, although the fragmentation of NPs with the formation of smaller clusters was also detected. The size distribution of both 10- and 40-nm NPs after CO_2 electrolysis was fitted well with a log-normal function, with a pronounced skewness toward larger sizes. In the case of 100-nm NPs, two new populations were distinguished with mode values of 11–13 nm and 170–200 nm after electrolysis. The mode values, particularly for the population of larger agglomerates, increased with electrolysis time (charge passed). The 100-nm NPs tended to form agglomerates consisting primarily of two or three initial particles. The population of smaller particles (mode of approximately 11–13 nm) was formed because of the fragmentation of initial NPs. The fragmentation appeared to be associated with cathodic corrosion of Ag NPs at negative potentials under conditions of intensive CO_2RR and HER. The GDE flooding with KOH solution, additional penetration of K^+ ions via a membrane, and accumulation of OH- ions due to cathodic reactions may facilitate the cathodic corrosion of Ag catalyst. Another sign of cathodic corrosion is the faceting of NPs, which was clearly distinguishable for the 100-nm NP-catalyst. We emphasise that the NP mass loading may also affect the degradation behavior.

Simultaneously, the correlation between the structural changes and the CO_2RR performance losses in a zero-gap electrolyzer was not able to be established because of the flooding and the harsh salt precipitation at the GDE within a short time (minutes). However, the results clearly indicated that on a long-term time scale, structural changes in catalysts play important roles in CO_2RR performance. NP agglomeration would decrease the electrochemically active surface area, whereas fragmentation/corrosion would promote the detachment of NPs.

Experimental Section

Catalyst preparation

PVP-capped Ag NPs of different sizes (~10 nm, ~40 nm, ~100 nm, and 1 mg mL^{-1} in water) were purchased from NanoComposix. Subsequently, 1 mL of as-received Ag NP suspension was diluted to 1.627 mL by the addition of isopropanol (VLSI Selectipur, BASF, Germany). Then 0.1765 mg of carbon powder (Vulcan XC 72R, Cabot, USA) was dispersed in 353 µL isopropanol by sonication for 1 hour. The two suspensions were subsequently mixed, and after the addition of 20 µL Nafion solution (5% Nafion, 15–20% water, Sigma-Aldrich), the new suspension with an Ag NP concentration of 0.5 mg mL^{-1} was sonicated for 5 min to yield a homogeneous catalyst ink. Next, 75 µL of the above suspension of carbon-supported Ag NPs was drop-cast on the hydrophobic surface of a GDE (circle with diameter d of 4 mm; Sigracet 36BB, Fuel Cell Store), as shown in Figure S2. The electrodes were dried under ambient conditions. The mass loading was 300 ± 17 µg cm^{-2} (Table 1), as determined by inductively coupled plasma mass spectrometry (ICP–MS). A GDE (Sigracet 36BB) circle (d = 4 mm) with an Ag-NP catalyst was inserted into the hole (d = 4 mm) in the center of a larger-area GDE (d = 20 mm, Freudenberg H23C8, Fuel Cell Store), as illustrated in Figure S2, and the assembled electrode was further inserted in an electrolyzer.

Assembly of the gas-fed zero-gap cell

The electrolyzer used in this work has been described elsewhere (Figure S1).[2, 3] It consists of a stainless-steel cell body with gas flow channels used to feed the CO_2 from the backside of the GDE. The prepared electrode was placed on the top of the gas flow channels, with its catalyst modified surface facing upward. Subsequently, a hydroxide-functionalized Sustainion alkaline membrane (X3750 RT, Dioxide materials) and a PTFE anolyte compartment were placed on top of the GDE. Then 10 mL of 2.0 M KOH was used as an electrolyte in the anolyte compartment. An Ag/AgCl (3 M KCl, double junction design, Metrohm) electrode and Ir wire (99.9%, Goodfellow GmbH) were used as reference and counter electrodes. The counter electrode was placed inside a glass capillary tube with a glass frit. The PTFE anolyte compartment had a central orifice of 3 mm diameter at its bottom, thereby providing direct contact between the electrolyte and the underlying anion-exchange membrane, whereas the GDE cathode was prevented from direct contact with the supporting anolyte. Thus, we defined the geometric area of the GDE electrode as the area of this orifice, i.e., 0.0707 cm^2. During electrolysis, a humidified CO_2 stream (17 mL min^{-1}, 99.999%, Carbagas, Switzerland) was continuously fed through the gas flow channels of the cell body, adjacent to the GDE.

Electrochemical measurements and product distribution studies

CO_2 electrolysis was performed at room temperature (22 ± 1 ºC) in galvanostatic mode with an ECi-200 potentiostat (Nordic Electrochemistry). The reported current and charge densities were normalized to the geometric surface area (0.0707 cm^2). The gaseous products of CO_2RR were quantitatively analyzed by on-line gas chromatography (SRI Instruments). A thermal conductivity detector for detecting H_2 and a flame ionization detector with a methanizer for detecting CO and hydrocarbons were applied in our studies. Among the possible dissolved products, only formate was detected in all experiments performed. Formate anions forming during CO_2 electrolysis diffused via the anion-exchange membrane to the anode compartment. Thus, formate was quantified by ion chromatography (Metrohm Ltd., Switzerland) analysis of anolyte samples collected after CO_2 electrolysis.

The faradaic efficiency (FE_i) of the gaseous product was calculated[33] as

$$FE_i = (x_i\ n_i\ F\ \upsilon_m\ /\ I)\ 100\% \qquad (1)$$

where x_i denotes the molar fraction of the products determined by gas chromatography with an independent calibration standard gas (Carbagas), n_i is the number of electrons involved in the reduction reaction to form a particular product (n_i = 2 for both CO and H_2 formation), F = 96485.3 C mol^{-1} is Faraday's constant, υ_m is the molar CO_2 gas flow rate measured by a universal flowmeter (7000 GC flowmeter, Ellutia), and I is the current set for the galvanostatic electrolysis.

The faradaic efficiency of formate FE_{HCOO-} is calculated as

$$FE_{HCOO^-} = (c_{HCOO^-}\ V_{anolyte}\ n_{HCOO^-}\ F\ /\ Q)\ 100\% \qquad (2)$$

where c_{HCOO^-} denotes the formate concentration in the anolyte determined by ion chromatography, $V_{anolyte}$ is the volume of anolyte in the electrolyzer, n_{HCOO^-} is the number of electrons involved in the formation of formate (n_{HCOO^-} = 2), and Q is the passed charge during galvanostatic CO_2 electrolysis. Every data point of *FE* (FE_{CO}, FE_{H2}, and FE_{HCOO-}) was obtained from three independent experiments with new GDEs, and error bars represent standard deviations.

In the "recovery" experiments, the GDE after the 1st electrolysis was carefully placed onto the surface of Milli-Q water in a beaker with the catalyst layer facing downward. Water was exchanged at least five times every 15 min. Then the GDE was dried and again used for the electrolysis (2nd electrolysis). Details have been previously reported [3].

Scanning electron microscopy (SEM) and energy-dispersive X-ray spectroscopy (EDX)

For morphological analysis of catalysts, a Zeiss Gemini 450 scanning electron microscope equipped with the InLens secondary electron (InLens SE) and back-scattering detectors was used. SEM images obtained with the InLens SE detector are presented herein unless otherwise specified. An acceleration voltage of 5 kV and currents of 120 pA and 200 pA were applied at a working distance of 2.9–4.0 mm. The particle size was measured in Smile View software, and the particle size distribution was based on size estimations of 500–1100 individual particles and agglomerates for each catalyst in three randomly selected areas. The particle/agglomerate size was defined as the longest dimension in the case of anisotropic NPs (Figure S16). EDX spectra and 2D surface elemental maps of samples were obtained with AZtec 5.0 software (Oxford Instruments). An acceleration voltage of 10 kV and a current of 1000 pA were applied at a working distance of 8.5 mm for EDX measurements.

Inductively coupled plasma mass spectrometry

The Ag mass loading of the electrodes was determined with a NExION 2000 ICP-MS instrument (Perkin Elmer). The Ag NPs on the GDE were dissolved in 1 mL HNO_3 (69.3%, BASF SE, Ludwigshafen, Germany). The obtained solutions were further diluted with 3% HNO_3 solution by a factor of 1000 and injected into the ICP-MS instrument to obtain the actual content of Ag on GDEs.

Total nitrogen content determination

To quantify PVP surfactant in the dispersion of Ag NPs, we determined the total nitrogen content (TN). Sample solutions with Ag NPs (Ag content is 0.5 mg mL^{-1}) were diluted by a factor of 4. Then 100 µL of diluted solution (Ag content is 0.125 mg cm^{-3}) was further centrifuged to separate NPs from the supernatant. The centrifugation rate was 35000 rpm (for 40 min) for solutions with 40- and 100-nm NPs, whereas a solution with 10-nm NPs was centrifuged for 40 min at 35000 rpm, then 40 min more at 50000 rpm. The obtained supernatant was further fed into a DIMATOC 2100 instrument (Dimatec, Essen, Germany) to determine TN in supernatant solution (TN_{sup}). The organic compounds were oxidized at 850 °C on a Pt catalyst to CO_2/NO. A non-dispersive infrared gas sensor with a reflective diffuser and a chemiluminescence detector was used to detect NO. The separated NPs were further redispersed in Milli-Q water, and these prepared dispersions with the same Ag content (0.5 mg mL^{-1}) were again analyzed to determine the TN_{NP}.

Acknowledgements

The work in this publication was part of NCCR Catalysis (grant number 180544), a National Centre of Competence in Research funded by the Swiss National Science Foundation. A.R. acknowledges support from the Ministry of Science and Higher Education of the Russian Federation. M.L., Y.K., and H.H. acknowledge financial support from the Chinese Scholarship Council (CSC).

Keywords: carbon dioxide electroreduction • gas diffusion electrodes • cathodic corrosion • nanoparticle degradation • nanoparticle agglomeration

[1] P. De Luna, C. Hahn, D. Higgins, S. A. Jaffer, T. F. Jaramillo, E. H. Sargent, *Science* **2019**, *364*, eaav3506.
[2] M. de Jesus Gálvez-Vázquez, P. Moreno-García, H. Xu, Y. Hou, H. Hu, I. Z. Montiel, A. V. Rudnev, S. Alinejad, V. Grozovski, B. J. Wiley, M. Arenz, P. Broekmann, *ACS Catal.* **2020**, *10*, 13096-13108.
[3] M. Liu, Y. Kong, H. Hu, N. Kovács, C. Sun, I. Zelocualtecatl Montiel, M. d. J. Gálvez Vázquez, Y. Hou, M. Mirolo, I. Martens, J. Drnec, S. Vesztergom, P. Broekmann, *Journal of Catalysis* **2021**, *404*, 371-382.
[4] J. He, Y. Li, A. Huang, Q. Liu, C. Li, *Electrochemical Energy Reviews* **2021**.
[5] Y. Gu, J. Wei, X. Wu, X. Liu, *Scientific Reports* **2021**, *11*, 11136.
[6] Y. Wu, S. Garg, M. Li, M. N. Idros, Z. Li, R. Lin, J. Chen, G. Wang, T. E. Rufford, *Journal of Power Sources* **2022**, *522*, 230998.
[7] A. Salehi-Khojin, H.-R. M. Jhong, B. A. Rosen, W. Zhu, S. Ma, P. J. A. Kenis, R. I. Masel, *J. Phys. Chem. C* **2013**, *117*, 1627-1632.
[8] A. V. Rudnev, K. Kiran, A. Cedeño López, A. Dutta, I. Gjuroski, J. Furrer, P. Broekmann, *Electrochim. Acta* **2019**, *306*, 245-253.
[9] Q. Lu, J. Rosen, F. Jiao, *ChemCatChem* **2015**, *7*, 38-47.
[10] S. Liu, H. Tao, L. Zeng, Q. Liu, Z. Xu, Q. Liu, J.-L. Luo, *J. Am. Chem. Soc.* **2017**, *139*, 2160-2163.
[11] W. H. Lee, Y.-J. Ko, Y. Choi, S. Y. Lee, C. H. Choi, Y. J. Hwang, B. K. Min, P. Strasser, H.-S. Oh, *Nano Energy* **2020**, *76*, 105030.
[12] S. Popović, M. Smiljanić, P. Jovanovič, J. Vavra, R. Buonsanti, N. Hodnik, *Angew. Chem. Int. Ed.* **2020**, *59*, 14736-14746.
[13] C. Spöri, J. T. H. Kwan, A. Bonakdarpour, D. P. Wilkinson, P. Strasser, *Angew. Chem. Int. Ed.* **2017**, *56*, 5994-6021.
[14] B. Vanrenterghem, M. Bele, F. R. Zepeda, M. Šala, N. Hodnik, T. Breugelmans, *Applied Catalysis B: Environmental* **2018**, *226*, 396-402.

[15] Y. Hou, N. Kovács, H. Xu, C. Sun, R. Erni, M. d. J. Gálvez-Vázquez, A. Rieder, H. Hu, Y. Kong, M. Liu, B. J. Wiley, S. Vesztergom, P. Broekmann, *Journal of Catalysis* **2021**, *394*, 58-66.
[16] J. Huang, M. Mensi, E. Oveisi, V. Mantella, R. Buonsanti, *J. Am. Chem. Soc.* **2019**, *141*, 2490-2499.
[17] J. Huang, N. Hörmann, E. Oveisi, A. Loiudice, G. L. De Gregorio, O. Andreussi, N. Marzari, R. Buonsanti, *Nat. Comm.* **2018**, *9*, 3117.
[18] W. T. Osowiecki, J. J. Nussbaum, G. A. Kamat, G. Katsoukis, M. Ledendecker, H. Frei, A. T. Bell, A. P. Alivisatos, *ACS Appl. Energy Mater.* **2019**, *2*, 7744-7749.
[19] H. Yun, J. Kim, W. Choi, M. H. Han, J. H. Park, H.-s. Oh, D. H. Won, K. Kwak, Y. J. Hwang, *Electrochim. Acta* **2021**, *371*, 137795.
[20] P. Grosse, D. Gao, F. Scholten, I. Sinev, H. Mistry, B. Roldan Cuenya, *Angew. Chem. Int. Ed.* **2018**, *57*, 6192-6197.
[21] M. E. Leonard, L. E. Clarke, A. Forner-Cuenca, S. M. Brown, F. R. Brushett, *ChemSusChem* **2020**, *13*, 400-411.
[22] L.-C. Weng, A. T. Bell, A. Z. Weber, *Energy Environ. Sci.* **2019**, *12*, 1950-1968.
[23] Y. Kong, H. Hu, M. Liu, Y. Hou, V. Kolivoška, S. Vesztergom, P. Broekmann, *Journal of Catalysis* **2022**, *408*, 1-8.
[24] R. Reske, H. Mistry, F. Behafarid, B. Roldan Cuenya, P. Strasser, *J. Am. Chem. Soc.* **2014**, *136*, 6978-6986.
[25] H. Mistry, R. Reske, Z. Zeng, Z.-J. Zhao, J. Greeley, P. Strasser, B. R. Cuenya, *J. Am. Chem. Soc.* **2014**, *136*, 16473-16476.
[26] J. J. Kaczur, H. Yang, Z. Liu, S. D. Sajjad, R. I. Masel, *Front. Chem.* **2018**, *6*.
[27] S. Alinejad, J. Quinson, G. K. H. Wiberg, N. Schlegel, D. Zhang, Y. Li, S. Reichenberger, S. Barcikowski, M. Arenz, *ChemRxiv* **2021**.
[28] M. M. Elnagar, J. M. Hermann, T. Jacob, L. A. Kibler, *Curr. Opin. Electrochem.* **2021**, *27*, 100696.
[29] T. J. P. Hersbach, I. T. McCrum, D. Anastasiadou, R. Wever, F. Calle-Vallejo, M. T. M. Koper, *ACS Applied Materials & Interfaces* **2018**, *10*, 39363-39379.
[30] J. Feng, D. Chen, A. S. Sediq, S. Romeijn, F. D. Tichelaar, W. Jiskoot, J. Yang, M. T. M. Koper, *ACS Applied Materials & Interfaces* **2018**, *10*, 9532-9540.
[31] M. M. Elnagar, J. M. Hermann, T. Jacob, L. A. Kibler, *Electrochim. Acta* **2021**, *372*, 137867.
[32] H. Hu, M. Liu, Y. Kong, Y. Hou, I. Zelocualtecatl Montiel, A. V. Rudnev, P. Broekmann, *Zenodo* **2022**. DOI: https://doi.org/10.5281/zenodo.6840454
[33] A. V. Rudnev, in *Encyclopedia of Interfacial Chemistry* (Ed.: K. Wandelt), Elsevier, Oxford, **2018**, pp. 321-325.

Entry for the Table of Contents

Insert graphic for Table of Contents here.

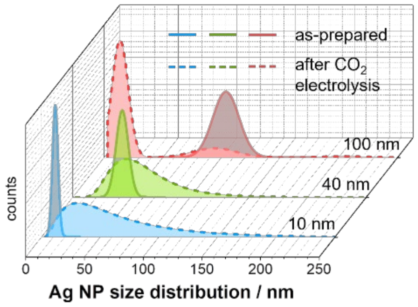

The exploration of catalyst structural changes during electrochemical CO_2 conversion under harsh conditions (at current densities > 0.2 A cm^{-2}) is highly essential. This article studies the size effect on degradation behavior of Ag nanoparticle catalysts during CO_2 electrolysis in a zero-gap electrolyzer. Small nanoparticles tend to agglomerate, while 100-nm particles undergo pronounced fragmentation related to cathodic corrosion.

7.5. Cracks as Efficient Tools to Mitigate Flooding in Gas Diffusion Electrodes Used for the Electrochemical Reduction of Carbon Dioxide

Authors: Ying Kong, Menglong Liu, Huifang Hu, Yuhui Hou, Soma Vesztergom, María de Jesus Gálvez-Vázquez, **Iván Zelocualtecatl Montiel**, Viliam Kolivoška, Peter Broekmann

Small Methods 2022, 2200369. DOI: https://doi.org/10.1002/smtd.202200369

Highlights: This work reported the advantages of using different GDEs coated with silver nanowires (Ag-NWs) for electrochemical reduction of CO_2 in a zero gap cell configuration. The experimental data revealed that the presence of cracks in the GDE showed high and sustained catalytic activity towards CO_2RR. However, using non-cracked electrodes leads to a fast transition to the parasitic reduction of water.

It is well known that during electrolysis conditions, GDEs tend to present electrolyte perspiration. Taking advantage of this phenomenon, the amount of the electrolyte perspiration was determined using ICP-MS, finding that the amount of perspirate electrolyte increases with the abundance of cracks. In combination with EDX mapping cross-sectional view analysis of the electrodes after CO2R, it was possible to obtain the absolute concentration profiles of perspirate electrolyte in the Ag-NWs@GDE, which provided microscopic evidence that cracks serve as preferential pathways for the electrolyte transport through the mesoporous layer in the GDEs.

GDEs with high crack abundance drain excess of electrolyte from the catalytic layer, preventing micropores' flooding and enabling them to function as efficient transport channels for gaseous CO2. While, in the absence of cracks, the electrolyte was found to flood micropores, reflecting itself as greatly reduced catalytic activity.

Contributions: In this project, I was involved in conducting ICP-MS. In addition, I participated in the manuscript revision process.

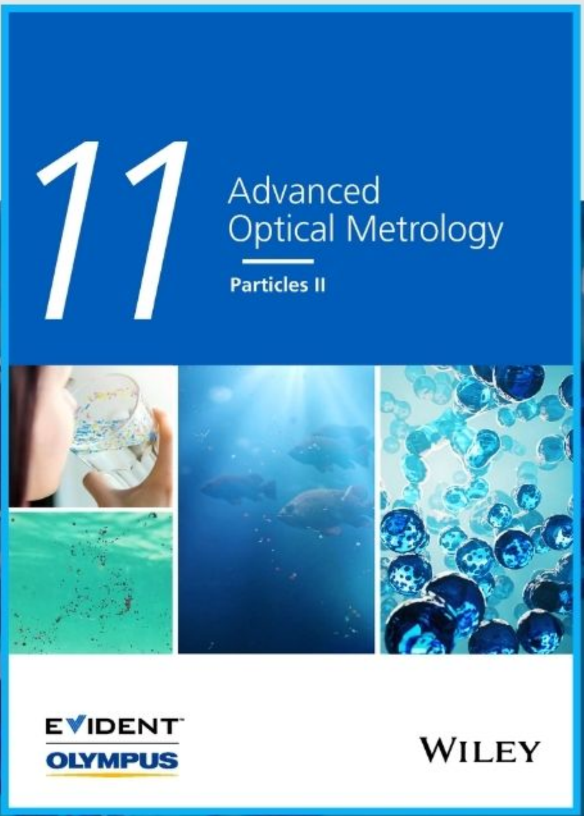
11
Advanced
Optical Metrology
Particles II
EVIDENT
OLYMPUS
WILEY

small methods
www.small-methods.com

Cracks as Efficient Tools to Mitigate Flooding in Gas Diffusion Electrodes Used for the Electrochemical Reduction of Carbon Dioxide

Ying Kong, Menglong Liu, Huifang Hu, Yuhui Hou, Soma Vesztergom, María de Jesus Gálvez-Vázquez, Iván Zelocualtecatl Montiel, Viliam Kolivoška, and Peter Broekmann**

The advantage of employing gas diffusion electrodes (GDEs) in carbon dioxide reduction electrolyzers is that they allow CO_2 to reach the catalyst in gaseous state, enabling current densities that are orders of magnitude larger than what is achievable in standard H-type cells. The gain in the reaction rate comes, however, at the cost of stability issues related to flooding that occurs when excess electrolyte permeates the micropores of the GDE, effectively blocking the access of CO_2 to the catalyst. For electrolyzers operated with alkaline electrolytes, flooding leaves clear traces within the GDE in the form of precipitated potassium (hydrogen)carbonates. By analyzing the amount and distribution of precipitates, and by quantifying potassium salts transported through the GDE during operation (electrolyte perspiration), important information can be gained with regard to the extent and means of flooding. In this work, a novel combination of energy dispersive X-ray and inductively coupled plasma mass spectrometry based methods is employed to study flooding-related phenomena in GDEs differing in the abundance of cracks in the microporous layer. It is concluded that cracks play an important role in the electrolyte management of CO_2 electrolyzers, and that electrolyte perspiration through cracks is paramount in avoiding flooding-related performance drops.

1. Introduction

Rising levels of atmospheric CO_2 as a dominant greenhouse gas have motivated endeavors to curb carbon emissions and utilize excess CO_2 to produce valuable resources.[1] The electrochemical reduction of CO_2 (denoted hereafter $ERCO_2$) allows not only its conversion to fuels and feedstock chemicals of high added value, but also the simultaneous storage of electrical energy originating from intermittent renewable sources.[2]

$ERCO_2$ operating at commercially relevant reaction rates (current densities) requires efficient and stable catalysts and facile mass transport of reactants and products with minimized energy losses.[3] Gas diffusion electrodes (GDEs) circumvent the problem of limited solubility and slow diffusion of CO_2 in aqueous media by delivering this reactant to the catalyst layer via gas phase.[3–6]

In GDEs, the catalyst layer is located on a supportive gas diffusion layer (GDL) that is composed of a carbon fiber layer (CFL) and a microporous layer (MPL),[4] as shown in **Figure 1**. Besides the reactant delivery, the GDL enables the release of gaseous reaction products, serves as a mechanical support and electrical contact for the catalyst, and plays important role in controlling the amount of electrolyte in the catalyst layer.[4,7,8] GDEs operating in alkaline aqueous electrolytes show highly active and selective $ERCO_2$ toward target products (like CO) due to the combination of reduced ohmic drops,[3,9] favorable electrode kinetics,[3,10–14] and suppression of the electrochemical reduction of water (ERH_2O) as a parasitic reaction.[15]

Y. Kong, M. Liu, H. Hu, Y. Hou, S. Vesztergom, M. de J. Gálvez-Vázquez, I. Zelocualtecatl Montiel, P. Broekmann
Department of Chemistry, Biochemistry and Pharmaceutical Sciences
University of Bern
3012 Bern, Switzerland
E-mail: peter.broekmann@unibe.ch

The ORCID identification number(s) for the author(s) of this article can be found under https://doi.org/10.1002/smtd.202200369.

DOI: 10.1002/smtd.202200369

Y. Kong, M. Liu, Y. Hou, P. Broekmann
National Centre of Competence in Research (NCCR) Catalysis
University of Bern
3012 Bern, Switzerland

S. Vesztergom
Department of Physical Chemistry
Eötvös Loránd University
1117 Budapest, Hungary

V. Kolivoška
J. Heyrovský Institute of Physical Chemistry of the Czech Academy of Sciences
18223 Prague, Czech Republic
E-mail: viliam.kolivoska@jh-inst.cas.cz

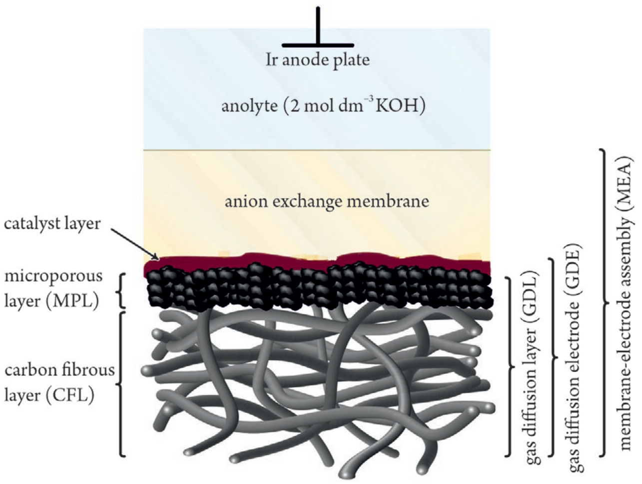

Figure 1. Schematic depiction of the zero-gap gas diffusion electrode (ZG GDE).

GDEs interfaced to ion exchange membranes, as shown in Figure 1, constitute membrane-electrode assemblies (MEAs),[16] allowing for decreased ohmic losses,[17] improved catalyst stability, and avoidance of problems due to the formation of gaseous products directly at electrode/electrolyte interfaces.[18]

Reactor arrangements based on MEAs were originally developed in the field of proton exchange membrane fuel cells (PEMFCs).[19] In PEMFCs, both the cathode and the anode are of a GDE structure, and are separated by a thin membrane. $ERCO_2$ electrolyzers often involve a configuration (see Figure 1 for a scheme; Figure S1, Supporting Information for detailed assembly) in which only the cathode is of a MEA structure.[20–22] This configuration is denoted further as a zero-gap GDE (ZG GDE) because the GDE cathode is in a direct contact with the membrane that separates it from the electrolyte solution (the anolyte) that contains the anode.

Despite differences in their mode of operation (electrical-to-chemical vs chemical-to-electrical energy conversion) and in their underlying chemistry, ZG GDE $ERCO_2$ electrolyzers and PEMFCs share several important aspects considering their water (electrolyte) management. In PEMFCs, H^+ ions resulting from the anodic oxidation of hydrogen are transported through the membrane to the cathode, where they are combined with electrons and oxygen to form water as the reaction product. In ZG GDE $ERCO_2$ electrolyzers, the membrane has essentially two roles: it controls the amount of water (that acts as a reactant of $ERCO_2$, and the absence of which can cause kinetic limitations[6]) and ensures that gaseous products formed by $ERCO_2$ in the catalyst layer cannot enter the anode compartment.

Insufficient hydration of the membrane can cause, both in PEMFCs and ZG GDE $ERCO_2$ electrolyzers, an increased cell resistance and pronounced energy losses, while excess hydration can lead to the flooding of the GDL and hence compromised transport of gaseous reactants toward the catalyst.[4]

The flooding of GDLs should be understood as a complex phenomenon that depends on diverse physico-chemical processes. System properties influencing flooding include the wettability of GDEs[8,23–29] and its dependence on the applied electrode potential (electrowetting),[30–40] the pH of the electrolyte,[30] the humidity of the reactant gases,[41,42] the presence of reaction intermediates[30] and products,[43] the temperature[30] and pressure[31,32,37,38] gradients across the cell, as well as the thickness of the employed membranes.[29]

In PEMFC research, the inspection of flooding phenomena has reached a significant degree of maturity.[19,44–47] The distribution of water in the interior of fuel cell structures has been visualized under operando conditions, for example, by optical microscopy (OM), magnetic resonance imaging, neutron imaging, environmental scanning electron microscopy (SEM), X-ray computed tomography, and fluorescence microscopy.[48–50]

Strategies to mitigate flooding in PEMFCs involve the use of MPLs with large voids[51,52] comprising both naturally formed structures (pores[53,54] and cracks[55–58]) and artificially designed architectures (holes[59] and grooves[60]). These bigger voids in the MPLs exhibit a smaller capillary pressure and hydrodynamic resistance compared to that of micropores. Thus, water formed in the cathode catalyst layer can preferentially be drained through the larger voids, reaching the CFL and finally escaping the fuel cell via flow channels and gas outlet. When large voids with appropriate abundance and distribution are present, micropores remain dry and keep their ability to function as efficient transport channels for gaseous reactants.

In the $ERCO_2$ field, flooding has been reported for GDEs either directly interfaced to liquid electrolytes[8,10,11,25,26,28,32–34,36–40,61–70] or blanketed by ion exchange membranes.[22,27,29,41,42,65,71–74] Flooding in $ERCO_2$ electrolyzers was often found to be accompanied by the appearance of precipitated salts inside or on the surface of GDEs.[9,11,22,28,33,34,36,38,39,41,42,61,64–66,68,69,74–76] These salts are either themselves constituents of the electrolyte solution or are formed when such a constituent reacts with CO_2. Both flooding and salt precipitation can hinder or even completely block the transport of CO_2 to the catalyst. As a result, a transition from $ERCO_2$ to ERH_2O is observed, leading to a significant drop of the overall Faradaic efficiency of $ERCO_2$.

In $ERCO_2$ electrolyzers employing alkaline electrolytes, the flooding of GDEs, and the appearance of precipitates within the GDE structure are mutually perpetuating processes. As some of the alkaline electrolyte appears in the GDE, it combines with the CO_2 supply gas to form potassium carbonate (or bicarbonate) precipitates. These salt formations decrease the hydrophobicity of the GDE, resulting in the permeation of even more electrolyte to the MPL and the formation of additional amounts of the precipitate.[68]

As a consequence, the appearance of carbonate precipitates within a GDE structure during electrolysis can be regarded as a tracer of flooding. In this vein, several authors have described flooding phenomena by visualizing potassium (as the electrolyte cation) on the surface[22,28,66] or within the interior[34,35,68,69,72,76] of GDEs, by the application of SEM complemented by energy dispersive X-ray (EDX) elemental mapping or by X-ray micro-computed tomography.[66,76] While these SEM-EDX works successfully showed that the appearance of potassium containing precipitates in GDE structures can be interpreted as a sign of flooding, they did not attempt to quantify the distribution of precipitates within the GDE, and to establish a correlation between the latter and the observed performance losses of the electrolyzer. The reason behind this is most likely that EDX is mostly considered a qualitative technique, yielding elemental maps that are not directly (that is, not quantitatively) comparable. This gap can however be bridged by the application of a novel method, based on the combination of cross-sectional EDX measurements with an inductively coupled plasma mass spectrometry (ICP-MS) based determination of the total potassium content accumulated within a GDE structure upon the electrolysis.[77]

Note here that from the viewpoint of catalytic performance and stability, not only the total electrolyte content in a GDE but also its spatial distribution may become decisive. While the occurrence of potassium inside the micropores of the MPL can be interpreted as a sign of flooding with high certainty, its appearance in the CFL is not necessarily to be linked to flooding of micropores. In several works, the transport of the liquid electrolyte through the entire GDE (further referred to as electrolyte perspiration) was reported.[37–39,41,66,68,70] It is likely—especially based on what was said above about PEMFCs[51–60]—that the electrolyte perspiration through larger structures in the MPL involving cracks can prevent or at least delay the flooding of the micropores.

In the $ERCO_2$ field, recent works have demonstrated that cracks in the MPL facilitate the reaction due to augmented mass transport of gaseous CO_2 to the catalyst[78] and removal of excess electrolyte from the catalyst layer.[37] To the best of our knowledge, however, there is no systematic work studying the impact of MPL cracks on the catalytic activity and water management in $ERCO_2$ electrolyzers, as was carried out for PEMFCs.[55,57] While flooding of GDEs by liquid water formed as the reaction product represents the only barrier for the gas transport in PEMFCs, $ERCO_2$ is further complicated by the intrusion of the electrolyte ions into GDEs, potentially leading to salt precipitation. Exploring the electrolyte transport through MPLs with systematically varied architectures thus becomes the aim of this paper, with the ultimate goal of avoiding electrode flooding and salt precipitation in commercial $ERCO_2$ reactors.

Here we perform a series of galvanostatic experiments in a ZG GDE electrolyzer operated with alkaline anolyte. We employ different GDEs, the MPLs of which exhibit a varied abundance of cracks. To allow for a straightforward monitoring of reaction rates, we employ silver as the $ERCO_2$ catalyst, capable of producing CO with near-unity Faradaic efficiency.[8,10,12–14,16,21,22,27–29,36,38,39,41,42,66,68,70,71,75,76] The evolution of the catalytic performance is inspected by online gas chromatographic monitoring of CO and H_2, the latter being the product of ERH_2O and hence a fingerprint of electrolyte management deficiencies. Additionally, cell resistance and voltage and surface wettability of GDEs are monitored in the course of the electrolysis. We further utilize potassium as the cation of the employed electrolyte to visualize and quantify flooding and perspiration in the interior of GDEs, based on a recently developed, robust analytical approach that combines cross-sectional EDX elemental mapping and ICP-MS methods.[77] In addition, we monitor the perspiration rate by determining the amount of potassium in the perspirate, employing ICP-MS.

To the best of our knowledge, we perform and present here the first systematic study of flooding phenomena in GDEs at varied stages of the electrolysis, for GDEs with systematically varied microarchitecture. Our results shed light on an important, yet still unaddressed question of $ERCO_2$ engineering, namely, that submillimeter cracks in the MPL of GDEs applied for CO_2 electrolysis play a key role in the electrolyte management, and that by providing direct means for electrolyte drainage, cracks can efficiently prevent (or at least delay) the flooding of the catalyst layer.

2. Results and Discussion

The presented work aims at exploring the impact of the MPL structure with the emphasis on naturally occurring cracks on the catalytic activity and electrolyte management in $ERCO_2$ realized in an alkaline ZG GDE-based electrolyzer (full and cross-sectional drawings are shown in Figure S1, Supporting Information).[22,79]

We have selected four commercial GDLs as catalyst supports for our experiments, all of them having a bilayer structure composed of a CFL and an MPL. Three GDLs (36BB, 39BB, and 39BC) contain cracks in their MPLs. The fourth GDL (H23C8) has a crack-free MPL and is utilized as a reference system. For all four GDLs, the CFL is composed of coarse fibers. The surfaces of all GDLs were air-brushed with a catalyst ink containing silver nanowires (see the Experimental Section for details). The use of a catalyst ink based on nanowires was motivated by the assumption that assemblies of these quasi-1D objects form thin layers uniformly covering MPL surfaces and crack walls, without permeating into the interior of micropores.[70] For all four GDEs, the mass loading of silver was constant and equal to ≈40 µg cm^{-2}, as verified by ICP-MS analysis (see the Experimental Section for details). Representative top-down OM images of as-prepared GDEs are shown in **Figure 2**.

The optical micrographs of Figure 2 are very similar to those shown in Figure S2, Supporting Information, taken from bare GDL surfaces unmodified by catalyst ink deposition. This suggests that the air brush deposition leads to uniform catalyst layers without localized accumulation of deposits on the GDL surface or in cracks.

To inspect the structure of the formed catalyst layers in more detail, surfaces of as-prepared GDEs were further imaged by top-down SEM (also shown in Figure 2). For all four GDEs, Ag nanowires are well discerned, appearing as a collection of cylindrical objects with a diameter of ≈100 nm and a length of several micrometers, oriented parallel to the electrode surface. The small spherical features seen in the top-down SEM images of Figure 2 are attributed to the carbon black particles of the catalyst ink. High-resolution cross-sectional focused ion beam SEM images of top parts of MPLs (Figure S3, Supporting Information) demonstrate that the formed catalyst layers are 100 to 300 nm thick and involve one to three layers of Ag nanowires.

To investigate the permeation of the catalyst ink into the interior features of MPLs (micropores and cracks), cross sections of as-prepared GDEs were further inspected by SEM imaging combined with the EDX mapping of silver (Figure 2). For the non-cracked MPL (H23C8), the silver signal is confined to the top part of the MPL, confirming that Ag nanowires do not permeate micropores.

For cracked MPLs (36BB, 39BB, and 39BC) we first focused (in Figure 2) on regions containing cracks appearing as shaded features in the centers of cross-sectional SEM images. The corresponding EDX maps show a strong silver signal in the cracks, confirming that the catalyst ink permeates into the interior of the GDE through the cracks. For all three cracked MPLs, we performed the same analysis for regions with no cracks, with results shown in Figure S3, Supporting Information. In all cases, the silver signal is confined to the top of MPLs, similarly as for the non-cracked MPL (H23C8, Figure 2).

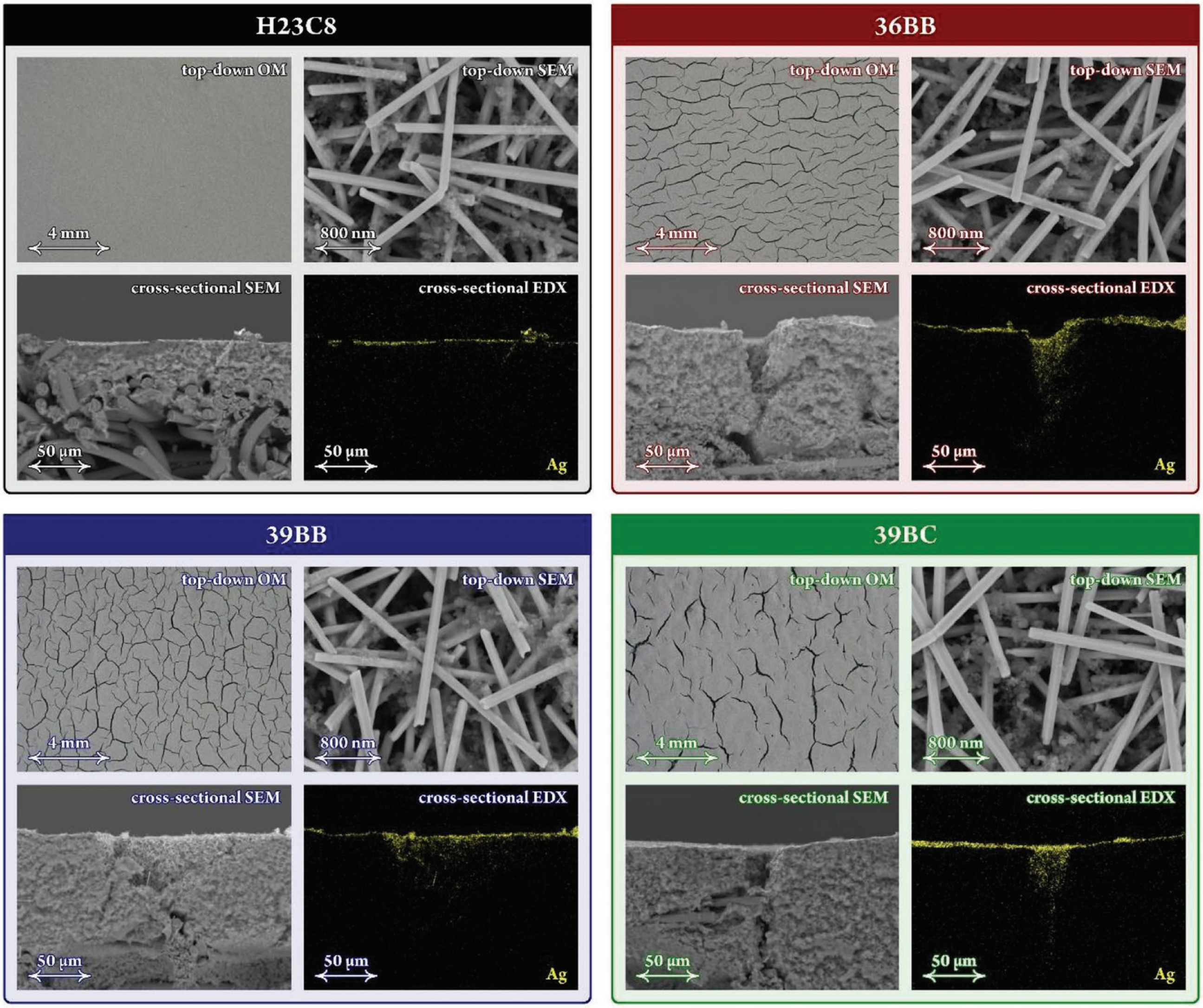

Figure 2. Representative top-down OM and SEM images, and cross-sectional SEM images and silver EDX maps of as-prepared GDEs.

One can conclude that the employed air brush deposition protocol leads to surfaces of MPLs completely covered by a thin catalyst layer that permeates into cracks, but leaves micropores unmodified. Such arrangement of the catalyst layer spatially decouples the target electrochemical process (ERCO$_2$) from the mass transport and charge transport phenomena occurring in the MPL, which is essential for the rigorous interpretation of relationships between the MPL structure, catalytic performance, and electrolyte management characteristics addressed in this work.

With regard to the distribution of cracks (see the optical micrographs of Figure 2 for catalyst ink-covered and Figure S2, Supporting Information for bare GDLs), it can be said that the H23C8 MPL has an almost featureless surface. Surfaces of the other three MPLs contain cracks that appear as distinct, elongated, and dark features. Cracks have no preferential orientation and enclose otherwise flat regions. White-light interferometry images of the pristine GDLs, as well as those of GDLs covered by a catalyst ink (taken before or following electrolysis, Figure S4, Supporting Information) exhibit the same crack distribution that seems undisturbed both by the catalyst ink coating and by subsequent electrolysis.

The pixel-by-pixel analysis of the top-down optical micrographs shown in Figure 2 allowed us to determine the relative occurrence of cracks on the MPL surface, denoted further as the surface crack ratio (CR). Obtained values are listed in **Table 1** and range from 0% to 21%. The characteristic width of cracks (≈100 µm for 36BB and 39BB, 100 to 200 µm for 39BC) is comparable to the thickness of the MPLs (also listed in Table 1), suggesting that most cracks span over the entire MPL depth.

Table 1 also lists void ratio values of entire GDLs, CFLs, and MPLs. These values were determined by densitometry, as described in the Experimental Section. The void ratio values of MPLs (further referred to as VR values) represent the cumulative porosity of MPLs; that is, the porosity that accounts for both cracks and micropores. The structure of micropores is partially resolved in SEM images presented in Figure S2, Supporting Information. As seen in Table 1, VR values scale with CR values, indicating that cracks are significant contributors to the overall porosity of MPLs. However, the differences

Table 1. Physical characteristics of GDLs used in this work. See the Statistical Analysis in the Experimental Section for more information on statistics.

	Entire GDL		CFL		MPL			
	Thickness [µm]	Void ratio [%]	Thickness [µm]	Void ratio [%]	Thickness [µm]	Void ratio (VR) [%]	Crack ratio (CR) [%]	Pores in solid (PS) [%]
H23C8	235 ± 3	60 ± 4	194 ± 5	67 ± 4	41 ± 2	30 ± 8	0 ± 0	30 ± 8
36BB	256 ± 9	70 ± 3	160 ± 20	73 ± 1	97 ± 11	68 ± 4	9 ± 2	64 ± 4
39BB	295 ± 15	81 ± 5	197 ± 22	82 ± 2	98 ± 7	78 ± 8	16 ± 4	74 ± 10
39BC	267 ± 7	72 ± 1	138 ± 21	66 ± 2	129 ± 14	78 ± 4	21 ± 4	72 ± 5

between VR values of cracked MPLs and the one obtained for the non-cracked MPL are more pronounced than the respective CR values, suggesting that cracked MPLs also exhibit a higher microporosity than crack-free MPLs. To quantify this observation, we introduce here a parameter termed the porosity of solid regions (PS) of MPLs, defined as

$$PS = \frac{VR - CR}{1 - CR} \tag{1}$$

Obtained PS values of all applied MPLs are also presented in Table 1. We presume that cracks formed in MPLs result from drying as a part of the manufacturing process of GDLs.[28] The comparison of PS and CR values suggests that the formation of cracks during the drying process is more likely for more porous MPLs. Results of combined OM and SEM imaging (Figure S2, Supporting Information) further show that the characteristic dimensions of cracks and micropores differ by at least two orders of magnitude. This difference has, as will be demonstrated, a huge impact on the capillary phenomena occurring in MPLs, being one of the key factors influencing the electrolyte management and hence catalytic performance of ZG GDEs.

For ERCO$_2$ testing, each GDE prepared and characterized as described above was blanketed by an anion exchange membrane and integrated in the electrolyzer, forming a ZG GDE (see Figure S1, Supporting Information for the arrangement of the electrolyzer and the Experimental Section for details). The electrolysis was performed and monitored under galvanostatic conditions with the GDE being continuously fed by a stream of humidified CO$_2$. **Figure 3** shows the evolution of the Faradaic efficiency (FE) values of CO obtained for all four ZG GDEs, expressed as a function of time as well as normalized charge passed in the electrolysis.

The charge normalization is based on the geometric area of the ZG GDE/anolyte interface, and the presented FE(CO) values were obtained by gas chromatography (GC) monitoring of the formed CO quantity during electrolysis (see the Experimental Section). For all ZG GDEs, CO is initially formed with near-unity FE, confirming that the catalyst shows high activity toward ERCO$_2$.

In the course of the electrolysis, significant differences in the evolution of FE(CO) values are noticed. For the crack-free MPL (H23C8), a fast decline in the CO production rate and a concomitant increase of the H$_2$ production rate are observed. The observed loss of CO production specificity may either be caused by a gradual degradation of the active catalyst sites, or by the retarded mass transport of CO$_2$ toward the catalyst layer.

For GDEs involving cracked MPLs, a markedly different evolution of FE(CO) values is observed. The GDE with the intermediate abundance of cracks (36BB, red) starts losing its catalytic activity roughly upon one-third of the electrolysis time. GDEs with higher crack abundance (39BB and 39BC, blue and green) continue to generate CO with near-unity FE values till the very end of the electrolysis. To reveal the origin of differences in the catalytic behavior, we performed identical location SEM studies of the catalyst layers deposited on H23C8 and 39BC GDLs (systems showing the smallest and the largest drop in the catalytic activity) before and after the electrolysis. For both systems, the obtained micrographs (Figure S5, Supporting Information) demonstrate that the electrolysis causes no visible changes in the nanomorphology of the catalyst. To exclude the influence of the electron beam used in SEM on the catalytic behavior and subsequent imaging,[80] we have further inspected random

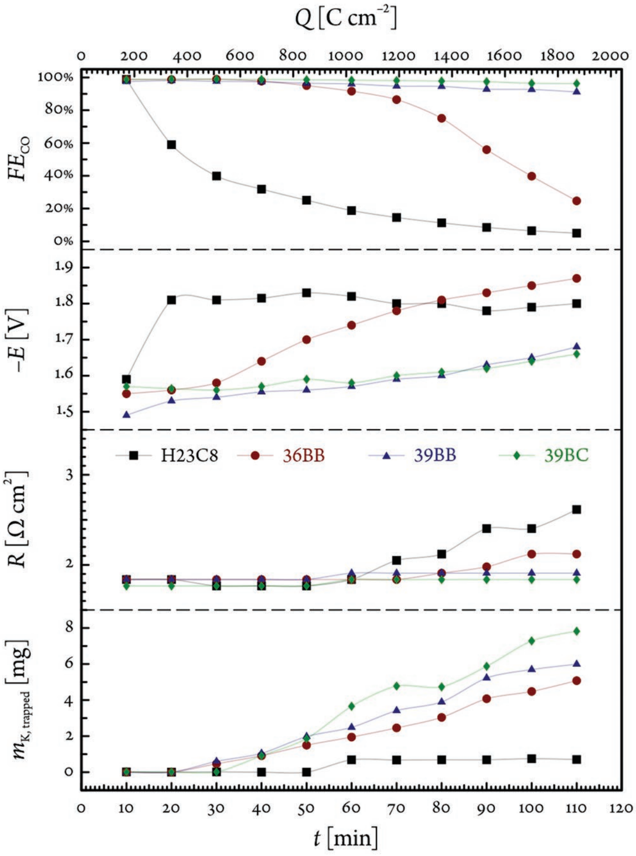

Figure 3. Faradaic efficiency of CO, ohmic drop-corrected cell voltage, normalized cell resistance, and the amount of potassium found by ICP-MS in the outlet trap plotted as a function of time and normalized charge passed in the electrolysis. Experiments were performed in the galvanostatic regime at −283 mA cm^{-2}, employing aqueous 2 M KOH as anolyte. A humidified CO$_2$ stream was fed to the GDE during the experiment at constant flow rate of 18 mL min^{-1}.

locations of the catalyst layer, not imaged prior to the electrolysis, again showing no signs of degradation (random location SEM micrographs are also shown in Figure S5, Supporting Information). Keeping in mind that catalyst loading and conditions applied in the electrolysis were identical for all four ZG GDEs, this suggests that a decline of the CO production rate observed for H23C8 and 36BB is not caused by the degradation of catalytic sites.

Employing a 36BB GDE selected for the demonstration, we further performed a follow-up electrolysis with a previously once-used electrode, preceded by a rinsing/drying step (see the Experimental Section for details). The catalytic activity of the electrode at the beginning of the follow-up electrolysis was largely restored (Figure S6, Supporting Information). This result not only confirms that the flooded electrolyte may be at least partially removed from the interior of the GDE, but additionally demonstrates that electrodes may be reused. The degradation of the catalyst was further excluded by identical and random location SEM studies performed before the initial and after the follow-up electrolysis (micrographs are also shown in Figure S6, Supporting Information).

The observed differences in the evolution of FE(CO) values among the investigated ZG GDEs are thus clearly attributed to the dissimilar rate of the CO_2 mass transport due to the different structure of MPLs.

It is important to remind that apart from the abundance of cracks (Figure 2; Figure S2, Supporting Information), the investigated MPLs also differ in void structure and, more specifically, in the porosity in solid regions, as documented by the CR, VR, and PS values (see Table 1). To investigate the effect of cracks and micropores on the observed differences in the catalytic behavior, we plotted FE(CO) values found at the end of the electrolysis as a function of the above three structural parameters in Figure S7, Supporting Information. FE(CO) data plotted on the CR basis shows more evident correlation compared to VR and PS parameters, suggesting that the crack abundance is the most important descriptor of differences in the catalytic behavior. Importantly, results of electrolysis experiments combined with the gas chromatographic product analysis suggest that cracks formed in the MPL prevent (39BB and 39BC) or at least delay (36BB) flooding as an adverse phenomenon frequently reported for $ERCO_2$ employing GDEs.

Apart from FE(CO) values, we also monitored the cell resistance as described in the Experimental Section, and plotted it as a function of time (as well as a function of the passed charge) in Figure 3. For MPLs with high crack abundance (39BB and 39BC), almost constant cell resistance values were found after a short initial period, suggesting that the concentration and mobility distribution of ions in these ZG GDEs reach a steady state. For the ZG GDE with lower crack abundance (36BB), a slight increase in resistance values is detected in later stages of the electrolysis, lagging the decrease of FE(CO) values. The resistance increase is either due to decreased electrolyte conductivity upon the reaction between CO_2 and OH^{-}[3,9] or a decrease of the active electrode area upon flooding or salt precipitation. Resistance values recorded for the non-cracked ZG GDE (H23C8) show an initial, transient decrease (presumably due to the accumulation of electrolyte ions in the catalyst layer and MPL, vide infra), followed by a pronounced increase toward the end of the electrolysis. The observed time shifts suggest that the cell resistance monitoring can only detect severe flooding events where the concentration and mobility of ions and/or active area of electrodes are affected significantly. The low flooding predicting power of cell resistance measurements is ascribed to significant resistance contributions originating from the anion exchange membrane and the anolyte, which are not affected by flooding of the GDE. The cell resistance thus cannot be used as an early warning signal to detect the onset of flooding.

Figure 3 further shows electrode potential values, mathematically corrected for the ohmic drop based on the measured cell resistance. Values obtained for ZG GDEs with high abundance of cracks (39BB and 39BC) show only subtle (and uniform) shifts, while more pronounced changes are noticed for the crack-free ZG GDE (H23C8) and the ZG GDE with moderate abundance of cracks (36BB). Such changes are probably due to the transition from the $ERCO_2$ to the ERH_2O regime. Importantly, the onset of changes observed in the electrode potential has no lag to the changes noticed in FE(CO) profiles. This suggests that electrode potential monitoring is applicable as an online tool for the detection of flooding of GDEs at commercially relevant current densities.

In experiments performed with all four ZG GDEs, small amounts of liquids and solids were observed at the back of CFLs, that is, in the gas flow channels and in the outlet equipped with a trap (see Experimental Section for details). After making sure that no electrolyte can escape the electrolyzer via leaking due to loosely assembled parts, we arrived at the conclusion that the observed liquids and solids originate from the transport of the electrolyte through ZG GDEs.

In the literature, the appearance of liquid electrolyte at the back of CFLs (termed as electrolyte perspiration) was attributed to the combination of pressure difference between the electrolyte and the gas phase and the electrowetting phenomena in the interior of GDEs.[37,38] For the ZG GDE electrolyzer employed in our study, the former contribution is given by the difference of the hydrostatic pressure acting on the top of the anion exchange membrane and the pressure in the gas flow channel beneath the CFL (see Figure S1, Supporting Information for the electrolyzer design). The magnitude of the hydrostatic pressure was estimated as 2.5 mbar, being much lower than the value needed to trigger electrolyte perspiration through the 39BC based GDE embedded in a flow-by electrolyzer (15 mbar) reported in the work of DeMot et al.[37]

In our study, the stream of gas (humidified CO_2) was fed to the flow channel at atmospheric pressure. Thus, we conclude that a differential pressure of 2.5 mbar (constant for all four ZG GDEs) was applied to the top of the anion exchange membrane. The pressure exerted on the top of GDE may additionally be influenced by the electroosmotic drag[29] resulting from the electric field (formed due to voltage applied across the cell), acting on the electric double layer in the interior of the membrane. The total pressure applied to the top of GDE is opposed by the capillary pressure originating from its hydrophobic interior structures. It is important to note that the ability of GDEs to resist external pressure may be compromised by electrowetting (an increase of wettability upon applying electric voltage between the electrode and the electrolyte).[30–40]

The magnitude of the capillary pressure is inversely proportional to the characteristic dimensions of interior structures. For hydrophobic surfaces, the electrolyte first enters structures with larger dimensions (cracks in this work), while leaving smaller structures (micropores) dry. For hydrophilic surfaces, the order of the electrolyte intrusion is just the opposite.[81] While wettability is not easily measurable in the interior of GDEs, it may be explored on their surfaces by contact angle measurements. In this work, we have monitored values of the contact angle on the surface of GDEs in the course of their preparation and upon subsequent electrolysis[22,26,27,66,70] performed with systematically varied charge consumption (Figures S8,S9, Supporting Information; see also the Statistical Analysis in the Experimental Section).

All four as-purchased (pristine) GDLs have strongly hydrophobic surfaces, with contact angle values obtained for cracked MPLs (164° ± 1°) being slightly lower than that of the crack-free MPL (170°). This is either due to crack walls having higher wettability than solid MPL regions or due to effects of highly curved surfaces. The deposition of the catalyst ink on MPLs leads to the uniform value of 143° ± 1°. This is in line with results of above-presented microscopic observations which demonstrate that the catalyst ink permeates to cracks (Figure 2).

Following electrolysis, the measured contact angle values diverge significantly among the employed electrodes. Values obtained for GDEs with high CR values (39BB and 39BC) are time-independent and equal to 106° ± 2°, indicating that their surfaces retain hydrophobic character. The value obtained for the GDE with the intermediate CR value (36BB) approaches 90°, being at the borderline between hydrophobicity and hydrophilicity. For the crack-free GDE (H23C8), contact angle values fall deep in the hydrophilic region. Washing GDEs with deionized water after completing the electrolysis led to uniform contact angle values of 135° ± 2°, being slightly lower than that obtained for as-prepared GDEs (143° ± 1°). This partial recovery implies that wettability changes observed upon the electrolysis are largely due to electrolyte accumulated in the GDE and not due to the catalyst degradation. This is in accord with results of identical and random location SEM studies of the catalyst layers presented in Figures S5,S6, Supporting Information.

Besides contact angle measurements, we further monitored the rate of electrolyte perspiration in the course of electrolysis by quantifying the amount of potassium in the outlet trap (Figure 3), employing ICP-MS analysis (see Experimental Section for details). For charge below 510 C cm^{-2}, no potassium was found. For non-cracked ZG GDE, the potassium amount remains low till the end of the electrolysis. For cracked ZG GDEs, amounts are significantly higher, scaling with passed charge and abundance of cracks.

As was already outlined above, the presence of cracks in MPLs helps to retain the catalytic activity of GDEs for a longer time (see the end-electrolysis FE(CO) values correlation with the CR parameter in Figure S7, Supporting Information). This is in agreement with the observation that the surface of GDE cathodes constructed of 39BB and 39BC GDLs show less hydrophobicity loss during electrolysis (Figures S8,S9, Supporting Information), because—as will be demonstrated below—of the cracks of these MPL surfaces act as dominant electrolyte transport pathways. For 36BB, the combination of lower CR value and hydrophobicity loss leads to slower electrolyte perspiration (Figure 3). Low amounts of potassium found for the non-cracked H23C8 suggest that the capacity of micropores to transport the electrolyte is very limited.

Besides the capillary action originating from interfacial forces, one also needs to consider that the flow of liquids through porous media is affected by viscous forces acting in the liquid. For laminar flow of water through pores of cylindrical geometry, Poiseuille law predicts that the flow rate is proportional to the second power of the cross-sectional pore area. This implies that cracks allow the passage of water at faster rate compared to micropores, additionally supporting the dominant role of cracks in the electrolyte transport. In addition to the presented reasoning, the difference in perspiration rates may further be rationalized by unequal rates of water consumption in the $ERCO_2$ and ERH_2O reactions. The two reactions proceed according to

$$CO_2 + H_2O + 2e^- \rightarrow CO + 2OH^- \tag{2}$$

and

$$2H_2O + 2e^- \rightarrow H_2 + 2OH^- \tag{3}$$

indicating that for ERH_2O, the consumption of water per unit passed charge is twice as high as for $ERCO_2$. For the non-cracked ZG GDE, where ERH_2O becomes the dominant process soon after the beginning of the electrolysis (Figure 3), higher consumption of water may contribute to the pronounced accumulation of electrolyte ions in the GDE interior, increasing the viscosity and impeding perspiration.

In the following, we further estimate the impact of the electrolyte perspiration on the carbon mass balance in $ERCO_2$, considering the data obtained for ZG GDEs based on 39BB and 39BC as best performing catalytic systems (Figure 3).

As mentioned above, the perspiration results in the accumulation of solids and liquids in gas flow channels and subsequently in the gas outlet equipped with the trap. During the electrolysis, it is not possible to monitor the amount of perspirate in gas flow channels and gas outlet and further analysis is thus restricted to the perspirate found in the trap (see Experimental Section for details). For both ZG GDEs (39BB and 39BC), the amount of potassium found in the trap scales linearly with the consumed charge. For the highest charge (1839 C cm^{-2}), it equals to 6.0 and 7.8 mg, respectively. The electrolyte transported through the GDE is in a permanent contact with gaseous CO_2 that is continuously delivered to flow channels. For stoichiometric excess of CO_2, we expect that its neutralization proceeds only to the first step, that is, producing HCO_3^- (and not CO_3^{2-}). Assuming this stoichiometry, the found mass of potassium corresponds to 1.53 and 1.99×10^{-4} mol of CO_2. We further discuss these amounts in the relation to the amount of CO_2 electrochemically converted to CO (6.74×10^{-4} mol) obtained considering FE(CO) of 100% for the sake of simplicity. The obtained CO_2 loss due to neutralization amounts to 23% and 30% indicating that the electrolyte perspiration cannot be ignored when drawing the total carbon mass balance of $ERCO_2$. Noteworthy, perspiration-related CO_2 losses in the ZG GDE electrolyzer as determined in this work are significantly lower than those reported for CO_2 neutralization in the interior of GDEs embedded in membrane-based flow-by electrolyzers (≈70%).[82,83]

To provide microscopic insight to the electrolyte intrusion in GDEs, we utilized post-experimental SEM imaging to visualize the surfaces and cross sections of electrodes subjected to the electrolysis (see Experimental Section for details). In all inspections, SEM imaging was complemented by EDX mapping of potassium (shown as purple) utilized in this work as the electrolyte cation, to specifically reveal locations to which the electrolyte has permeated. A collection of top-down and cross-sectional SEM images and EDX-K elemental maps are shown in Figure S10, Supporting Information for four different GDE samples and four different electrolysis treatments.

Here, **Figure 4** shows representative top-down EDX maps obtained for surfaces of GDEs subjected to electrolyzes terminated at the charge consumption of 2.8, 170, 510, and 1839 C cm^{-2}. In these surface maps, the deposited salt appears as fuzzy features, sometimes forming islands that, with on-going electrolysis, tend to cover the catalyst layer. Cross-sectional

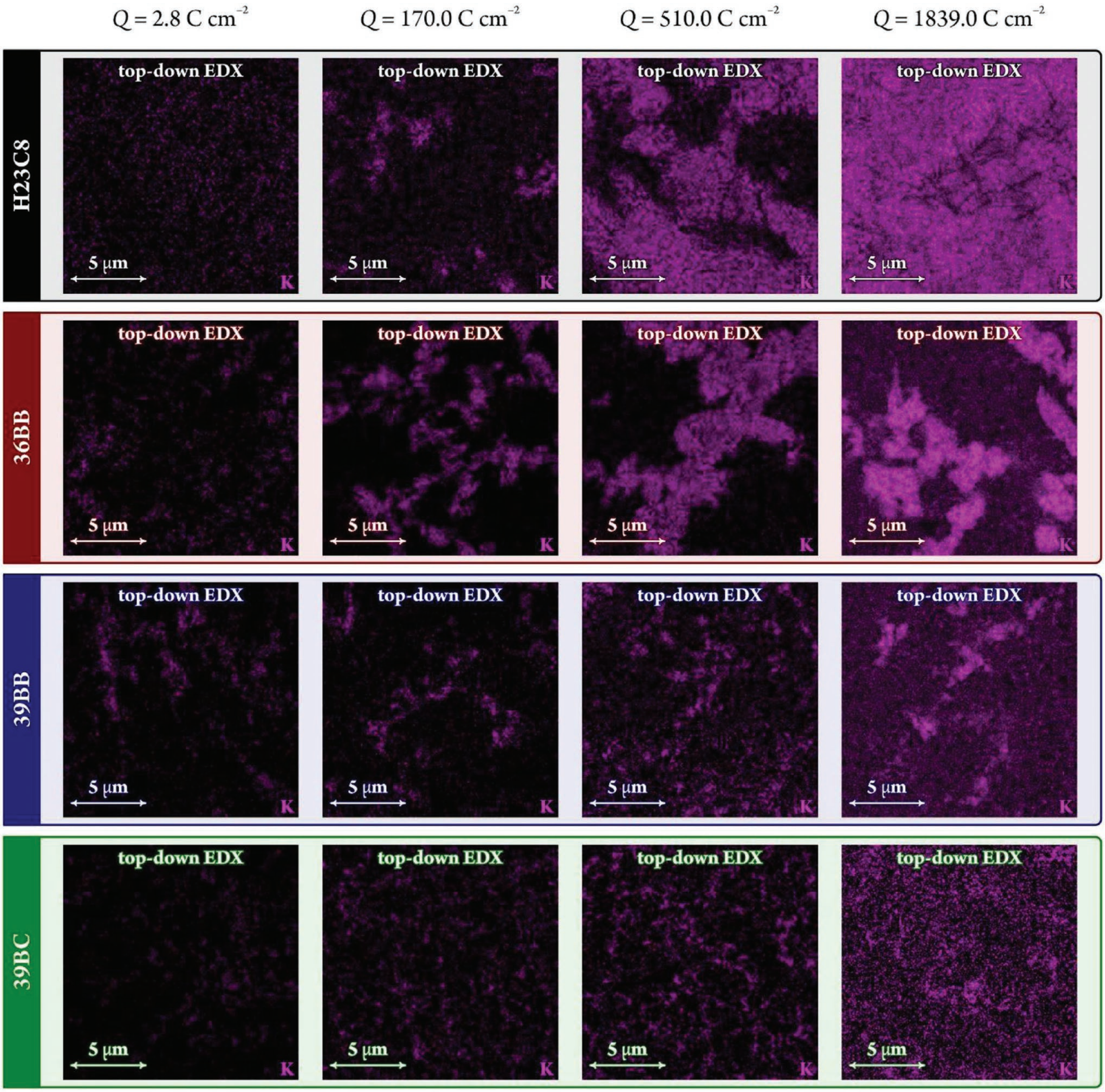

Figure 4. Representative top-down potassium EDX maps obtained for GDEs subjected to electrolyzes performed with varied charge consumption (for a comparison to corresponding top-down SEM images, as well as to cross-sectional SEM images and EDX maps, see Figure S10, Supporting Information).

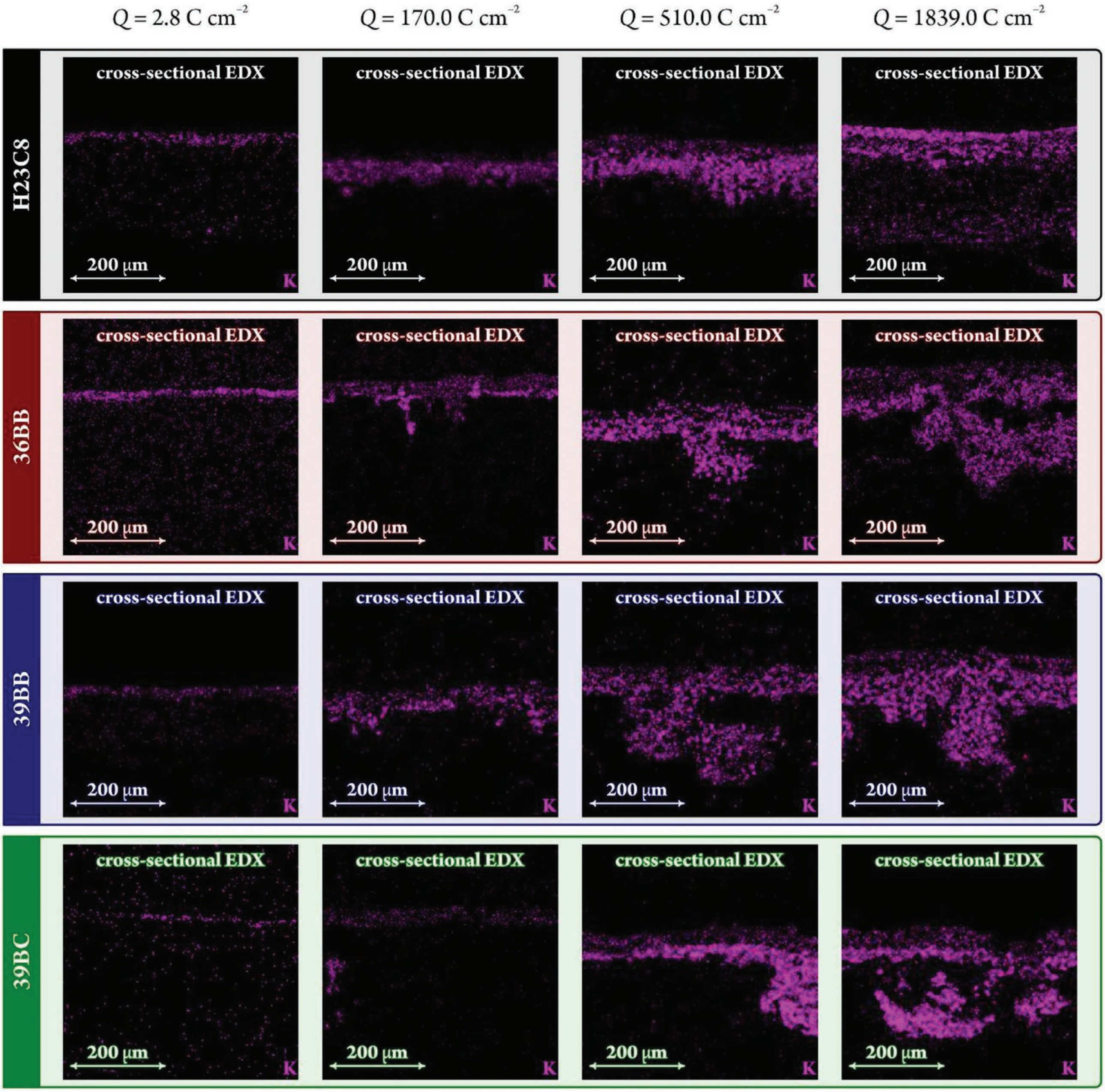

Figure 5. Representative cross-sectional potassium EDX maps obtained for GDEs subjected to electrolyzes performed with varied charge consumption (for a comparison to corresponding cross-sectional SEM images, as well as to top-down SEM images and EDX maps, see Figure S10, Supporting Information).

K EDX maps, shown in **Figure 5**, confirm that salt deposits (these are assumed to be potassium carbonates or hydrocarbonates), while initially formed only on the surface of the MPL, can later penetrate deeper layers of the GDL structure to different extent. Deposits appear already at the early stage of the electrolysis (2.8 C cm^{-2}) on all four GDE types, however they are confined to the surface of GDEs and show sparse coverage. For later stages of the electrolysis (170, 510, and 1839 C cm^{-2}) the amount and the pattern of deposits markedly differ among electrodes.

For the non-cracked GDE (H23C8), the electrolysis ends up with the deposit completely covering the electrode surface (Figure 4), being largely confined to the MPL (Figure 5). Only a minor amount of the deposit is found at the bottom of the CFL. This observation is in accordance with the low electrolyte perspiration rate found for this system (Figure 3). For the GDE with the intermediate CR value (36BB), the electrolysis leads to patched deposits covering significant portion of the electrode surface (Figure 4) and more pronounced electrolyte intrusion to the interior of the GDL (Figure 5). Higher amounts of the deposit found at the bottom of the CFL are consistent with higher perspiration rate. For GDEs with high CR values (39BB and 39BC), very little amounts of deposits were found at the electrode surface (Figure 4), with significant intrusion toward the bottom of the CFL (Figure 5), which is in line with the highest electrolyte perspiration rate.

To reveal relationships between the structure of MPLs and patterns of formed deposits, we further performed SEM imaging at higher magnification, together with combined EDX mapping of silver and potassium, with representative results shown in Figure S11, Supporting Information. All inspections were performed on GDEs subjected to electrolyzes terminated after 510 C cm^{-2}. The non-cracked GDE (H23C8) shows that the silver signal is confined to the top of the MPL and the potassium signal is evenly distributed mainly in the MPL, with little intrusion toward the CFL, all being in accord with the above-presented results (Figures 2,4,5). The SEM image obtained for 36BB shows a crack in the middle, with a corresponding region of increased silver signal. The potassium signal is localized mostly beneath this crack. A very similar scenario is observed for 39BB, with the crack, silver signal and potassium signal being in the left part of the inspected region. For 39BC, the SEM image depicts a horizontal rupture in the MPL in the central part of the micrograph with corresponding increase of the silver signal and the potassium signal located mostly below the rupture.

To conclude, high-resolution cross-sectional imaging of GDEs combined with EDX mapping of silver and potassium as signatures of cracks and electrolyte intrusion clearly demonstrate that these features correlate. This unique approach thus provides microscopic evidence that cracks drain excess electrolyte from the MPL, which is macroscopically observed in the form of electrolyte perspiration.

Samples of electrodes subjected to electrolyzes terminated at varied stages were further analyzed by ICP-MS with the goal of determining the total amount of potassium in their interior (see Experimental Section for details). Results are shown as potassium mass normalized to the electrode area (numbers stated in mg cm^{-2} shown in the panels of **Figure 6**). It is worth noting that the ICP-MS technique, while it can provide the absolute amount of potassium in the entire volume of the GDE,[74] lacks information about its spatial distribution. On the contrary, cross-sectional EDX mapping of potassium gives access to the spatial distribution,[34,35,68,69,72,76] but provides no information in terms of the absolute concentration. The two techniques may be combined to provide spatially resolved absolute potassium profiling as demonstrated by our recent contribution.

Following the approach described before,[77] we quantified the potassium distribution in GDEs subjected to electrolysis with the charge consumption varied as described above. Obtained local absolute potassium concentration values were averaged along horizontal lines of EDX maps and plotted as a function of the vertical position (i.e., depth in the GDE), with results depicted as shaded profiles in Figure 6. To provide statistically relevant information, such obtained profiles were further averaged over five individually prepared GDE cross sections, with results shown as thick curves. The concentration scale is established based on the ICP-MS based measurement of the total (surface area normalized) K content of the studied GDE section, providing the integral of the thick curves in Figure 6.

The MPL regions are visualized by shaded bands in Figure 6. The thickness of CFLs as imaged upon the electrolysis was generally found to differ a little from that determined for as-purchased GDLs (see Table 1). We attribute these differences to the swelling of the CFL structure due to electrolyte intrusion.

At early stages of electrolysis (charge consumption of 2.8 C cm^{-2}), little amounts of potassium were observed inside the investigated GDEs (Figure 6), being confined to the top of MPLs. At 170 C cm^{-2}, potassium permeated deeper to the GDE structure, with more pronounced accumulation noticed for systems losing their catalytic activity (H23C8 and 36BB, Figure 3) in top regions of the MPL. Differences among GDEs are most marked at later stages of the electrolysis (510 and 1839 C cm^{-2}). For H23C8, potassium stays localized mostly in the MPL and the top part of the CFL, with very little intrusion found in its bottom part, which is in line with the low perspiration rate observed for this GDE (Figure 3). For 36BB, the intrusion advances deeper to the CFL, being consistent with higher perspiration rate. Among all four GDEs, 36BB shows the highest total potassium content in the GDE presumably due to the combination of highly porous MPL (Table 1), high wettability of the catalyst layer (Figures S8,S9, Supporting Information) and low abundance of cracks as draining features (Table 1, Figure 2; Figure S2, Supporting Information). For 39BB and 39BC, overall lower concentration values in both MPL and CFL are observed, being in accord with the highest perspiration rates and the highest abundance of cracks.

For all four ZG GDEs, the total amount of potassium (numbers in mg cm^{-2} in Figure 6) grows up to 510 C cm^{-2} and converges to a plateau for 1839 C cm^{-2}, suggesting that a steady-state electrolyte intrusion is approached. No distinct correlations were found between the total amount of potassium in GDEs after completing the electrolysis at 1839 C cm^{-2} and the void parameters of MPLs (Figure S7, Supporting Information) suggesting that both cracks and micropores play a role in the accumulation of potassium in MPLs. The highest amount of potassium observed for 36BB presumably reflects a relatively high porosity of its MPL (Table 1) and high wettability of the catalyst layer (Figures S8,S9, Supporting Information), both favoring electrolyte intrusion, combined with low abundance of cracks (Figure 2; Figure S2, Supporting Information) impeding electrolyte perspiration.

For the three cracked GDEs (36BB, 39BB, and 39BC), the amount of potassium found in their interior (Figure 6) is insignificant compared to that determined in the outlet trap (Figure 3). This finding corroborates that cracks function as efficient pathways for the electrolyte transport and indicates that the total amount of CO_2 deposited as carbonates in the interior of GDEs can be neglected in the total carbon balance of $ERCO_2$.

We further inspected the back sides of GDEs subjected to the electrolysis by SEM/EDX analysis, finding only little amounts of potassium (Figure S12, Supporting Information). Contact angle measurements performed after the electrolysis with 1839 C cm^{-2} also confirmed that back sides of GDEs largely retained their hydrophobic character (Figure S13, Supporting Information).

To explore the extent of the electrolyte flooding in the absence of CO_2, we further carried out an electrolytic experiment employing argon-fed 36BB based ZG GDE selected for the demonstration. The catalytic activity of such treated

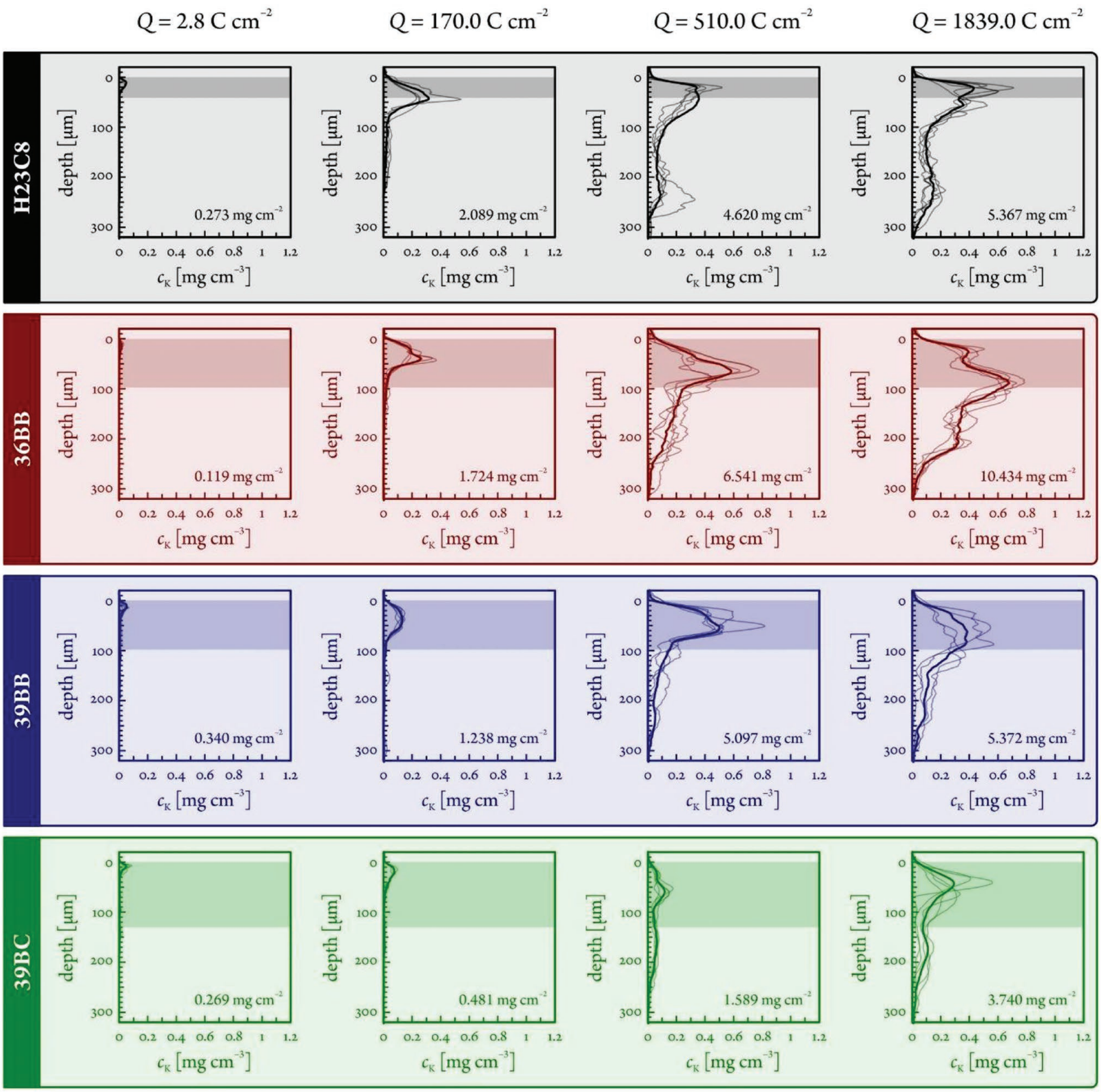

Figure 6. Potassium concentration as a function of depth in cross sections of GDEs subjected to electrolysis performed with varied charge consumption, obtained by combined EDX/ICP-MS approach. Shaded bands indicate MPL regions. The total amount of potassium found in the GDE by ICP-MS, normalized to its surface area, is indicated by numbers. See the Statistical Analysis in the Experimental Section for more information on data processing.

electrode was subsequently inspected in a follow-up electrolysis performed with CO_2. Resulting FE(CO) values (Figure S14, Supporting Information, left panel) were significantly lower compared to those obtained for the as-prepared GDE (Figure 3). This indicates that flooding in the GDE takes place also in the absence of CO_2 and in situ generated (hydrogen)carbonate salts. Nonetheless, when a cleaning/drying step (see the Experimental Section for details) was inserted between the argon-fed and the follow-up CO_2-fed electrolysis, the evolution of the catalytic activity (Figure S14, Supporting Information, right panel) well resembled that obtained for the as-prepared GDE. This demonstrates that flooded electrolyte may be removed from the interior of GDE when flooding has taken place in the absence of CO_2.

Results of the multi-methodological experimental approach presented above have revealed significant differences in the evolution of catalytic activity and the character of the electrolyte intrusion among inspected ZG GDEs due to varied structure of their MPLs. In the following, we aim to find relationships between the MPL structure, electrolyte intrusion pattern, and

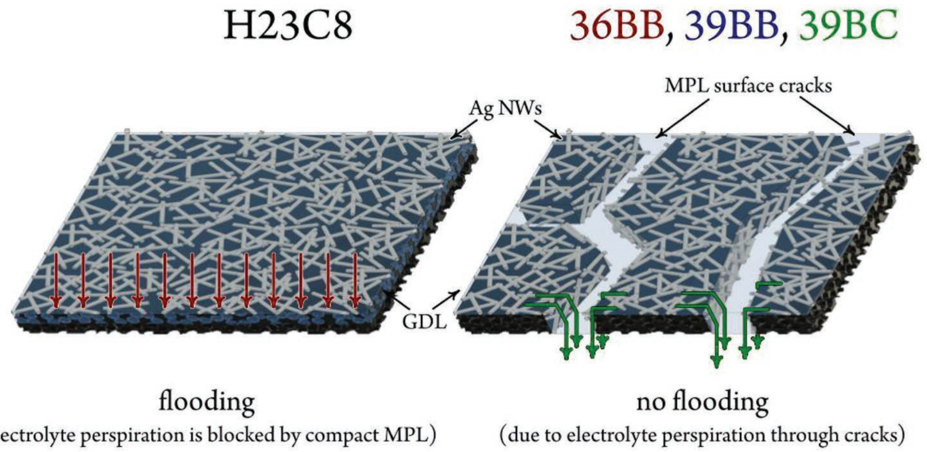

Figure 7. Schematic depiction of the catalyst layer supported with non-cracked (left) and cracked (right) MPL, visualizing electrode flooding and electrolyte perspiration phenomena.

catalytic activity, and provide mechanistic insights in these phenomena, employing a schematic depiction of the catalyst layers supported by non-cracked and cracked MPLs shown in **Figure 7**.

The MPL of H23C8 contains no cracks (Figure 2; Figure S2, Supporting Information) and shows low internal porosity (Table 1). The electrolysis performed with such ZG GDE leads to an immediate and pronounced decline in FE(CO), significant increase in cell resistance and voltage (Figure 3), loss of hydrophobilicy (Figures S8,S9, Supporting Information) and electrode surface completely covered with potassium (Figure 4) that additionally accumulates in the MPL and top part of CFL (Figures 4,5). All these characteristics are indicative of severe flooding of the MPL (Figure 7, left), with the proposed mechanism presented as follows. The combination of the hydrostatic pressure and electroosmotic drag drives the electrolyte through the anion exchange membrane to the catalyst layer, where water is partially consumed in cathodic processes (first $ERCO_2$, later mainly ERH_2O). In the absence of cracks in the MPL, the excess electrolyte floods its micropores.[81] The presence of the liquid electrolyte in micropores significantly reduces the diffusion coefficient of CO_2.[5] The diffusion rate slows down in the course of the electrolysis as the electrolyte intrudes deeper in the GDL (Figures 4,5). The ERH_2O takes place in the GDL,[70] causing more water to be consumed per unit charge. This accelerates the accumulation of OH^- ions (both originally present in the electrolyte and generated as the by-product of ERH_2O) in the GDL. Increased amounts of OH^- ions are balanced by potassium ions that reach the GDL by ionic migration via the anion exchange membrane that can generally have non-perfect permselectivity.[84] Increased ionic concentration may negatively impact the solubility of gases[85] and reaction kinetics.[3,86] The absence of cracks combined with low internal porosity of the MPL and increased electrolyte viscosity due to accumulated ions leads to low perspiration rate (Figure 3). Furthermore, OH^- ions react with CO_2 dissolved in the electrolyte to form (hydrogen)carbonate anions, reducing the electrolyte conductivity and increasing the risk of the salt precipitation in micropores. The accumulation of ions further leads to loss of hydrophobicity facilitating flooding of micropores.[68]

Based on the results of consecutive electrolytic experiments performed with argon and CO_2 (Figure S14, Supporting Information), we support the view that flooding is not initiated by the carbonate precipitation, being in contradiction to the interpretation presented by Leonard et al.[68] In fact, the intrusion of the electrolyte to micropores may be triggered by electrowetting at extreme cathodic potentials (Figure 3).[30–40] It is important to note that the ex situ SEM/EDX analysis of GDE cross sections, as performed in this work (Figures 4,5), can visualize areas to which the electrolyte has permeated during the electrolysis but cannot distinguish whether solid precipitates are formed during or after the electrolysis.[69]

The MPL of 36BB contains cracks in low abundance (Figure 2; Figure S2, Supporting Information) and has high internal porosity (Table 1). Compared to the crack-free system, this ZG GDE sustains $ERCO_2$ for longer time, shows lower increase in the cell resistance and voltage (Figure 3), less pronounced loss of hydrophobicity (Figures S8,S9, Supporting Information) and lower accumulation of potassium on the electrode surface (Figures 4,5). Compared to micropores, cracks have much greater characteristic dimensions (Figure 2; Figure S2, Supporting Information) and thus constitute preferred pathways for the electrolyte intrusion (Figure 7, right), which was microscopically confirmed by the SEM/EDX analysis (Figure S11, Supporting Information) and macroscopically observed as increased perspiration rate (Figure 3). The perspiration through cracks alleviates the flooding of micropores, enabling them to function as channels for the gas transport.[53,54,56–58] However, the loss of catalytic activity (Figure 3) accompanied by a significant buildup of potassium on the surface (Figure 4) and in the interior (Figure 5) of the GDE observed in later stages of the electrolysis indicate that the crack abundance in 36BB is not sufficient to maintain micropores dry. Values of contact angles found in later stages of the electrolysis are close to 90° (Figures S8,S9, Supporting Information), suggesting that capillary forces have minimal effect on the electrolyte transport through the MPL. In such case, the electrolyte transport rate via cracks and micropores is governed by their hydrodynamic resistance.

MPLs of 39BB and 39BC have high abundance of cracks (Figure 2; Figure S2, Supporting Information) and high internal porosity (Table 1). They differ in the architecture of cracks, with 39BB having higher amount of narrow cracks and 39BC having broader cracks with sparser abundance. Both ZG GDEs show near-unity FE(CO) values, no increase in the cell resistance, only subtle cell voltage shifts, high electrolyte perspiration rates (Figure 3), almost no loss of hydrophobicity (Figures S8,S9, Supporting Information) and little accumulation of potassium on the electrode surface (Figure 4) and in its interior (Figures 4,5), with all these characteristics being retained for the entire time span of the electrolysis. This indicates that MPLs of these two electrodes possess sufficient abundance of cracks enabling efficient electrolyte perspiration that prevents the flooding of micropores (Figure 7, right). A desired electrolyte management in the ZG GDE, with the liquid phase being largely confined to the catalyst layer, is thus established.[4] Slightly higher FE(CO) values obtained for the 39BC based system further corroborate that cracks, and not micropores, are the main drainage pathway for the electrolyte perspiration, providing valuable hints for the design of MPLs in future $ERCO_2$ electrolyzers. Near unity FE(CO) values combined with results of cross-sectional EDX mapping of silver indicate that Ag nanowires deposited on crack walls are catalytically active toward $ERCO_2$. In fact, the catalyst located in the interior of cracks may be more active than that deposited on the MPL surface due to facilitated CO_2 transport, as recently demonstrated by Welch et al.[78] Nevertheless, it is important to note that the electrolyte perspiration through cracks causes parasitic CO_2 losses due to neutralization occurring in gas flow channels, which needs to be accounted for when assessing the overall economic viability of newly designed electrolyzers.

3. Conclusions and Outlook

Cracks as structures naturally occurring in MPLs of GDEs have been reported as beneficial for the water removal in polymer electrolyte membrane fuel cells.

In this work, we have inspected the ability of cracks to improve the electrolyte management and the overall catalytic performance of zero gap GDEs for the electrochemical reduction of carbon dioxide. The employed electrodes contained silver nanowires in a thin catalytic layer and differed in the abundance of cracks in the MPL supporting the catalyst. Utilizing galvanostatic electrolyzes, we demonstrated that electrodes with appropriate abundance of cracks show high and sustained catalytic activity, while a fast transition to parasitic reduction of water was noticed for non-cracked electrodes.

Small amounts of liquids and solids were observed in flow channels and the outlet of the carbon dioxide delivery system indicating that the electrolyte is transported through zero gap GDEs (electrolyte perspiration). For the first time, the amount of the electrolyte in the perspirate was determined, employing ICP-MS, finding that this amount scales with the abundance of cracks.

Cross sections of GDEs subjected to electrolyzes were subsequently inspected by our recently developed analytical approach combining SEM imaging, EDX elemental analysis, and ICP-MS, to obtain absolute concentration profiles of potassium used as the electrolyte intrusion marker. The performed analysis provided the microscopic evidence that cracks serve as preferential pathways for the electrolyte transport through the MPL. Cracks thus drain excess electrolyte from the catalytic layer, which prevents flooding of micropores and enables them to function as efficient transport channels for gaseous carbon dioxide. In the absence of cracks, the electrolyte was found to flood micropores, reflecting itself as greatly reduced catalytic activity.

Our contribution presents the first study focusing on the effect of cracks on the electrolyte management and catalytic activity in the field of electrochemical CO_2 reduction. Besides monitoring the electrolyte intrusion in GDEs as a function of charge consumed in the electrolysis, we found correlations among the catalytic performance, electrochemical characteristics of cells, electrolyte perspiration rates, and surface wettability of electrodes, resolving the influence of cracks and micropores in the electrolyte transport.

While cracks were clearly proven to be beneficial for the electrolyte management, it should not be forgotten that the electrolyte perspiration occurring via these structures leads to non-negligible parasitic losses of carbon dioxide due to its neutralization. Therefore, efforts to optimize the utilization of carbon dioxide in electrolyzers must include searching for conditions under which both electrode flooding and perspiration-related reactant losses are minimized. Following the approaches reported for polymer electrolyte membrane fuel cells, we further aim at manufacturing and inspecting zero gap GDEs based on MPLs modified with artificially created draining elements such as holes or trenches formed by mechanical or laser perforation. The electrolyte perspiration through these structures may be controlled by their dimensions and predicted employing numerical models taking into account the capillary action, hydrodynamic resistance, and electroosmotic drag.

4. Experimental Section

Preparation of Gas Diffusion Electrodes: All experiments performed in this work employed commercial GDLs composed of supporting compressed CFL (carbon without additives) and MPL (carbon black treated with 5% PTFE). MPLs differ in their height, porosity, and abundance of cracks (for details see Results and Discussion). The GDL with crack-free MPL (H23C8) was obtained from Freudenberg, while GDLs involving cracked MPLs (36BB, 39BB, and 39BC) were purchased from Sigracet.

Silver nanowires used in this work as catalysts for $ERCO_2$ were synthesized following the procedure described in the previous work.[87] To prepare the catalyst ink, 4.5 mg of the as-synthesized Ag nanowires and 0.8 mg of carbon black (VULCAN VXC72R, Cabot) were separately dispersed in 20 mL of isopropanol (BASF SE, assay ≥ 99.0%) and sonicated for 30 min. Such prepared dispersions were intermixed, sonicated for 30 min, and dried by a rotary evaporator (Büchi R 210, 40 °C, 65 mbar). The resulting mixture was re-dispersed in 18 mL of isopropanol additionally containing 180 µL of Nafion 117 solution (≈5 wt% in a mixture of lower aliphatic alcohols and water, obtained from Sigma Aldrich) and sonicated for 20 min. The thus prepared catalyst ink was deposited on the MPL surfaces by airbrushing (hand-held Airbrushpistole Infinity CR plus, propelled by nitrogen gas, 99.999%, Carbagas, Switzerland), forming the catalyst layer. Such modified assemblies were dried and used as GDEs in electrolytic experiments performed as follows.

Assembly of the Electrolyzer: All electrochemical experiments performed in this work were realized in the electrolyzer shown in Figure S1, Supporting Information.[22,79] The electrolyzer was based on ZG GDE arrangement with GDEs prepared as described above, interfaced to the anodic compartment. The assembly of the electrolyzer was carried out as follows. The GDE with the catalyst layer facing upward was placed on a stainless steel support functioning as a current collector and a gas delivery system (it was equipped with flow channels connected to inlet and outlet tubing). The anion exchange membrane (X37-50 RT, Dioxide materials) was subjected to a pre-treatment suggested by the supplier, and gently placed on the top of the GDE. The formed ZG GDE was covered by a Teflon chamber, which was subsequently mounted to the stainless steel support by a clamp. The Teflon chamber was filled with aqueous KOH solution (10 mL, 2 м, pH = 14.3, solid KOH purchased from Sigma Aldrich, prepared employing Milli-Q water) serving as the anolyte. The Teflon chamber contained a central circular orifice (radius of 0.15 cm) in its bottom part defining the geometrical area of the ZG GDE/anolyte interface. Iridium wire (99.9%, MaTeck Material-Technologie & Kristalle GmbH, Germany) separated by glass frit and Ag/AgCl/3 м KCl electrode (double junction design, Metrohm) were immersed in the anolyte and were utilized as the counter electrode and the reference electrode. A flask containing 15 mL of Milli-Q water was placed downstream to the gas outlet and served as a trap to collect the perspirate resulting from the electrolyte transport through the ZG GDE.

Electrochemical Measurements: The catalytic activity of the ZG GDE (set as the working electrode) was inspected by galvanostatic experiments in the electrolyzer assembled as described above, employing an ECi-200 potentiostat (ECi-200, Nordic Electrochemistry). For all four GDEs, the electrolysis was performed at current of –20 mA (corresponding to geometric current density of –283 mA cm^{-2}) for systematically varied time, specifically 10, 600, 1800, and 6500 s. In the Results and Discussion section, the duration of electrolysis is presented as passed charge normalized to the geometrical area of the ZG GDE/anolyte interface (0.0707 cm^2). Unless otherwise specified, a freshly prepared GDE was used in the electrolysis. A humidified gaseous CO_2 stream (99.999%, Carbagas, Switzerland) was continuously supplied to the flow channels of the stainless steel support via the inlet at the rate of 18 mL min^{-1} employing a thermal mass flow controller (red-y smart, Vögtlin Instruments). The gaseous mixture leaving the outlet was fed through a drying tube and its composition was analyzed for CO and H_2 by online GC (SRI Instruments) in 10 min intervals.[21] The formed CO and H_2 quantities, measured during electrolysis, added up to about 100% ± 10% of the quantities that could be expected from the charge of electrolysis. Noting that while the formation of some other products (e.g., that of formate) was possible in very little amount in the studied electrolyzer, it was assumed that the H_2:CO formation ratios detectable by GC were, within range of experimental error, correct. Faradaic efficiency values (e.g., those presented in Figure 3) were thus re-scaled so that the measured H_2:CO ratios were respected, together accounting for a 100% Faradaic efficiency.

The cell voltage and resistance were monitored in 0.1 s intervals. The cell resistance was obtained by superimposing AC perturbation (5 000 Hz, 50 µA) to the current applied to the cell (20 mA) and monitoring the AC component of the cell voltage.

For the GDE based on 36BB GDL, a follow-up electrolysis experiment was performed with the goal of exploring the possibility of restoring the catalytic activity of once used electrode. First, the GDE was subjected to the electrolysis performed as described above. Afterward, the electrolyzer was disassembled and the GDE was immersed in ≈30 mL of quiescent Milli-Q water for 5 min, the procedure being repeated 7 times. Subsequently, the GDE was dried in a vacuum oven for 2 h at ambient temperature. Such treated GDE was reinstalled into the electrolyzer and its catalytic performance was inspected in a follow-up electrolysis carried out under the same conditions.

Also for the GDE based on 36BB GDL, an additional control electrolytic experiment was performed to inspect the occurrence of flooding in the absence of CO_2. First, the GDE was subjected to the electrolysis with humidified CO_2 being replaced by humidified argon (99.9999%, Carbagas, Switzerland). Subsequently, the electrolyzer was disassembled and the GDE was either subjected to the cleaning/drying procedure performed as described above or this step was omitted. Such treated GDE was reinstalled into the electrolyzer and its catalytic performance was inspected in a follow-up electrolysis carried out with humidified CO_2.

Characterization of Electrodes: Surfaces of pristine MPLs and as-prepared GDEs were inspected by optical microscopic imaging employing a VHX600 Keyence digital microscopes. The obtained images were utilized to determine the surface CR based on counting pixels corresponding to cracks and solid regions on the MPL surface. The void ratio of CFLs, MPLs, and entire GDLs was obtained by using a pycnometer, employing isopropanol as a liquid that was assumed to completely fill up the internal structures of layers. Surfaces of as-purchased (pristine) MPLs, as-prepared GDEs, and GDEs subjected to the electrolysis were additionally inspected by white light interferometry (Contour GT, Bruker) equipped with Vision64 software (Vision64, Bruker).

A Zeiss Gemini 450 SEM equipped with an EDX spectroscopy instrument (Aztec, Oxford instruments) was used to investigate the structure and content of silver and potassium on surfaces and in the interior of GDEs. Surfaces of GDEs were inspected before and after electrolytic measurements performed as described above. For selected samples, identical location SEM studies were performed. Subsequently, electrodes subjected to the electrolysis were frozen in liquid nitrogen and cut by a sharp blade and such obtained cross sections were examined by SEM/EDX. To obtain statistically significant information, at least five cross sections were prepared and analyzed for each GDE. The cross-sectional imaging was additionally performed for as-purchased GDLs, to determine the thickness of the CFL and the MPL.

The mass loading of silver in the catalyst layer of as-prepared GDEs was determined by means of ICP-MS (NexION 2000 ICP-MS instrument, PerkinElmer). For this purpose, GDEs of circular shape with the radius of 0.1 cm were prepared and examined. GDE samples were introduced to concentrated nitric acid (69.3%, VLSI selectipur, BASF), sonicated for 30 min and left overnight. Additionally, ICP-MS analysis following the same sample treatment was employed to determine the amount of potassium in the interior of GDEs upon the electrolysis. Furthermore, the ICP-MS was employed to determine the amount of potassium in the perspirate resulting from the electrolyte transport through GDEs, found in the trap following the gas outlet.

The wettability of as-purchased GDLs, as prepared GDEs and GDEs subjected to electrolysis performed as described above was assessed by contact angle measurement (Krüss Advance Drop Shape Analyzer DSA25, Krüss GmbH, Hamburg, Germany). Electrodes subjected to the electrolysis were dried for 2 h before actual measurements. All inspected samples were mounted on a flat stage, sessile water drops (Milli-Q water, 1.4 µL) were deposited on their top at room temperature and contact angles were recorded immediately after creating droplets.

Statistical Analysis: For data presented in the form expected value ± error in the paper, the expected value was determined as the arithemetic mean, and the error as the standard deviation of the dataset. Contact angle intervals reported in the text were calculated using values shown in Figure S7, Supporting Information, by averaging over different GDEs that underwent the same electrolysis treatment. The optical micrographs of the as-prepared GDEs (Figure 2) were used for the calculation of surface CRs of the GDEs. The micrographs were utilized to determine the surface CR based on counting pixels corresponding to cracks and solid regions on the MPL surface: the analysis was done by an in-house developed algorithm written in LabVIEW. The void ratios of the carbon fibrous and MPLs of GDLs, as well as the total void ratios of CFLs, MPLs, and entire GDLs, shown in Table 1, were determined by three parallel pycnometer-based densitometry measurements. The vertical depth profiles of K^+ concentrations, shown in Figure 6, were created using cross-sectional EDX maps obtained from the respective GDEs following electrolyzes. The total (average) K^+ concentrations, corresponding to the integrals of the averaged distribution curves, were determined by a single ICP-MS measurement. In case of each panel of Figure 6, several (five to eight) individual EDX maps were analyzed. These maps were obtained in a numerical format from the Aztec controlling software. Depth profiles were obtained by a row-to-row summation of the K signal intensity, followed by vertical alignment of the individual distributions. This alignment was based on the assignation of a 0 depth value to the first entry where the detected K intensity reached 3 times the initial noise level. For the alignment, subsequent averaging, and normalization of the distributions, a home-built software (written in LabVIEW) was used; more details of the calculations can be found elsewhere.[77] Raw data serving as a basis for the presented calculations are accessible at Zenodo.[88]

Supporting Information

Supporting Information is available from the Wiley Online Library or from the author.

Acknowledgements

This publication was created as part of NCCR Catalysis (Grant number 180544), a National Centre of Competence in Research funded by the Swiss National Science Foundation. V.K. acknowledges financial support from the Czech Science Foundation (Project number 18-09848S). Y.K., M.L., and H.H. acknowledge the financial support by the Chinese Scholarship Council (CSC). S.V. acknowledges support from the National Research, Development and Innovation Office of Hungary (NKFIH grant FK135375).

Open access funding provided by Universität Bern.

Conflict of Interest

The authors declare no conflict of interest.

Data Availability Statement

The raw data to this paper are made fully accessible to the public via Zenodo (https://doi.org/10.5281/zenodo.6421142) along with the publication of this manuscript.

Keywords

carbon dioxide electroreduction, cracks, flooding, gas diffusion electrodes, microporous layers, perspiration, precipitation

Received: April 7, 2022
Revised: June 28, 2022
Published online:

---

[1] I. Ganesh, *Renewable Sustainable Energy Rev.* **2016**, *59*, 1269.
[2] S. Nitopi, E. Bertheussen, S. B. Scott, X. Y. Liu, A. K. Engstfeld, S. Horch, B. Seger, I. E. L. Stephens, K. Chan, C. Hahn, J. K. Norskov, T. F. Jaramillo, I. Chorkendorff, *Chem. Rev.* **2019**, *119*, 7610.
[3] T. Burdyny, W. A. Smith, *Energy Environ. Sci.* **2019**, *12*, 1442.
[4] N. T. Nesbitt, T. Burdyny, H. Simonson, D. Salvatore, D. Bohra, R. Kas, W. A. Smith, *ACS Catal.* **2020**, *10*, 14093.
[5] D. M. Weekes, D. A. Salvatore, A. Reyes, A. X. Huang, C. P. Berlinguette, *Acc. Chem. Res.* **2018**, *51*, 910.
[6] E. W. Lees, B. A. W. Mowbray, F. G. L. Parlane, C. P. Berlinguette, *Nat. Rev. Mater.* **2022**, *7*, 55.
[7] A. Z. Weber, J. Newman, *J. Electrochem. Soc.* **2005**, *152*, A677.
[8] B. Kim, F. Hillman, M. Ariyoshi, S. Fujikawa, P. J. A. Kenis, *J. Power Sources* **2016**, *312*, 192.
[9] E. J. Dufek, T. E. Lister, M. E. McIlwain, *Electrochem. Solid-State Lett.* **2012**, *15*, B48.
[10] S. S. Bhargava, F. Proietto, D. Azmoodeh, E. R. Cofell, D. A. Henckel, S. Verma, C. J. Brooks, A. A. Gewirth, P. J. A. Kenis, *ChemElectroChem* **2020**, *7*, 2001.
[11] S. Verma, Y. Hamasaki, C. Kim, W. X. Huang, S. Lu, H. R. M. Jhong, A. A. Gewirth, T. Fujigaya, N. Nakashima, P. J. A. Kenis, *ACS Energy Lett.* **2018**, *3*, 193.
[12] S. Verma, X. Lu, S. C. Ma, R. I. Masel, P. J. A. Kenis, *Phys. Chem. Chem. Phys.* **2016**, *18*, 7075.
[13] B. Kim, S. Ma, H. R. M. Jhong, P. J. A. Kenis, *Electrochim. Acta* **2015**, *166*, 271.
[14] C. M. Gabardo, A. Seifitokaldani, J. P. Edwards, C. T. Dinh, T. Burdyny, M. G. Kibria, C. P. O'Brien, E. H. Sargent, D. Sinton, *Energy Environ. Sci.* **2018**, *11*, 2531.
[15] V. R. Stamenkovic, D. Strmcnik, P. P. Lopes, N. M. Markovic, *Nat. Mater.* **2017**, *16*, 57.
[16] J. Lee, J. Lim, C. W. Roh, H. S. Whang, H. Lee, *J. CO_2 Util.* **2019**, *31*, 244.
[17] L. C. Weng, A. T. Bell, A. Z. Weber, *Energy Environ. Sci.* **2019**, *12*, 1950.
[18] A. Angulo, P. van der Linde, H. Gardeniers, M. Modestino, D. F. Rivas, *Joule* **2020**, *4*, 555.
[19] L. Cindrella, A. M. Kannan, J. F. Lin, K. Saminathan, Y. Ho, C. W. Lin, J. Wertz, *J. Power Sources* **2009**, *194*, 146.
[20] M. L. Liu, Y. Kong, H. F. Hu, N. Kovacs, C. Z. Sun, I. Z. Montiel, M. D. G. Vazquez, Y. Hou, M. Mirolo, I. Martens, J. Drnec, S. Vesztergom, P. Broekmann, *J. Catal.* **2021**, *404*, 371.
[21] M. D. Galvez-Vazquez, S. Alinejad, H. F. Hu, Y. H. Hou, P. Moreno-Garcia, A. Zana, G. K. H. Wiberg, P. Broekmann, M. Arenz, *Chimia* **2019**, *73*, 922.
[22] M. D. Galvez-Vazquez, P. Moreno-Garcia, H. Xu, Y. H. Hou, H. F. Hu, I. Z. Montiel, A. V. Rudnev, S. Alinejad, V. Grozovski, B. J. Wiley, M. Arenz, P. Broekmann, *ACS Catal.* **2020**, *10*, 13096.
[23] M. Maja, C. Orecchia, M. Strano, P. Tosco, M. Vanni, *Electrochim. Acta* **2000**, *46*, 423.
[24] N. Wagner, M. Schulze, E. Gulzow, *J. Power Sources* **2004**, *127*, 264.
[25] Z. Xing, X. Hu, X. F. Feng, *ACS Energy Lett.* **2021**, *6*, 1694.
[26] Z. Xing, L. Hu, D. S. Ripatti, X. Hu, X. F. Feng, *Nat. Commun.* **2021**, *12*, 136.
[27] W. H. Lee, Y. J. Ko, Y. Choi, S. Y. Lee, C. H. Choi, Y. J. Hwang, B. K. Min, P. Strasser, H. S. Oh, *Nano Energy* **2020**, *76*, 105030.
[28] U. O. Nwabara, A. D. Hernandez, D. A. Henckel, X. Y. Chen, E. R. Cofell, M. P. De-Heer, S. Verma, A. A. Gewirth, P. J. A. Kenis, *ACS Appl. Energy Mater.* **2021**, *4*, 5175.
[29] A. Reyes, R. P. Jansonius, B. A. W. Mowbray, Y. Cao, D. G. Wheeler, J. Chau, D. J. Dvorak, C. P. Berlinguette, *ACS Energy Lett.* **2020**, *5*, 1612.
[30] T. Burchardt, *J. Power Sources* **2004**, *135*, 192.
[31] K. Liu, W. A. Smith, T. Burdyny, *ACS Energy Lett.* **2019**, *4*, 639.
[32] A. Lowe, C. Rieg, T. Hierlemann, N. Salas, D. Kopljar, N. Wagner, E. Klemm, *ChemElectroChem* **2019**, *6*, 4497.
[33] K. J. Puring, D. Siegmund, J. Timm, F. Mollenbruck, S. Schemme, R. Marschall, U. P. Apfel, *Adv. Sustainable Syst.* **2021**, *5*, 2000088.
[34] F. Bienen, A. Lowe, J. Hildebrand, S. Hertle, D. Schonvogel, D. Kopljar, N. Wagner, E. Klemm, K. A. Friedrich, *J. Energy Chem.* **2021**, *62*, 367.
[35] F. Bienen, J. Hildebrand, D. Kopljar, N. Wagner, E. Klemm, K. A. Friedrich, *Chem. Ing. Tech.* **2021**, *93*, 1015.
[36] K. L. Yang, R. Kas, W. A. Smith, T. Burdyny, *ACS Energy Lett.* **2021**, *6*, 33.
[37] B. De Mot, J. Hereijgers, M. Duarte, T. Breugelmans, *Chem. Eng. J.* **2019**, *378*, 122224.
[38] P. Jeanty, C. Scherer, E. Magori, K. Wiesner-Fleischer, O. Hinrichsen, M. Fleischer, *J. CO_2 Util.* **2018**, *24*, 454.
[39] M. Duarte, B. De Mot, J. Hereijgers, T. Breugelmans, *ChemElectroChem* **2019**, *6*, 5596.
[40] S. Sen, S. M. Brown, M. Leonard, F. R. Brushett, *J. Appl. Electrochem.* **2019**, *49*, 917.

[41] D. G. Wheeler, B. A. W. Mowbray, A. Reyes, F. Habibzadeh, J. F. He, C. P. Berlinguette, *Energy Environ. Sci.* **2020**, *13*, 5126.
[42] B. Endrodi, E. Kecsenovity, A. Samu, F. Darvas, R. V. Jones, V. Torok, A. Danyi, C. Janaky, *ACS Energy Lett.* **2019**, *4*, 1770.
[43] M. E. Leonard, M. J. Orella, N. Aiello, Y. Roman-Leshkov, A. Forner-Cuenca, F. R. Brushett, *J. Electrochem. Soc.* **2020**, *167*, 124521.
[44] H. Li, Y. H. Tang, Z. W. Wang, Z. Shi, S. H. Wu, D. T. Song, J. L. Zhang, K. Fatih, J. J. Zhang, H. J. Wang, Z. S. Liu, R. Abouatallah, A. Mazza, *J. Power Sources* **2008**, *178*, 103.
[45] K. Jiao, X. G. Li, *Prog. Energy Combust. Sci.* **2011**, *37*, 221.
[46] N. Yousfi-Steiner, P. Mocoteguy, D. Candusso, D. Hissel, A. Hernandez, A. Aslanides, *J. Power Sources* **2008**, *183*, 260.
[47] P. C. Pei, H. C. Chen, *Appl. Energy* **2014**, *125*, 60.
[48] M. B. Ji, Z. D. Wei, *Energies* **2009**, *2*, 1057.
[49] A. Bazylak, *Int. J. Hydrogen Energy* **2009**, *34*, 3845.
[50] S. Tsushima, S. Hirai, *Prog. Energy Combust. Sci.* **2011**, *37*, 204.
[51] R. Omrani, B. Shabani, *Int. J. Hydrogen Energy* **2017**, *42*, 28515.
[52] S. Tsushima, S. Hirai, *J. Therm. Sci. Technol.* **2015**, *10*, JTST0002.
[53] T. Sasabe, P. Deevanhxay, S. Tsushima, S. Hirai, *Electrochem. Commun.* **2011**, *13*, 638.
[54] E. A. Wargo, V. P. Schulz, A. Cecen, S. R. Kalidindi, E. C. Kumbur, *Electrochim. Acta* **2013**, *87*, 201.
[55] M. P. Manahan, S. Kim, E. C. Kumbur, M. M. Mench, *ECS Trans.* **2009**, *25*, 1745.
[56] H. Markotter, I. Manke, P. Kruger, T. Arlt, J. Haussmann, M. Klages, H. Riesemeier, C. Hartnig, J. Scholta, J. Banhart, *Electrochem. Commun.* **2011**, *13*, 1001.
[57] N. Karst, V. Faucheux, A. Martinent, P. Bouillon, J. P. Simonato, *J. Power Sources* **2010**, *195*, 5228.
[58] J. S. Ma, X. X. Zhang, Z. Y. Jiang, H. Ostadi, K. Jiang, R. Chen, *Fuel* **2014**, *136*, 307.
[59] D. Gerteisen, C. Sadeler, *J. Power Sources* **2010**, *195*, 5252.
[60] K. Nishida, T. Murakami, S. Tsushima, S. Hirai, *J. Power Sources* **2010**, *195*, 3365.
[61] R. L. Cook, R. C. Macduff, A. F. Sammells, *J. Electrochem. Soc.* **1990**, *137*, 607.
[62] G. L. De Gregorio, T. Burdyny, A. Loiudice, P. Iyengar, W. A. Smith, R. Buonsanti, *ACS Catal.* **2020**, *10*, 4854.
[63] M. Jouny, W. Luc, F. Jiao, *Nat. Catal.* **2018**, *1*, 748.
[64] J. J. Lv, M. Jouny, W. Luc, W. L. Zhu, J. J. Zhu, F. Jiao, *Adv. Mater.* **2018**, *30*, 1803111.
[65] C. M. Gabardo, C. P. O'Brien, J. P. Edwards, C. McCallum, Y. Xu, C. T. Dinh, J. Li, E. H. Sargent, D. Sinton, *Joule* **2019**, *3*, 2777.
[66] E. R. Cofell, U. O. Nwabara, S. S. Bhargava, D. E. Henckel, P. J. A. Kenis, *ACS Appl. Mater. Interfaces* **2021**, *13*, 15132.
[67] C. T. Dinh, T. Burdyny, M. G. Kibria, A. Seifitokaldani, C. M. Gabardo, F. P. G. de Arquer, A. Kiani, J. P. Edwards, P. De Luna, O. S. Bushuyev, C. Q. Zou, R. Quintero-Bermudez, Y. J. Pang, D. Sinton, E. H. Sargent, *Science* **2018**, *360*, 783.
[68] M. E. Leonard, L. E. Clarke, A. Forner-Cuenca, S. M. Brown, F. R. Brushett, *ChemSusChem* **2020**, *13*, 400.
[69] D. McLaughlin, M. Bierling, R. Moroni, C. Vogl, G. Schmid, S. Thiele, *Adv. Energy Mater.* **2020**, *10*, 2000488.
[70] D. Raciti, T. Braun, B. M. Tackett, H. Xu, M. Cruz, B. J. Wiley, T. P. Moffat, *ACS Catal.* **2021**, *11*, 11945.
[71] G. O. Larrazabal, P. Strom-Hansen, J. P. Heli, K. Zeiter, K. T. Therldldsen, I. Chorkendorff, B. Seger, *ACS Appl. Mater. Interfaces* **2019**, *11*, 41281.
[72] J. Li, G. X. Chen, Y. Y. Zhu, Z. Liang, A. Pei, C. L. Wu, H. X. Wang, H. R. Lee, K. Liu, S. Chu, Y. Cui, *Nat. Catal.* **2018**, *1*, 592.
[73] A. Patru, T. Binninger, B. Pribyl, T. J. Schmidt, *J. Electrochem. Soc.* **2019**, *166*, F34.
[74] B. De Mot, M. Ramdin, J. Hereijgers, T. J. H. Vlugt, T. Breugelmans, *ChemElectroChem* **2020**, *7*, 3839.
[75] B. Endrodi, E. Kecsenovity, A. Samu, T. Halmagyi, S. Rojas-Carbonell, L. Wang, Y. Yan, C. Janaky, *Energy Environ. Sci.* **2020**, *13*, 4098.
[76] B. Endrodi, A. Samu, E. Kecsenovity, T. Halmagyi, D. Sebok, C. Janaky, *Nat. Energy* **2021**, *6*, 439.
[77] Y. Kong, H. F. Hu, M. L. Liu, Y. Hou, V. Kolivoska, S. Vesztergom, P. Broekmann, *J. Catal.* **2022**, *408*, 1.
[78] A. J. Welch, A. Q. Fenwick, A. Bohme, H. Y. Chen, I. Sullivan, X. Q. Li, J. S. DuChene, C. X. Xiang, H. A. Atwater, *J. Phys. Chem. C* **2021**, *125*, 20896.
[79] G. K. H. Wiberg, M. Fleige, M. Arenz, *Rev. Sci. Instrum.* **2015**, *86*, 024102.
[80] Y. H. Hou, N. Kovacs, H. Xu, C. Z. Sun, R. Erni, M. D. Galvez-Vazquez, A. Rieder, H. F. Hu, Y. Kong, M. L. Liu, B. J. Wiley, S. Vesztergom, P. Broekmann, *J. Catal.* **2021**, *394*, 58.
[81] L. C. Weng, A. T. Bell, A. Z. Weber, *Phys. Chem. Chem. Phys.* **2018**, *20*, 16973.
[82] M. Ma, S. Kim, I. Chorkendorff, B. Seger, *Chem. Sci.* **2020**, *11*, 8854.
[83] M. Ma, E. L. Clark, K. T. Therkildsen, S. Dalsgaard, I. Chorkendorff, B. Seger, *Energy Environ. Sci.* **2020**, *13*, 977.
[84] G. M. Geise, M. A. Hickner, B. E. Logan, *ACS Appl. Mater. Interfaces* **2013**, *5*, 10294.
[85] M. Roehe, A. Botz, D. Franzen, F. Kubannek, B. Ellendorff, D. Oehl, W. Schuhmann, T. Turek, U. Krewer, *ChemElectroChem* **2019**, *6*, 5671.
[86] N. T. Nesbitt, W. A. Smith, *J. Phys. Chem. C* **2021**, *125*, 13085.
[87] H. F. Hu, M. L. Liu, Y. Kong, N. Mysuru, C. Z. Sun, M. D. Galvez-Vazquez, U. Muller, R. Erni, V. Grozovski, Y. H. Hou, P. Broekmann, *ACS Catal.* **2020**, *10*, 8503.
[88] Y. Kong, M. Liu, H. Hu, Y. Hou, S. Vesztergom, M. de J. Gálvez-Vázquez, I. Zelocualtecatl Montiel, V. Kolivoška, P. Broekmann, Raw data for the article "Cracks as efficient tools to mitigate flooding in gas diffusion electrodes used for the electrochemical reduction of carbon dioxide" **2022**, https://doi.org/10.5281/zenodo.6421142.

7.6. The capping agent is the key: Structural alterations of Ag NPs during CO_2 electrolysis probed in a zero-gap gas-flow configuration

Authors: Menglong Liu, Ying Kong, Huifang Hu, Noémi Kovács, Changzhe Sun, **Iván Zelocualtecatl Montiel**, María de Jesús Gálvez Vázquez, Yuhui Hou, Marta Mirolo, Isaac Martens, Jakub Drnec, Soma Vesztergom, Peter Broekmann

Journal of Catalysis **404** (2021) 371–382. DOI: https://doi.org/10.1016/j.jcat.2021.10.016

Highlights: This work reports the effect of Ag-NPs stabilized by different ligands like BPEI, PVP, PEG and Citrate dispersed in a gas diffusion layer (GDE) for CO_2 electroreduction in a zero-gap flow cell. Electrochemical studies show that product distribution and partial current densities are slightly affected depending on the stabilizing agent for all four capping agents. Using different characterization techniques, such as SEM, EDX mapping, ICP MS, and WAXS, the structural changes of the Ag-NPs before and after electrolysis experiments were analysed. These methods demonstrate that depending on the nature of their stabilizing ligands, Ag-NPs undergo different degradation pathways during electrolysis. It was found that amongst the studied capping agents, BPEI presents a protection effect; however, the selectivity towards CO formation seems to be affected. In the case of the PVP agent, mostly corrosion (particle shrinkage) was observed, while PEG and citrate lead more to particle coalescence. It is important to note that the excess ligand adsorbed on the carbon support surface plays an important role in determining the extent and mode of catalyst degradation.

Contributions: In this project, I was involved in conducting some electrochemical experiments and ICP-MS. In addition, I participated in the manuscript revision process.

Journal of Catalysis 404 (2021) 371–382

Contents lists available at ScienceDirect

Journal of Catalysis

journal homepage: www.elsevier.com/locate/jcat

The capping agent is the key: Structural alterations of Ag NPs during CO_2 electrolysis probed in a zero-gap gas-flow configuration

Menglong Liu [a,b], Ying Kong [a,b], Huifang Hu [a], Noémi Kovács [a], Changzhe Sun [a,b], Iván Zelocualtecatl Montiel [a], María de Jesús Gálvez Vázquez [a], Yuhui Hou [a,*], Marta Mirolo [c], Isaac Martens [c], Jakub Drnec [c], Soma Vesztergom [a,d,*], Peter Broekmann [a,b,*]

[a] University of Bern, Department of Chemistry, Biochemistry and Pharmaceutical Sciences Freiestrasse 3, 3012 Bern, Switzerland
[b] National Centre of Competence in Research (NCCR) Catalysis, University of Bern Freiestrasse 3, 3012 Bern, Switzerland
[c] European Synchrotron Radiation Facility, Experimental Division, Avenue des Martyrs 71, 38000 Grenoble, France
[d] Eötvös Loránd University, Department of Physical Chemistry Pázmány Péter sétány 1/A, 1117 Budapest, Hungary

ARTICLE INFO

Article history:
Received 16 August 2021
Revised 1 October 2021
Accepted 13 October 2021
Available online 21 October 2021

Keywords:
Power to value
Carbon dioxide electroreduction
Catalyst degradation
Particle sizing
Scanning electron microscopy
Wide-angle X-ray scattering

ABSTRACT

We apply silver nanoparticles (Ag NPs) as catalysts of CO_2 reduction in a zero-gap gas-flow electrolyser. Ag NPs stabilized by different ligands —branched polyethylenimine (BPEI), polyvinylpyrrolidone (PVP), polyethylene glycol (PEG), and citrate— are used in the experiments. The as-prepared NPs have almost identical initial size distributions, yet their catalytic performance, in terms of achievable current and CO selectivity, is different. During electrolysis all Ag NPs exhibit unambiguous morphology changes; the degradation pathway they follow, however, markedly depends on the chemical nature of the capping agent stabilizing them. Scanning electron micrographs obtained before and after constant-charge electrolyses carried out at different potentials reveal that amongst the studied ligands, BPEI seems to be the most effective stabilizer of Ag NPs; in turn, however, BPEI also limits CO formation the most. In case of PVP, mostly corrosion (particle shrinkage) is observed at practically relevant electrolysing potentials, while the application of PEG leads more to particle coalescence. Ostwald ripening seems to appear only at high applied (H_2 forming) potentials in case of the three afore-mentioned ligands while in case of citrate it becomes significant already at mild (CO forming) voltages. By studying the effects of capping agent removal and exchange we demonstrate that apart from ligands directly attached to the Ag NPs, also the excess of capping agents (adsorbed on the electrode surface) plays a decisive role in determining the extent and mode of catalyst degradation. The results of SEM-based particle sizing are also confirmed by synchrotron based wide-angle X-ray scattering measurements that provide further insight into the evolution of crystallite size and lattice strain in the applied Ag NPs during electrolysis.

1. Introduction

The electrochemical reduction of CO_2 into value-added products is a quickly developing field of electrocatalysis, mostly because it opens new perspectives in front of climate change mitigation [1]. Due to the considerable thermodynamic stability of carbon dioxide, the electrochemical CO_2 reduction reaction (CO_2RR) requires high negative potentials, and the application of catalyst materials that favour CO_2RR over the competing hydrogen evolution reaction (HER). The design of new catalyst materials that not only meet this requirement, but can also selectively direct CO_2RR towards the formation of a desired product at suitable rate and at low energy cost has thus become the forefront of electrochemical research in the past 20 years [2].

Although examples to the contrary already exist [3], metals or metal oxides (either in bulk [4], foam [5], or nanoparticulate [6] form) are still considered as catalysts of first choice for CO_2RR. While on bulk metal electrodes with large planar surfaces it is primarily the chemical nature of the metal [4] that determines the

---

* Corresponding authors at: University of Bern, Department of Chemistry, Biochemistry and Pharmaceutical Sciences, Freiestrasse 3, 3012 Bern, Switzerland (Y. Hou and P. Broekmann); Eötvös Loránd University, Department of Physical Chemistry, Pázmány Péter sétány 1/A, 1117 Budapest, Hungary (S. Vesztergom).

E-mail addresses: menglong.liu@unibe.ch (M. Liu), ying.kong@unibe.ch (Y. Kong), huifang.hu@unibe.ch (H. Hu), noemi.kovacs@unibe.ch (N. Kovács), changzhe.sun@unibe.ch (C. Sun), ivan.zelocualtecatl@unibe.ch (I. Zelocualtecatl Montiel), maria.galvez@dcb.ch (M.J. Gálvez Vázquez), yuhui.hou@unibe.ch (Y. Hou), marta.mirolo@esrf.fr (M. Mirolo), isaac.martens@esrf.fr (I. Martens), jakub.drnec@esrf.fr (J. Drnec), vesztergom@chem.elte.hu (S. Vesztergom), peter.broekmann@dcb.unibe.ch (P. Broekmann).

https://doi.org/10.1016/j.jcat.2021.10.016
0021-9517/

majority product (CO, formate, hydrocarbons, alcohols), in case of catalysts with nanosized features (nanoparticles or hierarchic foams) also the nanoscale structure has a pivotal role in determining selectivity [6,7]. In case of Cu nanoparticles (NPs), for example, a direct correlation between particle size and product distribution has already been established [8], and also for other metallic NPs (like Sn [9] or Ag [10]) intense research has been carried out to correlate the activity and selectivity of nanoparticulate catalysts to their morphology and physical structure. To use metals (or their oxides) in a nanoparticulate form for the catalysis of the CO_2RR is a very straightforward approach especially because of the many facile synthesis routes available that allow the design of NPs with fine-tuned catalytic properties.

Using metals in a nanoparticulate form for the catalysis of CO_2RR has the obvious advantage that comes with the low raw material cost — small sized NPs can be applied in a relatively low loading to achieve an already considerable current of CO_2 reduction [5]. A significant drawback of nanoparticulate catalysts stems, however, also from the small size of NPs, which makes them thermodynamically unstable. Maintaining the stability of NPs under the operating conditions of electrolysis, that is, at high applied potentials, strong flow of current and intense gas formation, thus becomes a key question of research. In other fields of electrocatalysis (*e.g.,* in fuel cell research [11]) the degradation of catalyst NPs is well studied. In relation to CO_2RR on the other hand, only a few researchers seem to place emphasis on elucidating possible degradation mechanisms [9,10,12–16].

Ag is considered an appealing catalyst material for CO_2 reduction because it produces a single yet very sought-after product over a broad potential window and under different operating conditions: CO. CO is a remarkably versatile precursor of the production of synthetic fuels [17], and industrial applications already exist, for example, for the coupling of CO_2-to-CO/water-to-H_2 electrolysers to a fermentation module where CO and H_2 are converted to butanol and hexanol with high carbon selectivity [18]. In addition, the two-electron transfer required by the CO_2-to-CO conversion provides a large profit margin compared to other multiple-electron transfer products requiring larger energy inputs [17].

While in existing industrial electrolysers Ag is usually applied in a bulk form for the production of CO [18], it was recently shown in lab scale experiments that when Ag is used in a nanoparticulate form, stable CO formation can be achieved over a much broader potential window, and thus better conversion metrics can be achieved compared to the case when electrolysis is carried out on planar Ag cathodes [10].

In a recent study we made the first step in the direction of upscaling towards practical application by using Ag NPs as catalysts of CO_2RR in a zero-gap gas-flow electrolyser unit [15]. Zero-gap gas-flow electrolysers allow the realisation of large current densities ($\gg 300$ mA cm^{-2}, normalized to geometric cathode surface area) and create an ideal playground for catalyst stability testing under harsh operating conditions.

The use of capping agents is essential in Ag nanoparticle synthesis as they control the shape and size of the grown nanoparticles, and prevent their aggregation over time [19]. Capping agents usually achieve long-term stabilization of the particle size [20] either by steric hindrance (such ligands usually have bulky protecting groups) or by an electrostatic repulsion between ligands bearing the same charge (such capping agents are usually ionic species). While essentially both types of ligands can work well in stabilizing NPs in dispersion, they both have significant drawbacks when it comes to fixing the NPs on an electrode surface and using them as electrocatalysts. In such cases NPs stabilized by charged ligands are often found to quickly agglomerate either due to screening effects arising from high ionic strengths or as a result of the electric field of the working electrode. NPs stabilized by steric hindrance are usually more stable, however in this case the strong adsorption of ligands often blocks the access of reactants to the NPs, leading to an overall decrease of the catalytic activity.

The structural changes metallic NP-based catalyst layers undergo in the course of the catalysed process can take many forms, including the *detachment* of particles from the support (which ultimately results in catalyst loss), the *corrosion* of the NPs (leading to an overall decrease of the average nanoparticle size), the *aggregation* of NPs on the catalyst support (leading to the formation of larger particles) and the phenomenon known as Ostwald ripening (as a result of which some particles grow larger on the expense of smaller ones disappearing). These structural changes (an illustration is shown in Fig. 1) all result in distortions of the particle size distribution of the NPs, and as such, they are commonly referred to as means of *degradation* — practically regardless to whether they have any measurable effect, either negative or positive, on the observed catalytic performance.

In practical electrolysers degradation rarely takes a single route, and in most cases it is a combination of several of the above-described degradation phenomena that determines the fate of catalyst NPs. The means and extent of degradation heavily depends on the operating conditions of the electrolyser (voltage and current, the intensity of gas formation, etc.), as well as on the chemical nature of the stabilizing (capping) agents applied either during the synthesis of the NPs or later for the formulation of the catalyst ink.

As capping agents not only adsorb on the surface of the NPs but also on the (usually carbon) cathode support, they may also play a decisive role in determining the surface adherence and the mobility of the NPs. While strongly bonding capping agents may preserve the initial particle size distribution of the NPs more efficiently than others, such ligands may also decrease catalytic performance by blocking the access of reactants to active catalyst sites. In such cases, the onset of "degradation" can even have an unexpected positive effect on the performance of electrolysis, as it can enable the participation of new, previously unaccessible sites in the catalysed process [21]. Apart from such exceptions, however, the degradation of NPs usually manifests in a long-term loss of the catalytic performance. This is primarily due to a loss of the active catalyst surface area that accompanies all degradation modes (including corrosion that often leads to the detachment of the smaller particles). A secondary degradation effect that may also account for performance losses is related not to the changing size distribution of the particles, but rather to a consequence of this: an internal structural change of the NPs, during which the (from a catalytic point of view, highly active) open crystalline sites re-organize to less ordered and more compact amorphous structures.

In this study we use Ag NPs capped by different ligands — branched polyethylenimine (BPEI), polyvinylpyrrolidone (PVP), polyethylene glycol (PEG), and citrate— with an initially narrow size distribution centred at ~ 40 nm for the preparation of catalyst inks that we disperse on a gas diffusion layer. The thus prepared Ag NP GDE (Fig. 2) is in direct contact with the anion exchange membrane of the zero-gap gas-flow electrolyser (see also Figure S1 of the Supporting Information) that contains an electrolyte solution only on the anode side. The reactant gas (CO_2) is directly fed by a constant flow to the GDE, and the configuration does not only assure reduced ohmic losses but it also attenuates complications that arise from poor membrane hydration and electrode flooding at high current densities [15].

We show that in case of all four applied capping agents, the efficiency of CO_2RR considerably drops over time in a manner that is similar for all capping agents. While this performance loss, occurring due to the formation of carbonate plaques at high current densities over the electrode surface, is not a direct result of the structural changes that catalyst NPs suffer during electrolysis, the zero-gap gas flow cell still provides means to study the morpholog-

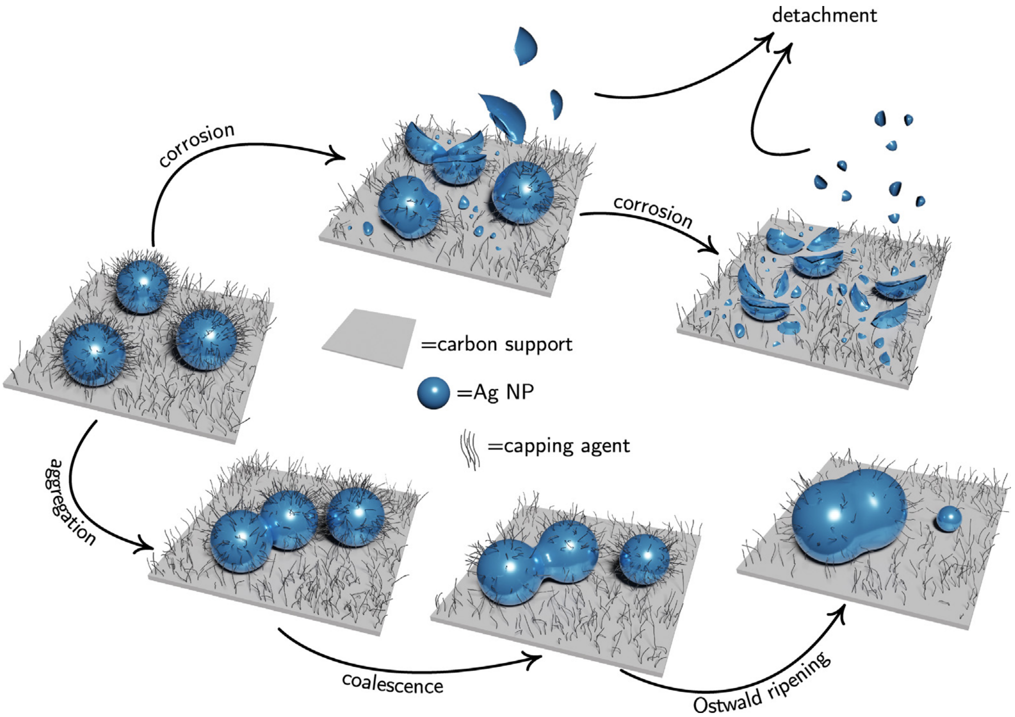

Fig. 1. Degradation pathways of Ag NPs used for CO_2RR.

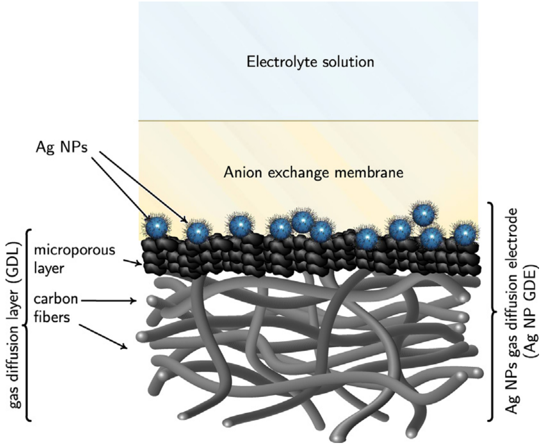

Fig. 2. The gas diffusion electrodes (Ag NP GDEs) used in this study are formed by drop-casting an Ag NPs containing catalyst ink on a gas diffusion layer (GDL). The latter is a bilayer structure consisting of a macroporous backing material (carbon fiber paper support) and a carbon-based microporous layer. The Ag NP GDE is separated by an anion exchange membrane from the electrolyte solution that contains the anode and a reference electrode.

ical changes of Ag NPs during intense CO_2RR/HER stressing. Following a removal of the formed carbonate plaques by careful dip-washing, structural changes can be investigated by a set of state-of-the-art nanoparticle characterization techniques including scanning electron microscopy (SEM) and wide-angle X-ray scattering (WAXS) measurements. These methods can clearly demonstrate that depending on the nature of their stabilizing ligands, Ag NPs undergo different degradation pathways on the course of electrolysis. By a set of ligand removal and exchange experiments we also demonstrate that apart from ligand molecules directly attached to the NPs, ligands adsorbed on the supporting carbon matrix also play a role in determining the dominant degradation mode.

2. Experimental Section

Preparation of the Ag NPs-containing catalyst ink. To prepare the carbon-supported Ag NP catalyst ink, 0.25 cm^3 of the as-received parent catalyst suspension (NanoComposix, Ag mass concentration of 1 mg cm^{-3}) was diluted to 0.55 cm^3 by the addition of Milli-Q water. A second suspension (volume: 0.44 cm^3) was made by dispersing carbon black (Vulcan XC 72r, Cabot) in isopropanol (VLSI Selectipur, BASF SE, Ludwigshafen, Germany) in a 0.1 mg cm^{-3} concentration. Both suspensions were sonicated separately for 10 and 30 min, respectively, following which the suspensions were intermixed and, after the addition of 10 $\mu\ell$ Nafion solution (5% Nafion, 15–20% water, Sigma–Aldrich), the new suspension was sonicated for further 10 min. The same ink preparation protocol was applied to all four nanoparticulate catalysts used herein. BPEI, PVP, PEG and citrate-capped Ag NPs with an average particle size of ~ 40 nm were purchased from a supplier (NanoComposix) and were used directly for the ink preparation. In order to carry out experiments by removing some of the excess PVP capping agent, the parent Ag NP suspension was first subjected to centrifugation (at 35 000 rpm, 40 min, Beckmann Coulter ultracentrifuge, SW60 rotor). This treatment allowed for a separation of the surfactant-capped Ag NPs and the free surfactants that remained, at least to a large extent, in the liquid (aqueous) phase. The separated Ag NPs were then suspended in Milli-Q water to keep the Ag concentration the same as that of the parent suspension, and the ink preparation protocol described above was followed. The separated Ag NPs and the aqueous matrix phase were both subjected to a total organic carbon concentration (TOC) analysis with the aim to estimate the amount of surfactants that is either attached to the Ag NPs or is present in solution (see Table S5 in Supporting Information).

Preparation of the Ag NP GDEs. GDEs were formed by drop-casting 40 $\mu\ell$ of either one of the above-described catalyst inks onto the masked hydrophobic surface of a GDL (H23C8, FuelCellStore, see Figure S2 of the Supporting Information for SEM characterization). The GDE was in contact with the membrane through a circular opening with a diameter of 3 mm, and the corresponding geometric area (7.07 mm^2) is used for the surface normalization of current to current density. The catalyst ink was percolated through the porous body of the GDE by a vacuum filtration system placed on the backside of the electrode, followed by drying at ambient conditions. The resulting mass loading was in the range of (43±5) $\mu g\ cm^{-2}$, as confirmed by inductively coupled plasma mass spectrometry (ICP–MS, see Table S1 in Supporting Information for detailed loading data).

Assembly of the gas flow-cell. The assembly and main components of the zero-gap gas-flow cell employed in this work have been described elsewhere [15]. The cell (see also Figure S1 in Supporting Information) consists of a stainless steel body with the gas flow channels used to feed the CO_2 from the backside of the prepared Ag NPs GDE mounted on the outermost location of the central portion. Other components incorporated into the cell include a current collector and a gas inlet and outlet to control the supply of the CO_2 reactant (99.999%, Carbagas, Switzerland) and analysis of gaseous products, respectively. All the CO_2 reduction experiments were set up by placing a freshly prepared Ag NPs GDE on top of the gas flow channels, with its catalyst modified surface facing upward. Subsequently, a new hydroxide-functionalised Sustainion alkaline membrane (X3750 RT, Dioxide materials) and a poly-(tetrafluoroethylene) anolyte compartment were placed on top of the GDE. A clamp was then used to guarentee cell tightness and mechanical stability. 10 cm^3 of 2.0 mol dm^{-3} KOH was used as electrolyte for the anolyte compartment. An Ag|AgCl|3 mol dm^{-3} KCl electrode (double junction design, Metrohm) was used as a reference, and an Ir wire (99.9%, MaTeck Material-Technologie & Kristalle GmbH, Germany) separated by a glass frit was used as a counter electrode. Note that the PTFE anolyte compartment has a central orifice (of 3 mm diameter, corresponding to a geometric surface area of 7.07mm^2) in its bottom part that provides direct contact between the electrolyte and the underlying anion-exchange membrane, while the Ag NPs GDE is prevented from direct contact with the supporting anolyte. During electrolysis, a humidified CO_2 stream (16 $cm^3\ min^{-1}$) was continuously fed through the gas flow channels of the stainless steel cell body, adjacent to the GDE.

Electrochemical measurements and product distribution studies. An ECi-200 potentiostat (Nordic Electrochemistry) was used to perform all electrolysis experiments. The electro-generated gaseous products (CO and H_2) were determined by means of on-line gas chromatography (SRI Instruments) in fixed (10 or 4 min) time intervals. The electrolyte solution was also analysed after full electrolyses, to check for any soluble products formed, by means of ion exchange chromatography (Metrohm Ltd., Switzerland). As formate (in different amounts, see Table S3 in Supporting Information) was found as the sole dissolved product in the electrolyte solution, it was assumed that whenever the GC-based detection of volatile products could not account for a 100% of Faradaic efficiency, the rest of the passed current was turned into formate production.

Electron microscopy measurements. For the morphological characterization of the Ag NPs on GDEs, a Zeiss Gemini 450 scanning electron microscope equipped with an InLens secondary electron detector and a back-scattering detector was used. An accelerating voltage of 5 kV and a current of 120 pA were applied at a working distance of 3.8–4.2 mm. Using the Smile View software for particle sizing, ca. 500–900 particles were analysed per experimental setting for the creation of the particles size distribution shown in Figs. 7, 9 and 10. The particle size was defined as the longest measurable dimension in case of anisotropic NPs, see Figure S13 in the Supporting Information. To acquire EDX point spectra and 2D surface mappings of selected samples, the AZtec 4.2 software (Oxford Instruments) was used. An acceleration voltage of 10 kV and a current of 500 pA were applied at a working distance of 8.5 mm for EDX measurements. For high-angle annular dark-field scanning transmission electron microscopy (HAADF–STEM) combined with energy-dispersive X-ray spectroscopy (EDX), a Talos F200X (Thermo Fisher Scientific) instrument equipped with a SuperEDX detector was used with an acceleration voltage of 200 kV.

Contact angle measurements. Contact angle measurements were carried out using a Krüss Advance Drop Shape Analyzer DSA25 (Krüss GmbH, Hamburg, Germany). Electrodes were mounted on a flat stage and water drops (milli-Q water, 1.4 μL) were deposited at room temperature.

Synchrotron Wide-Angle X-ray Scattering (WAXS) measurements. Crystallite size and microstrain were measured via WAXS measurements at the ID31 beamline of the European Synchrotron Radiation facility (ESRF) in Grenoble, France. The high energy X-ray beam (75 keV) was focused on the Ag NP GDEs, and the scattered signal was collected using a Dectris Pilatus CdTe 2 M detector positioned 520 mm behind the sample. The energy, detector distance and tilts were calibrated using a standard CeO_2 powder and the 2D diffraction patterns were reduced to the presented 1D curves using the pyFAI software package [22]. Rietveld refinement of the WAXS patterns was performed to extract the phase structure, crystallite size, lattice parameter and microstrain using the cubic *Fm–3 m* structure of Ag metal and the GSASII software [23], see Figure S14 in Supporting Information for a representative fit. The instrumental parameters were determined by the refinement of a CeO_2 standard sample. Air scattering was removed from each pattern. The measurement consists in a height scan acquiring WAXS pattern at different positions in the sample. The pattern of the GDE is considered as background and removed for each sample. The fitting is performed using crystallites of uniaxial orientation along the (111) direction.

White light interferometry (WLI) analysis. The mesoscopic surface morphology of the Ag NP GDEs was analyzed by means of white light interferometry (Contour GT, Bruker, see Figure S5). Vision64 software (Bruker) was used for operating the instrument and for data analysis.

Inductively coupled plasma mass spectrometry (ICP-MS). GDE samples were immersed for 24 h in 1 cm^3 HNO_3 (69.3%, BASF SE, Ludwigshafen, Germany) to dissolve all Ag NPs. The resulting solutions were diluted with 3% HNO_3 solution by a factor of 500 and were then fed into a NExION 2000 ICP-MS instrument (Perkin Elmer) to obtain the Ag mass loading of the electrodes (see Tables S1 and S4 in Supporting Information).

Total organic content (TOC) determination. To quantify surfactants in each solution, 100 $\mu\ell$ of free surfactant solutions obtained by centrifugation of Ag NP suspensions (0.25 mg cm^{-3}) and surfactant-capped Ag NP suspensions (0.25 mg cm^{-3}) which do not contain free surfactants were fed into a DIMATOC 2100 instrument (Dimatec, Essen, Germany). The organic compounds were oxidized at 850 °C with Pt as catalyst to CO_2/NO. Non-dispersive infrared (NDIR) gas sensor with a reflective diffuser and a chemiluminescence detector were used to detect CO_2 and NO, respectively.

3. Results and Discussion

Characterization of the as-prepared Ag NP GDEs. Essentially regardless to the nature of the stabilizing ligand (BPEI, PVP, PEG or citrate), all our studied Ag NP GDEs exhibited very similar physical characteristics (Fig. 3). Representative SEM images of (PVP-capped) Ag NP GDEs are shown in Fig. 3a and c, revealing isotropic and uniformly dispersed NPs with an almost uniform particle size

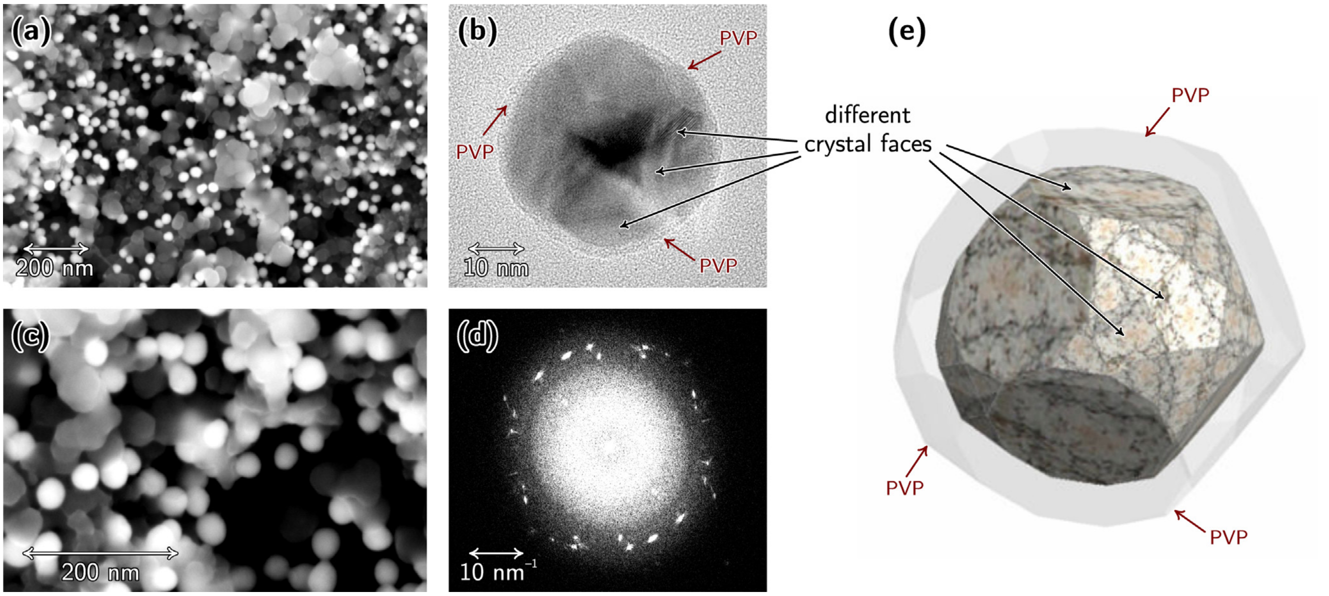

Fig. 3. Representative top-down SEM images (a, c) of PVP-capped Ag NPs dispersed on the carbon microporous layer of the GDE. The HR–TEM image (b) of an individual PVP-capped Ag NP, and its Fourier-transformed representation (d) demonstrate the polycrystalline nature of the nanoparticle, exhibiting different crystalline domains. Schematic drawing of the PVP-capped Ag NP is shown in (e). For a complete (top-down) SEM and TEM view of GDEs prepared by the use of Ag NPs capped with different ligands, see Figure S3 and S4 in the Supporting Information.

of about 37 nm. The HR–TEM image and the corresponding FFT representation of an individual PVP-capped Ag NP, shown in Fig. 3b and d, reveal the polycrystalline nature of the NPs. The drawing in Fig. 3e, inspired by the result of electron micrography, attempts to show a single Ag NP in three dimensions. Similar initial states were found in the case of Ag NPs capped by other ligands (BPEI, PEG and citrate). Independently of the nature of the capping agent used by the provider (NanoComposix) for the synthesis of the studied Ag NPs, we found that all NPs used in this work are of an (almost) spherical shape, as shown in Fig. 3e, and that the NPs exhibit no preferential faceting. The uniformly dispersed particles were isotropic but polycrystalline, and their average size was between 30 and 40 nm in all cases. Corresponding SEM and TEM images of all four types of surfactant-capped Ag NPs are shown in Figures S3 and S4, respectively, of the Supporting Information, where white-light interferometry images (top view of the catalyst layer, Figure S5), as well as cross-sectional (side view) SEM and EDX images (Figure S6) can also be found. The latter show that the majority of Ag NPs does not penetrate the GDE, and remains dispersed on top of the microporous layer.

CO_2RR/HER stressing. In order to study the electrochemical performance of Ag NP GDEs, potentiostatic electrolyses in the configuration shown in Fig. 2 were carried out at three different applied potentials. Keeping comparability in mind, all electrolyses were performed until the same amount of charge (300 C cm^{-2}, normalized to the geometric surface area of the circular opening of the zero-gap cell) passed through the electrolyser. The product distribution (that is, the partial current densities of CO and H_2 formation, see the dashed lines) were reconstructed on the basis of on-line GC measurements at given fixed time intervals, shown by the dots in Fig. 4.

As the amount of CO and H_2 detected by on-line GC measurements did not account for a 100% Faradaic efficiency, contents of the electrolyte were analysed post-electrolysis by ionic liquid chromatography (IC), which revealed a significant amount of formate production at each setting (see Table S3 in Supporting Information). As no water-soluble products apart from formate were detected after electrolysis by IC, it is safe to assign the missing fraction of the current density (hatched areas in Fig. 4 labelled "rest") to the production of formate [15,24].

Fig. 4 reveals a rather similar behaviour of three out of four studied catalysts. Namely, the PVP-, PEG- and citrate-capped Ag NPs all seem to exhibit a remarkable selectivity towards the production of CO, although especially at larger electrolysing potentials this selectivity, as well as the overall current, significantly decrease with time. That the catalytic performance of these NPs seems not to depend significantly on the nature of the applied capping agents suggests that already at initial stages of the electrolysis at least a partial removal of the capping shell from the surface of the NPs may have occurred, leaving catalytically active sites available to participate in CO_2RR [13,16,21].

As for BPEI-capped Ag NPs, both the overall current and the selectivity of CO production are considerably smaller (essentially at all three applied potentials), and this observation can be explained by the exceptionally strong bonding interactions between the amino groups of BPEI and the Ag NPs. Due to this strong bonding it seems plausible to assume that the BPEI-capped particles remain at least partially inaccessible for the reactants of electrolysis. As a result, the observed performance loss is in turn also smaller compared to the case of NPs capped by other agents (PVP, PEG or citrate).

In case of all four types of NPs, a clear decrease is observed in both the Faradaic efficiencies of CO formation and the current density as a function of time (*i.e.*, charge) at each potential. The performance decay is especially rapid at the electrolysing potential of –2.354 V, where the Faradaic efficiency of CO formation very quickly drops due to intense hydrogen evolution. Although less severe, performance losses can also be observed in the cases of lower electrolysing potentials in Fig. 4. The question whether the observed performance loss has anything to do with the actual morphology changes of the NPs during the electrolysis immediately follows: we found, however, that although by SEM and WAXS investigations significant morphology changes can indeed be monitored, these structural alterations are not the main cause of the performance losses observed in Fig. 4.

The obvious decrease of the overall current density and the relative selectivity of the catalyst NPs to produce CO is rather connected to another phenomenon, namely the formation of a mostly potassium carbonate-based precipitate over the GDE. This

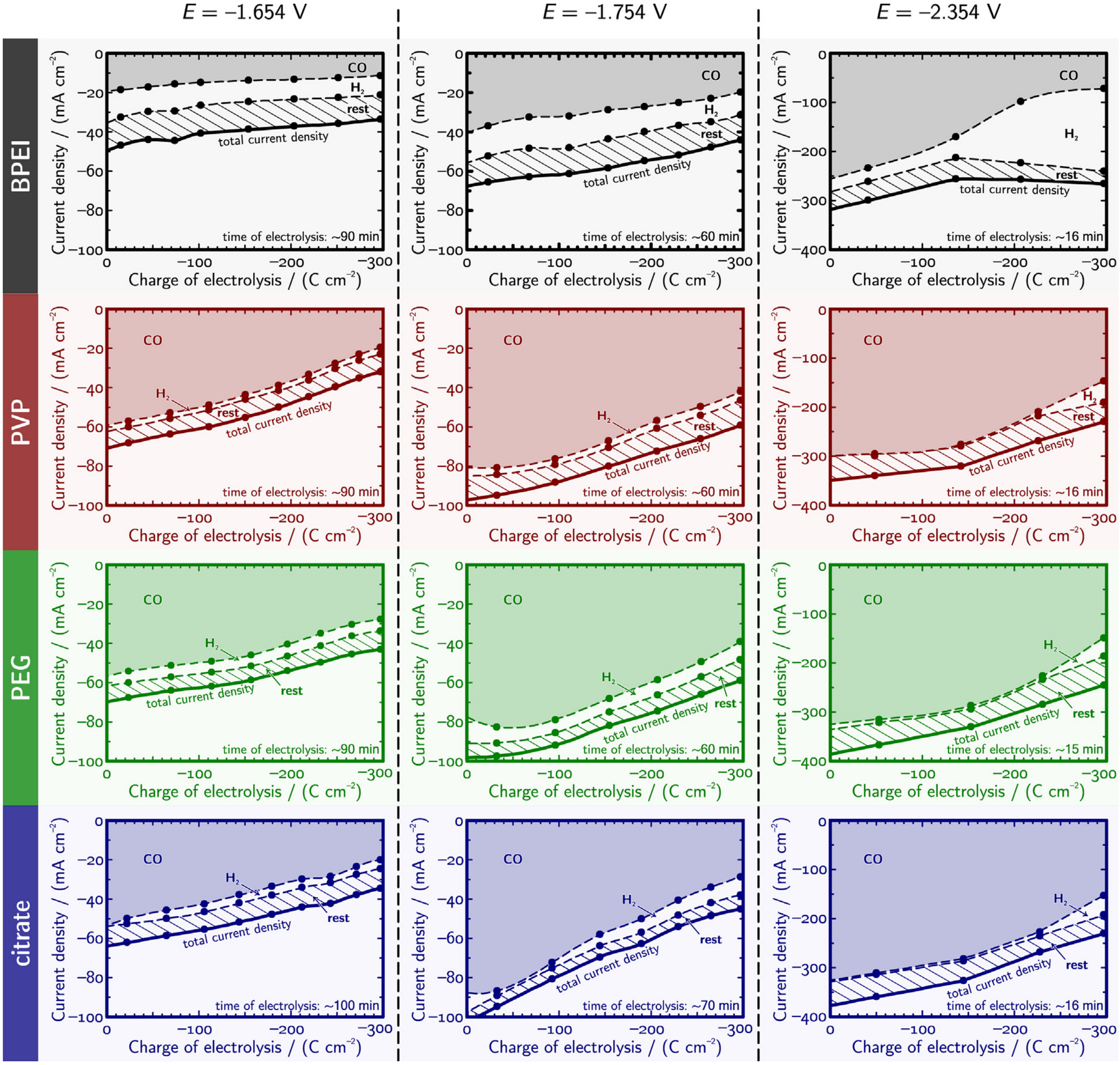

Fig. 4. Total current densities (full thick curves) plotted as a function of the passed charge density at different constant electrolysis potentials (measured vs. Ag/AgCl) for differently capped Ag NP GDEs. Electrolyses were stopped in all cases after the same amount of charge (-300 C cm^{-2}) was passed through the electrode. Shaded areas and dashed curves show the product distribution as reconstructed by GC measurements at different times (indicated by dots). Note that CO and H_2 were the only GC-detectable products that however did not account for a 100% of Faradaic efficiency. The "rest" of the current (hatched area in the graphs) can most probably be assigned to formate production (see the text and Tables S2 and S3 in Supporting Information for more details).

serious effect —that however does not hinder the observation of actual morphology changes on the nanoscale— is exemplified in Fig. 5.

As shown in Fig. 5, the pristine GDL we start out from (see Fig. 5a for a photograph) exhibits a clear surface, and the top- and side-view SEM images (Fig. 5b and c) reveal the expected structure of the surface microporous layer and the underlying carbon fibers. The surface of the top microporous layer is hydrophobic, as demonstrated by contact angle measurements on a sessile water drop, Fig. 5d. The EDX mapping analysis (Fig. 5q) reveals only carbon and fluorine signals in the elemental composition (the latter arises due to the PTFE treatment of the GDL applied by the manufacturer).

Fig. 5e shows a photograph of the (PVP-capped) catalyst ink drop-cast on the GDL. The circular area that will serve as the active cathode surface of the electrolyser (this will be in direct contact with the membrane) is shown here by a dashed circle. The catalyst NPs are clearly visible by SEM (Fig. 5f) and EDX-based elemental mapping (Fig. 5g) confirms that the NPs are clearly composed of Ag. Drop-casting the catalyst ink on the surface does not significantly decrease the hydrophobicity of the GDE (Fig. 5h), while in the EDX spectrum (Fig. 5h) the signal of Ag clearly appears.

When this GDE is subjected to CO_2RR/HER stressing, the formation of a potassium carbonate/bicarbonate based precipitate immediately becomes visible also to the bare eye, as shown in the photograph of Fig. 5i. An SEM image of the formed carbonate plaque is shown in Fig. 5j, and the elemental composition map of Fig. 5k reveals K as a major component of this plaque. Due to the formation of the carbonate precipitate the surface of the GDE becomes hydrophilic (Fig. 5l) and the signals of both K and O appear in the EDX spectra of Fig. 5q.

That the formed carbonate plaque is beyond doubt responsible for the performance losses observed before in Fig. 4 can be proven by a set of "recovery" experiments. These show (see Figure S12 in

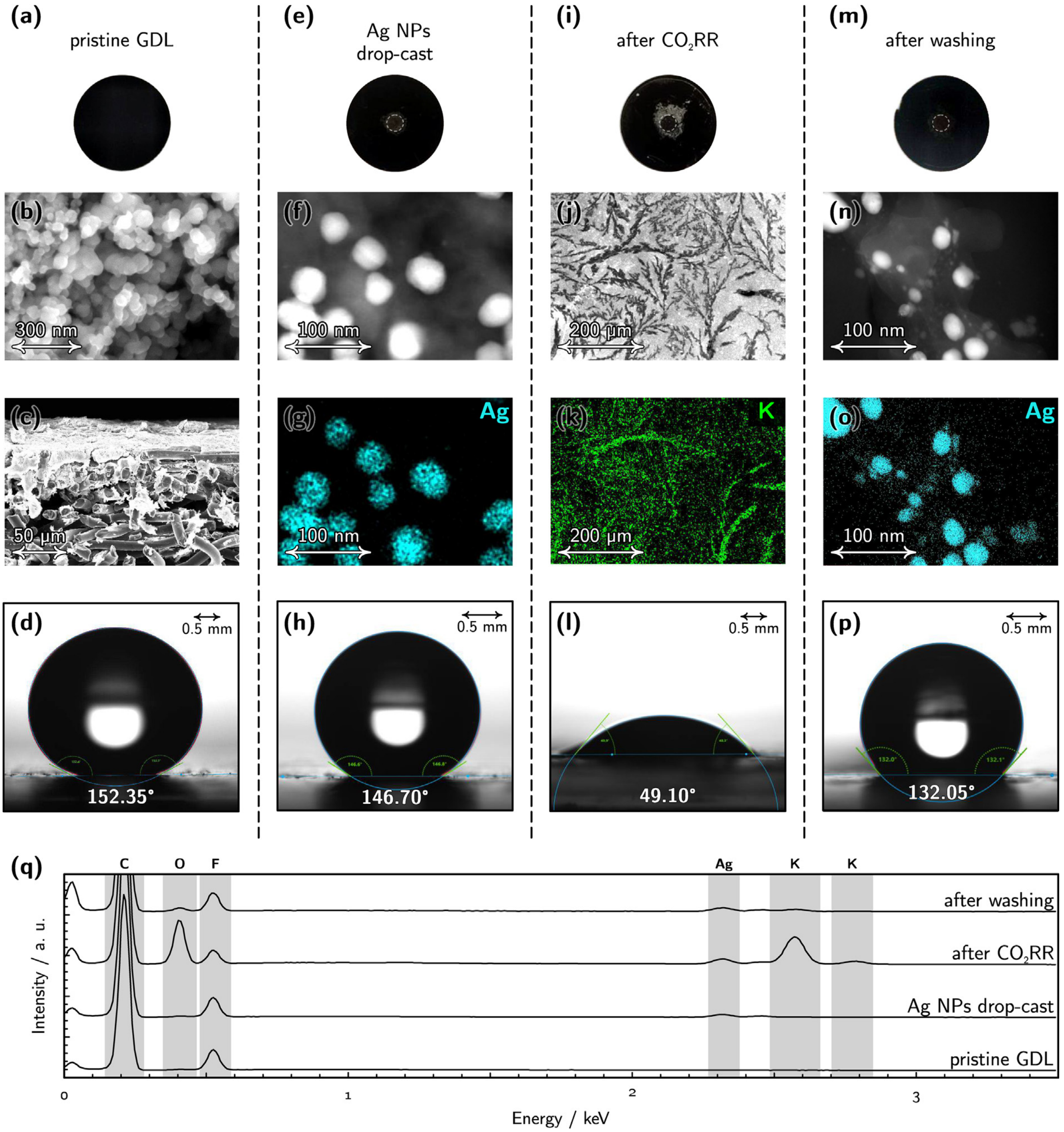

Fig. 5. The characteristic features of a pristine GDL significantly change after surfactant-capped Ag NPs are drop-cast on it, the thus prepared GDE is used for electrolysis, and finally, after the carbonate precipitate formed during CO_2RR/HER stressing is washed away. See the text for an exact description of each panel, and Figures S7–S11 of the Supporting Information for more details.

Supporting Information) that following a removal of the carbonate layer by dip-washing, already used GDEs can almost completely regain their efficiency in a subsequent electrolysis.

As the formed carbonate plaque makes us unable to study the degradation of NPs during CO2RR/HER stressing, the carbonate precipitate was removed from the surface following electrolysis by careful dip-washing (see Figure S8 in Supporting Information for details). A photograph of the GDE following the dissolution of the carbonate plaque is shown in Fig. 5m, and the subsequently taken SEM images (Fig. 5n and o) clearly indicate that this cleaning method does leave the actual catalyst NPs intact (compare panels n and o with f and g in Fig. 5). The accuracy of the dip-washing method is also proven by EDX (Fig. 5q) showing that the K and O signals almost fully disappear and the Ag signal is regained after washing. That the dip-washing technique we used to remove the carbonate plaque from over the catalyst surface did not result in any significant catalyst (Ag) loss was confirmed by ICP–MS analysis (see Table S4 in Supporting Information).

Morphology changes of Ag NPs on GDEs studied by SEM. The reliability of the applied dip-washing method allowed us to apply SEM analysis in order to study the structural changes that the differently capped Ag NPs undergo during extensive CO_2RR/HER stressing. Representative SEM images of pre- and post-electrolysis (dip-washed) samples are shown in Fig. 6 for the studied four types of surfactant-capped Ag NP catalysts. The histograms shown in Fig. 7 were prepared by manually processing several micrographs similar to those shown in Fig. 6: the size of each NP, regardless to form, was determined by measuring its longest dimension as illustrated by Figure S13 in the Supporting Information.

Expectation ranges of the particle sizes (mode±deviation) were determined by making the histograms shown in Fig. 7 subject to probability distribution fitting. Histograms exhibiting a single mode were fitted by log-normal distributions yielding an unsymmetrical (skewed) expectation range, while in case of bimodal distributions the linear combination of two (symmetric) Gaussians were used to describe our datasets. Expectation ranges for the average particle size are specified for all panels of Fig. 7, making it apparent that the morphology of the Ag NPs evolved differently in case of the four different capping agents.

In case of BPEI, the observed particle size distributions are bimodal both before and after electrolyses. Interestingly, the second characteristic particle size (corresponding to a smaller peak) is twice of the first one, which implies, taking into consideration that we used the longest measurable dimension for particle sizing, two-particle aggregates were present at the GDE surface, already before electrolysis. As also shown in Fig. 7, however, no significant change of the characteristic particle sizes are observed when BPEI-capped Ag NPs are exposed to electrolysis stressing at different potentials, and this is in agreement with the results of Fig. 4 that also show a relatively stable catalytic performance of BPEI-capped Ag NPs.

The situation is markedly different in the case of PVP-capped nanoparticles that, as shown in Fig. 7, tend to corrode during electrolysis. Corrosion in case of PVP-capped Ag NPs leads to a significant decrease of the characteristic particle size, as well as to a general broadening and a larger skewness of the distribution.

In the case of PEG, stressing by CO_2RR/HER seems to have rather the opposite effect. While the first characteristic particle size remains essentially unchanged, as a result of electrolysis a second peak becomes visible in the histograms, and the maximum of this peak is approximately twice of that of the first one. This is a clear hint [25] to that in case of PEG, particle coalescence is the most favoured mode of catalyst degradation (see also the micrographs of Fig. 6).

The general increase of particle sizes is also apparent in the case of citrate-capped Ag NPs, as shown in the last row of Fig. 7, although in this case no evolution of further, distinct modes are seen: the histograms, instead, get significantly broadened and skewed as a result of electrolysis. In this particular case we assume that due to the relative instability of the citrate shell at the applied (negative) potentials, the NPs quickly become almost totally unprotected [26]. As a result, their aggregation/coalescence becomes unhindered, and apart from the coalescence of neighbouring particles, also Ostwald ripening (either its two or three-dimensional form) occurs in this case [27,28].

To conclude, the SEM analyses seem to suggest that PVP-capped particles undergo more the corrosion pathway of degradation (Fig. 1), while PEG- and citrate-capped NPs tend more to aggregate, coalesce, and (especially in case of citrate) some form of Ostwald

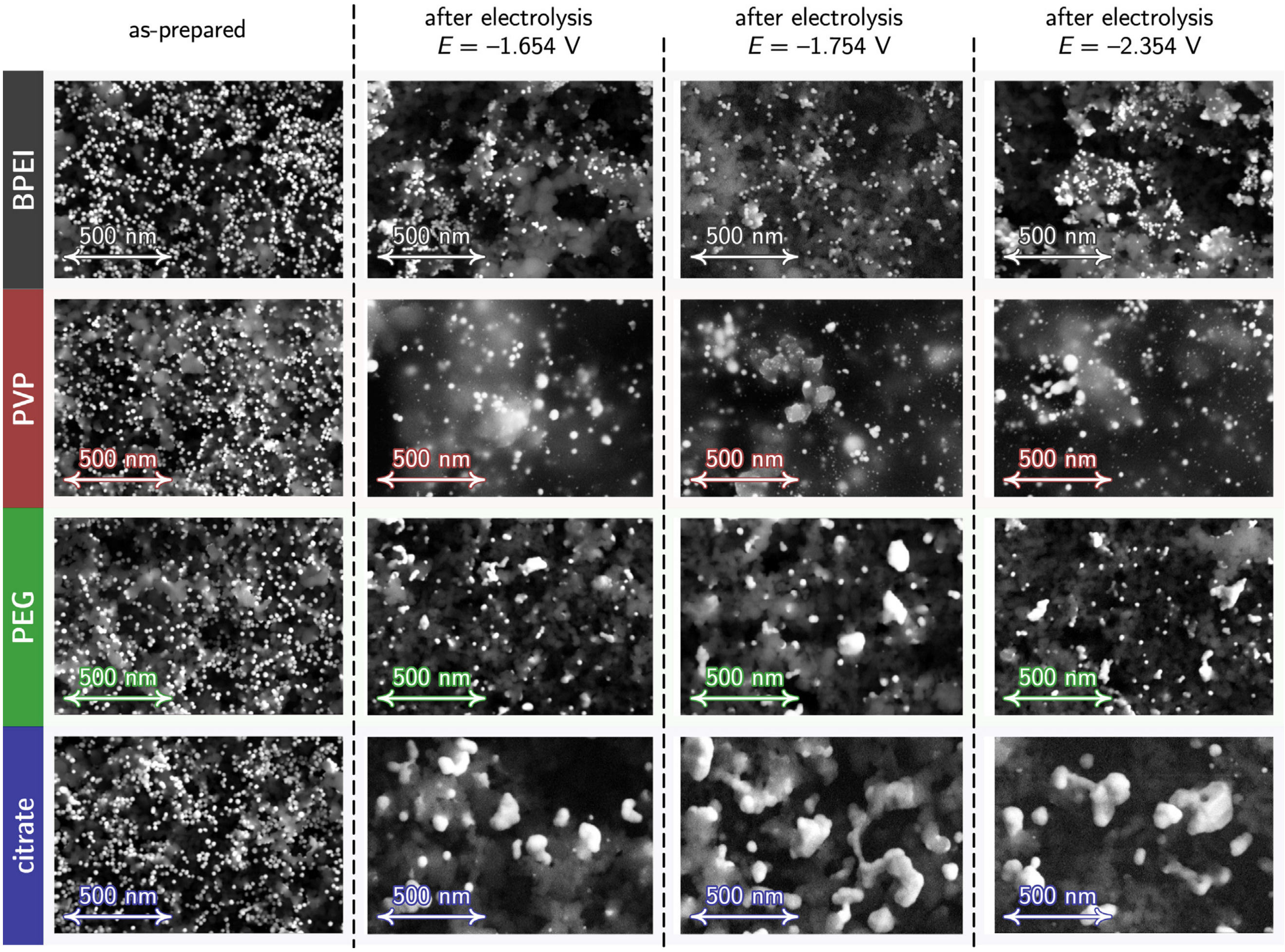

Fig. 6. Representative SEM micrographs of GDEs prepared using Ag NPs stabilized by different capping agents, recorded before ("as-prepared") and after constant charge electrolyses at different potentials (cf. to Fig. 4). These, as well as some other similar SEM images were used to construct the histograms shown in Fig. 7.

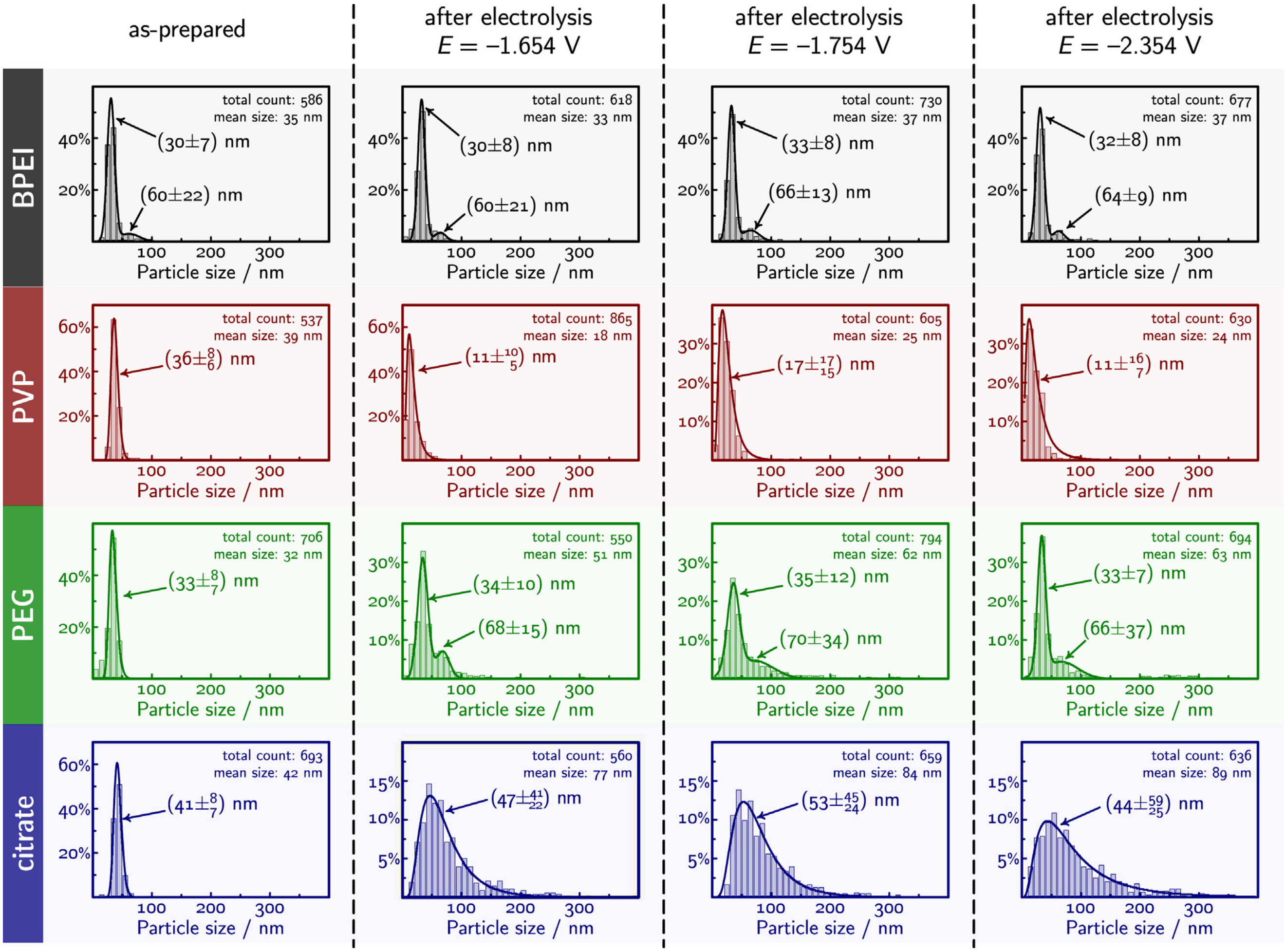

Fig. 7. Histograms showing the particle size distribution of Ag NPs, capped by different ligands, before and after electrolysis at a given potential. Expectation ranges of the particle size are shown for the fitted peak(s).

ripening also seems to take place. Amongst the studied capping agents, BPEI seems to be the most protecting one, as in this case no particular changes of the size distribution was observed when comparing post- to pre-electrolysis SEM images.

Morphology changes of Ag NPs on GDEs studied by WAXS analysis. The above picture can further be nuanced if we also use WAXS measurements to characterize the morphology changes of Ag NP catalysts during electrolysis (Fig. 8). The width of the WAXS peaks have two main contributions —apart from instrumental broadening—, and these are the size of coherently scattering domain (crystallite size) and microstrain (deviation from perfect order). These different characteristic parameters were determined by Rietveld fits of the diffraction pattern. Because the size determined by Rietveld fit maps crystallite sizes rather than full geometrical sizes, direct comparison between the WAXS and SEM-based analysis can reveal new insights about the degradation phenomena. First we note that using only the isotropic size model did not fit the data well. The fits improved significantly only after a size anisotropy had been included, implying that the nanoparticles have preferred growth orientation along the (111) direction (Fig. 8 and Figure S16 in Supporting Information). Along this direction, the crystallite size is about two times longer when compared to the short directions.

In the case of BPEI, the crystallite size is smaller than the particle size determined by the SEM analysis. This hints that the particles are composed from several crystallites, in agreement with the TEM observations. In this case the size does not change significantly, supporting the conclusions from the SEM analysis that the particles are stable during electrolysis. The microstrain shows a very low value for as-prepared NPs, but increases significantly for the samples measured after electrolysis. Given that the microstrain is a direct measure of internal disorder of the crystallites, the electrolysis seems to distort the local order which is typically linked to the increase of grain boundaries length. However, as in our case we do not observe any decrease in crystallite dimensions, the increase of microstrain should either be linked to surface phenomena caused by changes in the BPEI surface structure [29], or, alternatively, could be explained by some carbonate precipitates (that were not entirely removed by dip-washing) remaining adherent to the catalyst NPs (cf. to Fig. 5 exhibiting a small K signal even after washing).

The PVP case shows different behaviour. After electrolysis, the crystallite size increases in both directions, independently of the applied current, and the microstrain values increase moderately. This crystallite size increase is apparently opposite to the SEM-derived trend in particle size and the crystallites appear significantly larger than the physical size measured by SEM. This is caused by a broadening of the particle size distribution during electrocatalysis that is due to the formation of some amount of larger NPs while the average size shows a general decrease in the SEM measurements. It is of worth to note that while SEM results a number-weighted distribution, the diffraction amplitude is weighted by the volume of the NPs, therefore the crystallite size

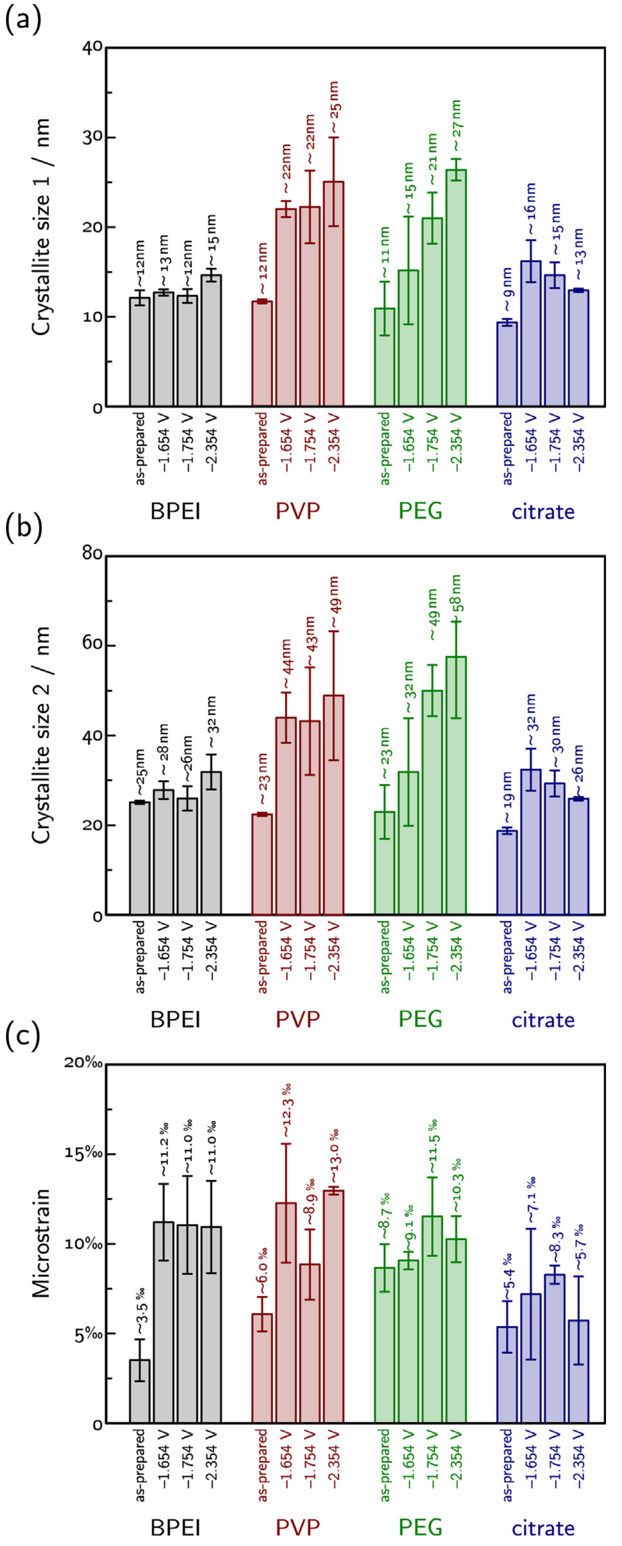

Fig. 8. Crystallite sizes (a, b) and microstrain (c) measured by WAXS of Ag NPs, capped by different ligands, before and after electrolysis at a given potential.

is much more sensitive to the appearance of larger NPs in the whole ensemble. This can result in crystallite sizes seemingly larger than the size of the NPs as determined by SEM using the distribution maximum. Based on the above observations we can conclude that apart from corrosion, that is a dominant pathway of the degradation of PVP-capped Ag NPs, Ostwald ripening also takes place in this case — and this causes both the increase of crystallite sizes (Fig. 8) and the broadening towards bigger sizes of the SEM-based size distribution (Fig. 7).

WAXS measurements on PEG-capped Ag NPs show a similar trend of increasing crystallite size, consistently with the appearance of bimodality in the SEM-based size distribution. PEG-capped NPs are not only aggregated, but the individual crystallites are also fused together through coalescence during electrolysis. The picture is somewhat different for citrate capped NPs that although as evidenced by SEM clearly undergo coalescence to a large extent during electrolysis, at the same time show only a moderate increase of the crystallite size. This is a hint to that the fusion of the NPs does not necessarily involve the merging of crystallites and that the enormously large Ag particles formed from citrate-capped Ag NPs during electrolysis (see, e.g, Fig. 6) can be composed of several distinct crystalline domains. The relatively low changes of microstrain observed in the case of PEG- and citrate-capped NPs are likely linked to the fact that the capping agent is only loosely bound to the surface of these NPs.

Ligand removal and exchange experiments. That in our investigations we saw the most severe degradation taking place in the case of citrate-capped Ag NPs can plausibly be explained by the fact that citrate stabilizes the NPs not by a steric effect as the other three studied ligands do, but by an electrostatic force. It can thus safely be assumed that under the operating conditions of electrolyses — that is, at high cathodic potentials— most of the negatively charged citrate ions will leave not only the surface of the NPs but they would also desorb from the surface of the carbon support. This can enhance the surface mobility of the particles, leading to their more rapid aggregation and then coalescence.

In order to check whether ligand molecules that may have remained adsorbed on the support in the three other (non-citrate) case have any role in determining the degradation pathway of the NPs, we designed a set of ligand exchange/removal experiments. These were based on separating the NPs from their parent dispersion by centrifugation, which left the majority of the capping agents —that would necessarily end up on the support surface during the GDE preparation— in the supernatant (see Table S5 and Figure S14 in Supporting Information). Filtering and re-dispersing the nanoparticles in Milli-Q water after centrifugation (see Section 2 for details) thus allowed us the (at least partial) removal of the carbon substrate-attached ligands or, if re-dispersion took place in the solution of another capping agent, the (again, at least partial) exchange of ligands.

The effect of ligand removal on electrolysis-induced degradation is shown in Fig. 9 for PVP-capped Ag NPs (this time, electrolysis took place at $E = -1.754$ V, see Figure S15a in Supporting Information for more details). We can see a notable difference if we compare this figure to the appropriate panels of Figs. 6 and 7: namely, that while the initial size distribution of the NPs is seemingly unaffected by the removal of excess PVP, the degradation pathway markedly changes. While in the previous case, when excess PVP was adsorbed on the carbon support layer, we primarily observed corrosion (and the change of the average particle size from around 39 to 25 nm), in Fig. 9 we see an increase of the average size (from 42 to 67 nm) and a significant broadening of the distribution. It seems to be a plausible assumption that the apparent coalescence we observe here was in the previous case hindered by support-adsorbed PVP, rendering the degrading NPs immobile. Alternatively, the removal of a significant portion of PVP from the surface of the NPs might have also lead to an increase of the average particle size by allowing quicker Ostwald ripening.

The role of support-adsorbed ligands can further be emphasized if we carry out a ligand exchange (as opposed to removal) experiment with citrate-capped Ag NPs that we in this case after centrifugation re-disperse in a PVP solution. As shown in Fig. 10, this

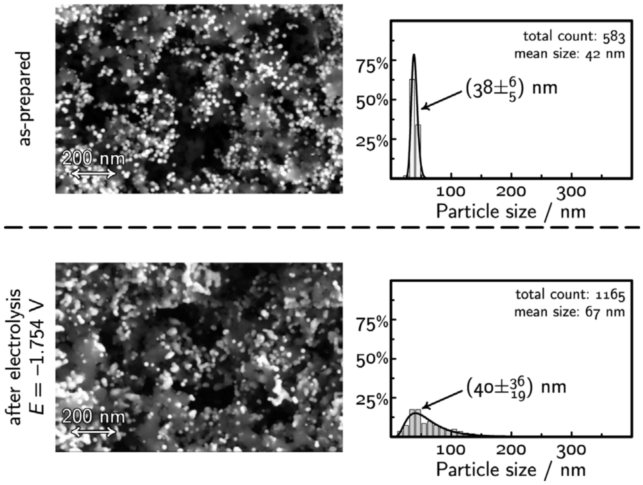

Fig. 9. The partial removal of the excess PVP from the catalyst ink results in less PVP adsorbed on the carbon support, facilitating more the aggregation (rather than the corrosion) of Ag NPs. (Cf. to Figs. 6 and 7).

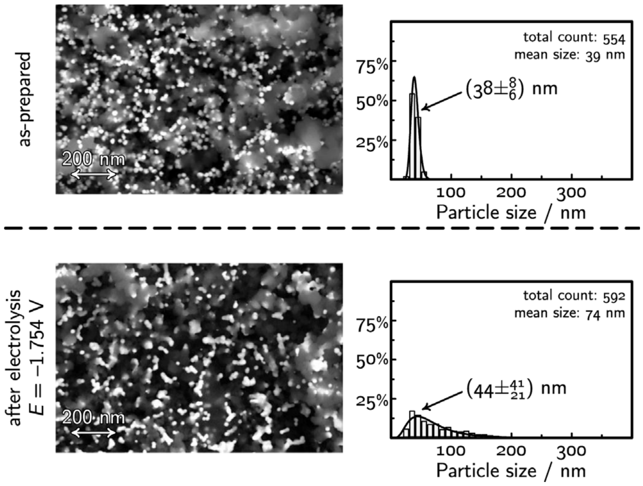

Fig. 10. The partial citrate → PVP ligand exchange in the catalyst ink results in more PVP adsorbed on the carbon support, somewhat hindering the coalescence degradation pathway otherwise observable for citrate-capped NPs. (Cf. to Figs. 6 and 7.).

can milden the coalescence of particles (otherwise characteristic for citrate-capped NPs, see Fig. 6 and 7), and this effect can also be explained by the adsorption of the extra PVP amount on the support surface, hindering the motion of the degrading NPs. (For more details of the electrolysis experiments, see Figure S15b of the Supporting Information.).

4. Conclusion

In this paper we used Ag NPs capped by different stabilizing ligands to prepare gas diffusion electrodes that we applied for CO_2 electroreduction in a zero-gap gas-flow electrolyser. This configuration allowed a high current stressing of the NPs. After careful cleaning of the GDE from the carbonate precipitates formed during electolysis, we compared SEM images of the catalyst NPs obtained before and after the high current testing, and made these subject to a statistical analysis.

We showed that amongst the studied capping agents, BPEI is the most protective one; in turn, however, it also limits CO formation the most. In case of PVP, mostly corrosion (particle shrinkage) was observed at practically relevant electrolysing potentials, while the application of PEG and that of citrate lead more to particle coalescence. In parallel with the SEM-based investigations, WAXS analysis was also used to follow the evolution of crystallite size and lattice strain during CO_2RR/HER stressing, and the results were compared to those of SEM mapping.

By studying the effects of capping agent removal and exchange we demonstrated that apart from ligands directly attached to the Ag NPs, also the excess of capping agents (adsorbed on the carbon support surface) plays a decisive role in determining the extent and mode of catalyst degradation.

Declaration of Competing Interest

The authors declare that they have no known competing financial interests or personal relationships that could have appeared to influence the work reported in this paper.

Acknowledgement

P. B. acknowledges financial support by NCCR Catalysis. S. V. acknowledges support from the National Research, Development and Innovation Office of Hungary (NKFIH grant FK135375). M. L., Y. K., H. H., and C. S. acknowledge the financial support by the Chinese Scholarship Council (CSC).

Appendix A. Supplementary material

Supplementary data associated with this article can be found, in the online version, at https://doi.org/10.1016/j.jcat.2021.10.016.

References

[1] D.R. Feldman, W.D. Collins, P.J. Gero, M.S. Torn, E.J. Mlawer, T.R. Shippert, Observational determination of surface radiative forcing by CO_2 from 2000 to 2010, Nature 519 (2015) (2000) 339–343, https://doi.org/10.1038/nature14240.
[2] D.T. Whipple, P.J.A. Kenis, Prospects of CO_2 utilization via direct heterogeneous electrochemical reduction, J. Phys. Chem. Lett. 1 (2010) 3451–3458, https://doi.org/10.1021/jz1012627.
[3] H. Coskun, A. Aljabour, P.D. Luna, D. Farka, T. Greunz, D. Stifter, M. Kus, X. Zheng, M. Liu, A.W. Hassel, W. Schöfberger, E.H. Sargent, N.S. Sariciftci, P. Stadler, Biofunctionalized conductive polymers enable efficient CO_2 electroreduction, Sci. Adv. 3 (8) (2017) e1700686, https://doi.org/10.1126/sciadv.1700686.
[4] Y. Hori, Electrochemical CO_2 reduction on metal electrodes, in: C.G. Vayenas, R.E. White, M.E. Gamboa-Aldeco (Eds.), Modern Aspects of Electrochemistry, Vol. 42, Springer, 2008, pp. 89–189.
[5] S. Vesztergom, A. Dutta, M. Rahaman, K. Kiran, I.Z. Montiel, P. Broekmann, Hydrogen bubble templated metal foams as efficient catalysts of CO_2 electroreduction, ChemCatChem 13 (2020) 1039–1058, https://doi.org/10.1002/cctc.202001145.
[6] F. Yu, P. Wei, Y. Yang, Y. Chen, L. Guo, Z. Peng, Material design at nano and atomic scale for electrocatalytic CO_2 reduction, Nano, Mater. Sci. 1 (2019) 60–69, https://doi.org/10.1016/j.nanoms.2019.03.006.
[7] D. Sun, X. Xu, Y. Qin, S.P. Jiang, Z. Shao, Rational design of Ag-based catalysts for the electrochemical CO_2 reduction to CO: A review, ChemSusChem 13 (2019) 39–58, https://doi.org/10.1002/cssc.201902061.
[8] R. Reske, H. Mistry, F. Behafarid, B.R. Cuenya, P. Strasser, Particle size effects in the catalytic electroreduction of CO_2 on Cu nanoparticles, J. Am. Chem. Soc. 136 (19) (2014) 6978–6986, https://doi.org/10.1021/ja500328k.
[9] A. Dutta, A. Kuzume, V. Kaliginedi, M. Rahaman, I. Sinev, M. Ahmadi, B. Roldán Cuenya, S. Vesztergom, P. Broekmann, Probing the chemical state of tin oxide NP catalysts during CO_2 electroreduction: A complementary operando approach, Nano Energy 53 (2018) 828–840, https://doi.org/10.1016/j.nanoen.2018.09.033.
[10] Y. Hou, N. Kovács, H. Xu, C. Sun, R. Erni, M. Gálvez-Vázquez, A. Rieder, H. Hu, Y. Kong, M. Liu, B.J. Wiley, S. Vesztergom, P. Broekmann, Limitations of identical location SEM as a method of degradation studies on surfactant capped nanoparticle electrocatalysts, J. Catal. 394 (2020) 58–66, https://doi.org/10.1016/j.jcat.2020.12.006.
[11] P.C. Okonkwo, O.O. Ige, E.M. Barhoumi, P.C. Uzoma, W. Emori, A. Benamor, A. M. Abdullah, Platinum degradation mechanisms in proton exchange membrane fuel cell (PEMFC) system: A review, Int. J. Hydrog. Energy 46 (29) (2021) 15850–15865, https://doi.org/10.1016/j.ijhydene.2021.02.078.

[12] J. Huang, N. Hörmann, E. Oveisi, A. Loiudice, G.L. De Gregorio, O. Andreussi, N. Marzari, R. Buonsanti, Potential-induced nanoclustering of metallic catalysts during electrochemical CO_2 reduction, Nat. Commun. 9 (1) (2018) 3117, https://doi.org/10.1038/s41467-018-05544-3.

[13] J.R. Pankhurst, P. Iyengar, A. Loiudice, M. Mensi, R. Buonsanti, Metal–ligand bond strength determines the fate of organic ligands on the catalyst surface during the electrochemical CO_2 reduction reaction, Chem. Sci. 11 (2020) 9296–9302, https://doi.org/10.1039/d0sc03061a.

[14] S. Popović, M. Smiljanić, P. Jovanovič, J. Vavra, R. Buonsanti, N. Hodnik, Stability and degradation mechanisms of copper-based catalysts for electrochemical CO_2 reduction, Angew. Chem. 132 (35) (2020) 14844–14854, https://doi.org/10.1002/ange.202000617.

[15] M.de.J. Gálvez-Vázquez, P. Moreno-García, H. Xu, Y. Hou, H. Hu, I. Zelocualtecatl Montiel, A.V. Rudnev, S. Alinejad, V. Grozovski, B.J. Wiley, M. Arenz, P. Broekmann, Environment matters: CO_2RR electrocatalyst performance testing in a gas-fed zero-gap electrolyzer, ACS Catal. 10 (21) (2020) 13096–13108, https://doi.org/10.1021/acscatal.0c03609.

[16] H. Hu, M. Liu, Y. Kong, N. Mysuru, C. Sun, M. d. J. Gálvez-Vázquez, U. Müller, R. Erni, V. Grozovski, Y. Hou, P. Broekmann, Activation matters: Hysteresis effects during electrochemical looping of colloidal Ag nanowire catalysts, ACS Catal. 10 (2020) 8503–8514. doi:https://doi.org/10.1021/acscatal.0c02026.

[17] C.-T. Dinh, F.P.G. de Arquer, D. Sinton, E.H. Sargent, High rate, selective, and stable electroreduction of CO_2 to CO in basic and neutral media, ACS Energy Lett. 3 (2018) 2835–2840, https://doi.org/10.1021/acsenergylett.8b01734.

[18] T. Haas, R. Krause, R. Weber, M. Demler, G. Schmid, Technical photosynthesis involving CO_2 electrolysis and fermentation, Nat. Catal. 1 (2018) 32–39, https://doi.org/10.1038/s41929-017-0005-1.

[19] C.V. Restrepo, C.C. Villa, Synthesis of silver nanoparticles, influence of capping agents, and dependence on size and shape: A review, Environ. Nanotechnol. Monit. Manag. 15 (2021) 100428, https://doi.org/10.1016/j.enmm.2021.100428.

[20] R. Szűcs, D. Balogh-Weiser, E. Sánta-Bell, E. Tóth-Szeles, T. Varga, Z. Kónya, L. Poppe, I. Lagzi, Green synthesis and in situ immobilization of gold nanoparticles and their application for the reduction of p-nitrophenol in continuous-flow mode, RSC Adv. 9 (2019) 9193–9197, https://doi.org/10.1039/c8ra10373a.

[21] M. d. J. Gálvez-Vázquez, H. Xu, P. Moreno-García, Y. Hou, H. Hu, B.J. Wiley, S. Vesztergom, P. Broekmann, Unwrap them first: Operando potential-induced activation is required when using PVP-capped Ag nanocubes as catalysts of CO_2 electroreduction, Chimia 75 (2021) 163–168. doi:https://doi.org/10.2533/chimia.2021.163.

[22] J. Kieffer, J.P. Wright, PyFAI: A Python library for high performance azimuthal integration on GPU, Powder Diffr. 28 (2013) S339–S350, https://doi.org/10.1017/s0885715613000924.

[23] B.H. Toby, R.B.V. Dreele, GSAS-II: The genesis of a modern open-source all purpose crystallography software package, J. Appl. Crystallogr. 46 (2013) 544–549, https://doi.org/10.1107/s0021889813003531.

[24] J.S. Yoo, R. Christensen, T. Vegge, J.K. Nørskov, F. Studt, Theoretical insight into the trends that guide the electrochemical reduction of carbon dioxide to formic acid, ChemSusChem 9 (2015) 358–363, https://doi.org/10.1002/cssc.201501197.

[25] C. Spöri, J.T.H. Kwan, A. Bonakdarpour, D.P. Wilkinson, P. Strasser, The stability challenges of oxygen evolving catalysts: Towards a common fundamental understanding and mitigation of catalyst degradation, Angew. Chem. Int. Ed. 56 (2017) 5994–6021, https://doi.org/10.1002/anie.201608601.

[26] I. Schrader, J. Warneke, S. Neumann, S. Grotheer, A.A. Swane, J.J.K. Kirkensgaard, M. Arenz, S. Kunz, Surface chemistry of "unprotected" nanoparticles: A spectroscopic investigation on colloidal particles, J. Phys. Chem. C 119 (31) (2015) 17655–17661, https://doi.org/10.1021/acs.jpcc.5b03863.

[27] J.A.S. Bett, K. Kinoshita, P. Stoneheart, Crystallite growth of platinum dispersed on graphitized carbon black II. Effect of liquid environment, J. Catal. 41 (1976) 124–133, https://doi.org/10.1016/0021-9517(76)90207-4.

[28] P.J. Ferreira, G.J. la O', Y. Shao-Horn, D. Morgan, R. Makharia, S. Kocha, H.A. Gasteiger, Instability of Pt/C electrocatalysts in proton exchange membrane fuel cells, J. Electrochem. Soc. 152 (2005) A2256. doi:https://doi.org/10.1149/1.2050347.

[29] R. Chattot, P. Bordet, I. Martens, J. Drnec, L. Dubau, F. Maillard, Building practical descriptors for defect engineering of electrocatalytic materials, ACS Catal. 10 (2020) 9046–9056, https://doi.org/10.1021/acscatal.0c02144.

7.7. Insights from *Operando* and Identical Location (IL) Techniques on the Activation of Electrocatalysts for the Conversion of CO_2: A Mini-Review

Authors: Abhijit Dutta, Kiran Kiran, Motiar Rahaman, **Ivan Zelocualtecatl Montiel**, Pavel Moreno-García, Soma Vesztergom, Jakub Drnec, Mehtap Oezasland, and Peter Broekmann

CHIMIA 2021, 75, No. 9. DOI: https://doi.org/10.2533/chimia.2021.733

Highlights: This work demonstrates the importance of using spectroscopic techniques like *operando* XAS, XRD, and Raman spectroscopy to study the chemical state evolution of Cu_xO and Bi_2O_3 metal foams during electrochemical reduction of CO_2. The metal foams were synthesized using the dynamic hydrogen bubble template electrodeposition approach. These catalysts show a great improvement in product selectivity after a thermal activation at 300˚C for 12 h, followed by an electroreduction of the oxide species before or after CO_2 electrolysis. It was found that in the case of Cu oxide, the pre-activation process is completed long before the CO_2 electroreduction sets in. Therefore, the main catalyst involved in the CO_2 reduction is the Cu metallic, which is derived from the Cu_xO precursor catalyst. In contrast, the opposite case occurs when a Bi_2O_3 foam catalyst is employed, this catalyst goes through a partial transformation (during CO_2 reduction) into an electrochemically active subcarbonate and metallic phase. This transition was followed by potential-dependent *operando* Raman experiments, giving a better understanding of the CO_2 electroreduction pathway. The use of IL-SEM demonstrates that the metal foams studied herein presented significant alterations in their morphology.

Contributions: In this project, I was involved in the synthesis, characterization, electrochemical screening, and *operando* Raman potential- and time-dependent experiments. In addition, I participated in the manuscript revision process.

doi:10.2533/chimia.2021.733 Chimia 75 (2021) 733–743

Insights from *Operando* and Identical Location (IL) Techniques on the Activation of Electrocatalysts for the Conversion of CO_2: A Mini-Review

Abhijit Dutta*[a], Kiran Kiran[a], Motiar Rahaman[a#], Ivan Zelocualtecatl Montiel[a], Pavel Moreno-García[a], Soma Vesztergom[a,b], Jakub Drnec[c], Mehtap Oezaslan[d], and Peter Broekmann*[a]

Abstract: In this mini-review we compare two prototypical metal foam electrocatalysts applied to the transformation of CO_2 into value-added products (*e.g.* alcohols on Cu foams and formate on Bi foams). A substantial improvement in the catalyst performance is typically achieved through thermal annealing of the as-deposited foam materials, followed by the electro-reduction of the pre-formed oxidic precursors prior or during the actual CO_2 electrolysis. Utilizing highly insightful and sensitive complementary *operando* analytical techniques (XAS, XRD, and Raman spectroscopy) we demonstrate that this catalyst pre-activation process is entirely accomplished in case of the oxidized Cu foams prior to the formation of hydrocarbons and alcohols from the CO_2. The actually active catalyst is therefore the metallic Cu derived from the precursor by means of oxide electro-reduction. Conversely, in their oxidic form, the Cu-based foam catalysts are inactive towards the CO_2 reduction reaction (denoted ec-CO_2RR). Oxidized Bi foams can be regarded as an excellent counter example to the above-mentioned Cu case as both metallic and the thermally derived oxidic Bi foams are highly active towards ec-CO_2RR (formate production). Indeed, *operando* Raman spectroscopy reveals that CO_2 electrolysis occurs upon its embedment into the oxidic Bi_2O_3 foam precursor, which itself undergoes partial transformation into an active sub-carbonate phase. The potential-dependent transition of sub-carbonates/oxides into the corresponding metallic Bi foam dictates the characteristic changes of the ec-CO_2RR pathway. Identical location (IL) microscopic inspection of the catalyst materials, *e.g.* by means of scanning electron microscopy, demonstrates substantial morphological alterations on the nm length scale on the material surface as consequence of the sub-carbonate formation and the potential-driven oxide reduction into the metallic Bi foam. The foam morphology on a mesoscopic length scale (macroporosity) remains, by contrast, fully unaffected by these phase transitions.

Keywords: Catalyst activation · CO_2 reduction reaction · Identical location (IL) technique · Metal foam · *Operando* spectroscopy

Dr. Abhijit Dutta obtained his PhD in chemistry from the Indian Institute of Engineering Science and Technology, Kolkata. During his PhD studies, his research mainly focused on the development of Pt and *non*-Pt based nanostructured materials for the application to fuel cells such as alcohol electro-oxidation, hydrogen oxidation, and the oxygen reduction reaction. He worked as a post-doctoral fellow at the National University of Singapore, Singapore. In 2015 he joined the interfacial electro-chemistry group of Prof. Peter Broekmann at the University of Bern, Switzerland, where he focuses on the development of various *operando* techniques (Raman, XAS, and XRD) to characterize novel electrocatalysts for the selective conversion of CO_2 into value-added products.

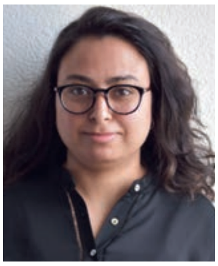

Kiran Kiran received her MSc in physics from Maharshi Dayanand University (M.D.U.) India in 2015. She is currently pursuing her PhD at the Department of Chemistry, Biochemistry and Pharmaceutical Sciences at the University of Bern under the supervision of Prof. Peter Broekmann. Her research interests are focused on the synthesis of novel electrocatalysts for CO_2RR applications.

Dr. Motiar Rahaman received his MSc in chemistry (2013) from the Indian Institute of Technology Madras, India. He obtained his PhD (2018) from the University of Bern (group of Peter Broekmann) on the topic of electrochemical conversion of CO_2 into value-added products. Currently he works as a post-doctoral fellow at the University of Cambridge (UK).

Correspondence: Prof. Dr. P. Broekmann[a], E-mail: peter.broekmann@dcb.unibe.ch; Dr. A. Dutta[a], E-mail: abhijit.dutta@dcb.unibe.ch
[a]University of Bern, Department of Chemistry, Biochemistry and Pharmaceutical Sciences; [b]Eötvös Loránd University, Department of Physical Chemistry, H-1117 Budapest, Pázmány Péter sétány 1/A, Hungary; [c]European Synchrotron Radiation Facility, Grenoble, France; [d]Institute of Technical Chemistry, Technical University of Braunschweig, Braunschweig, Germany; [#]Current address: Department of Chemistry, University of Cambridge, Cambridge, United Kingdom

Ivan Zelocualtecatl Montiel received his BSc and MSc in chemistry from the Meritorious Autonomous University of Puebla (BUAP) in 2013 and 2016, respectively. He is currently a PhD candidate at the Department of Chemistry, Biochemistry and Pharmaceutical Sciences at the University of Bern under the supervision of Prof. Dr. Peter Broekmann. His research interest is focused on the development of novel catalysts for the electroreduction of CO_2.

Dr. Pavel Moreno-García received his PhD in chemistry and molecular science from the University of Bern in 2013, under the supervision of Prof. Dr. Thomas Wandlowski. At that time, his work was devoted to the study of electron transport through nano-objects at electrified interfaces by *in situ* STM. In 2013, he joined the group of Prof. Dr. Peter Broekmann, where he is involved in research activities on electrocatalysis, metal corrosion and laser ablation mass spectrometry.

Dr. Soma Vesztergom obtained his MSc (2010) and PhD (2014) degrees in chemistry, working with Prof. Dr. G. G. Láng at Eötvös Loránd University, Hungary. He was a post-doctoral researcher in Prof. Dr. Peter Broekmann's group at the University of Bern for one year (2014) and is a regular collaborator of this group since then. His research primarily focuses on instrumental developments in electrochemistry and on the modelling of electrocatalytic processes. Currently, he is an assistant professor at Eötvös Loránd University in Budapest.

Dr. Jakub Drnec obtained his PhD degree at University of Victoria, Canada, in the field of surface electrochemistry. He is currently beamline scientist at the European Synchrotron (ESRF) in Grenoble (France), developing new high energy X-rays experimental techniques to study materials for energy conversion and storage. His main goal is to probe materials in their working environment in order to better understand their functioning. His current projects involve *operando* investigations of fuel cells and batteries, fundamental studies of electrocatalyst's degradation and structure-activity relationships, and development of *operando* electrochemical cells and data analysis routines.

Prof. Dr. Mehtap Oezaslan obtained her PhD degree (2012) in electrochemistry from Technische Universität Berlin, Germany. After a post-doctoral stay at the Electrochemistry Laboratory Group, Paul Scherrer Institute, Switzerland, she was a Junior professor for Electrochemistry at Carl von Ossietzky University of Oldenburg from 2014–2019. Since June 2019, she holds a Full (W3) Professorship at the Institute of Technical Chemistry, Technische Universität Braunschweig. Her research is focused on the development and characterization of electrocatalysts for PEM fuel cells and electrolysis.

Prof. Dr. Peter Broekmann obtained his MSc in chemistry (1998) and a PhD (2000) from the University of Bonn. After a postdoctoral stay at the University of Twente (The Netherlands) in 2001, he became project leader at the Institute of Physical Chemistry in Bonn. Since 2008 he holds a lecturer position for electrochemistry at the University of Bern. His research focuses on metal deposition processes for semiconductor and electrocatalysis applications.

1. Introduction

The conversion of CO_2 into value-added products by means of electrolysis (denoted hereafter ec-CO_2RR) is considered a promising approach to mitigate the negative impact that CO_2 is exerting on the global climate.[1] The vision of converting this environmentally harmful molecule into chemical platform chemicals or synthetic fuels on large industrial scale even offers the unique chance of decreasing the existing atmospheric CO_2 concentration, which already exceeds a level of 400 ppm. For this purpose, the ec-CO_2RR has to be coupled in the future to advanced direct air capture technologies.[2–4] The products of CO_2 reduction – typically light-weight molecules such as carbon monoxide, formic acid or alcohols – could be used as either chemical feedstock and transformed further into products of higher value, *e.g. via* Fischer–Tropsch synthesis or biotechnological transformations,[5] or directly as 'green' fuels. The latter is considered vital for the so-called 'energy transition'.[6,7] In particular, if a surplus of renewable energies, originating from solar, wind, or hydroenergy sources, is used to operate the highly endergonic and energy demanding ec-CO_2RR, this conversion process might become truly sustainable and possibly a key element of a future circular economy. Without doubt, ec-CO_2RR has the highest potential of contributing to the closing of the anthropogenic CO_2 cycle (see Fig. 1).[8]

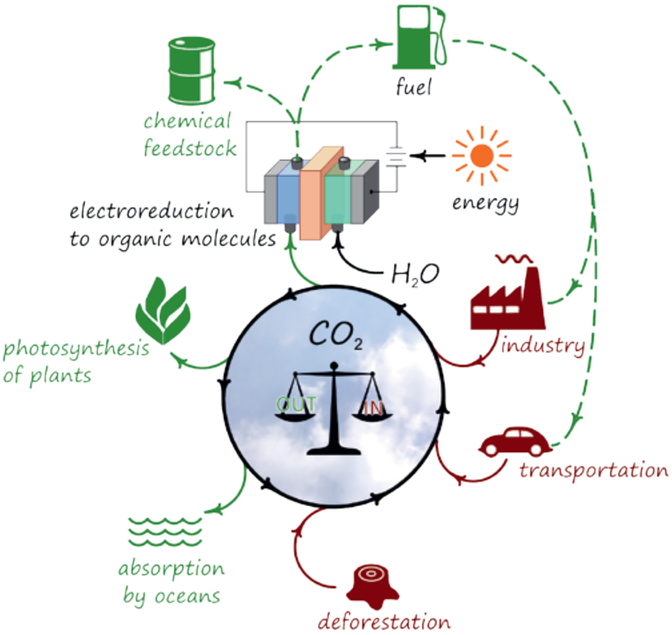

Fig. 1. Schematic depiction of the overall concept to close the anthropogenic carbon cycle by ec-CO_2RR: Towards sustainable conversion of CO_2 into synthetic fuels and chemical feedstock powered by solar energy. Adapted from ref. [8], with permission from John Wiley and Sons.

Most of the known electrochemical CO_2 transformations are, however, still immature and uneconomic.[9] One reason for this is related to electrocatalysts which still require substantial improve-

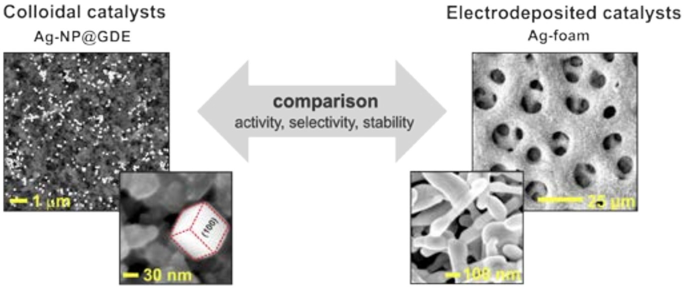

Fig. 2. Complementary catalyst concepts for the ec-CO_2RR: carbon-supported colloidal nanoparticles (left) *versus* electrodeposited metal foams (right) exemplified for Ag-based electrocatalysts. Adapted from refs [13,19], with permission of the American Chemical Society.

ments in terms of material costs, (energy) efficiency and catalyst reliability (stability).[8] Additionally, electrocatalysts are essential not only to accelerate the intrinsically slow ec-CO_2RR process but also to direct the electrolysis reaction towards the desired reaction products (selectivity).[10] It is, however, not only the chemical nature of the catalyst itself which governs the resulting ec-CO_2RR product distribution[10] but also its morphological characteristics on various length scales.[11] Some of the most common ec-CO_2RR catalyst concepts rely on the use of nanoparticulate materials.[12] A clear advantage of this classical approach of catalyst design is that the whole spectrum of (mature) colloid chemistry can be applied to synthesize nano-materials of various shapes, morphologies and size distributions. In addition, this approach offers a straightforward and well-established route to functionalize highly porous carbon supports (*e.g.* gas diffusion electrodes (GDEs), Fig. 2) that are used in gas-fed electrolyzer systems that can reach ec-CO_2RR current densities of technological relevance (> 200 mA × cm^{-2}).[13,14]

A relatively new and alternative concept of ec-CO_2RR catalyst design relies on the electrodeposition of foam-type materials[11,15–17] (Fig. 2), which, similar to their nanoparticulate counterparts, offer a large surface area that is not only accessible to reactants but also enables fast, multidimensional electron transport.[17] Moreover, self-standing foams can directly be employed as cathodes for the ec-CO_2RR often without the need for additional mechanical support, rendering the application of conductive binders unnecessary.[17]

Herein we review and compare the structural, compositional and performance characteristics of two prototypical foam electrocatalysts that are based on Cu and Bi systems published recently.[11,18–20] Among various materials studied so far, Cu stands out as the only known mono-metallic catalyst that can produce multiple hydrocarbons and alcohols of various chain lengths at elevated rates from the ec-CO_2RR.[10,21–26] In this context, C–C coupled (liquid) alcohols are of particular interest due to their high volumetric energy density (*e.g.* n-propanol: 27.0 MJ L^{-1}).[27] Note that, prior to their use in operating electrolyzers, numerous as-synthesized/as-deposited ec-CO_2RR catalysts require further activation as an essential pre-requisite to attain a highly selective CO_2 conversion into the targeted product(s).[28–33] The terms ‘as-synthesized’ and ‘as-deposited’ refer to the stage of catalyst preparation right after the initial electrodeposition of the catalyst material and prior to its further activation. A common approach of such catalyst activation involves the partial or complete surface oxidation of the as-deposited metallic foams, *e.g.* by thermal annealing in air.[20,29,31] An ultimate activation step of such formed oxidic catalyst precursors is often only achieved *in situ* under reductive conditions prior to or during the actual CO_2 electrolysis.[19,31,34] Such oxidation/electro-reduction treatments not only lead to the further increase of the electrochemically active surface area of the catalyst but also often create those active sites on the foam surface which are required for highly selective ec-CO_2RR.[28] It should be emphasized that, at least in the case of copper-based materials, the oxidic precursors (Cu_2O or CuO) formed upon thermal annealing are thermodynamically instable at electrolysis potentials typically applied during ec-CO_2RR,[35] which in turn results into the formation of so-called oxide-derived (OD) catalysts.[31,36] In general, one possible complication of this catalyst activation approach lies in the reduced electric conductivity of the formed ‘bulk’ oxides. This can, in principle, lead to a ‘kinetic’ stabilization of the formed oxidic catalyst precursor phases even under the extremely cathodic potentials applied. In some rare cases one might therefore observe oxidic catalyst species even at potentials far beyond the stability regime predicted by thermodynamics. The specific role of oxides for the ec-CO_2RR mechanism and in particular the occurrence of oxygen species embedded inside the hosting metallic Cu matrix under reductive conditions are still the subject of highly controversial debates. To date, there is no ultimate consensus achieved in the literature on the potential-dependent stability of surface and sub-surface oxide/oxygen species and their specific role for the ec-CO_2RR.[19,20,33,37–42] To address these mechanistic questions of catalyst activation, a highly complementary approach utilizing several *operando* techniques is needed, which provides various means of deriving structural and chemical information of the catalyst state under reactive conditions.[28] When further combined with high-resolution imaging techniques, *e.g.* identical-location electron microscopy (*e.g.* IL-SEM[28] or IL-TEM[43]), this holistic approach even permits discriminating *transient* phenomena of catalyst precursor reduction (activation). Fig. 3 depicts the set of complementary *operando* analytical techniques described herein.[19]

X-ray absorption spectroscopy (XAS)[19] provides information on (i) the oxidation state (XANES: X-ray Absorption Near

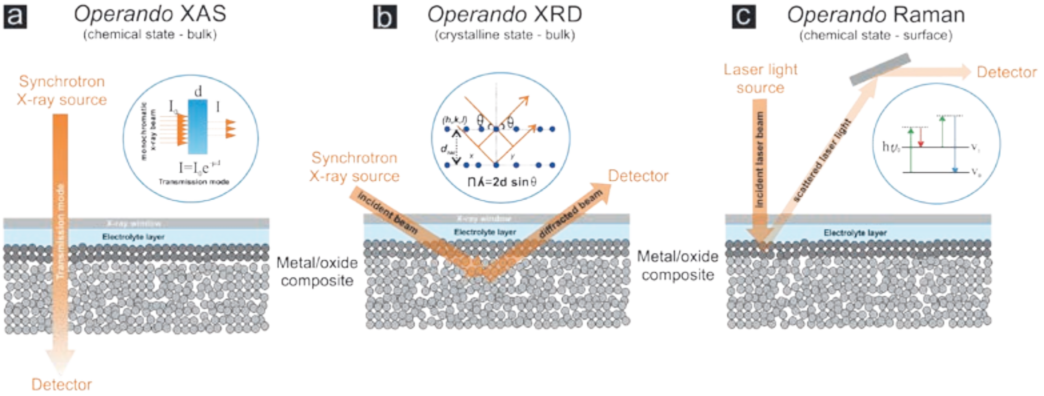

Fig. 3. Complementary *operando* analytical approaches to study the potential-dependent oxide precursor–metal conversion. a) *Operando* X-ray absorption spectroscopy (XAS); b) *Operando* X-ray diffraction (XRD); c) *Operando* Raman spectroscopy. Adapted from ref. [19], with permission of Elsevier.

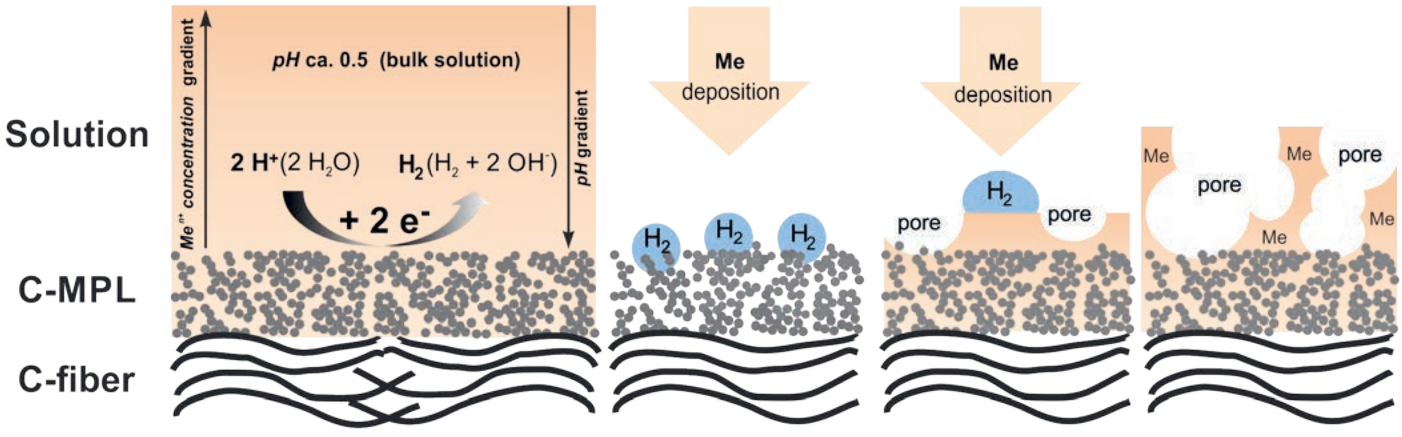

Fig. 4. Metal foam electrodeposition ('Me' deposition) by means of the dynamic hydrogen bubble template (DHBT) approach. The working principle is exemplified for a porous carbon support that finds use as gas-diffusion electrode (GDE). 'MPL' and 'Me' stand for microporous layer and metal, respectively. Adapted from ref. [18], with permission of the American Chemical Society.

Edge Structure) and (ii) the coordination number changes (EXAFS: Extended X-ray Absorption Fine Structure) that typically go along with the electro-reduction of the oxidic precursor materials. Compared to their nanoparticulate counterparts, metal foam electrocatalysts and their oxidic precursors exhibit a more unfavorable surface to volume (bulk) ratio (see *e.g.* Fig. 2). Therefore, information derived from XANES and EXAFS techniques originate predominantly from the 'bulk' of the foam material and comprise only marginal contributions from the respective catalyst surfaces. However, what makes the *operando* grazing-incidence X-ray absorption spectroscopy particularly valuable is its capability to probe these potential-dependent oxidation state transitions even when amorphous phases, lacking any long-range translational order, are involved. Note that the activation of Cu foam catalysts *via* thermal annealing and subsequent electroreduction often proceeds *via* amorphous Cu_xO phases.[19,20]

The *operando* X-ray diffraction (XRD) technique[19] is highly complementary to XAS as it permits probing changes in the crystal structure of the foam catalysts, which typically accompany the potential-driven oxidation state changes.

Raman spectroscopy[19] can be considered as the most surface sensitive *operando* technique among those employed herein. A particular strength of the *operando* Raman spectroscopy is that not only the potential-induced alterations of the catalyst themselves can be probed but, in addition, also the emergence of ec-CO_2RR intermediate species, which might be chemisorbed on the evolving 'active' metallic catalyst surface.[19,44]

Herein we introduce Cu foams and their oxidic precursors as prototypical model systems where the oxide–metal transition (catalyst activation) is completed prior to (or at the very onset of) the ec-CO_2RR.[19,20,28] The actual foam catalysts, being active towards alcohol and hydrocarbons, can therefore be considered as truly oxide-derived (OD).[19]

As a counter-example to that, we also discuss oxidized Bi foam catalysts[18] used for the highly selective production of formate. Our investigations reveal that both the oxidized as well as the corresponding metallic foams exhibit pronounced electrocatalytic activity towards the ec-CO_2RR. Finally, we hint at two ec-CO_2RR pathways that are distinctly active on oxide-derived Cu and Bi_2O_3/Bi foam electrocatalysts.[18]

2. Experimental[18,19]

Experimental details on the Cu and Bi foam preparation and the performed *operando*/IL investigations have already been detailed elsewhere.[11,18,19] We therefore restrict ourselves here to a brief description of the applied experimental approaches.

2.1 *Preparation of the Cu/Cu_xO and Bi/Bi_2O_3 Foam Catalysts*[11,19]

Metallic Cu foams were electrodeposited onto activated carbon foil substrates (0.25 mm thick, 99.8%, Alfa Aesar, Germany) using the dynamic hydrogen bubble template (DHBT)[15,16] approach (see Fig. 4). The carbon foil support was then immersed into a Cu plating bath containing 0.2 M $CuSO_4 \cdot 5H_2O$ and 1.5 M H_2SO_4. For the galvanostatic deposition process, a current density of $j = -3.0$ A × cm^{-2} (normalized to the geometric surface area of the carbon support) was applied for the duration of 5 seconds. The electrodeposited Cu foams were further subjected to thermal annealing in air for 12 h at a temperature of 300 °C using a tube furnace (GERO, GmbH, Germany).

For the *operando* Raman spectroscopy studies, metallic Bi foams were electrodeposited on graphitic carbon foils (Alfa Aesar) that were activated prior to the Bi deposition by annealing in air at 550 °C for 12 h in a tube furnace. To further increase the electrochemically active surface area Bi foams were deposited on highly porous carbon fiber cloths (gas diffusion electrodes, GDEs, Fuel Cell, USA) for the electrolysis experiments. The carbon fiber cloths were used as received. The standard plating bath for the Bi foam deposition was composed of 1.5 M H_2SO_4 (prepared from 96% H_2SO_4, ACS grade, Sigma-Aldrich) serving as the supporting electrolyte and 20 mM bismuth ammonium citrate ($C_{12}H_{22}BiN_3O_{14}$, purity ≥ 99.5 % Sigma Aldrich). The galvanostatic Bi foam deposition was carried by applying a current density of $j = -3.0$ A × cm^{-2} (referred to the geometric surface area of the support electrode) for 20 s. The as-prepared Bi foams were further subjected to thermal annealing in air at 300 °C for 12 h, thus transforming the metallic Bi into fully oxidized Bi_2O_3.

2.2 *Operando X-ray Absorption Spectroscopy*[19]

XAS experiments were carried out at the SuperXAS (X10DA) beamline at the Swiss Light Source (SLS) in Villigen, Switzerland. The storage ring was operated at 2.4 GeV and 400 mA. For the *operando* spectroscopic experiments a dedicated liquid flow-cell was used.[45] XAS experiments were carried out in CO_2-sat. 0.5 M $KHCO_3$ electrolyte solution (pH = 7.2) in the potential range from +0.8 V to –0.9 V vs. RHE. All potentials were iR-corrected.

2.3 *Operando X-ray Diffraction*[19]

Operando XRD experiments were performed at the high energy beamline ID31 of the European Synchrotron Radiation Facility (ESRF). The X-ray beam was mono-chromatized with a Laue-Laue monochromator to the energy of 69 keV and focused to the size of 5 × 20 µm^2 (vertical × horizontal) at the sample position. The 2D XRD patterns were collected with a Dectris Pilatus 2M CdTe detector. A custom-made PEEK electrochemical flow cell was used for the experiments.[46] The measurements were performed in grazing incidence geometry (the incidence angle was less than 1 degree), in CO_2-sat. 0.5 M $KHCO_3$ electrolyte. A continuous flow of fresh CO_2-sat. electrolyte solution through the spectro-electrochemical cell prevented any undesired accumulation of soluble Cu species in the investigated X-ray window. All potentials were iR-corrected.

2.4 *Operando Raman Spectroscopy*[19]

Raman spectra were recorded using a LabRAM HR800 confocal microscope (Horiba Jobin Yvon) at a working distance of 8 mm between the objective lens (LMPLFLN from Olympus, 50X magnification) and the sample with a numerical aperture of 0.1 in order to focus a diode-pumped solid-state or He-NE laser beam (excitation wavelength of 532 or 633 nm, power of 3 mW) on the sample. The Raman signal was collected in a back-scattering geometry using a lab-made spectro-electrochemical cell made of Kel-F.[47,48] CO_2-sat. 0.5 M $KHCO_3$ solution was used as the electrolyte. The ohmic drop was determined using the positive feedback technique and compensated during the measurement.

2.5 *Identical Location Scanning Electron Microscopy (IL-SEM)*

For the high-resolution (HR) identical location (IL) SEM imaging a Zeiss DSM 982 instrument was used.

2.6 *Product Analysis of the ec-CO_2RR*[11,18]

All electrolysis experiments were carried out in CO_2-sat. 0.5 M $KHCO_3$ solution using a custom-built, air-tight glass-cell (H-type) described elsewhere.[11] During electrolysis CO_2 was continuously purged through the catholyte at a flow rate of 13 mL × min^{-1}. The headspace of the electrolysis cell was directly connected to the gas sampling loop of the gas chromatograph (GC 8610C, SRI Instruments). The GC was equipped with a packed Hayesep D column and a packed Molesieve 5A column. Argon (99.9999 %, Carbagas) was used as the carrier gas. A flame ionization detector (FID) coupled to a methanizer was used to quantify CO and volatile hydrocarbons. A thermal conductivity detector (TCD) was used for the H_2 detection. Non-volatile products (*e.g.* alcohols) were quantified by a second FID detector. After the electrolysis, a 2 μL aliquot of the electrolyte solution was injected into a second Haysep D column (post-electrolysis alcohol detection). Other liquid products (*e.g.* formate) were analyzed by means of ion exchange chromatography (IC, Metrohm Advanced Modular Ion Chromatograph: L-7100 pump, Metrosep A Supp 7-250 column, conductivity detector).

3. Results and Discussion

3.1 *Activation of Cu Foam Electrocatalysts*[19]

Fig. 5 displays a prime example of Cu foams fabricated by means of the DHBT-assisted electrodeposition method.[11] The basic concept of this approach was adapted from the work by Shin *et al.*[15,16] As the Cu electrodeposition takes place under rather harsh hydrogen evolution reaction (HER) conditions (*e.g.* at current densities of $j = -3$ A × cm^{-2}, see Fig. 4), gas bubbles rapidly evolve on the support electrode and serve as geometric template for the actual metal plating process which is superimposed on the HER. Cu is deposited only in the bubble-free areas of the support and the emerging porous film. The process of hydrogen bubble

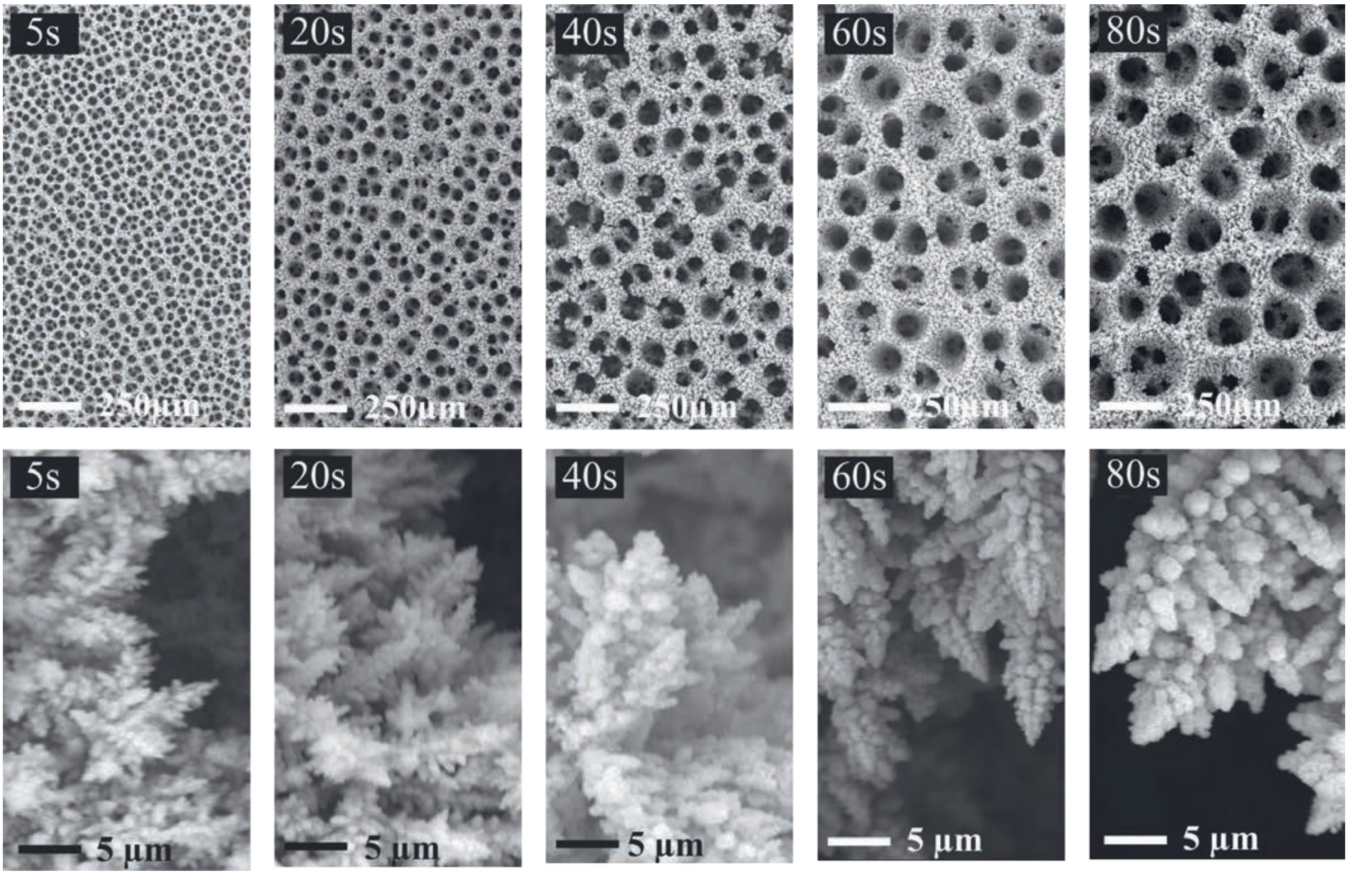

Fig. 5. Top-down SEM analysis showing the surface pore size (upper row) and dendrite size (lower row) evolution as function of the deposition time (exemplified for a Cu foam catalyst). Adapted from ref. [11], with permission of the American Chemical Society.

nucleation, growth and coalescence is continuous. This is why the average surface pore size increases as function of the deposition time and film thickness (Fig. 5).[11] A characteristic feature of the formed metal foams is a gradient in the pore sizes along the surface normal. Smallest pores are typically created close to the support electrode whereas the biggest ones are found at the outermost surface of the foam material which is exposed to the (liquid) electrolyte during the CO_2 electrolysis reaction.[11]

In addition to this primary macro-porosity (µm length scale), originated by the gaseous H_2-template during the metal deposition, the scaffold of the formed 3D foam itself is porous, too.[11,20,49] The macro-pore sidewalls are composed of randomly distributed Cu dendrites thus introducing a secondary porosity to the catalyst (nm length scale).[15] Such a dendritic growth mode originates from the applied experimental conditions that impose a deposition rate limited by mass transport of the metal ions and a reduced mobility of the deposited atoms on the emerging foam surface.[11]

In particular when alcohols are targeted as products, the electrodeposited catalysts often require further activation prior to the ec-CO_2RR, *e.g.* by thermal annealing in air.[28,50] Fig. 6 displays representative SEM micrographs of an 'as-deposited' Cu foam and its morphological evolution induced by thermal annealing at 300 °C for 12 h in air, and a subsequent 1 h CO_2 electrolysis in CO_2-sat. 0.5 M bicarbonate solution carried out at –0.67 V vs. RHE. Obviously, the macro-porous morphology of the Cu foam remains completely unaffected by both the thermal annealing in air (Cu oxidation) and the subsequent ec-CO_2RR, the latter involving the electro-reduction of the formed oxides.[19,20] However, the Cu foam undergoes substantial morphological alterations on the nm length scale particularly induced by the thermal treatment (see Fig. 6e–h). Following the 12 h annealing step at 300 °C, the surface of the pristine metallic Cu foam is completely transformed into a composite material consisting of cuprous (Cu_2O) and cupric (CuO) oxides[19,20,28] (denoted Cu_xO). This transformation requires substantial mass transport of oxygen and Cu species. A combination of *ex situ* (post-deposition, post-electrolysis) XRD and XPS analysis confirms the composite nature of the oxidic foam.[19,20] It should be noted that the applied annealing temperature of 300 °C is sufficient to form a crystalline Cu_2O phase whereas the cupric CuO remains largely in an amorphous state lacking any long range transitional order.[19,20] Consequently, Cu(II) species are detected in the XPS but not in the corresponding XRD analysis.[19,20] It should be noted here that, in full agreement with previous studies, the thermal annealing activates the Cu catalyst for C2 and C3 alcohol production.[19] For instance, the partial current density for ethanol formation increases from $j_{EtOH} = –0.86\ mA \times cm^{-2}$ ($FE_{EtOH} = 5\%$) at –0.77 V vs. RHE to $j_{EtOH} = –1.61\ mA \times cm^{-2}$ ($FE_{EtOH} = 6.7\%$) at –0.87 V vs. RHE. Similarly, the partial current density for n-propanol formation reaches a value of $j_{PrOH} = –1.72\ mA \times cm^{-2}$ ($FE_{PrOH} = 7.1\%$) at –0.87 V.[19] A full description of the electrocatalytic performance of the annealed Cu foam can be found in ref. [19].

More sophisticated *operando* analytical techniques are required to ultimately address how important oxide species are in particular for the alcohol electrosynthesis *via* the ec-CO_2RR on these Cu foams. Fig. 7 provides an overview on the results of the highly complementary XAS, XRD, and Raman spectroscopic investigations discussed by Dutta *et al*.[19] Changes in the potential-dependent Cu K-edge XANES spectra of the Cu_xO foam could be attributed to potential-dependent redox state changes of Cu species (Fig. 7, panel a; selected data set). Panel b in Fig.7 shows the result of a linear combination fitting (LCF) that was applied to the obtained XANES data using Cu K-edge XANES spectra of a Cu foil, Cu_2O and CuO as reference materials. The plot displays the relative concentrations of the Cu(0), Cu(I), and Cu(II) species present in the Cu_xO foam as a function of the potential applied.[19] The LCF analysis suggests that the Cu_xO foam at +0.6 V vs. RHE predominantly consists of CuO, whereas only a lower Cu_2O content was observed (25–35 wt.%). Upon potential excursion from +0.6 down to 0 V vs. RHE, the relative abundances of Cu(II) and Cu(I) anti-correlate and further negative polarization leads to the onset of oxide reduction to metallic Cu(0). At potentials below 0 V vs. RHE the Cu(II) abundance

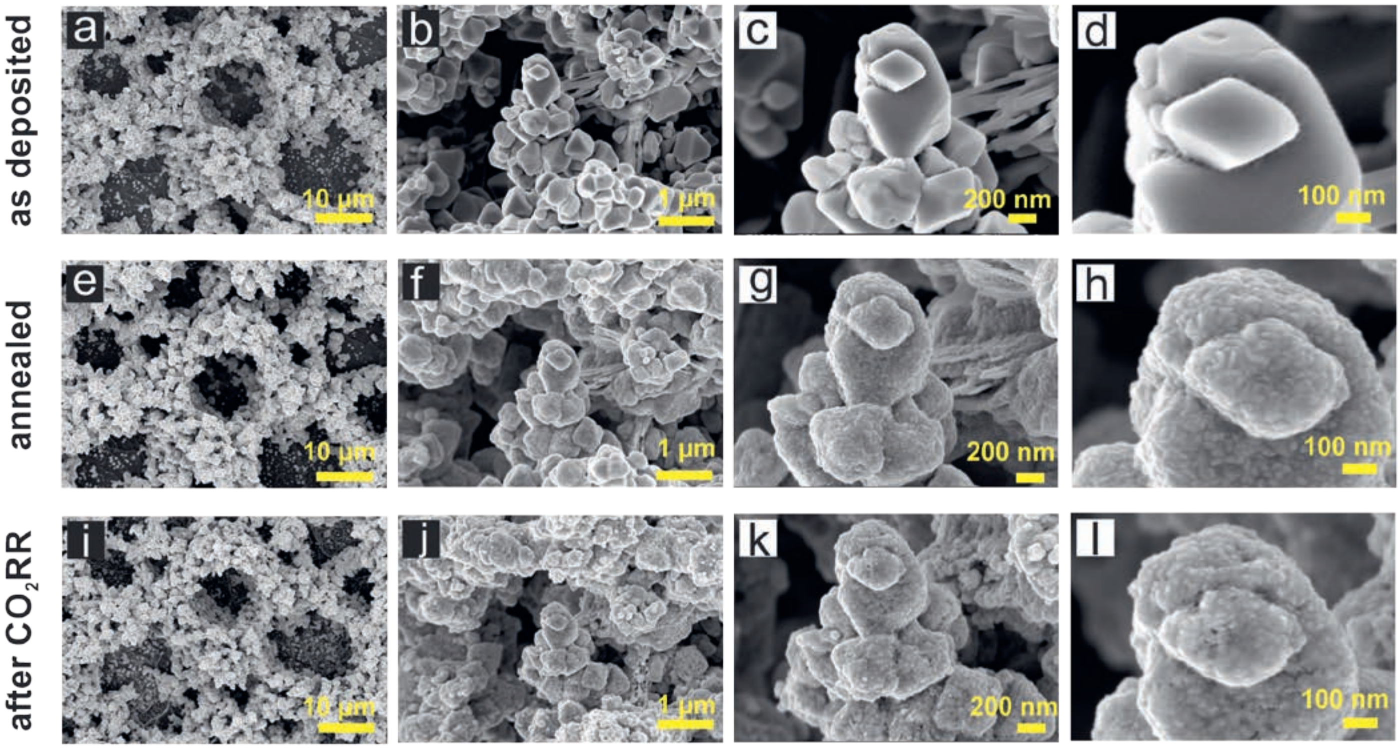

Fig. 6. Identical location (IL) SEM inspection of the Cu foam catalyst. (a–d) As-deposited Cu foam (5 s deposition at -3 A × cm^{-2}); (e–h) Thermally annealed Cu foam (300 °C for 12 h in air, denoted Cu_xO foam); (i–l) Oxide-derived (OD) Cu foam after 1 h CO_2RR in CO_2-sat. 0.5 M $KHCO_3$ solution at –0.67 V vs. RHE. Adapted from ref. [19], with permission of Elsevier.

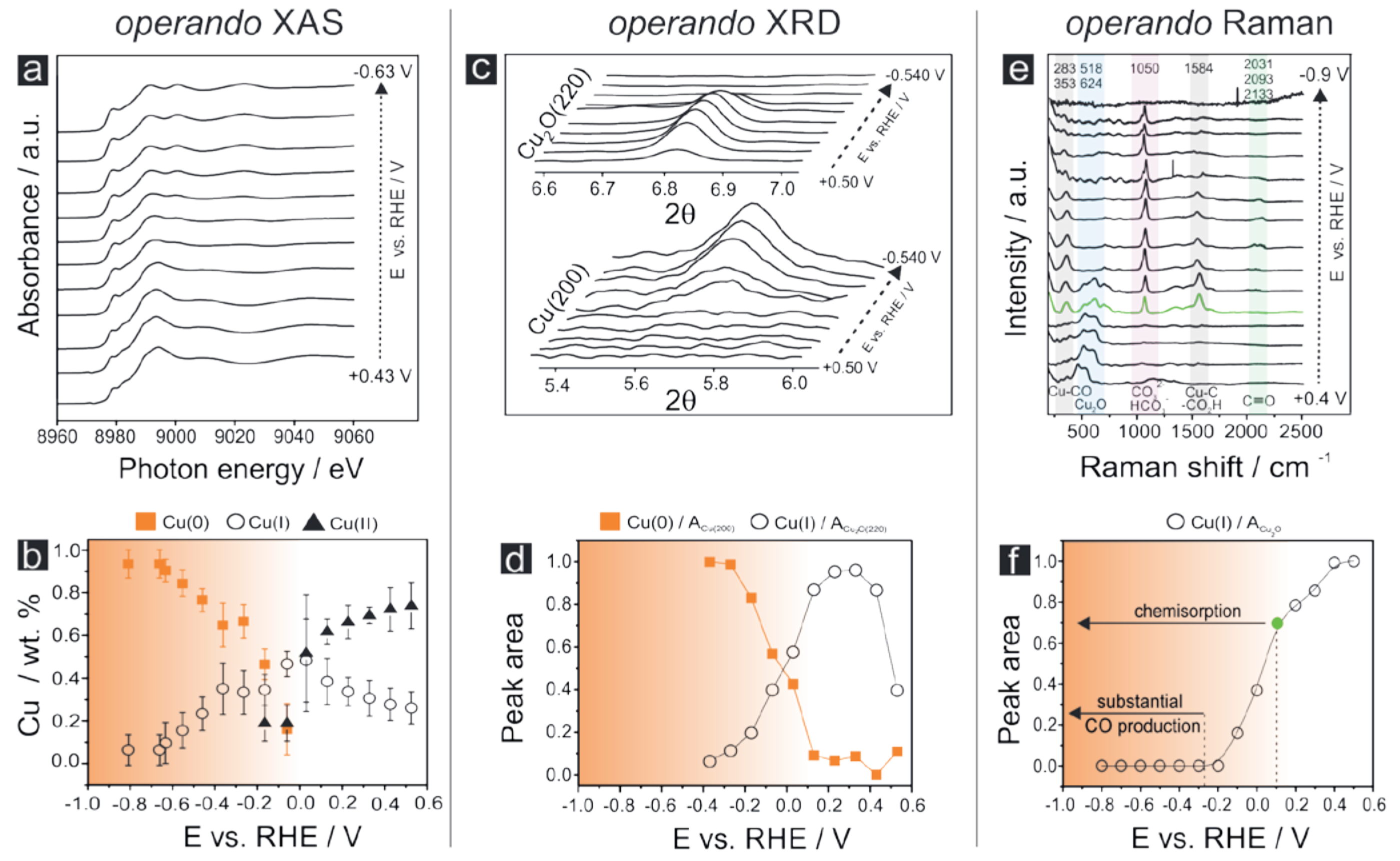

Fig. 7. Survey of experimental *operando* results demonstrating the potential-dependent oxide–metal transition of the oxidic catalyst precursor (Cu_xO foam). (a) Potential-dependent *operando* XANES spectra (Cu K-edge) of the thermally annealed Cu foam (Cu_xO) in CO_2-sat. 0.5 M $KHCO_3$ solution; (b) Potential-dependent composition of the Cu_xO foam (relative content of Cu species: Cu(0), Cu(I), and Cu(II) derived from a linear combination fitting (LCF) of the XANES spectra shown in (a)); (c) Potential-dependent *operando* grazing-incidence X-ray diffractograms of the $Cu_2O(220)$ and Cu(200) reflections; (d) Integrated and normalized peak intensities of the diffractograms shown in (c); (e) Corresponding potential-dependent *operando* Raman spectra; (f) Integrated and normalized peak intensities of the Cu_2O-related Raman peaks (518 cm^{-1} and 624 cm^{-1}) shown in (e). The peak areas were normalized with respect to the most intense peaks at most positive electrode potentials. The grey and orange areas in panel b, d, and f indicate the stability windows of the oxidic and metallic state of Cu, respectively. Adapted from ref. [19], with permission of Elsevier.

drops down to zero, whereas Cu(I) species are present in the bulk material down to potentials of -0.5V vs. RHE.[19] The potential-dependent decrease of the Cu(I) content below 0 V vs. RHE is clearly anti-correlated to the increase of the Cu(0) abundance. The transition from the oxidic precursor to metallic Cu in the bulk is completed at about –0.7 V vs. RHE.[19]

Operando XRD experiments basically confirm the XAS investigations (panel c and d in Fig. 7). As hypothesized on the basis of the XAS results the integrated intensity of the $Cu_2O(220)$ diffraction peak first increases when sweeping the cathode potential from +0.5 V to +0.2 V vs. RHE. This trend is consistent with the assumption of an intermediate crystalline Cu_2O phase which accumulates in the initial stage of the oxide–metal transition in the foam material at the expense of the amorphous CuO phase.[19] Interestingly, the disappearance of the Cu_2O related diffraction pattern with negative going potentials is already completed at –0.4 V vs. RHE, whereas the XAS experiment indicates the presence of Cu(I) species for potentials down to –0.8 V vs. RHE. These deviations in the particular potential-dependence of the Cu(I)(XAS)/Cu_2O(XRD) stability regime are related to the intrinsic characteristics of both *operando* techniques. The ultimate reduction of the Cu(I) to Cu(0) proceeds most likely *via* an intermediate amorphous Cu(I) phase.[19]

Among the *operando* techniques applied Raman spectroscopy is the most surface sensitive one.[19] Raman features observed at 148 cm^{-1}, 518 cm^{-1}, and 624 cm^{-1} can be ascribed to cuprous oxide species (Cu_2O), whereas vibrational modes at 298 cm^{-1} and 346 cm^{-1} originate from cupric oxides (panel e and f in Fig. 7).[19] Interesting to note is that after exposure to the 0.5 M $KHCO_3$ electrolyte at the open circuit potential, the CuO related vibrational modes have completely disappeared from the Raman spectra.[19] Only vibrational modes of the cuprous oxide (Cu_2O) are left which indicates that the initial catalyst surface is terminated exclusively by Cu(I) species when exposed to the electrolyte. Both XRD and XAS typically do not show these effects when the oxidic foam is exposed to the electrolyte at OCP.[19] This is due to the dominance of 'bulk' contributions to the data with only minor contributions from the foam surface. Integrated intensities of the Cu_2O specific Raman features (panel f) follow qualitatively the same trend as observed in the XAS and XRD. However, the 'surface oxide reduction' proceeds apparently faster than the corresponding transition of the oxidic 'bulk phases' probed by *operando* XAS and XRD and is therefore completed at less negative applied potentials.[19]

Operando Raman spectroscopy provides additional information on intermediate species associated to the ec-CO_2RR. Raman modes observed at 283 cm^{-1}/253 cm^{-1}, 1050 cm^{-1}, 1584 cm^{-1} and 2031 cm^{-1}/2093 cm^{-1}/2133 cm^{-1} are attributed to adsorbed CO, HCO_3^-, and HCOOH respectively. These intermediates appear only after partial reduction of the oxide to the metallic Cu.[19]

The 'holistic view' on the potential-dependent oxide–metal transition using different complementary *operando* techniques let us safely conclude that the surface and bulk Cu oxide reduction is completed at potentials more positive than the onset of hydrocar-

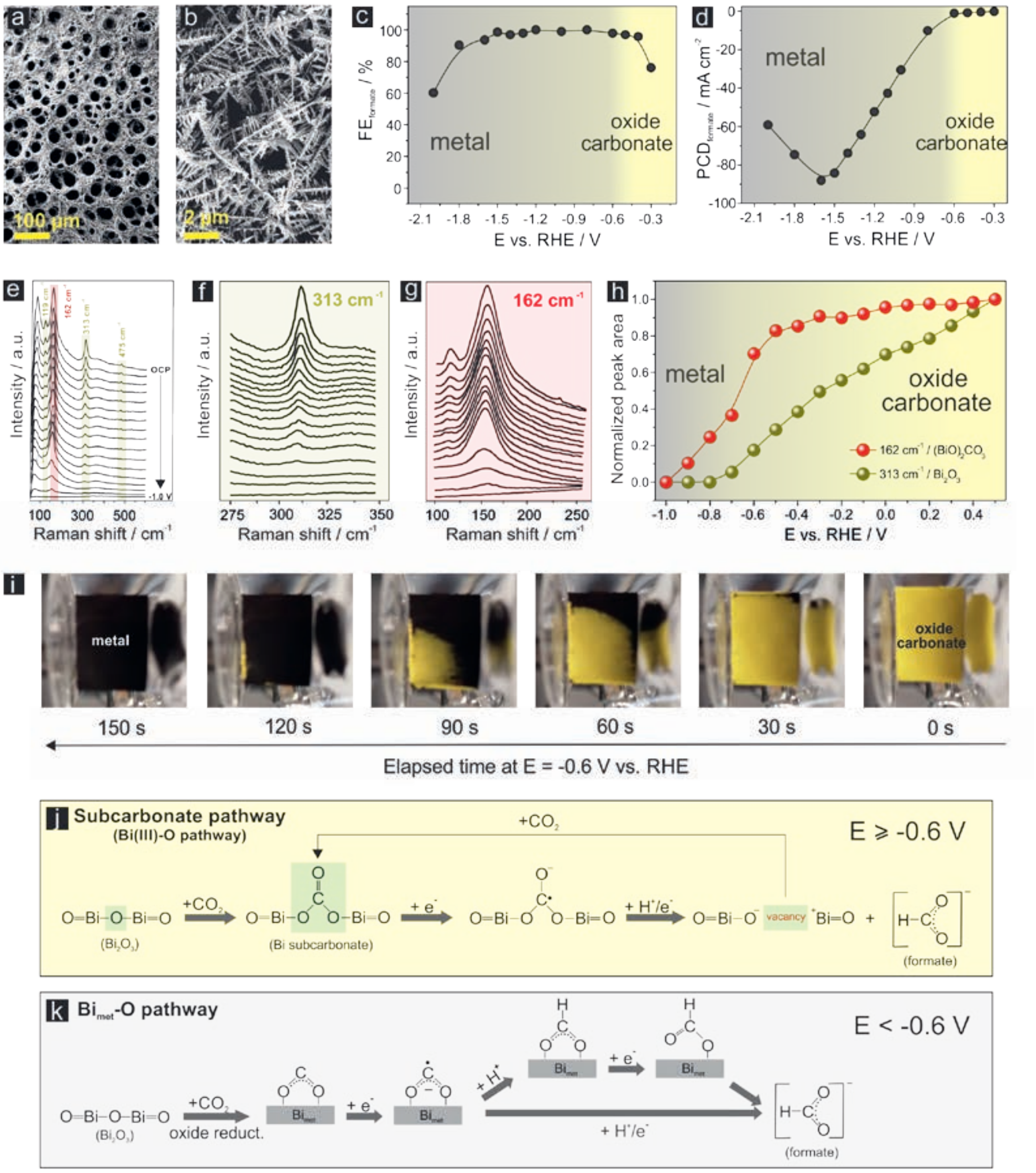

Fig. 8. (a,b) *ap* Bi/Bi$_x$O$_y$ foam deposited on a carbon cloth support (denoted Bi/Bi$_x$O$_y$@GDE); (c) CO$_2$RR product distribution represented as $FE_{formate}$ vs. E plot (*FE*: Faradaic efficiency). The annealed foam (denoted Bi$_2$O$_3$@GDE) was used as the catalyst; (d) Corresponding CO$_2$RR reaction rate represented as PCD$_{formate}$ vs. E plot (PCD: partial current density). Note that the only side-product of the CO$_2$RR is hydrogen; (e–h) *Operando* Raman spectroscopy results showing the potential-dependent oxide/sub-carbonate reduction. Raman bands at 313 cm^{-1} and 162 cm^{-1} were used to probe the presence of oxide and sub-carbonate species, respectively; (i) *Operando* optical inspection of the time-dependent oxide/sub-carbonate/metal transition in CO$_2$-sat. 0.5 M KHCO$_3$ solution at -0.6 V vs. RHE; (j,k) Proposed reaction mechanisms of formate formation. Adapted from ref. [18], with permission of the American Chemical Society.

bon and alcohol formation. Obviously, oxidic species do not play any significant role for the ec-CO$_2$RR on Cu in general and for the alcohol production in particular.

3.2 *Activation of Bi/Bi$_2$O$_3$ Foam Electrocatalysts*[18]

A novel bismuth oxide (Bi$_2$O$_3$) foam-type of catalyst (precursor) material has been produced by means of an additive-assisted DHBT electrodeposition followed by thermal annealing at 300 °C for 12 h.[18] This DHBT approach could successfully be applied to functionalize technical supports, *e.g.* gas diffusion electrodes (GDEs). This transfer of the foam catalyst from planar substrates (*e.g.* Cu foils[11]) to highly porous carbon supports is considered a crucial technical pre-requisite for any future application of this novel catalyst concept in gas-fed (CO$_2$) electrolyzer systems. The latter will be vital to achieve ec-CO$_2$RR current densities which are of technological relevance ($j_{CO2RR} > 200$ mA × cm^{-2}). It should be noted that the resulting (surface) pore sizes are altered when changing the support material.[18] In general, the pore size distribution is substantially broader when the foam materials are electrodeposited on porous carbon supports compared to respective metal foaming processes on planar metal foil supports. Fig. 8a,b shows representative top-down SEM images of the as-prepared Bi foam on the technical carbon support denoted hereafter *ap* Bi/Bi$_2$O$_3$@GDE. Note that the as-prepared oxophilic Bi foam is typically covered by an ultrathin Bi$_2$O$_3$ layer after its emersion from the Bi plating bath.[18]

The thermal treatment at 300 °C for 12 h in air leaves the macroporosity of *ap* Bi/Bi$_2$O$_3$ foam fully unaffected (see also Fig. 9), similar to the Cu case (Fig. 6). This annealing yields a fully oxidized Bi$_2$O$_3$ foam which shows a characteristic yellow color (Fig. 8i at 0 s).

The formed oxidic Bi foam exhibits a superior electrocatalytic selectivity toward formate production with Faradaic efficiencies (FEs) never falling below 90 % within an extraordinarily huge potential window of ~ 1100 mV (max. $FE_{formate}$ = 100% at –0.8 V vs. RHE).[18] Panel c and d of Fig. 8 depict the potential-dependent Faradaic efficiencies (c) and partial current densities (d) of formate production when the electrolysis is carried out from aqueous CO$_2$-sat. 0.5 M KHCO$_3$ solution.

For the first time, *operando* Raman spectroscopy provided clear experimental evidence for the embedment of CO$_2$ into an oxidic matrix (so-called 'sub-carbonate' formation) at low overpotentials prior to and during the CO$_2$ reduction reaction (Fig. 8e–h). We used the Raman bands at 313 cm^{-1} and 162 cm^{-1} as characteristic 'fingerprints' for the presence of Bi oxide and Bi subcarbonate species, respectively.[18] Note that

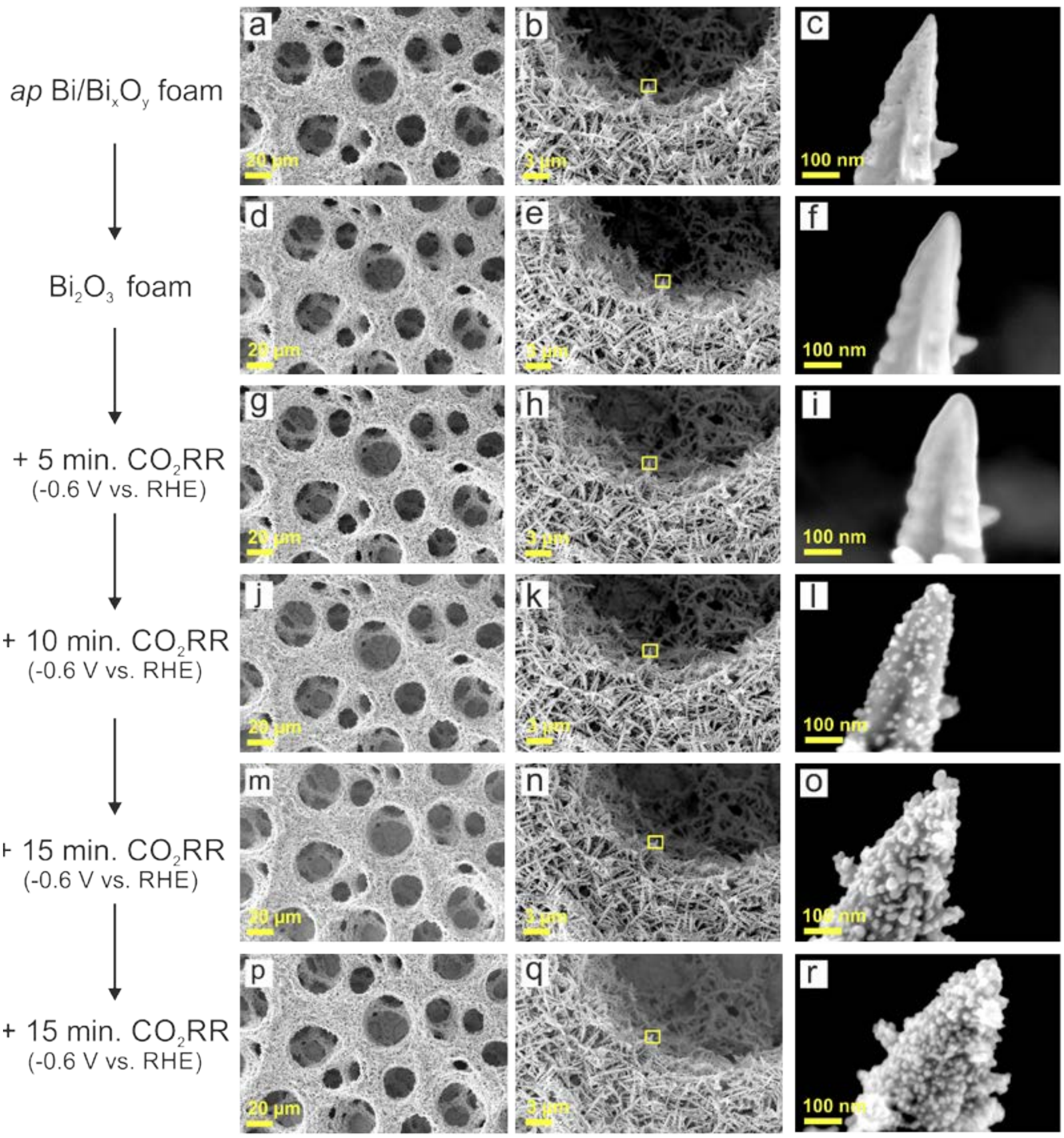

Fig. 9. (a-r) Identical location (IL) SEM inspection of morphological changes associated to the thermal annealing of the *ap* Bi/Bi$_x$O$_y$ foam, the sub-carbonate formation and subsequent potentiostatic CO$_2$ electrolysis in CO$_2$-sat. 0.5 M KHCO$_3$ solution at –0.6 V vs. RHE. Adapted from ref. [18] with permission of the American Chemical Society.

the exchange of the oxide by the sub-carbonate is a spontaneous and rather fast process which takes place in the CO$_2$-sat. 0.5 M KHCO$_3$ solution even at the open circuit potential without initiating the ec-CO$_2$RR. Indeed, the potential-dependent integrated intensities of the Raman bands at 313 cm^{-1} and 162 cm^{-1} suggest that formed sub-carbonate species are more stable than the corresponding oxides (Fig. 8h). As shown in Fig. 8i, this transition from the oxide/sub-carbonate to the metallic Bi state is accompanied by a characteristic color change from yellow (oxide) to black (metal).

These excellent electrocatalytic characteristics of the novel Bi foam catalysts result from the coupling of two distinct reaction pathways of formate formation which are active (i) in the presence of the (partly-reduced) Bi$_2$O$_3$ foam at low overpotentials (sub-carbonate pathway) and (ii) on the corresponding metallic Bi foam catalyst at medium and high overpotentials (Bi-O pathway). The reaction mechanisms, proposed also on the basis of the *operando* Raman results, are displayed in Fig. 8j,k. To probe in more detail the structural and morphological changes which take place on the nanometer length scale upon sub-carbonate formation and partial electro-reduction of the oxidic precursor during ec-CO$_2$RR we further applied the identical location (IL) scanning electron microscopy (SEM) technique by sequentially imaging the same single spot on the catalyst surface after the initial electrodeposition (as prepared), after the thermal annealing treatment, and after a series of dedicated CO$_2$ electrolyses. The results of this IL-SEM analysis are depicted in Fig. 9 and demonstrate severe morphological changes on the nm length scale which go along with (i) the oxidation upon thermal annealing, (ii) the sub-carbonate formation when exposed to the CO$_2$-sat. bicarbonate solution, and (iii) the ensuing catalyst electro-reduction into the metallic state at higher applied overpotentials.

These microscopic results impressively demonstrate that the actually active catalyst forms only under reactive conditions.

4. Conclusions

Herein we have demonstrated the usefulness of advanced *operando* analytical techniques to probe the (chemical) state evolution of foam-type catalysts under reactive conditions, *e.g.* in the course of CO$_2$ electrolysis. In particular for the case of Cu foams and their oxidic precursors it could be shown that a complementary *operando* analysis approach is mandatory to derive a full understanding of the catalyst activation process which involves the potential-driven electro-reduction of the oxidic precursors. Due to intrinsic technical limitations associated with each applied *operando* technique (*e.g.* XAS, XRD, and Raman spectroscopy) the probed potential dependence of the observed structural and compositional alterations is slightly different in all cases. However, from all applied *operando* techniques it can be concluded that the oxide–metal transition is completed prior to the onset of hydrocarbon or alcohol formation. The active Cu catalyst can be indeed considered as metallic (oxide-derived).

The understanding of the catalyst activation process is, however, much more complex in case of Bi foams and their oxidic counterparts. As evidenced by the comparison of *operando* Raman spectroscopy results and corresponding electrochemical performance testing, both the oxidic and the metallic foams are active towards ec-CO$_2$RR (formate production). The scenario becomes even more complex due to the rapid exchange of oxidic species by sub-carbonates in the presence of (dissolved) CO$_2$ in the electrolyte solution. It is the coupling of two distinct reaction pathways of formate production (sub-carbonate pathway at low overpotentials; Bi-O pathway at high overpotentials) that leads to the extraordinarily broad potential window of ~1100 mV in which the Faradaic efficiency of formate production does not fall below 90%.

Acknowledgments

M.R. and K.K. acknowledge the financial support by the Swiss Government Excellence Scholarship (ESKAS). S. V. acknowledges support from the National Research, Development and Innovation Office of Hungary (NKFIH grant FK135375). P.B. acknowledges the financial support by the NCCR Catalysis and by the Swiss National Science Foundation (SNSF, Grant code 200020_172507).

Received: July 1, 2021

[1] E. V. Kondratenko, G. Mul, J. Baltrusaitis, G. O. Larrazabal, J. Perez-Ramirez, *Energy Environ. Sci.* **2013**, *6*, 3112, https://doi.org/10.1039/C3EE41272E

[2] M. Fasihi, O. Efimova, C. Breyer, *J. Clean. Prod.* **2019**, *224*, 957, https://doi.org/10.1016/j.jclepro.2019.03.086

[3] S. Fujikawa, R. Selyanchyn, T. Kunitake, *Polym. J.* **2021**, *53*, 111, https://doi.org/10.1038/s41428-020-00429-z

[4] N. McQueen, K. V. Gomes, C. McCormick, K. Blumanthal, M. Pisciotta, J. Wilcox, *Prog. Energy* **2021**, *3*, 032001, https://doi.org/10.1088/2516-1083/abf1ce

[5] T. Haas, R. Krause, R. Weber, M. Demler, G. Schmid, *Nat. Catal.* **2018**, *1*, 32, https://doi.org/10.1038/s41929-017-0005-1

[6] N. Kittner, F. Lill, D. M. Kammen, *Nat. Energy* **2017**, *2*, 17125, https://doi.org/10.1038/nenergy.2017.125

[7] B. D. Solomon, K. Krishna, *Energy Policy* **2011**, *39*, 7422, https://doi.org/10.1016/j.enpol.2011.09.009

[8] A. V. Rudnev, Y.-C. Fu, I. Gjuroski, F. Stricker, J. Furrer, N. Kovács, S. Vesztergom, P. Broekmann, *ChemPhysChem* **2017**, *18*, 3153, https://doi.org/10.1002/cphc.201700737

[9] J. Durst, A. Rudnev, A. Dutta, Y. Fu, J. Herranz, V. Kaliginedi, A. Kuzume, A. A. Permyakova, Y. Paratcha, P. Broekmann, T. J. Schmidt, *Chimia* **2015**, *69*, 769, https://doi.org/10.2533/chimia.2015.769

[10] Y. Hori, in 'Modern Aspects of Electrochemistry', Springer, New York, **2008**, 89, https://doi.org/10.1007/978-0387-49489-0_3.

[11] A. Dutta, M. Rahaman, N. C. Luedi, M. Mohos, P. Broekmann, *ACS Catal.* **2016**, *6*, 3804, https://doi.org/10.1021/acscatal.6b00770

[12] J. Quinson, S. Neumann, T. Wannmacher, L. Kacenauskaite, M. Inaba, J. Bucher, F. Bizzotto, S. B. Simonsen, L. T. Kuhn, D. Bujak, A. Zana, M. Arenz, S. Kunz, *Angew. Chem. Int. Ed.* **2018**, *57*, 12338, https://doi.org/10.1002/anie.201807450

[13] M. de Jesus Gálvez-Vázquez, P. Moreno-García, H. Xu, Y. Hou, H. Hu, I. Z. Montiel, A. V. Rudnev, S. Alinejad, V. Grozovski, B. J. Wiley, M. Arenz, P. Broekmann, *ACS Catal.* **2020**, *10*, 13096, https://doi.org/10.1021/acscatal.0c03609

[14] M. d. J. Gálvez-Vázquez, S. Alinejad, H. Hu, Y. Hou, P. Moreno-García, A. Zana, G. K. H. Wiberg, P. Broekmann, M. Arenz, *Chimia* **2019**, *73*, 922, https://doi.org/10.2533/chimia.2019.922

[15] H. C. Shin, M. Liu, *Chem. Mater.* **2004**, *16*, 5460, https://doi.org/10.1021/cm048887b

[16] H. C. Shin, J. Dong, M. Liu, *Adv. Mater.* **2004**, *16*, 237, https://doi.org/10.1002/adma.200305660

[17] S. Vesztergom, A. Dutta, M. Rahaman, K. Kiran, I. Zelocualtecatl Montiel, P. Broekmann, *ChemCatChem* **2021**, *13*, 1039, https://doi.org/10.1002/cctc.202001145

[18] A. Dutta, I. Zelocualtecatl Montiel, K. Kiran, A. Rieder, V. Grozovski, L. Gut, P. Broekmann, *ACS Catal.* **2021**, *11*, 4988, https://doi.org/10.1021/acscatal.0c05317

[19] A. Dutta, M. Rahaman, B. Hecker, J. Drnec, K. Kiran, I. Zelocualtecatl Montiel, D. Jochen Weber, A. Zanetti, A. Cedeño López, I. Martens, P. Broekmann, M. Oezaslan, *J. Catal.* **2020**, *389*, 592, https://doi.org/10.1016/j.jcat.2020.06.024

[20] A. Dutta, M. Rahaman, M. Mohos, A. Zanetti, P. Broekmann, *ACS Catal.* **2017**, *7*, 5431, https://doi.org/10.1021/acscatal.7b01548

[21] M. G. Kibria, C.-T. Dinh, A. Seifitokaldani, P. De Luna, T. Burdyny, R. Quintero-Bermudez, M. B. Ross, O. S. Bushuyev, F. P. García de Arquer, P. Yang, D. Sinton, E. H. Sargent, *Adv. Mater.* **2018**, *30*, 1804867, https://doi.org/10.1002/adma.201804867

[22] Y. Hori, A. Murata, R. Takahashi, *J. Chem. Soc., Faraday Trans. 1* **1989**, *85*, 2309, https://doi.org/10.1039/F19898502309

[23] Y. Hori, I. Takahashi, O. Koga, N. Hoshi, *J. Phys. Chem. B* **2002**, *106*, 15, https://doi.org/10.1021/jp013478d

[24] S. Ma, M. Sadakiyo, R. Luo, M. Heima, M. Yamauchi, P. J. A. Kenis, *J. Power Sources* **2016**, *301*, 219, https://doi.org/10.1016/j.jpowsour.2015.09.124

[25] J. J. Kim, D. P. Summers, K. W. Frese, *J. Electroanal. Chem.* **1988**, *245*, 223, https://doi.org/10.1016/0022-0728(88)80071-8

[26] K. P. Kuhl, T. Hatsukade, E. R. Cave, D. N. Abram, J. Kibsgaard, T. F. Jaramillo, *J. Am. Chem. Soc.* **2014**, *136*, 14107, https://doi.org/10.1021/ja505791r

[27] M. Rahaman, K. Kiran, I. Z. Montiel, V. Grozovski, A. Dutta, P. Broekmann, *Green Chem.* **2020**, *22*, 6497, https://doi.org/10.1039/D0GC01636E

[28] M. Rahaman, A. Dutta, A. Zanetti, P. Broekmann, *ACS Catal.* **2017**, *7*, 7946, https://doi.org/10.1021/acscatal.7b02234

[29] R. Kas, R. Kortlever, A. Milbrat, M. T. M. Koper, G. Mul, J. Baltrusaitis, *Phys. Chem. Chem. Phys.* **2014**, *16*, 12194, https://doi.org/10.1039/C4CP01520G

[30] C. W. Li, J. Ciston, M. W. Kanan, *Nature* **2014**, *508*, 504, https://doi.org/10.1038/nature13249

[31] K. W. Frese, *J. Electrochem. Soc.* **1991**, *138*, 3338, https://doi.org/10.1149/1.2085411

[32] M. Ma, K. Djanashvili, W. A. Smith, *Phys. Chem. Chem. Phys.* **2015**, *17*, 20861, https://doi.org/10.1039/C5CP03559G

[33] D. Gao, I. Zegkinoglou, N. J. Divins, F. Scholten, I. Sinev, P. Grosse, B. Roldan Cuenya, *ACS Nano* **2017**, *11*, 4825, https://doi.org/10.1021/acsnano.7b01257

[34] C. W. Li, M. W. Kanan, *J. Am. Chem. Soc.* **2012**, *134*, 7231, https://doi.org/10.1021/ja3010978

[35] B. Beverskog, I. Puigdomenech, *J. Electrochem. Soc.* **1997**, *144*, 3476, https://doi.org/10.1149/1.1838036

[36] A. Verdaguer-Casadevall, C. W. Li, T. P. Johansson, S. B. Scott, J. T. McKeown, M. Kumar, I. E. L. Stephens, M. W. Kanan, I. Chorkendorff, *J. Am. Chem. Soc.* **2015**, *137*, 9808, https://doi.org/10.1021/jacs.5b06227

[37] H. Mistry, A. S. Varela, C. S. Bonifacio, I. Zegkinoglou, I. Sinev, Y. W. Choi, K. Kisslinger, E. A. Stach, J. C. Yang, P. Strasser, B. R. Cuenya, *Nat. Commun.* **2016**, 7, https://doi.org/10.1038/ncomms12123

[38] A. Eilert, F. Cavalca, F. S. Roberts, J. Osterwalder, C. Liu, M. Favaro, E. J. Crumlin, H. Ogasawara, D. Friebel, L. G. M. Pettersson, A. Nilsson, *J. Phys. Chem. Lett.* **2017**, *8*, 285, https://doi.org/10.1021/acs.jpclett.6b02273

[39] F. Cavalca, R. Ferragut, S. Aghion, A. Eilert, O. Diaz-Morales, C. Liu, A. L. Koh, T. W. Hansen, L. G. M. Pettersson, A. Nilsson, *J. Phys. Chem. C* **2017**, *121*, 25003, https://doi.org/10.1021/acs.jpcc.7b08278

[40] M. Fields, X. Hong, J. K. Nørskov, K. Chan, *J. Phys. Chem. C* **2018**, *122*, 16209, https://doi.org/10.1021/acs.jpcc.8b04983

[41] A. J. Garza, A. T. Bell, M. Head-Gordon, *J. Phys. Chem. Lett.* **2018**, *9*, 601, https://doi.org/10.1021/acs.jpclett.7b03180

[42] P. Grosse, D. Gao, F. Scholten, I. Sinev, H. Mistry, B. Roldan Cuenya, *Angew. Chem. Int. Ed.* **2018**, *57*, 6192, https://doi.org/10.1002/anie.201802083

[43] K. J. J. Mayrhofer, S. J. Ashton, J. C. Meier, G. K. H. Wiberg, M. Hanzlik, M. Arenz, *J. Power Sources* **2008**, *185*, 734, https://doi.org/10.1016/j.jpowsour.2008.08.003

[44] T. Kottakkat, K. Klingan, S. Jiang, Z. P. Jovanov, V. H. Davies, G. A. M. El-Nagar, H. Dau, C. Roth, *ACS Appl. Mater. Interfaces* **2019**, *11*, 14734, https://doi.org/10.1021/acsami.8b22071

[45] M. R. Antonio, L. Soderholm, I. Song, *J. Appl. Electrochem.* **1997**, *27*, 784, https://doi.org/10.1023/A:1018464526864

[46] I. Martens, R. Chattot, M. Rasola, M. V. Blanco, V. Honkimäki, D. Bizzotto, D. P. Wilkinson, J. Drnec, *ACS Appl. Energy Mater.* **2019**, *2*, 7772, https://doi.org/10.1021/acsaem.9b00982

[47] A. Dutta, A. Kuzume, M. Rahaman, S. Vesztergom, P. Broekmann, *ACS Catal.* **2015**, *5*, 7498, https://doi.org/10.1021/acscatal.5b02322

[48] A. Dutta, A. Kuzume, V. Kaliginedi, M. Rahaman, I. Sinev, M. Ahmadi, B. R. Cuenya, S. Vesztergom, P. Broekmann, *Nano energy* **2018**, *53*, 828, https://doi.org/10.1016/j.nanoen.2018.09.033

[49] A. Dutta, C. E. Morstein, M. Rahaman, A. Cedeño López, P. Broekmann, *ACS Catal.* **2018**, *8*, 8357, https://doi.org/10.1021/acscatal.8b01738

[50] A. Dutta, I. Z. Montiel, R. Erni, K. Kiran, M. Rahaman, J. Drnec, P. Broekmann, *Nano Energy* **2020**, *68*, 104331, https://doi.org/10.1016/j.nanoen.2019.104331

License and Terms

7.8. Suppression of the Hydrogen Evolution Reaction is the Key: Selective Electrosynthesis of Formate from CO_2 over Porous $In_{55}Cu_{45}$ Catalyst

Reprinted with permissions from ACS Appl. Mater. Interfaces 2021, 13, 35677−35688, Copyright 2021 American Chemical Society.

Authors: Motiar Rahaman, Kiran Kiran, **Ivan Zelocualtecatl Montiel**, Abhijit Dutta, Peter Broekmann

ACS Appl. Mater. Interfaces 2021, **13**, 35677-35688, DOI: https://doi.org/10.1021/acsami.1c07829

Highlights: This work reports the synthesis, characterization, and electrochemical performance in an H-type cell of a novel porous $In_{55}Cu_{45}$@Cu alloy catalyst for highly selective electrochemical reduction of CO_2 to formate. The $In_{55}Cu_{45}$ catalyst was synthesized using the dynamic hydrogen bubble template electrodeposition approach, giving a very high-surface-area material. Through an electrochemical performance was found that the FEformate never fell below 90% ($PCD_{formate}$ ~–8.9 $mA.cm^{-2}$) within a relatively broad potential range (–0.8 to –1.2 V *vs.* RHE); without leaving aside that the catalyst present high stability and high suppression of HER, which was demonstrated for a long-term experiment at –1.0 V *vs.* RHE. Both the faradaic efficiency ($FE_{formate}$ = 94.2%) and the partial current density ($PCD_{formate}$ = –8.2 mA cm^{-2}). Scanning electron microscopy images before and after electrolysis experiments shows that the catalyst morphology seems to be unaffected on a µm-length scale; however, minor morphological changes are visible on a nm-length scale. The use of *operando* Raman spectroscopy gives an idea about the possible pathway for formate production in the $In_{55}Cu_{45}$ alloy catalyst. Finally, the metal electrodeposition approach was transferred to a technically relevant porous GDE supports, where only small changes in the product distribution were observed; however, a dramatic increase in the PCD was obtained.

Contributions: In this project, I was involved in conducting ICP-MS studies and *operando* Raman experiments. In addition, I participated in the manuscript revision process.

ACS APPLIED MATERIALS & INTERFACES

Suppression of the Hydrogen Evolution Reaction Is the Key: Selective Electrosynthesis of Formate from CO_2 over Porous $In_{55}Cu_{45}$ Catalysts

Motiar Rahaman,*,§ Kiran Kiran,*,§ Ivan Zelocualtecatl Montiel, Abhijit Dutta, and Peter Broekmann*

Cite This: *ACS Appl. Mater. Interfaces* 2021, 13, 35677−35688 Read Online

ACCESS | Metrics & More | Article Recommendations | Supporting Information

ABSTRACT: Direct electrosynthesis of formate through CO_2 electroreduction (denoted CO_2RR) is currently attracting great attention because formate is a highly valuable commodity chemical that is already used in a wide range of applications (e.g., formic acid fuel cells, tanning, rubber production, preservatives, and antibacterial agents). Herein, we demonstrate highly selective production of formate through CO_2RR from a CO_2-saturated aqueous bicarbonate solution using a porous $In_{55}Cu_{45}$ alloy as the electrocatalyst. This novel high-surface-area material was produced by means of an electrodeposition process utilizing the dynamic hydrogen bubble template approach. Faradaic efficiencies (FEs) of formate production ($FE_{formate}$) never fell below 90% within a relatively broad potential window of approximately 400 mV, ranging from −0.8 to −1.2 V *vs* the reversible hydrogen electrode (RHE). A maximum $FE_{formate}$ of 96.8%, corresponding to a partial current density of $j_{formate} = -8.9$ mA cm^{-2}, was yielded at −1.0 V *vs* RHE. The experimental findings suggested a CO_2RR mechanism involving stabilization of the HCOO* intermediate on the $In_{55}Cu_{45}$ alloy surface in combination with effective suppression of the parasitic hydrogen evolution reaction. What makes this CO_2RR alloy catalyst particularly valuable is its stability against degradation and chemical poisoning. An almost constant formate efficiency of ∼94% was maintained in an extended 30 h electrolysis experiment, whereas pure In film catalysts (the reference benchmark system) showed a pronounced decrease in formate efficiency from 82% to 50% under similar experimental conditions. The identical location scanning electron microscopy approach was applied to demonstrate the structural stability of the applied $In_{55}Cu_{45}$ alloy foam catalysts at various length scales. We demonstrate that the proposed catalyst concept could be transferred to technically relevant support materials (e.g., carbon cloth gas diffusion electrode) without altering its excellent figures of merit.

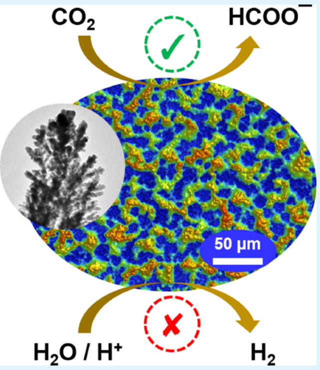

KEYWORDS: *CO_2 conversion, formate electrosynthesis, indium−copper alloy, hydrogen evolution reaction (HER) suppression, technical support*

1. INTRODUCTION

The electrochemical reduction of CO_2 (hereafter, CO_2RR) is considered a feasible approach to mitigate the constantly raising levels of CO_2 in the atmosphere and its harmful impact on the global climate.[1−4] CO_2RR provides a means of producing value-added platform chemicals from CO_2 in a highly sustainable manner, particularly when a surplus of renewables from solar, wind, and hydro energy sources is used to power the highly endergonic CO_2 conversion process.

Formate is regarded a valuable CO_2RR product that has utility in various sectors. Its potential as a future energy carrier in advanced fuel-cell technologies is currently being explored.[5,6] In the chemical industry, it finds wide use as a solvent and reactant for neutralization reactions. In the textile industry, it is used as a tanning agent in the production of leather goods.[7−9] In many products of our daily life, formate and formic acid serve as preserving agents.[10] Current efforts to use CO_2RR for the electrosynthesis of formate are further motivated by analyses suggesting that from an economic standpoint, the electrochemical approach might be competitive with existing mature synthesis routes.[11−15]

A key aspect of designing an efficient CO_2RR process concerns the catalyst material, which is essential not only to accelerate the inherently slow CO_2RR process but also to increase its energy efficiency by lowering the required overpotentials. In addition, the chemical nature and morphological characteristics of the catalyst material ultimately dictate the resulting CO_2RR product distribution.[16−19] In their pioneering work, Hori et al. grouped monometallic catalysts into three categories according to the observed main product of the CO_2RR process.[20] The first category of catalysts was

Received: April 28, 2021
Accepted: July 8, 2021
Published: July 21, 2021

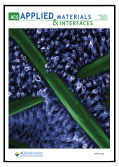

https://doi.org/10.1021/acsami.1c07829

found to predominantly produce formate (e.g., Sn, Pb, Hg, Cd, and Tl); the post-transition metal indium (In) also belongs to this formate-producing group of catalysts. The second category of metallic CO_2RR catalysts, which included but was not restricted to Ag and Au, showed a high product selectivity toward CO. Copper stands out as a unique material because it was identified as the only catalyst that can form hydrocarbons and alcohols from CO_2RR by allowing C−C coupling reactions.[20−28]

Combining two metallic catalysts from different groups of Hori et al.'s classification scheme has demonstrated promise in various aspects.[29−31] Among these, one benefit of such a two-component catalyst system could be the increase in CO_2RR selectivity toward a certain target product that is predominantly or exclusively formed on one of the catalyst constituents. The role of the secondary (nondominant) constituent is to further promote one particular CO_2RR pathway on the primary (dominant) catalyst component. A prime example is the combination of a CO former (e.g., Ag or Pd, nondominant constituent) with Cu (C−C coupler; dominant constituent), where spillover effects of CO intermediates from the nondominant constituent (Ag or Pd) to the Cu sites are discussed as the mechanistic origin of the improved faradaic yields toward higher alcohols (ethanol and 1-propanol).[32−36]

Another outcome of combining two metallic catalysts from different groups of Hori et al.'s classification scheme could be to alter the CO_2RR product selectivity in such a way that it becomes atypical for the respective two pure monometallic constituents of the mixed system. Examples are co-alloyed In_xCu_y systems, which often demonstrate high CO_2RR selectivities toward CO.[37−40] This is atypical in particular for the In component, which, in its monometallic form, belongs to the group of formate-producing catalysts.[20,41−44] In principle, CO forms on Cu but mainly as an intermediate that is typically converted further into hydrocarbons or higher alcohols, particularly at higher negative overpotentials. For the reported CO-forming In_xCu_y systems, Cu can be considered as the dominant catalyst component and In correspondingly as the nondominant (auxiliary) component. Its mechanistic role in the course of the multistep CO_2 conversion is to weaken the Cu−CO bond. This concept of weakening the metal−CO (M−CO) binding strength by a co-alloyed metal is well known from other two-component catalyst systems, for example, from binary Au_xCu_y, Ag_xCu_y, and Pd_xCu_y alloys.[45−47] This weakening of the Cu−CO bond, mediated by In, gives rise to the facile release of CO from the Cu sites of the alloy catalyst surface, thereby preventing any further reaction of intermediates in terms of C−C coupling or multicarbon formation. For monometallic systems, Kuhl et al. identified M−CO binding strength as a key descriptor for the resulting CO_2RR product distribution, demonstrating a volcano-like behavior, with (pure) Cu being located on the side of a high M−CO binding strength close to the volcano peak.[48] According to this consideration, the reported In_xCu_y alloys[37−40] need to be placed on the "low-binding" side of the volcano (compared with pure Cu), where catalysts such as Au and Ag are found to demonstrate lower M−CO binding strengths and facile release of CO as the main CO_2RR product.

In this study, we report a novel dendritic $In_{55}Cu_{45}$ alloy catalyst that differs substantially from those reported so far in the literature. In this $In_{55}Cu_{45}$ alloy, In is the dominant catalyst component governing CO_2RR product distribution, with a clear preference toward formate formation, whereas the electrocatalytic characteristics of Cu in terms of (intermediate) CO, hydrocarbon, and alcohol formation remain fully suppressed. Note that when brought into a highly dendritic form, a pure Cu catalyst also demonstrates a high formate selectivity of ∼50%, particularly at moderate overpotentials (at −0.7 V *vs* RHE).[28] Herein, we will demonstrate that the presence of Cu in the dendritic $In_{55}Cu_{45}$ alloy further boosts faradaic efficiency ($FE_{formate}$) values to 96.8% at −1.0 V *vs* RHE, yielding a partial current density ($PCD_{formate}$) of −8.9 mA cm^{-2}, which is considered excellent for electrolyses in H-type cells.

The most beneficial effect of co-alloying In and Cu on catalytic performance concerns, however, is its long-term stability. The $In_{55}Cu_{45}$ catalyst shows remarkable catalytic stability at −1.0 V *vs* RHE for 30 h with a constant production rate of formate ($FE_{formate} = 94.2 \pm 2.1\%$). On the other hand, pure In electrocatalysts undergo severe degradation during extended CO_2 electrolysis, which typically results in a drastic increase in the parasitic hydrogen evolution reaction (HER) at the expense of formate yields.

2. EXPERIMENTAL METHODS

2.1. Materials and Chemicals. The Cu foil (99.9% pure), serving as the support material for the alloy foam electrodeposition, was purchased from Alfa Aesar and cut into pieces of 8 mm × 30 mm. For X-ray diffraction (XRD) analysis, alloy foam was deposited on a graphite foil substrate (0.25 mm thick, 99.8%, Alfa Aesar) to omit the contribution from the Cu foil support to the XRD pattern.

$In_2(SO_4)_3{\cdot}xH_2O$ (Sigma-Aldrich, 99.99%) and $CuSO_4{\cdot}5H_2O$ (Sigma-Aldrich, 99.99%) were used as metal precursors for the metal foam electrodeposition. ACS-grade H_2SO_4 (Sigma-Aldrich) was used to prepare the plating bath. $KHCO_3$ (99.7%) was purchased from Sigma-Aldrich and used to prepare the electrolyte for the CO_2 electrolyses. All chemicals were used as received without further purification.

Milli-Q water (18.2 MΩ cm, 4 ppb of total organic carbon content; Millipore) was used to prepare all the solutions.

2.2. Catalyst Preparation. The Cu foil substrate was first electropolished in 50% orthophosphoric acid (ACS grade, Sigma-Aldrich) to remove contamination and the native oxide layer from its surface. For this purpose, a two-electrode arrangement was used, with graphite and Cu foil serving as a cathode and anode, respectively. For the electropolishing treatment, a potential difference of 2 V was applied for ∼2 min. The Cu foil was then thoroughly rinsed with Milli-Q water, sonicated for 15 min in absolute ethanol (Merck, Germany), and finally dried in air before using it as the support for the foam electrodeposition. Before electrodeposition, the Cu support was masked with insulating PTFE tape, defining a geometrical surface area (A_{geo}) of 1 cm^2. The $In_{55}Cu_{45}$ alloy electrodeposition was carried out from a 1.5 M H_2SO_4 electrolyte (pH ≈ 0.5) containing 20 mM indium sulfate and 5 mM copper sulfate precursor salts (25 mM total metal ion concentration). For the electrodeposition, a three-electrode arrangement was used, consisting of the electropolished and masked Cu foil, a Pt foil (4 cm × 3 cm), and an $Ag/AgCl_{3M}$ electrode (Metrohm) acting as the working electrode (WE), counter electrode (CE), and reference electrode (RE), respectively. The electrodeposition was carried out in galvanostatic mode (Metrohm Autolab 128N potentiostat; Autolab 10 A current booster; Metrohm Autolab, Utrecht, the Netherlands) by applying a constant current density of −3 A cm^{-2} for 30 s. The resulting catalyst film was denoted $In_xCu_y@Cu$. After the electrodeposition process, the alloyed In_xCu_y metal foams were carefully rinsed with Milli-Q water to remove residuals of the plating bath from the surface and interior of the porous catalyst material. The electrochemically active surface areas (ECSAs) of the alloy foam catalysts were determined by means of a cyclic voltammetry approach using dimethyl viologen as a reversible redox probe. The ECSA determination procedure and possible shortcomings have been described in detail elsewhere.[27]

The same deposition protocol was transferred to graphite and carbon (fiber) cloth (gas diffusion electrode, GDE) supports; the resulting catalyst films were denoted In_xCu_y@C and In_xCu_y@GDE, respectively. Before electrodeposition, the graphite foil (Alfa Aesar, 99.8%) was activated by annealing at 500 °C for 6 h, washing in a 1:1 acetone:water mixture, and finally drying at 100 °C for 1 h.

A 20 cm × 20 cm carbon cloth (GDE) was purchased from Fuel Cell (USA). This carbon cloth is covered on both sides with an extra mesoporous carbon layer (C-MPL, see the Supporting Information), facilitating the adhesion of the electrodeposited metallic foam to the support. The total thickness of the carbon cloth is ∼385 μm. The carbon fiber cloths were used as received.

2.3. CO_2 Electrolysis Experiments. A 128N potentiostat/galvanostat (Metrohm Autolab) was used for all electrochemical measurements. Cell resistance was measured by means of impedance spectroscopy before each CO_2 electrolysis experiment. A custom-made H-type glass cell was used for the CO_2RR experiments, where the cathode and anode compartments were separated by a proton exchange Nafion membrane (Nafion 117, Electrochem, USA). All experiments were performed at room temperature under ambient conditions. CO_2RR experiments were performed in a three-electrode configuration using aqueous 0.5 M $KHCO_3$ solution as the electrolyte. The dendritic In_xCu_y catalyst served as the WE, a leakless Ag/$AgCl_{3M}$ (EDAQ) electrode served as the RE, and a Pt foil (20 mm × 5 mm, 99.9%, Alfa Aesar) was used as the CE, where the water oxidation (counter reaction) took place. All potentials reported herein are *iR*-corrected. Prior to the CO_2 electrolysis, both the anode and cathode compartments (containing 0.5 M $KHCO_3$ electrolyte) were purged with CO_2 (99.9999%, Carbagas, Switzerland) for at least for 30 min to obtain a CO_2-saturated (sat.) 0.5 M $KHCO_3$ buffer electrolyte (pH = 7.2). The cathode compartment, having a headspace of approximately 12 mL, was constantly purged with CO_2 during the electrolysis.

Keeping pH dependency in mind, all the measured potentials *vs* the Ag/$AgCl_{3M}$ electrode were converted into RHE using the equation below:

$$E_{\mathrm{RHE}}(\mathrm{V}) = E_{\mathrm{Ag/AgCl}}3\mathrm{M}(\mathrm{V}) + 0.210\ \mathrm{V} + (0.0591\ \mathrm{V} \times \mathrm{pH}) \tag{1}$$

Quantification of gaseous and liquid products by gas chromatography and ion-exchange chromatography is described in detail elsewhere.[28]

From the X-ray photoelectron spectroscopy (XPS) and post-electrolysis inductively coupled plasma optical emission spectroscopy (ICP-OES) measurements, no traces of Pt were detected on the catalyst surface or in the electrolyte. Any Pt cross-contamination originating from the anode during electrodeposition or during the CO_2 electrolysis experiments can thus be excluded.

2.4. Scanning Electron Microscopy (SEM) and Energy-Dispersive X-ray Spectroscopy (EDX). An FE Zeiss DSM 982 and a Zeiss Gemini 450 scanning electron microscopy (SEM) instrument were used to analyze the catalyst morphology. The composition was studied by using a Noran SIX NSS200 energy-dispersive X-ray (EDX) spectrometer.

2.5. X-ray Diffraction (XRD) Analysis. XRD was carried out by means of powder XRD (Bruker D8) using Cu Kα radiation (λ = 0.1540 nm, 40 mA) at 40 keV. A range of 2θ value from 30° to 80° was recorded at a 1° min^{-1} scan rate. Joint Committee on Powder Diffraction (JCPD) standards for pure Cu and In metals, as well as for the bimetallic alloy, were used for comparison purposes to analyze the measured XRD patterns of the In_xCu_y material. To avoid undesired contributions from the Cu foil substrate to the measured XRD pattern, an activated graphite foil was used as the support for all XRD analyses.

2.6. X-ray Photoelectron (XPS) Spectroscopy. XPS analyses were carried out with an Escalab 250Xi ultrahigh-vacuum photoemission instrument equipped with a monochromatic Al Kα X-ray source (spot size, 100 μm). CasaXPS software was used for the peak fitting and the peak positions were referenced to the carbon C1s peak at 285.5 eV. It is important to note that the sample specimens were not subjected to any further modification (e.g., metal sputtering) before XPS analysis.

2.7. High-Resolution Transmission Electron Microscopy (HR-TEM) and High-Angle Annular Dark-Field Scanning Transmission Electron Microscopy (HAADF-STEM). A Talos F200X G2 TEM (FEI, operating voltage 200 kV; Thermo Scientific) electron microscope was used for high-resolution transmission electron microscopy (HR-TEM) and high-angle annular dark-field scanning transmission electron microscopy (HAADF-STEM) analyses. The sample was prepared by dispersing the electrodeposited catalyst material in ethanol using a bath sonicator and drop-casted on a carbon-coated Ni grid (300 mesh) that served as the support for the HR-TEM and HAADF-STEM analyses.

2.8. Inductively Coupled Plasma Optical Emission Spectrometry (ICP-OES) and Inductively Coupled Plasma Mass Spectrometry (ICP-MS). To determine the nominal bulk composition of the electrodeposited In_xCu_y catalyst material, ICP-OES analysis was performed using an iCAP 7400 ICP-OES DUO instrument (Thermo Scientific). Before the ICP-OES measurement, the bimetallic In_xCu_y alloy was chemically dissolved in 30% HNO_3 solution. To monitor the time-dependent changes in the metal content in the electrolyte solution (CO_2-sat. 0.5 M $KHCO_3$) during electrolysis, the ICP-MS technique was applied. For the ICP-MS analysis, aliquots of 20 μL of electrolyte (CO_2-sat. 0.5 M $KHCO_3$ solution) were taken from the electrolysis cell as a function of electrolysis time and diluted in 3% nitric acid solution (501 times dilution). Each ICP measurement was repeated five times by default, these repetitive measurements served as the basis for the determination of the sample-specific values of the relative standard deviation (RSD), and ICP-MS-related RSD values are typically between 1 and 2%. An extra measuring error of ∼1.5% needs to be taken into account and is caused by the dilution treatment required for certain samples. Error bars in Figure 4 include both the instrumental error (ICP-MS) and the additional error resulting from the dilution procedure.

3. RESULTS AND DISCUSSION

3.1. Physical Characterization of the *ap*-$In_{55}Cu_{45}$ Catalyst.

The In_xCu_y alloy discussed herein was produced using the dynamic hydrogen bubble template (DHBT) approach of metal foaming[49−54] adjusted to the needs of alloy deposition and specifically optimized toward efficient formate production from CO_2. Figure 1a shows a schematic diagram of the DHBT-assisted alloy deposition. In the following, we denote the catalyst used herein as *ap*-$In_{55}Cu_{45}$ (as-prepared) according to its bulk composition determined by the quantitative ICP-OES analysis of the alloy after its oxidative dissolution into a dilute nitric acid solution (for details, see Section 2). Note that the complementary EDX analysis of the bimetallic catalyst revealed a slightly different chemical composition of 59 at % In and 41 at % Cu (Figure S1). Semiquantitative EDX has, however, only a limited probing depth and does not, therefore, necessarily represent the true bulk composition of the respective catalyst material.[32,36]

A top-down SEM inspection revealed a highly porous appearance of the *ap*-$In_{55}Cu_{45}$ catalyst material deposited on a planar Cu foil support (*ap*-$In_{55}Cu_{45}$@Cu; Figure 1b,c and Figure S2). Although the experimental conditions applied were common for the DHBT approach,[27,51] for example, in terms of applied current density (−3 A cm^{-2}), no typical foam morphology developed during the InCu co-deposition. The ratio of the concentration-dependent exchange current density of metal deposition (j^0_{depo}) and of the competing hydrogen evolution reaction (j^0_{HER}) governs actual metal foaming and, thus, the resulting film morphology.[49] Clearly, the presence of

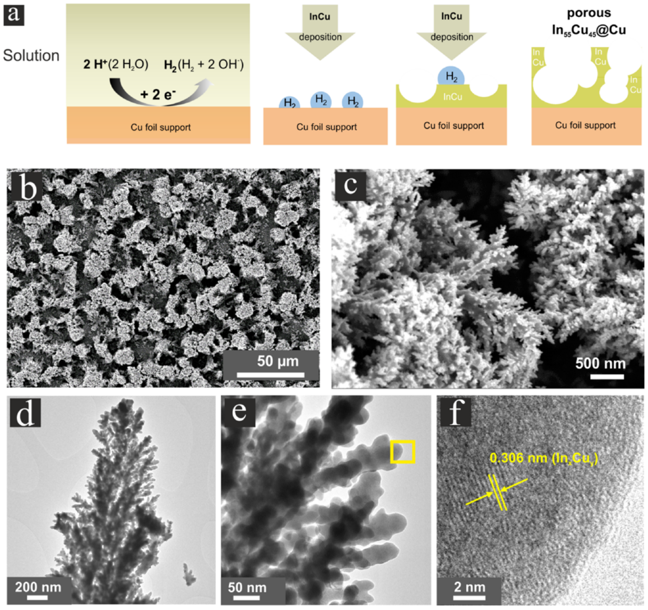

Figure 1. (a) Scheme demonstrating the principle of the dynamic hydrogen bubble template (DHBT) approach of metal foam electrodeposition using a planar Cu foil as the support. (b, c) Top-down SEM inspection of the *ap*-$In_{55}Cu_{45}$@Cu deposit. (d–f) Representative TEM and HR-TEM analysis of an isolated dendrite of the *ap*-$In_{55}Cu_{45}$@Cu sample.

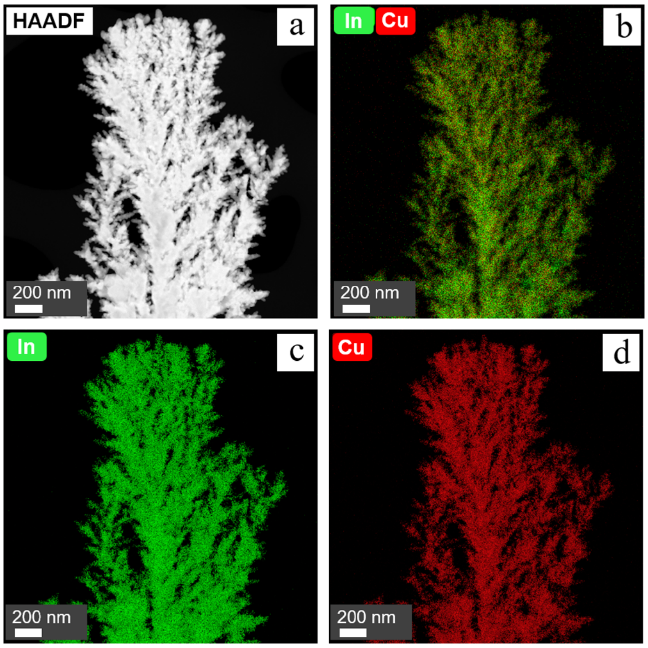

Figure 2. (a) HAADF and (b–d) STEM-EDX mapping of an isolated dendrite of the *ap*-$In_{55}Cu_{45}$ foam. This analysis confirms the homogeneous distribution of Cu and In in the bimetallic alloy material.

In had a substantial impact on the nucleation, growth, and the so-called break-off diameter of hydrogen bubbles formed on the emerging porous alloy during electrodeposition. Further support for this conclusion came from a comparative survey of morphologies showing pure Cu, pure In, and *ap*-$In_{55}Cu_{45}$ films after 30 s of deposition at an applied current density of −3 A cm^{-2} (Figure S3). Only the pure Cu deposit showed a well-developed multilevel foam morphology with interconnected open macropores,[27,51] whereas the electrodeposition of In on the Cu foil support, carried out under the same experimental conditions, resulted in a comparably smooth polycrystalline film composed of In grains with diameters in the micrometer range (In@Cu, Figure S3). In addition to their (primary) macroporosity, the *ap*-$In_{55}Cu_{45}$ deposit and the *ap*-Cu foam showed smaller dendritic features on the submicrometer length scale (Figure S3), thus introducing secondary porosity to both electrodeposits and further increasing their electrochemically active surface area (ECSA, Figure S4), which grow in the following sequence: In@Cu (1.5 cm^2) < $In_{55}Cu_{45}$@Cu (2.7 cm^2) < and Cu-foam@Cu (3.6 cm^2). The geometric surface area of the Cu foil support was identical in all three cases (A_{geo} = 1 cm^2).

White light interferometry (WLI) analysis of the *ap*-$In_{55}Cu_{45}$ deposit revealed an apparent thickness of ∼19 μm (Figure S2a,b), whereas the corresponding cross-sectional SEM inspection showed a slightly increased catalyst film thickness in the range of 20 to 23 μm (Figure S2c,d). This is because the WLI does not completely probe the porous catalyst film down to the Cu foil support.

TEM analysis showed the branch-like (dendritic) nanostructures of the $In_{55}Cu_{45}$ material (Figure 1d). A high-resolution TEM inspection (Figure 1e,f) of individual dendrites of the *ap*-$In_{55}Cu_{45}$ deposit confirmed the InCu co-alloying, resulting in the In_xCu_y fringe pattern corresponding neither to pure Cu nor to pure In (Figure 1f). The high degree of co-alloying was further supported by the spatially and chemically resolved STEM-EDX mapping of a representative dendrite feature demonstrating the homogeneous intermixing of Cu and In in the *ap*-$In_{55}Cu_{45}$ deposit (Figure 2). An XRD analysis of the *ap*-$In_{55}Cu_{45}$ material suggested the presence of well-defined intermetallic phases having an elemental composition close to an In-to-Cu ratio of 1:1 (Figure 3). Most prominent were the intermetallic InCu and In_9Cu_{11} phases (for a detailed analysis of the XRD patterns, see Table S1). Only minor contributions were visible in the diffractogram

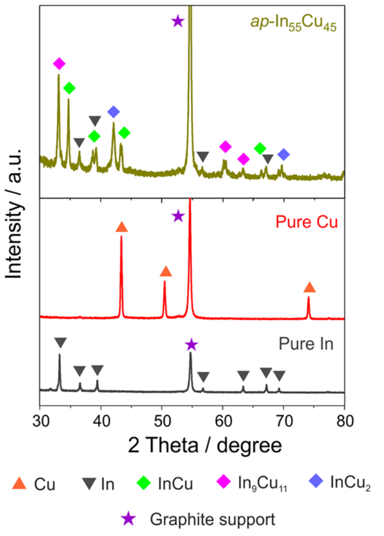

Figure 3. X-ray diffraction (XRD) pattern of the *ap*-$In_{55}Cu_{45}$ foam deposited on a graphite support. For comparison purposes, XRD patterns of pure (polycrystalline) Cu and In samples (deposited on graphite support) are also presented. For a detailed analysis based on JCPDS references, see Table S1.

https://doi.org/10.1021/acsami.1c07829
ACS Appl. Mater. Interfaces 2021, 13, 35677−35688

originating from InCu$_2$ and metallic In. All of these experimental observations were in full agreement with the phase diagram of the binary InCu system (Figure S5).[55] It is interesting to note that there is no indication in the diffractograms of the presence of (surface) oxides that are reported for pure (as-prepared) Cu foams.[27] This observation is remarkable insofar as the deposit certainly becomes more oxophilic when co-alloying Cu with In. The standard enthalpy changes of formation ($\Delta_f H^{\ominus}$) for the pure oxides might serve as a hint for the affinity of In and Cu toward (surface) oxide formation:

$$
\begin{aligned}
&|(\Delta_f H^{\ominus}_{\mathrm{In_2O_3}} = -923.5\ \mathrm{kJ\ mol^{-1}}| \\
&\quad \gg |(\Delta_f H^{\ominus}_{\mathrm{Cu_2O}} = -170\ \mathrm{kJ\ mol^{-1}}| \\
&\quad > |(\Delta_f H^{\ominus}_{\mathrm{CuO}} = -156\ \mathrm{kJ\ mol^{-1}}|
\end{aligned}
$$

The presence of a thin oxidic skin on the *ap*-In$_{55}$Cu$_{45}$ alloy, however, could be concluded from a more surface-sensitive XPS analysis (Figure S6). The spin-orbit split In3d photoemission, shown in Figure S6b, is deconvoluted by assuming two In species with a binding energies of BE(In3d$_{5/2}$) = 443.9 eV and BE(In3d$_{5/2}$) = 444.9 eV assigned to metallic In(0) and In(III), respectively. The dominance of the In(III) species in the In3d photoemission clearly indicates the presence of a thin oxide layer, whereas the In(0)-related photoemission most likely results from contributions of the metallic In$_{55}$Cu$_{45}$ bulk. The corresponding Cu2p$_{3/2}$ emission (Figure S6c) showed a prominent peak at BE(Cu2p$_{3/2}$) = 932.7 eV and a smaller satellite feature at BE(Cu2p$_{3/2}$) = 933.5 eV. The latter can be ascribed to traces of Cu(II) species. It is important to note that the *ex situ* XPS cannot discriminate between cuprous Cu(I) and metallic Cu(0).[56,57] The dominant emission at BE-(Cu2p$_{3/2}$) = 932.7 eV might be assigned to a mixture of both Cu(I) and Cu(0) species.[58]

3.2. Structural Alterations of the *ap*-In$_{55}$Cu$_{45}$ Catalyst under Potential Control.

Note that the partially oxidized catalyst surface experiences further alterations when exposed to the electrolyte at open-circuit potential (OCP) and subsequently set under potential control. Oxides are readily reduced, in particular under the harsh experimental conditions required to operate the CO$_2$RR.[56] Such oxide reduction is typically considered as an inherent part of the catalyst activation. From online ICP-MS studies on model electrodes, it is well known that metal ions are preferentially released into an electrolyte solution upon reduction of the formed (surface) oxides.[59−61] Similar observations have recently been made for the *in situ* activation of thermally annealed Pd$_x$Cu$_y$ alloy foam catalysts under CO$_2$ electrolysis conditions.[36] Time-dependent ICP-MS analysis of the electrolyte composition revealed, in that case, partial dissolution of the less precious Cu (E^0(Cu^{2+}/Cu^0) = +0.34 V *vs* standard hydrogen electrode (SHE)) in the very initial stage of the electrolysis, whereas the more precious Pd (E^0(Pd^{2+}/Pd^0) = +0.85 V *vs* SHE) was not released into the electrolyte solution at all and remained in a (metallic) state on the catalyst surface upon oxide reduction. One consequence of this corrosive behavior during the *in situ* catalyst activation via oxide precursor reduction is a slow (mass transport-limited) metal deposition process superimposed on the actual CO$_2$RR, even with an extended electrolysis time.[36] Similar dissolution processes are expected for the *ap*-In$_{55}$Cu$_{45}$ alloy catalyst discussed herein. Figure 4 depicts the time-dependent evolution of In and Cu ion content in the electrolyte for two extreme potentials of −0.5 V and −1.2 V *vs* RHE referring to the lower and upper limits of the potential window considered herein (see also Figure 5 below). All traces of the metal ion concentration *vs* time showed a rapid increase in the metal ion concentration within the initial 5 to 10 min of exposure to the electrolyte before a (quasi)plateau was reached. Note that due to the continuous bubbling of CO$_2$ gas through the catholyte during electrolysis, the released metal ions are readily distributed (diluted) in the entire electrolyte volume after

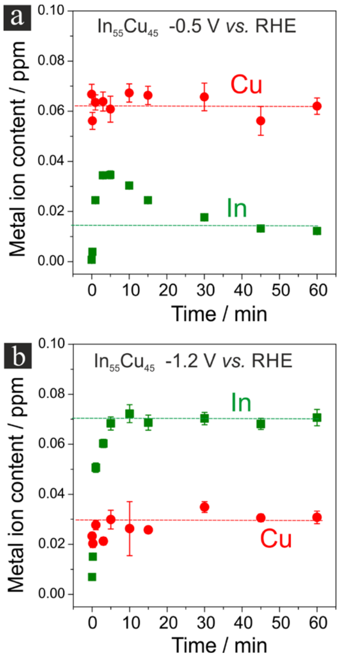

Figure 4. (a) Time-dependent ICP-MS analysis of the metal ion content (In and Cu) in the CO$_2$-sat. 0.5 M KHCO$_3$ electrolyte when −0.5 V *vs* RHE was applied for 1 h. (b) Corresponding ICP-MS data for an applied potential of −1.2 V *vs* RHE.

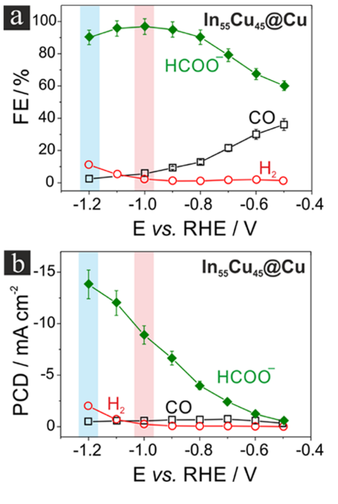

Figure 5. (a) Product distribution represented as the plot of the faradaic efficiency (FE) *vs* the electrolysis potential (E). The 1 h electrolysis was carried out using the CO$_2$-sat. 0.5 M KHCO$_3$ electrolyte. (b) Corresponding plot of the partial current densities (PCDs) *vs* E. Note that the current density is normalized to the geometric surface area of the support. Highlighted in red and blue are the data for the maximum FE$_{\mathrm{formate}}$ and PCD$_{\mathrm{formate}}$, respectively. FE and PCD data are listed in Tables S2 and S3.

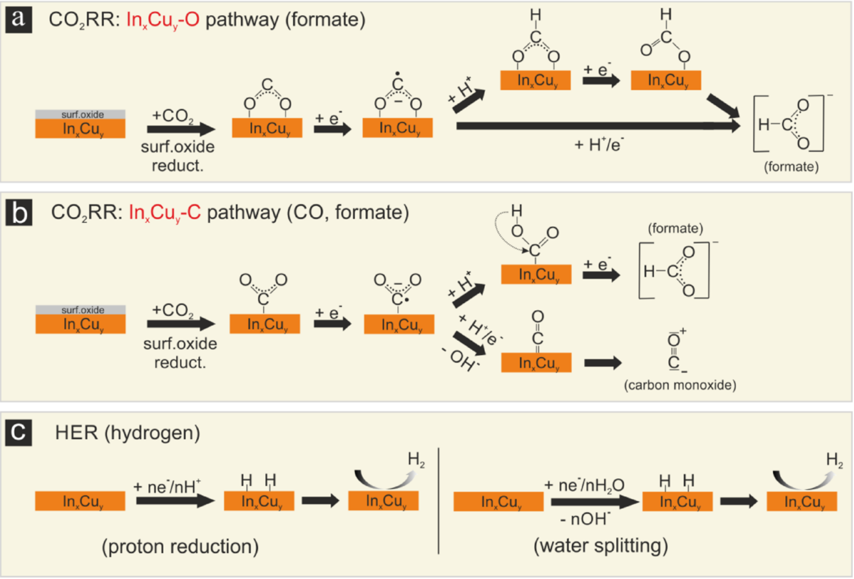

Figure 6. (a) Proposed In_xCu_y-O pathway of formate production (oxophilic case) and (b) In_xCu_y-C pathway of CO and formate production (carbophilic case). (c) Different reaction pathways of hydrogen evolution (proton reduction and water splitting).

completion of the oxide reduction. Figure 4 reveals that the dissolution characteristics depended on the applied electrolysis potential. At the lowest applied overpotentials (−0.5 V *vs* RHE, Figure 4a), it is the Cu component of the oxidic skin that gets preferentially dissolved into the electrolyte, whereas the In content of the electrolyte remains at a comparably low level. This is likely due to the more negative standard potential of the In(III)/In(0) redox transition ($E^0(In^{3+}/In^0) = -0.34$ V *vs* SHE). The reduction of indium oxide is assumed to be much slower and eventually not fully completed under these experimental conditions. Interestingly, the situation was reversed at the highest applied potentials (−1.2 V *vs* RHE, Figure 4b). It is now In that gets preferentially dissolved upon surface oxide reduction, whereas the Cu content in solution remains at a comparably low concentration. Obviously, the release of Cu ions into the electrolyte was more suppressed at higher overpotentials. It rapidly transformed into metallic Cu upon applying a potential of −1.2 V *vs* RHE. These ICP-MS analysis results demonstrate that activation of the catalyst by (surface) oxide reduction might lead to slightly different surface compositions when applying different electrolysis potentials.

3.3. Electrocatalytic Performance. The *ap*-$In_{55}Cu_{45}$ alloy samples were subjected to a series of potentiostatic electrolysis reactions (1 h each) within a broad range of applied electrode potentials (−0.5 to −1.2 V *vs* RHE). The electrolyses were carried out in a classical H-cell configuration using CO_2-sat. 0.5 M $KHCO_3$ as the electrolyte (pH = 7.2). For each electrolysis experiment, a freshly prepared catalyst was applied (multi-catalyst approach). Figure 5a,b depicts the resulting product distribution as plots of the faradaic efficiency (FE) *vs* the applied electrolysis potential (*E*) and the partial current densities (PCDs) *vs* *E*, respectively (Tables S2 and S3). The most striking observation is that the parasitic HER remains almost fully suppressed within the entire range of electrolysis potentials studied herein. Only below −1.0 V *vs* RHE did the FE_{H2} value start to rise, reaching 11.1% at −1.2 V *vs* RHE ($PCD_{H2} = -1.99$ mA cm^{-2}). The exclusive CO_2RR products are CO and formate, both involving a coupled two-electron/two-proton transfer reaction as follows:

$$CO_2 + 2\,e^- + 2\,H^+ \rightarrow HCOOH(\text{formic acid; acidic conditions}) \quad (2)$$

$$CO_2 + 2e^- + H_2O \rightarrow OH^- + HCOO^-(\text{formate; neutral and alkaline conditions}) \quad (3)$$

$$CO_2 + 2e^- + 2H^+ \rightarrow H_2O + CO(\text{CO; acidic conditions}) \quad (4)$$

$$CO_2 + 2e^- + H_2O \rightarrow 2OH^- + CO(\text{CO; neutral and alkaline conditions}) \quad (5)$$

Under neutral and alkaline conditions, water (solvent) itself serves as the proton source for the coupled electron-proton transfer reaction. The parasitic HER, typically superimposed on the CO_2RR, is fed by reductive water splitting rather than by proton reduction at an electrolyte pH of 7.3.[49]

$$2H^+ + 2e^- \rightarrow H_2(\text{proton reduction}) \quad (6)$$

$$2H_2O + 2e^- \rightarrow 2OH^- + H_2(\text{reductive water splitting}) \quad (7)$$

From the plot in Figure 5a, it is evident that the FEs of CO and formate formation are anticorrelated with each other. At the lowest applied overpotentials (−0.5 V *vs* RHE), the formate efficiency amounted to $FE_{formate} = 60.2\%$ ($PCD_{formate} = -0.54$ mA cm^{-2}), increasing to a maximum of 96.8% at −1.0 V *vs* RHE ($PCD_{formate} = -8.9$ mA cm^{-2}). A remarkable characteristic of the novel $In_{55}Cu_{45}$ catalyst is that $FE_{formate}$ values did not fall below 90% within a rather broad potential window of ~400 mV (−0.8 to −1.2 V *vs* RHE). The reaction selectivities toward CO were only substantial at the lowest

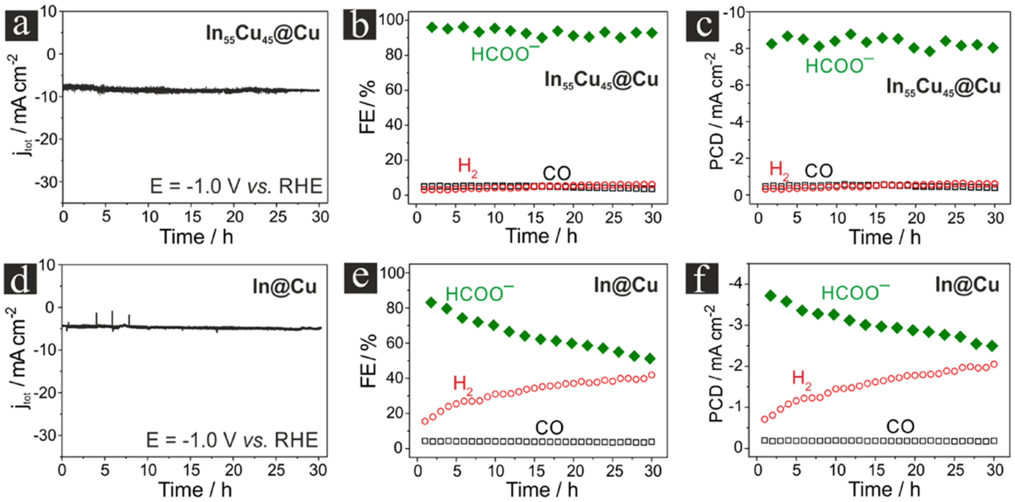

Figure 7. (a) Plot of the total (electrolysis) current density (j_{tot}) as a function of time using *ap*-In$_{55}$Cu$_{45}$@Cu as the catalyst. The extended electrolysis was carried out at $E = -1.0$ V *vs* RHE for 30 h; (b) plot of the faradaic efficiencies (FEs) as a function of electrolysis time; (c) plot of the partial current densities (PCDs) as a function of electrolysis time; (d−f) corresponding reference data of an extended electrolysis reaction carried out over an electrodeposited In@Cu (pure In deposit on Cu foil) catalyst (see also Figure S9). Note that the PCD values are normalized to the geometrical surface area of the support.

applied potentials (e.g., FE_{CO} = 36.1% at −0.5 V *vs* RHE) and gradually decreased with increasing overpotentials. The resulting PCDs in this low overpotential regime, however, remained low (PCD_{CO} = −0.34 mA cm^{-2} at −0.5 V *vs* RHE).

The absence of any hydrocarbons (e.g., CH_4, C_2H_4, and C_2H_6) or alcohols in the CO_2RR product distribution, in particular at higher negative overpotentials (<−0.7 V *vs* RHE), is indicative of effective suppression of the electrocatalytic characteristics of pure Cu in the binary In$_{55}$Cu$_{45}$ alloy. For a wide potential range, formate ($HCOO^-$) is the main CO_2RR product, proving that In (formate producer[20,41−44]) is the dominant catalyst component in the binary alloy governing the overall CO_2RR product distribution; Cu can be considered as a "modifier", amplifying the intrinsic catalytic characteristics of In in the In$_{55}$Cu$_{45}$ catalyst and further improving the degradation stability of the formed alloy (see discussion below). Only a few studies in the literature report increased product selectivities for formate when pure Cu is used as the CO_2RR catalyst. As an example, Rahaman et al. report on a dendritic Cu catalyst electrodeposited on a Cu mesh support that demonstrated an anomalously high selectivity toward formate, reaching $FE_{formate}$ = 49.2% at −0.7 V *vs* RHE.[28] This high formate efficiency, however, goes along with the production of hydrogen and decreases to $FE_{formate}$ = 5% at −1.2 V *vs* RHE. Note that the opposite trend in potential-dependent product distribution was observed for the porous In$_{55}$Cu$_{45}$ alloy catalyst discussed herein (Figure 5a).

In particular, oxophilic (post-transition) metals (e.g., Sn and In) favor CO_2RR reaction pathways involving reductive CO_2 adsorption through metal−oxygen (M−O) coordination via HCOO* intermediates (where * represents an adsorption state), denoted herein as the M−O pathway (Figure 6a). In some cases, the partially oxidized and oxygen-containing catalyst surface (e.g., SnO_2/SnO nanoparticles) is considered as the active catalyst species. For the M−O pathway, Feaster et al. proposed the HCOO* species as a key intermediate for the production of formate.[62] Its stabilization on the catalyst surface and, consequently, an increased abundance of HCOO* species are assumed to direct the CO_2RR product selectivity toward formate, thereby hindering the competitive adsorption of *COOH and *H species, which are considered key intermediates for the M−C pathway of the CO_2RR and the HER, respectively (see Figure 6b,c).[63]

For a number of transition metals, Yoo et al. described a scaling relationship between the Gibbs free energies of adsorption for *COOH (carboxyl intermediate, M−C pathway) and *H.[63] This consideration suggests that formate production via the M−C pathway is typically accompanied by the parasitic HER, as observed for some Cu catalysts. However, this scaling relation is a bit less pronounced for the post-transition metals (e.g., In and Sn).[63]

The effective suppression of the HER within the potential range studied herein (Figure 5a) is, based on the argument above, indicative of the prevalence of the M−O pathway (HCOO* intermediate) of formate formation on the porous In$_{55}$Cu$_{45}$ catalyst (Figure 6a). What makes this bimetallic In$_{55}$Cu$_{45}$ catalyst unique, however, is the fact that both CO and formate are formed as CO_2RR products over the porous bimetallic alloy. CO formation typically requires a carbophilic catalyst (the term "carbophilic" refers to CO_2RR pathways where the initial CO_2 adsorption occurs via M−C bonding and carboxyl intermediates (*COOH, Figure 6b)).[64−66]

From the physical characterization of the *ap*-In$_{55}$Cu$_{45}$ material, there is no indication of any phase separation into (nanometer-sized) domains of the pure components, as described for a bifunctional AgCu foam catalyst composed of a CO-forming component (pure Ag domains) and a C−C coupler (pure Cu domains).[32] Instead, all experimental observations suggested a rather homogeneous dispersion of Cu into In (or vice versa) in the *ap*-In$_{55}$Cu$_{45}$ material (e.g., Figure 2). These considerations suggest a "hybrid" characteristic of the bimetallic In$_{55}$Cu$_{45}$ catalyst that allows for M−C bonding or CO production at lower (negative) overpotentials and dominant M−O bonding or formate production at higher applied overpotentials.

In-depth mechanistic studies on the underlying CO_2RR pathway (e.g., by *operando* Raman spectroscopy that has successfully been applied to Cu and CuAg foam catalysts[32,56]) are impeded in the present case by the extraordinarily low

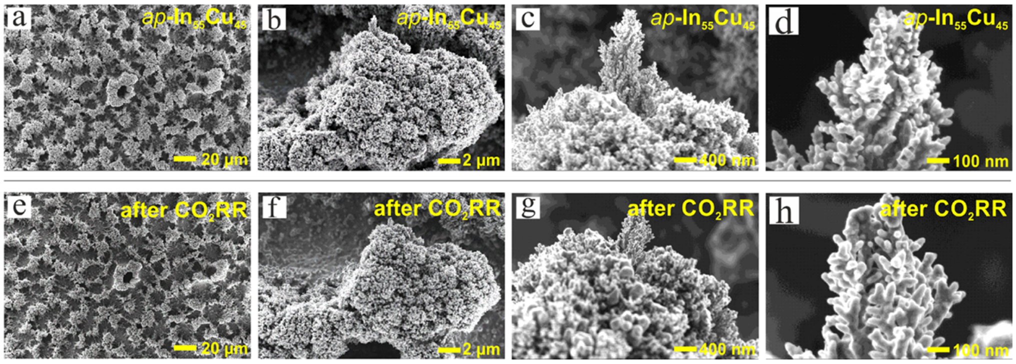

Figure 8. Identical location (IL) SEM analysis of the *ap*-$In_{55}Cu_{45}$@Cu alloy catalyst (a–d) before and (e–h) after the electrolysis. The CO_2 electrolysis experiment was carried out for 30 h at −1.0 V *vs* RHE in the CO_2-sat. 0.5 M $KHCO_3$ electrolyte.

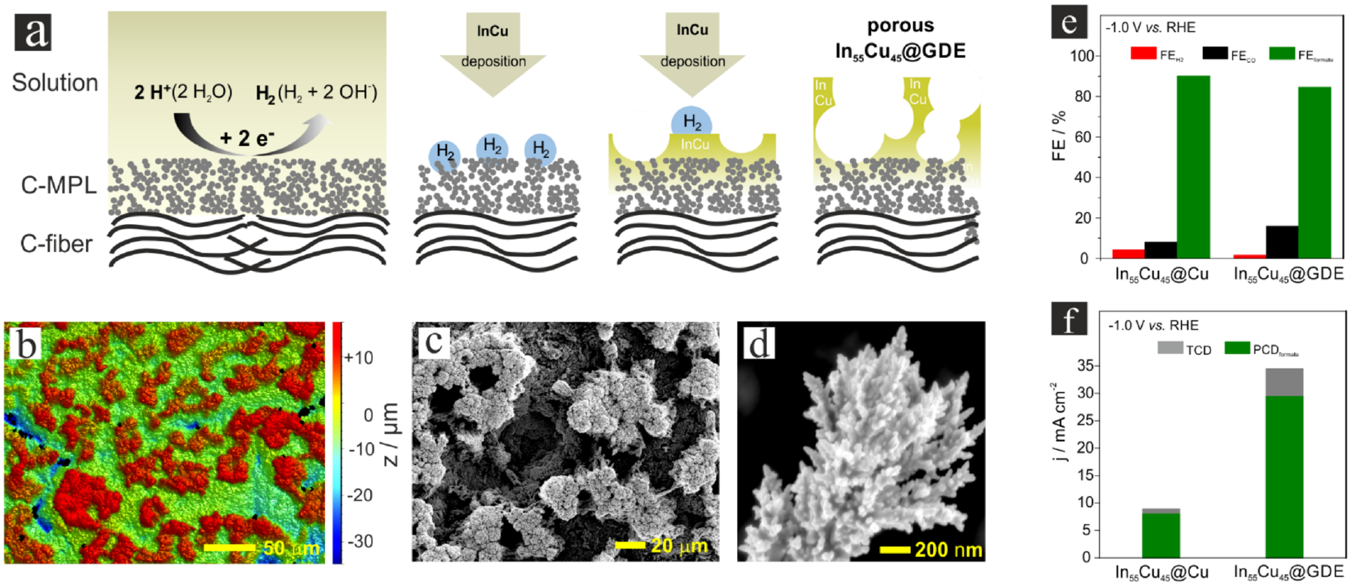

Figure 9. (a) Scheme demonstrating the DHBT approach of alloy deposition transferred to a carbon cloth support (GDE); (b) WLI image of the *ap*-$In_{55}Cu_{45}$@GDE catalyst; (c, d) top-down SEM inspection of the *ap*-$In_{55}Cu_{45}$@GDE catalyst. (e) Comparison of the product distribution using $In_{55}Cu_{45}$@Cu and $In_{55}Cu_{45}$@GDE as catalysts. (f) Corresponding total (TCD) and partial (PCD) current densities. The electrolyses were carried out for 1 h at −1.0 V *vs* RHE in CO_2-sat. 0.5 M $KHCO_3$ solution.

Raman intensities on the porous $In_{55}Cu_{45}$ material due to the alloying effect (see Figure S7).

The chemical composition of the $In_{55}Cu_{45}$ catalyst is optimized particularly for formate production and extended catalyst stability. A gradual increase in the Cu content in the deposit leads to an increase in CO yields at the expense of formate efficiencies. A survey of catalyst morphologies and resulting product distributions for $In_{55}Cu_{45}$, $In_{26}Cu_{74}$, and In_2Cu_{98} catalysts are presented in Figure S8. Cu foams containing only 2 at % In outperformed in terms of CO production, reaching a CO efficiency of almost 100% in the potential range from −0.4 to −0.6 V *vs* RHE. The production of hydrocarbons and alcohols remained suppressed at higher overpotentials, suggesting that a trace amount of In was already sufficient to substantially reduce the M−CO binding strength. This is why release of the formed CO is favored over C−C coupling and further transformations of the chemisorbed *CO intermediate into hydrocarbons/alcohols as reported for numerous Cu-based CO_2RR catalysts.[21,22,37,39]

What makes the bimetallic $In_{55}Cu_{45}$ catalyst outstanding, however, is its long-term stability during extended CO_2 electrolysis. Results of a representative 30 h potentiostatic CO_2RR carried out at −1.0 V *vs* RHE are presented in Figure 7a–c (Table S4). Corresponding reference experiments using an electrodeposited polycrystalline In film as the catalyst are shown in Figure 7d–f (Table S5). In both cases, the current density *vs* time traces (panels a and d) remained stable during the 30 h lasting electrolysis. The product distribution, however, underwent severe alterations in the case of the pure In catalyst (Figure 7e,f). This suggests that the current densities or changes thereof (panels a and d) cannot be considered suitable measures to probe the stability of the catalyst against chemical or structural degradation, both of which affect the resulting product distribution. The decrease in $FE_{formate}$ values from initially 82.1% ($PCD_{formate}$ = −3.67 mA cm^{-2}) to ultimately 50.2% ($PCD_{formate}$ = −2.45 mA cm^{-2}) after 30 h of continuous electrolysis was anticorrelated with the increase in FE_{H2} from 15.5% (PCD_{H2} = −0.71 mA cm^{-2}) to 41.9% (PCD_{H2} = −2.05 mA cm^{-2}). In contrast, both the faradaic efficiency ($FE_{formate}$ = 94.2 ± 2.1%) and the corresponding partial current density ($PCD_{formate}$ = −8.2 ± 0.4 mA cm^{-2}) remained stable during the electrolysis when the porous $In_{55}Cu_{45}$ material was used as the catalyst (see also Figure S9). These results strongly suggest that it is HER (Figure 6c) that causes an irreversible transformation of the comparatively planar In catalyst surface, thereby creating more of those (catalytic) surface sites that are active toward the HER. In this respect, we can consider the HER as a "self-accelerating" process that becomes increasingly dominant at the expense of other (competitive) reactions (e.g., the CO_2RR) with time. On the other hand, a 3D dendritic $In_{55}Cu_{45}$ alloy surface, with a higher ECSA, is capable to stabilize the CO_2RR intermediates (HCOO*), thereby suppressing the HER during the long-term electrolysis. This emphasizes the importance of complete suppression of HER right from the beginning of the electrolysis reaction as a crucial prerequisite for the long-term stability of the catalyst. A performance comparison based on the existing literature for InCu-based systems is presented in Table S6 and indicates the high performance of the $In_{55}Cu_{45}$ material studied herein. Further support for the excellent stability of the $In_{55}Cu_{45}$ catalyst comes from the identical location scanning electron microscopy (IL-SEM) analysis performed prior to and after 30 h of continuous electrolysis at −1.0 V *vs* RHE (Figure 8). The macroporosity on the micrometer-length scale remained unaffected by the extended electrolysis (Figure 8a,b,e,f). Minor morphological changes concern, however, the dendritic fine structure of the porous catalyst on the nanometer-length scale (Figure 8d,h).

3.4. Transfer of the Catalyst Concept to Technical GDE Substrates. The preparation of the bimetallic $In_{55}Cu_{45}$ catalyst has so far been restricted to DHBT-assisted alloy deposition on planar Cu foil supports. Future applications of the CO_2RR will apply gas-fed electrolyzer systems in which the gaseous CO_2 reactant is transported toward the actual catalyst layer through a porous (carbon cloth) support electrode.[26,40] By this approach, it is possible to substantially reduce CO_2 mass transport limitations, which are severe when the CO_2RR is carried from an aqueous electrolyte at high overpotentials. The actual CO_2 concentration in aqueous electrolytes is limited to ∼35 mM only.[67] It is therefore vital that the newly developed catalyst material can be transferred to a technical carbon cloth support that might serve as a gas diffusion electrode (GDE). The principle of DHBT-assisted alloy deposition on the GDE support is depicted in Figure 9a. Note that the electrolyte, when brought into contact with the carbon cloth, will penetrate to some extent into the topmost layers of the carbon microporous layer (C-MPL) of the GDE support. Catalyst deposition in the outermost part of the MPL is considered beneficial because it improves the overall adhesion (wetting) of the porous metallic catalyst deposit onto the carbon support. Figure S10a provides insights into the structure of the carbon cloth support, which consists of carbon fibers in its core that is further covered by a carbon MPL (panels b−d of Figure S10) on which the actual catalyst electrodeposition takes place. The macromorphology on the micrometer (μm)-length scale observed for *ap*-$In_{55}Cu_{45}$@Cu (Figure 1) is largely conserved on the GDE support (Figure 9b,c). Also, the dendritic features of the porous $In_{55}Cu_{45}$ catalyst are visible on the nanometer (nm)-length scale (Figure 9d). To exemplarily test the performance of the $In_{55}Cu_{45}$@GDE catalyst, a 1 h electrolysis was carried out from CO_2-saturated 0.5 M $KHCO_3$ solution at −1.0 V *vs* RHE and compared with data derived for the $In_{55}Cu_{45}$@Cu catalyst. In general, the excellent selectivity toward formate observed for $In_{55}Cu_{45}$@Cu is reproduced on the GDE support ($FE_{formate}$ ≈ 86%); also, hydrogen production remained largely suppressed (FE_{H2} ≈ 1%, Figure 9e). Compared with $In_{55}Cu_{45}$@Cu, however, FE_{CO} was slightly increased (∼15%). These slight changes in the catalytic activity of $In_{55}Cu_{45}$@GDE can be attributed to the minor morphological irregularity of the catalyst that could arise during the electrodeposition using the porous carbon network substrate unlike the planar Cu foil model substrate. It can be further assumed, however, that the ratio of formate/CO efficiencies can be further improved for the GDE support by optimizing the plating conditions (e.g., current density and deposition time).

Note that the GDE support had an intrinsically higher surface area compared to the Cu foil. This increased roughness is transferred during electrodeposition to the layer of the $In_{55}Cu_{45}$ catalyst. One consequence of this was improved total and partial CO_2RR current densities. For formate production, a partial current density of $PCD_{formate}$ ≈ −30 mA cm^{-2} was reached when using the carbon cloth as the support (Figure 9f).

4. CONCLUSIONS

A novel porous $In_{55}Cu_{45}$ alloy catalyst was produced on a Cu foil support by means of the DHBT deposition approach, which showed excellent electrocatalytic performance toward formate production, with $FE_{formate}$ values never falling below 90% within an extended (400 mV) potential window (−0.8 to −1.2 V *vs* RHE). Structural and compositional analysis of the as-prepared $In_{55}Cu_{45}$@Cu catalyst revealed homogeneous dispersion of Cu in In. The absence of pure domains of Cu in the bimetallic $In_{55}Cu_{45}$ alloy catalyst explains the complete suppression of CO_2RR pathways, which involve hydrocarbon/alcohol formation via C−C coupling. The most prominent characteristic of the $In_{55}Cu_{45}$@Cu catalyst is its high stability during extended CO_2 electrolysis reactions (30 h at −1.0 V *vs* RHE). Both the faradaic efficiency ($FE_{formate} = 94.2 \pm 2.1\%$) and the partial current density ($PCD_{formate} = -8.2 \pm 0.4$ mA cm^{-2}) were unaltered during the continuous CO_2 electrolysis. Essential for this long-term stability is a low rate of hydrogen formation. In the case of the In@Cu reference system, the HER has been identified as the source for severe degradation phenomena in terms of a self-amplifying process, creating further sites during the continued electrolysis reaction that are specifically active toward HER, thus reducing the CO_2RR yields.

The concept of DHBT-assisted alloy deposition could be transferred to technically relevant porous GDE supports. The CO_2RR product distribution experienced only marginal alterations, whereas the resulting PCDs were substantially increased (e.g., $PCD_{formate} = -30$ mA cm^{-2} at −1.0 V *vs* RHE). This was due to the intrinsic roughness of the support, which was substantially higher for the porous GDE compared with the plane Cu foil. Future work will focus on the transfer of this $In_{55}Cu_{45}$@GDE to gas-fed electrolyzer systems, where even higher PCDs are expected.

■ ASSOCIATED CONTENT

Supporting Information

The Supporting Information is available free of charge at https://pubs.acs.org/doi/10.1021/acsami.1c07829.

> Physical characterizations of the catalyst by SEM, WLI, and XPS analyses; electrochemically active surface area (ECSA) analysis; *operando* Raman spectroscopy, phase diagram of binary InCu systems, composition-dependent

activity, formate production rate, and supplementary tables (PDF)

AUTHOR INFORMATION

Corresponding Authors

Motiar Rahaman − *Department of Chemistry, Biochemistry and Pharmaceutical Sciences, University of Bern, Bern 3012, Switzerland;* Present Address: Yusuf Hamied Department of Chemistry, University of Cambridge, Lensfield Road, CB2 1EW Cambridge, United Kingdom (M.R.); orcid.org/0000-0002-8422-0566; Email: mr820@cam.ac.uk

Kiran Kiran − *Department of Chemistry, Biochemistry and Pharmaceutical Sciences, University of Bern, Bern 3012, Switzerland*; Email: kiran.kiran@dcb.unibe.ch

Peter Broekmann − *Department of Chemistry, Biochemistry and Pharmaceutical Sciences, University of Bern, Bern 3012, Switzerland;* orcid.org/0000-0002-6287-1042; Email: peter.broekmann@dcb.unibe.ch

Authors

Ivan Zelocualtecatl Montiel − *Department of Chemistry, Biochemistry and Pharmaceutical Sciences, University of Bern, Bern 3012, Switzerland*

Abhijit Dutta − *Department of Chemistry, Biochemistry and Pharmaceutical Sciences, University of Bern, Bern 3012, Switzerland;* orcid.org/0000-0002-3054-0492

Complete contact information is available at: https://pubs.acs.org/10.1021/acsami.1c07829

Author Contributions

[§]M.R. and K.K. contributed equally to this work. M.R. and P.B. conceived the idea and designed the project. M.R. and K.K. prepared and characterized the catalysts and performed the electrochemical experiments. I.Z.M. and K.K. conducted the ICP-MS analysis. A.D. and I.Z.M. performed the *operando* Raman experiments. M.R. prepared the figures and drafted the manuscript. P.B. revised and finalized the manuscript with inputs from all authors. M.R. and P.B. supervised the work.

Notes

The authors declare no competing financial interest.

ACKNOWLEDGMENTS

The financial support by the CTI Swiss Competence Center for Energy Research (SCCER, Heat and Electricity Storage) is gratefully acknowledged. M.R. and K.K. acknowledge the financial support by the Swiss Government Excellence Scholarship (ESKAS). P.B. acknowledges the financial support by the Swiss National Science Foundation (SNSF, grant code 200020_172507). The financial support by the NCCR Catalysis is gratefully acknowledged.

REFERENCES

(1) Whipple, D. T.; Kenis, P. J. A. Prospects of CO_2 Utilization via Direct Heterogeneous Electrochemical Reduction. *J. Phys. Chem. Lett.* **2010**, *1*, 3451−3458.

(2) Jhong, H.-R. M.; Ma, S.; Kenis, P. J. A. Electrochemical Conversion of CO_2 to Useful Chemicals: Current Status, Remaining Challenges, and Future Opportunities. *Curr. Opin. Chem. Eng.* **2013**, *2*, 191−199.

(3) Peter, S. C. Reduction of CO_2 to Chemicals and Fuels: A Solution to Global Warming and Energy Crisis. *ACS Energy Lett.* **2018**, *3*, 1557−1561.

(4) Kibria, M. G.; Edwards, J. P.; Gabardo, C. M.; Dinh, C.-T.; Seifitokaldani, A.; Sinton, D.; Sargent, E. H. Electrochemical CO_2 Reduction into Chemical Feedstocks: From Mechanistic Electrocatalysis Models to System Design. *Adv. Mater.* **2019**, *31*, 1807166.

(5) Jiang, J.; Wieckowski, A. Prospective direct formate fuel cell. *Electrochem. Commun.* **2012**, *18*, 41−43.

(6) Bartrom, A. M.; Ta, J.; Nguyen, T. Q.; Her, J.; Donovan, A.; Haan, J. L. Optimization of an anode fabrication method for the alkaline Direct Formate Fuel Cell. *J. Power Sources* **2013**, *229*, 234−238.

(7) Supronowicz, W.; Ignatyev, I. A.; Lolli, G.; Wolf, A.; Zhao, L.; Mleczko, L. Formic acid: a future bridge between the power and chemical industries. *Green Chem.* **2015**, *17*, 2904−2911.

(8) Szatmári, I.; Papp, G.; Joó, F.; Kathó, Á. Unexpectedly fast catalytic transfer hydrogenation of aldehydes by formate in 2-propanol−water mixtures under mild conditions. *Catal. Today* **2015**, *247*, 14−19.

(9) Zhang, F.; You, X.; Dou, H.; Liu, Z.; Zuo, B.; Zhang, X. Facile Fabrication of Robust Silk Nanofibril Films via Direct Dissolution of Silk in $CaCl_2$−Formic Acid Solution. *ACS Appl. Mater. Interfaces* **2015**, *7*, 3352−3361.

(10) Derbyshire, J. C.; Gordon, C. H.; Waldo, D. R. Formic Acid as a Silage Preservative for Milking Cows. *J. Dairy Sci.* **1976**, *59*, 278−287.

(11) Durst, J.; Rudnev, A.; Dutta, A.; Fu, Y.; Herranz, J.; Kaliginedi, V.; Kuzume, A.; Permyakova, A. A.; Paratcha, Y.; Broekmann, P.; Schmidt, T. J. Electrochemical CO_2 Reduction—A critical View on Fundamentals. *Mater. Appl. Chim.* **2015**, *69*, 769−776.

(12) Daiyan, R.; Lovell, E. C.; Bedford, N. M.; Saputera, W. H.; Wu, K.-H.; Lim, S.; Horlyck, J.; Ng, Y. H.; Lu, X.; Amal, R. Modulating Activity through Defect Engineering of Tin Oxides for Electrochemical CO_2 Reduction. *Adv. Sci.* **2019**, *6*, 1900678.

(13) Dutta, A.; Zelocualtecatl Montiel, I.; Kiran, K.; Rieder, A.; Grozovski, V.; Gut, L.; Broekmann, P. A tandem ($Bi_2O_3 \rightarrow Bi_{met}$) catalyst for highly efficient ec-CO_2 conversion into formate: Operando Raman spectroscopic evidence for a reaction pathway change. *ACS Catal.* **2021**, *11*, 4988−5003.

(14) Tran-Phu, T.; Daiyan, R.; Fusco, Z.; Ma, Z.; Amal, R.; Tricoli, A. Nanostructured β-Bi_2O_3 Fractals on Carbon Fibers for Highly Selective CO_2 Electroreduction to Formate. *Adv. Funct. Mater.* **2020**, *30*, 1906478.

(15) Rahaman, M.; Dutta, A.; Broekmann, P. Size-Dependent Activity of Palladium Nanoparticles: Efficient Conversion of CO_2 into Formate at Low Overpotentials. *ChemSusChem* **2017**, *10*, 1733−1741.

(16) Hori, Y. I. Electrochemical CO_2 Reduction on Metal Electrodes. In *Modern Aspects of Electrochemistry*; Springer: New York, 2008; pp. 89−189, .

(17) Kortlever, R.; Shen, J.; Schouten, K. J. P.; Calle-Vallejo, F.; Koper, M. T. M. Catalysts and Reaction Pathways for the Electrochemical Reduction of Carbon Dioxide. *J. Phys. Chem. Lett.* **2015**, *6*, 4073−4082.

(18) Qiao, J.; Liu, Y.; Hong, F.; Zhang, J. A Review of Catalysts for the Electroreduction of Carbon Dioxide to Produce Low-Carbon Fuels. *Chem. Soc. Rev.* **2014**, *43*, 631−675.

(19) Costentin, C.; Robert, M.; Savéant, J.-M. Catalysis of the electrochemical reduction of carbon dioxide. *Chem. Soc. Rev.* **2013**, *42*, 2423−2436.

(20) Hori, Y.; Wakebe, H.; Tsukamoto, T.; Koga, O. Electrocatalytic Process of CO Selectivity in Electrochemical Reduction of CO_2 at Metal Electrodes in Aqueous Media. *Electrochim. Acta* **1994**, *39*, 1833−1839.

(21) Kuhl, K. P.; Cave, E. R.; Abram, D. N.; Jaramillo, T. F. New Insights into the Electrochemical Reduction of Carbon Dioxide on Metallic Copper Surfaces. *Energy Environ. Sci.* **2012**, *5*, 7050−7059.

(22) Nitopi, S.; Bertheussen, E.; Scott, S. B.; Liu, X.; Engstfeld, A. K.; Horch, S.; Seger, B.; Stephens, I. E. L.; Chan, K.; Hahn, C.; Nørskov, J. K.; Jaramillo, T. F.; Chorkendorff, I. Progress and Perspectives of Electrochemical CO_2 Reduction on Copper in Aqueous Electrolyte. *Chem. Rev.* **2019**, *119*, 7610−7672.

(23) Peterson, A. A.; Abild-Pedersen, F.; Studt, F.; Rossmeisl, J.; Nørskov, J. K. How copper catalyzes the electroreduction of carbon dioxide into hydrocarbon fuels. *Energy Environ. Sci.* **2010**, *3*, 1311−1315.

(24) Nie, X.; Esopi, M. R.; Janik, M. J.; Asthagiri, A. Selectivity of CO_2 Reduction on Copper Electrodes: The Role of the Kinetics of Elementary Steps. *Angew. Chem., Int. Ed.* **2013**, *52*, 2459−2462.

(25) Luo, W.; Nie, X.; Janik, M. J.; Asthagiri, A. Facet Dependence of CO_2 Reduction Paths on Cu Electrodes. *ACS Catal.* **2016**, *6*, 219−229.

(26) Dinh, C.-T.; Burdyny, T.; Kibria, M. G.; Seifitokaldani, A.; Gabardo, C. M.; García de Arquer, F. P.; Kiani, A.; Edwards, J. P.; De Luna, P.; Bushuyev, O. S.; Zou, C.; Quintero-Bermudez, R.; Pang, Y.; Sinton, D.; Sargent, E. H. CO_2 electroreduction to ethylene via hydroxide-mediated copper catalysis at an abrupt interface. *Science* **2018**, *360*, 783−787.

(27) Dutta, A.; Rahaman, M.; Luedi, N. C.; Mohos, M.; Broekmann, P. Morphology Matters: Tuning the Product Distribution of CO_2 Electroreduction on Oxide-Derived Cu Foam Catalysts. *ACS Catal.* **2016**, *6*, 3804−3814.

(28) Rahaman, M.; Dutta, A.; Zanetti, A.; Broekmann, P. Electrochemical Reduction of CO_2 into Multicarbon Alcohols on Activated Cu Mesh Catalysts: An Identical Location (IL) Study. *ACS Catal.* **2017**, *7*, 7946−7956.

(29) Wang, Y.; Cao, L.; Libretto, N. J.; Li, X.; Li, C.; Wan, Y.; He, C.; Lee, J.; Gregg, J.; Zong, H.; Su, D.; Miller, J. T.; Mueller, T.; Wang, C. Ensemble Effect in Bimetallic Electrocatalysts for CO_2 Reduction. *J. Am. Chem. Soc.* **2019**, *141*, 16635−16642.

(30) Zhi, X.; Jiao, Y.; Zheng, Y.; Vasileff, A.; Qiao, S.-Z. Selectivity roadmap for electrochemical CO_2 reduction on copper-based alloy catalysts. *Nano Energy* **2020**, *71*, 104601.

(31) Vasileff, A.; Xu, C.; Jiao, Y.; Zheng, Y.; Qiao, S.-Z. Surface and Interface Engineering in Copper-Based Bimetallic Materials for Selective CO_2 Electroreduction. *Chem* **2018**, *4*, 1809−1831.

(32) Dutta, A.; Montiel, I. Z.; Erni, R.; Kiran, K.; Rahaman, M.; Drnec, J.; Broekmann, P. Activation of bimetallic AgCu foam electrocatalysts for ethanol formation from CO_2 by selective Cu oxidation/reduction. *Nano Energy* **2020**, *68*, 104331.

(33) Hoang, T. T. H.; Verma, S.; Ma, S.; Fister, T. T.; Timoshenko, J.; Frenkel, A. I.; Kenis, P. J. A.; Gewirth, A. A. Nanoporous Copper−Silver Alloys by Additive-Controlled Electrodeposition for the Selective Electroreduction of CO_2 to Ethylene and Ethanol. *J. Am. Chem. Soc.* **2018**, *140*, 5791−5797.

(34) Li, Y. C.; Wang, Z.; Yuan, T.; Nam, D.-H.; Luo, M.; Wicks, J.; Chen, B.; Li, J.; Li, F.; de Arquer, F. P. G.; Wang, Y.; Dinh, C.-T.; Voznyy, O.; Sinton, D.; Sargent, E. H. Binding Site Diversity Promotes CO_2 Electroreduction to Ethanol. *J. Am. Chem. Soc.* **2019**, *141*, 8584−8591.

(35) Clark, E. L.; Hahn, C.; Jaramillo, T. F.; Bell, A. T. Electrochemical CO_2 Reduction over Compressively Strained CuAg Surface Alloys with Enhanced Multi-Carbon Oxygenate Selectivity. *J. Am. Chem. Soc.* **2017**, *139*, 15848−15857.

(36) Rahaman, M.; Kiran, K.; Montiel, I. Z.; Grozovski, V.; Dutta, A.; Broekmann, P. Selective n-propanol formation from CO_2 over degradation-resistant activated PdCu alloy foam electrocatalysts. *Green Chem.* **2020**, *22*, 6497−6509.

(37) Rasul, S.; Anjum, D. H.; Jedidi, A.; Minenkov, Y.; Cavallo, L.; Takanabe, K. A Highly Selective Copper−Indium Bimetallic Electrocatalyst for the Electrochemical Reduction of Aqueous CO_2 to CO. *Angew. Chem.* **2015**, *54*, 2146−2150.

(38) Larrazábal, G. O.; Martín, A. J.; Mitchell, S.; Hauert, R.; Pérez-Ramírez, J. Enhanced Reduction of CO_2 to CO over Cu−In Electrocatalysts: Catalyst Evolution Is the Key. *ACS Catal.* **2016**, *6*, 6265−6274.

(39) Luo, W.; Xie, W.; Mutschler, R.; Oveisi, E.; De Gregorio, G. L.; Buonsanti, R.; Züttel, A. Selective and Stable Electroreduction of CO_2 to CO at the Copper/Indium Interface. *ACS Catal.* **2018**, *8*, 6571−6581.

(40) Xiang, H.; Rasul, S.; Hou, B.; Portoles, J.; Cumpson, P.; Yu, E. H. Copper−Indium Binary Catalyst on a Gas Diffusion Electrode for High-Performance CO_2 Electrochemical Reduction with Record CO Production Efficiency. *ACS Appl. Mater. Interfaces* **2020**, *12*, 601−608.

(41) Luo, W.; Xie, W.; Li, M.; Zhang, J.; Züttel, A. 3D hierarchical porous indium catalyst for highly efficient electroreduction of CO_2. *J. Mater. Chem. A* **2019**, *7*, 4505−4515.

(42) Hegner, R.; Rosa, L. F. M.; Harnisch, F. Electrochemical CO_2 reduction to formate at indium electrodes with high efficiency and selectivity in pH neutral electrolytes. *Appl. Catal., B* **2018**, *238*, 546−556.

(43) Bohlen, B.; Wastl, D.; Radomski, J.; Sieber, V.; Vieira, L. Electrochemical CO_2 reduction to formate on indium catalysts prepared by electrodeposition in deep eutectic solvents. *Electrochem. Commun.* **2020**, *110*, 106597.

(44) Ma, W.; Xie, S.; Zhang, X.-G.; Sun, F.; Kang, J.; Jiang, Z.; Zhang, Q.; Wu, D.-Y.; Wang, Y. Promoting electrocatalytic CO_2 reduction to formate via sulfur-boosting water activation on indium surfaces. *Nat. Commun.* **2019**, *10*, 892.

(45) Kim, D.; Resasco, J.; Yu, Y.; Asiri, A. M.; Yang, P. Synergistic geometric and electronic effects for electrochemical reduction of carbon dioxide using gold-copper bimetallic nanoparticles. *Nat. Commun.* **2014**, *5*, 4948.

(46) Kottakkat, T.; Klingan, K.; Jiang, S.; Jovanov, Z. P.; Davies, V. H.; El-Nagar, G. A. M.; Dau, H.; Roth, C. Electrodeposited AgCu Foam Catalysts for Enhanced Reduction of CO_2 to CO. *ACS Appl. Mater. Interfaces* **2019**, *11*, 14734−14744.

(47) Yin, Z.; Gao, D.; Yao, S.; Zhao, B.; Cai, F.; Lin, L.; Tang, P.; Zhai, P.; Wang, G.; Ma, D.; Bao, X. Highly selective palladium-copper bimetallic electrocatalysts for the electrochemical reduction of CO_2 to CO. *Nano Energy* **2016**, *27*, 35−43.

(48) Kuhl, K. P.; Hatsukade, T.; Cave, E. R.; Abram, D. N.; Kibsgaard, J.; Jaramillo, T. F. Electrocatalytic Conversion of Carbon Dioxide to Methane and Methanol on Transition Metal Surfaces. *J. Am. Chem. Soc.* **2014**, *136*, 14107−14113.

(49) Vesztergom, S.; Dutta, A.; Rahaman, M.; Kiran, K.; Zelocualtecatl Montiel, I.; Broekmann, P. Hydrogen Bubble Templated Metal Foams as Efficient Catalysts of CO_2 Electroreduction. *ChemCatChem* **2021**, *13*, 1039−1058.

(50) Plowman, B. J.; Jones, L. A.; Bhargava, S. K. Building with bubbles: the formation of high surface area honeycomb-like films *via* hydrogen bubble templated electrodeposition. *Chem. Commun.* **2015**, *51*, 4331−4346.

(51) Shin, H.-C.; Liu, M. Copper foam structures with highly porous nanostructured walls. *Chem. Mater.* **2004**, *16*, 5460−5464.

(52) Popov, K. I., Djokić, S.S., Nikolić, N.D., Jović, V.D.: *Morphology of Electrochemically and Chemically Deposited Metals*; Springer, 2016, DOI: 10.1007/978-3-319-26073-0.

(53) Daiyan, R.; Lu, X.; Ng, Y. H.; Amal, R. Highly Selective Conversion of CO_2 to CO Achieved by a Three-Dimensional Porous Silver Electrocatalyst. *ChemistrySelect* **2017**, *2*, 879−884.

(54) Li, D.; Wu, J.; Liu, T.; Liu, J.; Yan, Z.; Zhen, L.; Feng, Y. Tuning the pore structure of porous tin foam electrodes for enhanced electrochemical reduction of carbon dioxide to formate. *Chem. Eng. J.* **2019**, *375*, 122024.

(55) Bahari, Z.; Dichi, E.; Legendre, B.; Dugué, J. The equilibrium phase diagram of the copper−indium system: a new investigation. *Thermochim. Acta* **2003**, *401*, 131−138.

(56) Dutta, A.; Rahaman, M.; Hecker, B.; Drnec, J.; Kiran, K.; Zelocualtecatl Montiel, I.; Jochen Weber, D.; Zanetti, A.; Cedeño López, A.; Martens, I.; Broekmann, P.; Oezaslan, M. CO_2 electrolysis − Complementary *operando* XRD, XAS and Raman spectroscopy study on the stability of Cu_xO foam catalysts. *J. Catal.* **2020**, *389*, 592−603.

(57) Biesinger, M. C.; Lau, L. W. M.; Gerson, A. R.; Smart, R. S. C. Resolving surface chemical states in XPS analysis of first row transition metals, oxides and hydroxides: Sc, Ti, V, Cu and Zn. *Appl. Surf. Sci.* **2010**, *257*, 887−898.

(58) Dutta, A.; Rahaman, M.; Mohos, M.; Zanetti, A.; Broekmann, P. Electrochemical CO_2 Conversion Using Skeleton (Sponge) Type of Cu Catalysts. *ACS Catal.* **2017**, *7*, 5431−5437.

(59) Cherevko, S.; Geiger, S.; Kasian, O.; Kulyk, N.; Grote, J.-P.; Savan, A.; Shrestha, B. R.; Merzlikin, S.; Breitbach, B.; Ludwig, A.; Mayrhofer, K. J. J. Oxygen and hydrogen evolution reactions on Ru, RuO_2, Ir, and IrO_2 thin film electrodes in acidic and alkaline electrolytes: A comparative study on activity and stability. *Catal. Today* **2016**, *262*, 170−180.

(60) Löffler, M.; Khanipour, P.; Kulyk, N.; Mayrhofer, K. J. J.; Katsounaros, I. Insights into Liquid Product Formation during Carbon Dioxide Reduction on Copper and Oxide-Derived Copper from Quantitative Real-Time Measurements. *ACS Catal.* **2020**, *10*, 6735−6740.

(61) Topalov, A. A.; Cherevko, S.; Zeradjanin, A. R.; Meier, J. C.; Katsounaros, I.; Mayrhofer, K. J. J. Towards a comprehensive understanding of platinum dissolution in acidic media. *Chem. Sci.* **2014**, *5*, 631−638.

(62) Feaster, J. T.; Shi, C.; Cave, E. R.; Hatsukade, T.; Abram, D. N.; Kuhl, K. P.; Hahn, C.; Nørskov, J. K.; Jaramillo, T. F. Understanding Selectivity for the Electrochemical Reduction of Carbon Dioxide to Formic Acid and Carbon Monoxide on Metal Electrodes. *ACS Catal.* **2017**, *7*, 4822−4827.

(63) Yoo, J. S.; Christensen, R.; Vegge, T.; Nørskov, J. K.; Studt, F. Theoretical Insight into the Trends that Guide the Electrochemical Reduction of Carbon Dioxide to Formic Acid. *ChemSusChem* **2016**, *9*, 358−363.

(64) Zhu, W.; Michalsky, R.; Metin, O.; Lv, H.; Guo, S.; Wright, C. J.; Sun, X.; Peterson, A. A.; Sun, S. Monodisperse Au Nanoparticles for Selective Electrocatalytic Reduction of CO_2 to CO. *J. Am. Chem. Soc.* **2013**, *135*, 16833−16836.

(65) Hansen, H. A.; Varley, J. B.; Peterson, A. A.; Nørskov, J. K. Understanding Trends in the Electrocatalytic Activity of Metals and Enzymes for CO_2 Reduction to CO. *J. Phys. Chem. Lett.* **2013**, *4*, 388−392.

(66) Gao, F.-Y.; Bao, R.-C.; Gao, M.-R.; Yu, S.-H. Electrochemical CO_2-to-CO conversion: electrocatalysts, electrolytes, and electrolyzers. *J. Mater. Chem. A* **2020**, *8*, 15458−15478.

(67) Lucile, F.; Cézac, P.; Contamine, F.; Serin, J.-P.; Houssin, D.; Arpentinier, P. Solubility of Carbon Dioxide in Water and Aqueous Solution Containing Sodium Hydroxide at Temperatures from (293.15 to 393.15) K and Pressure up to 5 MPa: Experimental Measurements. *J. Chem. Eng. Data* **2012**, *57*, 784−789.

7.9. Hydrogen Bubble Templated Metal Foams as Efficient Catalysts of CO_2 Electroreduction

Authors: Soma Vesztergom, Abhijit Dutta, Motiar Rahaman, Kiran Kiran, **Iván Zelocualtecatl Montiel**, and Peter Broekmann

ChemCatChem 2021,**13**, 1039–1058. DOI: https://doi.org/10.1002/cctc.202001145

Highlights: This work presents a brief description of the synthesis of metal foams materials using the dynamic hydrogen bubble template (DHBT) electrodeposition approach. These materials present a highly porous surface applicable for CO_2 electroreduction. The appropriate conditions to perform DHBT-based foam deposition depend on different experimental parameters (potentiostatic or galvanostatic mode deposition) and the metal to be deposited (bath deposition). At the same time, this work discusses the product distribution selectivity of different metal foams for electrochemical reduction of CO_2.

Contributions: In this project, I was involved in the synthesis, characterization, and electrochemical experiments. In addition, I participated in the manuscript revision process.

ChemCatChem
Reviews
doi.org/10.1002/cctc.202001145

Chemistry Europe
European Chemical
Societies Publishing

Hydrogen Bubble Templated Metal Foams as Efficient Catalysts of CO_2 Electroreduction

Soma Vesztergom,*[a, b] Abhijit Dutta,[a] Motiar Rahaman,[a] Kiran Kiran,[a]
Iván Zelocualtecatl Montiel,[a] and Peter Broekmann*[a]

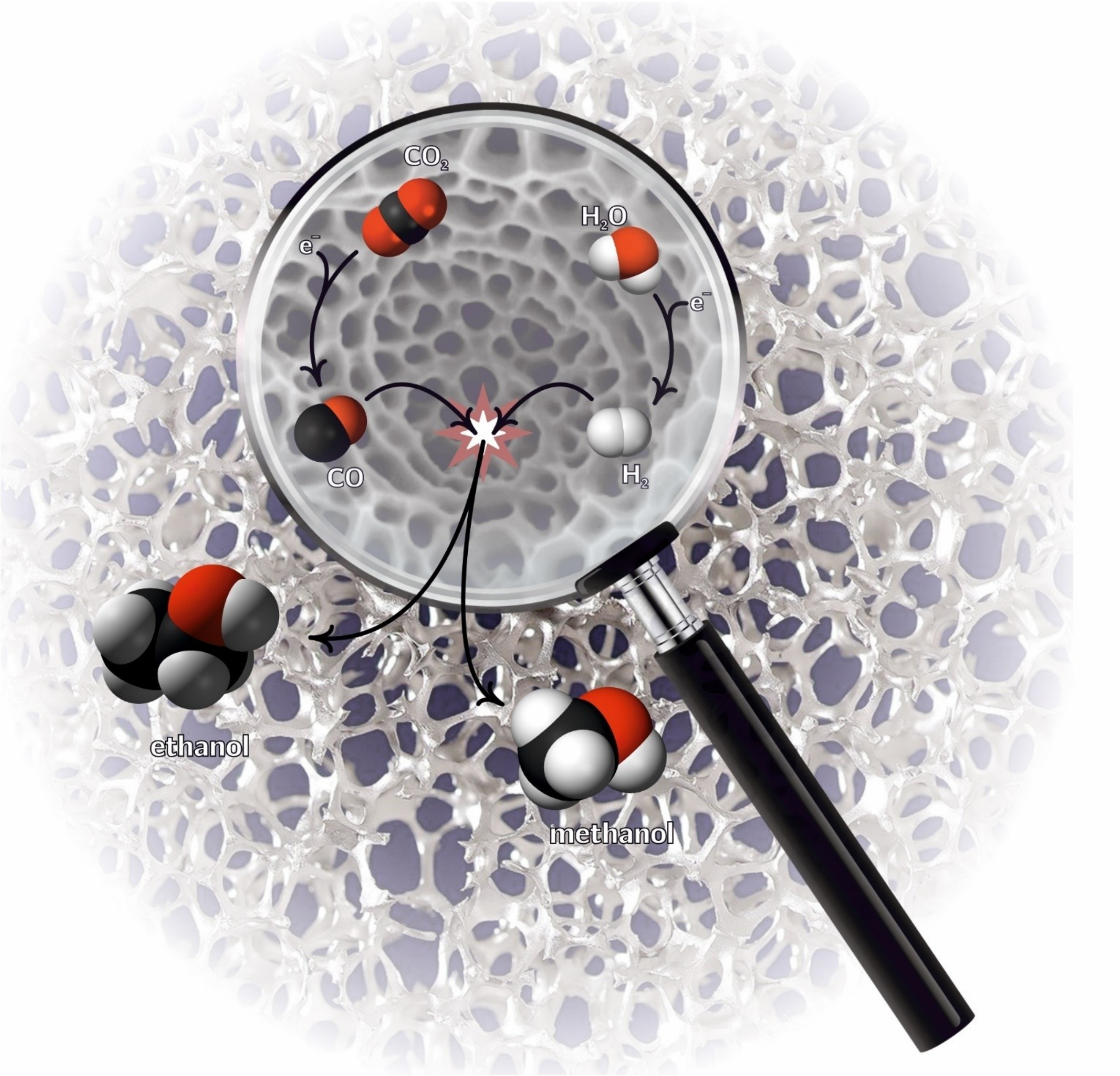

The creation of open porous structures with an extremely high surface area is of great technological relevance. The electrochemical deposition of metal foams around co-generated hydrogen bubbles that act as templates for the deposition is a promising, cheap and simple approach to the fabrication of new electrocatalyst materials. Metal foams obtained by dynamic hydrogen bubble templating (DHBT) offer an intrinsically high electrical conductance with an open porous structure that enables the fast transport of gases and liquids. As an additional benefit, the confined space within the pores of DHBT metal foams may act as small reactors that can harbour reactions not possible at an open electrode interface. The number, distribution, and size of the pores can be fine-tuned by an appropriate choice of the electrolysis parameters so that metal foam catalysts prepared by the DHBT technique meet certain requirements. In this paper, we review the preparation of certain metal foams, and their applications as catalysts for the electrochemical reduction of CO_2.

1. Introduction

The rising concentration of atmospheric carbon dioxide (CO_2) and its consequences on climate and related societal changes present a major challenge to humankind, necessitating the development of industries with a zero, or possibly negative, CO_2 footprint.[1] Electrochemical technologies provide an attractive solution to the problem, where electrons preferably gained from a renewable energy source can be used to turn CO_2 into value-added products.[2] Technologies already exist to achieve this goal, although their operation is still far from perfect. A key factor of developing CO_2 electrolysis technologies was, and probably still remains, the invention of new catalytic electrode materials. The application of proper catalysts can ensure higher yield and also a tailored selectivity toward the formation of certain sought-after products.

At recent technological levels, the most desired products of CO_2 electroreduction are syngas (a mixture of CO and H_2); C_2 hydrocarbons (primarily, C_2H_4); short carbon chain alcohols (like methanol, ethanol or propanol); and formate or formic acid. The formation of other products by electrochemical CO_2 reduction (*e.g.*, that of methane) would also be possible, but considering current market prices, the above aims are the ones that remain economically viable.[3]

Electrocatalysis plays a central role in lowering the energy barrier and thereby increasing the yield and decreasing the cost of CO_2 electroreduction, and in assuring that the reaction results in the desired product. Many efforts have thus been made to improve the performance of electrocatalysts, such as increasing the surface area, improving the intrinsic activity of the active sites, and manipulating the transport of reactants and products to and from the electrode surface.[4] Among these methods, the fabrication of three-dimensional porous structures (*i.e.*, metal foams[5]) and the application of these as electrode materials was proven to be an attractive way to improve electrocatalytic performance.[6]

The application of metal foams as electrocatalysts is advantageous, as self-standing foams can directly be employed as working electrodes, often without the need of additional mechanical support. They offer a large surface area that is not only accessible to reactants, but also enables fast, multidimensional electron transport pathways.[6,7] Also, metal foams can act as a support for other catalysts, rendering the application of conductive binders, like Nafion, unnecessary in catalyst design.

According to IUPAC,[8] "a foam is a dispersion in which a large proportion of gas by volume in the form of gas bubbles, is dispersed in a liquid, solid or gel." Foams can either be open-cell or closed-cell structured; for the purposes of electrocatalysis, foams with open-cell structures are the most useful.[9] Several non-electrochemical[10] and electrochemical[9] methods have been described for the preparation of metal foams, mainly including selective dissolution,[11–14] templating,[15,16] combustion,[17,18] and the sol-gel method.[19,20] Synthesis and characterization strategies of noble metal foams prepared by these methods, as well as their application for electrocatalysis purposes, were recently reviewed in detail by the Eychmüller group[9,20] and by Zhu *et al.*[6] A relatively newly developed, yet very promising method of the preparation of metal foams namely, dynamic hydrogen bubble templated (DHBT) electrodeposition[22] was, however, not addressed in these works. The aim of this survey is to fill this gap, and to review, in details, the use of DHBT for the preparation of metal foams that can be used, primarily, as electrocatalysts for CO_2 reduction.

2. DHBT Based Preparation of Metal Foams

2.1. General Considerations

When electrodepositing noble (*e.g.*, Au, Pt, Ag, Cu), or especially base metals (*e.g.*, Zn, Co, Fe, Ni) from solutions of their salts, concurrent hydrogen evolution is usually considered as a major problem that causes ramification of the deposited metal layer and accounts for often undesired changes in its mechanical and

---

[a] Dr. S. Vesztergom, Dr. A. Dutta, Dr. M. Rahaman, K. Kiran,
I. Zelocualtecatl Montiel, Prof. P. Broekmann
Department of Chemistry and Biochemistry
University of Bern
Freiestraße 3
Bern 3012 (Switzerland)
E-mail: peter.broekmann@dcb.unibe.ch
vesztergom@chem.elte.hu
[b] Dr. S. Vesztergom
Department of Physical Chemistry
Eötvös Loránd University
Pázmány Péter sétány 1/A
Budapest 1117 (Hungary)

This publication is part of a Special Collection on "Catalysis in Confined Spaces". Please check the ChemCatChem homepage for more articles in the collection.

optical properties, sometimes impairing the entire process.[26] Dynamic hydrogen bubble templating (DHBT) serves as a glaring counter-example, where the loss of some current due to hydrogen evolution is turned to a benefit, as the formed hydrogen bubbles aid the creation of spongy, high surface area metal foams that can be extremely useful for the purposes of electrocatalysis.

The co-generation of hydrogen along with metal deposition, in order to create high surface area electrode materials, has been part of the arsenal of electrochemists for quite some time now; *e.g.*, this was the method used for the creation of platinum black in the original recipe of Lummer and Kurlbaum[23] and of Kohlrausch[24] (Figure 1). Starting with the advent of the 21st century, the method experienced a boom, as it turned out to be quite useful for the creation of high surface area electrocatalyst materials – not necessarily platinum based ones. Among recent works directed at the development of tailored electrocatalyst materials using the DHBT method, the works of Chialvo and Marozzi,[27,28] Shin *et al.*,[29,30] Nikolić *et al.*,[31–36] Cherevko *et al.*,[37–43] as well as the works of the Bhargava group,[44–47] including a review[22] deserve further attention.

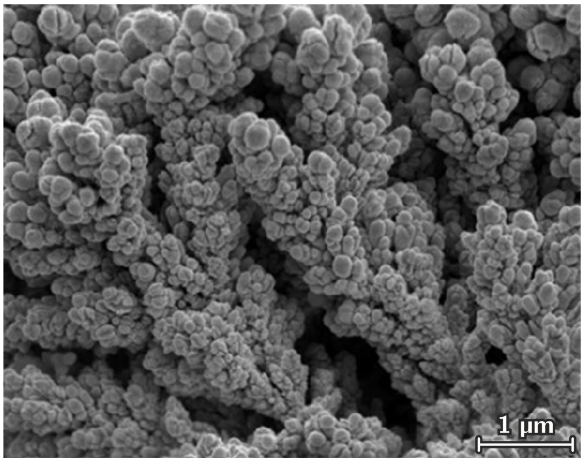

Figure 1. Scanning electron micrograph of platinum black, electrochemically deposited on a Pt surface from a hexachloroplatinate solution, using the recipe of Lummer and Kurlbaum[23] modified by Kohlrausch.[24] Reproduced from Ref. 25 with the permission of Nature.

In principle, there are two processes underlying the DHBT method that play a crucial role in the fabrication of metal foams. One is Reaction (R1), the deposition of the metal from a solution of its salt:

$$\mathrm{Me}^{z+} + z\mathrm{e}^- \rightarrow \mathrm{Me} \qquad \text{(R1)}$$

Soma Vesztergom obtained his M.Sc. (2010) and Ph.D. (2014) degrees in chemistry at Eötvös Loránd University of Budapest, Hungary. He was a post-doctoral researcher in Peter Broekmann's group at the University of Bern for a year (2014) and is a regular collaborator of this group since then. His research primarily focuses on instrumental developments in electrochemistry and on the modelling of electrocatalytic processes. Currently, he is an assistant professor at Eötvös Loránd University in Budapest.

Abhijit Dutta obtained his Ph.D in chemistry from the Indian Institute of Engineering Science and Technology, Kolkata. He worked as a post-doctoral fellow at the National University of Singapore. Afterwards, he joined the interfacial electrochemistry group of Peter Broekmann at the University of Bern, Switzerland. His research is focused on the development of various operando spectroscopies (Raman, XAS, and XRD) to characterize novel electrocatalysts for the selective conversion of CO_2 to value-added products.

Motiar Rahaman obtained his M.Sc. degree in chemistry at the Indian Institute of Technology Madras, Chennai (2013) and his Ph.D. (2018) at the University of Bern. The topic of his Ph.D. thesis was the electrochemical conversion of CO_2 into value-added products. Currently he is a post-doctoral researcher at the University of Cambridge.

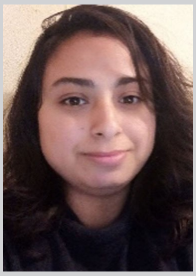

Kiran obtained her M.Sc. degree in physics at the Maharshi Dayanand University in Rohtak, India, in 2015 and currently pursues a Ph.D. in Peter Broekmann's research group at the University of Bern. Her primary research interests are in the preparation of nanomaterials and the application of these as catalysts for CO_2 electroreduction.

Ivan Zelocualtecatl Montiel received his B.Sc. and M.Sc. in Chemistry from the Meritorious Autonomus University of Puebla, Mexico, in 2013 and 2016, respectively. He is currently a Ph.D. candidate in the Department of Chemistry and Biochemistry at the University of Bern, under the supervision of Prof. Dr. Peter Broekmann. His research interest is focused on the development of novel catalysts for CO_2 electroreduction.

Peter Broekmann obtained his M.Sc. in chemistry (1998) and a Ph.D. (2000) from the University of Bonn, Germany. After a post-doctoral stay in 2001 at the University of Twente he became project leader at the Institute of Physical Chemistry in Bonn. Since 2008, Prof. Dr. Broekmann is lecturer for electrochemistry at the University of Bern (Switzerland). His research focuses on metal deposition processes for semiconductor and electrocatalysis applications.

The other is the hydrogen evolution reaction (HER) that in an acidic solution is supposed to proceed by Reaction (R2),

$$H^+ + e^- \rightarrow \frac{1}{2}H_2 \tag{R2}$$

while in solutions of pH >7, the primary source of hydrogen is the electroreduction of water itself:

$$H_2O + e^- \rightarrow \frac{1}{2}H_2 + OH^- \tag{R3}$$

Although for the preparation of metal foams using the DHBT technique, usually acidic solutions are applied, it has to be noted that under harsh cathodic conditions the surroundings of the electrode surface quickly get depleted in H^+, in which case direct water reduction, Reaction (R3), cannot be ignored.[48]

The fundamental idea of DHBT is that the H_2 bubbles generated in Reactions (R2) and (R3) disrupt the growth of the metal layer, acting as a dynamic template for the electrodeposition process. Micropores in the submicron range and macropores in the 10–100 μm size range are formed as a result of the growth of metal around small or coalesced bubbles generated on the surface, blowing up the specific surface area.[22]

When applying the DHBT method, high cathodic overpotentials are used, so that the rates of Reactions (R1) and (R2)–(R3) become comparable and decisive for the obtained foam structure. Apart from the reaction rates, however, other factors such as the nucleation, growth and detachment of the surface-generated bubbles, the intensive stirring and the related convective effects caused by bubble formation, the local alkalination of the near-electrode solution layers and its consequences on the chemistry of metal deposition, complex formation, the action of additives, etc. may also determine the surface morphology of the deposited foam. Below, we give a summary of these effects.

2.2. Mechanistic Aspects

In an excellent work, Nikolić[35] treats DHBT following Winand's classification of metals,[49] and shows contrary to previous claims[51] that metals from all three Winand groups can be obtained in three dimensional foam forms under the appropriate electrodeposition conditions. According to Winand, metals can be classed in the following three groups (Figure 2): *i.)* normal metals (such as Cd, Zn, Sn, Ag) that are characterized by low melting points, high ($j_{0,\mathrm{dep}} > 100\ \mathrm{A\,cm^{-2}}$) exchange current densities of metal deposition and low catalytic activities for hydrogen evolution; *ii.)* intermediate metals (such as Au, Cu and Ag, if in the case of Ag, deposition occurs from the solution of a complex and not of free Ag^+ ions) that are characterized by moderate melting points, intermediate ($1\ \mathrm{A\,cm^{-2}} \leq j_{0,\mathrm{dep}} \leq 100\ \mathrm{A\,cm^{-2}}$) exchange current densities of metal deposition and relatively low catalytic activities for hydrogen evolution; and *iii.)* inert metals (such as Fe, Ni, Co, Pt, Cr, Mn) that have high melting points, low ($j_{0,\mathrm{dep}} < 1\ \mathrm{A\,cm^{-2}}$) exchange current densities of metal deposition and relatively high catalytic activities for hydrogen evolution.

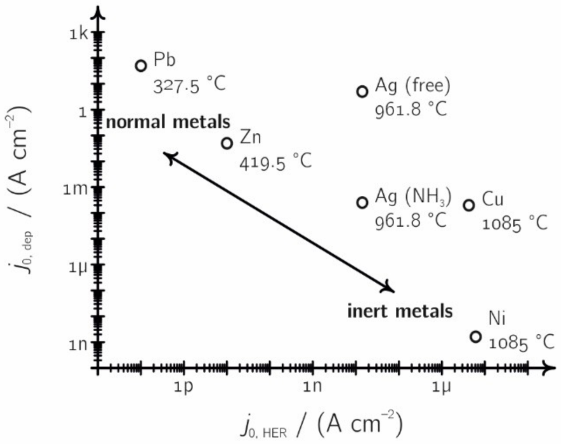

Figure 2. According to Winand,[49] metals can be classed into three groups (normal, intermediate and inert) based on their $j_{0,\mathrm{dep}}$ deposition exchange current densities and melting points. In his treatise on DHBT,[35] Nikolić extends Winand's original classification[49] based on the $j_{0,\mathrm{HER}}$ exchange current density of HER. The graph shown here was created using data obtained from Refs. 50 and 36.

In case of each three metal groups, the success of DHBT in creating metal foams depends on whether on the given metal, hydrogen is forming large enough bubbles (that is mostly a question of nucleation and growth kinetics and of surface thermodynamics) and on whether the rate of metal deposition is high enough to allow deposited dendritic metal structures to overgrow a hydrogen bubble, before it leaves the electrode surface.

As shown by Popov *et al.*,[53] in case of metals with low or moderate $j_{0,\mathrm{dep}}$ values, dendrite formation is possible only if the deposition overpotential η exceeds a minimum initiation overpotential

$$\eta_{\mathrm{ini}} = -\frac{RT}{zF}\frac{j_{lim,dep}}{j_{0,dep}} \tag{1}$$

where $j_{\mathrm{lim,dep}}$ is the effective limiting current density of metal deposition. Note that the value of $j_{\mathrm{lim,dep}}$ strongly depends on the prevailing hydrodynamic conditions and the vigorous mixing of the near-electrode solution caused by HER.

While for metal depositions in quiescent systems, the thickness of the diffusion layer of metal ions can (over time) extend to even a few hundreds of micrometers, it was shown that for quickly gas evolving electrodes (volumetric gas evolution rate normalized to surface area: $100\ \mathrm{cm^3\,min^{-1}}$, corresponding to hydrogen evolution occurring with a current density of about $5\ \mathrm{A\,cm^{-2}}$), the diffusion layer becomes only a few micrometers thick and the coverage of the surface by gas bubbles can exceed 30%.[54] Thus, at electrodes that evolve hydrogen at a high rate, due to the decrease of the diffusion layer thickness and the corresponding increase of $j_{lim,dep}$, the "effective overpotential" (a term coined by Nikolić *et al.*[31]) may be lower than what is required for efficient dendrite formation.

What was said above is nicely demonstrated in Ref. 31 for the deposition of honeycomb-like copper foams on plane copper substrates from an aqueous solution containing 0.10 mol dm^{-3} $CuSO_4$ and 0.50 mol dm^{-3} H_2SO_4. In Figure 3 we can observe the following: *i.)* that at $\eta = -0.550$ V, a value that falls inside the limiting current density of copper deposition where no hydrogen evolution takes place, cauliflower-like agglomerates of copper grains were formed; *ii.)* that at $\eta = -0.700$ V, just outside the limiting current region of copper deposition, where the Faradaic efficiency of HER is only about 5%, branch-like three dimensional dendrites are formed; and finally *iii.)* that at $\eta = -0.800$ or -1.000 V, holes formed of detached hydrogen bubbles surrounded by cauliflower-like agglomerates of copper grains are seen.

It is important to note with respect to the depositions occurring at high overpotentials that the number of holes formed at −1.000 V is larger than that at −0.800 V, which is due to the higher Faradaic efficiency of hydrogen evolution (almost 50% at −1.000 V and about 30% at −0.800 V). As communicated by Nikolić *et al.* elsewhere,[32] the critical Faradaic efficiency that hydrogen evolution should achieve in order to create hydrodynamic conditions that favour foam formation is 10% for copper depositing baths with a $CuSO_4$ concentration of 0.15 mol dm^{-3} and less, in 0.5 mol dm^{-3} H_2SO_4.

2.3. Creating Metal Foams with Hierarchic Porosity: The Effect of Deposition Time

As shown in Figure 4, at the initial stages (after the first 10 seconds) of the potentiostatic preparation of copper foams ($\eta = -1.000$ V, $c_{CuSO4} = 0.1$ mol dm^{-3}, $c_{H2SO4} = 0.5$ mol dm^{-3}), nucleation sites of H_2 bubbles and surrounding agglomerates of copper grains are already visible. Hydrogen evolution is initiated at irregularities of the surface, where small bubbles are formed, grow to a certain size and are then detached. The higher the current density, the more nucleation sites become active, and also the rate of growth of the bubbles increases. While at lower current densities, only the surface irregularities are active, at higher current densities bubbles are also formed on the more homogeneous parts of the surface.[56] After

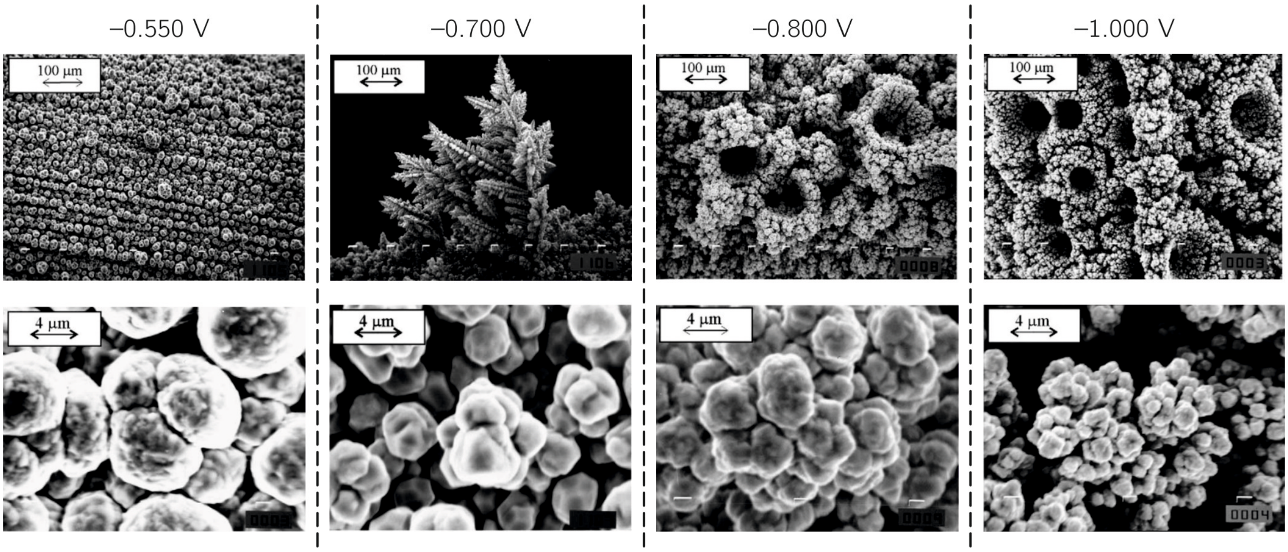

Figure 3. Morphologies of Cu deposits obtained after 60 s of potentiostatic electrolysis, at different values of the deposition overpotential from an aqueous solution containing 0.10 mol dm^{-3} $CuSO_4$ and 0.50 mol dm^{-3} H_2SO_4. Reproduced from Ref. 31 with the permission of Elsevier.

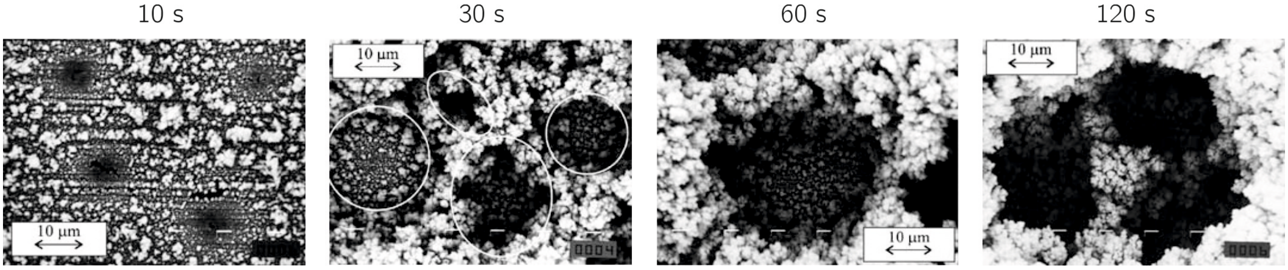

Figure 4. Morphologies of Cu deposits obtained after different times of potentiostatic electrolysis at a deposition overpotential of −1.000 V, from an aqueous solution containing 0.10 mol dm^{-3} $CuSO_4$ and 0.50 mol dm^{-3} H_2SO_4. Reproduced from Ref. 34 with the permission of Springer.

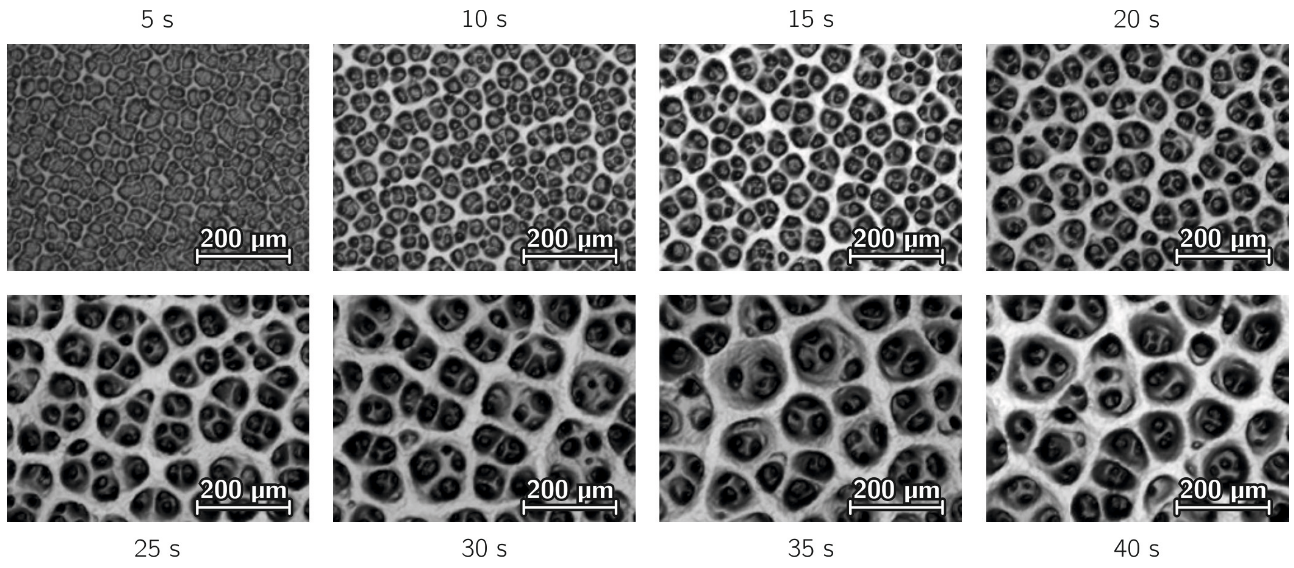

Figure 5. Morphologies of Cu deposits obtained after different times of galvanostatic electrolysis at −2.0 A cm^{-2}, from an aqueous solution containing 0.20 mol dm^{-3} $CuSO_4$ and 1.0 mol dm^{-3} H_2SO_4. Reproduced from Ref. 52 with permission of The Electrochemical Society.

30 seconds of potentiostatic electrolysis (Figure 4) we can notice that the deposited copper grows around the hydrogen bubbles that remained adherent to the surface, forming regular (circle-shaped) and irregular (from top view, ellipse shaped) cavities. As shown in Figure 5, an even more pronounced hierarchy is achieved if instead of potentiostatic control, we apply galvanostatic electrodeposition of foamed copper.[52]

As evident in Figures 3 and 4, the deposited metal foams exhibit two types of porosity: they show macropores, formed by the larger, coalesced bubbles; and micropores (porosities within the walls of the macropores) that are created as channels by the vigorous formation of small hydrogen bubbles over the copper dendrites.[34] As the electrolysis proceeds, the size of the macropores tends to increase, yielding a hierarchically structured foam deposit that has a bigger number of small pores close to the substrate, and fewer but bigger-sized pores close to the solution interface (Figures 6 and 7). This graded structure is ideally suited for the preparation of electrocatalyst materials with pore sizes specifically tuned by the selection of appropriate deposition times.[30]

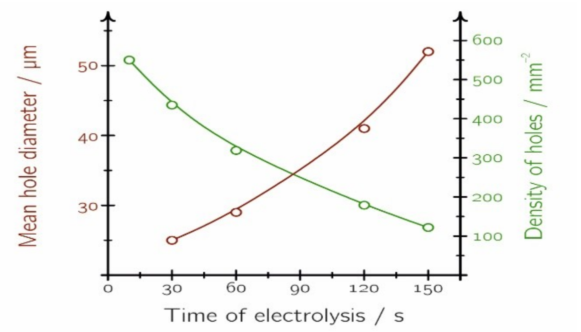

Figure 6. The size and number of H_2 bubble templated holes in Cu deposits obtained at a deposition overpotential of −1.000 V, from an aqueous solution containing 0.10 mol dm^{-3} $CuSO_4$ and 0.50 mol dm^{-3} H_2SO_4 are anti-correlated as the deposition proceeds. Graph created using data from Ref. 34.

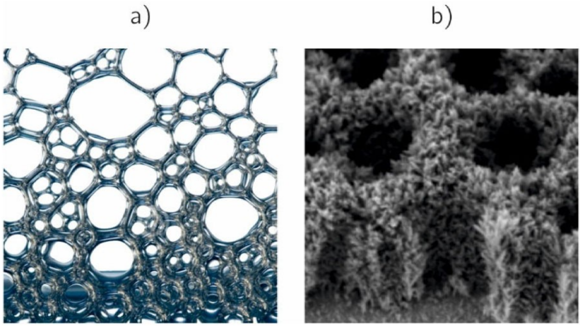

Figure 7. a) Illustration of the hierarchical porosity of metal foams and b) cross-sectional scanning electron micrographs of a potentiostatically obtained Cu foam deposit, reproduced from Ref. 30 with permission of the American Chemical Society.

2.4. Further Factors Affecting Foam Structure

As pointed out by Nikolić,[35] the formation of porous structures is possible for metals of all three Winand classes, provided that the deposition overpotential that is either directly applied or established as a result of galvanostatic polarization, exceeds the minimum initiation overpotential η_{ini}, defined by Equation (1), and that at this overpotential, hydrogen production is already vigorous.

Intensive hydrogen evolution will then have two effects: *i.)* that due to stirring the near-electrode solution, it decreases the thickness of the diffusion layer, increasing the limiting current density $j_{\mathrm{lim,dep}}$ of metal deposition; and *ii.)* that due to the at least, temporal adherence of the bubbles to the surface, it will increase the effective current density. In case θ denotes the ratio of the surface (in a time average) blocked by bubbles, the effective current density will be $1/(1-\theta)$ times bigger than the current density applied (that is the current normalized by the geometric surface area).[57]

When preparing metal foams, one must keep in mind that exchange current densities found in the literature (like those plotted in Figure 2) are concentration dependent quantities and values found in literature are usually (but not always) normalized to a unity concentration of the metal or H^+ ions in the bulk solution (for metal deposition and HER, respectively). Thus, the overall electrolyte composition will have a strong effect on determining actual hydrogen evolution/metal deposition current ratios.[58] When preparing metal foams from noble metals, *e.g.*, from silver,[38] gold[40] or palladium salts,[43] a larger metal salt concentration in the bath may be required than, for example, when depositing normal metals such as Sn or Pb, or even intermediate metals like Cu.

The success of metal foams preparation lies however not only in whether the right current densities for metal deposition and hydrogen evolution are achieved. The morphology of the deposit, especially on the macroscale, will be determined by the maximum size that H_2 bubbles formed during the electrolysis can reach before breaking off the surface, and also by the rate at which bubble growth occurs (Figure 8).[55,59]

The break-off diameter d was found to depend on the partial current density of hydrogen evolution j_{HER} according to the empirical formula

$$d = d_0\ (1 + a\ j_{HER})^b \tag{2}$$

where the constants $a \approx 0.2\ \mathrm{m^2\,A^{-1}}$ and $b \approx 0.45$ were determined by Vogt and Balzer[57] by fitting to experimental data; note that these constant values may be significantly different, depending on the system studied.

The parameter d_0 in Equation (2) is the break-off diameter in a current-free case, the value of which can be estimated by using a simplified form of the Fritz equation:[60]

$$d_0 = 1.20\,\vartheta\sqrt{\frac{\gamma}{g\,\rho}} \tag{3}$$

where g is the gravitational acceleration, ϑ denotes the contact angle of the bubble on the electrode surface, ρ is the density of the solution, and γ is the interfacial stress of the gas/liquid interface. Both the contact angle ϑ and the surface tension γ may vary as function of the applied electrode potential (and/or current),[61] as well as near-surface variations of the viscosity of the solution[62] may affect both the break-off diameter and the trajectory of bubbles leaving the electrode surface.

Additives affecting the surface energetics (either the solid/liquid or the gas/liquid interfacial stress, for example by preferential adsorption on one or both of these interfaces) may have a significant impact on both the macro- and the microporosity of the obtained deposit.[30] For example cationic surfactants like cetyltrimethylammonium bromide (CTAB), when used as additives in copper deposition baths, were shown to suppress the collision among hydrogen bubbles by specifically adsorbing on the gas/liquid interface. This leads to a mild rate of hydrogen evolution and smaller hydrogen bubbles, thus resulting in a smaller pore structure.[63] Eventually, it was also shown that CTAB can also be used to fine-tune the hydrophobicity of DHBT-deposited copper foams.[64]

Another important factor that has an effect on the structure of the finally obtained deposit is the concentration and form of available H^+ sources present in the depositing solutions. This parameter is probably even more important than the pH, which is only related to the concentration of free H^+ ions in the bulk solution. During intensive hydrogen evolution, however, when the near-electrode solution region gets alkalinated, additional H^+ sources such as NH_4^+ or citric acid can act as buffers, providing an excess amount of H^+ as a reactant supply for HER. Naturally, at large negative applied overpotentials or currents, even the direct reduction of H_2O can serve as means of HER. While in this case it is the autoprotolysis reaction of water that has to be taken into account to describe HER current densities,[48] for buffered systems additional (buffer) equilibria must be considered.[58]

Near-surface alkalination may have an adverse effect on the nature of the obtained deposits; *e.g.*, it can lead to the formation of hydroxides of the metal to be deposited.[64] While the application of buffers as bath components may successfully circumvent this effect, one also has to consider that some buffer components (especially due to complex formation) may also have other, indirect effects on the foam deposition process. For example, in case NH_4^+ ions are used as a buffer, the NH_3 molecules formed in the (alkaline) near-surface layers of the electrolyte solutions may act as complexing agents for the deposited metal, hindering its deposition. Although some experimental results do confirm this assumption,[38] the possibilities of complex formation are only scarcely treated in the literature of DHBT metal foam deposition.[22]

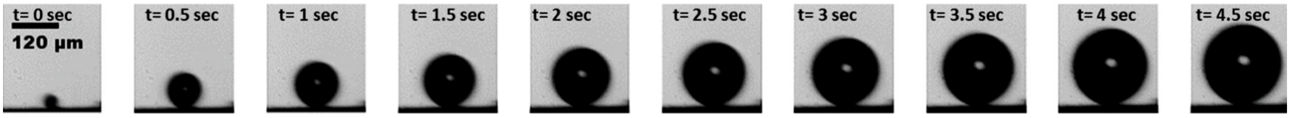

Figure 8. Sequence of images illustrating hydrogen bubble growth on an electrode surface at 60 mA cm^{-2} current density for HER. Reproduced from Ref. 55 with the permission of Elsevier.

2.5. Technical Challenges of DHBT Metal Foam Deposition

Although it is rarely mentioned in literature, one technical challenge that needs to be addressed with respect to DHBT metal foam deposition is the extreme high current that these methods require. Depositing hydrogen bubble templated metal foams necessitates the use of current densities in the range of 1 to 10 $A\,cm^{-2}$ (normalization is meant to the geometric surface area of the sample). This means that already in lab-scale experiments, the standard instrumentation (galvanostat/potentiostat) is to be equipped with current boosters. As standard boosters usually allow the control of currents up to 20 A, up-scaling may require specialized instruments as well. When using such high currents, secondary effects (such as that of Joule heat and *IR*-drop) should not be ignored, well-chosen cell geometries must be applied, and measures for electric shock protection must be taken.

3. Some Metal Foams Prepared by DHBT, with Potential Application in the Electroreduction of CO_2

Metals suited for catalysing electrochemical CO_2 reduction are usually those where hydrogen evolution proceeds only at high overpotentials. These metals can exhibit a relatively broad range of potentials where CO_2 reduction may already occur, while water splitting still remains relatively suppressed. These metals belong, according to Winand's classification, to the group of normal or intermediate metals. A non-exhaustive list includes pure metals such as Sn[66,67] Pb,[68] Zn,[69,70] Bi,[71] Ag[72–74] and Cu,[75–78] as well as bimetallic systems where Sn foams are deposited on Cu surfaces[79–84] or when smoothly dispersed Ag and Cu form one bimetallic foam structure.[85,86] In what follows, we summarize the DHBT-assisted preparation strategies of these metal foams, as well as some important aspects of CO_2 reduction occurring on them.

3.1. Sn Foams (Pure)

Sn is a prime example of normal metals having a low melting point, little activity for HER and high activity for metal deposition. Although on a Cu substrate, Sn foams were deposited relatively early by Shin *et al.*,[29] from a bath that contained 0.15 $mol\,dm^{-3}$ $SnSO_4$ dissolved in 1.5 $mol\,dm^{-3}$ H_2SO_4. By applying galvanostatic deposition at a (geometric surface area normalised) current density of $-3\,A\,cm^{-2}$ for 5 to 20 seconds, 100 to 300 μm thick deposits with surface pores of 100 to 400 μm diameter were obtained (Figure 9). The foam walls of Sn were composed of relatively long and dense, straight dendritic particles. The apparent microporosity (that is, the microscopic porosity of the walls of bigger pores) described in the same work by Shin *et al.*[29] for Cu, was not seen in the case of Sn, probably as a result of the suppressed electrocatalytic activity of Sn towards HER (Figure 2).

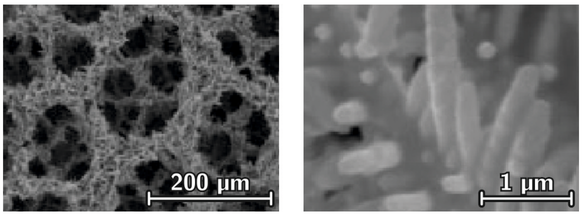

Figure 9. Scanning electron micrographs of a Sn foam deposited on a Cu substrate from a bath that contained 0.15 $mol\,dm^{-3}$ $SnSO_4$ dissolved in 1.5 $mol\,dm^{-3}$ H_2SO_4 by galvanostatic electrolysis at $-3\,A\,cm^{-2}$ nominal current density, lasting 5 seconds. Reproduced from Ref. 29, with the permission of Wiley.

Using a Sn instead of a Cu substrate, and $SnCl_2$ instead of $SnSO_4$ as a metal source bath component, deposits with qualities similar to those shown in Figure 9 were obtained by Du *et al.*[67] and were used for the electroreduction of CO_2. They showed that compared to planar Sn electrodes, Sn foams can deliver a higher yield and better selectivity for the production of formate. In a CO_2-saturated 0.1 $mol\,dm^{-3}$ $NaHCO_3$ solution, the maximum Faradaic efficiency of formate production could reach above 90% at a current density of about 23.5 $mA\,cm^{-2}$ ($E = -1.9$ V vs. SCE), which are among the highest reported to date under ambient conditions (H-type cell, aqueous solution, atmospheric pressure and room temperature).[67]

This improved production rate of formate can be attributed to the high surface area and porous structure. Moreover, Du *et al.*[67] demonstrated a high stability of their Sn foam catalyst; namely, the Faradaic efficiency remained unchanged during 16 hours of electrolysis. What cannot be inferred from Ref. 67 is, however, whether the outstanding tendencies towards the production of formate had any relation to the oxidation state of the Sn foam electrode. That oxide remnants on Sn catalysts have a guiding role in the production of formate has long been known,[66,87–89] and that surface oxidation promotes formate production (on the account of CO formation) was proven also for the case of large surface area Sn dendrites, the surface oxidation of which was induced by heating in air.[66]

3.2. Sn Foams (Deposited on Cu)

While reports on the use of pure Sn foams clearly point out that the large surface area of these foams lead to both a higher catalytic activity and an increased selectivity towards the production of formate,[66,67] the picture is not this clear in the case of foams composed of Sn deposited on top of Cu substrates (that is, Sn@Cu foams).

While browsing the literature, we can find works that advocate Sn@Cu foams for their excellent selectivity (>90%) towards formate production,[79,81,82] while for some other researchers,[83,84] Sn@Cu foams seem to be of more value if the selectivity towards CO production is higher (again, >90%). A comparison of two Sn foams deposited on Cu, with markedly different selectivities, is shown in Figure 10.

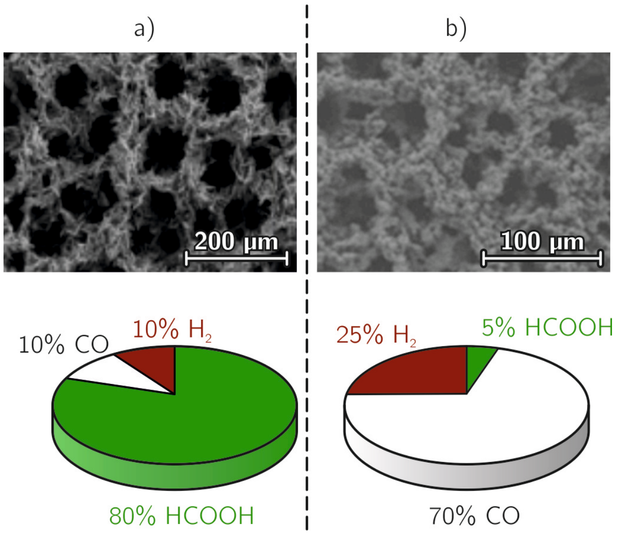

Figure 10. Sn foams deposited on a Cu substrate by a) Qin *et al.*[81] and by b) Li *et al.*[84] Scanning electron micrographs, reproduced from Ref. 81 with the permission of Elsevier and from Ref. 84 with that of MDPI, show similar surface morphologies, yet the product distribution is markedly different, as determined for potentiostatic electrolyses at −1.0 V *vs.* RHE in 0.1 mol dm^{-3} CO_2-saturated $KHCO_3$ solutions.

It is expected that also in case of these systems, the surface oxidation state of Sn particles has a pivotal role in determining selectivity. It was found, for example, by Li *et al.*[84] that the surface of Sn foams deposited on Cu substrates often contains SnO_2. We presume that stannic (or for that matter stannous) oxide domains in Sn foams may either be incorporated in the foam structure due to the local alkalination of the electrode as a result of DHBT deposition, or that even the entire foam surface may get partly oxidised after the foam is emerged from the depositing bath, and dried in air. Either way, it was found that these electrodes exhibit an SnO_x coverage-dependent catalysis – *i.e.*, a shift from CO selectivity to HCOOH selectivity with increasing SnO_2 coverage.[84]

We assume that in case of Sn@Cu systems, bimetallic corrosion effects may account for that some electrocatalytically active SnO_x particles may survive the reductive conditions of CO_2 electrolysis. This may explain that, as shown in Figure 10, in some Sn@Cu foams the selectivity of formate production is preserved.

3.3. Pb Foams

According to Winand's classification, Pb also belongs to the group of normal metals.[49] The preparation method of Pb foams was described by Cherevko *et al.*,[41] using perchloric acid both as a supporting electrolyte and an H^+ source. Deposition occurred on a Pt substrate from a solution containing 0.01 mol dm^{-3} $PbClO_4$ and 0.01–1.8 mol dm^{-3} $HClO_4$, under potentiostatic control at −2 V vs. Ag | AgCl. Good porous structures were only obtained above a $HClO_4$ concentration of 0.6 mol dm^{-3} (Figure 11). From a bath with a $HClO_4$ concentration of 0.6 mol dm^{-3}, deposited Pb layers exhibited pore sizes of about 300 μm. The walls of the pores showed a microstructure consisting of 200–300 nm diameter wires at lower perchloric acid concentrations, while at higher concentrations (>0.9 mol dm^{-3}) the Pb wires were either partially or fully covered by granular particles.

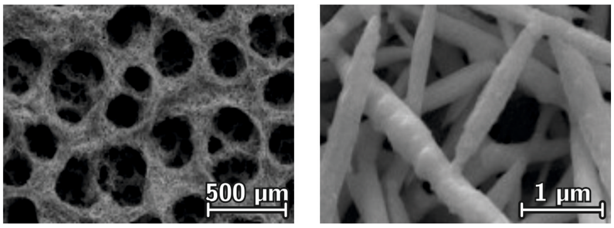

Figure 11. Scanning electron micrographs of a Pb foam deposited on a Pt substrate from a bath that contained 0.01 mol dm^{-3} $PbClO_4$ dissolved in 0.6 mol dm^{-3} $HClO_4$ by potentiostatic electrolysis lasting 2 seconds at −2 V *vs.* Ag | AgCl. Reproduced from Ref. 41, with the permission of Elsevier.

The above procedure was adapted by Wang *et al.*[68] in order to obtain Pb foams applicable for the electroreduction of CO_2. They showed that the porous Pb foam had a better electrocatalytic performance for the production of formate than a Pb plate: at 5 °C, the highest recorded Faradaic efficiency of formate production was 96.8% at an applied potential of −1.7 V vs. SCE in a 0.5 mol dm^{-3} $KHCO_3$ solution saturated by CO_2. In another study, Fan *et al.*[90] have shown that the selectivity towards formate seems to correlate with the proportion of surface sites with the (100) orientation.

3.4. Zn Foams

While also belonging to the normal group of metals, reports about the electrodeposition of Zn foams are recent. In the work of Luo *et al.*,[69] Zn foams were deposited on a Cu mesh from solutions containing 0.1 mol dm^{-3} $ZnSO_4$ and 1.5 mol dm^{-3} $(NH_4)_2SO_4$. They applied a current density of −1 A cm^{-2} for 30 seconds in order to obtain the deposited Zn foam shown by the micrographs of Figure 12. These reveal macropores with an average diameter of 30 μm and micropores with a diameter

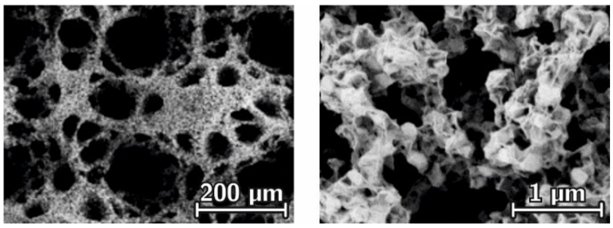

Figure 12. Scanning electron micrographs of a Zn foam deposited on a Pt substrate from a bath that contained 0.1 mol dm^{-3} $ZnSO_4$ dissolved in 1.5 mol dm^{-3} $(NH_4)_2SO_4$ by galvanostatic electrolysis at −3 A cm^{-2} nominal current density, lasting 5 seconds. Reproduced from Ref. 69, with permission of the American Chemical Society.

smaller than 2 μm, the latter formed as channels of the leaving, smaller H_2 bubbles.

Luo *et al.*[69] investigated the electroreduction of CO_2 on their highly porous Zn foam (Figure 12), and found a remarkably high Faradaic efficiency of 95 % towards the formation of CO at $E = -0.95$ V *vs.* RHE, where the current density was about -27 mA cm^{-2}, in a CO_2-purged 0.1 mol dm^{-3} $KHCO_3$ electrolyte. They argued that above the overall increase of the surface area, the Zn foam also offers a large number of active surface sites (compared to Zn foils) that play a decisive role in improving the catalytic activity. At the same time, the high local pH induced by the porous structure of Zn results in an enhanced CO selectivity because of suppressed H_2 evolution. Luo *et al.*[69] also transformed their Zn foam into a gas diffusion electrode, achieving a current density of 200 mA cm^{-2} for the reduction of CO_2 and an 84 % Faradaic efficiency for CO production at -0.64 V in a flow-cell reactor.

In another work,[70] we also developed a Zn-based alloy foam catalyst by the application of DHBT, using copper ions as a foaming agent and thereby obtaining an alloy with 6 atomic % copper content. We detected a >90 % Faradaic efficiency for CO production at -0.95 V *vs.* RHE in CO_2-purged 0.5 mol dm^{-3} $KHCO_3$. The high efficiency was ascribed to the combination of high density of low coordinated active sites and preferential Zn(101) over Zn(002) texturing,[70] and we pointed out by means of X-ray photoelectron spectroscopy investigations that the actual catalyst material is shaped upon reduction of an oxide/hydroxide-terminating surface, under CO_2 electrolysis conditions. In Ref. 70 we have also shown that intentional stressing by oxidation at ambient conditions proves to be beneficial for further activation of the catalyst.

3.5. Ag Foams

Silver is usually also considered a normal metal according to Winand's classification[49] but as long as silver is deposited not from a simple Ag^+ solution but from a solution of its complexes, it is usually treated as an intermediate metal.[35]

The first reports on the DHBT fabrication of silver foams originate from Cherevko *et al.*,[37,38] and these occurred from a thiocyanate complex solution of silver. The foam structure shown in Figure 13 was obtained by potentiostatic deposition at -3 V *vs.* Ag | AgCl lasting 30 seconds. For this deposition, Cherevko *et al.*[38] used a Pt substrate and a bath containing 0.01 mol dm^{-3} Ag_2SO_4, 1.5 mol dm^{-3} KSCN acting as a complexing agent, 0.75 mol dm^{-3} NH_4Cl, and 0.01 mol dm^{-3} sodium citrate. NH_4Cl acted as an H^+ source and the authors found that a minimum threshold concentration of >0.5 mol dm^{-3} of NH_4Cl is required for the deposit to show a foamy structure. A decrease in the diameter (from 45 to about 20 μm) and wall thickness of the surface pores, as well as an increase of the number of formed holes with increasing concentrations of NH_4Cl was observed. The authors found[38] that the microscale morphology of the formed Ag deposits changes, from exhibiting nanosized dendrites in case of foams deposited at low NH_4Cl concentrations towards small particle agglomerates, deposited from baths with higher NH_4Cl content.

As for the preparation of silver foams from normal (*i.e.*, noncomplexed) solutions, reports are relatively recent. In Ref. 72 we used a silver foil substrate and a bath containing 0.02 mol dm^{-3} Ag_2SO_4, 1.5 mol dm^{-3} H_2SO_4 and 0.1 mol dm^{-3} sodium citrate. Note that while the bulk of the solution was acidic enough not to allow complexation of silver by citrate, in the heavily alkaline near-electrode solution region, chelation of silver ions may occur. Silver foams obtained from citrate containing and citrate-free baths are compared in Figure 14. The thickness of the deposited foams is around 17 μm. Compared to the citrate-free deposition process, Ag foams deposited in the presence of citrate show a more uniform macroporosity with an open-cell architecture of interconnected pores. The average diameter of the macropores is significantly smaller, compared to deposits obtained from a citrate-free solution (Figure 14). This is probably related to the effect of citrate, decreasing the stress of the liquid/gas interface (cf. to Equation (3)). As expected, the inclusion of citrate in the depositing bath formulation does not only impact the obtained

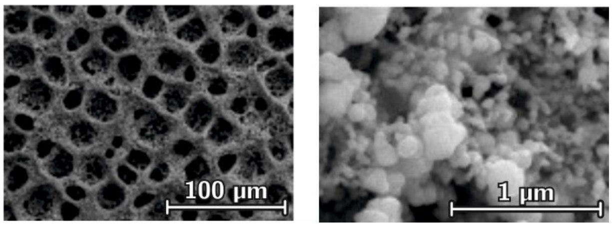

Figure 13. Scanning electron micrographs of an Ag foam deposited on a Pt substrate from a bath that contained 0.01 mol dm^{-3} Ag_2SO_4,

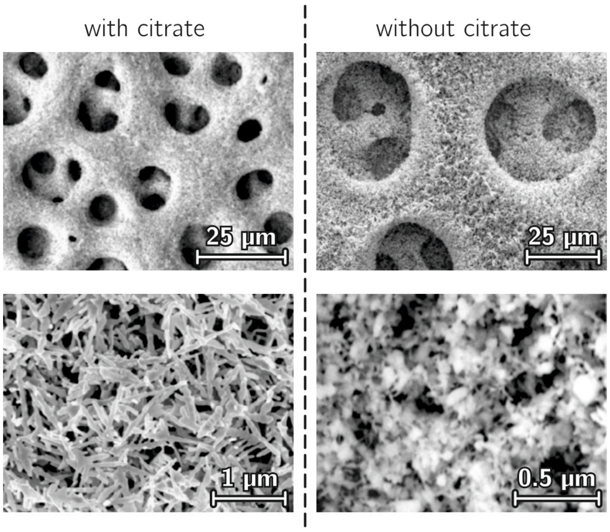

Figure 14. Scanning electron micrographs of an Ag foam deposited on an Ag substrate from a bath composed of 0.02 mol dm^{-3} Ag_2SO_4 and 1.5 mol dm^{-3} H_2SO_4. The effect of adding sodium citrate to the bath in a 0.1 mol dm^{-3} concentration can clearly be seen. Galvanostatic depositions with a nominal current density of -3 A cm^{-2}, lasting 20 seconds, were carried out in both cases. Reproduced from Ref. 72, with permission of the American Chemical Society.

foam morphology, but also its catalytic activity towards CO_2 electroreduction. Especially in terms of long-term stability, the multiporous Ag foams deposited from citrate containing baths perform better than the ones prepared from citrate-free depositing solutions.[72]

Silver foams deposited from a citrate-containing solution were used as electrocataysts for CO_2 reduction. Potentiostatic electrolyses in CO_2-saturated 0.5 mol dm^{-3} $KHCO_3$ solutions were carried out in a hermetically tight H-type cell, and the partial current densities corresponding to the formation of each products were determined by means of on-line gas chromatography.[91] The potential of using silver foams as electrocatalyst materials becomes evident by comparing the catalytic properties of foams to those of a plain silver plate, as in Figure 15.[72]

There are two features of DHBT-deposited silver foams that become immediately apparent in Figure 15: *i.)* that the silver foam produces CO with a much higher activity and over a considerably broader potential region, compared to a simple silver plate; and *ii.)* that due to the foam-like structure, the diversity of products is increased, and especially at high negative potentials, some rather significant amounts of hydrocarbons (primarily methane and ethylene) are also formed. While the former feature casts the silver foam catalyst described in Ref. 72 one of the best Ag-based CO forming catalysts reported so far in the literature for aqueous environments, the latter feature deserves attention because the formation of hydrocarbons was reported before only on Cu-based electrode materials, while Ag is traditionally considered a strictly CO-forming catalyst.[92] Note here that, as proven by control experiments in Ref. 72, the colourful product palette shown in Figure 15b is not due to artefacts caused by citrate that was applied as an additive to the deposition bath.

As shown in Figure 15b, some -20 μA cm^{-2} partial current of CO formation can already be detected at the potential of -0.3 V *vs.* RHE, while the onset potential of CO_2 reduction is about 300 mV more negative on planar silver surfaces. Note that onset potentials as low as -0.3 V *vs.* RHE were so far only reported for gold nano-needle catalysts.[93] As the potential is set to more and more cathodic values, the overall current density rises, with CO remaining the only or at least the majority reaction product, down until -0.8, respectively to -1.2 V.

At potentials less cathodic than -0.8 V *vs.* RHE, not even hydrogen evolution is observed, unlike the case of plain surface silver electrodes, at which HER competes with CO_2 reduction even at low overpotentials. As a result, the CO-selectivity of the silver foam prepared in Ref. 72 is not peak-like as is the case of planar silver electrodes, but it remains constantly above 90% over a more than 900 mV broad potential range.

This superior selectivity towards the formation of CO was not met by other silver foam catalysts reported in the literature,[73,74] in particular because of differences of the foam structure at the nanoscale. In Ref. 72 we hypothesized that the highly anisotropic, needle-like structures seen in Figure 14, obtained so far only by citrate-assisted deposition, may account for the superior selectivity towards CO production by increasing the bonding strength of adsorbed CO to the catalyst surface. For example, on commercially available silver foam electrodes with grain-like microstructure, the Faradaic efficiency of CO production is generally lower, although the potential regime of CO formation is still broader than that on pristine silver plates.[74]

Another hint that underlines the pivotal role of adsorbed CO played in the mechanism is the formation of C_1 (methane) and, to some extent, C_2 (ethylene) hydrocarbons, which also necessitates an adsorbed CO intermediate.[94] Of course, apart

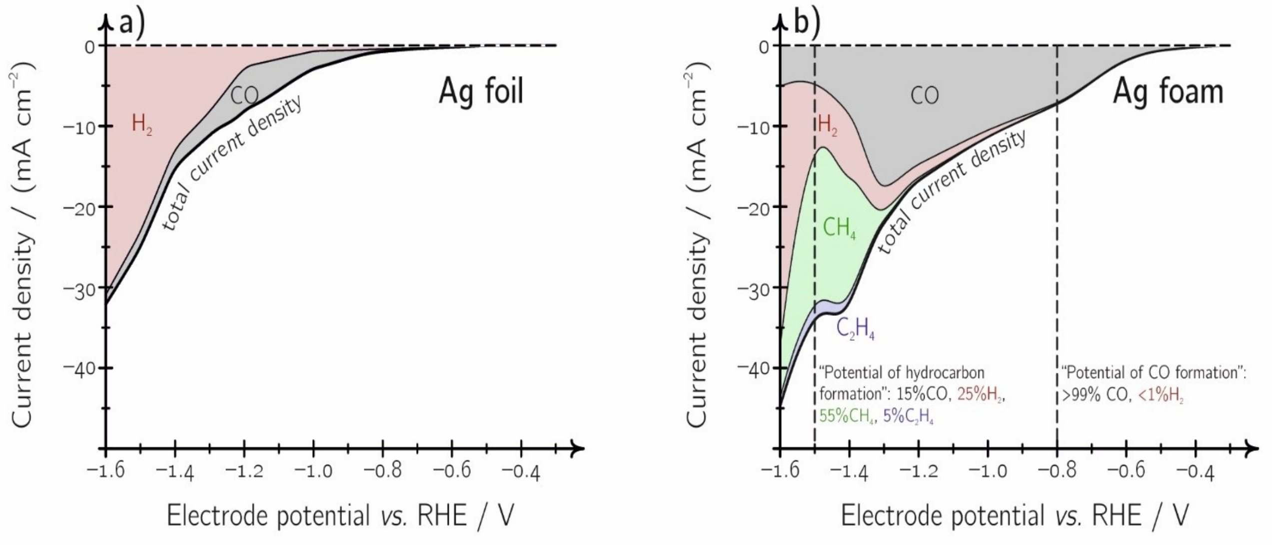

Figure 15. Polarization curves (interpolated) of a) a silver plate and b) the silver foam deposited from a citrate containing solution, shown in Figure 14. Electrolyses were carried out at distinct potentials in a CO_2-saturated 0.5 mol dm^{-3} $KHCO_3$ solution, and the product distribution was determined by online gas chromatography. Colour-shaded areas show the distribution of reaction products. Currents were normalized to the geometric (nominal) surface area of the electrodes. The graphs were prepared using data from Ref. 72.

from the higher bonding energy of adsorbed CO, and the longer residence time of surface-bound CO caused thereby, for the effective formation of hydrocarbons relatively intense H^+ reduction is also required to take place, so that surface-bound H atoms and CO molecules can effectively react.

From this point of view, the confinement of the reaction scenery to the small (macro)pores seems to be of primary importance. The hierarchical structure of the silver foam can make sure that potential intermediates (such as surface-bound CO or H_2) may not easily leave the electrode surface (and become a product), but instead get entrapped in the pores, at least for some time, having a higher chance to recombine.

The effect of confinement is illustrated by Figure 16a, showing a cavity of diameter *d* in contact with its surroundings through an opening of diameter *a* and length *L*. By theoretical studies on the random walk of a particle inside this cavity, it was shown by Berezhkovskii *et al.*[95] that the τ_{res} characteristic time of residence (*i.e.*, the average time a molecule would spend inside the void before diffusing out through the neck) can well be approximated using the simple formula

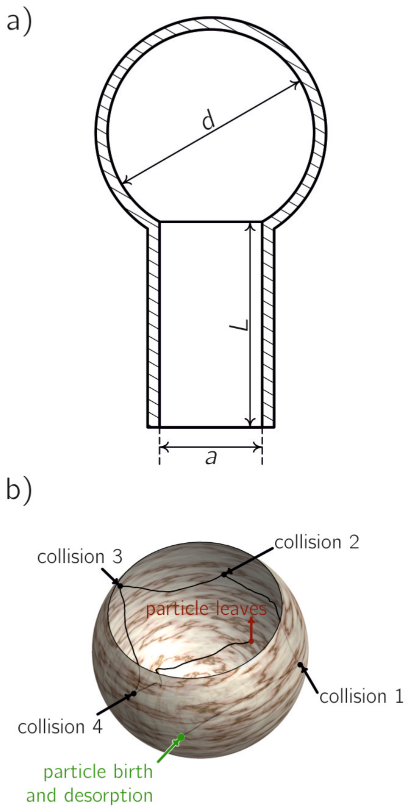

Figure 16. a) A spherical cavity of diameter *d*, connected to its surroundings by a neck with length *L* and diameter *a*. b) Simulated motion of a particle inside a spherical segment. After formed, the particle leaves the surface of the cavity and begins to traject, hitting in this case, four times the cavity wall before eventually leaving the void.

$$T_{res} = \frac{2d^3\ L}{3a^2\ D} \tag{4}$$

where *D* denotes the diffusion coefficient of the molecule.

Further taking into account that the characteristic time between two molecule-to-wall collisions can well be approximated as

$$T_{coll} = \frac{d^2}{6\ D} \tag{5}$$

it can be assumed that an average molecule, after born and before leaving the void, collides

$$N_{coll} = \frac{T_{res}}{T_{coll}} = \frac{4dL}{a^2} \tag{6}$$

times to the surface of the cavity. Using the arbitrary (but, based on the morphology shown for example in Figure 14, not unrealistic) parameter set of $d = 50\ \mu m$, $a = 25\ \mu m$, $L = 50\ \mu m$ and $D = 5 \cdot 10^{-6}\ cm^2 s^{-1}$, we get to a residence time of about 13 seconds, during which a formed molecule would impact about 16 times the wall of the cavity, having ample opportunity to re-adsorb, and act further as an intermediate.

As seen in Equations (4) and (6), the characteristic residence time and the mean collision number increases with the *L* length of the neck that separates the cavity from its surroundings. This hints to that the confinement effect in case of deep-buried cavities is bigger. For near-surface cavities (for which $L \approx 0$), another work of Berezhkovskii *et al.*[96] provides the formula

$$T_{res} = \frac{d^3 \pi}{12aD} \tag{7}$$

for the residence time, from which an average collision number

$$N_{coll} = \frac{d\pi}{2a} \tag{8}$$

follows. Using the above-mentioned parameters, the obtained residence time and collision number are about an order of magnitude smaller compared to when the escape occurs through a finite length neck. The concept is further illustrated by Figure 16b, showing the presumed Langevin trajectory[97] of a particle being formed and moving inside a void, before leaving it through an opening.

Although the above arguments are very simple and rather qualitative in nature, they well explain the effect of small-scale confinement on electrocatalytic processes. It is assumed that the above "multi-collision" effect is what lies behind the possibility of the formation of C_2 products on Ag foams, and a similar argument is often used for explaining CO_2 electroreduction mechanisms on-going on Cu electrodes, allowing even the formation of C_3 products.[98]

One has to note, however, that the Ag foam catalyst described in Ref. 72, although it is one of the most excellent catalyst material for CO production, is not the ideal playground for hydrocarbon formation. While it was observed that when operated on a long run at potentials of CO formation (see Figure 15b) the catalyst performs well without any significant degradation effects, as electrolyses are carried out at more negative potentials to form hydrocarbons, the performance of the catalyst decreases over time. This probably has to do with the poisoning of the silver foam by the formed methane, and can also be related to a mechanical degradation caused by the intensive gas evolution observed during long-lasting electrolyses.

In order to study degradation effects, we used identical location scanning electron microscopy[99] in Ref. 72. Figure 17 demonstrates degradation suffered by silver foams over long times of electrolyses at potentials where hydrocarbons are formed. Note here also, that long-lasting electrolysis at CO-forming potential does not cause any visible degradation of the catalyst.

From point of view of future applications of Ag foams in CO-producing electrolyzers, it also seems important in particular for future studies to fine-tune the foam preparation procedure in the direction of obtaining well-structured foams on substrates that are more challenging than a plain Ag foil. Deposition on gas diffusion electrodes (GDEs) seems to be a logical first step of up-scaling attempts. During our pilot studies in this direction, we found that the Ag foam preparation recipe mentioned before (and described in details in Ref. 72) needs further improvement, as it yields a less well-defined foam structure when we apply it for the deposition of Ag foams on GDEs (compare Figure 18a to Figure 14). Nonetheless, even though there is obviously space for further development, Ag foams on GDEs exhibit a superior activity towards CO formation, as shown by results of our recent (yet unpublished) investigations (Figure 18b).

3.6. Cu Foams

As opposed to silver and to the other metals discussed above, copper is usually considered as the only metal where the formation of C_1 (methane and methanol), C_2 (ethylene and ethyl-alcohol), or even C_3 products (propyl-alcohol) is possible, even if the applied catalyst is not of a foam structure.[92]

Several studies were conducted in the past with the aim of understanding the selectivity of Cu catalysts towards the formation of certain products.[75–78,94,100–107] These studies all

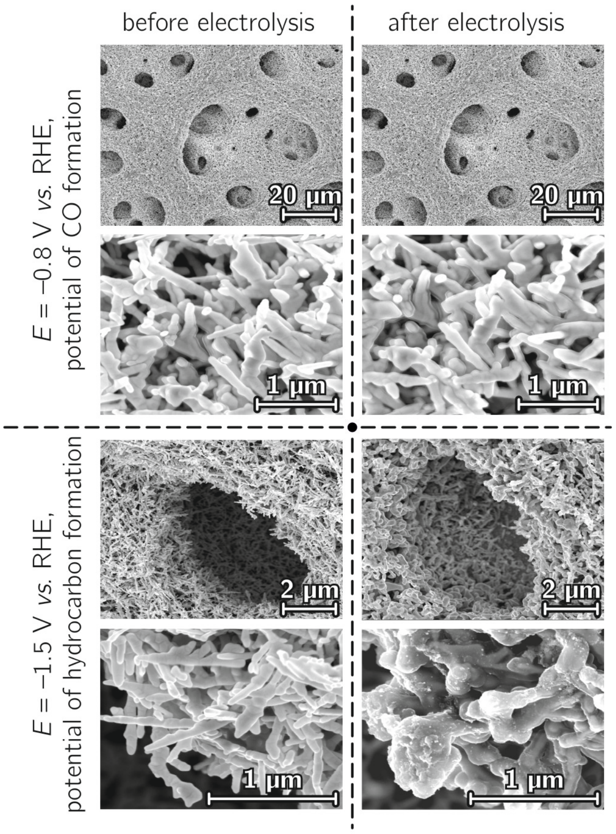

Figure 17. Scanning electron micrographs recorded at identical locations of an Ag foam catalyst, before and after being used for some hours for the electroreduction of CO_2. Mild potentials, where only CO is formed, cause no significant damage; however, long-time polarization in the range of extreme negative potentials where hydrocarbons are formed causes visible degradation, especially on the nanoscale.

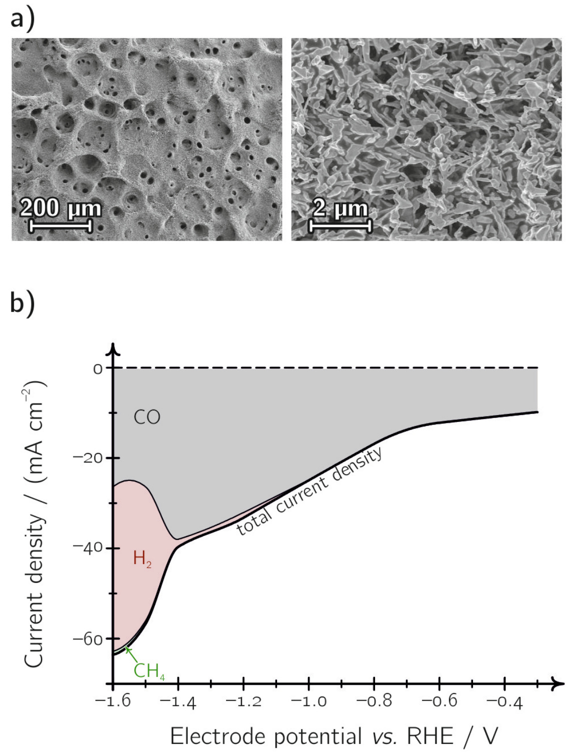

Figure 18. a) Scanning electron micrographs of a silver foam deposited by 20 s electrolysis using the recipe described in Ref. 72 onto a Sigracet 39 BC gas diffusion electrode (Fuel Cell Store). b) Interpolated product distribution and total current density plot measured on the GDE by electrolyses carried out in an H-type cell at distinct potentials in a CO_2-saturated 0.5 mol dm^{-3} $KHCO_3$ solution. (Unpublished data)

underline the importance of the bonding strength between the catalyst surface and the $\cdot CO_2^-$ radical anion that, following a coupled H^+/e^- (alternatively, direct adsorbed H) transfer, forms surface-bound CO, which acts as a second key intermediate.[75] By contrast to some other metals previously mentioned in this study, copper can bond CO strongly enough to allow its further reduction to C_1, C_2 or even to C_3 products. Both experimental[100] and theoretical investigations[104] indicate that C–C coupling is more probable on (100) oriented copper surfaces while the C_1 pathway is preferential on the (111) surface.[75] As a result, significant effort (relying on the use of sputtering and electropolishing,[103] as well as electrodeposition and anodization techniques[108]) has recently been devoted to find possibilities of tuning Cu surfaces towards the right (preferably, C_2) selectivity. Amongst these approaches, the oxidation of the copper surface,[105–107] yielding weekly coordinated structures, seems to be the most promising. Note here, however, that the thus obtained catalysts should not be referred to as copper oxide, but rather as oxide derived (OD) copper catalysts, since under the heavily cathodic operating conditions, the copper oxide is instantaneously reduced to an elementary Cu state.

In a recent paper,[75] we combined the activation of Cu catalysts via the reduction of its surface oxide with the DHBT-based foam deposition approach first developed by Shin *et al.*[30] We thus produced mesoporous, large surface area copper foams, shown in Figure 19. Several procedures for the potentiostatic (Figures 3 and 4) and galvanostatic (Figure 5) means of copper foam preparation were reported by the works of Nikolić *et al.*[31–36] and of Zhang *et al.*[52] These works, and the mechanistic description of copper foam deposition described therein, were reviewed here in the section before.

For purposes of CO_2 electrolysis, our group used galvanostatic deposition (nominal current density: $-3\ A\,cm^{-2}$) to deposit black copper foams on a Cu wafer substrate from a bath that contained $0.2\ mol\,dm^{-3}$ $CuSO_4$ and $1.5\ mol\,dm^{-3}$ H_2SO_4. As seen in Figure 19, deposits with a hierarchical macroporosity were obtained, with macropore sizes growing as a function of deposition time. The thus prepared Cu foams underwent a fast surface oxidation, following emersion from the plating bath. We demonstrated that these OD Cu foam catalysts show a superior selectivity toward C_2 product formation at particularly low overpotentials.[75]

In Figure 20 the electrocatalytic properties of the copper foam deposited with a 20 s deposition time are compared to those of a planar Cu wafer. Both surfaces exhibit a clear preference for hydrocarbon formation, in combination with a significantly reduced preference for formate production. Whereas on the Cu wafer methane is the primary product, the C_2 pathway seems to prevail on the Cu foam catalyst, with the C_1 pathway suppressed to such extent that not even traces of methane formation are detected.

The preference of OD Cu foams towards the C_2 pathway can probably be explained by two, synergistic effects: *i.)* that the OD Cu surface is composed more of (100) oriented (open) facets[75] and *ii.)* that due to the porous structure (confinement), key intermediates of the C_2 pathway may be entrapped and get readsorbed inside the catalyst pores. The latter effect is demonstrated by Figure 21, showing an anti-correlated variation of the Faradaic efficiencies of C_2 products and that of CO, as a function of the surface pore size of the copper foam catalyst.

With regard to the microscopic structure of the OD copper foam catalysts, we note that while thermal annealing can aid in the oxidation of the foam surface (and by altering the surface morphology, it may result in FE variations), the thus formed oxide is almost immediately reduced to elementary copper under the harsh cathodic conditions applied for CO_2 electrolysis, and has thus no role in the CO_2 reduction mechanism. The

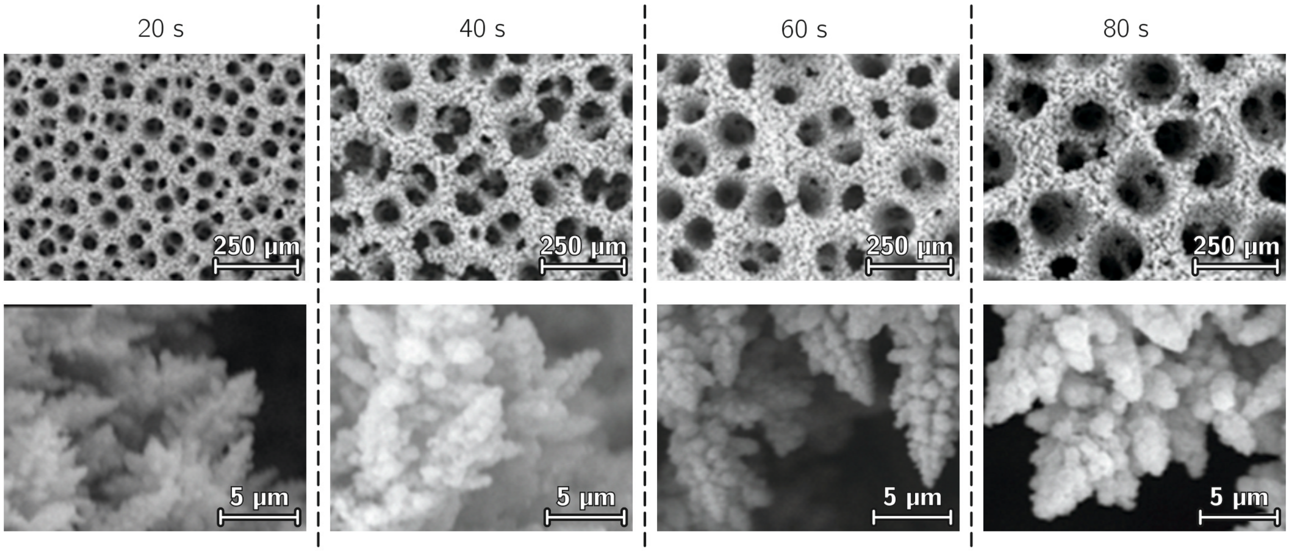

Figure 19. Scanning electron micrographs of Cu foams, deposited galvanostatically (nominal current density: $-3\ A\,cm^{-2}$) on a Cu wafer from a bath that contained $0.2\ mol\,dm^{-3}$ $CuSO_4$ and $1.5\ mol\,dm^{-3}$ H_2SO_4. Deposits obtained with different electrolysis times are shown. Reproduced from Ref. 75, with permission of the American Chemical Society.

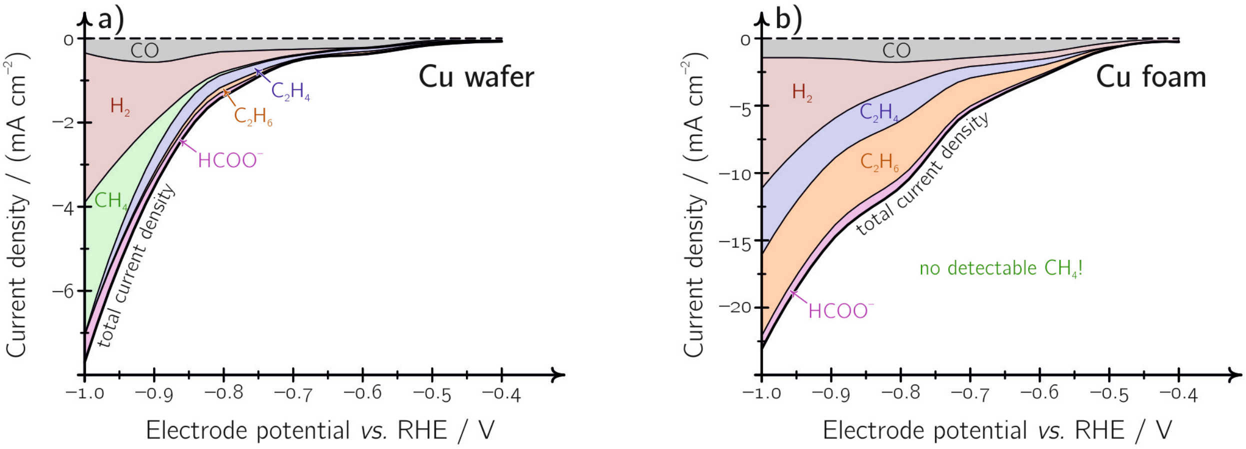

Figure 20. Polarization curves (interpolated) of a) a copper wafer and b) the copper foam shown in Figure 14 with the deposition time of 20 s. Electrolyses were carried out at distinct potentials in a CO_2-saturated 0.5 mol dm^{-3} $NaHCO_3$ solution, and the product distribution was determined by online gas, as well as post-electrolysis ionic liquid chromatography. Colour-shaded areas show the distribution of reaction products. Currents were normalized to the geometric (nominal) surface area of the electrodes. The graphs were prepared using data from Ref. 75.

disappearance (reduction) of surface copper oxides on Cu foam catalysts was recently proven by a combined operando X-ray diffraction (XRD), X-ray absorption spectroscopy (XAS) and Raman spectroscopy study.[76]

3.7. Ag–Cu Bimetallic Foams

By the combination of (primarily, CO forming) silver and (primarily, C_2 hydrocarbons forming) copper sites in the form of one bimetallic metal foam, it seems possible to direct the electroreduction of CO_2 towards the formation of products even more desired than either CO or hydrocarbons: ethyl- or even propylalcohol.[86]

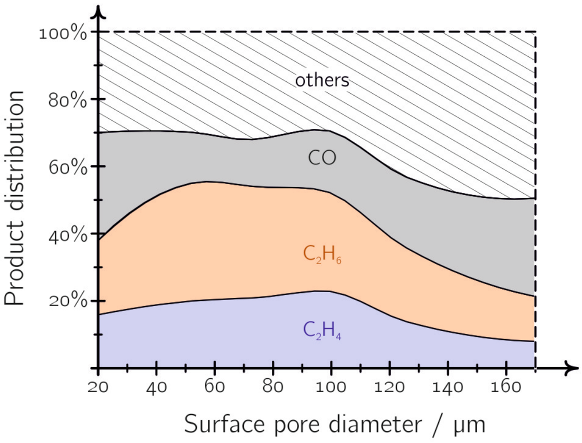

Figure 21. The distribution of CO_2 reduction products depend on the surface pore size of the Cu foam catalyst. Potentiostatic electrolyses lasting 1 hour were conducted at a potential of −0.8 V *vs.* RHE in a CO_2-saturated 0.5 mol dm^{-3} $NaHCO_3$ solution, and main gaseous products were analysed by means of online gas chromatography. Colour-shaded areas show the distribution of reaction products. The graph was prepared using data from Ref. 75.

The DHBT co-deposition of Ag–Cu bimetallic foams were first reported by Najdovski *et al.*,[46] who applied galvanostatic $|j| > 1\ \mathrm{A\,cm^{-2}}$ co-depositions in H_2SO_4-acidified baths that contained both $CuSO_4$ and $AgNO_3$. As expected,[109] no alloy formation was observed and Najdovski *et al.* showed that the Ag–Cu bimetallic foam consists of small segregates of silver and copper phases.[46]

They observed that the surface pore size obtained during codeposition increases with increasing the $c_{Ag+}:c_{Cu2+}$ ratio of the depositing bath. They argued that the increase of surface pore diameters, as well as the appearance of surface crack lines at higher silver contents is due to Ag exhibiting less catalytic activity towards HER than Cu (Figure 2), which favours the coalescence of H_2 bubbles.

The recipe of Najdovski *et al.*[46] was later applied by Kottakkat *et al.*[85] in order to create bimetallic Ag–Cu foams for purposes of CO_2 electroreduction. They used constant current (−1 A cm^{-2}, 10 s) co-deposition from baths containing 0.2 mol dm^{-3} $CuSO_4$, 1.5 mol dm^{-3} H_2SO_4 and 0.01–0.05 mol dm^{-3} $AgNO_3$. Kottakkat *et al.*[85] observed an improved CO selectivity and suppression of hydrogen evolution at low overpotentials, when comparing their bimetallic Ag–Cu foams to a plain Ag foil, and, similarly, a decrease of the Faradaic efficiency of formate production, compared to Cu foams.[85] The overall increase of the CO selectivity of bimetallic Ag–Cu foams was explained by an increased bonding strength of adsorbed CO, that Kottakkat *et al.*[85] verified by operando Raman spectroscopy. Although for other Ag–Cu bimetallic systems an enhanced selectivity towards multi-carbon oxygenate products was detected,[110] and it was attributed to near-surface alloying due to mechanical strain,[111] the formation of C_2 products, especially that of alcohols, was not observed by Kottakkat *et al.* on their Ag–Cu foams.[85]

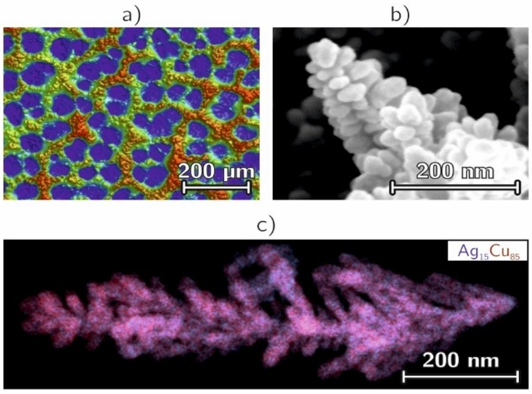

Figure 22. An Ag–Cu bimetallic foam deposited galvanostatically

In Ref. 86 we modified the original bath formulation of Najdovski *et al.*[46] by the inclusion of sodium citrate that, acting both as an adsorbent and a local chelating agent, changed the deposition mechanism,[86] resulting in honeycomb-like macropores and a fine dendritic microscopic structure. This is shown in Figure 22 for an $Ag_{15}Cu_{85}$ bimetallic foam deposited galvanostatically ($j = -3\ \mathrm{A\,cm^{-2}}$, $t = 20$ s) on a Cu foil substrate from a bath containing 1.5 mol dm^{-3} H_2SO_4, 0.02 mol dm^{-3} $CuSO_4$, 0.002 mol dm^{-3} $AgNO_3$ and 0.1 mol dm^{-3} sodium citrate.

Note that the notation $Ag_{15}Cu_{85}$ is based on an ICP–OES determination of the (bulk) atomic composition and by no means reflects compound formation. The white-light interferometric image of the Ag–Cu foam in Figure 22a reveals a near-surface pore diameter of ~25 µm; note, however, that the pore diameter is expected to vary also in this case along the surface normal, as was shown for other foams before (Figure 7). The side-walls of the macropores reveal dendrites with dimensions <50 nm, as shown in the electron micrograph of Figure 22b. The dendrites themselves are composed of small, individual Ag and Cu phases, as revealed by the energy-dispersive X-ray map in Figure 22c.

The electrocatalytic performance of $Ag_{15}Cu_{85}$ bimetallic foams was investigated in Ref. 86 by 1 hour long electrolysis experiments carried out at certain potentials in CO_2-saturated 0.5 mol dm^{-3} $KHCO_3$ solutions. Results of these electrolysis experiments are shown in Figure 23.a.

It can be seen in Figure 23a that within the range of low overpotentials ($-0.7\ \mathrm{V} < E < -0.3$ V *vs.* RHE) the predominant CO_2 reduction product is CO, assumed to take place preferentially on the Ag sites of the bimetallic catalyst. Accordingly, the Faradaic efficiency of formate production is suppressed, especially when compared to Cu foams, and in agreement with the observations of Kottakkat *et al.*[85] made on other bimetallic Ag–Cu foams. At potentials more cathodic than −0.5 V *vs.* RHE, hydrogen formation sets on, and along with it, pathways for the production of methane, ethylene and some small amounts ($<$ 1%) of ethane are opened.[86] At $E < -0.7$ V, the product distribution of CO_2 reduction is already obviously dominated by the Cu component, as C–C coupling reactions are enabled. It can be assumed, that the C–C coupling reaction benefits from the high abundance of CO inside the porous catalyst. Due to the small domain sizes of the metallic components of the as-deposited $Ag_{15}Cu_{85}$ foam, the CO intermediate is rapidly transported from the Ag (CO producer) to the Cu domains (C–C coupler), either by surface diffusion ("spill-over") or by diffusion through the liquid electrolyte phase inside the pores of the bimetallic foam (as depicted in Figure 16b). As shown in Figure 23a, CO_2 reduction already results in the formation of some little amount of ethanol at this potential range, while only traces of *n*-propanol are detected.

The product distribution becomes remarkably different if we make subject the deposited $Ag_{15}Cu_{85}$ foam to thermal annealing before it is used as an electrocatalyst of CO_2

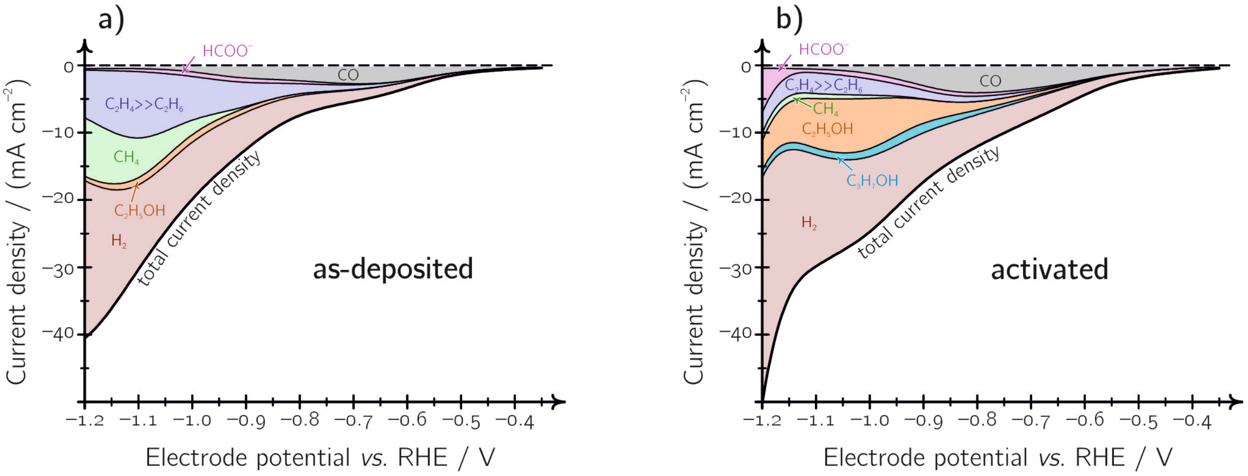

Figure 23. Polarization curves (interpolated) of CO_2 reduction recorded on a) an as-deposited $Ag_{15}Cu_{85}$ bimetallic foam and b) on the same foam following activation by mild thermal annealing in air (200 °C, 12 hours). Electrolyses were carried out at distinct potentials in a CO_2-saturated 0.5 mol dm^{-3} $KHCO_3$ solution, and the product distribution was determined by online gas, as well as by post-electrolysis ionic liquid chromatography. Colour-shaded areas show the distribution of reaction products. Currents were normalized to the geometric (nominal) surface area of the electrodes. The graphs were prepared using data from Ref. 86.

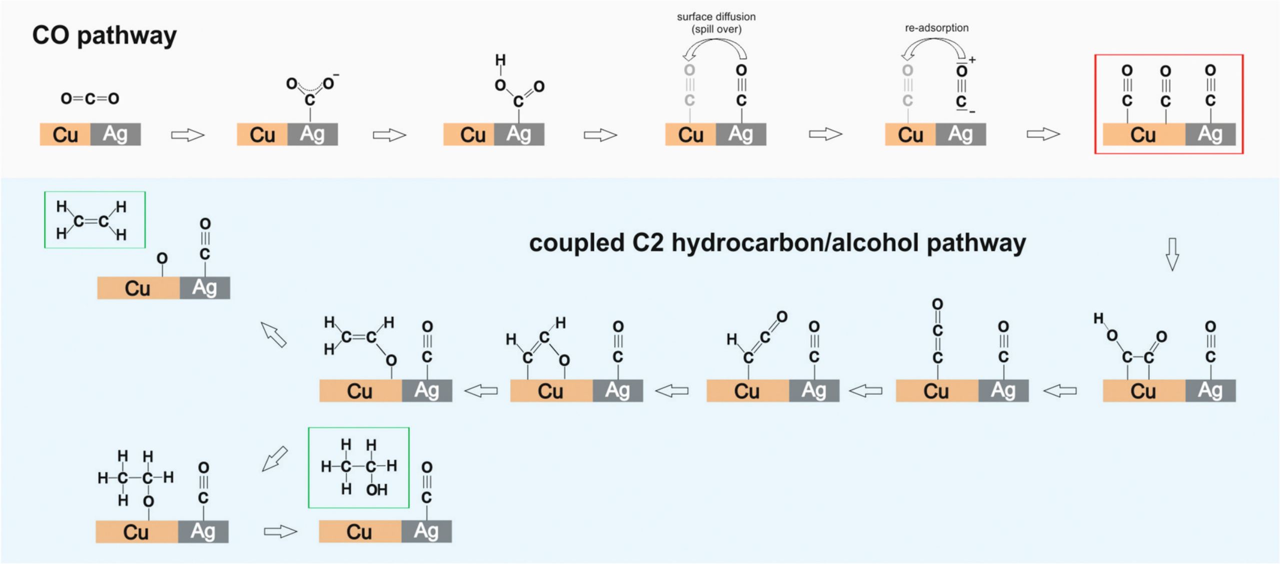

Figure 24. Proposed reaction scheme illustrating the coupling of the CO pathway and the C_2 hydrocarbon/alcohol reaction pathways on oxide-derived $Ag_{15}Cu_{85}$ bimetallic foams. Reproduced from Ref. 86 with the permission of Elsevier.

reduction (Figure 23b). It was shown in Ref. 86 that thermal annealing under mild conditions (200 °C for 12 hours) transforms the Cu in the bimetallic system into a mixture of crystalline Cu_2O and amorphous CuO, whereas the Ag islands remain in a metallic state due to the thermal instability of Ag_2O above temperatures of 180 °C. The selective oxidation of Cu in the bimetallic $Ag_{15}Cu_{85}$ catalyst goes along with an enrichment of Cu oxides on the surface of the formed mixed $AgCu_xO$ foam. Although both *operando* X-ray diffraction and *operando* Raman spectroscopy confirm that the cuprous/cupric oxide content of the catalyst is reduced back to the metallic state at potentials applied for CO_2 electrolysis, the formed oxide-derived bimetallic Ag–Cu foam was found to exhibit high selectivity towards alcohol formation (Figure 23b), with Faradaic efficiencies of about 34% and 7% for ethanol and *n*-propanol formation, respectively.

Extended electrolysis experiments (100 h) indicated a superior degradation resistance of the oxide-derived bimetallic catalyst, which was ascribed to the effective suppression of the C_1 hydrocarbon reaction pathway, assuring that irreversible carbon contaminations, appearing in particular during methane production, can be avoided.

The suggested mechanism of alcohol formation on the oxide derived, bimetallic Ag–Cu foam catalyst surface is shown in Figure 24. This mechanism is consistent with published models on alcohol formation on Cu,[112] with the addition that on the bimetallic foam CO forms selectively on the Ag domains, and is subsequently transported to the Cu domains via surface diffusion ("spillover") or alternatively via CO transport through the solution phase (desorption/readsorption). Besides the increased abundance of CO intermediates, it is the stabilization of the chemisorbed CO on the catalyst surface which further directs CO_2 reduction towards C–C coupling and alcohol formation, as confirmed by *operando* Raman experiments.[86]

3.8. Multimetallic Foams

The combination of multiple (more than two) metals in one foam structure has recently emerged as a new possibility of electrocatalyst design. In 2019 Lee *et al.*[113] described a Cu–In–Ag foam that was created by the deposition of a Cu foam that was electroplated by In and further modified by partial galvanic replacement of In with Ag (Figure 25). The preparation method is described briefly in Table 1, details can be found in Ref. 113. By the use of this trimetallic foam, Lee *et al.* achieved high Faradaic efficiency of CO production already at low overpotentials that, as they argued, was a result of synergistic effects arising from the high surface area of the Cu foam, the HER suppressing effect of In, and by Ag as a CO

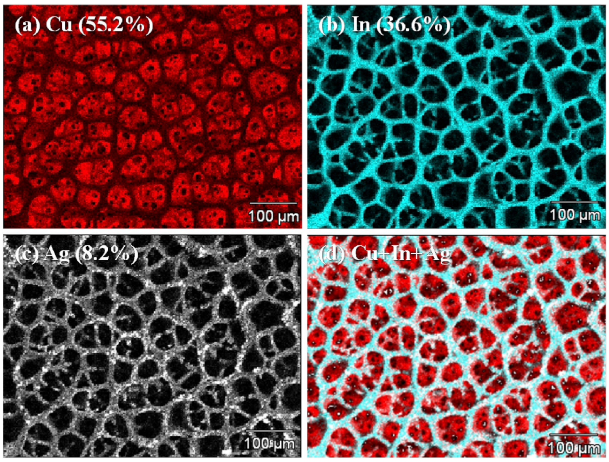

Figure 25. Elemental energy dispersive spectroscopy maps of the Ag–In–Cu foam prepared by Lee *et al.*[113] (a) Cu, (b) In, (c) Ag, and (d) Cu + In + Ag. Reproduced from Ref. 113, with the permission of Elsevier.

Table 1. Overview of the metal foams (preparation and CO_2 reduction characteristics) discussed in Section 3.

Metal (featured CO_2 reduction product)	Preparation using the DHBT technique	CO_2 reduction characteristics
Sn, pure (formate)[67]	0.15 mol dm^{-3} $SnSO_4$, 1.5 mol dm^{-3} H_2SO_4., galvanostatic deposition on Sn foil, typ. current density: −3 A cm^{-2}, typ. deposition time: 5 to 20 s.	In CO_2-sat. 0.1 mol dm^{-3} $NaHCO_3$, at $E = -1.9$ V vs. SCE $j \approx -23.5$ mA cm^{-2}; > 90% *FE* for formate production.
Sn@Cu (formate)[81]	0.1 mol dm^{-3} $SnCl_2$, 0.1 mol dm^{-3} sodium citrate, 1.2 mol dm^{-3} HCl, galvanostatic deposition on electro-polished Cu foil, typ. current density: −2 A cm^{-2}, typ. deposition time: 2 min.	In CO_2-sat. 0.1 mol dm^{-3} $KHCO_3$, at $E = -1.2$ V vs. RHE $j \approx -6.5$ mA cm^{-2}; > 90% FE for formate production.
Pb (formate)[68]	0.01 mol dm^{-3} $PbClO_4$, 0.01 mol dm^{-3} sodium citrate, 1.0 mol dm^{-3} $HClO_4$, galvanostatic deposition on Pb plate, typ. current density: −0.5 to −8 A cm^{-2}, typ. deposition time: 10 to 20 s.	In CO_2-sat. 0.5 mol dm^{-3} $KHCO_3$, at $E = -1.7$ V vs. SCE $j \approx -10$ mA cm^{-2}; > 97% FE for formate production at 5 °C.
Zn (CO)[69]	0.1 mol dm^{-3} $ZnSO_4$, 1.5 mol dm^{-3} $(NH_4)_2SO_4$, galvanostatic deposition on a Cu mesh, typ. current density: −1 A cm^{-2}, typ. deposition time: 30 s.	In CO_2-sat. 0.1 mol dm^{-3} $KHCO_3$, at $E = -0.95$ V vs. SCE $j \approx -27$ mA cm^{-2}; > 95% FE for CO formation.
Ag (CO)[72]	0.02 mol dm^{-3} Ag_2SO_4, 0.1 mol dm^{-3} sodium citrate, 1.5 mol dm^{-3} H_2SO_4, galvanostatic deposition on an Ag foil, typ. current density: −3 A cm^{-2}, typ. deposition time: 20 s.	In CO_2-sat. 0.5 mol dm^{-3} $KHCO_3$, at $E = -0.8$ V vs. RHE about −8 mA cm^{-2}; > 99% FE for CO formation. At $E = -1.5$ V vs. RHE $j \approx -36$ mA cm^{-2}; FEs: 15% CO, 25% H_2, 55% CH_4, 5% C_2H_4.
Cu (C_2 hydrocarbons)[75]	0.2 mol dm^{-3} $CuSO_4$, 1.5 mol dm^{-3} H_2SO_4, galvanostatic deposition on a Cu wafer, typ. current density: −3 A cm^{-2}, typ. deposition time: 20 s. See Ref..	In CO_2-sat. 0.5 mol dm^{-3} $KHCO_3$, at $E = -0.8$ V vs. RHE $j \approx -12$ mA cm^{-2}; FEs: 37% C_2H_6, 22% C_2H_4, 16% CO, 7% HCOOH, 17% H_2. See Ref. 75.
CuAg bimetallic ($C_{\geq 2}$ alcohols)[86]	0.02 mol dm^{-3} $CuSO_4$, 0.002 mol dm^{-3} $AgNO_3$, 1.5 mol dm^{-3} H_2SO_4, galvanostatic deposition on a Cu foil, typ. current density: −3 A cm^{-2}, typ. deposition time: 20 s, activated by annealing in air at 200 °C, 12 hours.	In CO_2-sat. 0.5 mol dm^{-3} $KHCO_3$, at $E = -1.05$ V vs. RHE $j \approx -27$ mA cm^{-2}; FEs: 28% C_2H_5OH, 4% C_3H_7OH, 10% C_2 hydrocarbons, 2.5% formate, 2.5% CH_4, 3% CO, 50% H_2.
AgInCu trimetallic (CO)[113]	Cu foam substrate is prepared from 0.12 mol dm^{-3} $CuSO_4$, 0.5 mol dm^{-3} H_2SO_4, 1.2 mol dm^{-3} $(NH_4)_2SO_4$ and 40 μmol dm^{-3} benzotriazole on a Ti foil, galvanostaticaly, at a current density of −1.2 A cm^{-2} for 40 s. In deposition then takes place on the Cu foam at a current density of −50 mA cm^{-2} for 900 s, in a 0.1 mol dm^{-3} $InCl_3$ and 0.5 mol dm^{-3} $HClO_4$ solution. Galvanic replacement by Ag follows by immersion into a solution of 10 mmol dm^{-3} $AgNO_3$ and 2 mmol dm^{-3} 2-nitrobenzoic acid.	In CO_2-sat. 0.5 mol dm^{-3} $KHCO_3$, at $E = -0.53$ V vs. RHE $j \approx -2$ mA cm^{-2}; > 74% FE for CO formation.

producer. Apart from minor amounts of formate produced, Lee *et al.* did not detect any products other than CO and H_2 on this trimetallic foam.

4. Summary and Outlook

In this review we attempted to provide an oversight on the current state-of-the-art of DHBT-based deposition of metal foams, and on the application of these materials as promising new catalysts of the electroreduction of CO_2.

We gave an introduction to the phenomenology and mechanism of DHBT-based deposition of metal foams, addressing the most important factors affecting the structure and surface morphology of the prepared foams. It was shown that by a careful selection of appropriate experimental parameters, foams of hierarchical structure can be created from various types of noble, intermediate and normal metals. The success of DHBT-based foam deposition depends on a set of parameters, and appropriate selection of the applied (potentiostatic/galvanostatic) mode of deposition, the value of the electrode potential or current at which the deposition is carried out, as well as the proper formulation of the depositing bath have a key impact on the deposited foam structure. With respect to bath formulation, most emphasis is laid on the concentration of the used metal salt and of the acid component, as well as on the concentration of buffering or complexing agents, and that of surfactants.

The review contains a brief description of several recipes, originating from works of our own or that of other groups, for the deposition of some metal foams, including pure metals such as Sn, Pb, Zn, Ag, Cu, as well as two-component systems like Sn foams deposited on Cu and the mixed Ag–Cu bimetallic foam. The reason why these metal foams and not some others like Pt, Pd, or Au were made subject of this study, is that the mentioned metals are the most promising candidates to be used as catalyst materials in electrochemical CO_2 reduction.

Accordingly, foams prepared by the DHBT technique from the above metals were also discussed from the point of view of CO_2 reduction, by placing special emphasis on the product distribution of this versatile process. While it is usually noted that on metal foams, mostly due to their increased surface area, electrocatalytic processes can occur at a higher rate compared to plain electrodes of the same metal, we found that hierarchical metal foams prepared by the DHBT technique often have a lot more to offer.

As it was pointed out especially in the cases of Ag, Cu and Ag–Cu bimetallic foams, the pores of these hierarchical three-dimensional structures can harbour reactions which would otherwise be unavailable on open surfaces due to the confinement (entrapping) of key reaction intermediates. In case of CO_2 electroreduction, confinement allows desorbed CO and H_2 to remain close and potentially re-adsorb on the electrode surface, ultimately leading to the formation of reaction products of a lower oxidation state (such as hydrocarbons and alcohols). Moreover, by the application of post-deposition, pre-electrolysis treatments (such as the oxidation of Cu-containing foams by annealing in air), the microstructure of the foams may further be fine-tuned towards the formation of certain, desired, CO_2 reduction products. Although most metal oxides never survive the reductive conditions of CO_2 electrolysis, oxide-derived surfaces have a different (usually, more open) structure, which opens a pathway before the formation of C_2 and even of C_3 products.

To conclude, the DHBT technique of metal foams preparation has the key advantage of meeting the most important structural and electronic factors that are considered essential for the electrocatalysis of CO_2 reduction. Processes fundamental to the technique, such as bubble nucleation, growth and detachment mechanisms, as well as the kinetics of metal deposition and dendrite formation are now understood at a level which will allow the rational design of mono- or multi-metallic foams that can act as new catalysts of CO_2 reduction. As it was shown, research on some metal foam catalysts is now ready to move in the direction of industrial upscaling (cf. to Figure 18), as foams with good structural qualities can even be deposited on gas diffusion electrodes. It is thus expected that in the coming years, metal foams will provide a viable alternative to, and may even outperform supported nanoparticle based (ink-like) catalysts in terms of yield, selectivity and, especially, stability.

Acknowledgements

Support by the CTI Swiss Competence Center for Energy Research (SCCER Heat and Electricity Storage) is gratefully acknowledged. P. B. acknowledges financial support from the Swiss National Foundation (grant 200020-172507). S. V. acknowledges support from the National Research, Development and Innovation Office of Hungary (NKFIH grants PD124079 and FK135375).

Conflict of Interest

The authors declare no conflict of interest.

Keywords: power-to-value · CO_2 reduction · Faradaic efficiency · selectivity · confinement

[1] S. J. Davis, K. Caldeira, H. D. Matthews, *Science* **2010**, *329*, 1330–1333.
[2] B. Khezri, A. C. Fisher, M. Pumera, *J. Mater. Chem. A* **2017**, *5*, 8230–8246.
[3] F. D. Meylan, V. Moreau, S. Erkman, *J. CO_2 Util.* **2015**, *12*, 101–108.
[4] W. Luc, F. Jiao, *ACS Catal.* **2017**, *7*, 5856–5861.
[5] P. Liu, G. Chen, *Porous Materials*, Butterworth-Heinemann, Oxford, **2014**, pp. 189–220.
[6] W. Zhu, R. Zhang, F. Qu, A. M. Asiri, X. Sun, *ChemCatChem* **2017**, *9*, 1721–1743.
[7] H. Zhao, Y.-P. Zhu, Z.-Y. Yuan, *Eur. J. Inorg. Chem.* **2016**, *2016*, 1916–1923.
[8] *IUPAC Compendium of Chemical Terminology* (Eds.: A. D. Mc-Naught, A. Wilkinson), Blackwell Scientific Publications, Oxford, 2nd ed, **1997**.
[9] R. Du, X. Jin, R. Hübner, X. Fan, Y. Hu, A. Eychmüller, *Adv. Energy Mater.* **2020**, *10*, 1901945.
[10] M. F. Ashby, T. Evans, N. A. Fleck, J. W. Hutchinson, H. N. G. Wadley, *Metal Foams: A Design Guide*, Butterworth-Heinemann, **2000**.
[11] H. W. Pickering, P. R. Swann, *Corrosion* **1963**, *19*, 373–389.
[12] K. Hashimoto, T. Goto, W. Suëtaka, S. Shimodaira, *Trans. Jpn. Inst. Met.* **1965**, *6*, 107–112.
[13] A. J. Forty, *Nature* **1979**, *282*, 597–598.
[14] J. Erlebacher, M. J. Aziz, A. Karma, N. Dimitrov, K. Sieradzki, *Nature* **2001**, *410*, 450–453.
[15] D. Walsh, L. Arcelli, T. Ikoma, J. Tanaka, S. Mann, *Nat. Mater.* **2003**, *2*, 386–390.
[16] H.-L. Gao, L. Xu, F. Long, Z. Pan, Y.-X. Du, Y. Lu, J. Ge, S.-H. Yu, *Angew. Chem. Int. Ed.* **2014**, *53*, 4561–4566; *Angew. Chem.* **2014**, *126*, 4649–4654.
[17] B. C. Tappan, M. H. Huynh, M. A. Hiskey, D. E. Chavez, E. P. Luther, J. T. Mang, S. F. Son, *J. Am. Chem. Soc.* **2006**, *128*, 6589–6594.
[18] B. C. Tappan, S. A. Steiner, E. P. Luther, *Angew. Chem. Int. Ed.* **2010**, *49*, 4544–4565; *Angew. Chem.* **2010**, *122*, 4648–4669.
[19] N. C. Bigall, A.-K. Herrmann, M. Vogel, M. Rose, P. Simon, W. Carrillo-Cabrera, D. Dorfs, S. Kaskel, N. Gaponik, A. Eychmüller, *Angew. Chem. Int. Ed.* **2009**, *48*, 9731–9734; *Angew. Chem.* **2009**, *121*, 9911–9915.
[20] W. Liu, A.-K. Herrmann, N. C. Bigall, P. Rodriguez, D. Wen, M. Oezaslan, T. J. Schmidt, N. Gaponik, A. Eychmüller, *Acc. Chem. Res.* **2015**, *48*, 154–162.
[21] S. Tang, S. Vongehr, Y. Wang, J. Cui, X. Wang, X. Meng, *J. Mater. Chem. A* **2014**, *2*, 3648–3660.
[22] B. J. Plowman, L. A. Jones, S. K. Bhargava, *Chem. Commun.* **2015**, *51*, 4331–4346.
[23] O. Lummer, F. Kurlbaum, *Ann. Phys. Chem.* **1892**, *282*, 204–224.
[24] F. Kohlrausch, *Ann. Phys. Chem.* **1897**, *299*, 423–430.
[25] S. E. Stanca, F. Hänschke, A. Ihring, G. Zieger, J. Dellith, E. Kessler, H.-G. Meyer, *Sci. Rep.* **2017**, *7*, 1074.
[26] *Modern Electroplating* (Eds.: M. Schlesinger, M. Paunovic), Wiley, New York, 5th ed, **2010**.
[27] C. Marozzi, A. Chialvo, *Electrochim. Acta* **2000**, *45*, 2111–2120.
[28] C. Marozzi, A. Chialvo, *Electrochim. Acta* **2001**, *46*, 861–866.
[29] H.-C. Shin, J. Dong, M. Liu, *Adv. Mater.* **2003**, *15*, 1610–1614.
[30] H.-C. Shin, M. Liu, *Chem. Mater.* **2004**, *16*, 5460–5464.
[31] N. D. Nikolić, K. I. Popov, Lj. J. Pavlović, M. G. Pavlović, *J. Electroanal. Chem.* **2006**, *588*, 88–98.
[32] N. Nikolić, K. Popov, Lj. Pavlović, M. Pavlović, *Sensors* **2007**, *7*, 1–15.
[33] N. Nikolić, G. Branković, M. Pavlović, K. Popov, *J. Electroanal. Chem.* **2008**, *621*, 13–21.
[34] N. D. Nikolić, K. I. Popov, *Mod. Aspects Electrochem.*, Springer, New York, **2010**, pp. 1–70.
[35] N. D. Nikolić, *Morphology of Electrochemically and Chemically Deposited Metals, Springer*, Cham, **2016**, pp. 171–203.
[36] N. D. Nikolić, *J. Electrochem. Sci. Eng.* **2020**, *10*, 111–126.
[37] S. Cherevko, X. Xing, C.-H. Chung, *Electrochem. Commun.* **2010**, *12*, 467–470.
[38] S. Cherevko, C.-H. Chung, *Electrochim. Acta* **2010**, *55*, 6383–6390.
[39] S. Cherevko, C.-H. Chung, *Talanta* **2010**, *80*, 1371–1377.
[40] S. Cherevko, C.-H. Chung, *Electrochem. Commun.* **2011**, *13*, 16–19.
[41] S. Cherevko, X. Xing, C.-H. Chung, *Appl. Surf. Sci.* **2011**, *257*, 8054–8061.
[42] S. Cherevko, N. Kulyk, C.-H. Chung, *Nanoscale* **2012**, *4*, 568–575.
[43] S. Cherevko, N. Kulyk, C.-H. Chung, *Nanoscale* **2012**, *4*, 103–105.
[44] I. Najdovski, P. R. Selvakannan, A. P. O'Mullane, S. K. Bhargava, *Chem. Eur. J.* **2011**, *17*, 10058–10063.
[45] A. Ott, L. A. Jones, S. K. Bhargava, *Electrochem. Commun.* **2011**, *13*, 1248–1251.
[46] I. Najdovski, P. R. Selvakannan, A. P. O'Mullane, *RSC Adv.* **2014**, *4*, 7207.
[47] V. E. Coyle, D. K. J. Oppedisano, L. A. Jones, A. E. Kandjani, Y. M. Sabri, S. K. Bhargava, *J. Electrochem. Soc.* **2016**, *163*, B689–B695.
[48] M. de J. Gálvez-Vázquez, V. Grozovski, N. Kovács, P. Broekmann, S. Vesztergom, *J. Phys. Chem. C* **2020**, *124*, 3988–4000.
[49] R. Winand, *Electrochim. Acta* **1994**, *39*, 1091–1105.
[50] S. Trasatti, *J. Electroanal. Chem. Interfacial Electrochem.* **1972**, *39*, 163–184.
[51] Y. Li, Y.-Y. Song, C. Yang, X.-H. Xia, *Electrochem. Commun.* **2007**, *9*, 981–988.
[52] H. Zhang, Y. Ye, R. Shen, C. Ru, Y. Hu, *J. Electrochem. Soc.* **2013**, *160*, D441–D445.

[53] K. Popov, S. S. Djokić, B. Grgur, *Fundamental Aspects of Electrometallurgy*, Springer, New York, **2013**.
[54] N. Ibl, *Chem. Ing. Tech.* **1961**, *33*, 69–74.
[55] P. Chandran, S. Bakshi, D. Chatterjee, *Chem. Eng. Sci.* **2015**, *138*, 99–109.
[56] L. J. J. Janssen, J. G. Hoogland, *Electrochim. Acta* **1970**, *15*, 1013–1023.
[57] H. Vogt, R. J. Balzer, *Electrochim. Acta* **2005**, *50*, 2073–2079.
[58] N. Kovács, V. Grozovski, P. Moreno-García, P. Broekmann, S. Vesztergom, *J. Electrochem. Soc.* **2020**, *167*, 102510.
[59] D. Fernández, P. Maurer, M. Martine, J. M. D. Coey, M. E. Möbius, *Langmuir* **2014**, *30*, 13065–13074.
[60] W. Fritz, *Phys. Z.* **1935**, *36*, 379–384.
[61] G. G. Láng, C. A. Barbero, *Laser Techniques for the Study of Electrode Processes*, Springer, Berlin, **2012**, pp. 41–73.
[62] S. A. Amadi, D. R. Gabe, M. Goodenough, *J. Appl. Electrochem.* **1991**, *21*, 1114–1119.
[63] H. Yang, X. Hao, J. Tang, W. Jin, C. Liu, H. Hou, X. Ji, J. Hu, *Appl. Surf. Sci.* **2019**, *494*, 731–739.
[64] Y. Li, W.-Z. Jia, Y.-Y. Song, X.-H. Xia, *Chem. Mater.* **2007**, *19*, 5758–5764.
[65] N. L. Ritzert, T. P. Moffat, *J. Phys. Chem. C* **2016**, *120*, 27478–27489.
[66] D. H. Won, C. H. Choi, J. Chung, M. W. Chung, E.-H. Kim, S. I. Woo, *ChemSusChem* **2015**, *8*, 3092–3098.
[67] D. Du, R. Lan, J. Humphreys, S. Sengodan, K. Xie, H. Wang, S. Tao, *ChemistrySelect* **2016**, *1*, 1711–1715.
[68] J. Wang, H. Wang, Z. Han, J. Han, *Front. Chem.* **2015**, *9*, 57–63.
[69] W. Luo, J. Zhang, M. Li, A. Züttel, *ACS Catal.* **2019**, *9*, 3783–3791.
[70] P. Moreno-García, N. Schlegel, A. Zanetti, A. C. López, M. de Jesús Gálvez-Vázquez, A. Dutta, M. Rahaman, P. Broekmann, *ACS Appl. Mater. Interfaces* **2018**, *10*, 31355–31365.
[71] M. Fan, S. Prabhudev, S. Garbarino, J. Qiao, G. A. Botton, D. A. Harrington, A. C. Tavares, D. Guay, *Appl. Catal. B* **2020**, *274*, 119031.
[72] A. Dutta, C. E. Morstein, M. Rahaman, A. Cedeño López, P. Broekmann, *ACS Catal.* **2018**, *8*, 8357–8368.
[73] H. Wang, Z. Han, L. Zhang, C. Cui, X. Zhu, X. Liu, J. Han, Q. Ge, *J. CO_2 Util.* **2016**, *15*, 41–49.
[74] Y. Yu, N. Zhong, J. Fang, S. Tang, X. Ye, Z. He, S. Song, *Catal.* **2019**, *9*, 57.
[75] A. Dutta, M. Rahaman, N. C. Luedi, M. Mohos, P. Broekmann, *ACS Catal.* **2016**, *6*, 3804–3814.
[76] A. Dutta, M. Rahaman, B. Hecker, J. Drnec, K. Kiran, I. Z. Montiel, D. J. Weber, A. Zanetti, A. C. López, I. Martens, P. Broekmann, M. Oezaslan, *J. Catal.* **2020**.
[77] S. Sen, D. Liu, G. T. R. Palmore, *ACS Catal.* **2014**, *4*, 3091–3095.
[78] S. Min, X. Yang, A.-Y. Lu, C.-C. Tseng, M. N. Hedhili, L.-J. Li, K.-W. Huang, *Nano Energy* **2016**, *27*, 121–129.
[79] Y. Wang, J. Zhou, W. Lv, H. Fang, W. Wang, *Appl. Surf. Sci.* **2016**, *362*, 394–398.
[80] W. Lv, J. Zhou, F. Kong, H. Fang, W. Wang, *Int. J. Hydrogen Energy* **2016**, *41*, 1585–1591.
[81] B. Qin, H. Wang, F. Peng, H. Yu, Y. Cao, *J. CO_2 Util.* **2017**, *21*, 219–223.
[82] C. Chen, Y. Pang, F. Zhang, J. Zhong, B. Zhang, Z. Cheng, *J. Mater. Chem. A* **2018**, *6*, 19621–19630.
[83] J. Zeng, K. Bejtka, W. Ju, M. Castellino, A. Chiodoni, A. Sacco, M. A. Farkhondehfal, S. Hernández, D. Rentsch, C. Battagliaand, C. F. Pirri, *Appl. Catal. B* **2018**, *236*, 475–482.
[84] Q. Li, M. Li, S. Zhang, X. Liu, X. Zhu, Q. Ge, H. Wang, *Catalysts* **2019**, *9*, 476.
[85] T. Kottakkat, K. Klingan, S. Jiang, Z. P. Jovanov, V. H. Davies, G. A. M. El-Nagar, H. Dau, C. Roth, *ACS Appl. Mater. Interfaces* **2019**, *11*, 14734–14744.
[86] A. Dutta, I. Z. Montiel, R. Erni, K. Kiran, M. Rahaman, J. Drnec, P. Broekmann, *Nano Energy* **2020**, *68*, 104331.
[87] Y. Chen, M. W. Kanan, *J. Am. Chem. Soc.* **2012**, *134*, 1986–1989.
[88] A. Dutta, A. Kuzume, M. Rahaman, S. Vesztergom, P. Broekmann, *ACS Catal.* **2015**, *5*, 7498–7502.
[89] A. Dutta, A. Kuzume, V. Kaliginedi, M. Rahaman, I. Sinev, M. Ahmadi, B. R. Cuenya, S. Vesztergom, P. Broekmann, *Nano Energy* **2018**, *53*, 828–840.
[90] M. Fan, S. Garbarino, G. A. Botton, A. C. Tavares, D. Guay, *J. Mater. Chem. A*, **2017**, *5*, 20747–20756.
[91] A. Rudnev in *Encyclopedia of Interfacial Chemistry* (Ed.: K. Wandelt), Elsevier, Amsterdam, **2018**, pp. 321–325.
[92] Y. Hori, *Modern Aspects of Electrochemistry, Vol. 42*, Springer, New York, **2008**, pp. 89–189.
[93] W. Zhu, Y.-J. Zhang, H. Zhang, H. Lv, Q. Li, R. Michalsky, A. Peterson, S. Sun, *J. Am. Chem. Soc.* **2014**, *136*, 16132–16135.
[94] R. Kortlever, J. Shen, K. J. P. Schouten, F. Calle-Vallejo, M. T. M. Koper, *J. Phys. Chem. Lett.* **2015**, *6*, 4073–4082.
[95] A. M. Berezhkovskii, A. V. Barzykin, V. Y. Zitserman, *J. Chem. Phys.* **2009**, *130*, 245104.
[96] I. V. Grigoriev, Y. A. Makhnovskii, A. M. Berezhkovskii, V. Y. Zitserman, *J. Chem. Phys.* **2002**, *116*, 9574–9577.
[97] N. G. van Kampen, *Stochastic Processes in Physics and Chemistry, Elsevier, Amsterdam* **2007**.
[98] T.-T. Zhuang, Y. Pang, Z.-Q. Liang, Z. Wang, Y. Li, C.-S. Tan, J. Li, C. T. Dinh, P. D. Luna, P.-L. Hsieh, T. Burdyny, H.-H. Li, M. Liu, Y. Wang, F. Li, A. Proppe, A. Johnston, D.-H. Nam, Z.-Y. Wu, Y.-R. Zheng, A. H. Ip, H. Tan, L.-J. Chen, S.-H. Yu, S. O. Kelley, D. Sinton, E. H. Sargent, *Nat. Can.* **2018**, *1*, 946–951.
[99] N. Hodnik, M. Zorko, M. Bele, S. Hočevar, M. Gaberšček, *J. Phys. Chem. C*, **2012**, *116*, 21326–21333.
[100] Y. Hori, I. Takahashi, O. Koga, N. Hoshi, *J. Mol. Catal. A* **2003**, *199*, 39–47.
[101] K. J. P. Schouten, Y. Kwon, C. J. M. van der Ham, Z. Qin, M. T. M. Koper, *Chem. Sci.* **2011**, *2*, 1902.
[102] K. P. Kuhl, E. R. Cave, D. N. Abram, T. F. Jaramillo, *Energy Environ. Sci.* **2012**, *5*, 7050.
[103] W. Tang, A. A. Peterson, A. S. Varela, Z. P. Jovanov, L. Bech, W. J. Durand, S. Dahl, J. K. Nørskov, I. Chorkendorff, *Phys. Chem. Chem. Phys.* **2012**, *14*, 76–81.
[104] J. H. Montoya, C. Shi, K. Chan, J. K. Nørskov, *J. Phys. Chem. Lett.* **2015**, *6*, 2032–2037.
[105] C. S. Chen, J. H. Wan, B. S. Yeo, *J. Phys. Chem. C* **2015**, *119*, 26875–26882.
[106] K. W. Frese, *J. Electrochem. Soc.* **1991**, *138*, 3338.
[107] C. W. Li, M. W. Kanan, *J. Am. Chem. Soc.* **2012**, *134*, 7231–7234.
[108] M. Le, M. Ren, Z. Zhang, P. T. Sprunger, R. L. Kurtz, J. C. Flake, *J. Electrochem. Soc.* **2011**, *158*, E45–E49.
[109] P. R. Subramanian, J. H. Perepezko, *J. Phase Equilib.* **1993**, *14*, 62–75.
[110] E. L. Clark, C. Hahn, T. F. Jaramillo, A. T. Bell, *J. Am. Chem. Soc.* **2017**, *139*, 15848–15857.
[111] J. L. Stevens, R. Q. Hwang, *Phys. Rev. Lett.* **1995**, *74*, 2078–2081.
[112] M. Rahaman, A. Dutta, A. Zanetti, P. Broekmann, *ACS Catal.* **2017**, *7*, 7946–7956.
[113] H. Lee, J. Kim, I. Choi, S. H. Ahn, *Electrochim. Acta* **2019**, *323*, 133102.

Manuscript received: July 13, 2020
Revised manuscript received: September 15, 2020
Accepted manuscript online: November 3, 2020
Version of record online: November 23, 2020

7.10. Environment Matters: CO_2RR Electrocatalyst Performance Testing in a Gas-Fed Zero-Gap Electrolyzer

Reprinted with permission from ACS Catal. 2020, 10, 21, 13096–13108. Copyright 2020 American Chemical Society.

Authors: María de Jesus Gálvez-Vázquez, Pavel Moreno-García, Heng Xu, Yuhui Hou, Huifang Hu, **Iván Zelocualtecatl Montiel**, Alexander V. Rudnev, Shima Alinejad, Vitali Grozovski, Benjamin J. Wiley, Matthias Arenz, and Peter Broekmann

ACS Catal. 2020, **10**, 13096−13108, DOI: https://doi.org/10.1021/acscatal.0c03609.

Highlights: This paper reports on the electrochemical performance of Ag-NC@GDE catalyst for CO_2RR to carbon monoxide in a zero-gap flow cell configuration at highly alkaline conditions. In addition, the catalyst morphological evolution during CO_2RR was studied by means of IL-SEM. The system exhibits remarkable CO_2 to CO conversion in terms of FE and PCD over a wide range of cathodic potentials. PCD_{CO} increases steeply as the cathodic potential increases from –1.54 to –1.87 V, reaching a maximum PCD_{CO} = ~–600 mA cm^{-2} at –1.85 V *vs.* Ag/AgCl with FE_{CO} = 85%. The missing FE is followed by the presence of hydrogen and formate, which was, surprisingly detected in the anode compartment. However, the FE was not more than 10%. The morphological evolution of the Ag-NC@GDE induced by the CO_2RR, as well as direct mechanical contact between the catalyst layer and the anion-exchange membrane, was analysed by IL-SEM before and after electrolysis experiments. This analysis reveals that the morphological evolution of the catalyst strongly depends on the applied electrolysis conditions. At low and mild potentials, the Ag-NC do not present significant alterations; however, at harsher cathodic potentials, smaller Ag nanoparticles begin to appear, adsorbed on formerly catalyst-free substrate regions. The catalyst degradation is mainly due to the local high alkalinity that inevitably develops at high current densities in the zero-gap cell and leads to the massive precipitation of carbonates which is not observed in the H-type cell configuration.

Contributions: In this project, I was involved in conducting some electrochemical experiments. In addition, I participated in the manuscript revision process.

ACS Catalysis

pubs.acs.org/acscatalysis

Research Article

Environment Matters: CO_2RR Electrocatalyst Performance Testing in a Gas-Fed Zero-Gap Electrolyzer

María de Jesus Gálvez-Vázquez,[⊥] Pavel Moreno-García,[*,⊥] Heng Xu, Yuhui Hou, Huifang Hu, Iván Zelocualtecatl Montiel, Alexander V. Rudnev, Shima Alinejad, Vitali Grozovski, Benjamin J. Wiley, Matthias Arenz, and Peter Broekmann*

Cite This: *ACS Catal.* 2020, 10, 13096−13108

Read Online

ACCESS | Metrics & More | Article Recommendations | Supporting Information

ABSTRACT: Among the electrolyzers under development for CO_2 electroreduction at practical reaction rates, gas-fed approaches that use gas diffusion electrodes (GDEs) as cathodes are the most promising. However, the insufficient long-term stability of these technologies precludes their commercial deployment. The structural deterioration of the catalyst material is one possible source of device durability issues. Unfortunately, this issue has been insufficiently studied in systems using actual technical electrodes. Herein, we make use of a morphologically tailored Ag-based model nanocatalyst [Ag nanocubes (NCs)] assembled on a zero-gap GDE electrolyzer to establish correlations between catalyst structures, experimental environments, electrocatalytic performances, and morphological degradation mechanisms in highly alkaline media. The morphological evolution of the Ag−NCs on the GDEs induced by the CO_2 electrochemical reduction reaction (CO_2RR), as well as the direct mechanical contact between the catalyst layer and anion-exchange membrane, is analyzed by identical location and post-electrolysis scanning electron microscopy investigations. We find that at low and mild potentials positive of −1.8 V versus Ag/AgCl, the Ag−NCs undergo no apparent morphological alteration induced by the CO_2RR, and the device performance remains stable. At more stringent cathodic conditions, device failure commences within minutes, and catalyst corrosion leads to slightly truncated cube morphologies and the appearance of smaller Ag nanoparticles. However, comparison with complementary CO_2RR experiments performed in H-cell configurations in a neutral environment clearly proves that the system failure typically encountered in the gas-fed approaches does not stem solely from the catalyst morphological degradation. Instead, the observed CO_2RR performance deterioration is mainly due to the local high alkalinity that inevitably develops at high current densities in the zero-gap approach and leads to the massive precipitation of carbonates which is not observed in the aqueous environment (H-cell configuration).

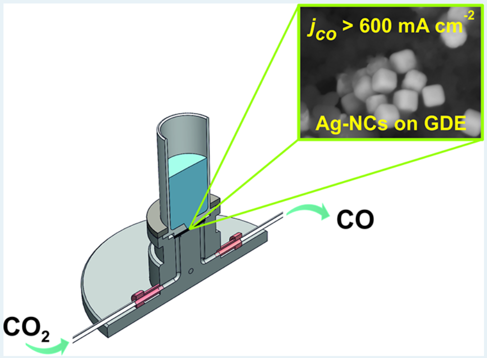

KEYWORDS: *CO_2 electroreduction, gas diffusion electrodes, zero-gap electrolyzer, carbon monoxide, exchange membrane electrode assembly*

■ INTRODUCTION

Powering the electrochemical reduction reaction of carbon dioxide (CO_2RR) with renewable energy sources has emerged as a compelling alternative to other approaches to CO_2 valorization,[1,2] toward meeting the increasing demand for commodity/platform chemicals and thereby contributing to efforts to close the anthropogenic carbon cycle.[3,4] In recent decades, significant progress has been made to understand the reaction mechanisms of this process through the development of cutting-edge catalyst materials that increase the activity [partial current density (PCD) of generated products] and selectivity (faradaic efficiency, FE) of the process. Strong cases of commercial viability have been made for formate ($HCOO^-$) and CO production, which require the transfer of only two electrons from the electrocatalyst to the CO_2 reactant molecule.[5,6] Formate is efficiently formed on Sn-, Bi-, In-, and Pb-based catalysts, whereas CO forms preferably on Ag-, Au-, and Zn-based catalysts.[7] CO is a particularly appealing product because it can be used as a stockpile for subsequent transformation either in the Fischer−Tropsch process[8] or in sequential electrochemical[9] and fermentation methods.[10]

Using catalyst screening methods based on H-cell experiments in which reactant CO_2 gas is usually dissolved in an aqueous bicarbonate-based electrolyte, a significant number of works have reported that Ag-,[11−13] Au-,[14,15] and Zn-based[16−18] cathode materials provide excellent CO selectivity and

Received: August 18, 2020
Revised: October 15, 2020
Published: October 27, 2020

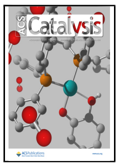

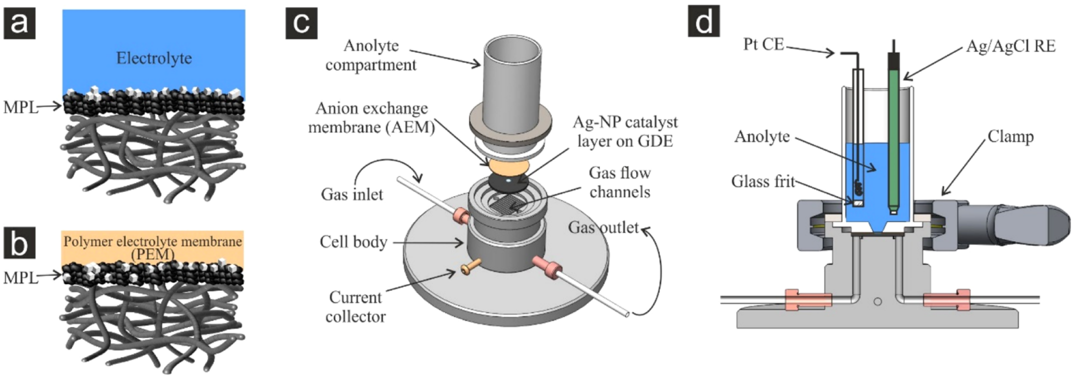

Figure 1. Schematics of the reaction interfaces in (a) liquid flow-cell electrolyzer and (b) exchange membrane electrode assembly (MEA) or zero-gap assembly. (c) Depiction and assembly of the zero-gap flow cell used in this work for the CO_2RR. (d) Cross-sectional view of the assembled cell with reference and counter electrodes (CE and RE, respectively) immersed in the anolyte compartment. MPL in panels (a,b) stands for the MPL on which the catalyst material (Ag−NCs) is embedded.

operational stability. Many works have also reported insightful correlations between the use of a tailored catalyst nanostructure and electrocatalytic performance.[19,20] In addition, diverging from the bicarbonate-based electrolyte that was once used almost ubiquitously, it has been found that highly concentrated (potassium) hydroxide-based catholyte solutions suppress the parasitic hydrogen evolution reaction (HER) and improve the CO_2RR performance because OH^- ions exhibit excellent ionic conductivity and reduce the activation energy barriers for CO_2 electroreduction.[9,21−24] Through these and other improvements, the field has reached a significant level of maturity so that currently, the associated research is driven by more ambitious endeavors, namely, scaling up the CO_2RR process to practical realization.[10,25] Toward this end, experimental platforms have been developed to circumvent or attenuate the mass transport limitations that are intrinsic to traditional H-type cell measurements[26−28] and arise from the low solubility of the dissolved CO_2 reactant in aqueous electrolytes. This pursuit opens a new avenue to the CO_2RR and related fields because the insights extracted from H-cell measurements with either stationary or rotating disk electrodes do not necessarily hold for their gas-fed homologues and both approaches bear fundamental kinetic differences that must be addressed to approach process commercialization.[29−31]

Among the various types of CO_2 electrolyzers under development, gas-fed approaches that use gas diffusion electrodes (GDEs) as cathodes and that are inspired by polymer electrolyte fuel cell technologies are considered to be the most promising.[1,21,30,32−36] Consequently, studies on Ag−GDEs in contact with flowing alkaline electrolytes (Figure 1a) have grown in popularity to achieve higher PCD_{CO} and FE_{CO} values as well as lower CO_2RR onset potentials and to explore possible enhancements to performance longevity.[37−41] However, electrolyzer designs that rely on this cell configuration are not without shortcomings that affect device performance and stability, thereby overshadowing their intrinsic electrocatalytic activity. These issues stem from (i) high ohmic losses owing to the electrolyte layer separating the electrodes,[30] (ii) electrolyte percolation through the microporous layer (MPL) of GDEs and concomitant carbonate salt precipitation,[42,43] and (iii) CO_2 crossover from the cathodic to the anodic compartment upon CO_2 neutralization by OH^- ions to HCO_3^-/CO_3^{2-}.[32,44,45]

Motivated by this, a few recent works on alternative cell designs with only an aqueous anolyte between the membrane and anode and no liquid electrolyte layer between the catalyst layer and (an)ion-exchange membrane [indistinctively called exchange membrane electrode assemblies (MEAs) or catholyte-free or zero-gap membrane assemblies, see Figure 1b][1,32,46] have been reported, enabling comparably reduced ohmic overpotentials, enhanced stability, and excellent CO selectivity.[25,47,48] This zero-gap configuration not only affords reduced ohmic losses but also attenuates complications that arise from poor membrane hydration and electrode flooding at high current densities, which are otherwise problematic to fully gas-fed electrolyzers[46,49] (note that exchange MEA electrolyzers may still suffer from the parasitic uptake of CO_2 at the interface of the cathode and anion-exchange membrane, thus facilitating the undesirable CO_2 discharge on the anode surface).[43,44,50] Nonetheless, one persistent hurdle that precludes the commercial deployment of these technologies is insufficient long-term device stability, which continues to fall short of the minimum target value of 8×10^4 h.[5] Efforts to identify the factors that lead to process failure have been undertaken, and strategies to alleviate such failures have been proposed (e.g., appropriate selection of the reactor design, electrode production method and hydrodynamics,[1] management of electrolyte percolation through the GDE,[39,51] and carbonation tolerance of the electrodes[43,44]).

In this context, another aspect that may also be a source of device durability issues and that has been minimally investigated using actual technical electrodes on which very large current densities (>300 mA cm^{-2}) are enforced is the structural deterioration of the catalyst material.[31,40] In particular, studies of the catalyst morphological evolution of Ag-based exchange MEAs induced by the CO_2RR reaction itself are lacking, as well as studies of the effect of direct mechanical contact between the catalyst layer and anion-exchange membrane (Figure 1b). To shed light on this unexplored aspect of CO_2RR on Ag−GDEs, we make use of morphologically tailored Ag-based model nanocatalysts [Ag nanocubes (Ag−NCs)] assembled on zero-gap GDEs to establish correlations between structure, environment, electrocatalytic performance, and degradation mechanisms under the abovementioned most favorable CO_2RR conditions (i.e., a highly alkaline membrane adjacent to the catalyst layer). Submonolayer surface coverages are purposely employed to unambiguously address possible structure degradation at the level of a single Ag−NC. Besides investigation of the catalyst activity and selectivity, we devote particular attention to the time evolution of both the electrochemical performance of the process and the material's nanostructure induced upon CO_2 electrolysis at large current densities, as enforced on the model exchange Ag−MEAs. We find that our testbed enables among the highest CO partial current densities and competitive FE_{CO} values (-625 mA cm^{-2} and 85%, respectively) even at the applied sub-monolayer catalyst coverages. Two distinct electrode potential regimes were observed, each exhibiting significantly different behaviors. At low and mild applied potentials ($E \geq -1.8$ V vs Ag/AgCl), stability prevails across the PCD_{CO} and FE_{CO}, electrolyzer performance, and catalyst structure. Conversely, at greater cathodic potentials, the process selectivity and activity severely degrade, leading to performance failure even though the catalyst morphology undergoes significantly less deterioration. Thus, this work enables the deconvolution of catalyst structural stability from system performance stability. Finally, a comparison with standard H-type reference measurements reveals that CO_2RR product selectivity is influenced by electrolyzer design and, therefore, that the knowledge developed using such batch-type approaches should not be regarded as directly transferable to gas-fed platforms. Overall, the results underscore that more effort must be devoted to the understanding and optimization of system design parameters (e.g., water management, prevention of salt precipitation, CO_2 flow rate, and electrolyte flow rate) that have a more significant impact on the product spectrum and longevity of the exchange MEA electrolyzers than that of the structural degradation of the catalyst, which is shown to be mild.

■ EXPERIMENTAL SECTION

Synthesis of Ag−NCs. Silver NCs were synthesized using a previously reported method with minor modification.[52] 5 mL of ethylene glycol (EG, J. T. Baker) was added to a 250 mL two-neck flask preheated to 160 °C. A light N_2 flow was introduced just above the EG for the first 10 min, followed by heating the solvent for another 50 min. Next, 3 mL EG solution of $AgNO_3$ (94 mM) and 3 mL EG solution containing polyvinylpyrrolidone (PVP, M_w = 55,000, 144 mM) and NaCl (0.22 mM) were simultaneously injected into the flask at a rate of 45 mL/h, with the solution observed to turn yellow during this process. Under continuous stirring at 160 °C, the solution exhibited a color transition series from yellow to clear yellow, brown, greenish, and finally ochre and opaque. The whole process required 16 h to 24 h for completion. After the solution had turned opaque, the reaction was quenched by adding 22 mL of acetone to the hot solution, followed by cooling in an ice-water bath. To purify the NCs, the solution was first centrifuged at 2000*g* for 30 min, and then, the precipitate was dispersed and centrifuged 3× in 10 mL of deionized water at 9000*g* for 10 min per run.[53] The product was finally dispersed in 5 mL of deionized water for future use.

Preparation of Ag−NC Catalyst Ink. To prepare the carbon-supported Ag−NC ink, 1.5 mg of the prepared Ag−NCs and 0.26 mg of carbon black (Vulcan XC 72R, Cabot) were separately dispersed in 10 mL of isopropanol (VLSI Selectipur, BASF SE, Ludwigshafen, Germany) by 1 h of sonication. Both suspensions were intermixed, sonicated for 1 h, and dried using a Rotary evaporator (Buchi R210, 45 °C, 85 mbar). The obtained carbon-supported Ag−NCs (85 wt % Ag−NC and 15 wt % C black) were then redispersed in 1 mL of isopropanol containing 50 μL of Nafion (5 wt %, 15−20% water, Sigma-Aldrich). The resulting suspension was subjected to sonication for 1 h yielding a homogeneous catalyst ink. For the sake of reproducibility and comparison, catalyst inks were also prepared with commercial Ag−NCs (NanoXact, nanoComposix) and used for complementary CO_2RR experiments.

Preparation of the Ag−NC−GDEs. The model catalyst material in this work consists of cubic Ag nanoparticles (Ag−NCs) with an average edge length of (113.1 ± 10.6) nm. The Ag−NC−GDEs for all electrochemical and characterization experiments were prepared as follows: a defined circular area of 7.07×10^{-2} cm^2 on the GDEs' hydrophobic surface (diameter of 2 cm, Sigracet 39 BC, Fuel Cell Store) was modified by dropcasting 50 μL of carbon-supported Ag−NC ink onto its top surface. This catalyst solution was percolated through the porous body of the GDEs by a vacuum filtration system placed on the backside of the electrode, and subsequent drying at ambient conditions was allowed for at least 30 min. Analysis by inductively coupled plasma−mass spectrometry (ICP−MS) of freshly prepared samples was used to determine the catalyst mass loading, which amounted to $\sim 7.1 \times 10^{-2}$ mg_{Ag} cm^{-2}.

Assembly of the Gas Flow Cell. The assembly and main components of the zero-gap gas-flow cell employed in this work to investigate correlations between the catalyst structure and process performance of CO_2RR to CO on Ag−NC−GDEs are schematically depicted in Figure 1c,d. This assembly consists of a stainless-steel cell body with the gas flow channels used to feed the CO_2 from the backside of the prepared Ag−NC−GDEs mounted on the outermost location of the central portion. Other components incorporated into the cell include a current collector and a gas inlet and outlet to control the supply of the CO_2 reactant (99.999%, Carbagas, Switzerland) and analysis of the gaseous products, respectively. All CO_2RR experiments were set up by placing a freshly prepared Ag−NC−GDE on top of the gas flow channels, with its catalyst-modified surface facing upward. Subsequently, a clean hydroxide-functionalized Sustainion alkaline membrane (X37-50 RT, Dioxide materials) and a poly(tetrafluoroethylene) (PTFE) anolyte compartment were carefully placed on top of the Ag−NC−GDE. A clamp was then used to ensure cell tightness and mechanical stability. KOH electrolyte-supporting solution (10 mL, 2 M; pH: 14.3, Sigma-Aldrich) was added to the anolyte compartment, and a Ag/AgCl (3 M KCl, double junction design, Metrohm) electrode and a Pt mesh (99.99%, MaTeck) separated by a glass frit served as the reference and counter electrodes, respectively. Note that the PTFE anolyte compartment has a central orifice (7.07×10^{-2} cm^2) in its bottom part that provides direct contact between the electrolyte and the underlying anion-exchange membrane, while the Ag−NC−GDE is prevented from establishing physical contact with the supporting anolyte. During electrolysis, a humidified CO_2 stream (16 mL min^{-1}) was continuously fed through the gas flow channels of the stainless-steel cell body adjacent to the prepared Ag−NC−GDEs.

Electrochemical Reduction of CO_2 (CO_2RR) Using Ag−NC−GDEs. All electrolytes were prepared using chemicals of at least ACS reagent grade and deionized water (Millipore, 18.2 MΩ cm, 3 ppb toc). Both ECi-200 (Nordic electrochemistry) and Autolab PGSTAT128 N (Metrohm) potentiostats were used to perform all electrochemical experiments. Electrochemical impedance spectroscopy measurements were conducted before and after every CO_2 electrolysis experiment, and the results were considered to build the potential-dependent product distributions and partial current densities displayed and mentioned throughout the text. Potentiostatic

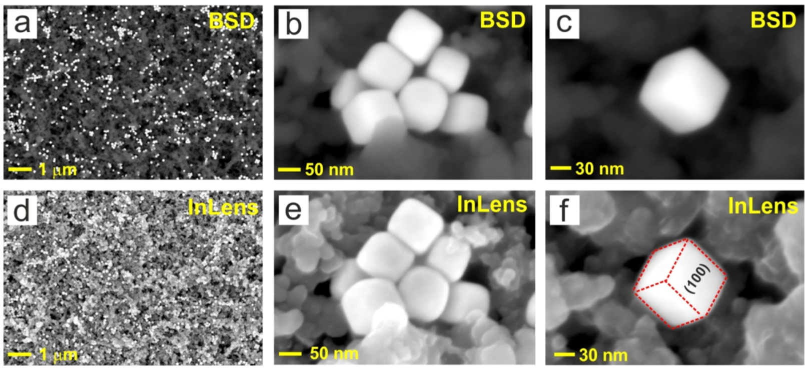

Figure 2. Representative SEM images at different magnifications showing the surface of an as-prepared Ag−NC−GDE cathode for CO_2RR. (a,d) Ag−NC catalyst sub-monolayer coverage on the MPL of the GDE. (b,c) and (e,f) reveal the well-defined cubic morphology of the Ag−NCs. Images (a−c) were acquired using the BSD detector of the scanning electron microscope. (d−f) Correspond to the same sample surface areas shown in the upper panels but were recorded with the InLens SE detector.

CO_2 electrolysis experiments were carried out at selected applied electrode potentials for 1 h, during which time the electrogenerated gaseous products were analyzed by online gas chromatography (SRI Instruments) in sequential intervals of 10 min. The electrolyte was analyzed after the applied electrolysis condition (post reaction) to quantify the produced formate by means of ion-exchange chromatography (Metrohm Ltd., Switzerland). For comparison, the performance of the Ag−NC−GDEs was also tested by dedicated reference measurements using 2 M $KHCO_3$ as the electrolyte in both the gas-flow cell and the conventional H-cell configurations. For the H-cell measurements, a proton-exchange membrane (Nafion 117, Sigma-Aldrich) separated the catholyte from the anolyte, and the working electrode consisted of a rectangular piece of carbon paper (0.8 × 3 cm) prepared in the same way as the Ag−NC−GDEs for zero-gap measurements. The back side and the edges of these electrodes were masked with the PTFE tape, thus leaving an uncovered geometric surface area of 0.2 cm^2. A single junction Ag/AgCl electrode (saturated KCl, Pine Research) and a Pt foil (2.5 × 0.8 cm, 99.99%, MaTeck) were used as the reference and counter electrodes, respectively. All electrode potential values in this work are in reference to the standard $Ag/AgCl_{3M}$ reference electrode. The data corresponding to the product selectivity and partial current densities of all experiments are displayed in Tables S2−S6. A thorough description of complementary experimental details is presented in a previous publication.[36]

Scanning Electron Microscopy and Energy-Dispersive X-ray Spectroscopy Characterization. Morphological characterization of the prepared Ag−NC−GDEs and assessment of the spatial distribution of the Ag−NCs over the samples was carried out with scanning electron microscopy (SEM) imaging experiments. Imaging was performed before (for the as-prepared electrodes) and after having sustained defined CO_2RR time intervals at selected applied electrode potentials. The analysis was conducted sequentially with a Zeiss Gemini 450 scanning electron microscope with both InLens secondary electron and backscattered electron detectors (Inlens SE and BSD detectors, respectively). An accelerating voltage of 5 kV and a current of 200 pA were applied at a working distance of 6.6−6.8 mm. The BSD detector enables clear identification of the Ag−NCs along the surface of the GDE's MPL because this technique is highly sensitive to the atomic number of the elements being imaged. However, the images acquired with the InLens SE detector provide better morphological resolution of the Ag−NCs. The use of both imaging operational modes coupled to energy-dispersive X-ray analysis (EDX) analysis made it possible to track morphological catalyst changes induced by CO_2 electrolysis and/or physical contact between the catalyst material and anion-exchange membrane on the Ag−NC−GDEs used. Complementary identical location (IL−SEM) experiments were conducted on Ag−NC−GDEs for which selected sample positions were imaged by the SEM instrument before and after CO_2RR experiments.

AZtec 4.2 software (Oxford Instruments) was used to acquire EDX spectra and surface mappings of selected Ag−NC−GDEs. An acceleration voltage of 10 kV and a current of 1.2 nA were applied at a working distance of 8.5 mm.

Catalyst Loading and Post-electrolysis Electrolyte and Ag−NC−GDE Analysis by ICP−MS. Freshly prepared Ag−NC−GDEs were immersed in 3 mL HNO_3 (BASF SE, Ludwigshafen, Germany) for 24 h to dissolve the Ag−NCs embedded on their surfaces. The resulting solutions were diluted with 3% HNO_3 solution by a factor of 500 and were then fed into a NExION 2000 ICP−MS instrument (PerkinElmer) to obtain the Ag mass loading of the electrodes. To identify possible Pt dissolution from the employed Pt counter electrode during CO_2 electrolysis, the following ICP−MS and EDX control experiments were conducted. First, 10 μL of post-reaction anolyte (after CO_2RR at −2.0 V for 60 min in 2 M KOH) was diluted with 10 mL of 3% HNO_3 solution for ICP−MS analysis. No Pt dissolution was detected in two independent measurements. Additionally, two post-electrolysis Ag−NC−GDEs were immersed in 3 mL aqua regia for 24 h and the solutions were diluted by factor 100 with 3% HNO_3. The corresponding ICP−MS spectra showed no signal other than the background further confirming the absence of Pt on the catalyst surface and supporting GDE. Finally, EDX analysis of a Ag−NC−GDE sample after being subjected to similar CO_2RR conditions also excluded the presence of any Pt deposited on the employed cathodes (see Figure S8).

X-ray Diffraction Catalyst Characterization. The crystallinity of the Ag−NCs was determined by means of X-ray diffraction (XRD) techniques (Bruker D8) using Cu Kα radiation (λ = 0.1540 nm, 40 mA) generated at 40 keV. Scans were recorded at 1° min^{-1} for 2θ values between 20 and 100°. The samples were prepared by dropcasting Ag−NCs dispersed in isopropanol on a graphite foil (0.13 mm, 99.8%, Alfa Aesar) and then allowing the solution to dry under ambient

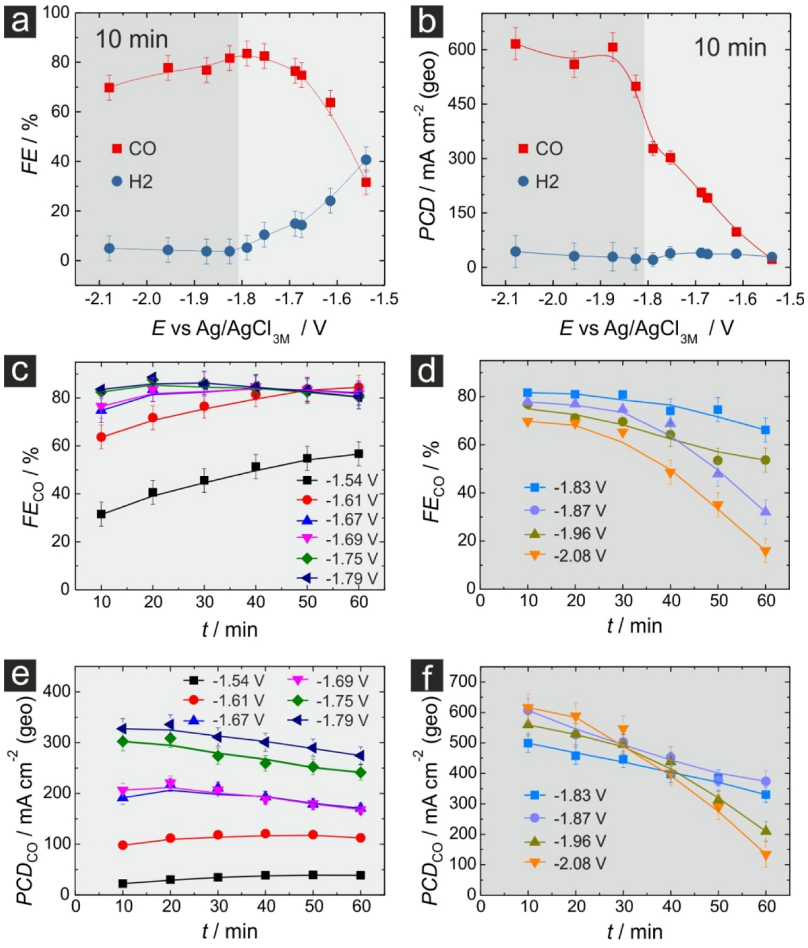

Figure 3. Potential-dependent FEs (a) and PCDs (b) of the gaseous products obtained from CO_2RR on the gas-fed Ag−NC−GDEs 10 min after beginning CO_2 electrolysis. Time evolution of the FE_{CO} at (c) mild (−1.5 V > E > −1.8 V) and (d) high applied potentials (−1.83 V > E > −2.1 V). Corresponding time evolution of the PCD_{CO} at mild (e) and high (f) applied potentials. All experiments were carried out using 2 M KOH in the anolyte compartment. The solid lines in all panels are guides to the eye to better observe the trends. The experimental error was accounted for using ±5% error bars.

conditions. The obtained XRD patterns were analyzed and compared with JCPD (Joint Committee on Powder Diffraction) for peak assignment.

RESULTS AND DISCUSSION

Characterization of Ag−NC−GDEs by SEM. Figure 2 shows representative SEM images of an as-prepared Ag−NC−GDE. We present data acquired sequentially at the same position with both the BSD and InLens SE detectors of the scanning electron microscope. Clear distinction between the Ag−NCs (bright) and the supporting GDE (dark) is provided by the BSD detector, which is sensitive to the atomic number of the analyzed material (Figure 2a−c). We observe a highly dispersed sub-monolayer of Ag−NC surface coverage built up by both single Ag−NCs and sparse groups of the particles (Figure 2b,c). This observation implies that the electrochemical performance of the Ag−NC−GDEs will be partially determined by parasitic side reactions (e.g., HER) taking place also on catalyst-free regions. This is supported by the combined SEM−EDX analysis of an as-prepared Ag−NC−GDE sample displayed in Figure S1a−d. The images acquired using the InLens SE detector (Figure 2d−f) offer improved morphological resolution of single Ag−NCs and their cubic shape, which is more easily observed at large magnifications (Figure 2e−f). Statistical analysis of more than 400 Ag−NCs provided an average edge length of 113.1 ± 10.6 nm, while XRD characterization confirmed the high crystallinity of the assembled Ag−NCs (Figure S1e,f). Recent theoretical and experimental studies in H-cell configurations have reported the superior and stable catalytic performance of cubic Ag nanoparticles compared to their octahedral and spherical counterparts.[19,20]

Electrocatalytic Performance of Ag−NC−GDEs for CO_2RR in Zero-Gap Electrolyzer. Potentiostatic CO_2RR experiments at selected applied potentials ranging between −1.55 and −2.1 V versus Ag/AgCl were conducted for 1 h using a dedicated Ag−NC−GDE as the cathode in a zero-gap gas flow-cell configuration (Figure 1b−d) for every potential. A favorable alkaline reacting environment was provided by the 2 M KOH electrolyte used in the anolyte compartment.[42] Figure 3a displays the potential-dependent product distribution of the gaseous products obtained after 10 min of CO_2 electrolysis. Besides the modest FE_{CO} observed at $E \sim -1.55$ V, all obtained FE_{CO} values at potentials more negative than −1.6 V surpassed 65%, reaching a maximum value of approximately 85% at −1.8 V. Diverging from previous reports in which an abrupt decay of FE_{CO} was observed with progressively higher potentials/current densities, only a slight decrease of CO

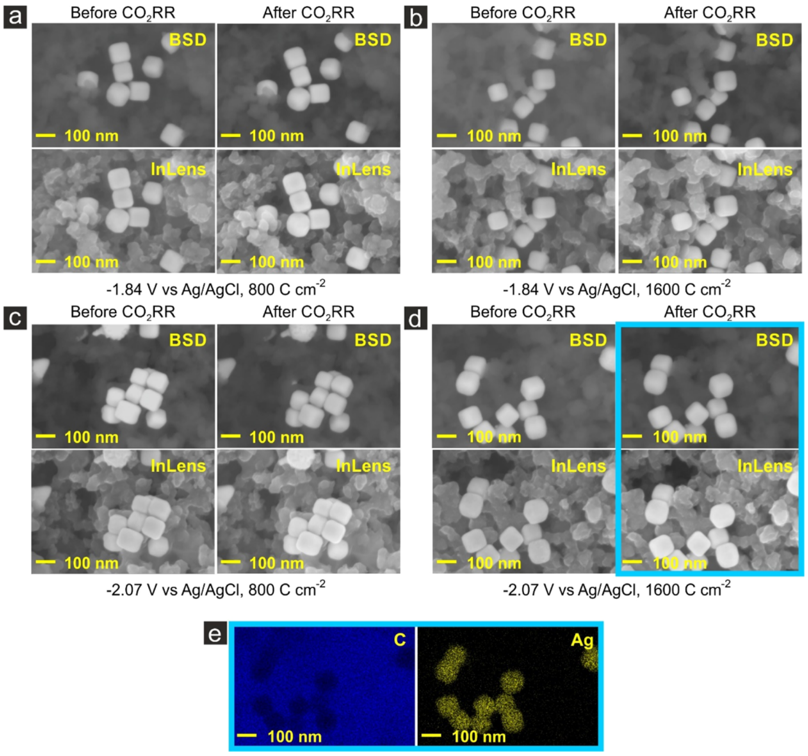

Figure 4. Representative IL−SEM images of Ag−NC−GDE cathode surfaces before and after having conducted dedicated gas-fed CO_2RR experiments at −1.84 V for (a) 30 min (800 C cm^{-2}) and (b) 60 min (1600 C cm^{-2}) and at −2.07 V for (c) 13 min (800 C cm^{-2}) and (d) 32 min (1600 C cm^{-2}) captured using both BSD and InLens SE detectors. (e) Elemental EDX mappings showing the spatial distribution of C (dark blue) and Ag (yellow) corresponding to the sample location highlighted by the blue rectangle in (d). All CO_2RR experiments were carried out using 2 M KOH in the anolyte compartment.

selectivity was detected at the harshest applied cathodic conditions due to an emerging formate contribution. However, it should be noted that in those previous reports either a bipolar membrane or a 0.5 M $KHCO_3$ buffer layer was used between the cathode and proton-exchange membrane.[32,54,55] The efficiency of parasitic H_2 stayed at FE_{H2} levels ≤10% for potentials more negative than −1.75 V. The corresponding dependence of the partial current densities PCD_{CO} and PCD_{H2} on the enforced potentials is shown in Figure 3b. The PCD_{CO} increases steeply as the cathodic potential increases from −1.54 to −1.87 V reaching highly competitive levels at approximately −600 mA cm^{-2} (see Table S1). Further cathodic polarization to approximately −2.1 V leads to a slightly increased PCD_{CO} reaching approximately −625 mA cm^{-2}. The PCD_{H2} did not exceed −50 mA cm^{-2} at all applied potentials. These CO selectivities and partial current densities stand out considering that for the as-prepared Ag−NC−GDEs, a significant portion of the three-phase boundary layer where the fed CO_2, polymer electrolyte, and catalyst material meet is constituted by the unmodified MPL of the support GDEs (Figure 2a). Clearly, an increase of the catalyst loading would lead to even better CO efficiencies and activities.[31] However, it is important to remember that a low catalyst surface coverage on the GDEs was deliberately applied to successfully monitor the morphological evolution of the Ag−NC catalyst at the single nanoparticle level (see below).

Distinct temporal evolution of both FE_{CO}s and PCD_{CO}s was found to depend on the magnitude of the applied potentials. Based on the temporal stability that these values promoted, two apparent potential regimes were identified for FE_{CO} and PCD_{CO}. These regimes are highlighted by different color codes in Figure 3. The panels corresponding to applied potentials that sustained the above-described performance throughout the duration of the experiments are highlighted by light gray rectangles (−1.5 V > E > −1.8 V). The panels highlighted in darker gray stand for results derived from applied potentials that led to the decay of FE_{CO} and PCD_{CO} values from their initial levels. Figure 3 panels c and e show that both CO selectivity and activity either improve or stay fairly stable across the lifespan of the experiments, provided that the applied potential was always less negative than −1.8 V. Conversely, when the potential surpassed this value, both CO production figures decreased over time. This decline was initially mild but intensified abruptly after 30 min with an increase of the applied potential (Figure 3 panels d and f).

Morphology Evolution of Ag−NC-Based Catalyst Induced by CO_2RR in Zero-Gap Flow Cell and H-Type Cell. To determine whether the observed decay in device performance during CO_2RR at the specific time intervals and applied potentials observed in Figure 3 panels d and f arises from morphological transformations of the cathodes (through morphological changes of the Ag−NCs or through their local rearrangement along the GDE surface), we analyzed Ag−NC−GDEs that were used for CO_2RR under those same conditions using *ex situ* SEM imaging experiments. Note that in the present study, our Ag−NC catalyst was subjected to significantly harsher cathodic conditions as compared to those reported in ref 61 reaching over two orders higher current densities and ∼400 mV more cathodic potentials.

In the first attempt, we employed the so-called IL−SEM-based technique.[56,57] This analysis is meant to provide the structural evolution of electrocatalyst materials by comparing

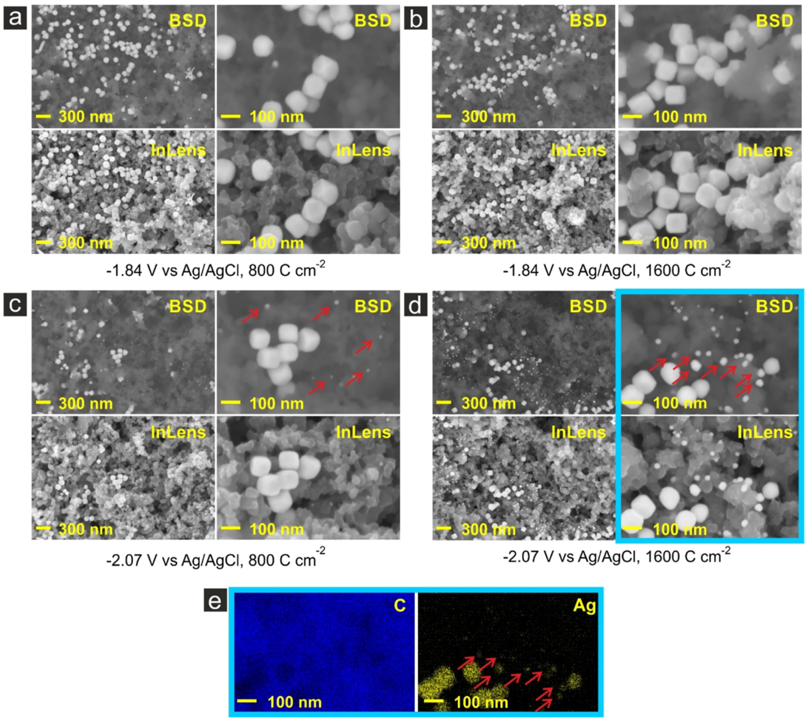

-1.84 V vs Ag/AgCl, 800 C cm^{-2}

-1.84 V vs Ag/AgCl, 1600 C cm^{-2}

-2.07 V vs Ag/AgCl, 800 C cm^{-2}

-2.07 V vs Ag/AgCl, 1600 C cm^{-2}

Figure 5. Representative SEM images of Ag−NC−GDE cathode surfaces after having conducted dedicated gas-fed CO_2RR experiments at −1.84 V for (a) 30 min (800 C cm^{-2}) and (b) 60 min (1600 C cm^{-2}) and at −2.07 V for (c) 13 min (800 C cm^{-2}) and (d) 32 min (1600 C cm^{-2}) captured using both BSD and InLens SE detectors. (e) Elemental EDX mappings showing the spatial distribution of C (dark blue) and Ag (yellow) of the sample location highlighted by the blue rectangle in (d). Red arrows identify Ag nanoparticles formed upon cathodic corrosion of the Ag−NC catalyst. All CO_2RR experiments were carried out using 2 M KOH in the anolyte compartment.

their morphology at the same sample location before and after being subjected to electrolysis.[56,57] We have previously employed this strategy to successfully assess structure−activity correlations caused by CO_2RR on bare porous metal electrocatalysts.[17,58] Herein, we monitored the structural evolution of Ag−NC−GDEs by IL−SEM for samples that were subjected to high cathodic potential values at which CO partial current densities reached −500 mA cm^{-2} and −620 mA cm^{-2} (−1.84 and −2.07 V, respectively). For each applied potential, the electrolysis was carried out until charge densities of 800 and 1600 C cm^{-2} were passed on dedicated Ag−NC−GDEs. These selected conditions are key for enabling insightful correlation between the SEM-based post-electrolysis studies and the data presented in Figure 3c−f.

Figure 4a−d presents representative IL−SEM images corresponding to Ag−NC−GDEs that were subjected to such CO_2RR conditions. Surprisingly, comparison of SEM images acquired before and after CO_2 electrolysis show that neither detachment nor degradation of the Ag−NCs seem to arise regardless of the specific applied potential, passed charge, or electrolysis duration. Post-electrolysis EDX mappings on sample regions that were scrutinized by IL−SEM also hint at the absence of cathodic corrosion and redeposition phenomena (compare Figures 4e and S1b,d). Furthermore, complementary IL−SEM experiments in which five sequential CO_2RR cycles were applied to a Ag−NC−GDE sample at the most stringent cathodic conditions are displayed in Figure S2. Although this sample was electrochemically stressed more severely (total cumulated Q = 13306 C cm^{-2} and $t \sim 4.5$ h), the combined IL−SEM−EDX analysis showed again no apparent sample degradation. These results alone would imply, at first sight, that the developed Ag−NC−GDEs tested in the proposed zero-gap flow cell do not undergo morphological degradation upon CO_2RR at all and that the undermined catalytic performance observed in Figure 3 at harsh cathodic conditions should originate from another failure source. However, an important aspect that did not need consideration in our previously reported IL−SEM structural CO_2RR studies and that can be the source of SEM imaging misinterpretation when studying colloidal nanocatalysts is the influence of surfactants that are left behind on their surfaces following their synthesis. Indeed, it has been shown that electron beam irradiation on nanomaterials synthesized by additive-assisted colloidal methods can lead to their improved structural stability through transformation of the adsorbed surfactants into dense carbonaceous shells.[59] Moreover, local surface passivation induced by SEM imaging has been identified on PVP-capped Ag NCs that hinders diffusion of Ag surface atoms.[60] This suggests that IL−SEM experiments might not accurately reveal the morphological evolution of colloidal catalyst materials as the initial electron irradiation conducted before the electrolysis step stabilizes and deactivates the scrutinized locations. Therefore, a second series of SEM imaging experiments were performed on the surface of Ag−NC−GDEs that were subjected to the same CO_2RR conditions as shown in Figure 4 but whose surfaces were not exposed to the electron beam of the SEM prior to the electrolysis.

Figure 5a−b displays representative images of Ag−NC−GDEs after having been subjected to −1.84 V. The Ag−NCs in panels a and b have undergone insignificant morphological changes after either 30 or 60 min of electrolysis (800 C cm^{-2} and 1600 C cm^{-2}, respectively). Furthermore, the images acquired with the BSD detector revealed the absence of

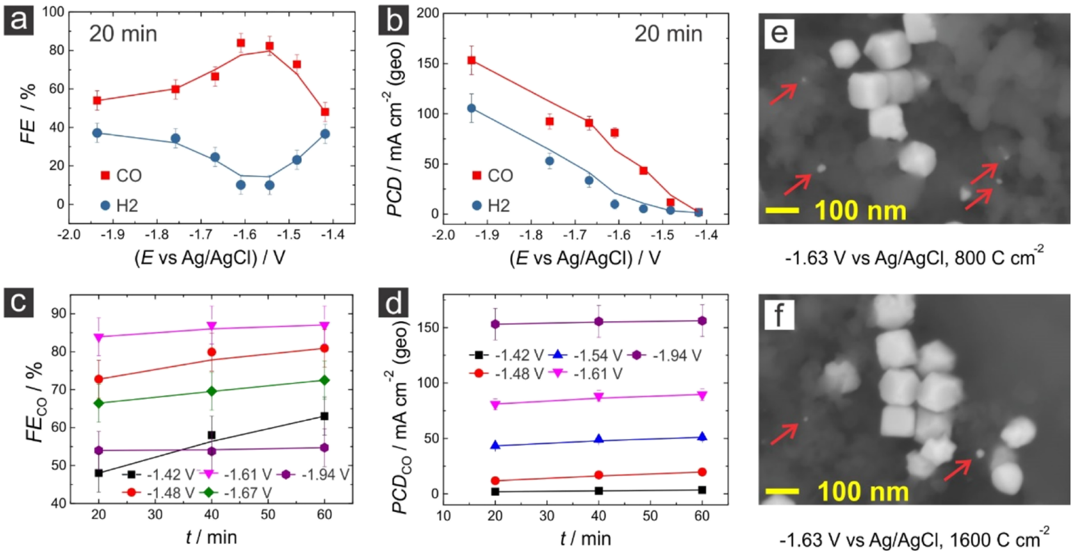

-1.63 V vs Ag/AgCl, 800 C cm^{-2}

-1.63 V vs Ag/AgCl, 1600 C cm^{-2}

Figure 6. Potential-dependent FEs (a) and PCDs (b) obtained on the Ag−NC−GDE in the H-cell configuration. Both variables were recorded 20 min after the CO_2 electrolysis experiment was initialized. Time evolution of the FE_{CO} (c) and PCD_{CO} (d) at (−1.42 V ≥ E ≥ −1.94 V). Representative SEM images of cathode surfaces after having conducted dedicated CO_2RR experiments at −1.63 V for (e) 196 min (800 C cm^{-2}) and (f) 304 min (1600 C cm^{-2}). Complementary SEM images of cathode surfaces subjected to −1.92 V are shown in Figure S6. These CO_2RR experiments were carried out with an H-type cell using 2 M $KHCO_3$ as the electrolyte. The solid lines in panels (a−d) are guides to the eye to better observe the trends. The experimental error was accounted for using ±5% error bars.

material removal from the Ag−NCs that would be redeposited in the form of smaller nanoparticles along the electrode surface under the applied cathodic conditions.[61] Importantly, excellent electrochemical performance figures (PCD_{CO} ≥ 300 mA cm^{-2} and FE_{CO} ~80%) are attained and sustained if the potential remains just positive of this applied value (−1.8 V vs Ag/AgCl, see Figure 3 panels c and e). Because of the morphological integrity of the actual catalyst observed under these conditions, it is reasonable to think that the purely electrochemical performance of the Ag−NCs−GDEs should be sustained over long electrolysis periods if the other system parameters do not lead to failure (e.g., salt precipitation, electrolyte penetration into the adjacent GDE, etc). However, diverging from what was observed in IL−SEM analysis, the electrodes exposed to more demanding cathodic conditions revealed alteration of the Ag−NC structure that may be linked to the deterioration of PCD_{CO}s and FE_{CO}s observed in Figure 3 panels d and f. Figure 5c shows representative images of a Ag−NC−GDE cathode that underwent CO_2RR at −2.07 V for 13 min (800 C cm^{-2}). Although the Ag−NCs maintained their overall cubic appearance, the BSD−SEM images reveal smaller, randomly distributed Ag nanoparticles (<5 nm) that arise from these more stringent CO_2 electrolysis conditions. The red arrows in the upper right image of Figure 5c indicate the appearance of particles adsorbed on regions of the GDE that were not covered by the Ag−NC catalyst material prior to CO_2RR. This phenomenon was more evident on cathodes subjected to 32 min (1600 C cm^{-2}) of electrolysis. Figure 5d demonstrates that the particles formed near the Ag−NCs when treated with these longer reaction times increased not only in size (~10 nm) but also in population along the formerly catalyst-free substrate regions. This is also supported by the EDX mapping shown in Figure 5e acquired on the sample location highlighted by the blue rectangle in Figure 5d. Additionally, analysis of single Ag−NCs indicated that the material source for these electrochemically formed particles stems mainly from the cube's vertices, eventually leading to the appearance of small (111) planes of truncated cube-like particles (Figure S3). Thus, it is clear that monitoring of the electrochemically induced morphological evolution of the colloidal catalyst is accurately described provided that the nanoparticles are not passivated by electron beam irradiation prior to electrolysis (as is the case in IL−SEM investigations). We suggest, however, that the observed mild morphological alteration of the Ag−NC catalyst on the GDE surfaces alone cannot be the physical origin for the significantly affected PCD_{CO}s and FE_{CO}s, as shown in Figure 3 panels d and f, at potentials more negative than −1.8 V.

To elucidate whether this decay in performance originates instead from the high bulk pH value (~14) of the electrolyte used, reference CO_2RR electrochemical and SEM experiments similar to those shown in Figures 3 and 5 were carried out on Ag−NC−GDEs, employing a significantly less basic 2 M $KHCO_3$ electrolyte (pH ~8). These results are displayed in Figures S4 and S5 following the same color code and image representation as of Figures 3 and 5. Figure S4a,b shows the corresponding FEs and PCDs of the electrogenerated gaseous products. Besides a slightly lower PCD_{CO} at most cathodic applied potentials (−1.86 V ≥ E ≥ −2.14 V), all other displayed quantities (PCD_{H2}, FE_{CO}, and FE_{H2}) exhibited the same qualitative potential- and time-dependent behaviors after 10 min CO_2 electrolysis, as discussed above, when the 2 M KOH electrolyte was used (compare Figure 3c−f with Figure S4c−f). The reduction in PCD_{CO} at high applied potentials might be related to the lower ionic conductivity of the HCO_3^- ion in comparison to that of OH^- and its relative deficiency to lower the CO_2 activation energy barrier.[42] Interestingly, suppression of the parasitic HER was equally effective when using both supporting electrolytes. The fact that the temporal dependence of FE_{CO} and PCD_{CO} as the electrolysis proceeded revealed again a stability bifurcation that depended on the potential window examined (Figure S4c−f) but not on the specific bulk pH is not surprising. Indeed, it has been predicted that the local pH adjacent to the three-phase boundary layer of a gas-fed GDE at CO_2RR reaction rates above 50 mA cm^{-2} becomes rather similar for both neutral and highly alkaline electrolytes due to the driven cathode half reactions (both CO_2 and water reduction generate OH^- as a byproduct).[30] The difference in the local pH at the cathode between both electrolyte solutions under CO_2RR reacting conditions at targeted $j_s \geq 200$ mA cm^{-2} might actually be negligible.[30] Similar to the experiments conducted in the 2 M KOH electrolyte, as shown in Figure 5, SEM analysis of a Ag−NC−GDE after 60 min CO_2RR at mild applied potential ($E = -1.84$ V, 1600 C cm^{-2}) in 2 M $KHCO_3$ showed minor structural degradation of the Ag−NCs (Figure S5). This finding suggests that the performance decay in our gas-fed zero-gap flow cell at large CO_2RR rates might be more significantly influenced by the increased local alkalinity rather than the relatively minor structural degradation of the Ag−NCs and the original bulk pH. Furthermore, an increasingly high alkalinity at the three-boundary layer in GDEs has been found to lead to issues related to electrolyte carbonation, electrolyte penetration through the GDE body (electrode flooding), and salt precipitation.[39,43,44,49,51] Electrolyte intrusion beyond the MPL of the Ag−NC−GDEs at high cathodic potentials also contributes to the decay in FE_{CO} and PCD_{CO}, as observed in Figure 3d,f and S4d,f, due to an increase of the CO_2 diffusion length. This is in agreement with recently reported work by Leonard et al.[43] who observed a clear increase of flooding propensity and loss of the nominal MPL hydrophobicity under stringent CO_2RR reductive conditions.

To further support this argument, we resorted to investigations performed in conventional H-cell configurations in which none of these detrimental aspects would influence the supply of dissolved CO_2 to the cathode through the liquid electrolyte. Figure 6a,b summarizes these experimental results. In comparison to the gas-fed experiments, significantly lower PCD_{CO}s are observed in all of the inspected potential window due to the dominant effect of the mass transport limitations of CO_2 dissolved in the used 2 M $KHCO_3$ electrolyte. In addition, the use of this non-optimal,[9,21−24] almost neutral electrolyte leads to larger PCD_{H2}s (as great as $PCD_{H2} \sim$ 100mA cm^{-2}) at high cathodic potentials relative to the values observed in the zero-gap experiments. The potential-dependent product selectivity shows an increase of FE_{CO} as the potential varied from low to mild applied values ($-1.4\text{ V} \geq E \geq -1.6$ V), although in contrast to the observed trends for the more technical approach, the CO efficiency significantly decreases as the competing HER benefits at more negative values. Moreover, in contrast to the results from the zero-gap experiments, neither FE_{CO} nor PCD_{CO} decays from its initial value as the electrolysis reaction proceeds, regardless of the applied potential (Figure 6c,d). Considering that the Ag−NCs used in these H-cell experiments seem to have undergone a similar degree of degradation and associated mechanism at mild and high applied potentials relative to that of the zero-gap counterparts (Figures 6e−f and S6), it seems evident that the system stability issues acting at high potentials and longer electrolysis times in the gas-fed configuration stem mainly from a sub-optimal reactor design and the high local alkalinity at high current densities. Indeed, we found a clear correlation between the decaying FE_{CO} and PCD_{CO} and occurrence of GDE flooding and salt precipitation, which cause device performance failure at high cathodic potentials in the gas-fed approach. Figure S7a,b shows typical contact angle images for water droplets on Ag−NC−GDEs before and after being submitted to CO_2RR at −2.07 V for 32 min. The decrease of contact angle indicates that the barrier properties of the MPL are to some extent undermined upon electrolysis. The corresponding EDX spectra additionally show a clear decay of the F signal due to degradation of the hydrophobic PTFE coating of the MPL (Figure S7c). Moreover, Figure S8a presents optical images showing the typical appearance of the employed GDEs at different experimental stages (as-received GDE, as-prepared Ag−NC−GDE and Ag−NC−GDE after having sustained CO_2RR at −2.07 V for 32 min and 1600 C cm^{-2}). The EDX spectra and mapping displayed in Figure S8b,c further support that, under these drastic cathodic conditions, carbonate/bicarbonate precipitation on the catalyst-modified GDE surface and its periphery takes place. Additionally, Figures S9 and S10 show that these undesired events (flooding and precipitation) can even be observed on the backside of such electrodes, irrespectively of the employed electrolyte. We would like to emphasize that this kind of massive salt precipitation is only observed in the GDE approach, irrespective of the used electrolyte, but not in the H-type cell configuration where the partial current densities of CO formation are mass transport limited and remain stable during electrolysis.

Comparison of CO_2RR Product Distribution in Zero-Gap Flow Cell and H-Type Cell. Finally, another important aspect that requires attention is the spectrum of products yielded from CO_2RR processes, which might also be affected by the specificities of the experimental approach employed (cell design and environment).[62] Along these lines, fundamental differences regarding the product selectivity were observed between the gas-fed- and H-cell-based approaches. As illustrated in Figure S11, formate was detected as a CO_2 electrolysis product over a large potential window using alkaline as well as almost basic electrolytes when the zero-gap testbed was used. This finding is in agreement with reports by Sargent, Sinton et al. on increased formate production on Ag−GDEs in highly alkaline aqueous environments (Figure 1a).[40] These authors proposed that the enhanced formate production when using highly alkaline environments adjacent to the Ag−GDE might be due to the limited ability of a temporary H_3O^+ molecule that is believed to assist the first protonation step of the adsorbed *COOH intermediate on the CO reaction pathway.[63] Accordingly, Figure S11 shows that both FE_{HCOO^-} and PCD_{HCOO^-} were more prominent when the hydroxide-based solution was employed and peaked at $E \sim -1.87$ V, amounting to non-negligible values of FE_{HCOO^-} ~20.1% and PCD_{HCOO^-} ~148 mA cm^{-2}, respectively. This result agrees with a recent report by Seger et al. who identified formate as a significant CO_2RR side reaction using a zero-gap electrolyzer combined with a basic anolyte at high current densities ≥200 mA cm^{-2}.[46] Conversely, our experiments in the H-cell yielded only a minor formate contribution at the highest applied potential (FE_{HCOO^-} ~2.6% and PCD_{HCOO^-} ~7.5 mA cm^{-2}). This result underlines the fact that the vast knowledge developed through batch-type CO_2RR experiments does not necessarily translate to more practical approaches aimed at industrial CO_2 reduction. Therefore, more effort must be devoted to understanding the particularities inherent to gas-fed CO_2RR platforms by going beyond a purely catalyst development-oriented approach and focusing more on rational electrolyzer design, engineering solutions, and process optimization to provide more robust and stable gas−liquid interfaces. Precipitation and flooding phenomena might, for instance, be prevented through incorporation of application-tailored microstructures and wettability into novel GDE designs.[43] Encouraging efforts in this direction are being made, for instance, by Schmid et al.[64] who have recently addressed the importance of optimized operating modes, electrolyzer design, and materials selection that enable nearly practical scale electrochemical CO_2-to-CO conversion. One key finding of these investigations that enables stable and long-term CO_2RR operation at −200 mA cm^{-2} is the attenuation of salt precipitation, GDE flooding, and CO_2 crossover to the anode compartment by utilizing a carbonate-free, sulfate-based neutral electrolyte in a liquid flow-cell electrolyzer.

■ CONCLUSIONS

We studied the performance of a model Ag−NC catalyst for CO_2RR to carbon monoxide on technical GDE in a zero-gap configuration and highly alkaline environments. The system exhibited remarkable CO_2 to CO conversion figures in terms of FE and PCD (FE_{CO} ~ 625 mA cm^{-2} and PCD_{CO} ~ 85%) even at sub-monolayer Ag−NC catalyst coverages on the GDEs. Based on the temporal system stability that they promoted, two apparent potential regimes were identified for FE_{CO} and PCD_{CO}. At mild applied potentials (-1.5 V > E vs Ag/AgCl > -1.8 V), the CO_2RR process improved or remained stable over time reaching PCD_{CO}s > 300 mA cm^{-2} and FE ~ 85%. However, at greater cathodic potentials, both CO production figures were initially more prominent but then weakened over time. This decline was initially mild but intensified abruptly after ~30 min with increasing applied potential. The morphological evolution of the Ag−NCs on the GDEs induced by the CO_2RR as well as the direct mechanical contact between the catalyst layer and anion-exchange membrane was analyzed by IL−SEM and post-electrolysis SEM investigations. The former approach turned out to be unsuitable for structural characterization of electrolysis-induced changes on colloidal catalysts that bear a surfactant shell on their surface left behind from the synthesis method. On the other hand, post-electrolysis SEM studies enabled the true morphological evolution of the catalyst that strongly depended on the applied electrolysis conditions. Regardless of the applied experimental conditions, no detachment of Ag−NC particles from the GDEs was detected. It was found that at low and mild potentials, the Ag−NCs undergo insignificant morphological alteration. However, at harsher cathodic conditions, smaller Ag nanoparticles begin to appear, adsorbed on formerly catalyst-free substrate regions. The material source of these electrochemically generated nanoparticles seems to come from the corners of the Ag−NCs. The observed mild cathodic corrosion of the catalyst leads to slightly truncated cube morphologies. However, complementary CO_2RR experiments in a neutral environment on Ag−NC−GDEs conducted in both zero-gap and conventional H-type cell configurations suggest that system failure is rooted in more factors than the observed morphological degradation of the catalyst. That is, the high alkalinity level at the three-phase boundary layer where the fed CO_2, catalyst material, and polymer electrolyte meet leads, to a significant degree, to the observed CO_2RR performance decline. The high alkalinity level inevitably develops at the reaction interface in the zero-gap electrolyzers at high cathodic reaction rates >300 mA cm^{-2} even when the starting bulk electrolyte is neutral, thereby causing electrolyte percolation through the GDEs, electrode flooding, and salt precipitation. Thus, this work enables the deconvolution of catalyst structural stability from system performance stability. Although the application of higher catalyst loadings on the GDEs would probably alleviate these issues, a more robust, long-lasting solution to the intrinsic challenges posed by gas-fed approaches must be proposed to near industrial CO_2RR deployment. Finally, as stated by some other recent works, we suggest that CO_2RR studies should increasingly be performed using technical approaches because the conclusions extracted from H-type cell experiments might not be directly translatable to electrolyzer-based studies.

■ ASSOCIATED CONTENT

Supporting Information

The Supporting Information is available free of charge at https://pubs.acs.org/doi/10.1021/acscatal.0c03609.

> SEM, EDX, XRD, and edge size distribution of Ag−NCs; literature survey on CO_2RR to CO on Ag−GDEs; IL−SEM of Ag−NC−GDEs subjected to zero-gap CO_2RR in 2 M KOH; SEM image of single Ag−NCs after zero-gap CO_2RR in 2 M KOH at high cathodic potentials; potential-dependent FEs and PCDs from zero-gap CO_2RR in 2 M $KHCO_3$; SEM imaging of Ag−NCs−GDEs after zero-gap CO_2RR in 2 M $KHCO_3$; SEM imaging of Ag−NCs−GDEs after CO_2RR in H-type cell; optical micrographs of employed GDEs at different experimental stages and EDX characterization of a Ag−NC−GDE after CO_2RR in 2 M KOH at stringent cathodic conditions; potential-dependent FE_{HCOO^-} and PCD_{HCOO^-} from zero-gap CO_2RR in 2 M KOH and 2 M $KHCO_3$; and complete database of all experiments (PDF)

■ AUTHOR INFORMATION

Corresponding Authors

Pavel Moreno-García − *Department of Chemistry and Biochemistry, University of Bern, Bern 3012, Switzerland;* orcid.org/0000-0002-6827-787X; Email: pavel.moreno@dcb.unibe.ch

Peter Broekmann − *Department of Chemistry and Biochemistry, University of Bern, Bern 3012, Switzerland;* orcid.org/0000-0002-6287-1042; Email: peter.broekmann@dcb.unibe.ch

Authors

María de Jesus Gálvez-Vázquez − *Department of Chemistry and Biochemistry, University of Bern, Bern 3012, Switzerland*

Heng Xu − *Department of Chemistry, Duke University, Durham, North Carolina 27708-0354, United States*

Yuhui Hou − *Department of Chemistry and Biochemistry, University of Bern, Bern 3012, Switzerland;* orcid.org/0000-0003-1616-562X

Huifang Hu − *Department of Chemistry and Biochemistry, University of Bern, Bern 3012, Switzerland*

Iván Zelocualtecatl Montiel − *Department of Chemistry and Biochemistry, University of Bern, Bern 3012, Switzerland*

Alexander V. Rudnev − *Department of Chemistry and Biochemistry, University of Bern, Bern 3012, Switzerland; A.N. Frumkin Institute of Physical Chemistry and Electrochemistry Russian Academy of Sciences, Moscow 119071, Russia*

Shima Alinejad − *Department of Chemistry and Biochemistry, University of Bern, Bern 3012, Switzerland;* orcid.org/0000-0002-1151-3333

Vitali Grozovski − *Department of Chemistry and Biochemistry, University of Bern, Bern 3012, Switzerland*

Benjamin J. Wiley − *Department of Chemistry, Duke University, Durham, North Carolina 27708-0354, United States;* orcid.org/0000-0002-1314-6223

Matthias Arenz − *Department of Chemistry and Biochemistry, University of Bern, Bern 3012, Switzerland;* orcid.org/0000-0001-9765-4315

Complete contact information is available at: https://pubs.acs.org/10.1021/acscatal.0c03609

Author Contributions

$^{\perp}$M.J.G.-V. and P.M.G. contributed equally. The manuscript was written through contributions of all authors. All authors have given approval to the final version of the manuscript.

Notes

The authors declare no competing financial interest.

■ ACKNOWLEDGMENTS

Support by the CTI Swiss Competence Center for Energy Research (SCCER Heat and Electricity Storage) is gratefully acknowledged. P.B. acknowledges financial support from the Swiss National Foundation (grant 200020-172507). M.d.J.G.-V. acknowledges the financial support by the Swiss Government Excellence Scholarships for Foreign Scholars (ESKAS) and thanks Antonio Calderon I. for the preparation of the cell's schematic drawings. A. R. acknowledges financial support from the Ministry of Science and Higher Education of the Russian Federation. M.A. acknowledges funding from the Swiss National Science Foundation (SNSF) via the project No. 200021_184742.

■ REFERENCES

(1) Vennekoetter, J.-B.; Sengpiel, R.; Wessling, M. Beyond the catalyst: How electrode and reactor design determine the product spectrum during electrochemical CO_2 reduction. *Chem. Eng. J.* **2019**, *364*, 89−101.

(2) Wang, Y.; Xia, Q.; Bai, X.; Ge, Z.; Yang, Q.; Yin, C.; Kang, S.; Dong, M.; Li, X. Carbothermal activation synthesis of 3D porous g-C_3N_4/carbon nanosheets composite with superior performance for CO_2 photoreduction. *Appl. Catal., B* **2018**, *239*, 196−203.

(3) Jhong, H.-R. M.; Ma, S.; Kenis, P. J. Electrochemical conversion of CO_2 to useful chemicals: current status, remaining challenges, and future opportunities. *Curr. Opin. Chem. Eng.* **2013**, *2*, 191−199.

(4) Seh, Z. W.; Kibsgaard, J.; Dickens, C. F.; Chorkendorff, I.; Nørskov, J. K.; Jaramillo, T. F. Combining theory and experiment in electrocatalysis: Insights into materials design. *Science* **2017**, *355*, No. eaad4998.

(5) Kibria, M. G.; Edwards, J. P.; Gabardo, C. M.; Dinh, C. T.; Seifitokaldani, A.; Sinton, D.; Sargent, E. H. Electrochemical CO_2 Reduction into Chemical Feedstocks: From Mechanistic Electrocatalysis Models to System Design. *Adv. Mater.* **2019**, *31*, 1807166.

(6) Fan, M.; Prabhudev, S.; Garbarino, S.; Qiao, J.; Botton, G. A.; Harrington, D. A.; Tavares, A. C.; Guay, D. Uncovering the Nature of Electroactive Sites in Nano Architectured Dendritic Bi for Highly Efficient CO_2 Electroreduction to Formate. *Appl. Catal., B* **2020**, *274*, 119031.

(7) Hori, Y. *Electrochemical CO2 Reduction on Metal Electrodes in Modern Aspects of Electrochemistry*; Springer: NY, 2008; p 89−189.

(8) Bushuyev, O. S.; De Luna, P.; Dinh, C. T.; Tao, L.; Saur, G.; van de Lagemaat, J.; Kelley, S. O.; Sargent, E. H. What Should We Make with CO_2 and How Can We Make It? *Joule* **2018**, *2*, 825−832.

(9) Jouny, M.; Luc, W.; Jiao, F. High-rate electroreduction of carbon monoxide to multi-carbon products. *Nat. Catal.* **2018**, *1*, 748−755.

(10) Haas, T.; Krause, R.; Weber, R.; Demler, M.; Schmid, G. Technical photosynthesis involving CO_2 electrolysis and fermentation. *Nat. Catal.* **2018**, *1*, 32−39.

(11) Ma, S.; Liu, J.; Sasaki, K.; Lyth, S. M.; Kenis, P. J. A. Carbon Foam Decorated with Silver Nanoparticles for Electrochemical CO_2 Conversion. *Energy Technol.* **2017**, *5*, 861−863.

(12) Dutta, A.; Morstein, C. E.; Rahaman, M.; Cedeño López, A.; Broekmann, P. Beyond Copper in CO_2 Electrolysis: Effective Hydrocarbon Production on Silver-Nanofoam Catalysts. *ACS Catal.* **2018**, *8*, 8357−8368.

(13) Hatsukade, T.; Kuhl, K. P.; Cave, E. R.; Abram, D. N.; Jaramillo, T. F. Insights into the electrocatalytic reduction of CO_2 on metallic silver surfaces. *Phys. Chem. Chem. Phys.* **2014**, *16*, 13814−13819.

(14) Chen, Y.; Li, C. W.; Kanan, M. W. Aqueous CO_2 Reduction at Very Low Overpotential on Oxide-Derived Au Nanoparticles. *J. Am. Chem. Soc.* **2012**, *134*, 19969−19972.

(15) Nursanto, E. B.; Jeon, H. S.; Kim, C.; Jee, M. S.; Koh, J. H.; Hwang, Y. J.; Min, B. K. Gold catalyst reactivity for CO_2 electroreduction: From nano particle to layer. *Catal. Today* **2016**, *260*, 107−111.

(16) Won, D. H.; Shin, H.; Koh, J.; Chung, J.; Lee, H. S.; Kim, H.; Woo, S. I. Highly Efficient, Selective, and Stable CO_2 Electroreduction on a Hexagonal Zn Catalyst. *Angew. Chem., Int. Ed.* **2016**, *55*, 9297−9300.

(17) Moreno-García, P.; Schlegel, N.; Zanetti, A.; Cedeño López, A.; Gálvez-Vázquez, M. d. J.; Dutta, A.; Rahaman, M.; Broekmann, P. Selective Electrochemical Reduction of CO_2 to CO on Zn-Based Foams Produced by Cu^{2+} and Template-Assisted Electrodeposition. *ACS Appl. Mater. Interfaces* **2018**, *10*, 31355−31365.

(18) Luo, W.; Zhang, Q.; Zhang, J.; Moioli, E.; Zhao, K.; Züttel, A. Electrochemical reconstruction of ZnO for selective reduction of CO_2 to CO. *Appl. Catal., B* **2020**, *273*, 119060.

(19) Yang, M.; Zhang, J.; Cao, Y.; Wu, M.; Qian, K.; Zhang, Z.; Liu, H.; Wang, J.; Chen, W.; Huang, W. Facet Sensitivity of Capping Ligand-Free Ag Crystals in CO_2 Electrochemical Reduction to CO. *ChemCatChem* **2018**, *10*, 5128−5134.

(20) Liu, S.; Tao, H.; Zeng, L.; Liu, Q.; Xu, Z.; Liu, Q.; Luo, J.-L. Shape-Dependent Electrocatalytic Reduction of CO_2 to CO on Triangular Silver Nanoplates. *J. Am. Chem. Soc.* **2017**, *139*, 2160−2163.

(21) Dinh, C.-T.; Burdyny, T.; Kibria, M. G.; Seifitokaldani, A.; Gabardo, C. M.; García de Arquer, F. P.; Kiani, A.; Edwards, J. P.; De Luna, P.; Bushuyev, O. S.; Zou, C.; Quintero-Bermudez, R.; Pang, Y.; Sinton, D.; Sargent, E. H. CO_2 electroreduction to ethylene via hydroxide-mediated copper catalysis at an abrupt interface. *Science* **2018**, *360*, 783−787.

(22) Hoang, T. T. H.; Verma, S.; Ma, S.; Fister, T. T.; Timoshenko, J.; Frenkel, A. I.; Kenis, P. J. A.; Gewirth, A. A. Nanoporous Copper−Silver Alloys by Additive-Controlled Electrodeposition for the Selective Electroreduction of CO_2 to Ethylene and Ethanol. *J. Am. Chem. Soc.* **2018**, *140*, 5791−5797.

(23) Kim, B.; Hillman, F.; Ariyoshi, M.; Fujikawa, S.; Kenis, P. J. A. Effects of composition of the micro porous layer and the substrate on performance in the electrochemical reduction of CO_2 to CO. *J. Power Sources* **2016**, *312*, 192−198.

(24) Liu, M.; Pang, Y.; Zhang, B.; De Luna, P.; Voznyy, O.; Xu, J.; Zheng, X.; Dinh, C. T.; Fan, F.; Cao, C.; de Arquer, F. P. G.; Safaei, T. S.; Mepham, A.; Klinkova, A.; Kumacheva, E.; Filleter, T.; Sinton, D.; Kelley, S. O.; Sargent, E. H. Enhanced electrocatalytic CO_2 reduction via field-induced reagent concentration. *Nature* **2016**, *537*, 382−386.

(25) Liu, Z.; Yang, H.; Kutz, R.; Masel, R. I. CO_2 Electrolysis to CO and O_2 at High Selectivity, Stability and Efficiency Using Sustainion Membranes. *J. Electrochem. Soc.* **2018**, *165*, J3371−J3377.

(26) Kas, R.; Hummadi, K. K.; Kortlever, R.; de Wit, P.; Milbrat, A.; Luiten-Olieman, M. W. J.; Benes, N. E.; Koper, M. T. M.; Mul, G. Three-dimensional porous hollow fibre copper electrodes for efficient

and high-rate electrochemical carbon dioxide reduction. *Nat. Commun.* **2016**, *7*, 10748.

(27) Ma, S.; Sadakiyo, M.; Luo, R.; Heima, M.; Yamauchi, M.; Kenis, P. J. A. One-step electrosynthesis of ethylene and ethanol from CO_2 in an alkaline electrolyzer. *J. Power Sources* **2016**, *301*, 219−228.

(28) Moreno-García, P.; Kovács, N.; Grozovski, V.; Gálvez-Vázquez, M. d. J.; Vesztergom, S.; Broekmann, P. Toward CO_2 Electroreduction under Controlled Mass Flow Conditions: A Combined Inverted RDE and Gas Chromatography Approach. *Anal. Chem.* **2020**, *92*, 4301−4308.

(29) Kim, C.; Dionigi, F.; Beermann, V.; Wang, X.; Möller, T.; Strasser, P. Alloy Nanocatalysts for the Electrochemical Oxygen Reduction (ORR) and the Direct Electrochemical Carbon Dioxide Reduction Reaction (CO_2RR). *Adv. Mater.* **2019**, *31*, 1805617.

(30) Burdyny, T.; Smith, W. A. CO_2 reduction on gas-diffusion electrodes and why catalytic performance must be assessed at commercially-relevant conditions. *Energy Environ. Sci.* **2019**, *12*, 1442−1453.

(31) De Gregorio, G. L.; Burdyny, T.; Loiudice, A.; Iyengar, P.; Smith, W. A.; Buonsanti, R. Facet-dependent selectivity of Cu catalysts in electrochemical CO_2 reduction at commercially viable current densities. *ACS Catal.* **2020**, *10*, 4854−4862.

(32) Delacourt, C.; Ridgway, P. L.; Kerr, J. B.; Newman, J. Design of an Electrochemical Cell Making Syngas (CO+H_2) from CO_2 and H_2 Reduction at Room Temperature. *J. Electrochem. Soc.* **2008**, *155*, B42.

(33) Dufek, E. J.; Lister, T. E.; McIlwain, M. E. Bench-scale electrochemical system for generation of CO and syn-gas. *J. Appl. Electrochem.* **2011**, *41*, 623−631.

(34) Higgins, D.; Hahn, C.; Xiang, C.; Jaramillo, T. F.; Weber, A. Z. Gas-Diffusion Electrodes for Carbon Dioxide Reduction: A New Paradigm. *ACS Energy Lett.* **2019**, *4*, 317−324.

(35) Weekes, D. M.; Salvatore, D. A.; Reyes, A.; Huang, A.; Berlinguette, C. P. Electrolytic CO_2 Reduction in a Flow Cell. *Acc. Chem. Res.* **2018**, *51*, 910−918.

(36) Gálvez-Vázquez, M. d. J.; Alinejad, S.; Hu, H.; Hou, Y.; Moreno-García, P.; Zana, A.; Wiberg, G. K. H.; Broekmann, P.; Arenz, M. Testing a Silver Nanowire Catalyst for the Selective CO_2 Reduction in a Gas Diffusion Electrode Half-cell Setup Enabling High Mass Transport Conditions. *Chimia* **2019**, *73*, 922−927.

(37) Verma, S.; Lu, X.; Ma, S.; Masel, R. I.; Kenis, P. J. A. The effect of electrolyte composition on the electroreduction of CO_2 to CO on Ag based gas diffusion electrodes. *Phys. Chem. Chem. Phys.* **2016**, *18*, 7075−7084.

(38) Verma, S.; Hamasaki, Y.; Kim, C.; Huang, W.; Lu, S.; Jhong, H.-R. M.; Gewirth, A. A.; Fujigaya, T.; Nakashima, N.; Kenis, P. J. A. Insights into the Low Overpotential Electroreduction of CO_2 to CO on a Supported Gold Catalyst in an Alkaline Flow Electrolyzer. *ACS Energy Lett.* **2018**, *3*, 193−198.

(39) Dinh, C.-T.; García de Arquer, F. P.; Sinton, D.; Sargent, E. H. High Rate, Selective, and Stable Electroreduction of CO_2 to CO in Basic and Neutral Media. *ACS Energy Lett.* **2018**, *3*, 2835−2840.

(40) Gabardo, C. M.; Seifitokaldani, A.; Edwards, J. P.; Dinh, C.-T.; Burdyny, T.; Kibria, M. G.; O'Brien, C. P.; Sargent, E. H.; Sinton, D. Combined high alkalinity and pressurization enable efficient CO_2 electroreduction to CO. *Energy Environ. Sci.* **2018**, *11*, 2531−2539.

(41) Dufek, E. J.; Lister, T. E.; McIlwain, M. E. Influence of Electrolytes and Membranes on Cell Operation for Syn-Gas Production. *Electrochem. Solid-State Lett.* **2012**, *15*, B48.

(42) Bhargava, S. S.; Proietto, F.; Azmoodeh, D.; Cofell, E. R.; Henckel, D. A.; Verma, S.; Brooks, C. J.; Gewirth, A. A.; Kenis, P. J. A. System Design Rules for Intensifying the Electrochemical Reduction of CO_2 to CO on Ag Nanoparticles. *ChemElectroChem* **2020**, *7*, 2001−2011.

(43) Leonard, M. E.; Clarke, L. E.; Forner-Cuenca, A.; Brown, S. M.; Brushett, F. R. Investigating Electrode Flooding in a Flowing Electrolyte, Gas-Fed Carbon Dioxide Electrolyzer. *ChemSusChem* **2020**, *13*, 400−411.

(44) Pătru, A.; Binninger, T.; Pribyl, B.; Schmidt, T. J. Design Principles of Bipolar Electrochemical Co-Electrolysis Cells for Efficient Reduction of Carbon Dioxide from Gas Phase at Low Temperature. *J. Electrochem. Soc.* **2019**, *166*, F34−F43.

(45) Ma, M.; Clark, E. L.; Therkildsen, K. T.; Dalsgaard, S.; Chorkendorff, I.; Seger, B. Insights into the carbon balance for CO_2 electroreduction on Cu using gas diffusion electrode reactor designs. *Energy Environ. Sci.* **2020**, *13*, 977−985.

(46) Larrazábal, G. O.; Strøm-Hansen, P.; Heli, J. P.; Zeiter, K.; Therkildsen, K. T.; Chorkendorff, I.; Seger, B. Analysis of Mass Flows and Membrane Cross-over in CO_2 Reduction at High Current Densities in an MEA-Type Electrolyzer. *ACS Appl. Mater. Interfaces* **2019**, *11*, 41281−41288.

(47) Liu, Z.; Masel, R. I.; Chen, Q.; Kutz, R.; Yang, H.; Lewinski, K.; Kaplun, M.; Luopa, S.; Lutz, D. R. Electrochemical generation of syngas from water and carbon dioxide at industrially important rates. *J. CO2 Util.* **2016**, *15*, 50−56.

(48) Kutz, R. B.; Chen, Q.; Yang, H.; Sajjad, S. D.; Liu, Z.; Masel, I. R. Sustainion Imidazolium-Functionalized Polymers for Carbon Dioxide Electrolysis. *Energy Technol.* **2017**, *5*, 929−936.

(49) Weng, L.-C.; Bell, A. T.; Weber, A. Z. Towards membrane-electrode assembly systems f or CO_2 reduction: a modeling study. *Energy Environ. Sci.* **2019**, *12*, 1950−1968.

(50) Yin, Z.; Peng, H.; Wei, X.; Zhou, H.; Gong, J.; Huai, M.; Xiao, L.; Wang, G.; Lu, J.; Zhuang, L. An alkaline polymer electrolyte CO_2 electrolyzer operated with pure water. *Energy Environ. Sci.* **2019**, *12*, 2455−2462.

(51) Jeanty, P.; Scherer, C.; Magori, E.; Wiesner-Fleischer, K.; Hinrichsen, O.; Fleischer, M. Upscaling and continuous operation of electrochemical CO_2 to CO conversion in aqueous solutions on silver gas diffusion electrodes. *J. CO2 Util.* **2018**, *24*, 454−462.

(52) Wiley, B.; Sun, Y.; Xia, Y. Polyol Synthesis of Silver Nanostructures: Control of Product Morphology with Fe(II) or Fe(III) Species. *Langmuir* **2005**, *21*, 8077−8080.

(53) Skrabalak, S. E.; Au, L.; Li, X.; Xia, Y. Facile synthesis of Ag nanocubes and Au nanocages. *Nat. Protoc.* **2007**, *2*, 2182−2190.

(54) Li, Y. C.; Zhou, D.; Yan, Z.; Gonçalves, R. H.; Salvatore, D. A.; Berlinguette, C. P.; Mallouk, T. E. Electrolysis of CO2 to Syngas in Bipolar Membrane-Based Electrochemical Cells. *ACS Energy Lett.* **2016**, *1*, 1149−1153.

(55) Salvatore, D. A.; Weekes, D. M.; He, J.; Dettelbach, K. E.; Li, Y. C.; Mallouk, T. E.; Berlinguette, C. P. Electrolysis of Gaseous CO_2 to CO in a Flow Cell with a Bipolar Membrane. *ACS Energy Lett.* **2018**, *3*, 149−154.

(56) Mayrhofer, K. J. J.; Meier, J. C.; Ashton, S. J.; Wiberg, G. K. H.; Kraus, F.; Hanzlik, M.; Arenz, M. Fuel cell catalyst degradation on the nanoscale. *Electrochem. Commun.* **2008**, *10*, 1144−1147.

(57) Hodnik, N.; Zorko, M.; Bele, M.; Hočevar, S.; Gaberščček, M. Identical Location Scanning Electron Microscopy: A Case Study of Electrochemical Degradation of PtNi Nanoparticles Using a New Nondestructive Method. *J. Phys. Chem. C* **2012**, *116*, 21326−21333.

(58) Rahaman, M.; Dutta, A.; Zanetti, A.; Broekmann, P. Electrochemical Reduction of CO_2 into Multicarbon Alcohols on Activated Cu Mesh Catalysts: An Identical Location (IL) Study. *ACS Catal.* **2017**, *7*, 7946−7956.

(59) Luo, B.; Fang, Y.; Li, J.; Huang, Z.; Hu, B.; Zhou, J. Improved Stability of Metal Nanowires via Electron Beam Irradiation Induced Surface Passivation. *ACS Appl. Mater. Interfaces* **2019**, *11*, 12195−12201.

(60) Tan, S. F.; Bosman, M.; Nijhuis, C. A. Molecular Coatings for Stabilizing Silver and Gold Nanocubes under Electron Beam Irradiation. *Langmuir* **2017**, *33*, 1189−1196.

(61) Huang, J.; Hörmann, N.; Oveisi, E.; Loiudice, A.; De Gregorio, G. L.; Andreussi, O.; Marzari, N.; Buonsanti, R. Potential-induced nanoclustering of metallic catalysts during electrochemical CO_2 reduction. *Nat. Commun.* **2018**, *9*, 3117.

(62) Wang, G.; Pan, J.; Jiang, S. P.; Yang, H. Gas phase electrochemical conversion of humidified CO_2 to CO and H_2 on proton-exchange and alkaline anion-exchange membrane fuel cell reactors. *J. CO2 Util.* **2018**, *23*, 152−158.

(63) Seifitokaldani, A.; Gabardo, C. M.; Burdyny, T.; Dinh, C.-T.; Edwards, J. P.; Kibria, M. G.; Bushuyev, O. S.; Kelley, S. O.; Sinton, D.; Sargent, E. H. Hydronium-Induced Switching between CO_2 Electroreduction Pathways. *J. Am. Chem. Soc.* **2018**, *140*, 3833−3837.

(64) Reinisch, D.; Schmid, B.; Martić, N.; Krause, R.; Landes, H.; Hanebuth, M.; Mayrhofer, K. J. J.; Schmid, G. Various CO_2-to-CO Electrolyzer Cell and Operation Mode Designs to avoid CO_2-Crossover from Cathode to Anode. *Z. Phys. Chem.* **2020**, *234*, 1115−1131.

NOTE ADDED AFTER ASAP PUBLICATION

This paper was published on October 27, 2020, before all final corrections were made. The corrected version was reposted on November 6, 2020.

7.11. CO_2 electrolysis - Complementary *operando* XRD, XAS and Raman spectroscopy study on the stability of Cu_xO foam catalysts

Authors: Abhijit Dutta, Motiar Rahaman, Burkhard Hecker, Jakub Drnec, Kiran Kiran, **Ivan Zelocualtecatl Montiel**, Daniel Jochen Weber, Alberto Zanetti, Alena Cedeño López, Isaac Martens, Peter Broekmann, Mehtap Oezaslan

Journal of Catalysis. **389** (2020) 592–603. DOI: https://doi.org/10.1016/j.jcat.2020.06.024

Highlights: This work reports the use of copper oxides foams (Cu_xO) as a novel precursor catalyst for CO_2 electroreduction towards C2 and C3 products like alcohols (ethanol, propanol) and ethylene. Using various sophisticated *operando* techniques, such as X-ray diffraction (XRD), X-ray absorption spectroscopy (XAS), and Raman spectroscopy, it was possible to study the chemical state evolution of the Cu oxides foams and the possible reaction pathways for C2 and C3 products through potential and time-dependent electrolysis experiments during electrochemical reduction of CO_2. These studies indicate that the reduction of the Cu_xO foams into metallic Cu is completed before the electrochemical reduction of CO_2 sets in. However, a comparison of bulk-sensitive techniques such as XAS and XRD indicates that the metal transition is delayed on the potential widow scale concerning what is observed in the surface-sensitive Raman spectroscopy. These studies demonstrate that close *operando* studies are required to understand the oxide-reduction evolution during CO_2RR. Complementary identical location SEM analysis before and after electrolysis experiments reveals changes in the morphology structure of Cu foams like a particle formation by the reduction process to which they have been subjected.

Contributions: In this project, I was involved in conducting the synthesis, characterization, and electrochemical experiments and in conducting *operando* potential- and time-dependent Raman experiments. In addition, I participated in the manuscript revision process.

Journal of Catalysis 389 (2020) 592–603

Contents lists available at ScienceDirect

Journal of Catalysis

journal homepage: www.elsevier.com/locate/jcat

CO_2 electrolysis – Complementary *operando* XRD, XAS and Raman spectroscopy study on the stability of Cu_xO foam catalysts

Abhijit Dutta [a,*,1], Motiar Rahaman [a,1], Burkhard Hecker [b], Jakub Drnec [c], Kiran Kiran [a], Ivan Zelocualtecatl Montiel [a], Daniel Jochen Weber [b,d], Alberto Zanetti [a], Alena Cedeño López [a], Isaac Martens [c], Peter Broekmann [a,*], Mehtap Oezaslan [b,d,*]

[a] *Department of Chemistry and Biochemistry, University of Bern, Freiestrasse 3, Bern 3012, Switzerland*
[b] *Department of Chemistry, University of Oldenburg, 26111 Oldenburg, Germany*
[c] *European Synchrotron Radiation Facility, 38000 Grenoble, France*
[d] *Technical Electrocatalysis Laboratory, Institute of Technical Chemistry, Technical University of Braunschweig, 38106 Braunschweig, Germany*

ARTICLE INFO

Article history:
Received 25 February 2020
Revised 18 June 2020
Accepted 20 June 2020
Available online 30 June 2020

Keywords:
CO_2 electro-reduction
Operando X-ray absorption spectroscopy
Operando X-ray diffraction
Operando Raman spectroscopy
Cu foam

ABSTRACT

Copper oxides have recently emerged as promising precursor catalyst materials demonstrating enhanced reactivity and selectivity towards C2 and C3 products like ethylene, ethanol, and n-propanol generated from the direct electro-reduction reaction of CO_2 (denoted as CO_2RR). Advanced *operando* X-ray absorption spectroscopy (XAS), X-ray diffraction (XRD) and Raman spectroscopy were employed to probe the potential-dependent changes of the chemical states of Cu species in the Cu oxide foams (referred to as Cu_xO) before and during the CO_2RR. This complementary and holistic approach of 'bulk'- and surface-sensitive techniques demonstrates that the electro-reduction of Cu_xO foams into metallic Cu is completed before hydrocarbon (e.g., ethylene, ethane) and alcohol (e.g., ethanol, n-propanol) formation sets in. There are, however, substantial differences in the potential dependence of the oxide reduction when comparing the 'bulk' with the respective 'surface' processes. Only in the very initial stage of the CO_2RR, the reduction of the Cu oxide precursor species is temporarily superimposed on the production of CO and H_2. Complementary identical location (IL) SEM analysis of the Cu_xO foams prior to and after the CO_2RR reveals a significant alteration in the surface morphology caused by the appearance of smaller Cu nanoparticles formed by the reduction process of Cu_xO species.

1. Introduction

The energy supply of modern society does still rely to a large extent on the combustion of fossil fuels (coal, oil, and gas) being the major source for the drastic increase of the CO_2 content in the atmosphere. Today, there is a general consensus within the scientific community that this raises in the atmospheric CO_2 concentration, already exceeding a level of 400 ppm [1], is the physical origin of global warming, one of the major threats to humankind. Clearly, a paradigm shift is required in the energy sector, also known as the 'energy transition' [2,3]. However, such a shift from fossil fuels towards more sustainable energy sources (wind, solar, and hydro) will heavily affect the entire chemistry sector as well. For instance, fossil feedstocks (e.g., natural gas) stand at the beginning of product and supply chains in the chemical industry. Therefore, the chemical sector will have to follow the energy sector in its transition from fossil to renewables, denoted the 'chemistry transition' [4]. Among the technological approaches that are currently under evaluation, electrochemical conversion processes stand out as they can convert CO_2 directly into the desired 'eco'-fuels or chemical feedstocks by using the surplus of renewable electricity from solar and wind plants. Not only might this approach contribute to the desired closing of the anthropogenic carbon cycle, it also provides means of storing intermittently produced excess electricity in the form of chemical energy which is considered as a key element of the 'energy transition'.

Most electrochemical CO_2 conversions are, however, still immature, very costly and short-lived. This is mainly due to insufficient electrocatalysts which need substantial improvements in terms of (i) (energy) efficiency, (ii) product selectivity (faradaic efficiency), (iii) material costs, and (iv) longterm durability. In the context of the electrochemical reduction of CO_2 (denoted hereinafter as CO_2RR) copper-based catalysts have attracted particular attention over

---

* Corresponding authors.
E-mail addresses: abhijit.dutta@dcb.unibe.ch (A. Dutta), peter.broekmann@dcb.unibe.ch (P. Broekmann), m.oezaslan@tu-braunschweig.de (M. Oezaslan).

[1] These authors contributed equally to this work.

https://doi.org/10.1016/j.jcat.2020.06.024
0021-9517/

the last decades as they can convert CO_2 directly into C-C coupled hydrocarbons [5–13] and alcohols [7,10,13–20] Previous studies have demonstrated that the pre-treatment of Cu-based catalysts is of eminent importance not only for their overall electrocatalytic activity but also for the resulting CO_2RR product distribution [21–23]. The fabrication of Cu catalysts for the CO_2RR often starts with the (electro-)synthesis of precursor materials where copper is present in an oxidized state (+1 or +2). An ultimate activation of these Cu oxide-based precursor materials is often achieved in the electrochemical environment prior to or during the CO_2RR [13,17,24–30].

Various approaches towards precursor synthesis and catalyst activation have been reported including but not restricted to electrode anodization [16], electropolishing [31], and cathodic electrodeposition processes [11,12,17]. Most successful strategies rely on the formation of a thin oxide layer on the respective catalyst surface, e.g. by chemical oxidation [16], thermal annealing treatments [11,21,24,25] or by exposure to oxygen plasma [22,32]. It should be pointed out that such formed cuprous or cupric oxides (Cu_2O or CuO) are thermodynamically unstable under such harsh cathodic conditions relevant to the CO_2RR, thus leading to so-called oxide-derived (OD) Cu catalysts [33]. However, massively precipitated cuprous/cupric oxides result in reduced electric conductivity, which might lead in some cases to the kinetic stabilization of the oxidic catalyst precursor phases even under reductive conditions. Effects such as the embedment of oxygen species into the forming metallic Cu matrix during oxide reduction are controversially discussed in the literature [22,34–36]. To date, there is no ultimate consensus achieved on the potential-dependent stability of surface and sub-surface oxide/oxygen species and their specific role for the CO_2RR [30,32,37–39].

To shine light on the question how stable cuprous and cupric oxides are under electrochemical conditions prior to and during the CO_2RR, we applied a set of highly complementary techniques ranging from ex situ (before and after electrolysis) chemical (XPS) and morphological (identical location (IL)-SEM) analyses to advanced *operando* XAS (X-ray absorption spectroscopy), XRD (X-ray diffraction), and more surface-sensitive Raman spectroscopy approaches. The unique combination of complementary *operando* techniques combined with various levels of structural and chemical information allows discriminating the different transient phenomena of the electro-reduction of Cu oxide species. This is a crucial pre-requisite for the interpretation of faradaic efficiency data derived from potential-dependent CO_2RR product analyses. As model system of choice we used Cu foams that were electrodeposited on a conductive carbon support and transformed into their corresponding Cu_xO bulk phases by means of a thermal annealing treatment in air at 300 °C (12 h) [12,17,40,41].

2. Experimental section

2.1. Chemicals

$KHCO_3$ (Sigma-Aldrich, ACS grade), $CuSO_4 \cdot 5\ H_2O$ (Sigma-Aldrich, ACS grade), H_2SO_4 (Sigma-Aldrich, ACS grade), and Milli-Q water (Millipore, 18.2 MΩ cm, 4 ppb of total organic carbon) were used for the preparation of solutions without further purification.

2.2. Electrodeposition of porous Cu/Cu_xO foams

Cu foams were electrodeposited onto activated carbon foil substrates (0.25 mm thick, 99.8%, Alfa Aesar, Germany) using the dynamic hydrogen bubble template approach [11,17,42–44]. Prior to the Cu electrodeposition, the carbon foils were activated by a thermal treatment at 550 °C for 12 h in air, followed by a cleaning step in an acetone/water mixture (volume ratio of 1:1) and subsequent drying at 100 °C for 1 h. The geometric surface area (A_{geo}) of the carbon foil, exposed to the plating bath, was 1 cm^2. The activated carbon foil was then immersed into a Cu plating bath containing 0.2 M $CuSO_4 \cdot 5\ H_2O$ and 1.5 M H_2SO_4. The Cu plating was carried out in a 250 mL glass beaker with a Cu plate (5 cm × 5 cm) and a leak-less double-junction Ag/AgCl(3 M KCl, Metrohm) serving as the counter and reference electrode, respectively [11,40,44,45]. For the galvanostatic deposition process, a current density of $j = -3.0\ A\ cm^{-2}$ (normalized to the geometric surface area of the carbon support) was applied for the duration of 5 s. After the electrodeposition, all Cu foam samples were thoroughly rinsed with Milli-Q water and subsequently dried in a gentle Ar gas stream (99.999%, Carbagas, Switzerland). The electrodeposited Cu foams were further subjected to a thermal annealing treatment in air for 12 h at a temperature of 300 °C using a tube furnace (GERO, GmbH, Germany).

2.3. Ex situ material characterization

The crystal structure of the electrodeposited and annealed Cu foams was investigated by means of powder XRD (Bruker D8) with Cu Kα radiation (λ = 0.1540 nm) operated at 40 mA and 40 kV. Scans were recorded at a rate of 1° min^{-1} for 2θ values between 20 and 90°. The obtained XRD patterns of the electrodeposited and annealed Cu foams were analyzed and compared to JCPD (Joint Committee on Powder Diffraction) standards (Cu_2O: 050667, CuO: 410254, and polycrystalline Cu: 040836) [46,47].

Ex situ X-ray photoelectron spectroscopy (XPS) studies were carried out using a PHI VersaProbeII scanning XPS micro-probe (Physical Instruments AG, Germany) equipped with a monochromatic Al Kα X-ray source operated at 24.8 W with a spot size of 100 μm. Peak positions were referenced to the carbon C*1s* peak at 284.5 eV. A graphite foil served as the reference material. The peak deconvolution and fitting of the XPS spectra were performed using the Casa-XPS software. After completion of the electrolysis reactions, all samples were stored under Ar gas atmosphere prior to the XPS analysis.

The morphology of the Cu foams was characterized by means of scanning electron microscopy (SEM). For the high-resolution SEM imaging a Zeiss DSM 982 instrument was used (working distance of 8 mm).

2.4. CO_2RR and product analysis

Potentiostatic CO_2RR experiments were performed in an air-tight H-type glass cell using a classical three electrode configuration. A leakless miniature Ag/AgCl(3 M KCl, EDAQ) electrode served as the reference electrode and was checked with a leakless double junction Ag/AgCl(3 M KCl, Metrohm) master reference electrode prior to each experiment. A 18 mm × 7 mm Pt foil (0.1 mm of thickness, 99.95%, Alfa Aesar) served as the counter electrode. Prior to its use the Pt foil was treated by flame annealing. The two compartments of the glass cell were separated by a cation exchange membrane (Nafion 117, Sigma Aldrich). Both the cathode and the anode compartments were filled with 30 mL of 0.5 M $KHCO_3$ solution. Prior to the electrolysis the solutions were purged with CO_2 (99.999%, Carbagas, Switzerland) for at least 30 min. The pH of the CO_2-saturated 0.5 M $KHCO_3$ solution was 7.2.

All electrochemical measurements (galvanostatic Cu deposition, cyclic voltammetry and potentiostatic CO_2RR experiments) were carried out using a potentiostat/galvanostat (Metrohm Autolab 128 N, The Netherlands). Automatic iR compensation (~85%, the exact value was determined by the positive feedback technique) was applied during these measurements, following the determination of the cell resistance by electrochemical impedance spectroscopy (EIS) or alternatively by the current interrupt method; both methods provide similar results of the cell resistance. For the sake of comparability and to eliminate the pH dependency, all potentials measured versus Ag/AgCl(3 M KCl) were converted to the reversible hydrogen electrode (RHE) scale using Eq. (1):

$$E_{RHE}(V) = E_{Ag/AgCl(3M)}(V) + 0.210V + (0.059V \times pH) \quad (1)$$

The headspace gas of the cathode compartment was vented with CO_2 to transport gaseous electrolysis products into the sampling loop of the gas chromatograph (GC 8610C, SRI Instruments). Online headspace GC measurements (detection of volatile products, e.g. H_2, CO, C_2H_4, C_2H_6) were conducted every 20 min at each potential step. The total duration of each electrolysis reactions was 1 h. The GC was equipped with two packed Hayesep D columns. Argon (99.9999%, Carbagas, Switzerland) served as the carrier gas. A flame ionization detector (FID) coupled to a methanizer was used for the quantification of all gaseous CO_2RR products, whereas a thermal conductivity detector (TCD) was applied for the quantitative hydrogen detection. The partial current density for a given gaseous product was determined using the Eq. (2):

$$j(i) = x_i \cdot n_i \cdot F \cdot v_m \quad (2)$$

where x_i represents the volume fraction of each product measured via online GC using an independent calibration standard gas (Carbagas, Switzerland); n_i is the number of electrons involved into the reduction reaction to form a particular product; v_m represents the molar CO_2 flow rate; and F – the Faraday constant. The partial current density for a given reaction product was normalized to the total current density to estimate the faradaic efficiency (FE) for a given reaction product.

Non-volatile products (e.g. alcohols) were quantified by a second FID detector. After the electrolysis, 2 μL aliquot of the electrolyte solution was injected into a second Haysep D column equipped with a pre-column to prevent the electrolyte salt entering into the main column (post-electrolysis alcohol detection). Other liquid products (e.g. formate) were detected and quantified by means of ion exchange chromatography (IC, Metrohm Advanced Modular Ion Chromatograph: L-7100 pump, Metrosep A Supp 7–250 column, conductivity detector). Electrolyte aliquots were diluted 20 times with Milli-Q water before injection into the IC instrument (post-electrolysis formate detection).

Note that all (partial) current densities given in the paper were normalized with respect to the geometric surface area of the electrode (A = 1 cm^2). The surrace roughness factors (RF) of the as prepared (RF = 1.54) and the oxide-derived Cu foams (RF = 1.8) were determined by means of voltammetric measurements in an inert 0.1 M $HClO_4$ electrolyte (determination of the double layer capacitance). In a further attempt, the electrochemically active surface area (ECSA) was determined by the viologen method [11,48,49] using di-methyl viologen as a reversible redox probe (see supplementary file). Scan-rate dependent cyclic voltammograms (CVs) were recorded in aqueous solution containing 1 M Na_2SO_4 (ACS grade, Sigma-Aldrich) and 10 mM $DMVCl_2$ (Sigma-Aldrich). The estimated ECSA of the 'as prepared' Cu foam was 3.68 cm^2 (referring to 1 cm^2 geometric surface area). It is important to note that the ECSA of the Cu foam was further increased to 4.89 cm^2 after the thermal annealing treatment and the subsequent 1 h electrolysis at −0.9 V vs RHE. Partial current densities of the CO_2RR were also normalized to the ECSA (see supplementary file).

2.5. Operando Quick-X-ray absorption spectroscopy (Quick-XAS)

Quick-XAS investigations were performed at the SuperXAS (X10DA) beamline, Swiss Light Source (SLS), Switzerland. The storage ring was operated at 2.4 GeV and 400 mA. A home-made spectro-electrochemical flow cell was used for the measurements (Fig. S1). The classical three-electrode configuration consisted of the Cu foam as the working electrode, an Au foil served as the counter and a non-leakage Ag/AgCl (3 M KCl, EDAQ) was used as the reference electrode. All potentials were corrected for the ohmic iR drop. The basic design of the spectro-electrochemical flow-cell was published elsewhere [50]. For the Quick-XAS experiments at the Cu K-edge, the cell was adjusted in a way that the electrolyte thickness in the X-ray window was about 1 mm and the porous Cu foam was only 30–40 μm thick to obtain sufficient signal-to-noise ratio in the transmission mode. XAS experiments were carried out in CO_2-saturated 0.5 M $KHCO_3$ electrolyte solution (pH = 7.2) in the potential range from +0.8 V to −0.9 V vs. RHE. A syringe pump was used to establish a constant flow of CO_2-saturated electrolyte through the spectro-electrochemical cell. For the potential-dependent Quick-XAS measurements, a fast oscillating channel cut crystal monochromator with a frequency of 40 Hz (~40 scans per second) was employed. The ionization chambers for the detection of incident (I_0) and transmitted (I_1 and I_2) X-ray radiation were filled with N_2. IFEFFIT software suite [51] was used for the data processing which included the background subtraction, edge step normalization and conversion of the energy units (eV) to photoelectron wave vector k units ($Å^{-1}$) by assigning the photoelectron energy origin, E_0, corresponding to k = 0, to the first inflection point of the absorption edge. The resulting χ(k) functions were weighted with k^2 to compensate for the dampening of the XAS amplitude with increasing k. Linear combination fitting (LCF) analysis of the X-ray absorption near edge structure (XANES) spectra at the Cu K-edge was performed to establish the contribution of different chemical Cu species based on the reference spectra of Cu foil, Cu_2O and CuO. In addition, the extended X-ray absorption fine structure (EXAFS) spectra were Fourier-transformed to obtain pseudo radial structure functions (RSFs). The amplitude reduction factor (S_0^2) was obtained from the fit of the EXAFS spectrum of a Cu foil to be 0.78. Using the ARTEMIS software [51], the coordination number (N), interatomic bond length (R), mean squared bond length disorder (σ^2), and correction to the energy origin (ΔE_0), together with its error bars were established for Cu-Cu and Cu-O scattering pairs by fitting theoretical EXAFS signals to the data in R-space.

2.6. Operando X-ray diffraction (XRD)

Operando XRD experiments were performed at ID31 high energy beamline of the European Synchrotron Radiation Facility (ESRF). The X-ray beam was mono-chromatized with a Laue-Laue monochromator to the energy of 69 keV and focused to the size of 5 × 20 μm^2 (vertical × horizontal) at the sample position. The 2D XRD patterns were collected with a Dectris Pilatus 2 M CdTe detector. A custom made PEEK electrochemical flow cell [41,52] was used for the experiments (Fig. S2). The cell consists of a Pt wire serving as the counter electrode, a Ag/AgCl (3 M KCl, EDAQ) as the reference electrode and an oxidized Cu foam sample supported on carbon paper electrically connected with Au wire as the working electrode. The measurements were performed in grazing incidence geometry, incidence angle less than 1°, in CO_2-saturated 0.5 M $KHCO_3$ electrolyte. A continuous flow of fresh CO_2-saturated electrolyte solution through the spectro-electrochemical cell avoids any undesired accumulation of soluble Cu species in the investigated X-ray window. The sample was first measured at OCP and then the potentials were changed from +0.5 V to −0.5 V vs. RHE by applying potential steps of 100 mV. The resting time at each potential before the measurement was around 2 min and 15 s. The cell resistance was measured by the current-interrupt method. Potentials were corrected manually after the measurements. The raw 2D diffraction patterns were radially integrated using the pyFAI software package [53]. All reflections were normalized taking into the account different electron densities of the crystalline structures, such that they can be compared on an absolute scale. The initial powder pattern at OCP was subtracted from following data to correct for the complex background signal from the cell and substrate material.

2.7. Operando Raman spectroscopy

Raman spectra were collected by a LabRAM HR800 confocal microscope (Horiba Jobin Yvon) [54]. Calibration was performed using a silicon wafer standard (520.6 cm^{-1}). Raman spectroscopy was performed using a working distance of 8 mm between the objective lens (LMPLFLN from Olympus, 50X magnification) and the sample with a numerical aperture of 0.1 in order to focus a diode-pumped solid-state laser beam (excitation wavelength 633 nm, power 3 mW) on the sample. The Raman signal was collected in a back-scattering geometry using a lab-made spectro-electrochemical cell made of Kel-F (Fig. S3) [54–57]. For *operando* Raman experiments, the air-annealed Cu foam was electrodeposited on an activated carbon foil and placed on glassy carbon (3 mm diameter) support. A Ag/AgCl (3 M KCl, EDAQ) and a Au ring served as the reference and counter electrode, respectively. CO_2-saturated 0.5 M $KHCO_3$ solution was used as the electrolyte. A μ-Autolab III (EcoChemie) potentiostat was used for the electrochemical Raman measurements. The ohmic drop was determined using the positive feedback technique and compensated during the measurement. Steady-state Raman spectra were acquired after five minutes at each potential set point (from +0.5 V to −0.9 V vs. RHE, applied potential steps of 100 mV).

3. Results

3.1. Ex situ characterization of as deposited and annealed Cu foam catalysts

Fig. 1 shows white light interferometry (panel a) and SEM images of the Cu foam prior to (panels b-d) and after (panels e–g) the annealing treatment at 300 °C (12 h in air). A hierarchical pore structure was formed on the activated carbon foil support as a result of the Cu electrodeposition process that was superimposed on the vigorous hydrogen evolution reaction (HER) [11,12,44]. Fig. S4 in the supplementary file demonstrates the basic principle of the hydrogen bubble assisted metal foam electrodeposition. A Cu electrodeposition at -3.0 A cm^{-2} for 5s yielded a two-level foam architecture of interconnected open-cell pores with surface pore diameters ranging from 15 to 25 μm and a total foam thickness of approximately 30–43 μm, assuming that the deepest pores reach the carbon foil substrate (Fig. 1a, see also Fig. S5). These results are further corroborated by the side-view SEM inspection of the as deposited Cu foam showing a foam thickness of ~43 μm (Fig. S5j).

The mean pore diameter and foam thickness slightly deviate from those values for Cu foams supported on a Cu wafer substrate reported by Dutta et al. [11]. This is due to faradaic efficiencies of Cu deposition and the competing HER which are slightly different on the previously used Cu wafer substrate. Carbon was used as the support material in the present study to avoid any undesired contribution of the Cu wafer support to Cu related signals in the *operando* XAS and XRD experiments.

Important to note is that the thermal annealing does not affect the primary macro-porosity of the Cu foam (Fig. S6). In contrast to that, the secondary meso-porosity of the pore side-walls and particularly their dendritic fine structure undergoes substantial structural and compositional alterations during the annealing process. Prior to such thermal treatment, individual dendrites are composed of faceted Cu nanoparticles as evidenced by the high-

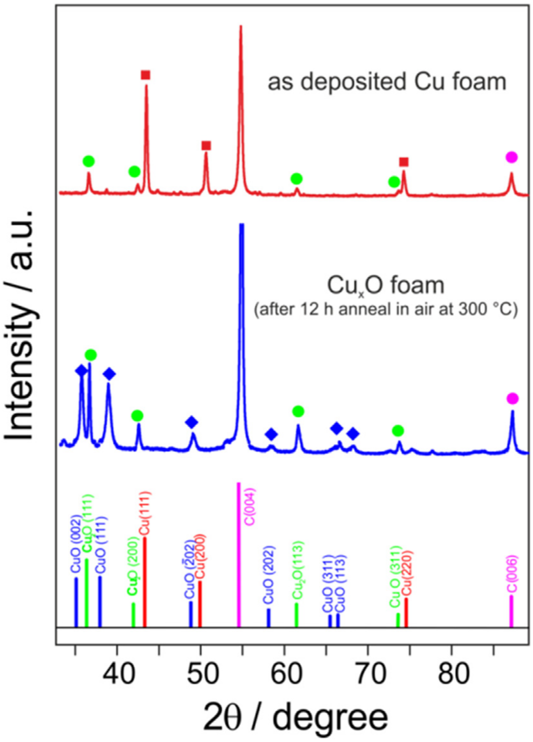

Fig. 2. X-ray diffractograms of the as deposited (red) and the thermally annealed (blue) Cu foam (300 °C, 12 h, in air). For comparison purposes the corresponding JCPDS reference data is indicated (Cu_2O: 050667, CuO: 410254, and polycrystalline Cu: 040836).

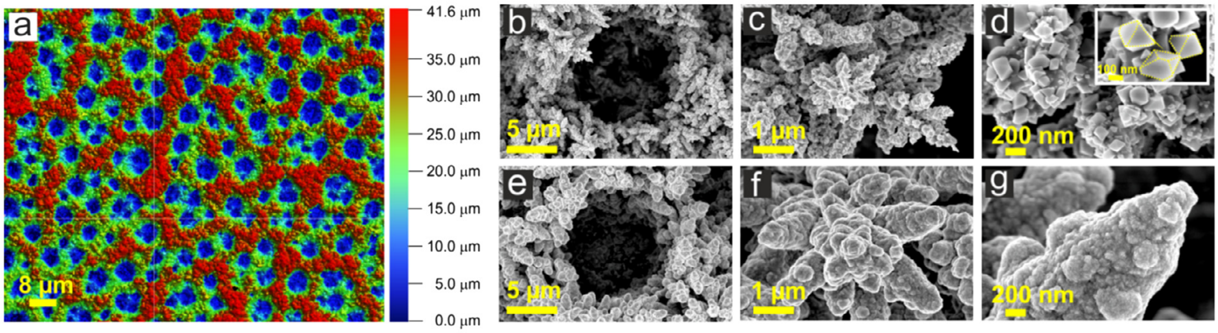

Fig. 1. (a) White-light interferometric characterization of the as deposited Cu foam (5 s deposition time at −3 A cm^{-2}); (b–d) SEM micrographs of the as deposited Cu foam; (e-g) SEM micrographs of the thermally annealed Cu foam (300 °C, 12 h, in air) denoted as Cu_xO foam.

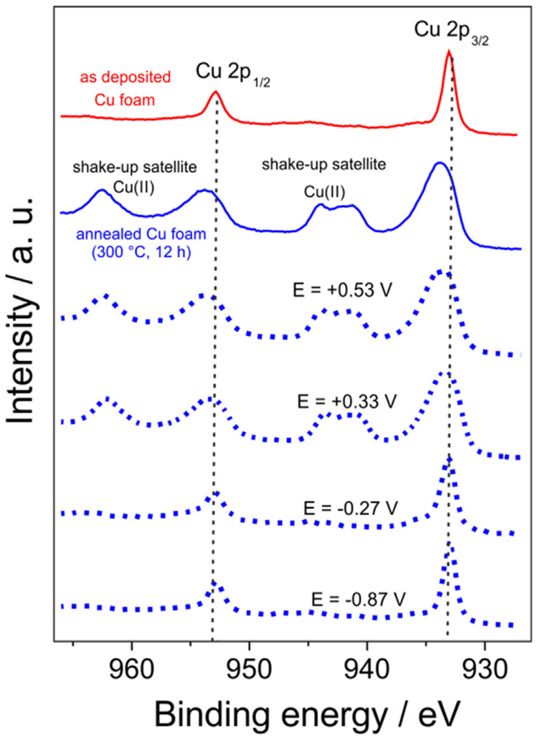

Fig. 3. XPS spectra (Cu$2p$ emission) of the Cu/Cu$_x$O foams. The red curve represents the as deposited foam sample, the blue curve shows the Cu$2p$ emission of the thermally annealed one (300 °C, 12 h, in air). The blue dotted spectra represent post-electrolysis XPS measurements carried out after 1 h potentiostatic electrolysis in CO_2 saturated 0.5 M $KHCO_3$ solution. The respective electrolysis potentials vs. RHE are indicated.

resolution SEM micrograph (see inset in Figs. 1d and S5g–i). The annealing of the Cu foam at 300 °C induces the coalescence of the faceted nano-crystallites leaving non-textured dendrites behind (Figs. 1g, S6g–i). These morphological alterations taking place on the meso-scale result from the formation of intermixed CuO/Cu_2O phases (denoted hereinafter as Cu_xO) which involve the concerted mass transport of oxygen and copper into and out of the pristine crystalline dendrite structure.

This scenario becomes further supported by the corresponding ex situ XRD analysis presented in Fig. 2. As expected, XRD patterns of the as deposited Cu foam show all characteristic diffraction features of polycrystalline face-centered cubic (fcc) Cu and in addition minor contribution originating from crystalline cuprous oxide (Cu_2O). Note that electrodeposited metal foams are prone to surface oxidation right after their emersion from the respective Cu plating bath and exposure to air [11,12]. All diffraction features related to metallic Cu have disappeared after the 12 h annealing treatment at 300 °C in air. Obviously, the as deposited metallic Cu foam has completely been transformed by the applied thermal treatment into an oxidic Cu_xO composite (mixture of Cu_2O and CuO). Note that thicker Cu foams deposited under similar experimental conditions (current density, metal ion concentration in solution), but using more extended deposition times, remain partly metallic in their interior upon annealing at 300 °C for 12 h in air as reported by Dutta et al. [12].

Complementary surface-sensitive XPS analysis of the as deposited Cu foam shows the spin-orbit split photoemissions of metallic Cu and cuprous oxide with binding energies (BE) of Cu$2p_{3/2}$ = 932.9 eV (FWHM = 1.26 eV) and Cu$2p_{1/2}$ = 952.6 eV (Fig. 3). Note that the XPS cannot discriminate between Cu(I) and Cu(0) species [12,58–60]. Thermal annealing at 300 °C leads to an up-ward shift of the Cu related photoemissions which goes along with a peak broadening and the appearance of characteristic shake-up satellites. These observations are clearly pointing to the presence of cupric oxide (CuO) at the surface of the Cu_xO foam [12]. The Cu$2p_{3/2}$ peak can be de-convoluted by considering two components with binding energies (peak maxima) at 932.8 eV and 933.7 eV which are assigned to Cu(I) and Cu(II), respectively (Fig. S7). The assignment of the photo-emission at 932.8 eV to Cu(I) species is based on the *ex situ* XRD data showing no experimental evidence for the presence of metallic Cu after the thermal treatment (Fig. 2). The deconvolution of both components (Fig. S7) yields a relative abundance of 68 at% Cu(I) as Cu_2O and 32 at% Cu(II) as CuO. Note that these values do not necessarily represent the bulk composition of the annealed Cu foam (Cu_xO) as the XPS is a surface-sensitive technique.

3.2. CO_2RR product analysis

To probe the performance of the annealed Cu foams, a dedicated campaign of potentiostatic electrolysis experiments (1 h duration) was carried out in the potential range from +0.07 V vs. RHE to −0.87 V vs. RHE. Note that a so-called multi-catalyst approach [61] was applied. A freshly prepared catalyst was used for each individual electrolysis experiment. Fig. 4 shows the CO_2RR product analysis derived from the thermally annealed Cu (Cu_xO) foam catalyst (see also Tables S1 and S2). For comparison purposes, the respective results of the as deposited Cu foam are presented in

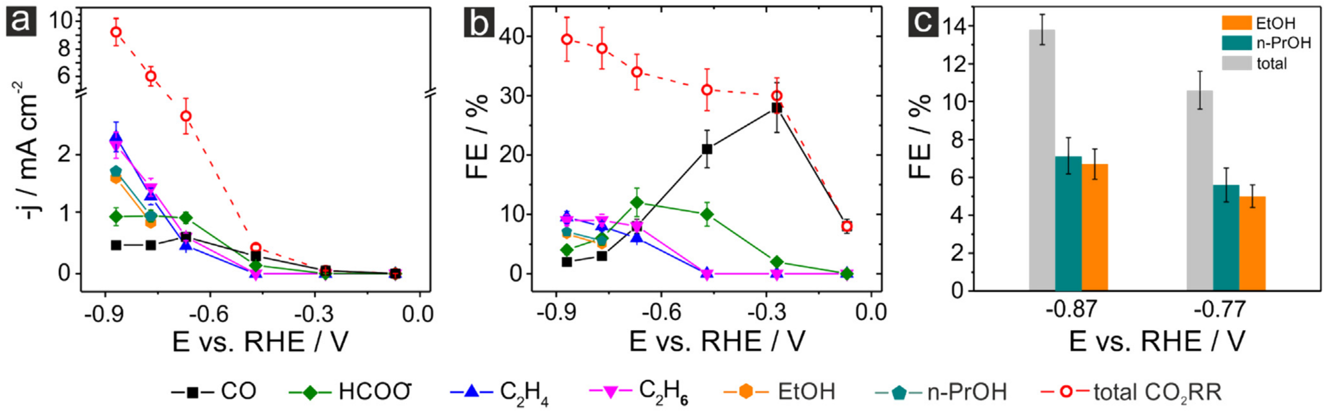

Fig. 4. Product distribution after 1 h CO_2RR electrolysis carried out in CO_2-saturated 0.5 M $KHCO_3$ using the Cu_xO foam (300 °C, 12 h, in air) as the catalyst; (a) CO_2RR product distribution represented as partial current densities; (b) CO_2RR product distribution represented as faradaic efficiencies (FEs); (c) Faradaic efficiencies for alcohol formation (EtOH, n-PrOH, and total alcohol efficiency) highlighted for two selected electrolysis potentials.

Fig. S8 (see also Tabled S3 and S4). The product distribution of the CO_2RR carried out over the as deposited Cu foam (Fig. S8) shows qualitatively the same trends as previously reported for other Cu foam electrocatalysts [11]. CO is the main CO_2RR product in the low overpotential regime reaching a maximum of faradaic efficiency (FE) of CO, FFCO = 19% (j_{CO} = −0.18 mA cm^{-2}) at −0.47 V vs. RHE. The hydrocarbon pathways are opened at electrolysis potentials more neagtive than −0.8 V vs RHE. A characteristic feature of the electrodeposited Cu foam catalysts is the full suppression of the C1 (methane) reaction pathway [11]. A C2 hydrocarbon efficiency of 20% is yielded at −0.77 V vs. RHE (see Table S3) with a slight preference towards C_2H_6 (FE_{C2H6} = 11%). The unusual appearance of ethane as CO_2RR product has previously been rationalized on the basis of particular intermediate trapping effects inside the pores of the Cu foam electrocatalysts [11] facilitating in particular the re-adsorption of ethylene on the catalyst surface and its subsequent reductive hydrogenation. It should be noted that the faradaic efficiencies yielded for ethane and ethylene are lower as compared to the ones previously reported by Dutta et al. [11]. Both the total CO_2RR efficiency and the ratio of ethylene/ethane formation were, however, shown to be strongly depending on the (surface) pore size distribution and catalyst film thickness (controlled by the deposition time). Note that the Cu foams used herein were optimized with regard to the *operando* investigations (see below) in terms of film thickness and not with regard to the CO_2RR product distribution. A much smaller film thickness was chosen in the present study (see Fig. S5) as compared to the conditions yielding optimum CO_2RR efficiencies [11].

In Fig. 4a, the potential dependent product analysis of the CO_2RR carried out over the oxide-derived Cu foam is represented in terms of partial current densities whereas in panel b the corresponding faradaic efficiencies (FEs) are shown. Minor CO_2RR activity towards CO starts already at −0.07 V vs. RHE. The partial current density for CO remains, however, on an extremely low level of only j_{CO} = −4 μA cm^{-2} (FE_{CO} = 8%) close to the detection limit in the GC analysis (Fig. 4). Changing the electrolysis potential to −0.27 V vs. RHE let the CO partial current increase by about one order of magnitude to j_{CO} = −0.05 mA cm^{-2} (FE_{CO} = 28%). This potential is identified as on-set of substantial CO evolution (see also discussion of Fig. 5f below). In addition, minor amounts of formate were detected ($j_{formate}$ = −4 μA cm^{-2}, $FE_{formate}$ = 2%). At −0.47 V vs. RHE the total CO_2RR current density has already raised to −0.44 mA cm^{-2}. The only CO_2RR products are CO (j_{CO} = −0.3 mA cm^{-2}, FE_{co} = 21%) and formate ($j_{formate}$ = −0.14 mA cm^{-2}, $FE_{formate}$ = 10%) again. At electrolysis potentials more negative than −0.6 V the hydrocarbon pathway is activated, thus leading to a further increase of the total CO_2RR current density to j_{CO2RR} = −2.65 mA cm^{-2} at −0.67 V. At this electrolysis potential ethylene (j_{C2H4} = −0.47 mA cm^{-2}, FE_{C2H4} = 6%) and ethane (j_{C2H6} = −0.62 mA cm^{-2}, FE_{C2H6} = 8%) were detected. The total CO_2RR efficiency shows a constantly increasing trend in the potential range studied, and reaches a value of ~40% at −0.87 V vs. RHE (Fig. 4b).

In agreement with previous studies, the thermal annealing activates the Cu catalyst for C2 and C3 oxygenate production (Fig. 4). Note that no methanol production was observed in the product analysis. As already observed for the hydrocarbons, the C1 alcohol

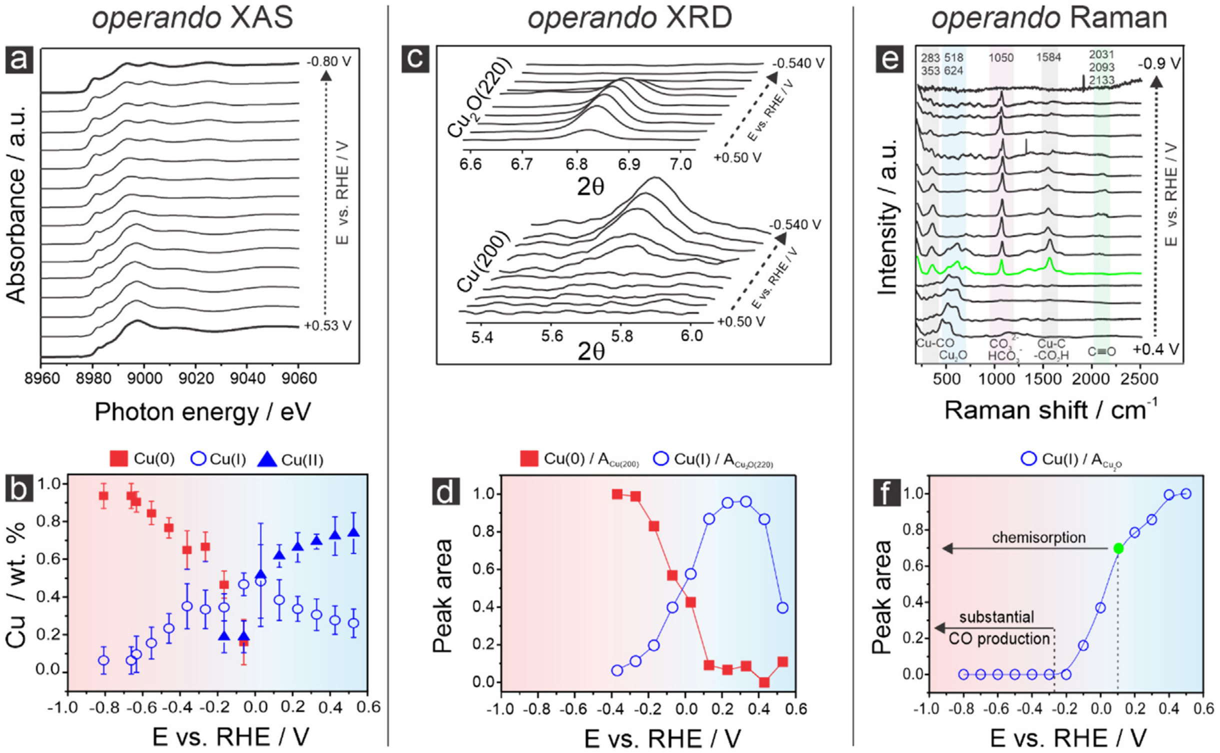

Fig. 5. Survey of experimental *operando* results demonstrating the potential-dependent oxide-metal transition of the catalyst precursor (Cu_xO foam). (a) Potential-dependent *operando* XANES spectra (Cu K-edge) of the thermally annealed Cu foam (Cu_xO) in CO_2-saturated 0.5 M $KHCO_3$; (b) Potential-dependent composition of the Cu_xO foam (relative content of Cu species: Cu(0), Cu(I), and Cu(II) derived from a linear combination fitting (LCF) of the XANES spectra shown in (a)); (c) Potential-dependent *operando* grazing-incidence X-ray diffractograms of the Cu_2O(220) and Cu(200) reflections; (d) Integrated and normalized intensities of the diffractograms shown in (c); (e) Corresponding potential-dependent *operando* Raman spectra; (f) Integrated and normalized peak intensities of the Cu_2O related Raman peaks (518 cm^{-1} and 624 cm^{-1}) shown in (e), the peak areas were normalized with respect to the most intense peaks at most positive electrode potentials. The red and blue colours in panel b, d, and f indicate the transition from the oxide to the metallic state of Cu.

pathway is fully blocked on the oxide-derived Cu foam catalyst. The partial current density for ethanol formation increases from $j_{EtOH} = -0.86$ mA cm^{-2} (FE_{EtOH} = 5%) at −0.77 V vs. RHE to $j_{EtOH} = -1.61$ mA cm^{-2} (FE_{EtOH} = 6.7%) at −0.87 V vs. RHE (Fig. 4c). The partial current density for n-propanol formation reaches a value of $j_{PrOH} = -1.72$ mA cm^{-2} (j_{PrOH} = 7.1%) at −0.87 V (Fig. 4c). All current densities discussed herein were normalized to the geometric surface area of the carbon support. Corresponding FE and partial current density (PDC) data normalized to the electrochemically active surface (ECSA, Fig. S13), determined by the viologen method, is provided in the supporting information (see Fig. S14 and Tables S5 and S6).

3.3. Post electrolysis XPS inspection

After completion of the 1 h lasting electrolysis, the used foam samples were transferred to an airtight and Ar containing (99.9999%, Carbagas, Switzerland) sample container to minimize further oxidation when exposed to air prior to the XPS inspection. CuO related photoemission features are clearly visible in the XPS spectra down to applied electrolysis potentials of +0.33 V vs. RHE (Fig. 3). Holding the potential for 1 h at −0.27 V is already sufficient to let all CuO related features disappear from the XPS spectrum which shows only characteristics of metallic Cu similar to the as deposited Cu foam. Note that the potential range where the reduction process of cupric and cuprous oxides is observed is fully consistent with thermodynamic predictions [33,62]. Our post electrolysis XPS results suggest that the surface of the thermally formed Cu oxides is already reduced at very low cathodic potentials, where only minimal traces of CO could be detected during CO_2RR (Fig. 4). Substantial CO_2RR activity on the thermally annealed Cu foam catalysts was observed only at potentials below −0.3 V vs. RHE, where the surface oxide layers are entirely transformed into metallic Cu. Therefore, the active catalyst for the CO_2RR can be indeed denoted as oxide-derived (OD) [11,12,21,23]. It should be noted, however, that these results do not exclude the presence of residual traces of sub-surface oxygen [22,32,34,35,37,38]. Its concentration might, however, be below the XPS detection limit.

3.4. Identical location (IL)-SEM study

The thermally induced formation of oxide phases from the metallic precursors and their subsequent electrochemical reduction back to the metallic state go along with changes in the morphology of the deposit, thus often considered as an important factor of the desired catalyst activation process [17]. To probe these morphological alterations, identical location (IL) SEM analysis was applied to the Cu foam catalysts in their different chemical states. Panels a–d in Fig. S9 represent the as deposited Cu foam whereas panels e-h show the corresponding Cu_xO foam obtained by the 12 h thermal annealing at 300 °C in air. In addition, panels i-l depict the metallic OD-Cu foam after the 1 h CO_2RR at −0.67 V vs. RHE. The primary macro-porosity of the Cu foam catalyst remains unaffected by the thermal treatment and the subsequent electrochemical reduction of the oxide phases under CO_2RR conditions. This observation demonstrates the structural benefits and robustness of the self-assembled Cu foam catalysts. Changes occur, however, on a smaller length scale starting with the disappearance of the facetted crystallites as a result of the thermal annealing and followed by a grain coarsening process upon the electrochemical reduction of the thermally formed oxides under CO_2RR conditions. A more fissured and rough surface appears along with a high density of nm-sized spherical Cu particles (Fig. S9l). Similar changes have recently been reported for dendritic Cu deposited on Cu mesh supports by Rahaman et al. [17]. This oxide-derived (OD)-Cu, which only forms under *operando* conditions, needs to be considered as the actual catalyst for the CO_2RR being active for hydrocarbon and alcohol production.

3.5. Operando Quick X-ray absorption spectroscopy (Quick-XAS)

To probe changes in the chemical state of copper before and during CO_2RR, Cu K-edge Quick-XAS measurements were carried out in CO_2-saturated 0.5 M $KHCO_3$ for both the annealed foam (Figs. 5a, b, S10, and 6) and the as deposited one (Fig. S11). Note that no substantial changes in the electronic state of copper were observed for the as deposited Cu foam sample within the entire range of potentials applied (Fig. S11). Changes in the potential-dependent Cu K-edge XANES (X-ray Absorption Near Edge Spectroscopy) spectra of the Cu_xO foam can clearly be attributed to potential-dependent redox state changes of Cu species (Fig. 5a). For instance, the observed shifts of the transition energy are due to changes of the ion charges and their potential-dependent redox-state (8984.3 eV, 8981.1 eV and 8979.7 eV for CuO, Cu_2O and Cu, respectively). The trend of decreasing Cu K-edge (transition) energies by applying more cathodic potentials is clearly pointing to the reduction of the Cu_xO foam mediated by the

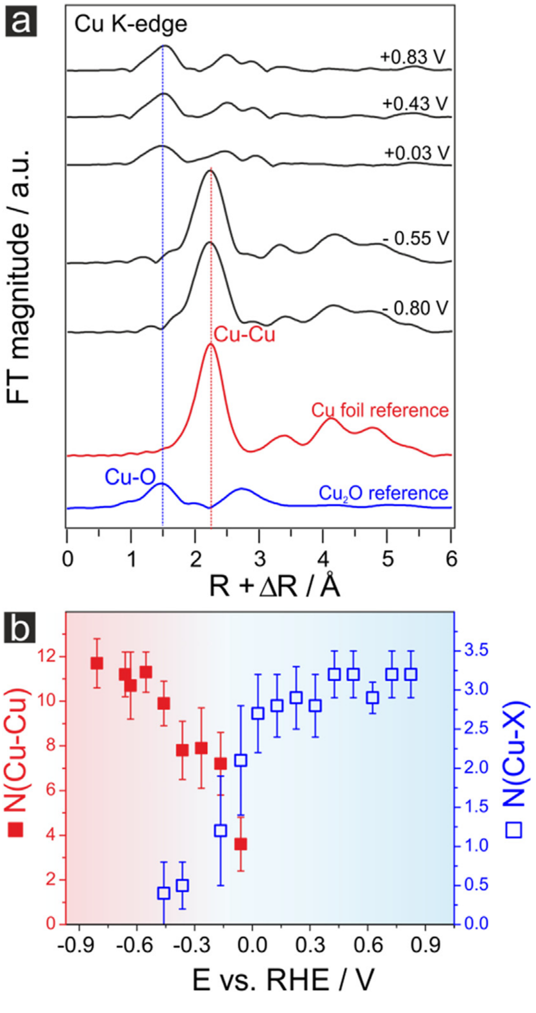

Fig. 6. (a) Changes of the Fourier-transform magnitudes of the k^2-weighted EXAFS data at the Cu K-edge as function of the applied potential for the Cu_xO foam. For comparison purposes also the EXAFS reference spectra for Cu_2O (blue) and metallic Cu (red) are provided; (b) Dynamic behavior of the partial coordination numbers for Cu-Cu and Cu-X (X = O or C) scattering pairs as function of the applied potential. The red and blue colours in panel b indicate the transition from the oxide to the metallic state of the oxidized copper. See also Table S7.

applied electrode potential. Obviously this chemical transition is already completed at potentials more positive than the onset of substantial hydrocarbon and alcohol formation (Fig. 4), which is in full agreement with the post electrolysis XPS analysis (Fig. 3).

A linear combination fitting (LCF) analysis was applied to the XANES data. Cu K-edge XANES spectra of the Cu foil, Cu_2O and CuO served as references for the LCF analysis. Note that the quality of the reference spectra used substantially influences the accuracy of the LCF analysis. As a result of this fitting, Fig. 5b shows changes of the Cu(0), Cu(I), and Cu(II) contents in the Cu_xO foam as a function of the potential applied. The LCF analysis suggests that the Cu_xO foam at + 0.6 V vs. RHE predominantly consists of Cu(II) species, assigned to cupric CuO, whereas only a lower Cu(I) content was observed (25–35 wt%). The latter is assigned to cuprous Cu_2O. Note that this Cu(I)/Cu(II) ratio is different from that derived from the more surface sensitive post electrolysis XPS inspection (Figs. 3, S7). When gradually changing the potential to more cathodic values, Cu(II) and Cu(I) species are in principle retained in the range between 0 and 0.6 V vs. RHE. Their relative abundance change, thus pointing to a potential-induced transition from Cu (II) to Cu(I) prior to the reduction of the oxidic precursor to metallic Cu(0) which starts in the 'bulk' of the foam material at 0 V vs. RHE. At potentials below 0 V vs. RHE the Cu(II) abundance drops down to zero, whereas Cu(I) species are present in the bulk down to potentials of −0.5 V vs. RHE. The potential-dependent decrease of the Cu(I) content below 0 V vs. RHE is clearly anti-correlated to the increase of the Cu(0) abundance (Fig. 5b). The transition from the oxidic precursor to metallic Cu in the bulk is completed at about −0.7 V vs. RHE.

Further, the Fourier-transformed k^2-weighted EXAFS spectra for the electrodeposited and annealed Cu foams as a function of the applied potential are illustrated in Figs. 6 and S10. From the EXAFS data, the coordination number (N), the interatomic bond length (R), the mean squared bond length disorder (σ^2), and correction to the energy origin (ΔE_0) for the Cu-Cu and Cu-O scattering pairs were derived and listed in Tables S7 and S8. Fig. 6a displays a representative set of EXAFS spectra of the Cu_xO foam. For comparison the reference spectra for metallic Cu (foil) and Cu_2O are also provided. Results of the analysis are displayed in Fig. 6b showing changes of the Cu-X (X = O, C) and Cu-Cu coordination numbers as function of the potential applied. Due to the scattering properties of light elements, it is impossible to distinguish between Cu-O and Cu-C by EXAFS. A very minor contribution from Cu-C coordination to the overall EXAFS signal might result from the appearance of chemisorbed CO_2RR intermediates adsorbed via the carbon to the Cu catalyst surface (see Discussion section below). At the applied potential of +0.8 V vs. RHE the mean (averaged) coordination number (N) for Cu-X is 3.2 ± 0.2 in agreement with the assumption of an oxidic foam material (catalyst precursor) that is composed of a Cu_2O/CuO mixture. Note that for an annealing temperature of 300 °C, applied for the preparation of the Cu_xO foam, the Cu_2O is expected to be crystalline (space group of Pn-3 m with a coordination number N(Cu-O) = 4 in the first shell), whereas the CuO remains largely in an amorphous state [11,12,17]. Substantially higher annealing temperatures are typically required to yield a fully crystalline CuO phase than for crystalline Cu_2O. In the potential range between +0.8 V and 0 V vs. RHE the mean coordination number N(Cu-X) drops down moderately. A substantial alteration occurs, however, at potentials below 0 V vs. RHE, which involves the appearance of metallic Cu (see also Figs. 3 and 5b). In the very initial stage of this transition, the metallic Cu is highly under-coordinated. Values of the N(Cu-Cu) start from 3.6 ± 1.2 at 0 V vs. RHE and gradually approach the target value of 12 for a face-centered cubic (*fcc)* bulk copper at highest cathodic potentials applied herein (e.g., N(Cu-Cu) = 11.7 ± 1.1 at −0.8 V vs. RHE).

3.6. Operando X-ray diffraction (XRD)

To further study the structural transition of the Cu_2O/CuO composite to the metallic *fcc* Cu we applied *operando* XRD in a gracing incidence geometry [63]. For the survey in Fig. 5c we restrict ourselves on the evolution of the $Cu_2O(220)$ (fingerprint for the oxide precursor) and Cu(200) (fingerprint for the metallic *fcc* Cu) diffraction peaks. Their noise to signal ratio was most appropriate for the quantitative analysis. Interestingly, the integrated intensity of the $Cu_2O(220)$ diffraction peak first increases when going from +0.5 V to +0.2 V vs. RHE. This trend is consistent with the assumption of an intermediate crystalline Cu_2O phase which accumulates in the initial stage of the oxide-metal transition in the foam material on the expense of the partially amorphous/crystalline CuO phase. A qualitatively similar trend of increasing Cu(I) content was observed in the corresponding XAS experiment (Fig. 5b). However, the disappearance of the Cu_2O related diffraction pattern with negative going potentials is already completed at −0.4 V vs. RHE, whereas the XAS experiment indicates the presence of Cu(I) species for potentials down to −0.8 V vs. RHE. These deviations in the particular potential-dependence of the Cu(I)(XAS)/Cu_2O(XRD) stability regime are most likely related to the intrinsic characteristics of both *operando* techniques (see Discussion section below). Our XRD results are in full agreement with the work by Ahn et al. also demonstrating the disappearance of copper oxide species prior to the CO_2RR onset [64]. An important finding of the XRD analysis concerns the average size of the coherent domains for Cu_2O and *fcc* Cu calculated on the basis of the Scherrer formula. The mean crystallite size of the Cu_2O in the range between 0 V and 0.7 V vs. RHE is 13.3 nm whereas a mean crystallite size drops down to 6.7 nm when the *fcc* Cu has formed below −0.2 V vs. RHE. This large shift of the mean domain size cannot solely be rationalized by changes of the unit-cell volume during the oxide-metal transition. The identical location (IL)-SEM analysis demonstrates morphological changes on the nm length-scale upon oxide reduction involving the appearance of smaller nanoparticles on the dendritic foam structure. In general, the reduction of the oxidic precursor typically leads to an increase of the electrochemically active surface area (ECSA, see also Figs. S12 and S13) [11,12,41,49,61]. Such change in the micro- and nano-structure upon reduction of the oxidic precursor is most likely the origin of the different performances of Cu nanomaterials prepared from similar precursors. These effects are also known from other types of catalyst materials, e.g. those used for the oxygen reduction reaction (ORR) [65–67]. Not only is the ECSA affected by these morphological alteration but also the density of low-coordinated surface sites and the grain boundary density are altered, explain changes in the overall catalytic activity and product selectivity for the CO_2RR.

3.7. Operando Raman spectroscopy

Whereas XRD and XAS are techniques which are both sensitive to the bulk of the catalyst material, the *operando* Raman spectroscopy provides additional and highly valuable insights into chemical state changes of the catalyst surface. In addition, chemisorption phenomena of CO_2RR intermediates become accessible thereby providing insights into the CO_2RR reaction mechanism [68]. The highly porous nature of the foam material might further facilitate the Raman experiment due to the SERS (Surface Enhanced Raman Spectroscopy) effect, at least when the Cu_xO precursor has been (partially) transformed to its metallic state [69].

In the potential-dependent Raman experiment (shown in Fig. 5e) the potential applied was started at the open circuit potential (OCP) followed by a stepwise change of the potential from +0.5 V vs. RHE to −0.8 V vs. RHE. Note that a significant change

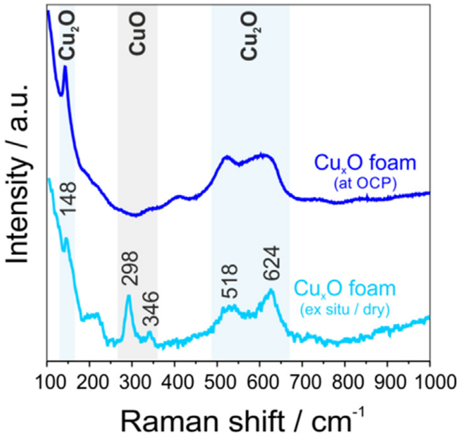

Fig. 7. Raman spectra of the Cu$_x$O foam (after annealing of the as deposited Cu foam at 300 °C, 12 h, in air). The bright blue spectrum (bottom) represents the dry Cu$_x$O foam (ex situ) whereas the blue one (top) shows the Cu$_x$O foam exposed to the CO$_2$-saturated 0.5 M KHCO$_3$ solution under OCP conditions (OCP = +0.504 V vs. RHE; see also Fig. S15).

in the surface condition takes already place, when the Cu$_x$O foam is brought into the contact with the CO$_2$-saturated 0.5 M KHCO$_3$ electrolyte solution under OCP conditions. This pronounced surface effect is highlighted in Fig. 7 comparing the Raman spectrum of the dry Cu$_x$O foam sample with the one measured under steady-state conditions at the OCP. Raman modes observed at 148 cm^{-1}, 518 cm^{-1}, and 624 cm^{-1} are ascribed to cuprous oxide species (Cu$_2$O), whereas peaks at 298 cm^{-1} and 346 cm^{-1} have to be assigned to cupric oxide [40,70,71]. After exposure to the electrolyte at OCP, the CuO related vibrational modes have completely disappeared from the spectrum. Only vibrational modes of the cuprous oxide (Cu$_2$O) are left thus demonstrating that the catalyst precursor surface is exclusively terminated by Cu(I) species in the initial stage of the potential step experiment presented in Fig. 5e. Note that no alteration of this kind were observed in the corresponding XRD and XAS experiments confirming once more that these techniques are largely insensitive to the catalyst surface, when applied to foam type of materials. These materials exhibit a large and dominating contribution of the bulk to the XRD and XAS signals. For the quantitative analysis of the Raman spectra we focused on the vibrational modes at 518 cm^{-1} and 624 cm^{-1} as spectroscopic fingerprints for the presence of cupric surface oxide species. Their integrated intensities are displayed in Fig. 5f as function of the applied potential. The overall trend of decreasing integrated intensities with decreasing applied potentials is qualitatively similar to the one derived from the *operando* XRD (Fig. 5d). Slight deviations concern, however, the initial stage of the oxide reduction process in the potential range from +0.5 V to +0.1 V vs. RHE, where the XRD shows an initial increase of the Cu$_2$O(2 2 0) related intensities passing a maximum at +0.1 V vs. RHE (Fig. 5d). The latter trend has been ascribed to the transient increase of the Cu$_2$O content in the bulk of the foam material, originating from the partial reduction of the amorphous CuO phases. Note that this transition occurs spontaneously at the surface when brought into contact to the electrolyte (Fig. 7). Obviously the 'surface oxide reduction' proceeds faster and at slightly more positive potentials than the corresponding transition of the oxidic 'bulk phases' probed by operando XAS and XRD. Delayed (on the potential scale) is in particular the disappearance of the Cu(I) in the XAS experiment (Fig. 5b) suggesting that the reduction of residual Cu(I) in the final state of the transition process (between −0.3 and −0.6 V vs. RHE) occurs from a largely disordered state which is still detectable by the XAS but invisible in the XRD.

Operando Raman spectroscopy provides not only insights into the chemical state of the catalyst (precursor) surface but also on the appearance and disappearance of chemisorbed intermediates associated to the CO$_2$RR. Raman modes observed at 283 cm^{-1}/253 cm^{-1}, 1050 cm^{-1}, 1584 cm^{-1} and 2031 cm^{-1}/2093 cm^{-1}/2133 cm^{-1} can be, in full agreement to the literature, assigned to CO$_{ads}$, HCO$^{-2}_{3ads}$ and HCOOH$_{ads}$ species [71,72]. These intermediates start to appear only from potentials of +0.2 V vs. RHE on (see green highlighted spectrum in Fig. 5e), where a certain fraction of the surface Cu$_2$O has already been disappeared from the surface (see also Discussion section below for further information on the Raman spectroscopy's results).

4. Discussion

Understanding the activation of oxidic precursor catalyst materials for the CO$_2$RR requires the application of highly complementary *operando* techniques. Fig. 8 demonstrates the basic working principles of the approaches applied herein. It further indicates their particular strengths and weaknesses for the analysis of the potential-mediated oxide-metal transition which is considered essential for the activation process of the oxidic Cu$_x$O precursor in particular when alcohols are targeted as CO$_2$RR products.

The XAS technique (XANES, EXAFS) is sensitive to the bulk of the catalyst (precursor) material and provides valuable information on the oxidation state and related coordination number changes which go along with the electrochemical reduction of the Cu$_x$O foam. Although considered as high-surface area catalysts, Cu foams exhibit a more unfavorable volume (bulk) to surface ratio as compared to nanoparticulate catalyst materials. This is why the XAS data acquired from the Cu$_x$O electro-reduction predominantly originate from the bulk with rather minor contribution from the surface of the oxide/metal foam (see Fig. S10). A clear strength of the XAS is, however, related to its capability of probing oxidation state changes even when (partially) amorphous phases are involved. This is particularly important for those structurally demanding samples where the crystalline oxide phases are not fully developed [12], e.g. in the case of the Cu$_x$O foam discussed herein. It has been demonstrated that oxide-metal transitions may occur via non-crystalline intermediate states, particularly in their final stage (see 'delayed' Cu(I) disappearance in Fig. 5b (XAS) compared to Fig. 5d (XRD)). This is why XAS is superior to all other techniques used herein in determining the ultimate completion of the (bulk) oxide-metal transition [11,12,41].

Operando XRD is highly complementary to the XAS technique as it allows monitoring changes in the crystal structure which often go along with the oxidation state alterations. In this present case, XRD could identify the crystalline Cu$_2$O as an intermediate phase whose abundance temporarily increases in the bulk phase during the Cu$_x$O reduction process (Fig. 5d) in full accordance with the XAS (Fig. 5b). Particularly valuable is the comparison of the XAS and XRD data in the highly cathodic potential regime suggesting the persistence of structurally disordered Cu$_2$O (and therefore not visible in the XRD, see Fig. 5d) at potentials more negative than those expected from the structure-sensitive XRD.

More sensitive to the very initial stage of the oxide-metal transition is the *operando* Raman spectroscopy (Figs. 5e, f and 7). *Operando* Raman spectroscopy probes predominantly the surface of the Cu/Cu$_x$O foams with little contributions from the near surface bulk regime.

Structural alterations already occur when the Cu$_x$O is exposed to electrolyte under OCP conditions. The presence of cupric oxide (CuO) at the surface of the dry sample has been confirmed by both ex situ XPS (Fig. 3) and Raman spectroscopy (Fig. 7). It instantaneously disappears from the outermost surface of the Cu$_x$O foam

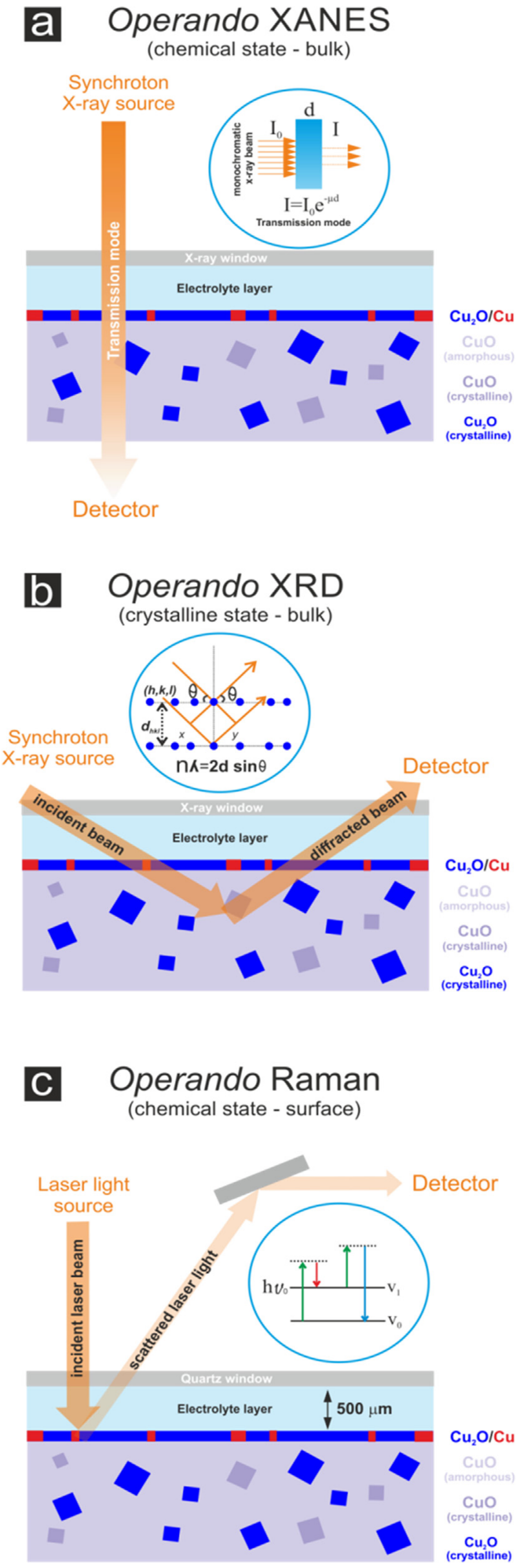

Fig. 8. Schematic drawings demonstrating the complementary approach of operando analytical techniques applied; (a) *Operando* X-ray absorption spectroscopy (XAS); (b) *Operando* X-ray diffraction (XRD); (c) *Operando* Raman scattering. The sample condition corresponds to the applied potential of +0.1 V vs. RHE where the surface is partially reduced (Fig. 5f) and the bulk is composed of a mixed Cu_2O and CuO (amorphous and crystalline).

when brought into contact with the electrolyte phase, whereas the Cu(II) → Cu(I) transition is completed in the bulk material only at potentials more negative than −0.2 V vs. RHE (Fig. 5b and d). Note that the Raman spectroscopy does not detect any CuO related vibrational modes at the OCP (Fig. 7) and at any applied potential (Fig. 5e), whereas the *operando* XAS clearly proves CuO as the main constituent of the Cu_xO foam material in the potential range between +0.6 and +0.1 V vs. RHE (Fig. 5b). This experimental observation clearly indicates that, under the given experimental conditions, the Raman spectroscopy has a highly limited probing depth making it to a surface sensitive technique with little or even negligible contributions from the 'bulk' material.

The comparison of the *operando* techniques applied (Fig. 5) clearly points to a huge difference in the potential-dependent surface phase behavior and corresponding structural and compositional transitions in the respective 3D volume of the foam material. Based on our comprehensive analysis, we conclude that all compositional and redox state changes in the bulk of the Cu_xO foam are 'delayed' on the potential scale compared to corresponding processes taking place at the oxide precursor surface which is in contact to the electrolyte solution.

Generally, the disappearance of the Cu_2O is anti-correlated to the appearance of metallic Cu (see Fig. 5b).

According to the *operando* Raman spectroscopy, concerted chemisorption phenomena of carbonate/bicarbonate and CO_2 related species set in at a potential of +0.1 V vs. RHE (highlighted green in Fig. 5e and f). This also involves the appearance of Raman features at 283 cm^{-1}/353 cm^{-1} that are commonly ascribed to Cu(0)–CO vibrational modes involving metallic Cu as binding partner [72–74]. This particular feature in the Raman spectrum can therefore be considered as a clear spectroscopic fingerprint for the appearance of metallic Cu. Raman features of the adsorbed species might be further enhanced by the SERS effect originating from the appearance of metallic domains on the foam surface (Fig. 5e, highlighted green).

Important to note is that all Raman features not related to the oxides (Cu_2O: 148 cm^{-1}, 518 cm^{-1}, and 624 cm^{-1}; CuO: 298 cm^{-1} and 346 cm^{-1}) appear along with the ones at 283 cm^{-1}/353 cm^{-1} (Cu fingerprint). This observation let us conclude that the chemisorption of carbonate/bicarbonate and CO_2 related species takes preferentially place on metallic Cu domains that obviously co-exist already at these potentials (+0.1 V vs. RHE) with surface domains of cuprous Cu_2O (Fig. 5e). These surface-confined processes at most positive applied potentials remain invisible for the *operando* XAS and XRD.

When comparing the acquired *operando* Raman data (Fig. 5f), which reflect those surface properties most relevant for the electrocatalytic activity of the Cu foam, with the potential-dependent CO_2RR product distribution in Fig. 4, it becomes evident that neither CuO nor Cu_2O species are detectable at the catalyst surface when substantial CO evolution sets in at applied potentials close to −0.3 V vs. RHE (Fig. 4b). Note, however, that the overall oxide reduction process in the bulk is not yet completed under these experimental conditions (Fig. 5b and 5d). The foam as a whole needs at these potentials to be considered as a mixed metal/oxide composite in the very initial stage of CO_2RR. The question, whether and if yes to which extent, the remaining oxide domains in the bulk of the foam catalyst actively participate in the initial CO_2RR, cannot be ultimately answered herein. What becomes, however, obvious from the comprehensive survey of the applied *operando* techniques (Fig. 5) is that both hydrocarbon formation and alcohol production take place on an activated Cu foam catalysts where the oxidic species have completely disappeared not only from the surface but also from the bulk of the foam material. These findings are in full agreement with the work by Mandal et al. [29].

Note that the *operando* XAS and Raman measurements were not extended to potentials more negative than −0.8 vs. RHE (potential range of hydrocarbon and alcohol formation) as it is rather unlikely that oxidic species re-appear under these extremely cathodic conditions.

5. Conclusion

We applied herein a set of highly complementary *operando* techniques sensitive to potential-dependent alteration of oxidic precursor materials used for the electrochemical reduction of CO_2 into value-added products such as hydrocarbons and higher alcohols.

Our analyses strongly suggest that the overall oxide-metal transition commences at the oxidic precursor surface. When brought into contact with the CO_2-saturated solution cupric oxide (CuO) species spontaneously disappear from the surface leaving a Cu_2O enriched interface behind as starting point for further potential-mediated surface transformations. *Operando* Raman spectroscopy further indicates that chemisorption phenomena of CO_2 related species preferentially occurs on metallic Cu and not on oxidic Cu species.

Particularly valuable is the comparison with the bulk-sensitive XAS and XRD techniques which both indicate oxide-metal transitions that are 'delayed' on the potential scale with respect to what is observed in the surface-sensitive Raman spectroscopy. The in-depth analysis of XAS and XRD data further revealed that the ultimate formation of metallic Cu at most cathode potentials applied herein occurs from Cu_2O lacking long-range transitional order. XRD showed the disappearance of crystalline Cu_2O before completion of the Cu(I) → Cu(0) transition as probed by the XAS.

All three *operando* techniques applied herein consistently prove, however, that the oxides are entirely reduced to the metallic state of Cu before the production of hydrocarbons and alcohols sets in.

This study demonstrates that a complementary approach of *operando* investigations is required to derive a complete view on the potential induced metal-oxide transition required to activate the Cu catalyst in particular towards alcohol formation.

Declaration of Competing Interest

The authors declare that they have no known competing financial interests or personal relationships that could have appeared to influence the work reported in this paper.

Acknowledgement

The financial support by the CTI Swiss Competence Center for Energy Research (SCCER Heat and Electricity Storage) is gratefully acknowledged. PB acknowledges the financial support by the Swiss National Science Foundation (SNSF) via the project No. 200020_172507. This study was performed with the support of the interfaculty Microscopy Imaging Centre (MIC) of the University of Bern. MO acknowledges the financial support by the Federal Ministry of Education and Research (BMBF, ECatPEMFC, FKZ 03SF0539) and by the German Research Foundation (DFG, INST 184/154-1 FUGG). BH thanks the Georg Lichtenberg scholarship of the RTG Nano- and Energy Research, Oldenburg. The Swiss Light Source (SLS) at the Paul Scherrer Institute, Switzerland is thanked - in particular Dr. Adam Clark and Dr. Maarten Nachtegaal - for access to synchrotron beamline SuperXAS (proposal-IDs 20161388 and 20182014).

Appendix A. Supplementary material

Supplementary data to this article can be found online at https://doi.org/10.1016/j.jcat.2020.06.024.

References

[1] G.M.D. Earth System Research Laboratory, https://www.esrl.noaa.gov/gmd/ccgg/trends/, in, Earth System Research Laboratory, Global Monitoring Division, https://www.esrl.noaa.gov/gmd/ccgg/trends/, 2018.
[2] N. Kittner, F. Lill, D.M. Kammen, Energy storage deployment and innovation for the clean energy transition, Nat. Energy 2 (2017) 17125.
[3] B.D. Solomon, K. Krishna, The coming sustainable energy transition: History, strategies, and outlook, Energy Policy 39 (2011) 7422–7431.
[4] Change is in the air, Nat. Catalysis, 1 (2018) 93-93.
[5] M.G. Kibria, C.-T. Dinh, A. Seifitokaldani, P. De Luna, T. Burdyny, R. Quintero-Bermudez, M.B. Ross, O.S. Bushuyev, F.P. García de Arquer, P. Yang, D. Sinton, E. H. Sargent, A surface reconstruction route to high productivity and selectivity in CO_2 electroreduction toward C2+ hydrocarbons, Adv. Mater. 30 (2018) 1804867.
[6] Y. Zhou, F. Che, M. Liu, C. Zou, Z. Liang, P. De Luna, H. Yuan, J. Li, Z. Wang, H. Xie, H. Li, P. Chen, E. Bladt, R. Quintero-Bermudez, T.-K. Sham, S. Bals, J. Hofkens, D. Sinton, G. Chen, E.H. Sargent, Dopant-induced electron localization drives CO_2 reduction to C2 hydrocarbons, Nat. Chem. 10 (2018) 974–980.
[7] Y. Hori, A. Murata, R. Takahashi, Formation of hydrocarbons in the electrochemical reduction of carbon dioxide at a copper electrode in aqueous solution, J. Chem. Soc., Faraday Trans. 1: Phys. Chem. Condens. Phases 85 (1989) 2309–2326.
[8] Y. Hori, A. Murata, R. Takahashi, S. Suzuki, Enhanced formation of ethylene and alcohols at ambient temperature and pressure in electrochemical reduction of carbon dioxide at a copper electrode, J. Chem. Soc., Chem. Commun. (1988) 17–19.
[9] Y. Hori, K. Kikuchi, S. Suzuki, Production of CO and CH_4 in electrochemical reduction of CO_2 at metal electrodes in aqueous hydrogencarbonate solution, Chem. Lett. 14 (1985) 1695–1698.
[10] S. Ma, M. Sadakiyo, R. Luo, M. Heima, M. Yamauchi, P.J.A. Kenis, One-step electrosynthesis of ethylene and ethanol from CO_2 in an alkaline electrolyzer, J. Power Sources 301 (2016) 219–228.
[11] A. Dutta, M. Rahaman, N.C. Luedi, M. Mohos, P. Broekmann, Morphology matters: tuning the product distribution of CO_2 electroreduction on oxide-derived Cu foam catalysts, ACS Catal. 6 (2016) 3804–3814.
[12] A. Dutta, M. Rahaman, M. Mohos, A. Zanetti, P. Broekmann, Electrochemical CO_2 conversion using skeleton (sponge) type of Cu catalysts, ACS Catal. 7 (2017) 5431–5437.
[13] R.M. Arán-Ais, F. Scholten, S. Kunze, R. Rizo, B. Roldan Cuenya, The role of in situ generated morphological motifs and Cu(i) species in C2+ product selectivity during CO_2 pulsed electroreduction, Nat. Energy 5 (2020) 317–325.
[14] K.W. Frese, S. Leach, Electrochemical reduction of carbon dioxide to methane, methanol, and CO on Ru electrodes, J. Electrochem. Soc. 132 (1985) 259–260.
[15] K.P. Kuhl, T. Hatsukade, E.R. Cave, D.N. Abram, J. Kibsgaard, T.F. Jaramillo, Electrocatalytic conversion of carbon dioxide to methane and methanol on transition metal surfaces, J. Am. Chem. Soc. 136 (2014) 14107–14113.
[16] M. Le, M. Ren, Z. Zhang, P.T. Sprunger, R.L. Kurtz, J.C. Flake, Electrochemical reduction of CO_2 to CH_3OH at copper oxide surfaces, J. Electrochem. Soc. 158 (2011) E45.
[17] M. Rahaman, A. Dutta, A. Zanetti, P. Broekmann, Electrochemical reduction of CO_2 into multicarbon alcohols on activated Cu mesh catalysts: an identical location (IL) study, ACS Catal. 7 (2017) 7946–7956.
[18] D. Ren, N.T. Wong, A.D. Handoko, Y. Huang, B.S. Yeo, Mechanistic insights into the enhanced activity and stability of agglomerated Cu nanocrystals for the electrochemical reduction of carbon dioxide to n-propanol, J. Phys. Chem. Lett. 7 (2016) 20–24.
[19] K. Zhao, Y. Liu, X. Quan, S. Chen, H. Yu, CO2 electroreduction at low overpotential on oxide-derived Cu/carbons fabricated from metal organic framework, ACS Appl. Mater. Interfaces 9 (2017) 5302–5311.
[20] Y.C. Li, Z. Wang, T. Yuan, D.-H. Nam, M. Luo, J. Wicks, B. Chen, J. Li, F. Li, F.P.G. de Arquer, Y. Wang, C.-T. Dinh, O. Voznyy, D. Sinton, E.H. Sargent, Binding site diversity promotes CO_2 electroreduction to ethanol, J. Am. Chem. Soc. 141 (2019) 8584–8591.
[21] K.W. Frese, Electrochemical reduction of CO_2 at intentionally oxidized copper electrodes, J. Electrochem. Soc. 138 (1991) 3338–3344.
[22] D. Gao, I. Zegkinoglou, N.J. Divins, F. Scholten, I. Sinev, P. Grosse, B. Roldan Cuenya, Plasma-activated copper nanocube catalysts for efficient carbon dioxide electroreduction to hydrocarbons and alcohols, ACS Nano 11 (2017) 4825–4831.
[23] C.W. Li, M.W. Kanan, CO_2 reduction at low overpotential on Cu electrodes resulting from the reduction of thick Cu_2O films, J. Am. Chem. Soc. 134 (2012) 7231–7234.
[24] R. Kas, R. Kortlever, A. Milbrat, M.T.M. Koper, G. Mul, J. Baltrusaitis, Electrochemical CO_2 reduction on Cu_2O-derived copper nanoparticles: controlling the catalytic selectivity of hydrocarbons, PCCP 16 (2014) 12194–12201.
[25] C.W. Li, J. Ciston, M.W. Kanan, Electroreduction of carbon monoxide to liquid fuel on oxide-derived nanocrystalline copper, Nature 508 (2014) 504–507.

[26] M. Ma, K. Djanashvili, W.A. Smith, Selective electrochemical reduction of CO_2 to CO on CuO-derived Cu nanowires, PCCP 17 (2015) 20861–20867.

[27] D. Ren, Y. Deng, A.D. Handoko, C.S. Chen, S. Malkhandi, B.S. Yeo, Selective electrochemical reduction of carbon dioxide to ethylene and ethanol on copper (I) oxide catalysts, ACS Catal. 5 (2015) 2814–2821.

[28] F.S. Roberts, K.P. Kuhl, A. Nilsson, High selectivity for ethylene from carbon dioxide reduction over copper nanocube electrocatalysts, Angew. Chem. Int. Ed. 54 (2015) 5179–5182.

[29] L. Mandal, K.R. Yang, M.R. Motapothula, D. Ren, P. Lobaccaro, A. Patra, M. Sherburne, V.S. Batista, B.S. Yeo, J.W. Ager, J. Martin, T. Venkatesan, Investigating the role of copper oxide in electrochemical CO_2 reduction in real time, ACS Appl. Mater. Interfaces 10 (2018) 8574–8584.

[30] Y. Lum, J.W. Ager, Stability of residual oxides in oxide-derived copper catalysts for electrochemical CO_2 reduction investigated with 18O labeling, Angew. Chem. Int. Ed. 57 (2018) 551–554.

[31] W. Tang, A.A. Peterson, A.S. Varela, Z.P. Jovanov, L. Bech, W.J. Durand, S. Dahl, J. K. Nørskov, I. Chorkendorff, The importance of surface morphology in controlling the selectivity of polycrystalline copper for CO_2 electroreduction, PCCP 14 (2012) 76–81.

[32] H. Mistry, A.S. Varela, C.S. Bonifacio, I. Zegkinoglou, I. Sinev, Y.-W. Choi, K. Kisslinger, E.A. Stach, J.C. Yang, P. Strasser, B.R. Cuenya, Highly selective plasma-activated copper catalysts for carbon dioxide reduction to ethylene, Nat. Commun. 7 (2016) 12123.

[33] B. Beverskog, I. Puigdomenech, Revised Pourbaix diagrams for copper at 25 to 300°C, J. Electrochem. Soc. 144 (1997) 3476–3483.

[34] F. Cavalca, R. Ferragut, S. Aghion, A. Eilert, O. Diaz-Morales, C. Liu, A.L. Koh, T. W. Hansen, L.G.M. Pettersson, A. Nilsson, Nature and distribution of stable subsurface oxygen in copper electrodes during electrochemical CO_2 reduction, J. Phys. Chem. C 121 (2017) 25003–25009.

[35] A. Eilert, F. Cavalca, F.S. Roberts, J. Osterwalder, C. Liu, M. Favaro, E.J. Crumlin, H. Ogasawara, D. Friebel, L.G.M. Pettersson, A. Nilsson, Subsurface oxygen in oxide-derived copper electrocatalysts for carbon dioxide reduction, J. Phys. Chem. Lett. 8 (2017) 285–290.

[36] H. Mistry, R. Reske, Z. Zeng, Z.-J. Zhao, J. Greeley, P. Strasser, B.R. Cuenya, Exceptional size-dependent activity enhancement in the electroreduction of CO_2 over Au nanoparticles, J. Am. Chem. Soc. 136 (2014) 16473–16476.

[37] M. Fields, X. Hong, J.K. Nørskov, K. Chan, Role of subsurface oxygen on Cu surfaces for CO_2 electrochemical reduction, J. Phys. Chem. C 122 (2018) 16209–16215.

[38] A.J. Garza, A.T. Bell, M. Head-Gordon, Is subsurface oxygen necessary for the electrochemical reduction of CO_2 on copper?, J Phys. Chem. Lett. 9 (2018) 601–606.

[39] P. Grosse, D. Gao, F. Scholten, I. Sinev, H. Mistry, B. Roldan Cuenya, Dynamic changes in the structure, chemical state and catalytic selectivity of Cu nanocubes during CO_2 electroreduction: size and support effects, Angew. Chem. Int. Ed. 57 (2018) 6192–6197.

[40] M. Balkanski, M.A. Nusimovici, J. Reydellet, First order Raman spectrum of Cu_2O, Solid State Commun. 7 (1969) 815–818.

[41] A. Dutta, I.Z. Montiel, R. Erni, K. Kiran, M. Rahaman, J. Drnec, P. Broekmann, Activation of bimetallic AgCu foam electrocatalysts for ethanol formation from CO_2 by selective Cu oxidation/reduction, Nano Energy 68 (2020) 104331.

[42] A. Abbas, M. Ullah, Q. Ali, I. Zahid, S. Abbas, X. Wang, An overview of CO_2 electroreduction into hydrocarbons and liquid fuels on nanostructured copper catalysts, Green Chem. Lett. Rev. 9 (2016) 166–178.

[43] H.C. Shin, J. Dong, M. Liu, Porous tin oxides prepared using an anodic oxidation process, Adv. Mater. 16 (2004) 237–240.

[44] H.-C. Shin, M. Liu, Copper foam structures with highly porous nanostructured walls, Chem. Mater. 16 (2004) 5460–5464.

[45] H.C. Shin, J. Dong, M. Liu, Nanoporous structures prepared by an electrochemical deposition process, Adv. Mater. 15 (2003) 1610–1614.

[46] R. Jenkins, Profile data acquisition for the JCPDS-ICDD database s, Aust. J. Phys. 41 (1988) 145–154.

[47] R. Jenkins, T.G. Fawcett, D.K. Smith, J.W. Visser, M.C. Morris, L.K. Frevel, JCPDS — international centre for diffraction data sample preparation methods in X-ray powder diffraction, Powder Diffr. 1 (2013) 51–63.

[48] H.-J. Kim, W.S. Jeon, Y.H. Ko, K. Kim, Inclusion of methylviologen in cucurbit[7]uril, PNAS 99 (2002) 5007.

[49] S. Sen, D. Liu, G.T.R. Palmore, Electrochemical reduction of CO_2 at copper nanofoams, ACS Catal. 4 (2014) 3091–3095.

[50] T. Binninger, E. Fabbri, A. Patru, M. Garganourakis, J. Han, D.F. Abbott, O. Sereda, R. Kötz, A. Menzel, M. Nachtegaal, T.J. Schmidt, Electrochemical Flow-Cell Setup for In Situ X-ray Investigations, J. Electrochem. Soc. 163 (2016) H906–H912.

[51] M. Newville, IFEFFIT: interactive XAFS analysis and FEFF fitting, J. Synchrotron Radiat. 8 (2001) 322–324.

[52] I. Martens, R. Chattot, M. Rasola, M.V. Blanco, V. Honkimäki, D. Bizzotto, D.P. Wilkinson, J. Drnec, Probing the dynamics of platinum surface oxides in fuel cell catalyst layers using in situ X-ray diffraction, ACS Appl. Energy Mater. 2 (2019) 7772–7780.

[53] G. Ashiotis, A. Deschildre, Z. Nawaz, J. Wright, D. Karkoulis, F. Picca, J. Kieffer, The fast azimuthal integration Python library: PyFAI, J. Appl. Crystallogr. 48 (2015).

[54] A. Dutta, A. Kuzume, M. Rahaman, S. Vesztergom, P. Broekmann, Monitoring the chemical state of catalysts for CO2 electroreduction: an in operando study, ACS Catal. 5 (2015) 7498–7502.

[55] V. Stancovski, S. Badilescu, In situ Raman spectroscopic–electrochemical studies of lithium-ion battery materials: a historical overview, J. Appl. Electrochem. 44 (2014) 23–43.

[56] A. Dutta, A. Kuzume, V. Kaliginedi, M. Rahaman, I. Sinev, M. Ahmadi, B. Roldán Cuenya, S. Vesztergom, P. Broekmann, Probing the chemical state of tin oxide NP catalysts during CO_2 electroreduction: a complementary operando approach, Nano Energy 53 (2018) 828–840.

[57] A. Kuzume, A. Dutta, S. Vesztergom, P. Broekmann, Operando Raman Spectroscopy: Studies on the Reactivity and Stability of SnO2 Nanoparticles During Electrochemical CO2 Reduction Reaction, in: K. Wandelt (Ed.) Encyclopedia of Interfacial Chemistry, Elsevier, Oxford, Encyclopedia of Interfacial Chemistry,Surface Science and Electrochemistry, Elsevier, Amsterdam, 2018, pp. 217–2262018, pp. 217-226.

[58] A.C. Miller, G.W. Simmons, Copper by XPS, Surf. Sci. Spectra 2 (1993) 55–60.

[59] H. Rupp, U. Weser, X-ray photoelectron spectroscopy of copper(II), copper(I), and mixed valence systems, Bioinorg. Chem. 6 (1976) 45–59.

[60] C.-K. Wu, M. Yin, S. O'Brien, J.T. Koberstein, Quantitative analysis of copper oxide nanoparticle composition and structure by X-ray photoelectron spectroscopy, Chem. Mater. 18 (2006) 6054–6058.

[61] A. Dutta, C.E. Morstein, M. Rahaman, A. Cedeño López, P. Broekmann, Beyond copper in CO2 electrolysis: effective hydrocarbon production on silver-nanofoam catalysts, ACS Catal. 8 (2018) 8357–8368.

[62] N. Ibl, Atlas d'équilibres électrochimiques à 25 °C. Von M. Pourbaix, unter Mitwirkung zahlreicher Fachgelehrter. Verlag: Gauthier-Villars & Cie., Paris 1963. 1. Aufl., 644 S., zahlr. Abb., geb. NF 140.—, Angew. Chem., 76 (1964) 444-444.

[63] T. Kondo, T. Masuda, K. Uosaki, In situ SXS and XAFS measurements of electrochemical interface, in: C.S.S.R. Kumar (Ed.), X-ray and Neutron Techniques for Nanomaterials Characterization, Springer, Berlin Heidelberg, Berlin, Heidelberg, 2016, pp. 367–449.

[64] S. Ahn, K. Klyukin, R.J. Wakeham, J.A. Rudd, A.R. Lewis, S. Alexander, F. Carla, V. Alexandrov, E. Andreoli, Poly-amide modified copper foam electrodes for enhanced electrochemical reduction of carbon dioxide, ACS Catal. 8 (2018) 4132–4142.

[65] R. Chattot, T. Asset, P. Bordet, J. Drnec, L. Dubau, F. Maillard, Beyond strain and ligand effects: microstrain-induced enhancement of the oxygen reduction reaction kinetics on various PtNi/C nanostructures, ACS Catal. 7 (2017) 398–408.

[66] R. Chattot, O. Le Bacq, V. Beermann, S. Kühl, J. Herranz, S. Henning, L. Kühn, T. Asset, L. Guétaz, G. Renou, J. Drnec, P. Bordet, A. Pasturel, A. Eychmüller, T.J. Schmidt, P. Strasser, L. Dubau, F. Maillard, Surface distortion as a unifying concept and descriptor in oxygen reduction reaction electrocatalysis, Nat. Mater. 17 (2018) 827–833.

[67] L. Dubau, J. Nelayah, S. Moldovan, O. Ersen, P. Bordet, J. Drnec, T. Asset, R. Chattot, F. Maillard, Defects do catalysis: CO monolayer oxidation and oxygen reduction reaction on hollow PtNi/C nanoparticles, ACS Catal. 6 (2016) 4673–4684.

[68] X. Chang, A. Malkani, X. Yang, B. Xu, Mechanistic insights into electroreductive C-C coupling between CO and acetaldehyde into multicarbon products, J. Am. Chem. Soc. 142 (2020) 2975–2983.

[69] M. Fleischmann, P.J. Hendra, A.J. McQuillan, Raman spectra from electrode surfaces, J. Chem. Soc., Chem. Commun. (1973) 80–81.

[70] Y. Deng, A.D. Handoko, Y. Du, S. Xi, B.S. Yeo, In Situ Raman spectroscopy of copper and copper oxide surfaces during electrochemical oxygen evolution reaction: identification of CuIII oxides as catalytically active species, ACS Catal. 6 (2016) 2473–2481.

[71] S. Jiang, K. Klingan, C. Pasquini, H. Dau, New aspects of operando Raman spectroscopy applied to electrochemical CO_2 reduction on Cu foams, J. Chem. Phys 150 (2018) 041718.

[72] W. Akemann, A. Otto, The effect of atomic scale surface disorder on bonding and activation of adsorbates: vibrational properties of CO and CO_2 on copper, Surf. Sci. 287–288 (1993) 104–109.

[73] I. Oda, H. Ogasawara, M. Ito, Carbon monoxide adsorption on copper and silver electrodes during carbon dioxide electroreduction studied by infrared reflection absorption spectroscopy and surface-enhanced Raman spectroscopy, Langmuir 12 (1996) 1094–1097.

[74] W. Akemann, A. Otto, Vibrational modes of CO adsorbed on disordered copper films, J. Raman Spectrosc. 22 (1991) 797–803.

7.12. Selective n-propanol formation from CO_2 over degradation-resistant activated PdCu alloy foam electrocatalyst

Authors: Motiar Rahaman, Kiran Kiran, **Ivan Zelocualtecatl Montiel**, Vitali Grozovski, Abhijit Dutta and Peter Broekmann

Green Chem. 2020, **22**, 6497-6509, DOI: 10.1039/D0GC01636E

Highlights: A highly porous and selective PdCu alloy catalyst for propanol formation through CO_2 electroreduction was synthesized using the dynamic hydrogen bubble template metal deposition approach followed by thermal activation in the air at 200 ˚C for 12h, which transforms the as prepared PdCu foam into a totally oxidized PdCu alloy. However, the ultimate catalyst activation was achieved by reducing the oxide species into the metallic state at –0.65 V *vs.* RHE for 45 min. The electrochemical performance of the PdCu catalyst after thermal and electrochemical pre-treatment shows high production of n-Propanol at relatively low overpotentials with a maximum $FE_{n\text{-propanol}}$ = 13.7% ($PCD_{n\text{-propanol}}$ = –1.15 mA cm^{-2}) over ethanol $FE_{ethanol}$ = 7.1% ($PCD_{ethanol}$ = –0.60 mA cm^{-2}) at –0.65 V *vs.* RHE. One of the main factors for the high selectivity to n-propanol is the complete suppression of methane. The stability of the PdCu catalyst was tested by a long term experiment for 102 h, at –0.65 V *vs.* RHE (combined with a continuous and discontinuous mode). IL-SEM was carried out before and after activation treatment and electrolysis experiments to monitor the morphological changes in the catalyst, showing phase segregation into nm-range Pd-rich and Cu-rich domains that helps to increase the n-Propanol selectivity. While the use of ICP-MS analysis of the electrolyte solution demonstrates, preferential Cu dissolution flowed by slow Cu redeposition on the catalyst surface. Because the CO_2RR was superimposed on the oxide reduction of the PdCu catalyst, *operando* Raman spectroscopy was employed to study the reduction of oxides species and propose the pathway for the highly n-propanol formation.

Contributions: In this project, I was involved in conducting ICP-MS studies and *operando* Raman experiments, and I participated in the manuscript revision process.

Green Chemistry

PAPER

View Article Online
View Journal | View Issue

Check for updates

Cite this: *Green Chem.*, 2020, **22**, 6497

Selective *n*-propanol formation from CO_2 over degradation-resistant activated PdCu alloy foam electrocatalysts†

Motiar Rahaman, *‡§ Kiran Kiran,‡ Ivan Zelocualtecatl Montiel, Vitali Grozovski, Abhijit Dutta * and Peter Broekmann *

Received 13th May 2020,
Accepted 7th September 2020

DOI: 10.1039/d0gc01636e

rsc.li/greenchem

We present a novel, foam-type, high surface area electrocatalyst for the CO_2 reduction reaction (CO_2RR) that is not only highly selective toward *n*-propanol (PrOH) formation (FE_{PrOH} = 13.7%, j_{PrOH} = −1.15 mA cm^{-2}) at relatively low overpotentials (−0.65 V *vs.* RHE) but also demonstrates an excellent long-term stability during CO_2 electrolysis experiments of 102 h in duration. A dynamic hydrogen bubble template approach is applied to electrodeposit a binary PdCu alloy foam yielding a nominal bulk composition of 9 at% Pd and 91 at% Cu (denoted as Pd_9Cu_{91}). The material is further modified by means of thermal annealing (12 h at 200 °C in air), which completely transforms the as-prepared metallic Pd_9Cu_{91} alloy foam into its oxidic state. The ultimate catalyst activation is achieved by subsequent reduction (at −0.65 V *vs.* RHE for 45 min) of the oxidic precursors (composite of Cu_2O, CuO, and $CuPdO_3$) into metallic state, as indicated by *operando* Raman spectroscopy. Identical location scanning electron microscopy (IL-SEM) analysis, carried out prior to and after the activation treatments, demonstrates significant morphological alterations of the Pd_9Cu_{91} foam on the nm length scale, which go along with a phase segregation into nm-range Pd-rich and Cu-rich domains that helps to increase the PrOH selectivity. Time-dependent ICP-MS analyses of the electrolyte solution, carried out during the catalyst activation, demonstrate preferential (rapid) Cu dissolution followed by (slow) Cu redeposition on the catalyst surface. These processes are found to be superimposed on the actual oxide reduction. A two-fold selectivity of PrOH was observed over ethanol (EtOH). The excellent long-term stability of the activated Pd_9Cu_{91} foam catalyst is rationalized by the full suppression of the C1 hydrocarbon (methane) pathway. The improved product selectivity towards the highly valuable C3 alcohol is rationalized by an efficient and concerted spillover of chemisorbed carbon monoxide (*CO) and atomic hydrogen (*H) species from the Pd-rich domains to the activated Cu-rich domains of the oxide-derived Pd_9Cu_{91} foam catalyst where the C–C coupling and subsequent hydrogenation processes take place to form the targeted oxygenate product.

Introduction

The electrochemical conversion of CO_2 into high energy density fuels or valuable chemicals is considered a promising approach for mitigating anthropogenic contributions to the steadily increasing CO_2 content (currently ∼410 ppm) of our atmosphere.[1–4] This so-called *power-to-X* concept becomes particularly appealing when the surplus of renewable electric energy from hydro, solar, or wind sources is used to power the highly endergonic CO_2 conversion process. Catalysts are needed for this electrochemical transformation not only to accelerate the kinetically hindered CO_2 reduction reaction (CO_2RR) but also to guide the process towards the desired reaction products.[5,6] Recent studies have demonstrated that, not only the chemical nature of the catalyst but also its morphology at various length scales which dictates the resulting CO_2RR product distribution.[7,8]

Among the various catalysts studied thus far, Cu stands out as the only mono-metallic material that can produce multiple hydrocarbons and oxygenates of various chain lengths from CO_2.[9–14] Higher alcohols are particularly desirable due to their high volumetric energy density (*e.g.* *n*-propanol: 27.0 MJ L^{-1}). They can be considered synthetic energy carriers of high

---

Department of Chemistry and Biochemistry, University of Bern, Freiestrasse 3, 3012 Bern, Switzerland. E-mail: mr820@cam.ac.uk, abhijit.dutta@dcb.unibe.ch, peter.broekmann@dcb.unibe.ch

† Electronic supplementary information (ESI) available. See DOI: 10.1039/d0gc01636e

‡ These authors contributed equally to this work.

§ Current address: Department of Chemistry, University of Cambridge, Lensfield Road, CB2 1EW Cambridge, UK.

added-value that are essential for the so-called energy transition.[9,11,15–21]

In early related studies, Hori *et al.* observed the formation of *n*-propanol on Cu foil.[22] However, the reported faradaic efficiency was rather low (FE_{PrOH} = 3.0% at −1.44 V *vs.* NHE). In principle, an improvement of the selectivity towards alcohols can be achieved by a partial or complete oxidation of the Cu catalyst prior to the CO_2 electrolysis. The formed cuprous and cupric oxides are considered to be precursors of the active catalyst material and, under the harsh experimental conditions commonly applied for the CO_2RR, typically undergo rapid electroreduction thereby accomplishing catalyst activation and the formation of the low-coordinated sites that are required for C–C coupling and subsequent alcohol formation.[23–25]

As an example, Rahaman *et al.* reported improved efficiencies of ethanol (EtOH) and *n*-propanol (PrOH) formation of FE_{EtOH} = 10.4% and FE_{PrOH} = 13.1%, respectively, at −0.90 V *vs.* RHE on oxide-derived dendritic Cu catalysts.[26] A similar mixture of EtOH and PrOH was obtained by Ren *et al.* with Cu nanocrystal agglomerates (FE_{PrOH} = 10.6% and FE_{EtOH} = 7.7% at −0.85 V *vs.* RHE).[27] Activation by plasma treatment also yields a slightly higher selectivity towards the C2 alcohol (FE_{EtOH} = 17% and FE_{PrOH} = 8.1% at −0.95 V *vs.* RHE).[28] To date, the highest reported PrOH efficiency still do not exceed 15% (FE_{EtOH} = 13% and FE_{PrOH} = 15% at −0.95 V *vs.* RHE).[29] So there is much room to improve the PrOH selectivity.

One crucial requirement for the production of higher alcohols is the sufficient abundance of chemisorbed carbon monoxide (*CO, the asterisk refers to an adsorbed state) which forms as a key intermediate in the course of the CO_2RR.[30] The further stabilization of *CO on the catalytically active surface is particularly important as the CO dimerization (C–C coupling) process ideally takes place in an early stage of alcohol formation.

Attempting to further increase the product selectivity towards C2 or C3 oxygenates therefore, often relies on the addition of a second catalyst component to the activated Cu (C–C coupler, alcohol producer), which selectively produces CO (CO producer).[31] Obvious candidates for the CO forming catalysts, according to the CO_2RR catalyst classification scheme introduced by Hori *et al.*, are Zn, Ag, Au, and Pd.[22] Pd nanoparticles have recently been employed to produce CO at medium overpotentials with a high selectivity reaching FE_{CO} values of ~90%.[32] However, one particular drawback of Pd as the CO-producing component is related to its comparably high affinity for CO chemisorption, which can lead to irreversible catalyst poisoning in the course of extended CO_2 electrolyses as demonstrated in several studies.[33,34] One promising approach for tackling the shortcoming of this CO_2RR catalyst is based on the co-alloying of Pd, *e.g.*, with Cu. This approach is known to reduce the binding strength of *CO to the catalyst sites[35,36] with the result that CO can be released more easily from the catalyst during extended electrolyses thus preventing any irreversible poisoning of the catalyst by strong CO chemisorption.[37] At the same time, co-alloying Pd with Cu introduces the required C–C coupling component and, if further activated, the actual ‘alcohol forming phases’ to the catalytic system. A further beneficial role of the Pd, embedded into the Cu matrix of the binary alloy, is associated to the required hydrogenation reaction of the C–C coupled reaction intermediates. This is due to the moderate hydrogen adsorption energy of the *H reactant on the Pd in combination with its facile transfer to the adjacent Cu sites where the actual hydrogenation reaction of the C–C coupled intermediated is supposed to take place.[38]

In this study, we apply the so-called dynamic hydrogen bubble template approach[7,39,40] to form binary high surface area alloy catalysts containing Cu and Pd as the major and minor components, respectively. This approach was originally developed by Shin *et al.* for mono-metallic Cu[40] and Sn[39] systems, based on the superposition of the metal electroplating (primary process) by a massive hydrogen evolution reaction (HER, secondary process) at high cathodic current densities of up to −3 A cm^{-2}. H_2 bubbles, which evolve at the cathode surface due to the rigorous HER, act as a temporary geometric template for the metal foaming process.[7,8,39–42]

In particular when C–C coupled alcohols are targeted as the CO_2RR product, it is mandatory to further activate the Cu component prior to the actual CO_2RR, *e.g.* by oxidation.[26] For this purpose we applied a thermal annealing treatment (200 °C for 12 h in air) to the as-deposited homogeneous alloy foam, which resulted in significant morphological and compositional changes of the material, a process that can be probed by so-called identical location scanning electron microscopy (IL-SEM) imaging. The catalyst pretreatment was completed by applying −0.65 V *vs.* RHE cathodic potentials that transforms the oxides into a phase-separated metallic catalyst (oxide-derived) which is essential for multicarbon alcohol formation. A maximum efficiency of 13.7 ± 0.8% PrOH (j_{PrOH} = −1.15 mA cm^{-2}) was obtained by this approach at relatively low overpotentials of −0.65 V *vs.* RHE, with only 7.1 ± 0.3% of EtOH (j_{EtOH} = −0.60 mA cm^{-2}) as a minor oxygenate product, providing a remarkable C3 alcohol selectivity that was two times higher than the respective C2 alcohol yield.

Extended catalyst stressing experiments of >100 h in duration demonstrate a superior degradation stability of the binary CuPd alloy foam catalyst with average total faradaic efficiencies of alcohol formation never decreasing to values less than 18%. More importantly, the high PrOH selectivity is also maintained during the extended electrolyses experiments.

Experimental

Materials and chemicals

The Cu foil (99.99% pure) was purchased from Goodfellow (initial dimension 10 cm × 10 cm) and cut into pieces measuring 8 mm × 25 mm. The Cu foils served as substrates for catalyst preparation by means of hydrogen bubble assisted alloy electrodeposition. Na_2PdCl_4 (Sigma Aldrich, 99.99%) and

$CuSO_4{\cdot}5H_2O$ (Sigma Aldrich, 99.99%) served as metal precursors for the plating step. $KHCO_3$ (ACS grade) and K_2SO_4 (ACS grade) were purchased from Sigma Aldrich. ACS grade H_2SO_4 (Sigma) was used to prepare the plating bath. All chemicals were used without further purification. Milli-Q water (Millipore, 18.2 MΩ cm, 4 ppb of total organic carbon content) was used for the preparation of all solutions.

Catalyst preparation

Prior to alloy electrodeposition the Cu foil substrate was electropolished in 50% phosphoric acid (ACS grade, Sigma Aldrich) to remove the native oxide layer from its surface. For this pre-treatment step, a two electrode arrangement that consisted of a graphite foil and the Cu foil serving as cathode and anode, respectively, was used. A potential difference of 2.0 V was applied for 2 min. After electropolishing, the Cu foil was thoroughly rinsed in Milli-Q water, subsequently sonicated in ethanol for 15 min, and finally dried in air before use.

To obtain a well-defined geometric surface area of 1 cm^2 the Cu foil substrate was masked with an insulating PTFE tape. Unless otherwise stated, alloy deposition was carried out using a plating bath containing Na_2PdCl_4 and $CuSO_4{\cdot}5H_2O$ metal ion sources (1 : 9 ratio, 25 mM) in 1.5 M H_2SO_4 electrolyte (pH ∼ 0.5). A three-electrode arrangement, consisting of a Pt foil (4 cm × 3 cm, counter electrode), an $Ag/AgCl_{3M}$ reference electrode (Metrohm), and the Cu foil substrate serving as the working electrode, was used for electrodeposition. A constant current density of -3 A cm^{-2} was applied for 40 s. After deposition, the formed metal foams were gently rinsed with Milli-Q water to remove excess electrolyte.

For the majority of the CO_2 electrolysis experiments the PdCu foam catalyst were further activated by 12 h of thermal annealing in air at a temperature of 200 °C using a tube furnace (GERO, GmbH, Germany). Catalyst activation was completed by an electrochemical reduction of the formed oxidic precursor in CO_2-saturated 0.5 M $KHCO_3$ solution for 45 min at an applied potential of -0.65 V *vs.* RHE. The individual steps of the catalyst preparation and activation procedure are schematically shown in Fig. 1.

The electrochemically active surface area (ECSA) of the as-deposited as well as the activated PdCu foam catalysts was determined based on voltammetric measurements using dimethyl viologen as a reversible redox probe. This procedure has been described in detail elsewhere.[7]

CO_2 electrolysis experiments

All electrochemical measurements were carried out using a potentiostat/galvanostat (Metrohm Autolab 128N, The Netherlands). Prior to the electrolysis experiments, the cell resistance was measured by means of impedance spectroscopy. All potentials reported herein are *iR*-corrected. The CO_2RR was carried out at room temperature using a custom-made H-type glass cell where the two compartments were separated by a cation exchange membrane (Nafion 117, Electrochem, USA). Aqueous 0.5 M $KHCO_3$ solution was used as electrolyte. A leak-less $Ag/AgCl_{3M}$ (EDAQ) served as the reference electrode, a Pt foil (15 mm × 5 mm, 99.95%, Alfa Aesar) was used as the counter (anode), and the CuPd foam catalyst served as the working electrode (cathode). Prior to commencing CO_2 electrolysis, both the anolyte and the catholyte were purged with CO_2 (99.9999%, Carbagas, Switzerland) at a flow rate of ∼30 mL min^{-1} at least for 30 min. During the electrolysis, the catholyte was constantly purged with CO_2 at a flow rate of ∼13 mL min^{-1}.

For the sake of comparability, all potentials, recorded *versus* the $Ag/AgCl_{3M}$ electrode, were converted to the reversible hydrogen electrode (RHE) scale using the following equation:

$$E_{\mathrm{RHE}}\ (\mathrm{V}) = E_{\mathrm{Ag/AgCl_{3M}}}\ (\mathrm{V}) + 0.210\ \mathrm{V} + (0.0591\ \mathrm{V} \times \mathrm{pH})$$

The quantification of the gaseous and non-gaseous reaction products by means of gas-chromatography and ion-exchange chromatography is described elsewhere.[7,26]

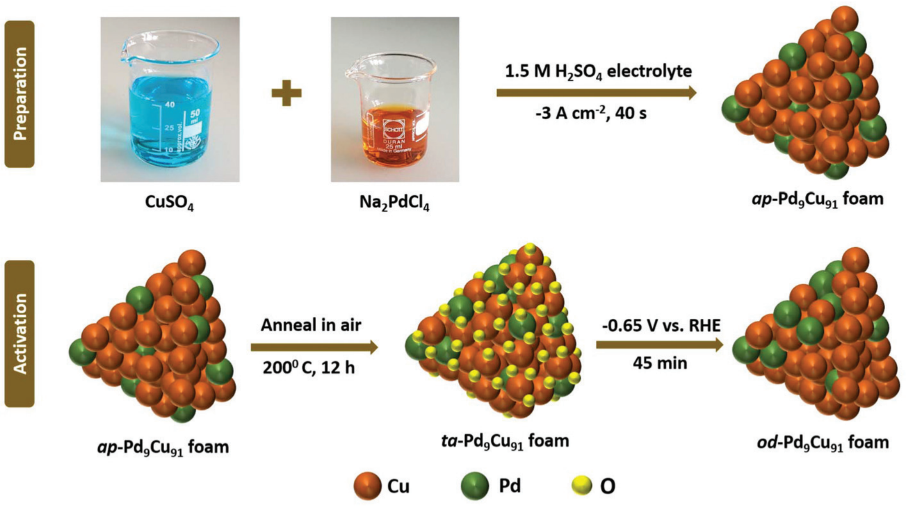

Fig. 1 Scheme illustrating individual preparation and activation steps of the Pd_9Cu_{91} catalyst.

According to the post-electrolysis inductively coupled plasma optical emission spectroscopy (ICP-OES) and X-ray photoelectron spectroscopy (XPS) measurements, Pt was detected neither in the separated catholyte compartment nor on the catalyst surface. Any interference of Pt dissolution at the anode during electrolysis can thus be excluded.

X-ray diffraction (XRD) analysis

XRD analyses of the as-prepared (*ap*), thermally annealed (*ta*), and oxide-derived (*od*) PdCu catalysts were carried out by means of powder XRD (Bruker D8) using CuKα radiation (λ = 0.1540 nm, 40 mA) generated at 40 keV. Scans were recorded at 1° min^{-1} for 2θ values ranging from 20 to 90°. The obtained XRD patterns were analyzed and compared with JCPD (Joint Committee on Powder Diffraction) standards for different pure metals, bimetallic alloy materials (Cu, Pd, and CuPd alloy) and corresponding oxide phases (CuO, Cu_2O, $CuPdO_3$). An activated graphite foil was used as the substrate for all XRD analyses to avoid undesirable contributions of the substrate to the XRD pattern of the PdCu alloy sample of interest.

Scanning electron microscopy (SEM) and energy-dispersive X-ray spectroscopy (EDX)

The morphology and composition of the as-prepared and oxide-derived CuPd catalysts were studied by means of a FE Zeiss DSM 982 SEM instrument equipped with a Noran SIX NSS200 energy dispersive X-ray spectrometer.

X-ray photoelectron spectroscopy

XPS studies were performed by means of Al-Kα radiation sources which was operated at 150 W with an Omicron Multiprobe (Omicron Nano Technology) spectrometer coupled to an EA 125 (Omicron) hemi-spherical analyzer. C 1s peak was used as reference and the fitting was performed using CasaXPS software. Note that, the samples were used for the XPS analyses without any further modifications (*e.g.* metal sputtering).

High resolution transmission electron microscopy (HR-TEM) and high-angle annular dark-field scanning transmission electron microscopy (HAADF-STEM)

HR-TEM and HAADF-STEM were carried out by a Thermo Scientific Talos F200X G2 TEM (FEI, operating voltage 200 kV). For these measurements, the catalyst materials were gently removed from the Cu foil substrate, dispersed in ethanol by sonication, and subsequently drop-casted on a carbon coated Ni grid (300 mesh).

Inductively coupled plasma optical emission spectrometry (ICP-OES) and inductively coupled plasma mass spectrometry (ICP-MS)

The bulk elemental composition has been studied by ICP-OES analysis (Thermo Scientific iCAP 7400 ICP-OES DUO). The PdCu metal foams have been dissolved in 30% HNO_3 for ICP-OES analysis. The time-dependent monitoring of the electrolyte chemical composition (metal content) has been carried out using a NexION 2000 ICP-MS instrument (PerkinElmer).

Operando Raman spectroscopy

Details of the *operando* Raman spectroscopy have been described elsewhere.[43] The spectroscopic analysis was conducted by means of a LabRAM HR800 confocal microscope (Horiba Jobin Yvon). Spectral data were collected with Lab Space 3.0 software. A large working distance objective lens (50× magnification, 8 mm focal length) was applied with a numerical aperture of 0.1 in order to focus a diode-pumped solid-state laser beam (excitation wavelength 633 nm, DPSS laser, power 3 mW) on the sample and collect the incident and scattered laser light. A home-made spectro-electrochemical cell made of Kel-F was used for the spectro-electrochemical experiments. The spectro-electrochemical cell consisted of a Ag/AgCl reference (EDAQ) electrode whereas a Au-wire served as the counter electrode. A μ-Autolab III (EcoChemie) potentiostat was used for the electrochemical measurements. Raman spectra were collected in the spectral range of 100–2500 cm^{-1}. For the data acquisition during the potentiostatic experiments, the holding time was 120 s at each applied electrolysis potential.

Results and discussion

Characterization of the catalyst

The PdCu alloy foam, used herein for the CO_2RR experiments, contains a nominal composition of 9 at% Pd (minor component) and 91 at% Cu (major matrix component) and thus named as Pd_9Cu_{91}. This 'integral' bulk composition was determined on the basis of quantitative ICP-OES measurements. EDX analysis, which is more sensitive to the near-surface region of the catalyst and thus is a more spatially-confined method, yielded, however, comparable results of 7 at% Pd and 93 at% Cu (see Fig. S1, ESI†). Note, however, that the EDX analysis is only semi-quantitative and that chemical composition of the outermost surface and the near-surface 'bulk' region of the deposit might slightly deviate from that of the bulk material. In the following we denote the catalysts analyzed herein according to their stage of preparation/activation as *ap*-Pd_9Cu_{91} (as-prepared), *ta*-Pd_9Cu_{91} (thermally-annealed), and *od*-Pd_9Cu_{91} (oxide-derived). This notation assumes that thermal annealing and the subsequent electrochemical (*ec*) reduction of the oxidic precursor don't lead substantial changes in the integral 'bulk' composition of the foam material. This assumption is in agreement with ICP-OES analyses of *ap*-Pd_9Cu_{91} and *od*-Pd_9Cu_{91} samples which provide similar % of Pd and Cu as bulk compositions of the materials. The term 'oxide-derived' (*od*) refers to the state of the annealed catalyst after the electrochemical pretreatment (45 min at −0.65 V *vs.* RHE in CO_2-saturated 0.5 M $KHCO_3$ solution, pH 7.2), assuming that it represents the stable metallic state under reactive conditions during the CO_2RR experiments.

Fig. 1 depicts the individual preparation and activation steps of the bimetallic Pd_9Cu_{91} catalyst used throughout this study.

Fig. 2 shows a collection of representative identical location (IL)-SEM micrographs of the *ap*-Pd_9Cu_{91} (panels a–d), the *ta*-Pd_9Cu_{91} (panels e–h), and the *od*-Pd_9Cu_{91} sample (panels i–l), demonstrating morphological alterations of the as-prepared alloy foam that are due to thermal annealing treatment and the subsequent electrochemical reduction of the oxidic catalyst precursor. The SEM images (panel a) reveal a three-dimensional architecture of meso-pores (primary porosity) with a mean surface diameter of 23 ± 3 µm. This value corresponds well to the respective depth of the topmost meso-pores of 25 ± 2 µm, as determined by white-light interferometry analysis (Fig. S2, ESI†). As it can be seen, the porosity on the µm length scale neither changes upon thermal annealing (panel e) nor upon oxide reduction (panel i). Due to their dendritic nature, the sidewalls of the 3D foam structure reveal a secondary porosity on the nanometer length scale that is, in contrast to the meso-pores, significantly affected by the combined thermal and electrochemical catalyst pre-treatment. One prominent feature of the *ap*-Pd_9Cu_{91} is the presence of textured nanometer-sized (~50 nm) crystallites that often exhibit a cubic shape ((100) texture, *e.g.*, see Fig. 2, panel d). SEM results of as-prepared pure Cu and pure Pd foams are also shown in Fig. S3 (ESI†). The cubic-shaped crystallites (in *ap*-Pd_9Cu_{91}) completely disappear upon thermal treatment due to the partial coalescence of the fine dendritic features that compose the pore sidewalls (Fig. 2, panel h). The *ta*-Pd_9Cu_{91} foam undergoes further morphological changes in the course of the electrochemical oxide reduction at −0.65 V *vs.* RHE. Under these reductive conditions, nm-sized (10–50 nm) particles appear on the catalyst surface, further increasing the electrochemically active surface area (ECSA) upon catalyst activation (see Fig. S4, ESI†). Similar morphological alterations, as demonstrated in Fig. 2, have also been reported for the activation of dendritic Cu and can be rationalized by the significant migration of oxygen and Cu associated with oxide precursors formation (thermal annealing) and their subsequent electroreduction.[26]

The IL-SEM analysis results are further supported by the complementary *ex situ* XRD analysis of the metallic and oxidic foams, as presented in Fig. 3. For comparison purposes, XRD data of pure Cu and Pd metallic foams are included in Fig. 3a. A comparison of the three diffractograms confirms the co-alloying of Pd and Cu in the *ap*-Pd_9Cu_{91} sample. The (111), (200), and (220) diffraction peaks of the face centered cubic (fcc) *ap*-Pd_9Cu_{91} sample appear at 2θ values of 42.73°, 49.74°, and 73.18°, which reside between the corresponding peaks reported for Cu (43.3°, 50.4°, and 74.1°; JCPDS: 85-1326) and Pd (40.2°, 46.8°, and 68.3°; JCPDS: 87-0638). The intense diffraction feature at $2\theta \sim 56°$ corresponds to the C(004) diffraction of the graphite foil support on which the metal foams were deposited for XRD inspection.

Fig. 3b demonstrates alterations in the crystal structure of the *ap*-Pd_9Cu_{91} that are associated with the thermal treatment and the subsequent oxide reduction. Clearly, all diffraction features of the fcc *ap*-Pd_9Cu_{91} sample disappear after thermal annealing (see diffractogram of *ta*-Pd_9Cu_{91}), indicating the transformation of the metallic alloy into an oxidic form, which obviously affects not only the catalyst surface but the entire 'bulk' of the alloy foam. Note that this oxidation process causes a partial phase segregation into domains of copper oxide(s) and a mixed PdCu oxide phase. The Cu_2O (200) and CuO (111) diffraction peaks appear at $2\theta = 40.9°$ (JCPDS: 74-1230) and at $2\theta = 38.76°$ (JCPDS: 80-1268), respectively. The

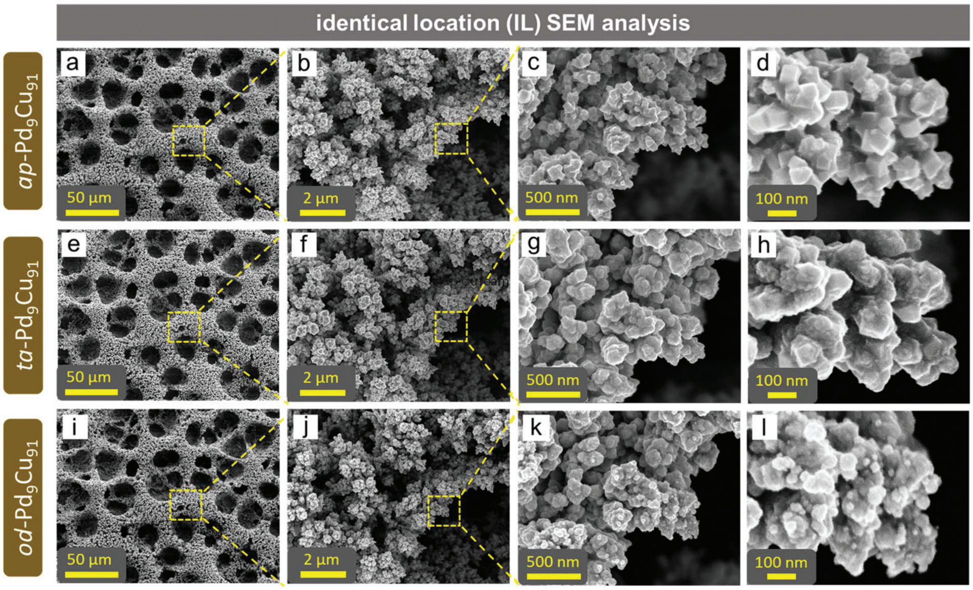

Fig. 2 Identical location (IL) SEM analysis of the co-alloyed foam catalyst depending on the processing stage; (a)–(d) as-prepared (*ap*) alloy foam; (e)–(h) thermally annealed (*ta*) alloy foam (200° C, 12 h, in air); (i)–(l) oxide-derived (*od*) alloy foam (after *ec* pretreatment at −0.65 V *vs.* RHE for 45 min).

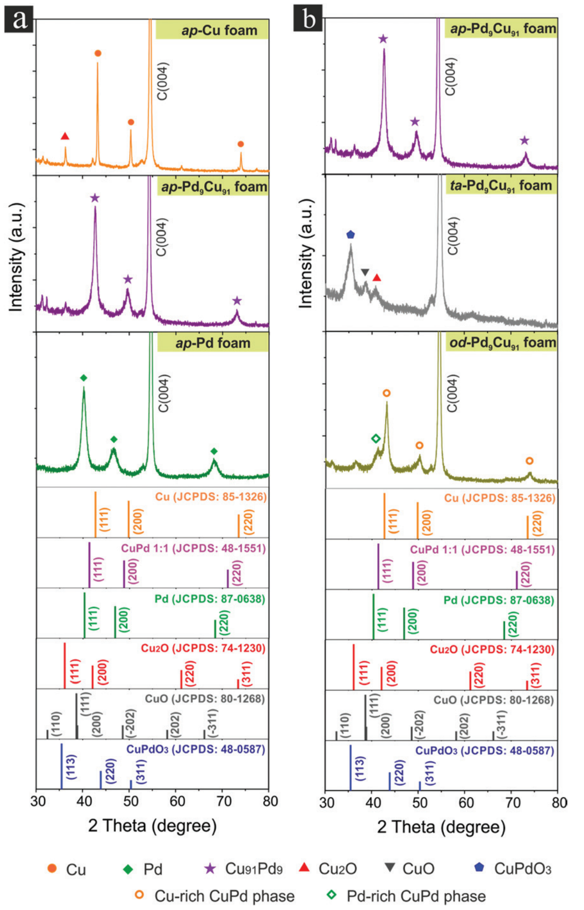

Fig. 3 (a) X-ray diffraction pattern of the as-prepared (*ap*) pure Cu, pure Pd, and the Pd_9Cu_{91} foam samples. (b) X-ray diffraction pattern of the Pd_9Cu_{91} sample depending on the processing stage (as-prepared (*ap*), thermally annealed (*ta*), and oxide-derived (*od*)). Standard diffraction peaks and their corresponding JCPDS files are shown.

mixed $CuPdO_3$ oxide phase was identified *via* its (113) diffraction peak at $2\theta = 35.32°$ (JCPDS: 48-0587).

Under reductive conditions, applied during the electrochemical part of the catalyst pre-treatment, these oxide phases are thermodynamically unstable and undergo rapid compositional and structural transitions back into their metallic state. Thus, there is no indication for the presence of any oxide phase with long-range transitional order after the electrochemical treatment (see diffractogram of the *od*-Pd_9Cu_{91} sample in Fig. 3b). However, the partial phase segregation, initially started after thermal annealing treatment, is retained after the subsequent oxide reduction. As a consequence, a Cu-rich phase is formed which exhibits a Cu-like diffraction pattern with (111) plane at $2\theta = 43.18°$ (JCPDS for Cu: 85-1326). Besides this major Cu-enriched phase, a second Pd-rich alloy phase develops, as deduced from the shift of the main (111) diffraction peak from 42.73° (*ap*-Pd_9Cu_{91}) to 41.34° (*od*-Pd_9Cu_{91}). An expansion of the crystal lattice towards the fcc Pd thus confirms enrichment by Pd (JCPDS for Pd: 87-0638) in the second phase (see Fig. 3).

The (metal → oxide → metal) transitions, observed in the XRD patterns, are also in full agreement with a complementary XPS analysis presented in Fig. S5 (ESI†), which shows the spin–orbit split Cu 2p (panel a) and Pd 3d (panel b) photoemissions of the Pd_9Cu_{91} samples in their respective processing states. The appearance of characteristic shake-up satellites in the Cu 2p photoemission spectrum after thermal treatment indicates the presence of cupric CuO in the *ta*-Pd_9Cu_{91} sample. It should be noted, however, that XPS cannot discriminate between metallic Cu and cuprous oxide (Cu_2O) as both phases exhibit the same binding energy of BE(Cu $2p_{3/2}$) = ~933 eV.[44] The Pd 3d peak broadened after the annealing treatment and a Pd(II) component (PdO, BE($3d_{5/2}$) = ~336.7 eV) was evident after peak deconvolution (Fig. S5, ESI†). After completion of the electrochemical pre-treatment, both the Cu 2p and Pd 3d emissions in the *od*-Pd_9Cu_{91} exhibit the same features as the metallic *ap*-Pd_9Cu_{91} sample, thus indicating the complete conversion of the intermediately formed oxide into a metallic catalyst under the applied reductive conditions (45 min at −0.65 V *vs.* RHE). Survey XPS analysis further proves that there is no contamination of other metals on the catalyst surface (Fig. S6, ESI†).

Operando Raman spectroscopy (Fig. 4) further confirms the instability of the oxides, formed during thermal annealing of the alloy foam, under those electrochemical conditions applied for the catalyst activation (−0.65 V *vs.* RHE) and PrOH production (see below discussion of Fig. 7 and 8). Note the Raman spectroscopic experiment probes to some extent the bulk but in particular the surface conditions of the catalyst material.[45] Fig. 4a shows the potential-dependent evolution of *operando* Raman spectra for *od*-Pd_9Cu_{91} in CO_2 saturated 0.5 M $KHCO_3$ electrolyte where the potential is stepped from the open circuit potential (OCP) to those potentials relevant for the oxygenate production. Raman features at 518 cm^{-1} and 624 cm^{-1} are typically assigned to the presence of cuprous oxides.[45–47] It becomes obvious that the oxides have already disappeared at 0 V *vs.* RHE prior to the actual onset of the CO_2RR which in full agreement with previous results on pure Cu foam catalysts.[31,45] Important to note is that the chemisorption of reactants, intermediate and products of the CO_2RR starts only after the disappearance of the oxidic species from the catalyst surface at 0 V *vs.* RHE (Fig. 4a). The Raman features at 283 cm^{-1} and 353 cm^{-1} (Fig. 4a, inset) can be assigned to the restricted rotational and vibrational modes of chemisorbed CO (*CO) on the binary PdCu catalyst which forms as key intermediate for the oxygenate products formation on Cu-based catalysts.[45]

Fig. 4b directly compares to the electrochemical part of the catalyst pre-treatment protocol where the potential is stepped from the OCP directly to −0.65 V *vs.* RHE using a *ta*-Pd_9Cu_{91} sample. Within a few minutes (time needed to record the Raman spectrum) the oxide features have completely disappeared under the applied cathodic potential.

As suggested by the XRD data (Fig. 3), the consecutive (metal → oxide → metal) transitions leads to a phase segregation into Cu-rich and Pd-enriched domains. This hypothesis

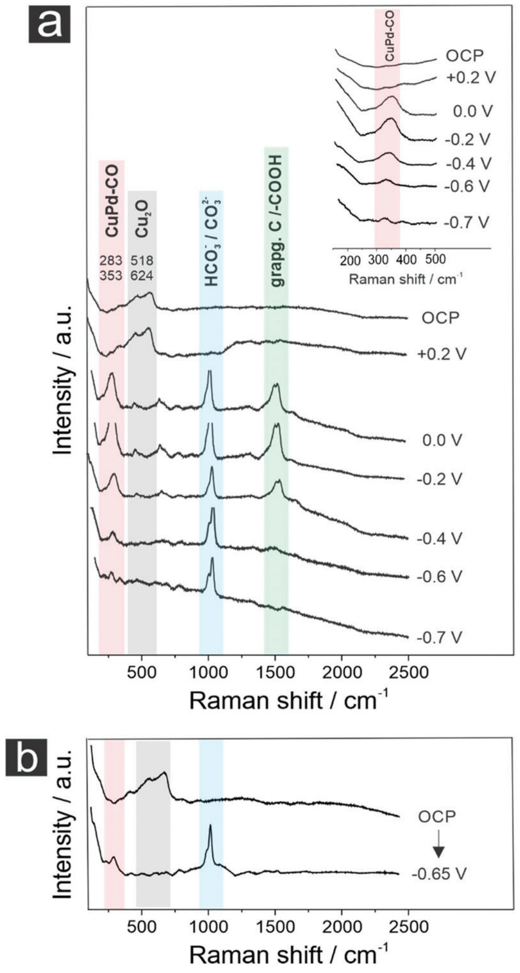

Fig. 4 (a) Potential-dependent *operando* Raman spectra of the *od*-Pd_9Cu_{91} foam sample in the CO_2-saturated 0.5 M $KHCO_3$ electrolyte starting at the OCP, inset is showing zoomed PdCu–CO adsorption features; (b) *operando* Raman spectra corresponding to the catalyst activation procedure by stepping the potential from the OCP to −0.65 V *vs.* RHE using a *ta*-Pd_9Cu_{91}.

is further experimentally corroborated by combined TEM, HR-TEM, HAADF, and STEM-EDX analyses of the *ap*-Pd_9Cu_{91} (a–d) and the *od*-Pd_9Cu_{91} (e–h) sample, presented in Fig. 5. HR-TEM analysis identifies almost pure Cu domains in the dendrites of the foam after electrochemical oxide reduction (Fig. 5, panel f). Local changes in the chemical composition (Pd/Cu ratio) as a consequence of the oxidation/reduction treatment are further corroborated by the spatially-resolved STEM-EDX maps shown in panels d and h of Fig. 5. Three spots, indicated by the yellow frames (panel d), were analyzed in more detail by means of STEM-EDX. The EDX spot analysis reveals a chemical composition of 9 at% Pd and 91 at% Cu (scattering of ± 0.5%) which is in excellent agreement with the bulk composition of the *ap*-Pd_9Cu_{91} sample determined on the basis of ICP-OES analysis. Visual inspection of the STEM-EDX mapping (panel d) confirms the homogeneous distribution of the Pd (minor component) in the Cu matrix prior to the catalyst activation treatment.

In total 10 different spots were analyzed by the STEM-EDX for their chemical composition on the *od*-Pd_9Cu_{91} sample (Fig. 5, panel h). Two different kinds of surface domains can be distinguished on the catalyst surface as indicated by the black and green frames, respectively. Those regions, highlighted by the black frames, indicate Cu-rich domains with a mean chemical composition of ∼2 at% Pd and 98 at% Cu (± 1% scattering) which can be found predominantly at the center of the dendritic features. Regions indicated by the green frames represent a PdCu alloy which is substantially enriched by Pd. The respective EDX analysis reveals a mean composition of ∼22 at% Pd and 78 at% Cu (± 5% scattering). These Pd-enriched domains are preferentially observed at the outermost periphery of the dendritic features of the alloy foam. To demonstrate the reproducibility of the proposed preparation and activation procedure respective repetition experiments are presented in Fig. S7 (ESI†) demonstrating a similar phase segregation phenomenon as shown in Fig. 5.

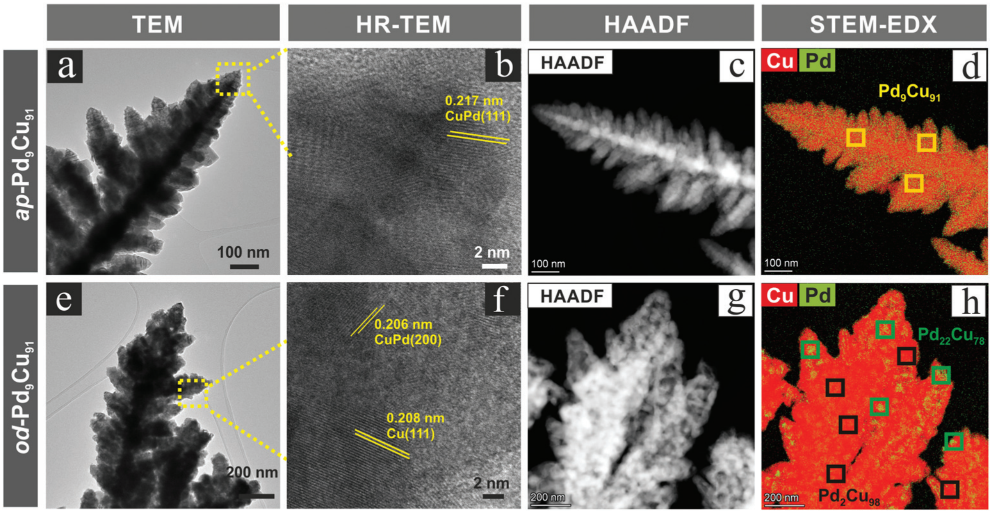

Fig. 5 (a)–(d) TEM, HR-TEM, HAADF and elemental STEM-EDX analysis of the *ap*-Pd_9Cu_{91} sample; (e)–(h) TEM, HR-TEM, HAADF and STEM-EDX analysis of the *od*-Pd_9Cu_{91} sample (after annealing (12 h at 200 °C in air) and *ec* pre-treatment (45 min at −0.65 V *vs.* RHE)).

Not only the initial thermal annealing contributes to the observed phase segregation (see Fig. 3) of the *ap*-Pd_9Cu_{91} catalyst but also its further activation under potential control. This can be concluded from complementary time-dependent ICP-MS analyses of the electrolyte solution during the oxide reduction reaction at −0.65 V *vs.* RHE. Form the work by Mayrhofer *et al.*[48,49] it is known that a release of metal ions from an oxidized electrode surface into the bulk of the electrolyte preferentially takes place upon oxide reduction. The same phenomenon can be observed in the present case for the reductive activation of the *ta*-Pd_9Cu_{91} foam catalyst. Fig. 6 depicts the time-dependent change of the Cu and Pd content in the CO_2-saturated electrolyte during the electrolysis at −0.65 V *vs.* RHE. Also for the experiment shown in Fig. 6, the potential was stepped right after the sample immersion into electrolyte from the OCP to −0.65 V *vs.* RHE. It has, however, to be noted that already the contact of the *ta*-Pd_9Cu_{91} sample to the electrolyte at OCP leads to a certain release of Cu components into the solution phase ($c_{Cu} = 0.3$ mg L^{-1} prior to the potential step to −0.65 V *vs.* RHE). This dissolution process is accelerated during the first minutes (<30 min) of the oxide-reduction which is superimposed on the electrolysis reaction (HER, CO_2RR). The Cu content in the solution reaches a maximum of 0.54 mg L^{-1} at $t = 5$ min before it slowly drops down as a function of time. This experiment clearly demonstrates that the 45 min lasting catalyst pre-treatment at −0.65 V *vs.* RHE involves both (i) the initial dissolution and (ii) the subsequent partial re-deposition of Cu material on the alloy surface from the electrolyte phase. The applied potential of −0.65 V *vs.* RHE is well below the respective reversible Nernst potential for Cu deposition/dissolution. Interestingly these sequential dissolution and re-deposition processes are selective with regard to the less noble Cu component of the binary alloy whereas the minor Pd component is not affected by the oxide reduction. The Pd content in the solution phase remains almost 0 ppm over the entire analysis time.

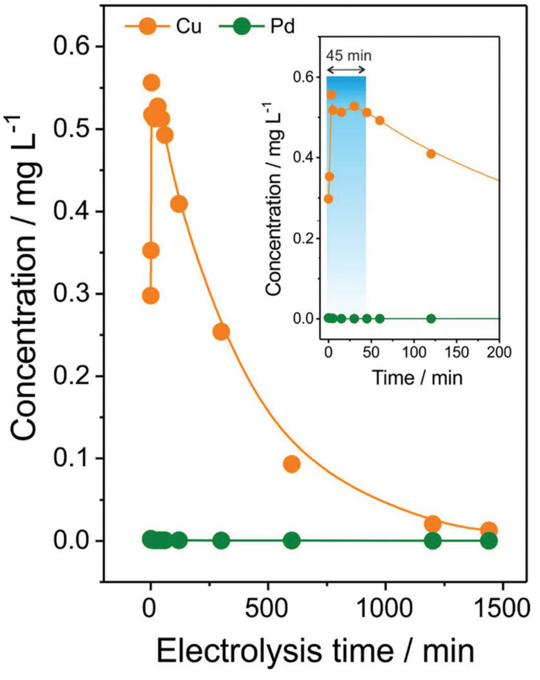

Fig. 6 Time-dependent ICP-MS analysis of the CO_2-saturated 0.5 M $KHCO_3$ solution during the CO_2RR at −0.65 V *vs.* RHE starting with the *ta*-Pd_9Cu_{91} foam as the catalyst. The inset highlights the first 200 min of the electrolysis.

Electrochemical performance

Systematic catalyst performance testing was carried out by potentiostatic electrolysis experiments in CO_2 saturated 0.5 M $KHCO_3$ (pH 7.2) using both the *ap*-Pd_9Cu_{91} and the *od*-Pd_9Cu_{91} samples. The applied electrolysis potentials ranged from −0.45 V to −0.95 V *vs.* RHE. A multi-catalyst approach has been applied for this screening where a newly-prepared catalyst was used for each screening experiment (3 h duration). Fig. 7a depicts the potential (E) dependent evolution of the product distribution (faradaic efficiency (FE)), represented as a plot of FE *vs* E for the *ap*-Pd_9Cu_{91} sample.

Formate is the main CO_2RR product at low applied overpotentials reaching a maximum faradaic efficiency of $FE_{formate} = 42.7\%$ ($j_{formate} = -1.2$ mA cm^{-2}) at −0.55 V *vs.* RHE. Both pure Pd and PdCu alloys have already been identified as excellent catalysts showing high efficiencies towards formate production at particularly low overpotentials.[33,34,37] In the present case, the formate efficiency steadily decreases with increasing overpotentials reaching a value of $FE_{formate} = 12.5\%$ at −0.95 V *vs.* RHE (see Table S1, ESI†). A similar trend is also observed for CO, starting from a maximum value of $FE_{CO} = 35.6\%$ ($j_{CO} = -0.52$ mA cm^{-2}) at lowest applied potentials of −0.45 V *vs.* RHE.[37,50] Within the entire window of applied electrolysis potentials, hydrocarbon formation remains at a relatively low level and reaches a maximum C2 hydrocarbon efficiency of $FE_{C2} = 12.3\%$ ($FE_{C_2H_4} = 8.2\%$, $FE_{C_2H_6} = 4.1\%$) at −0.75 V *vs.* RHE. The sum of the FE values detected by online (headspace) gas-chromatography (for CO, H_2, C_2H_4, and C_2H_6 detection) and post-electrolysis ion-exchange chromatography (for formate detection) reaches close to 100% irrespective of the applied electrolysis potential and thus demonstrating that all relevant major products were covered by this analysis approach. The result is obviously different when the CO_2RR is carried out over the *od*-Pd_9Cu_{91} catalyst, for which as much as 20% appears to be missing in the balance of total faradaic efficiencies (Fig. 7b). The reason for this discrepancy is due to the appearance of oxygenates as major CO_2RR products. The results are depicted in panels c and d of Fig. 7. Both C2 (EtOH) and C3 (PrOH) alcohols form as CO_2RR products, however, with a clear preference for PrOH. A maximum selectivity of $FE_{PrOH} = 13.7\%$ ($j_{PrOH} = -1.15$ mA cm^{-2}) is observed at −0.65 V *vs.* RHE (Table S2, ESI†). The onset potential of PrOH formation (−0.45 V *vs.* RHE) and the electrolysis potential of maximum PrOH efficiency (−0.65 V *vs.* RHE) are both significantly shifted towards the positive direction (≈200 mV) in comparison to the CO_2 electrolysis reactions carried out over 'pure' oxide-derived copper catalysts (Fig. S8, ESI†).[9,26,27] The presented potential-dependent product distribution clearly

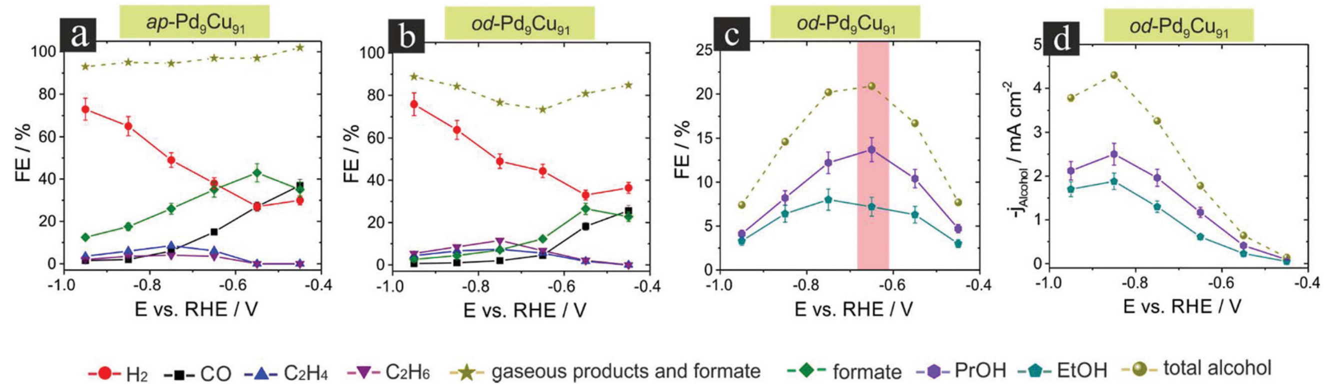

Fig. 7 (a) Product distribution of the electrolyses (3 h) carried out over the *ap*-Pd_9Cu_{91} sample. (b) Product distribution of the electrolyses (3 h) carried out over the *od*-Pd_9Cu_{91} sample. (c) Alcohol efficiencies derived from the electrolysis carried out over the *od*-Pd_9Cu_{91} sample. (d) Partial current densities of multicarbon alcohols.

demonstrates the beneficial catalytic effect of the co-alloyed Pd particularly in regard to the C3 alcohol formation (see discussion of the proposed reaction mechanism in Fig. 9 below). In contrast, the EtOH efficiency remains at a comparably low level (*e.g.*, FE_{EtOH} = 7.1% with j_{EtOH} = −0.60 mA cm^{-2}). Under these optimum electrolysis conditions, the PrOH efficiency is actually twice as high as that for EtOH. A representative GC chromatogram is provided in Fig. S9 (ESI†). In both the FE *vs.* *E* and the *j* *vs.* *E* plots, the trends of EtOH follow the ones for PrOH but at a significantly lower level. In contrast, previous studies indicated either similar FE values for PrOH and EtOH under optimized experimental conditions or a higher selectivity towards EtOH (see Table S3 for a comparison data, ESI†).[26–29] Note that the maximum faradaic efficiency (FE_{PrOH}) and the optimum rate of production (j_{PrOH}) are obtained at different electrolysis potentials. The maximum partial current density for PrOH production, j_{PrOH} = −2.50 mA cm^{-2}, was observed at −0.85 V *vs.* RHE where the FE_{PrOH} was 8.2% (Table S4, ESI†).

To demonstrate the excellent stability of the novel PdCu foam catalyst against degradation, extended CO_2 electrolysis experiments were performed at an applied potential of −0.65 V *vs.* RHE using *od*-Pd_9Cu_{91} as the catalyst. Gaseous and liquid (PrOH, EtOH) products were quantified in intervals of 1 h for a total duration of 102 h (Fig. 8). The electrolyses consisted of an initial continuous section (first 30 h) and an extra sequence of discontinuous electrolysis experiments of variable duration (six 10 h and one 12 h experiments). The potential control was switched off after each electrolysis experiment, and the catalyst was stored in pure Milli-Q water at the open circuit potential (OCP) before the next electrolysis was started. The main purpose of these continuous-discontinuous, long-term experiments was to demonstrate whether the catalyst could be successfully stored for long time periods and reused whenever necessary. This long-term experiment actually represents a two-fold stressing of the catalyst achieved by (i) the prolonged CO_2RR itself and (ii) the repetitive loss of potential control in combination with the storage of catalyst in an aqueous environment (Milli-Q water) at the OCP. Fig. 8a shows the current transient (wine curve) of the 102 h of electrolyses. The average steady state current density reached −7.5 mA cm^{-2}. Slightly higher current densities were observed at the beginning of the individual electrolysis experiments (discontinuous 10/12 h section), likely corresponding to the reduction of surface oxides formed during the resting time when the catalyst was kept at the OCP in Milli-Q water. Irrespective of the applied interruptions the resulting steady-state current density remained largely stable over the entire period of 102 h. This can be considered as a first experimental indication for an excellent structural and compositional stability of the catalyst. As already argued for pure Cu catalysts, one important factor contributing to the chemical stability of the catalyst is the successful total suppression of the C1 hydrocarbon pathway.[26]

Methane production was identified as the mechanistic origin of an irreversible poisoning of the Cu surface with chemisorbed carbon species. In the present case, the absence of methane as one of the CO_2RR products can also be considered beneficial for the observed long-term stability of the catalyst. During the first 30 h of continuous electrolysis, both the partial current density (panel a) and the corresponding faradaic efficiency (panel b) of PrOH formation increase with elapsing electrolysis time, from an initial value of j_{PrOH} = −1.11 mA cm^{-2} (FE_{PrOH} = 12.9%) to j_{PrOH} = −1.25 mA cm^{-2} (FE_{PrOH} = 13.9%). This trend is consistent with a slight decrease of the EtOH selectivity and the respective rate of production with time. However, the overall alcohol production rate does increase within the first 30 h period of the electrolysis reaction, thus proving that a continuous electrolysis does not cause any significant loss of catalytic performance, in particular with regard to the targeted C3 alcohol formation. Alterations in the catalyst's CO_2RR activity appear to be more complex when the sequence of discontinuous electrolyses is applied. The initial reduction of the surface oxide species, which likely formed during the resting period under the OCP conditions, leads to a temporary increase in the overall current density as well as partial currents of both PrOH and EtOH (panel a) right after restarting of the electrolysis which, however, steadily drops down in the further course of the reaction. However, in the first four 10 h discontinuous electrolyses, FE_{PrOH} reaches a

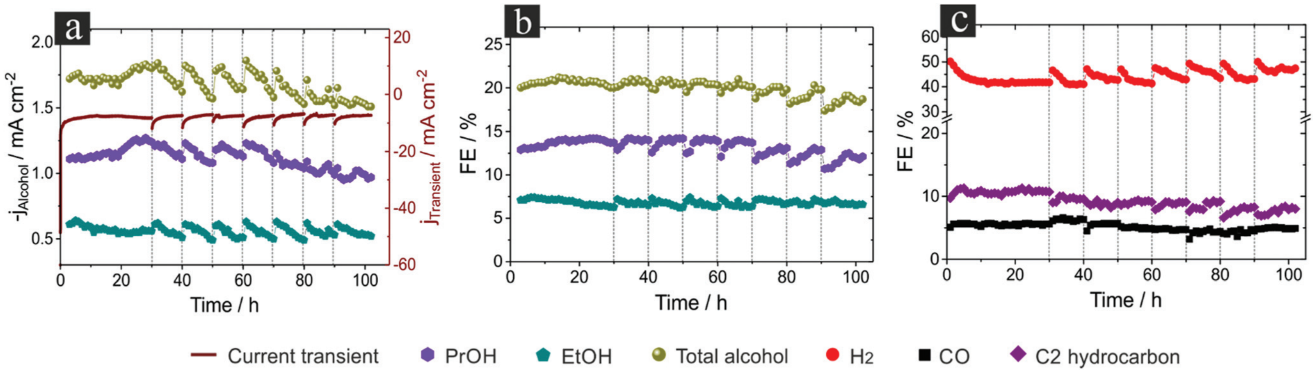

Fig. 8 (a) Current transient and time-dependent partial current densities of alcohols from the extended electrolysis carried out at −0.65 V *vs.* RHE over the *od*-Pd_9Cu_{91} sample; (b) corresponding alcohol efficiencies; (c) corresponding CO, H_2 and C2 hydrocarbon efficiencies. This set of long term experiments shows that we could store the catalyst for long time and reuse it when necessary.

steady state value of ~13.4 ± 0.9% after approximately 4 h of electrolysis time, keeping the low FE_{EtOH} of ~6.8 ± 0.3% and thus maintaining the steady PrOH selectivity until nearly 70 h (Fig. 8b). After that time, FE_{PrOH} starts to decrease slightly, which affects the PrOH selectivity. This result demonstrates that repetitive switching between the off and on state of electrolysis leads to a more significant degradation pattern than the (initial) continuous electrolysis experiment. CO and C2 hydrocarbon efficiencies decreased slightly with time whereas FE_{H_2} increased with time (see panel c of Fig. 8). Combined HAADF, STEM-EDX, and SEM analyses confirm that the compositional and structural characteristics of the *od*-Pd_9Cu_{91} catalyst are preserved even after prolonged electrolysis at −0.65 V *vs.* RHE (Fig. S10 and S11, ESI†).

Mechanistic explanation

The experimental data presented herein can be considered as a prime example of a CO_2RR catalyst material that undergoes significant structural and compositional changes during the activation stage of subsequent thermal and electrochemical pre-treatment thereby creating those electrocatalytically active sites that govern the resulting product distribution. The design of our catalyst is based on the combination of a *CO and *H forming component with a C–C coupler and alcohol-former component, which follows the similar concept of recently published bimetallic AgCu catalysts for selective ethanol production where the ethanol selectivity was rationalized by a spillover effect and the improved abundance of CO as the key intermediate of C–C coupled CO_2RR products in comparison to pristine Cu.[31,51,52] According to Dutta *et al.*, segregated domains of pure Ag take over the role of the CO formation whereas the Cu, activated by thermal annealing prior to the CO_2RR, transforms the formed CO into ethanol with a high selectivity, reaching FE_{EtOH} = 33.7% at −1.0 V *vs.* RHE.[31] Due to the limited miscibility of Ag and Cu, efficient phase segregation is easily achieved during the initial foam electrodeposition stage.[31,53] In contrast, Pd and Cu show a strong tendency towards co-alloying, thus resulting in a rather homogeneous distribution of the Pd in the Cu matrix of the as-prepared foam (Fig. 5, panels b and d). In our PdCu alloy foam, the spatial separation into *CO and *H forming and C–C coupling (alcohol forming) domains does not occur in the initial electroplating step but rather in the sequential activation steps of oxide formation and their subsequent electrochemical reduction (Fig. 1, 3 and 5). The thermally annealed Pd_9Cu_{91} foam consists of copper oxides (CuO, Cu_2O) and a mixed PdCu oxide phase ($CuPdO_3$, see Fig. 3). Subsequent electro-reduction of these oxide phases forms the phase separated Cu-rich and Pd-rich metallic domains. Kenis *et al.* also discussed the effect of phase separation in a bimetallic PdCu catalyst where ethylene and ethanol were produced from CO_2RR on phase-separated bimetallic PdCu nanoparticles.[54]

The domain of a Pd-rich PdCu alloy, formed after the electrochemical oxide reduction, can take over the role of the *CO and *H former (see Fig. 3 and 5h). Recent studies have already shown that both pure Pd and PdCu alloys are promising CO_2RR catalysts with excellent selectivity towards formate particularly at low overpotentials[33,34,37] (see also Fig. 7a) and towards CO at medium and high overpotentials.[32] However, pure Pd catalysts suffer from strong CO chemisorption, which leads to an irreversible poisoning of the active sites in the course of the CO_2RR.[33,34] One possible approach to tackling this challenge is to co-alloy the Pd with a second transition metal that exhibits CO_2RR activity in its own pure state but has a lower affinity towards CO adsorption/absorption in comparison to pure Pd.

A number of bimetallic systems have already been reported as CO_2RR catalysts including PdAu,[55] PdNi,[56] and PdCu.[57,58] Among these, copper is the most promising candidate for such a co-alloying approach because it shows a moderate binding strength towards CO, and allows for the C–C coupling reaction, towards oxygenate formation.[9,10,59] In this case, the C–C coupling role is taken over by Cu-rich PdCu domains (Fig. 3, 5h, and Fig. S7, ESI†).

Fig. 9 summarizes the proposed mechanism of C3 alcohol formation on the *od*-Pd_9Cu_{91} catalyst surface. *CO and *H form preferentially on the Pd-rich PdCu domains and they are

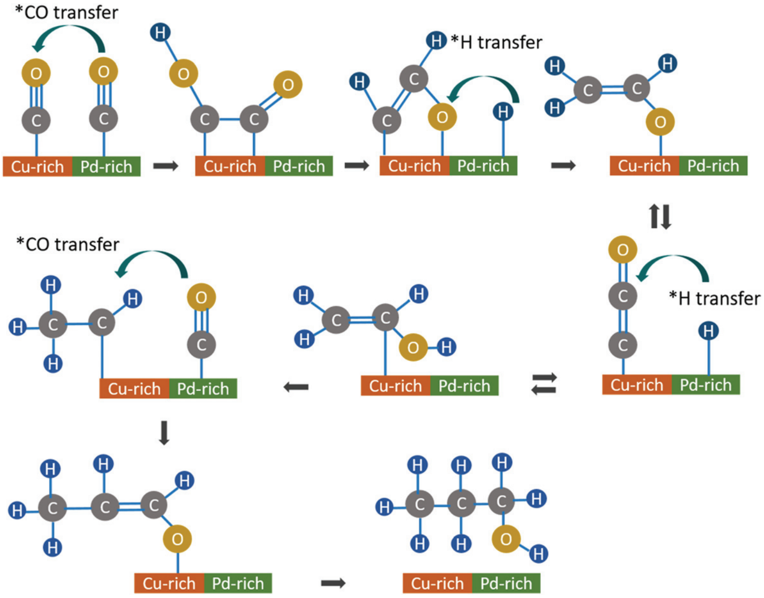

Fig. 9 Proposed reaction scheme for *n*-propanol formation from CO_2 over a phase-separated *od*-Pd_9Cu_{91} catalyst.

subsequently transported to the Cu-rich domain *via* surface diffusion or, alternatively, *via* CO and H transport through the solution phase (coupled desorption and re-adsorption processes). Besides the increased abundance of *CO and *H intermediates, it is the stabilization of the chemisorbed *CO on the catalyst surface and the efficient *H-transfer for the hydrogenation of the C–C coupled intermediates further direct the CO_2RR towards multicarbon alcohol formation.[38] This stabilization is achieved by the presence of Pd-rich domains next to the Cu-rich domains, which help to bind *CO and *H intermediates stronger than pure Cu.[10,60] *Operando* Raman spectroscopy provides a proof of *CO adsorption on the catalyst surface as it shows clear bands at 283 cm^{-1} and 353 cm^{-1} which can be assigned to the chemisorbed *CO (Fig. 4a, inset). EtOH formation most likely proceeds *via* a combined C2 hydrocarbon–oxygenate pathway, as discussed by Nie *et al.* and Kortlever *et al.*[61,62] In addition, another *CO further binds to the stabilized C2 intermediate to form the key-intermediate of PrOH, which is the adsorbed C3 aldehyde species ($*CH_3CHCHO$).[9] Additional control experiments in Ar-saturated CO_2-free 0.5 M K_2SO_4 electrolyte using CH_3CH_2CHO as the reactant demonstrated that PrOH can be obtained from the respective C3 aldehyde (see Fig. S12, ESI†) under similar electrochemical conditions.

Conclusions

A novel PdCu alloy electrocatalyst was prepared by means of a hydrogen bubble-assisted foam deposition process. The Pd (minor component, 9 at%) was homogeneously dispersed in the Cu matrix (major component, 91 at%) of the as-prepared alloy foam sample.

The basic bimetallic catalyst concept, followed herein, is based on the combination of a *CO and *H forming catalyst component and a second component, active for C–C coupling and subsequent alcohol formation. Additional catalyst activation, involving the thermal annealing of the *ap*-Pd_9Cu_{91} foam at 200 °C (12 h in air) and the subsequent reduction of the formed oxidic precursor under electrochemical conditions (at −0.65 V *vs.* RHE, 45 min), led to segregation into Pd-rich and Cu-rich domains which took over the role of *CO, *H-producer and C–C coupler (alcohol producer), respectively.

Highly selective *n*-propanol formation was observed (FE_{PrOH} = 13.7%, j_{PrOH} = −1.15 mA cm^{-2}) over ethanol (FE_{EtOH} = 7.1%, j_{EtOH} = −0.60 mA cm^{-2}) at −0.65 V *vs.* RHE, which led the selectivity of the C3 alcohol over the C2 alcohol by a factor of two. Key to the extraordinary performance of the oxide-derived *od*-Pd_9Cu_{91} foam catalyst was the complete suppression of methane formation (C1 hydrocarbon pathway). Extended CO_2 electrolyses, carried out for 102 h in a combined continuous and discontinuous mode, demonstrated rather stable PrOH selectivity and efficiencies that did not decrease during the continuously performed electrolysis but eventually were affected by the repetitive (intended) loss of potential control during the discontinuously performed catalyst stressing experiments. The continuous–discontinuous electrolyses indicated that the catalyst could be stored for long time and then used again when necessary.

Future work will focus on the transfer of these promising electrocatalysts to flow-cell electrolyzer with the aim of studying the catalyst degradation characteristics under well-defined mass transport conditions at elevated current densities relevant to industrial applications.

Conflicts of interest

The authors declare no competing financial interest.

Acknowledgements

The financial support by the CTI Swiss Competence Center for Energy Research (SCCER Heat and Electricity Storage) is gratefully acknowledged. M. R. and K. K. acknowledge Swiss Govt. Excellence Scholarship (ESKAS) for financial support. PB acknowledges the financial support by the Swiss National Science Foundation (SNSF) *via* the project no. 200020_172507.

References

1 *Nat. Catal.*, 2018, **1**, 93.
2 H.-R. M. Jhong, S. Ma and P. J. A. Kenis, *Curr. Opin. Chem. Eng.*, 2013, **2**, 191–199.
3 J.-P. Jones, G. K. S. Prakash and G. A. Olah, *Isr. J. Chem.*, 2014, **54**, 1451–1466.
4 J. Durst, A. Rudnev, A. Dutta, Y. Fu, J. Herranz, V. Kaliginedi, A. Kuzume, A. A. Permyakova, Y. Paratcha, P. Broekmann and T. J. Schmidt, *Chimia*, 2015, **69**, 769–776.
5 Y. Hori, in *Modern Aspects Electrochem.*, Springer, New York, 2008, pp. 89–189.
6 A. J. Martín, G. O. Larrazábal and J. Pérez-Ramírez, *Green Chem.*, 2015, **17**, 5114–5130.
7 A. Dutta, M. Rahaman, N. C. Luedi, M. Mohos and P. Broekmann, *ACS Catal.*, 2016, **6**, 3804–3814.
8 A. Dutta, C. E. Morstein, M. Rahaman, A. Cedeño López and P. Broekmann, *ACS Catal.*, 2018, **8**, 8357–8368.
9 K. P. Kuhl, E. R. Cave, D. N. Abram and T. F. Jaramillo, *Energy Environ. Sci.*, 2012, **5**, 7050–7059.
10 K. P. Kuhl, T. Hatsukade, E. R. Cave, D. N. Abram, J. Kibsgaard and T. F. Jaramillo, *J. Am. Chem. Soc.*, 2014, **136**, 14107–14113.
11 S. Nitopi, E. Bertheussen, S. B. Scott, X. Liu, A. K. Engstfeld, S. Horch, B. Seger, I. E. L. Stephens, K. Chan, C. Hahn, J. K. Nørskov, T. F. Jaramillo and I. Chorkendorff, *Chem. Rev.*, 2019, **119**, 7610–7672.
12 M. Gattrell, N. Gupta and A. Co, *J. Electroanal. Chem.*, 2006, **594**, 1–19.
13 W. Ma, S. Xie, T. Liu, Q. Fan, J. Ye, F. Sun, Z. Jiang, Q. Zhang, J. Cheng and Y. Wang, *Nat. Catal.*, 2020, **3**, 478–487.
14 C. Guo, P. He, R. Cui, Q. Shen, N. Yang and G. Zhao, *Adv. Energy Mater.*, 2019, **9**, 1900364.
15 Y. Hori, A. Murata and R. Takahashi, *J. Chem. Soc., Faraday Trans. 1*, 1989, **85**, 2309–2326.
16 S. Kaneco, K. Iiba, N.-H. Hiei, K. Ohta, T. Mizuno and T. Suzuki, *Electrochim. Acta*, 1999, **44**, 4701–4706.
17 O. A. Baturina, Q. Lu, M. A. Padilla, L. Xin, W. Li, A. Serov, K. Artyushkova, P. Atanassov, F. Xu, A. Epshteyn, T. Brintlinger, M. Schuette and G. E. Collins, *ACS Catal.*, 2014, **4**, 3682–3695.
18 C.-T. Dinh, T. Burdyny, M. G. Kibria, A. Seifitokaldani, C. M. Gabardo, F. P. García de Arquer, A. Kiani, J. P. Edwards, P. De Luna, O. S. Bushuyev, C. Zou, R. Quintero-Bermudez, Y. Pang, D. Sinton and E. H. Sargent, *Science*, 2018, **360**, 783–787.
19 C. Costentin, M. Robert and J.-M. Saveant, *Chem. Soc. Rev.*, 2013, **42**, 2423–2436.
20 G. Keerthiga, B. Viswanathan and R. Chetty, *Catal. Today*, 2015, **245**, 68–73.
21 J. Lee and Y. Tak, *Electrochim. Acta*, 2001, **46**, 3015–3022.
22 Y. Hori, H. Wakebe, T. Tsukamoto and O. Koga, *Electrochim. Acta*, 1994, **39**, 1833–1839.
23 C. W. Li, J. Ciston and M. W. Kanan, *Nature*, 2014, **508**, 504–507.
24 A. Verdaguer-Casadevall, C. W. Li, T. P. Johansson, S. B. Scott, J. T. McKeown, M. Kumar, I. E. L. Stephens, M. W. Kanan and I. Chorkendorff, *J. Am. Chem. Soc.*, 2015, **137**, 9808–9811.
25 Y. Lum, B. Yue, P. Lobaccaro, A. T. Bell and J. W. Ager, *J. Phys. Chem. C*, 2017, **121**, 14191–14203.
26 M. Rahaman, A. Dutta, A. Zanetti and P. Broekmann, *ACS Catal.*, 2017, **7**, 7946–7956.
27 D. Ren, N. T. Wong, A. D. Handoko, Y. Huang and B. S. Yeo, *J. Phys. Chem. Lett.*, 2016, **7**, 20–24.
28 D. Gao, I. Zegkinoglou, N. J. Divins, F. Scholten, I. Sinev, P. Grosse and B. Roldan Cuenya, *ACS Nano*, 2017, **11**, 4825–4831.
29 K. Jiang, R. B. Sandberg, A. J. Akey, X. Liu, D. C. Bell, J. K. Nørskov, K. Chan and H. Wang, *Nat. Catal.*, 2018, **1**, 111–119.
30 K. J. P. Schouten, Y. Kwon, C. J. M. van der Ham, Z. Qin and M. T. M. Koper, *Chem. Sci.*, 2011, **2**, 1902–1909.
31 A. Dutta, I. Z. Montiel, R. Erni, K. Kiran, M. Rahaman, J. Drnec and P. Broekmann, *Nano Energy*, 2020, **68**, 104331.
32 D. F. Gao, H. Zhou, J. Wang, S. Miao, F. Yang, G. X. Wang, J. G. Wang and X. H. Bao, *J. Am. Chem. Soc.*, 2015, **137**, 4288–4291.
33 X. Q. Min and M. W. Kanan, *J. Am. Chem. Soc.*, 2015, **137**, 4701–4708.
34 M. Rahaman, A. Dutta and P. Broekmann, *ChemSusChem*, 2017, **10**, 1733–1741.
35 J. Ko, H. Kwon, H. Kang, B. K. Kim and J. W. Han, *Phys. Chem. Chem. Phys.*, 2015, **17**, 3123–3130.
36 S. Sakong, C. Mosch and A. Gross, *Phys. Chem. Chem. Phys.*, 2007, **9**, 2216–2225.
37 Y. Hou, R. Erni, R. Widmer, M. Rahaman, H. Guo, R. Fasel, P. Moreno-García, Y. Zhang and P. Broekmann, *ChemElectroChem*, 2019, **6**, 3189–3198.
38 J. Li, A. Xu, F. Li, Z. Wang, C. Zou, C. M. Gabardo, Y. Wang, A. Ozden, Y. Xu, D.-H. Nam, Y. Lum, J. Wicks, B. Chen, Z. Wang, J. Chen, Y. Wen, T. Zhuang, M. Luo, X. Du, T.-K. Sham, B. Zhang, E. H. Sargent and D. Sinton, *Nat. Commun.*, 2020, **11**, 3685.
39 H. C. Shin, J. Dong and M. Liu, *Adv. Mater.*, 2004, **16**, 237–240.
40 H. C. Shin and M. Liu, *Chem. Mater.*, 2004, **16**, 5460–5464.
41 A. Dutta, M. Rahaman, M. Mohos, A. Zanetti and P. Broekmann, *ACS Catal.*, 2017, **7**, 5431–5437.

42 A. V. Rudnev, K. Kiran, A. Cedeño López, A. Dutta, I. Gjuroski, J. Furrer and P. Broekmann, *Electrochim. Acta*, 2019, **306**, 245–253.

43 A. Dutta, A. Kuzume, M. Rahaman, S. Vesztergom and P. Broekmann, *ACS Catal.*, 2015, **5**, 7498–7502.

44 C. K. Wu, M. Yin, S. O'Brien and J. T. Koberstein, *Chem. Mater.*, 2006, **18**, 6054–6058.

45 A. Dutta, M. Rahaman, B. Hecker, J. Drnec, K. Kiran, I. Zelocualtecatl Montiel, D. Jochen Weber, A. Zanetti, A. Cedeño López, I. Martens, P. Broekmann and M. Oezaslan, *J. Catal.*, 2020, **389**, 592–603.

46 H. Y. H. Chan, C. G. Takoudis and M. J. Weaver, *J. Phys. Chem. B*, 1999, **103**, 357–365.

47 Y. Deng, A. D. Handoko, Y. Du, S. Xi and B. S. Yeo, *ACS Catal.*, 2016, **6**, 2473–2481.

48 S. Cherevko, T. Reier, A. R. Zeradjanin, Z. Pawolek, P. Strasser and K. J. J. Mayrhofer, *Electrochem. Commun.*, 2014, **48**, 81–85.

49 M. Löffler, P. Khanipour, N. Kulyk, K. J. J. Mayrhofer and I. Katsounaros, *ACS Catal.*, 2020, **10**, 6735–6740.

50 R. Cui, Q. Shen, C. Guo, B. Tang, N. Yang and G. Zhao, *Appl. Catal., B*, 2020, **261**, 118253.

51 J. Gao, H. Zhang, X. Guo, J. Luo, S. M. Zakeeruddin, D. Ren and M. Grätzel, *J. Am. Chem. Soc.*, 2019, **141**, 18704–18714.

52 Y. C. Li, Z. Wang, T. Yuan, D.-H. Nam, M. Luo, J. Wicks, B. Chen, J. Li, F. Li, F. P. G. de Arquer, Y. Wang, C.-T. Dinh, O. Voznyy, D. Sinton and E. H. Sargent, *J. Am. Chem. Soc.*, 2019, **141**, 8584–8591.

53 T. Kottakkat, K. Klingan, S. Jiang, Z. P. Jovanov, V. H. Davies, G. A. M. El-Nagar, H. Dau and C. Roth, *ACS Appl. Mater. Interfaces*, 2019, **11**, 14734–14744.

54 S. Ma, M. Sadakiyo, M. Heima, R. Luo, R. T. Haasch, J. I. Gold, M. Yamauchi and P. J. A. Kenis, *J. Am. Chem. Soc.*, 2017, **139**, 47–50.

55 R. Kortlever, I. Peters, C. Balemans, R. Kas, Y. Kwon, G. Mul and M. T. M. Koper, *Chem. Commun.*, 2016, **52**, 10229–10232.

56 S. W. Kim, M. Park, H. Kim, K. J. Yoon, J. W. Son, J. H. Lee, B. K. Kim and J. Hong, *Appl. Catal., B*, 2017, **200**, 265–273.

57 T. Takashima, T. Suzuki and H. Irie, *Electrochim. Acta*, 2017, **229**, 415–421.

58 Z. Yin, D. Gao, S. Yao, B. Zhao, F. Cai, L. Lin, P. Tang, P. Zhai, G. Wang, D. Ma and X. Bao, *Nano Energy*, 2016, **27**, 35–43.

59 D. Raciti, K. J. Livi and C. Wang, *Nano Lett.*, 2015, **15**, 6829–6835.

60 S. Zhu, B. Jiang, W.-B. Cai and M. Shao, *J. Am. Chem. Soc.*, 2017, **139**, 15664–15667.

61 X. Nie, M. R. Esopi, M. J. Janik and A. Asthagiri, *Angew. Chem., Int. Ed.*, 2013, **52**, 2459–2462.

62 R. Kortlever, J. Shen, K. J. Schouten, F. Calle-Vallejo and M. T. Koper, *J. Phys. Chem. Lett.*, 2015, **6**, 4073–4082.

7.13. Photonic Curing: Activation and Stabilization of Metal Membrane Catalysts (MMCs) for the Electrochemical Reduction of CO_2

*Reprinted with permission from ACS Catal. 2019, **9**, 9518−9529. Copyright 2019 American Chemical Society.*

Authors: Yuhui Hou, Sami Bolat, Aline Bornet, Yaroslav E. Romanyuk, Huizhang Guo, Pavel Moreno-García, **Ivan Zelocualtecatl Montiel**, Zhiqiang Lai, Ulrich Müller, Vitali Grozovski and Peter Broekmann

ACS Catal. 2019, **9**, 9518−9529. DOI: https://doi.org/10.1021/acscatal.9b03664

Highlights: This work reports the use of photonic curing as an effective and versatile method to activate and stabilize Cu-NWs catalyst for electrochemical reduction of CO_2. Photonic curing was found as a suitable technique to remove surfactants from the catalyst surface without affecting the structural characteristics of the Cu-NWs, after applying the optimum conditions (50 µs, 5.9 kW. cm^{-2}). Through electrochemical experiments, the as-prepared Cu-NWs-GC predominantly produce H_2 (FE_{H2} = 73.3%, PCD_{H2} = –13.9 mA cm^{-2}) followed by formate ($FE_{formate}$ = 12.0%, $PCD_{formate}$ = –2.3 mA cm^{-2}) as reduction products from CO_2. However, the photonically cured Cu-NWs-GC show high selectivity towards ethylene formation, reaching a maximum faradaic efficiency of 42.4% at –1.1 V *vs.* RHE ($PCD_{ethylene}$ = –7.8 mA cm^{-2}). The high ethylene selectivity was preserved during a prolonged electrolysis time of 100 h. The most important factor obtained by photonic curing is that it leads to the substantial mechanical stability of the NW when they are used in aqueous electrolytes.

Contributions: In this project, I was involved in conducting some electrochemical experiments, and I participated in the manuscript revision process.

ACS Catalysis
Research Article
Cite This: *ACS Catal.* 2019, 9, 9518−9529
pubs.acs.org/acscatalysis

Photonic Curing: Activation and Stabilization of Metal Membrane Catalysts (MMCs) for the Electrochemical Reduction of CO_2

Yuhui Hou,*[,†] Sami Bolat,[‡] Aline Bornet,[†] Yaroslav E. Romanyuk,[‡] Huizhang Guo,[§,†] Pavel Moreno-García,[†] Ivan Zelocualtecatl Montiel,[†] Zhiqiang Lai,[†] Ulrich Müller,[‖] Vitali Grozovski,[†] and Peter Broekmann*[,†]

[†]Department of Chemistry and Biochemistry, University of Bern, Freiestrasse 3, Bern 3012, Switzerland

[‡]Laboratory of Thin Films and Photovoltaics, Empa—Swiss Federal Laboratories for Materials Science and Technology, Ueberlandstrasse 129, Dübendorf 8600, Switzerland

[§]Wood Materials Science, Institute for Building Materials, ETH Zürich, Stefano-Franscini-Platz 3, Zürich 8093, Switzerland

[‖]Nanoscale Materials Science, Empa—Swiss Federal Laboratories for Materials Science and Technology, Dübendorf 8600, Switzerland

Supporting Information

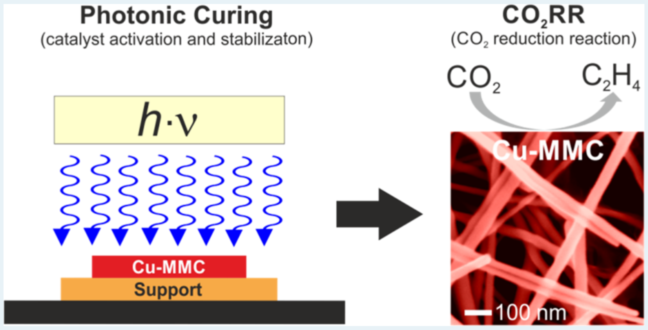

ABSTRACT: Photonic curing, an exposure of matter to intense and short (μs) light pulses, is herein demonstrated as an effective and versatile method to activate and stabilize electrocatalysts for the electrochemical reduction of CO_2. Catalyst preparation by colloidal synthesis often makes use of surfactants (capping agents) that control the size and morphology of target nano-objects during and after their synthesis. However, this approach can severely compromise the catalytic properties of the as-synthesized nanomaterials. Photonic curing is suitable to gently remove surfactants from the catalyst surface without severely altering its overall structural properties (e.g., surface faceting), thereby increasing the abundance of these surface active sites that can participate in the desired (electro)catalytic reaction. This catalyst activation is exemplarily demonstrated on the basis of Cu nanowire (Cu-NW) catalysts synthesized by an oleylamine route and transferred to a glassy carbon (GC) support electrode. Although the 3D networks of the as-synthesized Cu-NW catalysts predominantly produce hydrogen as the product of the electrolysis reaction, photonically cured Cu-NWs, denoted hereinafter as Cu metal membrane catalysts (MMCs), show a high selectivity toward ethylene formation, reaching a Faradaic efficiency of $FE_{C_2H_4} = 42.4\%$ ($J_{C_2H_4} = -7.8$ mA cm^{-2}, $E = -1.1$ V vs RHE). This high ethylene yield can even be maintained during prolonged electrolysis of 110 h. A further beneficial effect of the photonic curing treatment is related to the substantially increased mechanical stabilization of the Cu-NW film on the support electrode induced by a "mild" sintering of Cu-NWs, which remains locally confined to their points of contact. A loss of catalyst material or a delamination of the catalyst film from the support electrode during massive gas evolution can thus be prevented.

KEYWORDS: *CO_2 reduction, colloid synthesis, copper nanowires, photonic curing, catalyst activation, metal membrane catalyst, catalyst degradation*

INTRODUCTION

The environmental crisis, our society currently faces, demands a substantial reduction of greenhouse gas emissions as well as an increase of power generation based on renewable resources.[1] In addition, the CO_2, already released into the atmosphere, needs to be captured and, most preferably, transformed back into value-added products.[2−4] Among various concepts proposed, it is the electrochemical CO_2 reduction reaction (hereinafter referred to as CO_2RR) that has the potential to become a technologically and economically feasible approach toward the conversion of CO_2 into chemical feedstock, fine chemicals or high energy density fuels,[5] thereby contributing to the future closing of the anthropogenic carbon cycle.[6,7] This so-called power-to-value concept becomes particularly appealing when the surplus of renewable electricity from wind, solar and hydro sources is exploited.[2,3] However, the CO_2RR kinetics and the selectivity toward specific products still need to be improved to bring the CO_2RR into an economically feasible industrial application. Substantial efforts have already been made in the development of new

Received: August 27, 2019
Revised: September 5, 2019
Published: September 10, 2019

DOI: 10.1021/acscatal.9b03664

CO_2RR electrocatalysts with tunable particle size,[8,9] morphology,[10,11] grain boundary, and defect densities[12,13] to either directly produce value-added products from CO_2 (e.g., C_1−C_n alcohols[14−18]) or to obtain reaction intermediates (e.g., CO[19−23]) which can be further converted into hydrocarbons or alcohols in the course of subsequent nonelectrochemical reactions (e.g., by Fischer−Tropsch synthesis[24] or fermentation[25]), following the primary CO_2RR.

Not only is the availability of specific active sites (e.g., surface facets or defects) is important for the resulting CO_2RR catalyst but also its morphology on various length scales.[10,11] The particular morphology of the three-dimensional porous catalyst architecture determines the transport characteristics of the reactants into the electroactive material and influences therefore the mean residence time of reaction intermediates (e.g., alkenes[10]) inside its porous structure. Note that the probability for reaction intermediates to undergo consecutive reactions (e.g., hydrogenation of unsaturated hydrocarbons) also depends on the catalyst porosity.[10,11] Further, the three-dimensional structure of the catalyst material needs to be taken into account with regard to the chemical and mechanical stability of the electrode, in particular when high electrolysis current densities (>200 mA cm^{-2}) are targeted. Massive gas evolution, for example, caused by the parasitic hydrogen evolution reaction (HER) superimposed to the CO_2RR in aqueous reaction media, can induce mechanical stress on the catalyst layer, which might lead to its degradation, for example, by the loss of catalyst material into the electrolyte[26] or even the complete delamination of the active layer.

A bottom-up design of CO_2RR catalysts controlling the hierarchy of individual structural elements is suited to tackle these challenges. Among others, colloid chemistry can be considered as a promising approach to produce high-surface area electrode materials having a well-defined morphology and electrocatalytic properties in terms of an engineering of active sites.[27] Nonetheless, this colloidal synthesis approach often makes use of organic surfactants controlling nucleation and growth of the desired nano-objects (e.g., particles, wires, etc.), stabilizing thus their shape and preventing undesired precipitation and aggregation during and after their synthesis.[28−30] However, when left on the catalyst surface, these surfactants might compromise the performance of the material by sterically blocking the catalytically active sites. This is why several postsynthesis treatments have been proposed for the surfactant removal, for example, chemical washing,[28,29] thermal annealing under reductive or inert conditions,[30] and exposure to oxidative environments (e.g., O_2 plasma or ozone).[9,31] However, these approaches often require a nonsatisfying long treatment time (e.g., thermal annealing), producing huge amounts of organic waste (chemical washing) or can further alter the surface properties of the catalyst (e.g., plasma treatment).[32,33] The postsynthesis activation of surfactant-stabilized nanocatalysts remains, therefore, a challenge for the electrode fabrication process.

In this present study, we introduce photonic curing as a novel, fast, and versatile alternative to common catalyst activation methods. Note that, in this context, the term catalyst activation primarily refers to the selective removal of the surfactant (capping agent) from the catalyst surface and not to any further structural or compositional alteration of the as-synthesized catalyst material itself. The latter is well known, for instance, from copper-based CO_2RR catalysts that perform particularly well after being chemically activated by the electroreduction of cupric or cuprous precursor materials.[18,34,35]

Photonic curing, which is often called intense pulse light[36] or flash lamp annealing,[37] is based on the exposure of matter to intense light from a xenon flash lamp, thereby inducing an ultra-fast local heating of the surface area exposed to these light pulses. This rapidly emerging technology already finds applications in various industrial fields, for example, in the manufacturing of printed electronic devices as it allows the replacement of glass or ceramic substrates by less expensive and more flexible materials such as polymer sheets or paper.[38,39] More importantly, photonic curing substantially reduces process times from hours or minutes down to sub-milliseconds.[40]

In this present study, we exemplarily demonstrate the usability of photonic curing for the effective activation of CO_2RR electrocatalysts by selective surfactant removal. As a model system, we have chosen highly anisotropic copper nanowires (denoted hereinafter as Cu-NWs) that show preferential (100) texturing on their sidewalls. Early studies on single-crystalline Cu catalysts have claimed that the C−C coupling (C2 pathway) is more efficient on the (100)-textured catalyst, whereas the C1 hydrocarbon pathway was demonstrated to be preferred on (111) facets.[41−43] More recent studies utilizing the Cu nanocube-type of catalysts with preferential (100) texturing emphasize the need for an optimized ratio of (100) surface sites and certain edge sites in particular for the formation of ethylene from CO_2.[8]

For the colloidal synthesis of Cu-NWs, oleylamine (IUPAC name: (*Z*)-octadec-9-enylamine, $CH_3(CH_2)_7CH{=}CH(CH_2)_7CH_2NH_2$, denoted in the following as OAm) is often used as the organic reaction medium and reducing agent. At the same time, it serves as the surfactant that selectively stabilizes (100) facets during the anisotropic nanowire growth in solution.[44,45] The primary amine functionality thereby serves as an anchor group to the Cu surface.

In what follows, we will demonstrate that photonic curing enables the removal of the OAm surfactant from the catalyst surface without altering the structure of the Cu-NWs. The performance of the photonic curing approach is compared to other surfactant removal methods, such as thermal annealing, ozone treatment, plasma treatment, and deep UV annealing. To further demonstrate the versatility of photonic curing, we will show that this catalyst activation approach is transferable (i) to other catalyst morphologies [e.g., Cu nanoparticles (Cu-NPs)], (ii) to alternative catalyst materials (e.g., Ag-NWs), and (iii) to other organic surfactants [e.g., polyvinylpyrrolidone (PVP)]. Of equal importance is that photonic curing provides means of mechanically stabilizing the three-dimensional network of Cu-NWs, which is of particular importance for those electrode processes that involve massive gas evolution (e.g., HER and CO_2RR from aqueous electrolytes). Li et al. recently described a loss of Cu-NW material into the electrolyte under CO_2RR conditions when drop-casted on a glassy carbon (GC) support electrode without any further treatment.[26] One approach to prevent such mechanical catalyst degradation, proposed by the same authors, is the embedment of Cu-NWs into a carbon black (Ketjen) matrix (catalyst loading 20 wt %) that provides sufficient mechanical stability and prevents Cu-NW detachment from the electrode.[26] It should be noted that the presence of a carbon support exposed to the electrolyte will inevitably affect the resulting Faradaic efficiencies of the electrolysis products. In the latter case, the

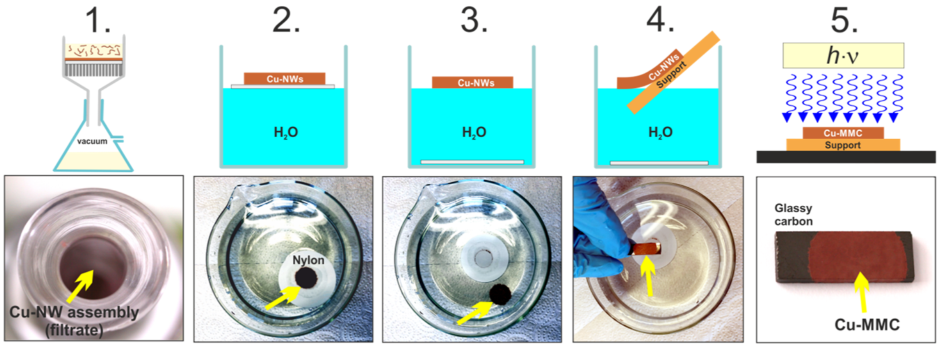

Figure 1. Schematic representations and top-down optical micrographs of individual steps followed for the preparation of the Cu-MMC (copper MMC) on the GC support.

resulting product distribution originates from superposition of the inherent catalyst characteristics and the contribution of the surrounding carbon matrix (see also the Supporting Information file). On the other hand, photonic curing provides mechanical stability of the three-dimensional network of Cu-NWs without the need of a stabilizing carbon matrix. The resulting layer of the activated and stabilized Cu-NWs assembly is denoted hereinafter as the Cu metal membrane catalyst (Cu-MMC).

■ EXPERIMENTAL SECTION

Cu-NW Synthesis. Cu nanowires (Cu-NWs) were synthesized according to a modified protocol introduced by Guo et al.[46] Nickel(II) acetylacetonate (0.4 mmol, $Ni(acac)_2$, Aldrich, assay 95%) and 0.8 mmol of copper(II) chloride monohydrate ($CuCl_2 \cdot H_2O$, Aldrich, assay >99.99%) were dissolved in 9 mL of oleylamine (OAm, Aldrich, assay 70%) in a three-necked flask. The solution was kept for 10 min at 100 °C under strong magnetic stirring conditions and continuous flow of high-purity nitrogen gas (99.995%, Carbagas, Switzerland). Subsequently, the solution was rapidly heated up to 180 °C and kept for 3 h at this temperature. After cooling down to room temperature, an excess of hexane was added to the aforementioned solution thus leading to the appearance of a black precipitate which could be isolated by 6 min centrifugation at 4000 rpm. The precipitate was thoroughly washed in a mixture of hexane and toluene and subsequently dried in a vacuum oven at 50 °C for 1 h, yielding a dry powder sample. Afterward, 9 mg of the as-synthesized Cu nanowires was dispersed in 30 mL toluene by ultrasonication.

For comparison purposes (see the Supporting Information file), Ag-NWs and Cu nanocubes (Cu-NCs) were synthesized also following a colloidal synthesis approach.

Ag-NWs were synthesized according to a modified protocol introduced by da Silva et al.[47] $AgNO_3$ (100 mM, Sigma-Aldrich, 99%) and 50 mM NaBr (Sigma-Aldrich, 99.99%) solutions were prepared using ethylene glycol (EG, Acros Organics, 99.5%) as a solvent. PVP (125 mg, $M_r \approx 1\,300\,000$ g mol^{-1}, Acros Organics) was dissolved in 20 mL of EG, subsequently heated up to a temperature of 160 °C and continuously stirred (320 rpm) for 1 h at this temperature. Subsequently, 250 μL of the NaBr solution was injected into the reaction vessel. After 15 min, 7.5 mL of $AgNO_3$ was dropwise added to the solution at a rate of 0.15 mL min^{-1}. After the complete addition of the $AgNO_3$ solution, the reaction mixture was thermally quenched by immersing the reaction vessel into an ice-water bath. After addition of 75 mL of acetone, the obtained suspension of Ag-NWs was centrifuged. Subsequently, the Ag-NWs were carefully washed with H_2O.

Cu-NCs were synthesized according to a modified protocol introduced by Guo et al.[48] CuBr (0.3 mmol, Acros Organics, 98%) and 0.5 mmol TOPO (Acros Organics, 99%) were dissolved at 80 °C under continuous stirring (15 min at 250 rpm) in 7 mL OAm (Sigma-Aldrich, 70%). This solution was then further heated up to 260 °C and kept at this temperature under reflux for 2.5 h. After cooling down to room temperature, an excess of toluene was added to the resulting reddish solution. The obtained suspension of Cu-NCs was centrifuged at 4000 rpm for 10 min (Hettich Universal 16). The reddish Cu-NCs were further purified by five cycles of redispersion/centrifugation in a solvent mixture of toluene (10 mL) and hexane (1 mL).

Electrode Preparation. A standard assembly of Cu-NWs was formed by vacuum filtration of 1 mL of the prepared Cu-NW suspension (0.3 mg Cu-NWs/mL) using a Nylon cloth (pore size 0.22 μm, Fisher Scientific). The resulting Cu-NW assembly (1.2 cm in diameter) was lifted off from the Nylon cloth in a glass beaker filled with Milli-Q water. While the Nylon cloth membrane dropped down to the bottom of the glass beaker, the lighter and free-standing assembly of Cu-NWs remained floating on the surface of the Milli-Q water. With the help of a supporting substrate (e.g., Cu foil, GC, carbon cloth, carbon paper, etc.) the Cu-NW assembly could be picked-up, dried, and then further subjected to catalyst activation procedures (e.g., photonic curing, thermal annealing, etc.). Individual steps of the Cu-MMC preparation are shown in Figure 1.

For comparison purposes, Cu-NWs were dispersed also on a technical carbon support (see Supporting Information file). For the preparation of such carbon-supported Cu-NW film, 7.0 mg of the as-prepared Cu-NWs was dispersed in 15 mL of hexane by 1 h sonication. Further, 3.0 mg of carbon powder (Vulcan XC 72R, Cabot, USA) was dispersed in 15 mL of isopropanol by 1 h sonication. Both suspensions were then intermixed, homogenized by sonication, and subsequently dried overnight in vacuum. The thus obtained carbon-supported Cu-NWs were redispersed in 1.9 mL of isopropanol (Sigma, assay ≥99.5%) containing 100 μL of Nafion solution (Aldrich, 5 wt % in lower aliphatic alcohols and water). This suspension was subjected to sonication (probe sonicator, Sonics, probe diameter: 3.2 mm, frequency: 10 kHz) for 30 min, thus yielding a homogeneous catalyst ink. This ink (50 μL) was then drop-casted and dried on a GC plate (A = 0.8 cm^2, Alfa Aesar, 2 mm thickness, type1). The GC plate had been mirror-polished (0.5 μm, alumina suspension, Buehler, USA) prior to the drop-casting of the catalyst ink. Activated carbon-supported Cu-NW samples were prepared in the same way. The Cu-NWs were, however, subjected to various activation treatments (i.e., thermal annealing, photonic curing, etc.) prior to their dispersion in the hexane solvent.

Catalyst Activation. For the photonic curing treatment, a PulseForge 1300 system from NovaCentrix was used (xenon flash lamp, optimized conditions: irradiance 5.9 kW cm^{-2}, 50 μs pulse duration). Light pulses of variable duration in the range from 20 to 150 μs were applied to the Cu-NW assemblies in an inert N_2 gas atmosphere, thus preventing surface oxidation during the photonic curing. For comparison purposes, the Cu-NW assemblies were also subjected to the thermal annealing under a protective N_2 gas atmosphere using a Nabertherm tube furnace. For the ozone treatment, a UV ozone system (PSD Series, Novascan) was used. The total duration of the ozone treatment was 2 h. The ozone chamber was, however, opened every 30 min to refresh the atmosphere as the oxygen gets consumed during the treatment. For the N_2-plasma treatment, the Cu-NW assemblies were activated for 10 min in a plasma etcher (Plasma Prep III, SPI supplies) at a gas pressure of 300 mT of N_2 and a power of 20 W. For the deep UV treatment, the Cu-NW assemblies were exposed to UV light in the deep UV chamber (UV253HR from Filgen) for 1 h under a N_2 atmosphere.

Electrode Characterization. The Cu-NW assemblies were characterized by means of scanning electron microscopy (Zeiss DSM 982). Identical location (IL) transmission electron microscopy was carried out using a FEI Titan Themis system operated at 300 kV. The thickness of the Cu-NW assemblies was determined on the basis of white-light interferometry (ContourGT profilometer, Bruker). The crystallinity of the catalysts was characterized by means of powder X-ray diffraction (XRD) techniques. An STOE Stadi P system with a Cu Kα radiation source (λ = 0.1540 nm, 40 mA) generated at 40 keV was used. XRD spectra were recorded in reflection mode (Bragg−Brentano geometry) with 2θ values ranging between 30 and 80° in steps of 1° min^{-1}. The obtained XRD patterns were analyzed and compared to (powder diffraction file) standards for Cu. Fourier transform infrared spectra were acquired between 4000 and 400 cm^{-1} using a FT/IR 4700 spectrometer (Jasco, Germany) in air in an attenuated total reflection mode. For this latter measurement, the Cu-MMCs were deposited on glass slides (see Figure S1).

X-ray photoelectron spectroscopy (XPS) spectra were acquired on a physical electronics (PHI) Quantum 2000 Scanning ESCA Microprobe System using monochromated Al Kα radiation ($h\nu$ = 1486.7 eV) and a hemispherical capacitor electron-energy analyzer equipped with a channel plate and a position-sensitive detector. The electron take-off angle was 45°, and the analyzer was operated in the constant pass energy mode at 23.5 eV for the detailed spectra of the Cu $2p_{3/2}$, O 1s, C 1s, and N 1s peaks with a step size of 0.20 eV. The beam diameter was typically 150 μm. The binding energy was calibrated using Cu $2p_{3/2}$, Ag $3d_{5/2}$, and Au $4f_{7/2}$ emissions at 932.62, 368.21, and 83.96 eV, respectively, to within ±0.1 eV. To compensate for eventual surface charging, built-in electron and argon ion neutralizers were used. The base pressure of the system was below 5×10^{-7} Pa. The spectra were analyzed using the software Multipak 8.2B, and the peaks are shown after a Shirley background subtraction. The atomic concentrations were calculated using the corrected relative sensitivity factors as given by the manufacturer and normalized to 100 at. %. The uncertainty is about 10% relative.

Electrochemical Characterization. CO_2 electrolysis experiments were performed using a potentiostat/galvanostat (Metrohm Autolab 302N, The Netherlands) attached to a custom-built, air-tight glass-cell (H-type), which has been described elsewhere.[10] The current interrupt approach (Autolab Nova, Metrohm) was used to determine the iR drop (cell resistance). All potentials given herein are iR-compensated. The three-electrode arrangement used consisted of a leakless Ag/AgCl$_{3M}$ reference electrode (EDAQ), a bright Pt-foil (15 mm × 5 mm) serving as the counter electrode, and the GC-supported Cu-MMC catalysts serving as working electrodes. For the sake of comparability, all potentials measured versus Ag/AgCl$_{3M}$ were referenced with respect to the RHE (reversible hydrogen electrode). Technical details of the CO_2RR product analysis based on online gas chromatography (GC) and ion exchange chromatography (IC) have been described elsewhere.[10] Electrolysis experiments were carried out in 0.5 M $KHCO_3$ (ACS grade, Sigma-Aldrich) electrolyte solutions saturated with Ar or CO_2 gas (99.999%, Carbagas, Switzerland). Note that, unless otherwise mentioned, a newly prepared catalyst electrode has been used for each CO_2 electrolysis experiment.

RESULTS AND DISCUSSION

Catalyst Activation (Surfactant Removal). Figure 2a,b depicts representative white-light interferometric images of the catalyst material that has been transferred after its filtration to a GC support (see also Figure 1). This microscopic inspection reveals a rather homogeneous but highly porous catalyst film with a root-mean-squared roughness of $R_q \approx 340$ nm (see also Figure S2). From the corresponding interferometric analysis of the catalyst film edge, a mean layer thickness of ∼400 nm could be determined (panel c and d in Figure 2). Note that the electrode was masked by an insulating Teflon tape prior to the CO_2 electrolysis so that a defined geometric surface area of 0.8 cm^2 was exposed to the electrolyte (Figure S3).

The analysis of the catalyst film by scanning electron microscopy (SEM) shows a three-dimensional network of randomly distributed Cu-NWs (Figure 3a). Their length can exceed tens of micrometers whereas the nanowire diameter is typically in the range of 50−70 nm (see representative high-resolution transmission electron microscopy (HR-TEM) in Figure 3b). Selective area electron diffraction (SAED) analysis obtained from an individual Cu-NW (Figure 3c) confirms, in full accordance with the literature, the five-fold twinned face centered cubic structure of the Cu-NWs and their preferential orientation along the [110] crystallographic direction.[49] The sidewalls of the Cu-NWs consist of 5 (100)-textured facets whereas the pentagonal apex of the Cu-NW is (111) terminated (Figure 3d). These (111) facets represent the actual growth front where precursor ions get preferentially reduced and added to the developing nanowire. Earlier studies[50] suggest a preferential and stronger adsorption of the organic surfactants on the (100) facets, thereby sterically blocking these sites for further addition of metal atoms. The anisotropy of the metal growth originates, at least in this scenario, from the weaker surfactant adsorption on the (111) facets, thus allowing for the continuous unidirectional addition of metal atoms. More recent studies emphasize, however, the important role of chloride anions for this highly anisotropic growth of Cu-NWs in particular when carried out in aqueous

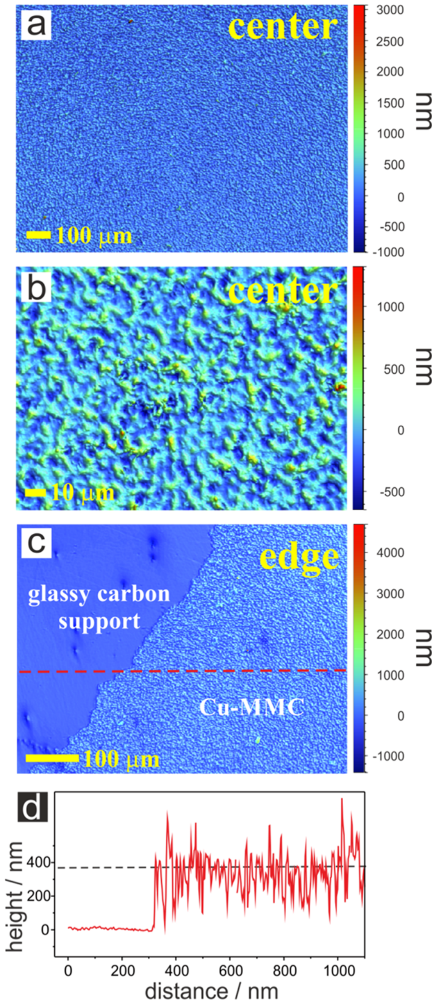

Figure 2. White-light interferometric analysis of the Cu-MMC after the photonic curing (5.9 kW cm^{-2}; 50 μs); (a,b) representative location in the center of the Cu-MMC; (c) representative location at the edge of the Cu-MMC; and (d) cross-sectional line-scan indicated in (c).

solutions.[51] Note that, cupric chloride is typically used as the copper source for the Cu-NW growth. Chloride anions tend to strongly chemisorb on Cu surfaces.[52−58] Wiley et al. discussed the competitive adsorption of chloride and alkylamine-based surfactants as the origin of the anisotropic Cu growth. Chloride anions were demonstrated to remove the surfactant more effectively from the (111) oriented facets, thereby keeping them active for the metal growth.[51]

The presence of surfactants on the surface of the Cu-NWs after the wet chemical synthesis represents a severe drawback for their application as catalysts because of the active reaction sites being sterically blocked by the surfactants. A mild catalyst activation process is therefore required that selectively removes the surfactant molecules from the NW surfaces while preserving their unique structural properties. In order to identify optimum experimental conditions for the surfactant removal and catalyst activation, Cu-NW assemblies were subjected to photonic curing at constant irradiance (5.9 kW cm^{-2}) but variable pulse lengths (single pulse approach). The photonic curing was carried out in a nitrogen gas atmosphere to avoid any extra compositional or structural change of the Cu-NWs that might go along with oxidation of the nanomaterial when exposed to oxygen during the photonic treatment. After activation, the resulting catalytic performance was studied by means of CO_2RR product analysis following 1 h potentiostatic electrolysis of a CO_2-saturated 0.5 M $KHCO_3$ solution at −1.1 V versus RHE. Results of this prescreening step are presented in Figure 4a (note that the irradiance dependence was already screened beforehand, see Figure S4). As expected, the as-prepared Cu-NW assemblies show only a minor activity toward CO_2RR. H_2, originating from the parasitic HER, is the predominant product of the electrolysis reaction, reaching a Faradaic efficiency of $FE_{H_2} = 73.3\%$ ($J_{H_2} = -13.9$ mA cm^{-2}). Formate is clearly the main CO_2RR product with a Faradaic yield of 12.0% ($J_{\text{formate}} = -2.3$ mA cm^{-2}), followed by minor yields of ethylene ($FE_{C_2H_4} = 5.1\%$, $J_{C_2H_4} = -0.97$ mA cm^{-2}). Also, traces of CO could be detected ($FE_{CO} = 1.9\%$, $J_{CO} = -0.36$ mA cm^{-2}). Note that, formate is the least demanding CO_2RR product with regard to the Cu catalyst (Cu−O binding) whereas formation of ethylene requires a high abundance of next neighbor adsorption sites that can

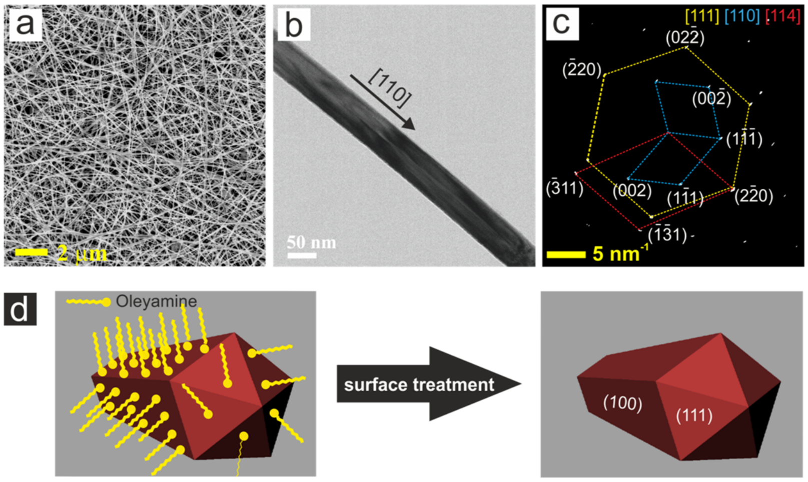

Figure 3. (a) Top-down SEM inspection of the Cu-MMC after the photonic curing; (b) HR-TEM micrograph of an individual Cu-NW; (c) SAED analysis obtained from an individual Cu-NW after the photonic curing; (d) schematic drawing showing the Cu-NW before (left panel) and after (right panel) the activation treatment.

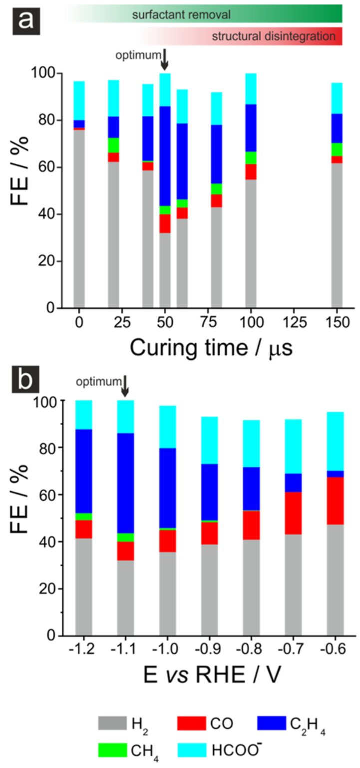

Figure 4. (a) CO_2RR product distributions from various Cu-MMCs photonically cured using a constant irradiance of 5.9 kW cm^{-2} but varying pulse times; the CO_2RRs were carried out for 1 h at −1.1 V vs RHE in each case; (b) potential-depending CO_2RR product distributions derived from the optimum catalyst at 50 µs curing time.

strongly bind CO (Cu−C binding), thus being a mechanistic prerequisite for subsequent C−C coupling reactions.[59,60] CO forms as the key intermediate in the course of the CO_2 electroreduction. In particular, the (100) facets, key structural motifs of the NW sidewalls, have been discussed in the literature as being active for the C−C coupling reaction.[43,60,61] The hydrocarbon pathways remain, however, largely suppressed on the nonactivated Cu-NW electrocatalyst when the OAm surfactant is still present (Figure 4a).

When considering ethylene as the most valuable CO_2RR product, there is a clear optimum at 50 µs pulse duration (Figure 4a), resulting in a maximum ethylene efficiency of $FE_{C_2H_4}$ = 42.4% ($J_{C_2H_4}$ = −7.8 mA cm^{-2}), thus being indicative for an effective OAm surfactant removal (for details see Table S1). Note that, the SEM and HR-TEM analyses in Figure 3 were carried out after the photonic curing proving that, at least under the given experimental conditions, this activation treatment does not severely affect the structural characteristics of the Cu-NWs. After applying optimum curing conditions, the Faradaic efficiency for H_2 production is substantially reduced to FE_{H_2} = 32% (J_{H_2} = −5.9 mA cm^{-2}), whereas the total CO_2RR efficiency reaches FE_{CO_2RR} = 69% (J_{CO_2RR} = −12.8 mA cm^{-2}). More extended photonic curing leads, however, to the gradual drop down of the total CO_2RR efficiencies, for example, FE_{CO_2RR} = 34% (J_{CO_2RR} = −5.8 mA cm^{-2}) when pulses of 150 µs duration are applied (Figure 4a). This trend can be regarded as an experimental hint for an undesired structural degradation of the Cu-NW catalyst taking place upon prolonged photonic curing times at the given irradiance of 5.9 kW cm^{-2}. This conclusion is consistent with an SEM inspection of the photonically cured Cu-MMCs, demonstrating that the 50 µs photonic curing at 5.9 kW cm^{-2} does not induce structural changes of the Cu-NW assembly on larger macroscopic length scales or on the length scale of individual Cu-NWs (Figure S5). By contrast, prolonged photonic curing times lead to severe structural alterations of the Cu-NWs (Figure S6a). As a result, semihemispheric droplets appear on the NW sidewalls. Similar morphological and structural changes were observed after thermal annealing at temperatures ≥300 °C (Figure S6b). One might assume that these substantial structural changes also involve a decrease in the relative abundance of those specific surface sites needed for the C−C coupling.

Figure 4b displays the complete potential-dependent CO_2RR product analysis for the optimum photonic curing conditions (50 µs, 5.9 kW cm^{-2}). A maximum of $FE_{C_2H_4}$ = 42.4% ($J_{C_2H_4}$ = −7.8 mA cm^{-2}) is observed for an electrolysis potential of −1.1 V versus RHE that is anticorrelated with the minimum in the Faradaic efficiency for hydrogen production (FE_{H_2} = 32.0%, J_{H_2} = −5.9 mA cm^{-2}). At higher overpotentials, for example, at −1.2 versus RHE, the hydrogen efficiency starts to increase (FE_{H_2} = 41.3%, J_{H_2} = −10.2 mA cm^{-2}) at the expense of the ethylene yield ($FE_{C_2H_4}$ = 35.6%, $J_{C_2H_4}$ = −8.8 mA cm^{-2}). Note that this trend does not necessarily point to the loss of catalytic performance of the Cu-MMC at higher overpotentials but might, instead, be ascribed to the onset of CO_2 mass transport limitations in quiescent aqueous electrolytes where the CO_2 solubility is limited to ~35 mM.[3,6] The high reproducibility of the electrode preparation and catalyst activation procedure is demonstrated in Figure S7, showing the CO_2RR product distribution of five independent electrolysis experiments performed at −1.1 V versus RHE.

Comparable or even higher ethylene efficiencies than the one achieved in this present study were already reported in the literature.[8,34,61−63] For example, Mistry et al.[33] obtained an ethylene selectivity of $FE_{C_2H_4}$ ≈ 60% at comparably low overpotentials of −0.9 V versus RHE. These extraordinarily high C_2H_4 yields are typically observed only when using so-called oxide-derived (OD) Cu catalysts. Facile approaches to activate Cu-based CO_2RR catalysts by oxidation are the exposure to oxygen plasma, thermal annealing in air,[64,65] or electrode anodization.[35] These formed cupric and cuprous oxides typically get reduced under CO_2RR conditions, thereby creating these low-coordinated sites and grain boundaries, which are particularly active for hydrocarbon or alcohol formation.[15] An extra activation of the Cu-NW catalyst, for example, by surface oxidation, was excluded herein as the photonic curing was carried out in an inert N_2 atmosphere (see Experimental Section). Further chemical activation of the Cu-MMCs will be treated separately in a forthcoming study.

It is interesting to note that no substantial ethane formation is observed for the Cu-MMC catalyst (Figure 4b). From porous Cu foam catalysts, it is known that because of the prolonged residence time of the intermediates inside the three-dimensional catalyst, formed ethylene gets, to some extent, further reduced to ethane as consequence of readsorption and subsequent reduction steps. The Cu-foam catalysts, studied by Dutta et al.,[10] show a primary macroporosity with pore sizes on the micrometer length scale and a secondary porosity of their dendritic sidewalls on the nm length scale. These previous

DOI: 10.1021/acscatal.9b03664
ACS Catal. 2019, 9, 9518−9529

studies indicate that the electrolyte can penetrate into the micrometer-sized macropores of the Cu foams, giving rise to a pronounced pore-size dependence of the resulting CO_2RR product distribution.[10]

The absence of ethane in the present case (Figure 4b) can be regarded as the first experimental hint for an electrolyte which does not completely penetrate the entire three-dimensional network of the Cu-NWs. Apparently, the wetting of the Cu-MMC remains confined to the outermost volume of the 3D network of Cu-NWs. To support this hypothesis, we carried out two extra control experiments. The first one was based on a thickness variation of the Cu-MMC (see Figures S2, S8 and S9). The CO_2RR product distribution is found to be largely insensitive to the further increase of the Cu-NW layer thickness (Figure S8a). A slight increase of the H_2 efficiency was, however, observed when the Cu-MMC thickness was further reduced (Figure S8a). This latter observation might point to a certain contribution of the GC substrate to the resulting CO_2RR product distribution when the MMC thickness falls below a critical value (Figure S8b). Exchanging the GC support of the Cu-MMC by an Ag foil does not lead to a substantial alteration of the CO_2RR product distribution provided the Cu-MMC layer thickness is sufficiently high (Figure S10a). These control experiments are indicative for an electrolysis reaction that takes place within a spatially confined and constant volume of the three-dimensional Cu-MMC as illustrated in Figures S8b and S10b.

For comparison purposes, we present in Figure S11 a similar potential-dependent product analysis for Cu-MMC samples treated by thermal annealing in an inert nitrogen gas atmosphere at 200 °C. Also, this approach leads to certain catalyst activation but on a significantly lower level as compared to the photonic curing (Figure 4a,b). A maximum of $FE_{C_2H_4} = 15.5\%$ ($J_{C_2H_4} = -2.5$ mA cm^{-2}) is yielded after the 2 h annealing at 200 °C. Obviously, there is no clear preference for C−C coupled hydrocarbons after the thermal annealing, no matter what annealing times have been applied. Methane efficiencies are, however, comparably high after the thermal treatment, for example, $FE_{CH4} = 9.2\%$ at −1.1 V versus RHE (Figure S11). A C2/C1 hydrocarbon ratio of ∼1.7 clearly points to poor product selectivity toward ethylene. In case of the catalyst activated by photonic curing, the respective C2/C1 hydrocarbon ratio at −1.1 V versus RHE electrolysis potentials is 12.1 (Figure 4b). Annealing temperatures above 200 °C lead to a further decrease of the CO_2RR performance most likely due to structural catalyst degradation as observed in the SEM analysis (Figure S6b).

A more complete overview over the performance of different surfactant removal approaches is provided in Figure 5 that includes thermal annealing, the exposure of the catalyst to ozone, deep UV treatment, and plasma activation. Among these, it is indeed the photonic curing that demonstrates the most promising results, in particular when ethylene is targeted as the CO_2RR product. It can be hypothesized that the observed differences in the CO_2RR performance are due to different efficiencies in the OAm surfactant removal. To support this hypothesis, surface-sensitive XPS analyses were carried out after applying the activation treatments to the Cu-NW catalyst films (Figure 6). The ratio of the integrated N 1s and Cu $2p_{3/2}$ intensities can be considered as a measure for the effectiveness of the respective surfactant removal. As expected, the as-prepared sample shows the highest N 1s/Cu $2p_{3/2}$ ratio followed by the thermally annealed one. This observation is fully consistent with the nonsatisfying CO_2RR performance of the as-prepared and annealed catalyst samples (Figures 5 and S11). A more efficient surfactant removal is observed for the plasma and ozone treatments. Obviously, the photonic curing and the deep UV treatment lead to an almost complete surfactant removal (Figure 6b). The comparison of Figures 5 and 6 demonstrates a quite good correlation between the surfactant removal, probed by XPS via the N 1s/Cu $2p_{3/2}$ ratio, and the resulting CO_2RR performance. An effective surfactant removal is further confirmed by the IR inspection of the photonically cured Cu-MMC sample (Figure S12).

It should be emphasized at this point that the catalyst activation by photonic curing is highly versatile and not limited to Cu-based materials. Photonic curing can be applied to other colloidal systems prepared by various surfactant-assisted synthesis routes. As an example, we present in the Supporting Information file analogous investigations on Ag-NWs synthesized by the assistance of PVP. Their selectivity toward CO formation can substantially be improved by applying the novel photonic curing activation method (see Figure S13). These supporting experiments further demonstrate that the surfactant removal is not only limited to monomeric OAm surfactants but can be successfully applied also to polymeric capping agents

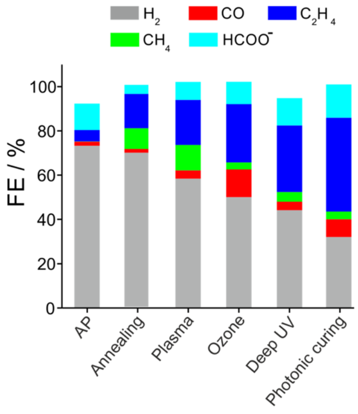

Figure 5. CO_2RR product distribution at −1.1 V vs RHE (1 h electrolysis) derived from catalysts treated by various procedures for the removal of the surfactant. For comparison purposes, also the results from the as-prepared (AP) sample are shown.

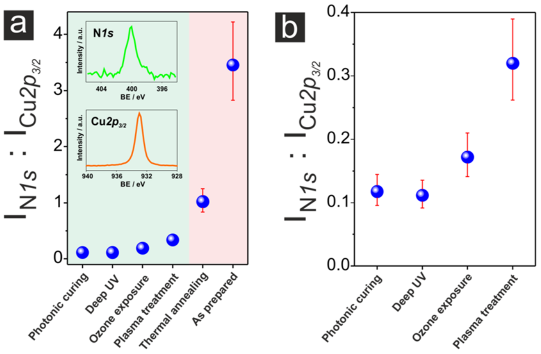

Figure 6. (a) XPS analyses of the Cu-NW assemblies carried out after applying different activation treatments (for details see text). The ratio of the integrated N 1s and Cu $2p_{3/2}$ emissions serves as the measure for the removal of the surfactants, which preferably bind via their nitrogen functionality to the copper surface; (b) enlarged section of (a) focusing on the well-performing surfactant removal treatments.

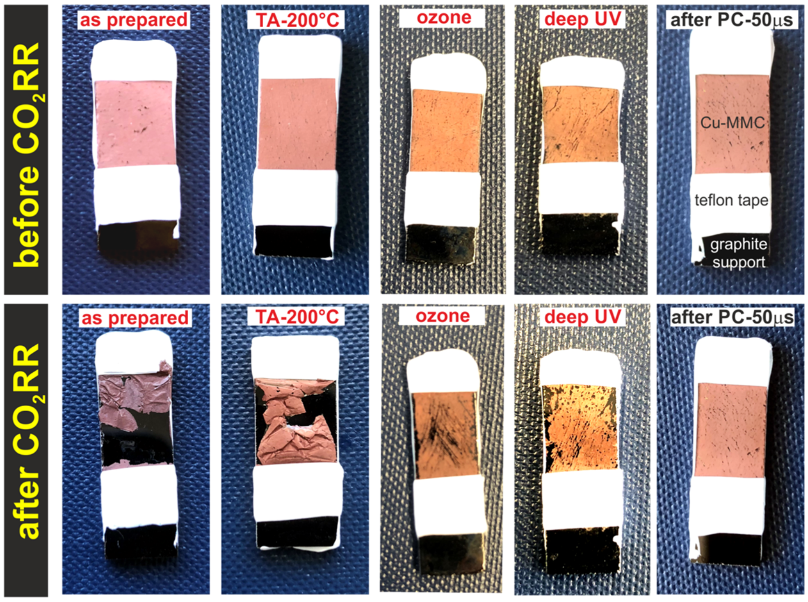

Figure 7. Optical micrographs of the Cu-NW catalysts prior to and after 1 h CO_2RR at −1.1 V vs RHE. Considered are the as-prepared sample, the one thermally annealed at 200 °C, the ones exposed to ozone and deep UV light, and the photonically cured Cu catalyst.

(e.g., PVPs). Furthermore, the catalyst activation by photonic curing is also transferable to other catalyst morphologies, for example, shaped nanoparticles (see Figure S14).

Catalyst Stability. Not only are the product selectivity and the achieved partial CO_2RR current densities of importance for the evaluation of the overall catalyst performance but also the mechanical robustness and the long-term chemical stability of the electrode assembly.

In order to demonstrate the superior mechanical stability of the photonically cured Cu-MMCs, optical micrographs were taken before and after 1 h CO_2RR at −1.1 V versus RHE (Figure 7). Gas evolution reactions (e.g., HER and CO_2RR) can induce substantial mechanical stress to the electrode assembly particularly when exposed to an aqueous environment. This stress often leads to a loss of active catalyst material into the solution phase during the electrolysis reaction[26] or even to a partial or complete delamination of the catalyst layer from the support electrode. Delamination phenomena upon CO_2RR are observed in particular for the as-prepared Cu-NW sample and the thermally annealed one whereas substantial losses of the catalyst material into the solution phase become apparent from the optical micrographs of these samples treated by deep UV light and by ozone exposure (Figure 7). The only catalyst sample which obviously remains unaffected by the CO_2RR at −1.1 V versus RHE is the photonically cured one (respective repetition experiments are shown in Figure S15). This observation is also consistent with an IL microscopic inspection of the photonically cured Cu-MMC prior to and after the CO_2RR not showing any severe morphological alterations after the electrolysis reaction at −1.1 V versus RHE (Figure S16). Such mechanical stabilization is most likely achieved by the "mild" sintering of the Cu-NWs upon photonic curing which remains locally confined to their points of contact, at least for the given curing conditions (50 μs, 5.9 kW cm^{-2}). Further, the photonic curing not only improves the rigidity of the 3D Cu-NW assembly itself but also improves the adhesion to the underlying support material (e.g., to the GC electrode). Massive losses of the Cu-NW material into the electrolyte during the electrolysis, as reported by Li et al.,[26] can thus be prevented even without using a stabilizing carbon matrix (e.g., Vulcan, Ketjen; Nafion).

With regard to the structural stability on a nanometer scale, nanowire-based catalysts seem to be superior over nanoparticles of the same catalyst material (see Figure S17). Cube-shaped Cu-NPs of the similar diameter as the Cu-NWs studied herein undergo comparably fast structural degradation, involving the loss of the extended and preferential (100) texturing upon CO_2RR (Figure S17).[66] This might be an important finding for the application of CO_2RR catalysts under industrial conditions where their reliability is key.

At this point, the question arises whether the observed trend in the CO_2RR performance (Figure 5) can solely be ascribed to differences in the OAm removal efficiency as concluded from Figure 6 or whether extra effects due to the observed degradation phenomena (Figure 7) also contribute, at least to some extent, to the resulting CO_2RR product distribution. In particular, the delamination of the Cu-NW films from the GC support will necessarily lead to a certain contribution of the support material to the overall electrolysis reaction. As the GC support electrode is active only toward the HER, an increase of the FE_{H_2} is indeed expected. However, cyclic voltammetric control experiments carried out in the Ar-saturated and CO_2-saturated 0.5 M $KHCO_3$ solution (Figure S18) clearly demonstrate a comparably low activity of the GC electrode toward the HER at the relevant electrolysis potential of −1.1 V versus RHE. From this control experiment, we therefore conclude that the main contribution to the FE_{H_2} in case of the as-prepared and thermally annealed samples (Figure 5) originates from the inefficient removal of surfactants from the Cu catalyst surface with only minor contributions from the GC support after the partial delamination of the catalyst film.

Further, to avoid the undesired structural degradation processes at elevated current densities (Figure 7), selected CO_2 electrolysis experiments were carried out also at −0.8 V versus RHE. Because of the reduced overall current densities at −0.8 V versus RHE in the order of ~2.5 mA cm^{-2}, all the pretreated catalyst films remain structurally intact as evidenced by the optical inspection shown in Figure S19a. Important to note is that also at these lower overpotentials, the same trend of an improved CO_2RR performance is observed after the photonic curing treatment (Figure S19b) as already seen for the electrolysis at −1.1 V versus RHE (Figure 5). The comparably higher Faradaic efficiency toward hydrogen in case of the thermally annealed sample can solely be ascribed to an insufficient surfactant removal whereas undesired side effects originating from the GC support after partial delamination of the catalyst layer can be excluded in this case (Figure S19b).

An alternative route to avoid losses of catalyst material into the aqueous electrolyte phase during the electrolysis reaction is the embedment of Cu-NWs into a carbon support matrix as recently discussed by Li et al.[26] Also, in this case, the photonic curing of the Cu-NWs, carried out prior to the catalyst ink preparation, leads to a further improvement of the CO_2RR performance (Figure S20). It should, however, be noted that catalyst films based on C-supported Cu-NWs predominantly yield methane as the major hydrocarbon product of the CO_2RR in full agreement with the recent work by Li et al.[26] This observation again points to the fact that the resulting CO_2RR product distribution is not solely governed by the intrinsic structural properties of the catalyst material on the atomic scale [e.g., (100) versus (111) surface faceting] but, as already pointed out by Dutta et al.,[10] results from the complex convolution of several effects involving also the catalyst film morphology on various length scales which affects the local reaction environment (e.g., local pH) and the reactant/product transport characteristics inside the three-dimensional catalyst material.

To further demonstrate the superior chemical stability of the photonically cured Cu-MMC, an extended 110 h lasting CO_2 electrolysis has been carried out at an applied potential of −1.1 V versus RHE (Figure 8). Within this period of electrolysis time, the ethylene efficiency remains well above >40%. At least on this time scale, there is no noticeable catalyst degradation. The photonically cured Cu-MMC also withstands stressing experiments where the electropotential is periodically switched from the OCP to −1.1 V versus RHE (Figure S21).

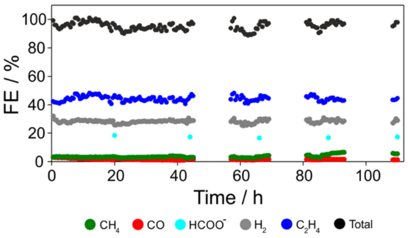

Figure 8. Long-term (110 h) continuous CO_2 electrolysis experiment carried out over the photonically cured Cu-MMC at −1.1 V vs RHE (note that the product detection by online gas chromatography was not carried out over the full electrolysis time).

When using (polycrystalline) Cu catalysts, it is often the coupled C1/2 hydrocarbon pathway (Figure 9) which causes a fast and irreversible catalyst degradation.[15] According to early work by Hori et al.,[67] Akhade et al.,[68] and Dewulf et al.,[69] hydrocarbon formation might involve an irreversible chemisorption of *C surface species on the catalyst surface, which blocks these sterically demanding reactive sites that are required for the *CH_2 dimerization.[15] More recent DFT results by Nie et al.[70] discuss C1 and C2 pathways that also share key intermediates such as *CO, *COH and *CH_2 but do not involve the formation of poisoning *C species. The long term stability of the photonically cured Cu-MMC catalyst suggests that both methane and ethylene formation occur in the present case rather via the *COH route[70] than via the *C pathway. The latter would lead to an irreversible poisoning of the catalyst surface as shown by Rahaman et al. for dendritic Cu.[15]

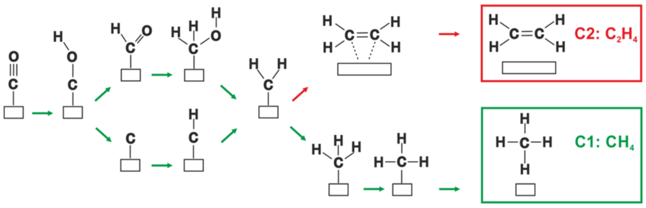

Figure 9. Proposed reaction mechanism of ethylene formation on Cu catalysts.

CONCLUSIONS

Photonic curing in an inert gas atmosphere has been introduced as an effective and highly versatile method to remove surfactants (capping agents) from the surface of stabilized nanomaterials (e.g., nanowires, nanoparticles etc.), thereby activating them for electrocatalytic reactions, for example, the CO_2 electroreduction reaction (CO_2RR). Crucial is the right balance of the energy input, depending on factors such as the irradiance (kW cm^{-2}) and the irradiation time (typically in the range of μs), to remove the surfactant from the as-synthesized catalyst without degrading these structural features (e.g., surface sites) of the nanomaterial that are particularly active toward the targeted (electro)catalytic reaction. One prime example, discussed in detail herein, is the activation of oleylamine-stabilized Cu-NWs which yield up to 42% ethylene as the CO_2RR product at −1.1 V versus RHE after applying one single pulse of 50 μs duration at 5.9 kW cm^{-2} irradiance. Optimized curing conditions depend on the chemical nature of the catalyst material, the support electrode, and the capping agent used during synthesis. Photonic curing also leads to a substantial mechanical stabilization of the NW assembly (denoted as metal membrane catalyst: MMC), thus being important in particular for electrocatalytic reactions involving massive gas evolution which can induce mechanical stress to the electrode assembly.

Future method development will focus on multistep catalyst activation steps, for example, involving reactive gas environments with the aim to direct the CO_2RR product distribution toward alcohol formation.

ASSOCIATED CONTENT

Ⓢ Supporting Information

The Supporting Information is available free of charge on the ACS Publications website at DOI: 10.1021/acscatal.9b03664.

> White-light interferometric analysis; irradiance-dependent product analysis; layer thickness-dependent product analysis; voltammetric determination of roughness factors; IL TEM analysis of the MMCs; linear sweep voltammetry; comparison of MMCs and carbon-supported catalysts; and discontinuous catalyst stressing experiments (PDF)

AUTHOR INFORMATION

Corresponding Authors

*E-mail: yuhui.hou@dcb.unibe.ch (Y.H.).
*E-mail: peter.broekmann@dcb.unibe.ch (P.B.)

ORCID

Yuhui Hou: 0000-0003-1616-562X
Huizhang Guo: 0000-0002-9695-5092
Pavel Moreno-García: 0000-0002-6827-787X
Peter Broekmann: 0000-0002-6287-1042

Notes

The authors declare no competing financial interest.

ACKNOWLEDGMENTS

Financial support by the CTI Swiss Competence Center for Energy Research (SCCER Heat and Electricity Storage) is gratefully acknowledged. P.B. acknowledges financial support by the Swiss National Science Foundation (SNSF) via the project no. 200020_172507. This study was performed with the support of the interfaculty Microscopy Imaging Centre (MIC) of the University of Bern.

REFERENCES

(1) Qiao, J.; Liu, Y.; Hong, F.; Zhang, J. A Review of Catalysts for the Electroreduction of Carbon Dioxide to Produce Low-Carbon Fuels. *Chem. Soc. Rev.* **2014**, *43*, 631−675.

(2) Jones, J.-P.; Prakash, G. K. S.; Olah, G. A. Electrochemical CO_2 Reduction: Recent Advances and Current Trends. *Isr. J. Chem.* **2014**, *54*, 1451−1466.

(3) Jhong, H.-R. M.; Ma, S.; Kenis, P. J. Electrochemical Conversion of CO_2 to Useful Chemicals: Current Status, Remaining Challenges, and Future Opportunities. *Curr. Opin. Chem. Eng.* **2013**, *2*, 191−199.

(4) Appel, A. M.; Bercaw, J. E.; Bocarsly, A. B.; Dobbek, H.; DuBois, D. L.; Dupuis, M.; Ferry, J. G.; Fujita, E.; Hille, R.; Kenis, P. J. A.; Kerfeld, C. A.; Morris, R. H.; Peden, C. H. F.; Portis, A. R.; Ragsdale, S. W.; Rauchfuss, T. B.; Reek, J. N. H.; Seefeldt, L. C.; Thauer, R. K.; Waldrop, G. L. Frontiers, Opportunities, and Challenges in Biochemical and Chemical Catalysis of CO_2 Fixation. *Chem. Rev.* **2013**, *113*, 6621−6658.

(5) Li, C. W.; Ciston, J.; Kanan, M. W. Electroreduction of Carbon Monoxide to Liquid Fuel on Oxide-Derived Nanocrystalline Copper. *Nature* **2014**, *508*, 504−507.

(6) Durst, J.; Rudnev, A.; Dutta, A.; Fu, Y.; Herranz, J.; Kaliginedi, V.; Kuzume, A.; Permyakova, A. A.; Paratcha, Y.; Broekmann, P.; Schmidt, T. J. Electrochemical CO_2 Reduction—A Critical View on Fundamentals, Materials and Applications. *Chimia Int. J. Chem.* **2015**, *69*, 769−776.

(7) Whipple, D. T.; Kenis, P. J. A. Prospects of CO_2 Utilization via Direct Heterogeneous Electrochemical Reduction. *J. Phys. Chem. Lett.* **2010**, *1*, 3451−3458.

(8) Loiudice, A.; Lobaccaro, P.; Kamali, E. A.; Thao, T.; Huang, B. H.; Ager, J. W.; Buonsanti, R. Tailoring Copper Nanocrystals towards C2 Products in Electrochemical CO_2 Reduction. *Angew. Chem., Int. Ed.* **2016**, *55*, 5789−5792.

(9) Reske, R.; Mistry, H.; Behafarid, F.; Roldan Cuenya, B.; Strasser, P. Particle Size Effects in the Catalytic Electroreduction of CO_2 on Cu Nanoparticles. *J. Am. Chem. Soc.* **2014**, *136*, 6978−6986.

(10) Dutta, A.; Rahaman, M.; Luedi, N. C.; Mohos, M.; Broekmann, P. Morphology Matters: Tuning the Product Distribution of CO_2 Electroreduction on Oxide-Derived Cu Foam Catalysts. *ACS Catal.* **2016**, *6*, 3804−3814.

(11) Dutta, A.; Rahaman, M.; Mohos, M.; Zanetti, A.; Broekmann, P. Electrochemical CO_2 Conversion Using Skeleton (Sponge) Type of Cu Catalysts. *ACS Catal.* **2017**, *7*, 5431−5437.

(12) Li, J.; Chen, G.; Zhu, Y.; Liang, Z.; Pei, A.; Wu, C.-L.; Wang, H.; Lee, H. R.; Liu, K.; Chu, S.; Cui, Y. Efficient Electrocatalytic CO_2 Reduction on a Three-Phase Interface. *Nat. Catal.* **2018**, *1*, 592−600.

(13) Mariano, R. G.; McKelvey, K.; White, H. S.; Kanan, M. W. Selective Increase in CO_2 Electroreduction Activity at Grain-Boundary Surface Terminations. *Science* **2017**, *358*, 1187−1192.

(14) Kuhl, K. P.; Hatsukade, T.; Cave, E. R.; Abram, D. N.; Kibsgaard, J.; Jaramillo, T. F. Electrocatalytic Conversion of Carbon Dioxide to Methane and Methanol on Transition Metal Surfaces. *J. Am. Chem. Soc.* **2014**, *136*, 14107−14113.

(15) Rahaman, M.; Dutta, A.; Zanetti, A.; Broekmann, P. Electrochemical Reduction of CO_2 into Multicarbon Alcohols on Activated Cu Mesh Catalysts: An Identical Location (IL) Study. *ACS Catal.* **2017**, *7*, 7946−7956.

(16) Hori, Y.; Murata, A.; Takahashi, R.; Suzuki, S. Enhanced formation of ethylene and alcohols at ambient temperature and pressure in electrochemical reduction of carbon dioxide at a copper electrode. *J. Chem. Soc., Chem. Commun.* **1988**, *1*, 17−19.

(17) Ma, S.; Sadakiyo, M.; Luo, R.; Heima, M.; Yamauchi, M.; Kenis, P. J. A. One-Step Electrosynthesis of Ethylene and Ethanol from CO_2 in an Alkaline Electrolyzer. *J. Power Sources* **2016**, *301*, 219−228.

(18) Ren, D.; Deng, Y.; Handoko, A. D.; Chen, C. S.; Malkhandi, S.; Yeo, B. S. Selective Electrochemical Reduction of Carbon Dioxide to Ethylene and Ethanol on Copper(I) Oxide Catalysts. *ACS Catal.* **2015**, *5*, 2814−2821.

(19) Hori, Y.; Kikuchi, K.; Suzuki, S. Production of CO and CH_4 in Electrochemical Reduction of CO_2 at Metal-Electrodes in Aqueous Hydrogencarbonate Solution. *Chem. Lett.* **1985**, *14*, 1695−1698.

(20) Dufek, E. J.; Lister, T. E.; McIlwain, M. E. Bench-Scale Electrochemical System for Generation of CO and Syn-Gas. *J. Appl. Electrochem.* **2011**, *41*, 623−631.

(21) Hansen, H. A.; Varley, J. B.; Peterson, A. A.; Nørskov, J. K. Understanding Trends in the Electrocatalytic Activity of Metals and Enzymes for CO_2 Reduction to CO. *J. Phys. Chem. Lett.* **2013**, *4*, 388−392.

(22) Verdaguer-Casadevall, A.; Li, C. W.; Johansson, T. P.; Scott, S. B.; McKeown, J. T.; Kumar, M.; Stephens, I. E. L.; Kanan, M. W.; Chorkendorff, I. Probing the Active Surface Sites for CO Reduction on Oxide-Derived Copper Electrocatalysts. *J. Am. Chem. Soc.* **2015**, *137*, 9808−9811.

(23) Mistry, H.; Choi, Y.-W.; Bagger, A.; Scholten, F.; Bonifacio, C. S.; Sinev, I.; Divins, N. J.; Zegkinoglou, I.; Jeon, H. S.; Kisslinger, K.; Stach, E. A.; Yang, J. C.; Rossmeisl, J.; Roldan Cuenya, B. Enhanced Carbon Dioxide Electroreduction to Carbon Monoxide over Defect-Rich Plasma-Activated Silver Catalysts. *Angew. Chem., Int. Ed.* **2017**, *56*, 11394−11398.

(24) Li, J.; He, Y.; Tan, L.; Zhang, P.; Peng, X.; Oruganti, A.; Yang, G.; Abe, H.; Wang, Y.; Tsubaki, N. Integrated tuneable synthesis of liquid fuels via Fischer-Tropsch technology. *Nat. Catal.* **2018**, *1*, 787−793.

(25) Haas, T.; Krause, R.; Weber, R.; Demler, M.; Schmid, G. Technical Photosynthesis Involving CO_2 Electrolysis and Fermentation. *Nat. Catal.* **2018**, *1*, 32−39.

(26) Li, Y.; Cui, F.; Ross, M. B.; Kim, D.; Sun, Y.; Yang, P. Structure-Sensitive CO_2 Electroreduction to Hydrocarbons on Ultrathin 5-fold Twinned Copper Nanowires. *Nano Lett.* **2017**, *17*, 1312−1317.

(27) Gawande, M. B.; Goswami, A.; Felpin, F.-X.; Asefa, T.; Huang, X.; Silva, R.; Zou, X.; Zboril, R.; Varma, R. S. Cu and Cu-Based Nanoparticles: Synthesis and Applications in Catalysis. *Chem. Rev.* **2016**, *116*, 3722−3811.

(28) Aditya, T.; Jana, J.; Singh, N. K.; Pal, A.; Pal, T. Remarkable Facet Selective Reduction of 4-Nitrophenol by Morphologically Tailored (111) Faceted Cu_2O Nanocatalyst. *ACS Omega* **2017**, *2*, 1968−1984.

(29) Xi, Z.; Li, J.; Su, D.; Muzzio, M.; Yu, C.; Li, Q.; Sun, S. Stabilizing CuPd Nanoparticles via CuPd Coupling to $WO_{2.72}$ Nanorods in Electrochemical Oxidation of Formic Acid. *J. Am. Chem. Soc.* **2017**, *139*, 15191−15196.

DOI: 10.1021/acscatal.9b03664
ACS Catal. 2019, 9, 9518−9529

(30) Yin, Z.; Gao, D.; Yao, S.; Zhao, B.; Cai, F.; Lin, L.; Tang, P.; Zhai, P.; Wang, G.; Ma, D.; Bao, X. Highly Selective Palladium-Copper Bimetallic Electrocatalysts for the Electrochemical Reduction of CO_2 to CO. *Nano Energy* **2016**, *27*, 35−43.

(31) Menard, L.; Xu, F.; Nuzzo, R.; Yang, J. Preparation of TiO_2-Supported Au Nanoparticle Catalysts from a Au-13 Cluster Precursor: Ligand Removal Using Ozone Exposure Versus a Rapid Thermal Treatment. *J. Catal.* **2006**, *243*, 64−73.

(32) Gao, D.; Scholten, F.; Roldan Cuenya, B. Improved CO_2 Electroreduction Performance on Plasma-Activated Cu Catalysts via Electrolyte Design: Halide Effect. *ACS Catal.* **2017**, *7*, 5112−5120.

(33) Mistry, H.; Varela, A. S.; Bonifacio, C. S.; Zegkinoglou, I.; Sinev, I.; Choi, Y. W.; Kisslinger, K.; Stach, E. A.; Yang, J. C.; Strasser, P.; Roldan Cuenya, B. Highly Selective Plasma-Activated Copper Catalysts for Carbon Dioxide Reduction to Ethylene. *Nat. Commun.* **2016**, *7*, 12123.

(34) Handoko, A. D.; Ong, C. W.; Huang, Y.; Lee, Z. G.; Lin, L.; Panetti, G. B.; Yeo, B. S. Mechanistic Insights into the Selective Electroreduction of Carbon Dioxide to Ethylene on Cu_2O-Derived Copper Catalysts. *J. Phys. Chem. C* **2016**, *120*, 20058−20067.

(35) Le, M.; Ren, M.; Zhang, Z.; Sprunger, P. T.; Kurtz, R. L.; Flake, J. C. Electrochemical Reduction of CO_2 to CH_3OH at Copper Oxide Surfaces. *J. Electrochem. Soc.* **2011**, *158*, E45−E49.

(36) Wang, B.; Wang, Y.; Li, J.; Guo, X.; Bai, G.; Tong, X.; Jin, G.; Guo, X. Photocatalytic Sonogashira reaction over silicon carbide supported Pd-Cu alloy nanoparticles under visible light irradiation. *Catal. Sci. Technol.* **2018**, *8*, 3357−3362.

(37) McMahon, R. A.; Smith, M. P.; Seffen, K. A.; Voelskow, M.; Anwand, W.; Skorupa, W. Flash-lamp annealing of semiconductor materials-Applications and process models. *Vacuum* **2007**, *81*, 1301−1305.

(38) Qin, G.; Watanabe, A.; Tsukamoto, H.; Yonezawa, T. Copper Film Prepared from Copper Fine Particle Paste by Laser Sintering at Room Temperature: Influences of Sintering Atmosphere on the Morphology and Resistivity. *Jpn. J. Appl. Phys.* **2014**, *53*, 096501.

(39) Lim, H. S.; Kim, S. J.; Jang, H. W.; Lim, J. A. Intense Pulsed Light for Split-Second Structural Development of Nanomaterials. *J. Mater. Chem. C* **2017**, *5*, 7142−7160.

(40) Troughton, J.; Carnie, M. J.; Davies, M. L.; Charbonneau, C.; Jewell, E. H.; Worsley, D. A.; Watson, T. M. Photonic Flash-Annealing of Lead Halide Perovskite Solar Cells in 1 ms. *J. Mater. Chem. A* **2016**, *4*, 3471−3476.

(41) Hori, Y.; Takahashi, I.; Koga, O.; Hoshi, N. Electrochemical Reduction of Carbon Dioxide at Various Series of Copper Single Crystal Electrodes. *J. Mol. Catal. A: Chem.* **2003**, *199*, 39−47.

(42) Montoya, J. H.; Shi, C.; Chan, K.; Nørskov, J. K. Theoretical Insights into a CO Dimerization Mechanism in CO_2 Electroreduction. *J. Phys. Chem. Lett.* **2015**, *6*, 2032−2037.

(43) Takahashi, I.; Koga, O.; Hoshi, N.; Hori, Y. Electrochemical reduction of CO_2 at copper single crystal Cu(S)-[n(111)×(111)] and Cu(S)-[n(110)×(100)] electrodes. *J. Electroanal. Chem.* **2002**, *533*, 135−143.

(44) Mourdikoudis, S.; Liz-Marzán, L. M. Oleylamine in Nanoparticle Synthesis. *Chem. Mater.* **2013**, *25*, 1465−1476.

(45) Yang, H.-J.; He, S.-Y.; Tuan, H.-Y. Self-Seeded Growth of Five-Fold Twinned Copper Nanowires: Mechanistic Study, Characterization, and SERS Applications. *Langmuir* **2014**, *30*, 602−610.

(46) Guo, H.; Chen, Y.; Ping, H.; Jin, J.; Peng, D.-L. Facile Synthesis of Cu and Cu@Cu-Ni Nanocubes and Nanowires in Hydrophobic Solution in the Presence of Nickel and Chloride Ions. *Nanoscale* **2013**, *5*, 2394−2402.

(47) da Silva, R. R.; Yang, M.; Choi, S.-I.; Chi, M.; Luo, M.; Zhang, C.; Li, Z.-Y.; Camargo, P. H. C.; Ribeiro, S. J. L.; Xia, Y. Facile Synthesis of Sub-20 nm Silver Nanowires through a Bromide-Mediated Polyol Method. *ACS Nano* **2016**, *10*, 7892−7900.

(48) Guo, H.; Chen, Y.; Cortie, M. B.; Liu, X.; Xie, Q.; Wang, X.; Peng, D. L. Shape-Selective Formation of Monodisperse Copper Nanospheres and Nanocubes via Disproportionation Reaction Route and Their Optical Properties. *J. Phys. Chem. C* **2014**, *118*, 9801−9808.

(49) Guo, H.; Büchel, M.; Li, X.; Wäckerlin, A.; Chen, Q.; Burgert, I. Dictating Anisotropic Electric Conductivity of a Transparent Copper Nanowire Coating by the Surface Structure of Wood. *J. R. Soc. Interface* **2018**, *15*, 20170864.

(50) Jin, M.; He, G.; Zhang, H.; Zeng, J.; Xie, Z.; Xia, Y. Shape-Controlled Synthesis of Copper Nanocrystals in an Aqueous Solution with Glucose as a Reducing Agent and Hexadecylamine as a Capping Agent. *Angew. Chem., Int. Ed.* **2011**, *50*, 10560−10564.

(51) Kim, M. J.; Alvarez, S.; Chen, Z.; Fichthorn, K. A.; Wiley, B. J. Single-Crystal Electrochemistry Reveals Why Metal Nanowires Grow. *J. Am. Chem. Soc.* **2018**, *140*, 14740−14746.

(52) Broekmann, P.; Wilms, M.; Kruft, M.; Stuhlmann, C.; Wandelt, K. In-situ STM Investigation of Specific Anion Adsorption on Cu(111). *J. Electroanal. Chem.* **1999**, *467*, 307−324.

(53) Polewska, W.; Behm, R. J.; Magnussen, O. M. In-Situ Video-STM Studies of Cu Electrodeposition on Cu(100) in HCl Solution. *Electrochim. Acta* **2003**, *48*, 2915−2921.

(54) Magnussen, O. M. Ordered Anion Adlayers on Metal Electrode Surfaces. *Chem. Rev.* **2002**, *102*, 679−726.

(55) Huemann, S.; Minh Hai, N. T.; Broekmann, P.; Wandelt, K.; Zajonz, H.; Dosch, H.; Renner, F. X-ray Diffraction and STM Study of Reactive Surfaces under Electrochemical Control: Cl and I on Cu(100). *J. Phys. Chem. B* **2006**, *110*, 24955−24963.

(56) Huynh, T. M. T.; Hai, N. T. M.; Broekmann, P. Quasi-Reversible Interaction of MPS and Chloride on Cu(100) Studied by In Situ STM. *J. Electrochem. Soc.* **2013**, *160*, D3063−D3069.

(57) Wilms, M.; Broekmann, P.; Kruft, M.; Stuhlmann, C.; Wandelt, K. STM Investigation of Step orientation and Surface Dynamics of Cu(111) in Hydrochloric Acid Electrolyte. *Appl. Phys. A* **1998**, *66*, S473−S475.

(58) Wilms, M.; Broekmann, P.; Kruft, M.; Park, Z.; Stuhlmann, C.; Wandelt, K. STM Investigation of Specific Anion Adsorption on Cu(111) in Sulfuric Acid Electrolyte. *Surf. Sci.* **1998**, *402-404*, 83−86.

(59) Schouten, K. J. P.; Kwon, Y.; van der Ham, C. J. M.; Qin, Z.; Koper, M. T. M. A New Mechanism for the Selectivity to C1 and C2 Species in the Electrochemical Reduction of Carbon Dioxide on Copper Electrodes. *Chem. Sci.* **2011**, *2*, 1902−1909.

(60) Calle-Vallejo, F.; Koper, M. T. M. Theoretical Considerations on the Electroreduction of CO to C2 Species on Cu(100) Electrodes. *Angew. Chem., Int. Ed.* **2013**, *52*, 7282−7285.

(61) Hori, Y.; Takahashi, I.; Koga, O.; Hoshi, N. Selective Formation of C2 Compounds from Electrochemical Reduction of CO_2 at a Series of Copper Single Crystal Electrodes. *J. Phys. Chem. B* **2002**, *106*, 15−17.

(62) Baturina, O. A.; Lu, Q.; Padilla, M. A.; Xin, L.; Li, W.; Serov, A.; Artyushkova, K.; Atanassov, P.; Xu, F.; Epshteyn, A.; Brintlinger, T.; Schuette, M.; Collins, G. E. CO_2 Electroreduction to Hydrocarbons on Carbon-Supported Cu Nanoparticles. *ACS Catal.* **2014**, *4*, 3682−3695.

(63) Lee, S. Y.; Jung, H.; Kim, N.-K.; Oh, H.-S.; Min, B. K.; Hwang, Y. J. Mixed Copper States in Anodized Cu Electrocatalyst for Stable and Selective Ethylene Production from CO_2 Reduction. *J. Am. Chem. Soc.* **2018**, *140*, 8681−8689.

(64) Frese, K. W. Electrochemical Reduction of CO_2 at Intentionally Oxidized Copper Electrodes. *J. Electrochem. Soc.* **1991**, *138*, 3338−3344.

(65) Li, C. W.; Kanan, M. W. CO_2 Reduction at Low Overpotential on Cu Electrodes Resulting from the Reduction of Thick Cu_2O Films. *J. Am. Chem. Soc.* **2012**, *134*, 7231−7234.

(66) Grosse, P.; Gao, D.; Scholten, F.; Sinev, I.; Mistry, H.; Roldan Cuenya, B. Dynamic Changes in the Structure, Chemical State and Catalytic Selectivity of Cu Nanocubes during CO_2 Electroreduction: Size and Support Effects. *Angew. Chem., Int. Ed.* **2018**, *57*, 6192−6197.

(67) Hori, Y.; Murata, A.; Takahashi, R. Formation of Hydrocarbons in the Electrochemical Reduction of Carbon dioxide at a Copper Electrode in Aqueous Solution. *J. Chem. Soc., Faraday Trans. 1* **1989**, *85*, 2309−2326.

(68) Akhade, S. A.; Luo, W.; Nie, X.; Bernstein, N. J.; Asthagiri, A.; Janik, M. J. Poisoning Effect of Adsorbed CO during CO_2

Electroreduction on Late Transition Metals. *Phys. Chem. Chem. Phys.* **2014**, *16*, 20429−20435.

(69) DeWulf, D. W.; Jin, T.; Bard, A. J. Electrochemical and Surface Studies of Carbon Dioxide Reduction to Methane and Ethylene at Copper Electrodes in Aqueous Solutions. *J. Electrochem. Soc.* **1989**, *136*, 1686−1691.

(70) Nie, X.; Esopi, M. R.; Janik, M. J.; Asthagiri, A. Selectivity of CO_2 Reduction on Copper Electrodes: The Role of the Kinetics of Elementary Steps. *Angew. Chem., Int. Ed.* **2013**, *52*, 2459−2462.

8. Appendix

8.1. List of Publications

1. **Zelocualtecatl Montiel, I.**; Dutta, A.; Kiran, K.; Rieder, A.; Iarchuk A.; Vesztergom, S.; Mirolo, M.; Martens, I.; Drnec, Jakub.; Broekmann, P., CO_2 Conversion at High Current Densities: Stabilization of Bi(III)-Containing Electrocatalysts under CO_2 Gas Flow Conditions. *ACS Catal*. **2022**, *12*, 17, 10872–10886.

2. Dutta, A.; **Zelocualtecatl Montiel, I.**; Kiran, K.; Rieder, A.; Grozovski, V.; Gut, L.; Broekmann, P., A Tandem (Bi_2O_3 → Bimet) Catalyst for Highly Efficient ec-CO_2 Conversion into Formate: Operando Raman Spectroscopic Evidence for a Reaction Pathway Change. *ACS Catalysis* **2021**, *11* (9), 4988-5003.

3. Dutta, A.; **Montiel, I. Z**.; Erni, R.; Kiran, K.; Rahaman, M.; Drnec, J.; Broekmann, P., Activation of bimetallic AgCu foam electrocatalysts for ethanol formation from CO_2 by selective Cu oxidation/reduction. *Nano Energy* **2020**, *68*, 104331.

4. Hu, H.; Liu, M.; Kong, Y.; **Montiel, I. Z.**; Hou, Y.; Rudnev, A. V.; Broekmann, P., Size-dependent Structural Alterations in Ag Nanoparticles During CO_2 Electrolysis in a Gas-fed Zero-gap Electrolyzer. ChemElectroChem n/a (n/a).

5. Kong, Y.; Liu, M.; Hu, H.; Hou, Y.; Vesztergom, S.; Gálvez-Vázquez, M. d. J.; **Zelocualtecatl Montiel, I**.; Kolivoška, V.; Broekmann, P., Cracks as Efficient Tools to Mitigate Flooding in Gas Diffusion Electrodes Used for the Electrochemical Reduction of Carbon Dioxide. Small Methods n/a (n/a), 2200369.

6. Liu, M.; Kong, Y.; Hu, H.; Kovács, N.; Sun, C.; **Zelocualtecatl Montiel, I**.; Gálvez Vázquez, M. d. J.; Hou, Y.; Mirolo, M.; Martens, I.; Drnec, J.; Vesztergom, S.; Broekmann, P., The capping agent is the key: Structural alterations of Ag NPs during CO_2 electrolysis probed in a zero-gap gas-flow configuration. *Journal of Catalysis* **2021**, *404*, 371-382.

7. Dutta, A.; Kiran, K.; Rahaman, M.; **Montiel, I. Z.**; Moreno-García, P.; Vesztergom, S.; Drnec, J.; Oezaslan, M.; Broekmann, P., Insights from Operando and Identical Location (IL) Techniques on the Activation of Electrocatalysts for the Conversion of CO_2: A Mini-Review. *CHIMIA International Journal for Chemistry* **2021**, *75* (9), 733-743.

8. Rahaman, M.; Kiran, K.; **Zelocualtecatl Montiel, I**.; Dutta, A.; Broekmann, P., Suppression of the Hydrogen Evolution Reaction Is the Key: Selective Electrosynthesis of Formate from CO_2 over Porous $In_{55}Cu_{45}$ Catalysts. *ACS Applied Materials & Interfaces* **2021**, *13* (30), 35677-35688.

9. Vesztergom, S.; Dutta, A.; Rahaman, M.; Kiran, K.; **Zelocualtecatl Montiel, I**.; Broekmann, P., Hydrogen Bubble Templated Metal Foams as Efficient Catalysts of CO2 Electroreduction. *ChemCatChem* **2021**, *13* (4), 1039-1058.

10. de Jesus Gálvez-Vázquez, M.; Moreno-García, P.; Xu, H.; Hou, Y.; Hu, H.; **Montiel, I. Z.**; Rudnev, A. V.; Alinejad, S.; Grozovski, V.; Wiley, B. J.; Arenz, M.; Broekmann, P., Environment Matters: CO_2RR Electrocatalyst Performance Testing in a Gas-Fed Zero-Gap Electrolyzer. *ACS Catalysis* **2020**, *10* (21), 13096-13108.

11. Dutta, A.; Rahaman, M.; Hecker, B.; Drnec, J.; Kiran, K.; **Zelocualtecatl Montiel, I.**; Jochen Weber, D.; Zanetti, A.; Cedeño López, A.; Martens, I.; Broekmann, P.; Oezaslan, M., CO_2 Electrolysis-Complementary operando XRD, XAS and Raman spectroscopy study on the stability of Cu_xO foam catalysts. *Journal of Catalysis* **2020**, *389*, 592-603.

12. Rahaman, M.; Kiran, K.; **Montiel, I. Z**.; Grozovski, V.; Dutta, A.; Broekmann, P., Selective n-propanol formation from CO_2 over degradation-resistant activated PdCu alloy foam electrocatalysts. *Green Chemistry* **2020**, *22* (19), 6497-6509.

13. Hou, Y.; Bolat, S.; Bornet, A.; Romanyuk, Y. E.; Guo, H.; Moreno-García, P.; **Zelocualtecatl Montiel, I**.; Lai, Z.; Müller, U.; Grozovski, V.; Broekmann, P., Photonic Curing: Activation and Stabilization of Metal Membrane Catalysts (MMCs) for the Electrochemical Reduction of CO_2. *ACS Catalysis* **2019**, *9* (10), 9518-9529.

8.2. Conferences and Presentations

- *“Bimetallic CuAg nano foam catalyst: Towards electrochemical CO_2 conversion into selecetive Ethanol”* (Poster presentation). In the International Summer School on Power to X: Fundamentals and Applications of Modern Electro synthesis. Villars-sur-Ollon, CH. (August 27 - 31, 2018).
- *“Confined insertion of Sn^{x+} ions into Nafion-supported cathodes for efficient electrochemical reduction of CO_2 to formate”* (Poster presentation). In the Annual meeting of the SCCER (Swiss Competence Center for Energy Research) Heat and Electricity Storage. At the Hochschule für Technik in Rapperswil, CH. (November 2018).
- “*Activation of Bimetallic AgCu Foam Electrocatalysts for Ethanol formation from CO_2 by Selective Cu Oxidation/Reduction”* (Poster presentation). In the 8th Symposium of the SCCER (Swiss Competence Center for Energy Research) Heat and Electricity Storage. Empa Dübendorf, CH. (November 2019).
- Participation in the Analysis of *In-situ* and *Ex-situ* Bi_2O_3@GDE electrodes for CO_2 electroreduction in the *“Soleil Beamtime, Proposal 20191897”*. SOLEIL Synchrotron. L’Orme des Merisieres, Saint-Aubin BP 48, France. (October 2021)
- “*CO_2 Conversion at High Current Densities: Stabilization of Bi(III) Containing Electrocatalysts in a Flow Cell Electrolyzer*” (Poster presentation) in the National Centres of Competence in Research (NCCR) Catalysis Annual Event 2022 Symposium. ETH Zurich, Campus Hönggerberg, CH. (June 2022).
- “*CO_2 electro-reduction on porous Bi_2O_3 in a Fluidic Flow cell Electrolyzer*” (Poster presentation) in the 15th International Fischer Symposium a meeting on nanoscale electrochemistry. Kloster Seeon, Germany. (June 2022).

8.3. Acknowledgments

In life, we do not meet anyone by coincidence. It is destiny that brings us together with incredible people. I would like to thank Prof. Dr. Peter Broekmann so much for giving me the fantastic opportunity to work in his research group and for trusting me to work on this project without knowing me first. I really appreciate all the support and understanding you provided me during these four years. You are a great human being, and I will always be grateful to you. Thank you so much.

A very special thanks to Prof. Dr. Siegfried R. Waldvogel (University of Mainz) and Prof. Dr. Andreas Türler for their kindness in agreeing to be the reviewers of my thesis and above all for taking the time to read my work.

I would also like to thank Dr. Abhijit Dutta, who helped me a lot during my PhD studies. Thank you for the things I learnt from you, the good advice, and the nice scientific and non-scientific talks we had.

A very special thanks to Dr. Pavel Moreno Garcia, who helped me to get this great work opportunity in Bern and because of his very nice and funny stories. Thank you so much.

To all my friends in the lab, Aline, Kiran, Alain, Renan, Sasha, Valentine, and specially to all my Chinese friends, Ying Kong, Huifang, Menglong, Yühui, Yuzhen, and Changze, I'd like to say thank you so much for your friendship, all the support and motivation on this path, and the great moments we spent together. Most importantly, thank you so much for making me laugh every single day in the lab. I will miss you guys, but I am thrilled to have met all of you.

Thank you so much to Beatrice Frey for all her support and patient of analysing my thousands of SEM samples.

To Nicola, Mike, Sven, Lorine, and Denis, thank you for being a such a nice guys and for helping not only me, but all of us who work in the laboratory.

Mary (amiwi) thank you so much not only for being my friend but also my family. Thank you for helping me through this process. I will always be grateful to you for always pointed me in the right direction. And Lili thank you for sharing with me a very charming moments. Las quiero mucho.☺

Vitali, I do not have enough words to thank you for what a good person you were with me. Thank you so much for your friendship and, above all, for giving me the opportunity to meet your family. Cheers.

Craig, thank you for the adventures by your side and for being like a brother to me (and accomplice). You are a great friend. Te quiero mucho.

Sometimes we are scared to try something new, to go out of our comfort zone. Thankfully, there is always someone who pushes you to make something that can change your life for the better. That is why I would like to say a very special thanks to Rocío Aguilar Sánchez for all her support and for motivating me to study abroad. Thank you very much not only for being a good boss but also a true friend.

Mariel thank you very much for your friendship and for be there when I need you. Te quiero mucho, and I miss you.

Most importantly, thank you, God, for the beautiful family that you gave me. I cannot imagine how my life would be without them. Mami and Papi, thank you so much for all support that I have received from you throughout my entire life. I will be eternally grateful. I know that, despite living so far away, I can always count on you. Thank you to my siblings, Beto and Matilde, Lala and Isaac, Lupis and Valentin, Tele and Bety, and Fer and Sandy, for believing in me, for the time that we spent together, and for the amazing nephews and nieces that I have: Alan and Mariela, Johan, Brays, Kike, Jimena, Emily, Matias, David, Martin, Mateo, Estefany, and Angel. I miss you, but you are always in my mind and heart. I love you so much.

Last but not least, thank you to everyone who is reading this.

8.4. Declaration of Consent

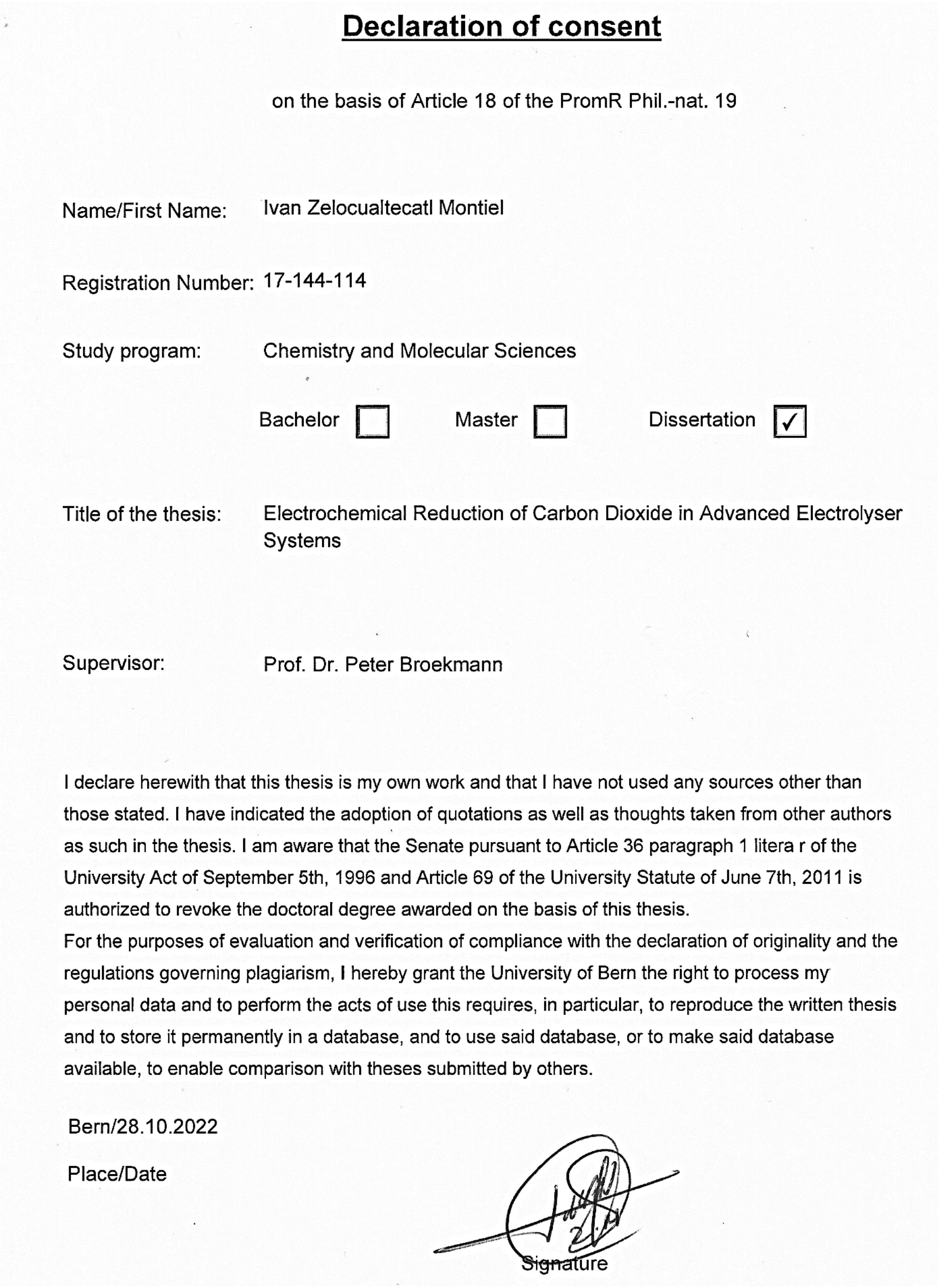

Declaration of consent

on the basis of Article 18 of the PromR Phil.-nat. 19

Name/First Name:	Ivan Zelocualtecatl Montiel
Registration Number:	17-144-114
Study program:	Chemistry and Molecular Sciences
	Bachelor ☐ Master ☐ Dissertation ☑
Title of the thesis:	Electrochemical Reduction of Carbon Dioxide in Advanced Electrolyser Systems
Supervisor:	Prof. Dr. Peter Broekmann

I declare herewith that this thesis is my own work and that I have not used any sources other than those stated. I have indicated the adoption of quotations as well as thoughts taken from other authors as such in the thesis. I am aware that the Senate pursuant to Article 36 paragraph 1 litera r of the University Act of September 5th, 1996 and Article 69 of the University Statute of June 7th, 2011 is authorized to revoke the doctoral degree awarded on the basis of this thesis.

For the purposes of evaluation and verification of compliance with the declaration of originality and the regulations governing plagiarism, I hereby grant the University of Bern the right to process my personal data and to perform the acts of use this requires, in particular, to reproduce the written thesis and to store it permanently in a database, and to use said database, or to make said database available, to enable comparison with theses submitted by others.

Bern/28.10.2022

Place/Date

Signature